NOVEMBER 2021

AJNR

VOLUME 42 • PP 1919–2107

AJNR

AMERICAN JOURNAL OF NEURORADIOLOGY

NOVEMBER 2021
VOLUME 42
NUMBER 11
WWW.AJNR.ORG

THE JOURNAL OF DIAGNOSTIC AND INTERVENTIONAL NEURORADIOLOGY

Machine learning in multiple sclerosis
Susceptibility vessel sign in patients undergoing mechanical thrombectomy
Thrombectomy model based on ex vivo whole human brains
MRI findings in patients with IIH after venous sinus stenting

Official Journal ASNR • ASFNR • ASHNR • ASPNR • ASSR

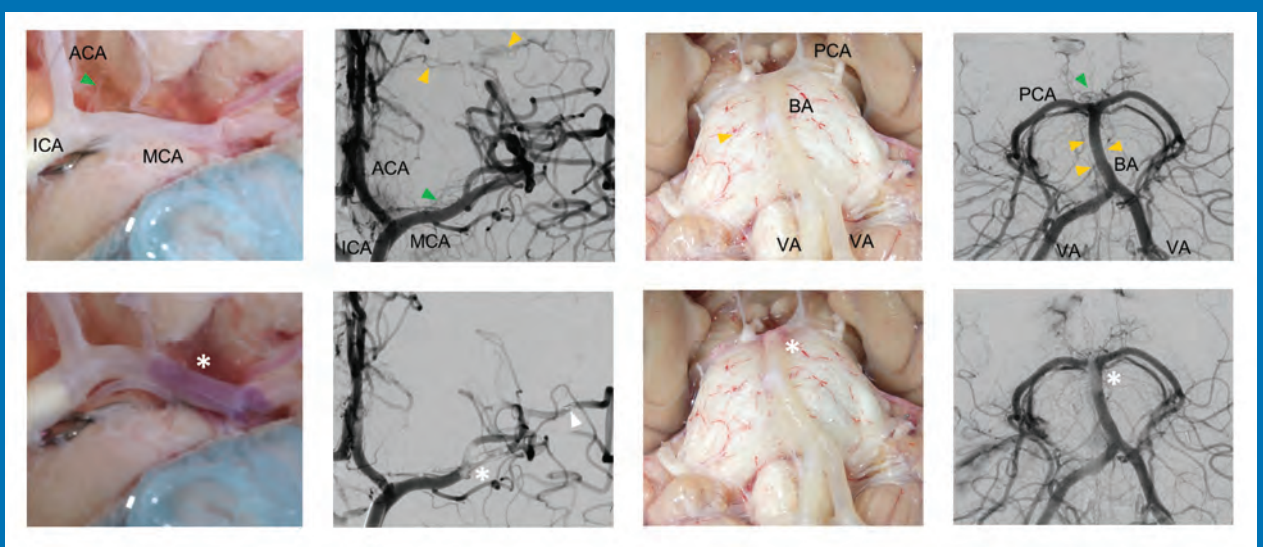

FRED™

Flow **R**e-**D**irection
Endoluminal **D**evice

FLOW DIVERSION.

SIMPLIFIED.

MicroVention™
TERUMO

MicroVention Worldwide Innovation Center
35 Enterprise
Aliso Viejo, CA 92656 USA
PH +1 714.247.8000

MicroVention UK Limted
PH +1 44 (0) 191 258 6777

MicroVention Europe S.A.R.L.
PH +33 (1) 39 21 77 46

MicroVention Deutschland GmbH
PH +49 211 210 798-0

Web
microvention.com

The New Standard of **Ease and Simplicity** in Flow Diversion Treatment.

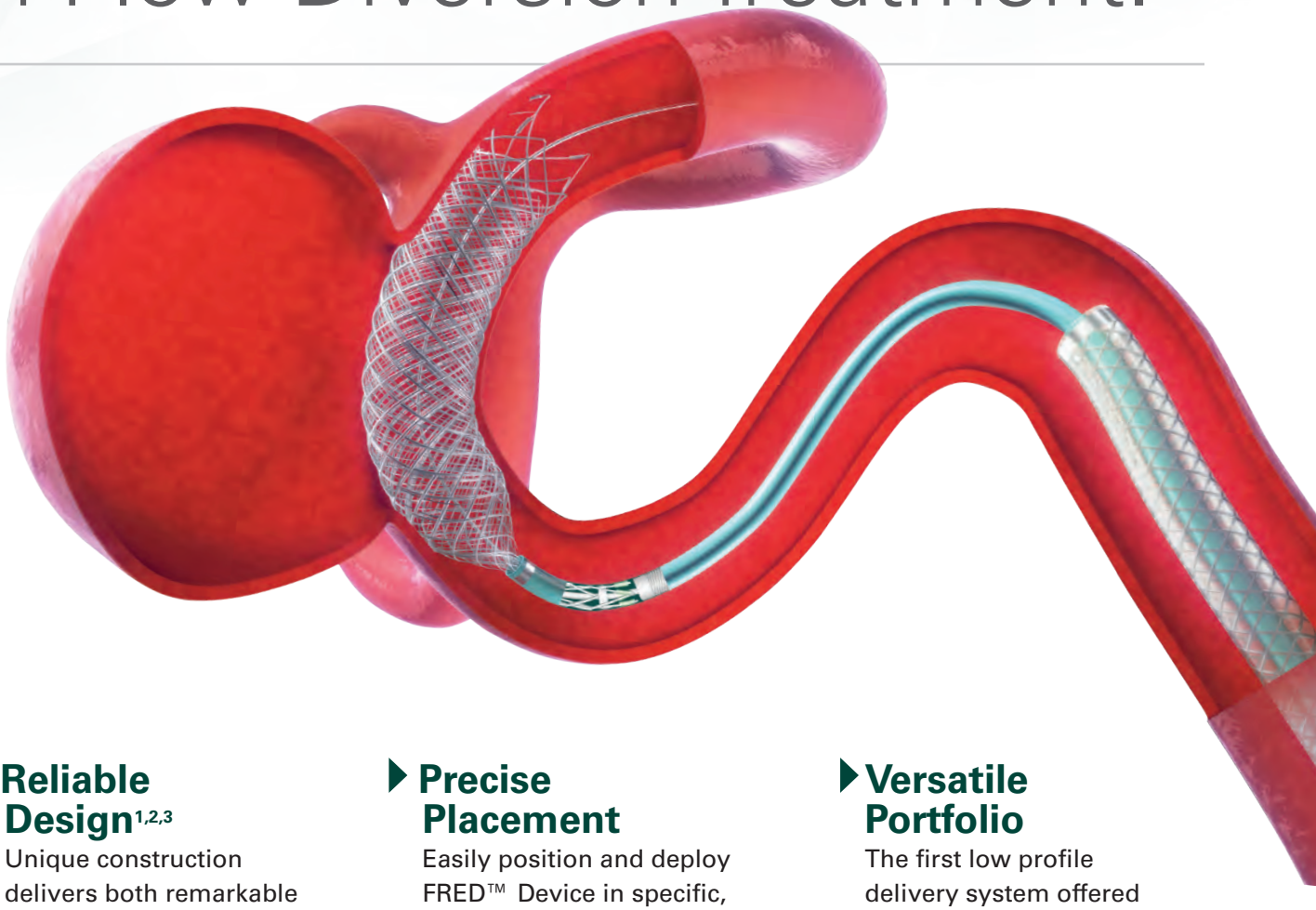

Reliable Design[1,2,3]

Unique construction delivers both remarkable ease of use and excellent flow diversion[1,2,3]

Precise Placement

Easily position and deploy FRED™ Device in specific, targeted locations[4,5,6]

Versatile Portfolio

The first low profile delivery system offered in combination with large diameter and long length options

References:
1. TR11-211 2. TR13-171 3. TR15-055 4. TR13-192 5. TR15-072 6. TR19-145

The Flow Re-Direction Endoluminal Device (FRED™) System is indicated for use in the internal carotid artery from the petrous segment to the terminus for the endovascular treatment of adult patients (22 years of age or older) with wide-necked (neck width ≥ 4 mm or dome-to-neck ratio < 2) saccular or fusiform intracranial aneurysms arising from a parent vessel with a diameter ≥ 2.0 mm and ≤ 5.0 mm.

Use of the FRED™ System is contraindicated under these circumstances: Patients in whom anticoagulant, anti-platelet therapy, or thrombolytic drugs are contraindicated. Patients with known hypersensitivity to metal such as nickel-titanium and metal jewelry. Patients with anatomy that does not permit passage or deployment of the FRED™ System. Patients with an active bacterial infection. Patients with a pre-existing stent in place at the target aneurysm. Patients in whom the parent vessel size does not fall within the indicated range. Patients who have not received dual anti-platelet agents prior to the procedure. For complete indications, contraindications, potential complications, warnings, precautions, and instructions, see instructions for use (IFU provided in the device).

RX Only: Federal (United States) law restricts this device to sale by or on the order of a physician.

Dotarem®
(gadoterate meglumine) Injection

Guerbet

A Stable MRI Contrast Solution Approved for Children

The safety and efficacy of Dotarem have been established in pediatric patients from birth (term neonates ≥ 37 weeks gestational age) to 17 years of age.[1-3]

- **Available in a wide variety of dosing options, including 5mL vials**
- In a pediatric study of 1,568 patients, image quality was rated either good or very good by radiologists in 98.4% of cases when using Dotarem[4]
- The first imaging contrast with a macrocyclic and ionic structure for high thermodynamic and kinetic stability[1,2]
- Following repeated administration, no visible T1 signal intensity detected on non-contrast images within the brain[6-10]

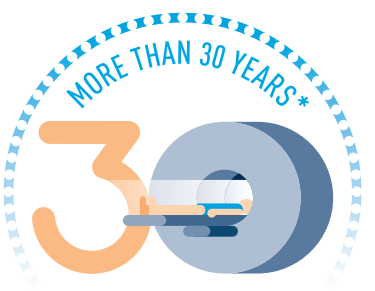

Dotarem®
(gadoterate meglumine) Injection

1-877-729-6679 | Dotarem-us.com

DOTAREM (GADOTERATE MEGLUMINE) INJECTION IMPORTANT SAFETY INFORMATION

WARNING: NEPHROGENIC SYSTEMIC FIBROSIS (NSF)

Gadolinium-based contrast agents (GBCAs) increase the risk for NSF among patients with impaired elimination of the drugs. Avoid use of GBCAs in these patients unless the diagnostic information is essential and not available with non-contrasted MRI or other modalities. NSF may result in fatal or debilitating fibrosis affecting the skin, muscle and internal organs.

- The risk for NSF appears highest among patients with:
  - Chronic, severe kidney disease (GFR < 30 mL/min/1.73m2), or
  - Acute kidney injury.
- Screen patients for acute kidney injury and other conditions that may reduce renal function. For patients at risk for chronically reduced renal function (e.g. age > 60 years, hypertension, diabetes), estimate the glomerular filtration rate (GFR) through laboratory testing.
- For patients at highest risk for NSF, do not exceed the recommended DOTAREM dose and allow a sufficient period of time for elimination of the drug from the body prior to any re-administration.

INDICATIONS AND USAGE

DOTAREM® (gadoterate meglumine) injection is a prescription gadolinium-based contrast agent indicated for intravenous use with magnetic resonance imaging (MRI) in brain (intracranial), spine and associated tissues in adult and pediatric patients (including term neonates) to detect and visualize areas with disruption of the blood brain barrier (BBB) and/or abnormal vascularity.

CONTRAINDICATIONS

History of clinically important hypersensitivity reactions to DOTAREM.

WARNINGS AND PRECAUTIONS

- Hypersensitivity Reactions: Anaphylactic and anaphylactoid reactions have been reported with DOTAREM, involving cardiovascular, respiratory, and/or cutaneous manifestations. Some patients experienced circulatory collapse and died. In most cases, initial symptoms occurred within minutes of DOTAREM administration and resolved with prompt emergency treatment.
- Before DOTAREM administration, assess all patients for any history of a reaction to contrast media, bronchial asthma and/or allergic disorders. These patients may have an increased risk for a hypersensitivity reaction to DOTAREM.
- Administer DOTAREM only in situations where trained personnel and therapies are promptly available for the treatment of hypersensitivity reactions, including personnel trained in resuscitation.
- Gadolinium Retention: Gadolinium is retained for months or years in several organs. The highest concentrations have been identified in the bone, followed by brain, skin, kidney, liver and spleen. The duration of retention also varies by tissue, and is longest in bone. Linear GBCAs cause more retention than macrocyclic GBCAs.
- Consequences of gadolinium retention in the brain have not been established. Adverse events involving multiple organ systems have been reported in patients with normal renal function without an established causal link to gadolinium retention.
- Acute Kidney Injury: In patients with chronically reduced renal function, acute kidney injury requiring dialysis has occurred with the use of GBCAs. The risk of acute kidney injury may increase with increasing dose of the contrast agent; administer the lowest dose necessary for adequate imaging.
- Extravasation and Injection Site Reactions: Ensure catheter and venous patency before the injection of DOTAREM. Extravasation into tissues during DOTAREM administration may result in tissue irritation.

ADVERSE REACTIONS

- The most common adverse reactions associated with DOTAREM in clinical trials were nausea, headache, injection site pain, injection site coldness and rash.
- Serious adverse reactions in the Postmarketing experience have been reported with DOTAREM. These serious adverse reactions include but are not limited to: arrhythmia, cardiac arrest, respiratory arrest, pharyngeal edema, laryngospasm," bronchospasm, coma and convulsion.

USE IN SPECIFIC POPULATIONS

- **Pregnancy:** GBCAs cross the human placenta and result in fetal exposure and gadolinium retention. Use only if imaging is essential during pregnancy and cannot be delayed.
- **Lactation:** There are no data on the presence of gadoterate in human milk, the effects on the breastfed infant, or the effects on milk production. However, published lactation data on other GBCAs indicate that 0.01 to 0.04% of the maternal gadolinium dose is present in breast milk.
- **Pediatric Use:** The safety and efficacy of DOTAREM at a single dose of 0.1 mmol/kg has been established in pediatric patients from birth (term neonates ≥ 37 weeks gestational age) to 17 years of age based on clinical data. The safety of DOTAREM has not been established in preterm neonates. No cases of NSF associated with DOTAREM or any other GBCA have been identified in pediatric patients age 6 years and younger.

You are encouraged to report negative side effects of prescription drugs to the FDA. Visit www.fda.gov/medwatch or call 1-800-FDA-1088.

Please see the full Prescribing Information, including Boxed Warning and the patient Medication Guide, for additional important safety information.

References: 1. Port M et al. Efficiency, thermodynamic and kinetic stability of marketed gadolinium chelates and their possible clinical consequences: a critical review. Biometals. 2008;21:469-90. **2.** Frenzel T et al. Stability of gadolinium-based magnetic resonance imaging contrast agents in human serum at 37°C. Invest Radiol. 2008;43:817-828. **3.** Dotarem [package insert]. Princeton, NJ: Guerbet LLC; Oct 2019. **4.** De-Hua, Chang, and Pracros Jean-Pierre. "Safety of Gadoterate Meglumine in over 1600 Children Included in the Prospective Observational SECURE Study." Acta Radiologica, 2019. **5.** Mithal LB, Patel PS, Mithal D, Palac HL, Rozenfeld MN. Use of gadolinium-based magnetic resonance imaging contrast agents and awareness of brain gadolinium deposition among pediatric providers in North America. Pediatr Radiol. 2017 Mar10.doi: 10.1007/s00247-017-3810-4. [Epub ahead of print] **6.** Radbruch A et al. Gadolinium retention in the dentate nucleus and globus pallidus is dependent on the class of contrast agent. Radiology. 2015 Jun;275(3):783-91. **7.** Radbruch A et al. Intraindividual analysis of signal intensity changes in the dentate nucleus after consecutive serial applications of linear and macrocyclic gadolinium-based contrast agents. Invest Radiol. 2016 Nov;51(11):683- 690. **8.** Eisele P et al. Lack of increased signal intensity in the dentate nucleus after repeated administration of a macrocyclic contrast agent in multiple sclerosis: An observational study. Medicine (Baltimore). 2016 Sep;95(39):e4624. **9.** Radbruch A et al. Pediatric brain: no increased signal intensity in the dentate nucleus on unenhanced T1-weighted MR images after consecutive exposure to a macrocyclic gadolinium-based contrast agent. Radiology. 2017 Mar 8:162980. [Epub ahead of print]. **10.** Tibussek D et al. Gadolinium Brain Deposition after Macrocyclic Gadolinium Administration: A Pediatric Case-Control Study. Radiology. 2017 161151 [Epub ahead of print].

*Dotarem was launched globally in 1989 and approved by the FDA for use in the US in 2013

Explore the New ASNR Career Center

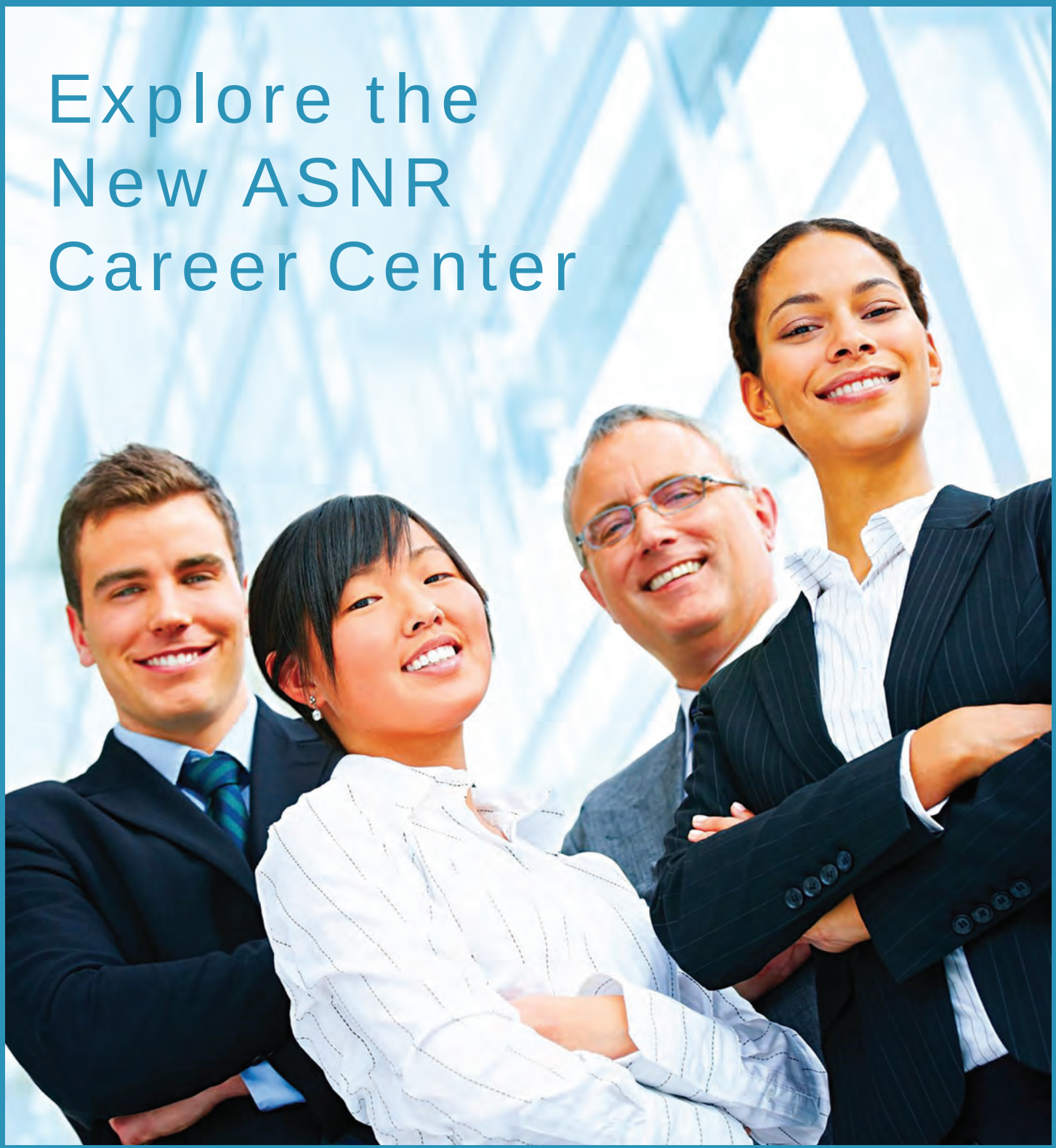

Your Premier Resource for Professional Development

- Access to jobs in the National Healthcare Career Network
- Confidential resume posting
- One-time free resume review
- Professional online profile
- Saved jobs capability

Start here: careers.asnr.org

ASNR
American Society of Neuroradiology

AJNR
AMERICAN JOURNAL OF NEURORADIOLOGY

CALL FOR AJNR EDITORIAL FELLOWSHIP CANDIDATES

2022 Candidate Information and Requirements

ASNR and AJNR are pleased once again to join efforts with other imaging-related journals that have training programs on editorial aspects of publishing for trainees or junior staff (<5 years on staff), including Radiology (Olmsted fellowship), AJR (Figley and Rogers fellowships), JACR (Bruce J. Hillman fellowship), and Radiologia.

GOALS

- Increase interest in editorial and publication-related activities in younger individuals.
- Increase understanding and participation in the AJNR review process.
- Incorporate into AJNR's Editorial Board younger individuals who have previous experience in the review and publication process.
- Fill a specific need in neuroradiology not offered by other similar fellowships.
- Increase the relationship between "new" generation of neuroradiologists and more established individuals.
- Increase visibility of AJNR among younger neuroradiologists.

ACTIVITIES OF THE FELLOWSHIP

- Serve as Editorial Fellow for one year. This individual will be listed on the masthead as such.
- Review at least one manuscript per month for 12 months. Evaluate all review articles submitted to AJNR.
- Learn how electronic manuscript review systems work.
- Be involved in the final decision of selected manuscripts together with the Editor-in-Chief.
- Participate in all monthly Senior Editor telephone conference calls.
- Participate in all meetings of the Editors during the annual meetings of ASNR and RSNA and the Radiology Editors Forum as per candidate's availability. The Foundation of the ASNR will provide $2000 funding for this activity.
- Evaluate progress and adjust program to specific needs in annual meeting or telephone conference with the Editor-in-Chief.
- Embark on an editorial scientific or bibliometric project that will lead to the submission of an article to AJNR or another appropriate journal as determined by the Editor-in-Chief. This project will be presented by the Editorial Fellow at the ASNR annual meeting.
- Recruit trainees as reviewers as determined by the Editor-in-Chief.
- Organize and host a Fellows' Journal Club podcast.
- Serve as Guest Editor for an issue of AJNR's News Digest with a timely topic.

QUALIFICATIONS

- Be a fellow in neuroradiology from North America, including Canada (this may be extended to include other countries).
- Be a junior faculty neuroradiology member (< 5 years) in either an academic or private environment.
- Be an "in-training" or member of ASNR in any other category.

APPLICATION

- Include a short letter of intent with statement of goals and desired research project. CV must be included.
- Include a letter of recommendation from the Division Chief or fellowship program director. A statement of protected time to perform the functions outlined is desirable.
- Applications will be evaluated by AJNR's Senior Editors prior to the ASNR annual meeting. The name of the selected individual will be announced at the meeting.
- Applications should be received by March 1, 2022 and sent to Ms. Karen Halm, AJNR Managing Editor, electronically at khalm@asnr.org.

AJNR go green

AJNR urges American Society of Neuroradiology members to reduce their environmental footprint by voluntarily suspending their print subscription.

The savings in paper, printing, transportation, and postage directly fund new electronic enhancements and expanded content.

The digital edition of *AJNR* presents the print version in its entirety, along with extra features including:

- **Publication Preview**
- **Case Collection**
- **Podcasts**
- **The *AJNR* News Digest**
- **The *AJNR* Blog**

It also reaches subscribers much faster than print. An electronic table of contents will be sent directly to your mailbox to notify you as soon as it publishes.

Readers can search, reference, and bookmark current and archived content 24 hours a day on www.ajnr.org.

ASNR members who wish to opt out of print can do so by using the AJNR Go Green link on the *AJNR* Website (http://www.ajnr.org/content/subscriber-help-and-services). Just type your name in the email form to stop print and spare our ecosystem.

MIDRC

MEDICAL IMAGING AND DATA RESOURCE CENTER.

Medical Imaging in the Fight against COVID-19
Call for Contributions

The Medical Imaging and Data Resource Center (MIDRC) is a multi-organizational initiative in the fight against the ongoing worldwide pandemic co-led by the ACR®, the RSNA, and the AAPM and is hosted at the University of Chicago.

The primary goal is to accelerate machine learning research by creating a high quality COVID-19 image commons linked to relevant clinical data made available as a public resource.

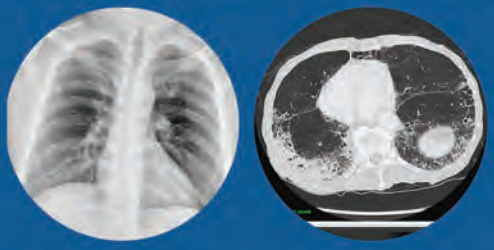

ASNR has teamed up with MIDRC to advance the understanding of the neuroimaging manifestations of COVID-19 and to enhance the MIDRC image commons.

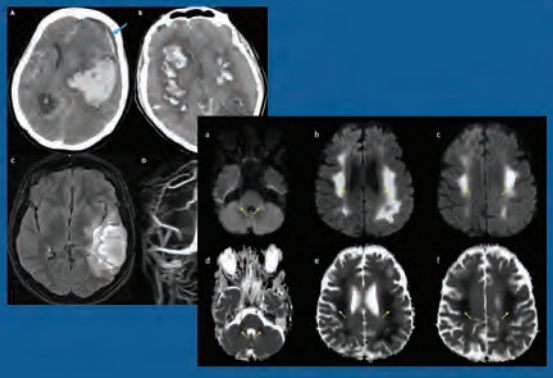

- To ensure success, MIDRC encourages all institutions and hospitals, both small and large, to donate their COVID-19 medical images and data to the cause.
- MIDRC provides a HIPAA-compliant mechanism to securely submit medical images and clinical metadata, and is committed to helping institutions throughout the submission process.

Visit midrc.org for more information

ACR American College of Radiology

RSNA Radiological Society of North America

AAPM American Association of Physicists in Medicine

The University of Chicago

NIH National Institute of Biomedical Imaging and Bioengineering

Creating Biomedical Technologies to Improve Health

PS Form 3526 — **Statement of Ownership, Management, and Circulation (All Periodicals Publications Except Requester Publications)**

1. Publication Title	2. Publication Number	ISSN	3. Filing Date
AMERICAN SOCIETY OF NEURORADIOLOGY/ AJNR-AMERICAN JOURNAL OF NEURORADIOLOGY	532630		09/15/2021

4. Issue Frequency	5. Number of Issues Published Annually	6. Annual Subscription Price
MONTHLY	12	$ 430.00

7. Complete Mailing Address of Known Office of Publication
800 ENTERPRISE DRIVE
SUITE 205
OAK BROOK, DU PAGE, IL 60523

Contact Person KAREN HALM
Telephone (630) 574-1487 Ext. 238

8. Complete Mailing Address of Headquarters or General Business Office of Publisher
AMERICAN SOCIETY OF NEURORADIOLOGY
800 ENTERPRISE DRIVE, SUITE 205
OAK BROOK, IL 60523

9. Full Names and Complete Mailing Addresses of Publisher, Editor, and Managing Editor

Publisher *(Name and complete mailing address)*
AMERICAN SOCIETY OF NEURORADIO
800 ENTERPRISE DRIVE
SUITE 205
OAK BROOK, IL 60523

Editor *(Name and complete mailing address)*
JEFFREY S. ROSS
800 ENTERPRISE DRIVE
SUITE 205
OAK BROOK, IL 60523

Managing Editor *(Name and complete mailing address)*
KAREN E. HALM
800 ENTERPRISE DRIVE
SUITE 205
OAK BROOK, IL 60523

10. Owner *(Do not leave blank. If the publication is owned by a corporation, give the name and address of the corporation immediately followed by the names and addresses of all stockholders owning or holding 1 percent or more of the total amount of stock. If not owned by a corporation, give names and addresses of the individual owners. If owned by a partnership or other unincorporated firm, give its name and address as well as those of each individual owner. If the publication is published by a nonprofit organization, give its name and address.)*

Full Name	Complete Mailing Address
AMERICAN SOCIETY OF NEURORADIO	800 ENTERPRISE DRIVE, SUITE 205, OAK BROOK, IL 60523
AMERICAN SOCIETY OF NEURORADIO	800 ENTERPRISE DRIVE, SUITE 205, OAK BROOK, IL 60523

11. Known Bondholders, Mortgagees, and Other Security Holders Owning or Hoding 1 Percent or More of Total Amount of Bonds. Mortgages, or Other Securities. If none, check box [X] None

Full Name	Complete Mailing Address

PS Form **3526**, September 2007 *(Page 1)* — **PRIVACY NOTICE:** See our privacy policy on *www.usps.com*

13. Publication Title AMERICAN SOCIETY OF NEURORADIOLOGY/AJNR-AMERICAN JOURNAL OF NEURORADIOLOGY

14. Issue Date for Circulation Data Below 09/07/2021

15. Extend and Nature of Circulation			Average No. Copies Each Issue During Preceding 12 Months	No. Copies of Single Issue Published Nearest to Filing Date
a. Total Numbers of Copies *(Net press run)*			2415	1600
b. Paid Circulation *(By Mail and Outside the Mail)*	(1)	Mailed Outside County Paid Subscriptions Stated on PS Form 3541*(include paid distribution above nominal rate, advertiser's proof copies, and exchange copies)*	1920	1197
	(2)	Mailed In-County Paid Subscriptions Stated on PS Form 3541*(include paid distribution above nominal rate, advertiser's proof copies, and exchange copies)*	0	0
	(3)	Paid Distribution Outside the Mails Including Sales Through Dealers and Carriers, Street Vendors, Counter Sales, and Other Paid Distribution Outside USPS	91	91
	(4)	Paid Distribution by Other Classes of Mail Through the USPS *(e.g. First-Class Mail)*	192	169
c. Total Paid Distribution *(Sum of 15b (1), (2), (3), (4))*			2203	1457
d. Free or Nominal Rate Distribution *(By Mail and Outside the Mail)*	(1)	Free or Nominal Rate Outside County Copies included on PS Form 3541	33	30
	(2)	Free or Nominal Rate In-County Copies included on PS Form 3541	0	0
	(3)	Free or Nominal Rate Copies Mailed at Other Classes Through the USPS *(e.g. First-Class Mail)*	0	0
	(4)	Free or Nominal Rate Distribution Outside the Mail *(Carriers or other means)*	0	0
e. Total Free or Nominal Rate Distribution *(Sum of 15d (1), (2), (3), (4))*			33	30
f. Total Distribution *(Sum of 15c and 15e)*			2236	1487
g. Copies not Distributed			201	113
h. Total *(Sum of 15f and 15g)*			2437	1600
i. Percent Paid *((15c / 15f) times 100)*			98.52 %	97.98 %

16. If total circulation includes electronic copies, report that circulation on lines below.

a. Paid Electronic Copies	0	0
b. Total Paid Print Copies*(Line 15C)* + Paid Electronic Copies	0	0
c. Total Print Distribution*(Line 15F)* + Paid Electronic Copies	0	0
d. Percent Paid*(Both Print and Electronic Copies)*	0.00 %	0.00 %

[ ] **I Certify that 50% of all my distributed copies (Electronic and Print) are paid above a nominal price.**

17. Publication of Statement of Ownership
[X] If the publication is a general publication, publication of this statement is required. Will be printed in the 11/15/2021 issue of this publication. [ ] Publication not required.

18. Signature and Title of Editor, Publisher, Business Manager, or Owner	Title	Date
Karen E. Halm	Managing Editor	09/15/2021 13:51:47 PM

I certify that all information furnished on this form is true and complete. I understand that anyone who furnishes false or misleading information on this form or who omits material or information requested on the form may be subject to criminal sanctions (including fines and imprisonment) and/or civil sanctions (including civil penalties).

PS Form **3526**, September 2007 *(Page 2)* — **PRIVACY NOTICE:** See our privacy policy on *www.usps.com*

OPTIMAX

FEEL THE DIFFERENCE:
VOLUME, SOFTNESS AND STABILITY

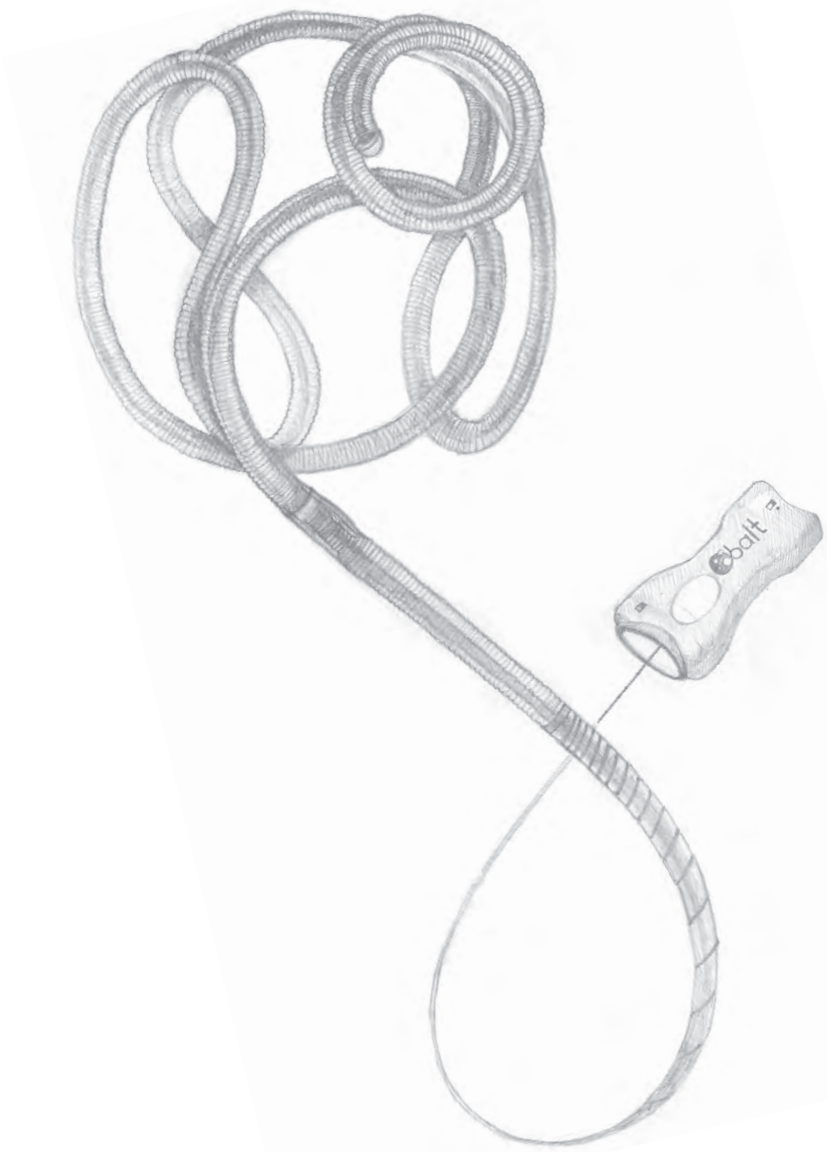

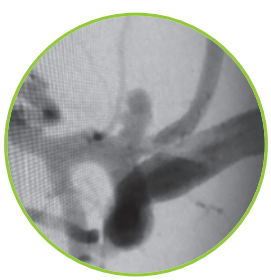

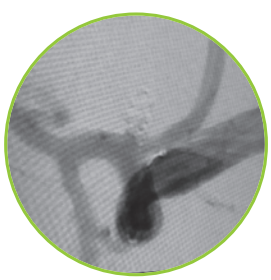

Complete and Unique Offerings:
The only large volume coil available in a **Super Soft** configuration in 1mm to 3.5mm diameters, including half sizes.

Visit our products page at www.Balt-USA.com to learn more.

Balt USA
29 Parker, Irvine, CA 92618
tel 949.788.1443 fax 949.788.1444
balt-usa.com

balt
inspiring innovation

AJNR

AMERICAN JOURNAL OF NEURORADIOLOGY

NOVEMBER 2021
VOLUME 42
NUMBER 11
WWW.AJNR.ORG

Publication Preview at www.ajnr.org features articles released in advance of print. Visit www.ajnrblog.org to comment on AJNR content and chat with colleagues and AJNR's News Digest at http://ajnrdigest.org to read the stories behind the latest research in neuroimaging.

1919 **PERSPECTIVES** *B. Thomas*

REVIEW ARTICLE

1920 **Sodium MR Neuroimaging** *A. Hagiwara, et al.* — ADULT BRAIN

GENERAL CONTENTS

1927 **A Combined Radiomics and Machine Learning Approach to Overcome the Clinicoradiologic Paradox in Multiple Sclerosis** *G. Pontillo, et al.* — ADULT BRAIN

1934 **Imaging Features of Symptomatic MCA Stenosis in Patients of Different Ages: A Vessel Wall MR Imaging Study** *H. Kang, et al.* — ADULT BRAIN

1942 **The First Examination of Diagnostic Performance of Automated Measurement of the Callosal Angle in 1856 Elderly Patients and Volunteers Indicates That 12.4% of Exams Met the Criteria for Possible Normal Pressure Hydrocephalus** *M. Borzage, et al.* — ADULT BRAIN

1949 **SWI Susceptibility Vessel Sign in Patients Undergoing Mechanical Thrombectomy for Acute Ischemic Stroke** *N.F. Belachew, et al.* — ADULT BRAIN, INTERVENTIONAL

1956 **Impact of Implementing an Elaborated CT Perfusion Protocol for Aneurysmal SAH on Functional Outcome: CTP Protocol for SAH** *V. Malinova, et al.* — ADULT BRAIN

1962 **Spiral 2D T2-Weighted TSE Brain MR Imaging: Initial Clinical Experience** *E. Sartoretti, et al.* — ADULT BRAIN

1968 **A Thrombectomy Model Based on Ex Vivo Whole Human Brains** *Y. Liu, et al.* — INTERVENTIONAL

1973 **Evaluation of Outcome Prediction of Flow Diversion for Intracranial Aneurysms** *S. Hadad, et al.* — INTERVENTIONAL

1979 **Outcomes of Mechanical Thrombectomy in the Early (<6-hour) and Extended (≥6-hour) Time Window Based Solely on Noncontrast CT and CT Angiography: A Propensity Score–Matched Cohort Study** *P. Hendrix, et al.* — INTERVENTIONAL

1986 **Local Intra-arterial Thrombolysis during Mechanical Thrombectomy for Refractory Large-Vessel Occlusion: Adjunctive Chemical Enhancer of Thrombectomy** *S.H. Baik, et al.* — INTERVENTIONAL

1993 **Evolution of MRI Findings in Patients with Idiopathic Intracranial Hypertension after Venous Sinus Stenting** *N.F. Belachew, et al.* — INTERVENTIONAL

AJNR (Am J Neuroradiol ISSN 0195–6108) is a journal published monthly, owned and published by the American Society of Neuroradiology (ASNR), 800 Enterprise Drive, Suite 205, Oak Brook, IL 60523. Annual dues for the ASNR include approximately 21% for a journal subscription. The journal is printed by Intellicor Communications, 330 Eden Road, Lancaster, PA 17601; Periodicals postage paid at Oak Brook, IL and additional mailing offices. Printed in the U.S.A. POSTMASTER: Please send address changes to American Journal of Neuroradiology, P.O. Box 3000, Denville, NJ 07834, U.S.A. Subscription rates: nonmember $410 ($480 foreign) print and online, $320 online only; institutions $470 ($540 foreign) print and basic online, $935 ($1000 foreign) print and extended online, $380 online only (basic), $825 online only (extended); single copies are $35 each ($40 foreign). Indexed by PubMed/MEDLINE, BIOSIS Previews, Current Contents (Clinical Medicine and Life Sciences), EMBASE, Google Scholar, HighWire Press, Q-Sensei, RefSeek, Science Citation Index, SCI Expanded, Meta/CZI, ReadCube, and Semantic Scholar.

2001 **Dual-Energy Parathyroid 4D-CT: Improved Discrimination of Parathyroid Lesions from Thyroid Tissue Using Noncontrast 40-keV Virtual Monoenergetic Images** *P.M. Bunch, et al.* HEAD & NECK

2009 **Intraindividual Comparison between the Contrast-Enhanced Golden-Angle Radial Sparse Parallel Sequence and the Conventional Fat-Suppressed Contrast-Enhanced T1-Weighted Spin-Echo Sequence for Head and Neck MRI** *S.-J. Hur, et al.* HEAD & NECK

2016 **Measuring 3D Cochlear Duct Length on MRI: Is It Accurate and Reliable?** *M.B. Eser, et al.* HEAD & NECK

2023 **Protuberant Fibro-Osseous Lesion of the Temporal Bone: "Bullough Bump"—Multimodality Imaging Case Series and Literature Review** *N. Shekhrajka, et al.* HEAD & NECK

2030 **Pulsatility Attenuation along the Carotid Siphon in Pseudoxanthoma Elasticum** *J.W. Bartstra, et al.* HEAD & NECK

2034 **A Uniform Description of Perioperative Brain MRI Findings in Infants with Severe Congenital Heart Disease: Results of a European Collaboration** *R. Stegeman, et al, for the European Association Brain in Congenital Heart Disease Consortium* PEDIATRICS

2040 **DWI in Brains of Fetuses with Congenital Heart Disease: A Case-Control MR Imaging Study** *J.-Y. Ren, et al.* PEDIATRICS

2046 **Grading of Pediatric Intracranial Tumors: Are Intravoxel Incoherent Motion and Diffusional Kurtosis Imaging Superior to Conventional DWI?** *D. She, et al.* PEDIATRICS

2054 **Selective Motor Control is a Clinical Correlate of Brain Motor Tract Impairment in Children with Spastic Bilateral Cerebral Palsy** *A. Vuong, et al.* PEDIATRICS

2062 **MR Imaging Differences in the Circle of Willis between Healthy Children and Adults** *K.P. Guilliams, et al.* PEDIATRICS

2070 **Heterotopia in Individuals with 22q11.2 Deletion Syndrome** *E. Neuhaus, et al.* PEDIATRICS

2077 **MRI Patterns in Pediatric CNS Hemophagocytic Lymphohistiocytosis** *P. Malik, et al.* PEDIATRICS

2086 **Mapping Human Fetal Brain Maturation In Vivo Using Quantitative MRI** *V.U. Schmidbauer, et al.* PEDIATRICS

2094 **Prenatal Diagnosis of Third and Fourth Branchial Apparatus Anomalies: Case Series and Comparison with Lymphatic Malformation** *Y. Li, et al.* PEDIATRICS

2101 **Filtered Diffusion-Weighted MRI of the Human Cervical Spinal Cord: Feasibility and Application to Traumatic Spinal Cord Injury** *S.A. Murphy, et al.* SPINE

2107 35 YEARS AGO IN AJNR

ONLINE FEATURES

LETTERS

E77 **From Dysembryoplastic Neuroepithelial Tumors to Myxoid Glioneuronal Tumors, a New Entity** *C. Zamora, et al.*

BOOK REVIEWS *R.M. Quencer, Section Editor*

Please visit www.ajnrblog.org to read and comment on Book Reviews.

From Liu Y, et al in this issue: Concurrent direct transmural observation and DSA of the brain model pre- and post-LVO.

Indicates Editor's Choices selection
Indicates Fellows' Journal Club selection
Indicates open access to non-subscribers at www.ajnr.org
Indicates article with supplemental online data
Indicates article with supplemental online video
Evidence-Based Medicine Level 1
Evidence-Based Medicine Level 2

AJNR

AMERICAN JOURNAL OF NEURORADIOLOGY

Publication Preview at www.ajnr.org features articles released in advance of print. Visit www.ajnrblog.org to comment on AJNR content and chat with colleagues and AJNR's News Digest at http://ajnrdigest.org to read the stories behind the latest research in neuroimaging.

NOVEMBER 2021 • VOLUME 42 • NUMBER 11 • WWW.AJNR.ORG

Title: Canadian Autumn, 21 cm × 14 cm, Brustro watercolor on 300 GSM hot-pressed paper. Falling in love with the "Fall," with light green to luminescent yellows and bright oranges to flaming red! These are memories of my fellowship days; if I miss anything, it's the Fall.

Bejoy Thomas, MD, DNB, PDCC, Trivandrum, Kerala, India

Sodium MR Neuroimaging

A. Hagiwara, M. Bydder, T.C. Oughourlian, J. Yao, N. Salamon, R. Jahan, J.P. Villablanca, D.R. Enzmann, and B.M. Ellingson

ABSTRACT

SUMMARY: Sodium MR imaging has the potential to complement routine proton MR imaging examinations with the goal of improving diagnosis, disease characterization, and clinical monitoring in neurologic diseases. In the past, the utility and exploration of sodium MR imaging as a valuable clinical tool have been limited due to the extremely low MR signal, but with recent improvements in imaging techniques and hardware, sodium MR imaging is on the verge of becoming clinically realistic for conditions that include brain tumors, ischemic stroke, and epilepsy. In this review, we briefly describe the fundamental physics of sodium MR imaging tailored to the neuroradiologist, focusing on the basics necessary to understand factors that play into making sodium MR imaging feasible for clinical settings and describing current controversies in the field. We will also discuss the current state of the field and the potential future clinical uses of sodium MR imaging in the diagnosis, phenotyping, and therapeutic monitoring in neurologic diseases.

ABBREVIATIONS: ESC = extracellular sodium concentration; IDH = isocitrate dehydrogenase; ISC = intracellular sodium concentration; NHE1 = Na+/H+ exchanger isoform 1; TSC = total sodium concentration

Routine clinical MR imaging is performed exclusively by using hydrogen nuclei (ie, protons, H^+) because it is the most abundant element in the human body in the form of water. However, other nuclei are also detectable with MR imaging and may provide complementary physiologic information to conventional proton MR imaging. Referred to collectively as "X-nuclei," elements including sodium (^{23}Na), potassium (^{35}K), chloride (^{35}Cl), and phosphorus (^{31}P) all have detectable magnetic moments and all play critical roles in the biochemistry of living tissues.

Received March 12, 2021; accepted after revision May 28.

From the UCLA Brain Tumor Imaging Laboratory (A.H., M.B., T.C.O., J.Y., B.M.E.), Center for Computer Vision and Imaging Biomarkers, and Department of Bioengineering (J.Y., B.M.E.), Henry Samueli School of Engineering and Applied Science, University of California, Los Angeles, Los Angeles, California; and Department of Radiological Sciences (A.H., M.B., J.Y., N.S., R.J., J.P.V., D.R.E., B.M.E.), Neuroscience Interdepartmental Program (T.C.O., B.M.E.), and Department of Psychiatry and Biobehavioral Sciences (B.M.E.), David Geffen School of Medicine, University of California, Los Angeles, Los Angeles, California.

This work was supported by American Cancer Society Research Scholar Grant (RSG-15-003-01-CCE), the UCLA SPORE in Brain Cancer grant (NIH/NCI 1P50CA211015-01A1), and the UCLA Department of Radiology Sodium Imaging Program.

Please address correspondence to Benjamin M. Ellingson, PhD, UCLA Brain Tumor Imaging Laboratory, Departments of Radiology and Psychiatry and Radiological Sciences and Psychiatry, David Geffen School of Medicine, University of California, Los Angeles, 924 Westwood Blvd, Suite 615, Los Angeles, CA 90024; e-mail: bellingson@mednet.ucla.edu

http://dx.doi.org/10.3174/ajnr.A7261

Sodium is the second most abundant element in the body detectable on MR imaging. Sodium homeostasis is crucial for life because it is a major determinant of body fluid osmolality, and sodium sensing is performed in the brain by specialized sodium channels within the circumventricular organs to maintain a range of 135–145 mM.[1] Sodium also plays a crucial role in the propagation of neural signals in and between neurons,[2,3] and disruption in sodium homeostasis as well as structural and metabolic integrity has been identified in a variety of neurologic disorders including brain tumors,[4] stroke,[5] and epilepsy.[6] Hence, sodium MR imaging has remarkable potential for use in diagnosis, characterization, and treatment monitoring in neurologic diseases.

The fundamental limitation to translational use of sodium MR imaging for clinical care is the low inherent MR signal. The MR imaging signal is approximately 10,000 times lower than that of protons, which is due to a combination of the following: 1) a concentration of about 0.055% of that of water protons; 2) a gyromagnetic ratio (γ, relates the main magnetic field strength, B_0, to the resonance frequency) of about 26.5% of that of the proton, thus a lower energy ($\Delta E = \gamma \hbar B_0$) and lower inherent bulk magnetization; and 3) a nuclear spin of 3/2, leading to electric quadrupolar interactions between the nucleus and its environment resulting in faster T2* decay. Overcoming these issues and achieving adequate MR signal levels necessitates acquisition schemes with low spatial resolution, short TE, multiple measurements, and long scan times.

Researchers have put considerable effort into optimizing these various factors and taking advantage of both the acquisition algorithm and hardware improvements. In this review, we briefly describe the fundamental physics of sodium MR imaging tailored to the neuroradiologist, focusing on the basics necessary to understand factors that are involved in making sodium MR imaging feasible for clinical settings and describing current controversies in the field, including the measurement of intracellular sodium concentration. We will also discuss the current state of the field and the potential future clinical uses of sodium MR imaging in the diagnosis, phenotyping, and therapeutic monitoring in neurologic diseases.

Sodium MR Imaging Physics and Acquisition

In practice, MR imaging of sodium ions is essentially the same as imaging protons, but with lower SNR and shorter (and more complex) T2 relaxation characteristics. Due to the inherent nuclear spin of 3/2, the sodium ion exhibits electric quadrupolar interactions between the nucleus and its environment,[7,8] leading to what appears to be a biexponential T2 decay in many biologic tissues. The short T2 species appears to occur most often in viscous liquids or semisolid tissues, where there is a continuum of electric field gradients (depending on the orientation of the sodium ion and the position of an anion) that produces a broad range of energy levels and gives rise to short T2 relaxation. A longer T2 component is observed from the energy levels unperturbed by the electric field gradients,[7] such as those in CSF and other nonviscous liquids because the motion of the ions causes electric field gradients to average to zero over the measurement time scale, resulting in a single, longer T2 relaxation. This observation has been replicated in the human brain, where parenchyma, including both white and gray matter, exhibits a characteristic biexponential T2 decay, while the nonviscous CSF displays monoexponential T2 relaxation.[9]

Most measurements used in clinical sodium MR imaging focus on estimation of the total sodium concentration (TSC) or the volume-weighted average of the intra- and extracellular sodium concentrations (ISC and ESC, respectively). Notably, ISC and ESC do not correspond to short and long sodium T2 relaxation (explained later in this section). Because ESC is stable at around 140 mM, TSC is mainly affected by changes in ISC and alterations in the volume fractions between the intra- and extracellular space. TSC in the brain was reported to range from 30 to 56 mM[10-12] and remain constant throughout adulthood in cognitively healthy individuals, and its regional variation in the brain was reported to be minimal.[12] Sodium concentration in the CSF has been known to show circadian fluctuation;[13] however, whether TSC in the brain tissue also shows circadian fluctuation and whether the degree of fluctuation is different between normal and pathologic brain tissues are unknown. Remarkable effort has been made to measure ISC during the past decades in animal models to elucidate cellular homeostasis, energetic state, and functionality of sodium pumps; however, these measurements involve the use of highly toxic extracellular paramagnetic "frequency shift reagents" that are trapped within the extracellular space and shift the resonance frequency of extracellular sodium, resulting in isolation of purely intracellular sodium ions.[14,15] Unfortunately, due to their toxicity and the fact they do not cross the blood-brain barrier, shift reagents for sodium MR imaging are not used in humans.

Two major physics approaches to measure the ISC in humans that have been explored include the use of inversion recovery[16-19] and multiple quantum filtering[20-22] techniques. Similar to FLAIR, the inversion recovery approach assumes that a simple inversion pulse can suppress the sodium signals free from macromolecules; hence, the sodium signal in the extracellular space is also presumed to be suppressed. However, there is evidence that the T1 relaxation times of intra- and extracellular sodium are very similar,[23-28] and there is little reason to assume that the T1 of the sodium within the extracellular compartment is more similar to that in CSF than in the intracellular compartment. Indeed, extracellular fluid in brain tissue is largely different from CSF in composition.[29]

Multiple quantum filtering is a relatively sophisticated approach that works on the premise that the slow-moving sodium, presumably in the intracellular space, can be selectively detected on the basis of the underlying biexponential T2 relaxation of sodium.[30] However, molecular interactions that result in equivalently small T2 values in both intra- and extracellular compartments are expected to result in similar multiple quantum coherences.[27] Indeed, previous experiments have shown a contribution of the extracellular sodium to the multiple quantum coherences detected by multiple quantum-filtering sodium MR imaging, and the degree of contamination is largely unexplored.[31-33] Therefore, direct measurement of the ISC solely using sodium MR imaging physics without the use of exogenous contrast agents is not yet plausible, and such claims in previous literature using the relaxation behavior of sodium should be cautiously interpreted. Furthermore, the exchange rate of sodium between intra- and extracellular space, which might affect the measurement of the ISC, has not been considered in previous studies. Future studies aimed at using multiparametric input from proton diffusion MR imaging and/or PET may be useful for using estimates of cell density[34] to disentangle the ISC from the TSC measured by sodium MR imaging, but as of now, TSC is the most reliable measurement parameter for routine sodium MR imaging examinations.

The primary challenge for clinical sodium MR imaging is the very short T2, meaning that most of the sodium MR imaging signal is lost within a few milliseconds. Hence, imaging with a very short, ultrashort, or zero TE (ie, TE of <1 ms) is almost mandatory for any sodium MR imaging application. High quantification accuracy of the sodium concentration with ultrashort TE imaging has been reported.[10,35] To reduce the duration of signal readout while maintaining sufficient SNR, non-Cartesian sequences (eg, radial or spiral trajectories) are preferred.[36,37] For example, Ridley et al[38] used a 3D radial projection for whole-brain imaging, with 3-mm isotropic resolution on a 3T clinical scanner in 34 minutes. On the other hand, Thulborn et al[39] showed that a twisted radial *k*-space imaging trajectory could be used for whole-brain coverage with 5-mm isotropic resolution (44 slices) on a 3T clinical scanner in approximately 8 minutes, which was sufficient for brain tumor imaging applications.

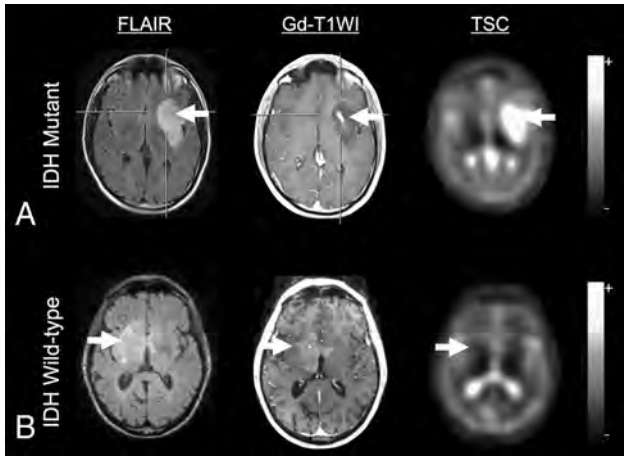

FIG 1. *A*, MR imaging of a 38-year-old male patient with an *IDH*-mutated glioblastoma, World Health Organization grade IV. The tumor (*white arrows*) shows focal contrast enhancement in the T1-weighted image and is clearly depicted in the FLAIR image. Sodium imaging shows increased TSC. *B*, MR imaging of a 78-year-old male patient with an *IDH* wild-type anaplastic astrocytoma, World Health Organization grade III, in the right basal ganglia. The tumor (*white arrows*) shows focal contrast enhancement in the T1-weighted image and diffuse abnormalities in the FLAIR image. Sodium imaging shows no abnormality. Adapted and reproduced with permission from Shymanskaya et al.[22]

In addition to creative *k*-space trajectories, advancements in hardware have also made sodium MR imaging more clinically realizable. The use of high- and ultra-high-field strength scanners, for example, proportionally increases the SNR, making commercial 7T MR imaging scanners feasible for faster or higher resolution sodium imaging.[11] Of note, higher resolution, especially with 3D imaging, helps reduce partial volume effects. In addition to the use of high-field-strength scanners, receiver coil architecture is also of great importance because the design of this coil predetermines the maximum attainable SNR. Because proton MR imaging is often performed concurrently with sodium imaging, the same physical coil housing (ie, "dual tuned" coils) is desired. Dual-tuned designs of different Larmor frequencies come with unique challenges, however, such as coupling between the sodium and proton coils.[40] This issue could be addressed by using 2-coil geometries that are intrinsically decoupled, dual-tuning a single coil, or strategies to actively decouple the 2 coils.[40] Use of array coils is an attractive approach in sodium imaging to further increase the SNR and reduce scan time by using parallel imaging strategies.[41] For example, Lee et al[42] demonstrated up to a 400% increases in the SNR using a 4-channel coil >20 years ago. To date, the highest number of channels reported for a head sodium coil is 32,[28] while 20- to 30-channel coils are commercialized and available through third-party coil vendors. However, despite remarkable progress, array coils are still rarely used in sodium imaging because of hardware and software limitations and additional costs.[41] For using array coils in sodium MR imaging, the receivers should be capable of handling the frequencies relevant to sodium acquired with analog-to-digital converters and having processing engines capable of sorting and combining the signals from each coil properly. Most commercial scanners have offered only a single broadband X-nuclei receiver channel, limiting the use of array coils.

Neurologic Applications

Brain Tumors. In brain tumors, sodium MR imaging has the potential to reveal molecular information related to cell viability, proliferation, migration, invasion, and immunogenicity[43-45] and may enable us to reveal molecular responses to treatment before morphologic changes can be observed. TSC is reportedly elevated in brain tumors both in humans[19,22,39,46-48] and animals,[49,50] a feature that may be due to the ISC, the volume of the extracellular space, or both, considering that the ESC remains relatively constant and much higher than the ISC as long as there is moderate tissue perfusion.[51] Increases of the ISC in tumors are partly related to the increased energy demand arising from cell proliferation, because negative sodium gradients across the cell membranes are maintained by consumption of adenosine triphosphate.[52] In addition, the Na^+/H^+ exchanger isoform (NHE1) (*SLC9A1*) is upregulated in gliomas and is a potential therapeutic target due to its role in the progression of malignant gliomas,[53-55] influence on pH homeostasis in glioma cells,[54-57] influence on seizure activity,[6] and potential increased resistance to both chemoradiation[58] and anti-PD-1 immunotherapy.[56]

Although the literature is sparse, studies have shown differences in sodium MR imaging contrast among different tumor grades[48,59] and between active tumors and peritumoral edema[46] or other types of lesions,[60] and these differences appear to reflect the general prognosis,[59] with higher TSC in areas of more aggressive tumor. Despite this general trend, a number of studies have shown differences in sodium MR imaging contrast between isocitrate dehydrogenase (*IDH*) mutant and wild-type gliomas,[22,59,61] with *IDH*-mutant human gliomas showing higher TSC than *IDH* wild-type gliomas (Fig 1).[22,61] While this finding is counterintuitive, it could be due to the lower cellular density of *IDH*-mutant gliomas,[62] leading to a larger extracellular space and higher TSC. Alternatively, *IDH*-mutant gliomas often result in more frequent seizures compared with more aggressive high-grade *IDH* wild-type malignant gliomas,[63,64] and because expression of NHE1s is strongly linked to seizure activity,[6] this finding may also explain the differences in TSC observed between *IDH*-mutant and wild-type gliomas.

Sodium MR imaging has also shown some promise in identifying the early treatment response in brain tumors.[39,65,66] For example, in rat glioma models, response to chemotherapy using sodium MR imaging was detectable even earlier than in proton diffusion MR imaging.[67] In rat models of subcutaneously implanted gliomas, lower total sodium signals were observed in gliomas treated with 1,3-Bis(2-chloroethyl)-1-nitrosourea compared with untreated gliomas.[68] Another study showed a pronounced increase in the TSC following 1,3-Bis(2-chloroethyl)-1-nitrosourea treatment in orthotropic rat gliomas compared with untreated gliomas.[50] Notably, the increase in TSC after treatment occurred before tumor shrinkage. Even though the discrepancy in the results between these 2 studies may partly lie in differences in the implantation sites of gliomas and acquisition methods, the increase in TSC observed in the latter study may also be due to a combination of treatment response leading to necrosis and an

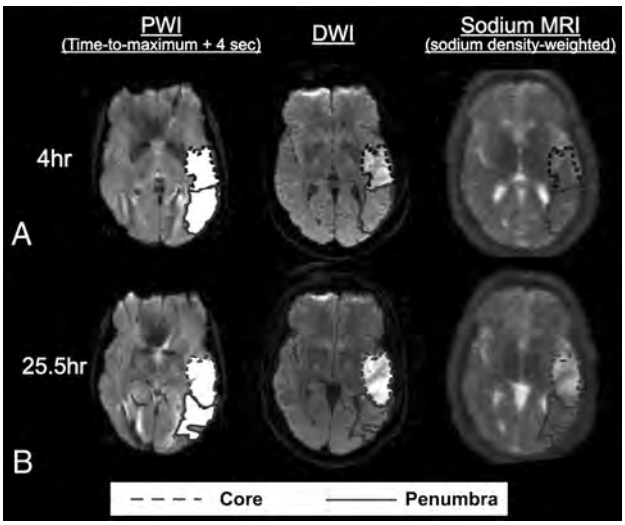

FIG 2. Images of a representative section from a patient with ischemic stroke showing the hypoperfused (time-to-maximum + 4 seconds) perfusion maps, the DWI with a DWI-hyperintense core in the *dotted outline*, the PWI-DWI mismatch tissue (penumbra) in the *solid outline*, and sodium images for (*A*) 4 and (*B*) 25.5 hours after the onset. This patient had a perfusion/diffusion mismatch at the first time point. The absolute lesion volume of the core enlarged from the first to the second time point, while the penumbral volume diminished. Note that the sodium signal is not increased in the first time point, while the high sodium signal is matched with DWI hyperintensity at the second time point. Adapted and reproduced with permission from Tsang et al.[76]

increase in the extracellular space. Additionally, Thulborn et al[39] evaluated the effects of the standard chemoradiotherapy on 20 patients with human glioblastomas using sodium MR imaging and noted an increase in TSC after successful treatment.

Acute Ischemic Stroke. Acute ischemic stroke occurs due to sudden occlusion of arteries within the brain, resulting in reductions of adenosine triphosphate production and Na^+/K^+-ATPase activity. Inadequate Na^+/K^+-ATPase activity disrupts the ion homeostasis, leading to an increase in the ISC, cytotoxic cell swelling, and eventual cell death.[69] Sodium MR imaging may be useful as a surrogate marker of Na^+/K^+-ATPase activity and cell viability in the ischemic tissue, with potential implications for determining tissue viability.[70] Monotonic increases in the TSC after acute ischemic stroke have been reported both in animals[71,72] and humans,[73,74] using time scales relevant for patient management (ie, 0–24 hours following onset), and this increase does not appear to normalize in the natural course following stroke. In contrast, decreased ADC in the acute phase normalizes when vasogenic edema starts in the subacute phase (ie, 24–72 hours following onset).[75] Hussain et al[73] demonstrated that there was a 10% increase in sodium signal in the first 7 hours, followed by a rapid increase in sodium until a plateau of a 69% increase at 48 hours relative to baseline values, during which time the ADC did not fluctuate. Because sodium concentration correlates with the duration of ischemia, the onset time may be more accurately estimated by the sodium concentration than diffusion MR imaging changes, providing potential utility in "wake-up" strokes.

Additional studies have demonstrated that sodium MR imaging signals in the region with a perfusion-diffusion mismatch may not differ from those in contralateral normal tissue until around 32 hours after symptom onset, indicating that sodium MR imaging may help identify the viable tissue in the penumbra, even when the onset time of a stroke is unknown (Fig 2).[76] Despite these initial studies, the specific thresholds of TSC for determining reversible and irreversible ischemic tissues and the vulnerability of infarcted tissues to hemorrhage following reperfusion therapy are yet to be determined. Conceivably, sodium MR imaging in combination with conventional imaging techniques may enable more judicious selection of candidates for endovascular thrombectomy in the future, rather than using a fixed time window as is the current practice.

Epilepsy. Because sodium homeostasis affects neuronal excitability,[6] sodium MR imaging has the potential to detect subtle disturbances in sodium concentration in seizure disorders including epilepsy. Several pathologic mechanisms in epilepsy are implicated in the change of the TSC observed in the brain, with the primary mechanism being dysfunction of sodium channels and Na^+/K^+-ATPase in patients with epilepsy due to genetic mutation and mitochondrial dysfunction, leading to depolarization and the increase in the ISC.[77-79] Additionally, reduction in the size of the extracellular space due to an increase in the intracellular osmolarity can occur during seizure activity,[80,81] and an increase in the extracellular space due to neuronal loss, gliosis, and blood-brain barrier disruption, arising from chronic epilepsy or underlying diseases such as stroke or trauma, can lead to alterations in TSC measurements using sodium MR imaging.[82]

Despite the potential impact, to date, very few sodium MR imaging studies have been performed in epilepsy and seizure disorders. Wang et al[83] reported a dynamic postictal temporal change in proton ADC and TSC using sodium MR imaging after the administration of kainic acid to rats. In the pyriform cortex and amygdala, decreases in the ADC were noted as early as 5 hours after kainic acid administration, and the ADC values further decreased until 24 hours after the seizures. ADC values returned to normal levels 7 days postictally. Meanwhile, the TSC did not change at 5 hours postictally but increased at 24 hours and remained elevated even at 7 days postictally. These changes in ADC and TSC were interpreted as being influenced by sodium entry into the excited neurons and accompanying cellular swelling, followed by energy deficiencies and cell death, in line with pathologically-confirmed extensive neuronal cell loss by day 7. However, future research is desired to elucidate the relationship between the change in sodium concentration and pathophysiology in more detail by using shift reagents in animal models, to determine the degree of contribution by the change in the ISC to the increased TSC.

Additionally, Ridley et al[38] used sodium MR imaging to examine 9 patients with epilepsy during interictal periods and 1 patient who incidentally presented with several seizures during the MR imaging examination. TSC in the intracerebral electroencephalogram-defined epileptogenic regions was increased in the interictal group, a finding that can be explained by an increase in the ISC due to voltage-gated sodium channel mutations leading to a persistent

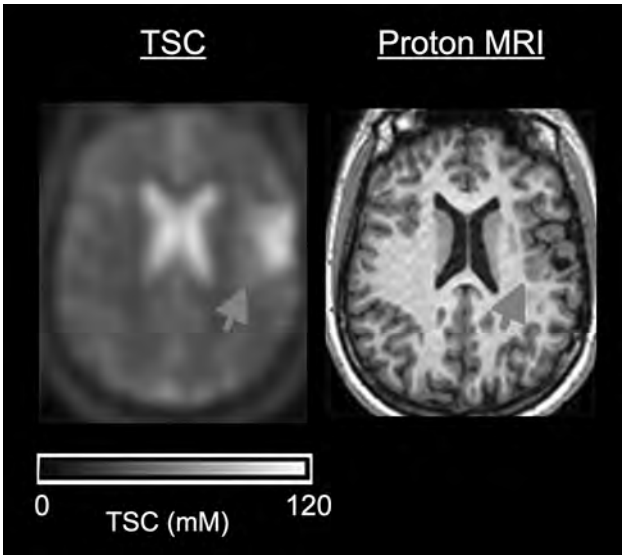

FIG 3. A patient with a cortical malformation. The TSC map shows high value on a cortical malformation that is subtle on high-resolution proton 3D-T1-weighted image (*arrows*) (adapted and reproduced with permission from Ridley et al[38]). However, the effect of the partial volume effect should be examined in a future study with the achievement of higher-resolution sodium MR imaging.

inward sodium current, along with an increase in the extracellular space due to cell loss and glial formation (Fig 3).[6,82] In contrast to patients in the interictal period and consistent with preclinical studies, the TSC was slightly decreased in the epileptogenic area in the patient who presented with multiple seizures during the MR imaging examination. Together, these preliminary studies suggest that sodium MR imaging may be useful for identification and illumination of epileptic activity, but important questions remain, including the precise temporal changes in TSC that occur during and after seizure activity, the effects of antiepileptic medication, the sensitivity of sodium MR imaging for epileptic foci detection compared with standard proton MR imaging, and the value of sodium MR imaging as a tool to predict surgical outcome in patients with refractory epilepsy.

CONCLUSIONS

Sodium MR imaging has the potential to complement routine proton MR imaging examinations with the goal of improving diagnosis, disease characterization, and clinical monitoring in neurologic diseases. In the past, the utility and exploration of sodium MR imaging as a valuable clinical tool have been limited due to the extremely low MR signal, but with recent improvements in imaging techniques and hardware, sodium MR imaging is on the verge of becoming clinically feasible for conditions including brain tumors, stroke, and epilepsy.

Disclosures: Akifumi Hagiwara—*RELATED*: *Grant*: Japan Society for the Promotion of Science Grants-in-Aid for Scientific Research, *Comments*: 19K17150.

REFERENCES

1. Noda M, Hiyama TY. **Sodium sensing in the brain.** *Pflugers Arch* 2015;467:465–74 CrossRef Medline
2. Hernandez CM, Richards JR. *Physiology, Sodium Channels*. StatPearls Publishing; 2021
3. Joseph D, Pidathala S, Mallela AK, et al. **Structure and gating dynamics of Na(+)/Cl(-) coupled neurotransmitter transporters**. *Front Mol Biosci* 2019;6:80 CrossRef Medline
4. Dekker LJM, Wu S, Jurriens C, et al. **Metabolic changes related to the IDH1 mutation in gliomas preserve TCA-cycle activity: an investigation at the protein level.** *FASEB J* 2020;34:3646–57 CrossRef Medline
5. Lo WD, Betz AL, Schielke GP, et al. **Transport of sodium from blood to brain in ischemic brain edema.** *Stroke* 1987;18:150–57 CrossRef Medline
6. Kaplan DI, Isom LL, Petrou S. **Role of sodium channels in epilepsy.** *Cold Spring Harb Perspect Med* 2016;6:a022814 CrossRef Medline
7. Madelin G, Regatte RR. **Biomedical applications of sodium MRI in vivo.** *J Magn Reson Imaging* 2013;38:511–29 CrossRef Medline
8. Rooney WD, Springer CS Jr. **The molecular environment of intracellular sodium: 23Na NMR relaxation.** *NMR Biomed* 1991;4:227–45 CrossRef Medline
9. Tsang A, Stobbe RW, Beaulieu C. **Triple-quantum-filtered sodium imaging of the human brain at 4.7 T.** *Magn Reson Med* 2012;67:1633–43 CrossRef Medline
10. Liao Y, Lechea N, Magill AW, et al. **Correlation of quantitative conductivity mapping and total tissue sodium concentration at 3T/4T.** *Magn Reson Med* 2019;82:1518–26 CrossRef Medline
11. Qian Y, Zhao T, Zheng H, et al. **High-resolution sodium imaging of human brain at 7 T.** *Magn Reson Med* 2012;68:227–33 CrossRef Medline
12. Thulborn K, Lui E, Guntin J, et al. **Quantitative sodium MRI of the human brain at 9.4 T provides assessment of tissue sodium concentration and cell volume fraction during normal aging.** *NMR Biomed* 2016;29:137–43 CrossRef Medline
13. Harrington MG, Salomon RM, Pogoda JM, et al. **Cerebrospinal fluid sodium rhythms.** *Cerebrospinal Fluid Res* 2010;7:3 CrossRef Medline
14. Bansal N, Germann MJ, Seshan V, et al. **Thulium 1,4,7,10-tetraazacyclododecane-1,4,7,10-tetrakis(methylene phosphonate) as a 23Na shift reagent for the in vivo rat liver.** *Biochemistry* 1993;32:5638–43 CrossRef Medline
15. Winter PM, Bansal N. **TmDOTP(5-) as a (23)Na shift reagent for the subcutaneously implanted 9L gliosarcoma in rats.** *Magn Reson Med* 2001;45:436–42 CrossRef Medline
16. Stobbe R, Beaulieu C. **In vivo sodium magnetic resonance imaging of the human brain using soft inversion recovery fluid attenuation.** *Magn Reson Med* 2005;54:1305–10 CrossRef Medline
17. Madelin G, Kline R, Walvick R, et al. **A method for estimating intracellular sodium concentration and extracellular volume fraction in brain in vivo using sodium magnetic resonance imaging.** *Sci Rep* 2014;4:4763 CrossRef Medline
18. Barrett T, Riemer F, McLean MA, et al. **Quantification of total and intracellular sodium concentration in primary prostate cancer and adjacent normal prostate tissue with magnetic resonance imaging.** *Invest Radiol* 2018;53:450–56 CrossRef Medline
19. Nunes Neto LP, Madelin G, Sood TP, et al. **Quantitative sodium imaging and gliomas: a feasibility study.** *Neuroradiology* 2018;60:795–802 CrossRef Medline
20. Hancu I, Boada FE, Shen GX. **Three-dimensional triple-quantum-filtered (23)Na imaging of in vivo human brain.** *Magn Reson Med* 1999;42:1146–54 CrossRef Medline
21. Fiege DP, Romanzetti S, Mirkes CC, et al. **Simultaneous single-quantum and triple-quantum-filtered MRI of 23Na (SISTINA).** *Magn Reson Med* 2013;69:1691–96 CrossRef Medline
22. Shymanskaya A, Worthoff WA, Stoffels G, et al. **Comparison of [18F] Fluoroethyltyrosine PET and sodium MRI in cerebral gliomas: a pilot study.** *Mol Imaging Biol* 2020;22:198–207 CrossRef Medline
23. Shinar H, Navon G. **NMR relaxation studies of intracellular Na+ in red blood cells**. *Biophys Chem* 1984;20:275–83 CrossRef Medline

24. Burstein D, Fossel ET. **Intracellular sodium and lithium NMR relaxation times in the perfused frog heart.** *Magn Reson Med* 1987;4:261–73 CrossRef Medline
25. Foy BD, Burstein D. **Interstitial sodium nuclear magnetic resonance relaxation times in perfused hearts.** *Biophys J* 1990;58:127–34 CrossRef Medline
26. Jelicks LA, Paul PK, O'Byrne E, et al. **Hydrogen-1, sodium-23, and carbon-13 MR spectroscopy of cartilage degradation in vitro.** *J Magn Reson Imaging* 1993;3:565–68 CrossRef Medline
27. Burstein D, Springer CS Jr. **Sodium MRI revisited.** *Magn Reson Med* 2019;82:521–24 CrossRef Medline
28. Lachner S, Ruck L, Niesporek SC, et al. **Comparison of optimized intensity correction methods for ^{23}Na MRI of the human brain using a 32-channel phased array coil at 7 Tesla.** *Z Med Phys* 2020;30:104–15 CrossRef Medline
29. Lei Y, Han H, Yuan F, et al. **The brain interstitial system: anatomy, modeling, in vivo measurement, and applications.** *Prog Neurobiol* 2017;157:230–46 CrossRef Medline
30. LaVerde G, Nemoto E, Jungreis CA, et al. **Serial triple quantum sodium MRI during non-human primate focal brain ischemia.** *Magn Reson Med* 2007;57:201–05 CrossRef Medline
31. Jelicks LA, Gupta RK. **Multinuclear NMR studies of the Langendorff perfused rat heart.** *J Biol Chem* 1989;264:15230–35 CrossRef Medline
32. Hutchison RB, Malhotra D, Hendrick RE, et al. **Evaluation of the double-quantum filter for the measurement of intracellular sodium concentration.** *J Biol Chem* 1990;265:15506–10 Medline
33. Jelicks LA, Gupta RK. **On the extracellular contribution to multiple quantum filtered ^{23}Na NMR of perfused rat heart.** *Magn Reson Med* 1993;29:130–33 CrossRef Medline
34. Gaw N, Hawkins-Daarud A, Hu LS, et al. **Integration of machine learning and mechanistic models accurately predicts variation in cell density of glioblastoma using multiparametric MRI.** *Sci Rep* 2019;9:10063 CrossRef Medline
35. Lu A, Atkinson IC, Claiborne TC, et al. **Quantitative sodium imaging with a flexible twisted projection pulse sequence.** *Magn Reson Med* 2010;63:1583–93 CrossRef Medline
36. Shah NJ, Worthoff WA, Langen KJ. **Imaging of sodium in the brain: a brief review.** *NMR Biomed* 2016;29:162–74 CrossRef Medline
37. Zaric O, Juras V, Szomolanyi P, et al. **Frontiers of sodium MRI revisited: from cartilage to brain imaging.** *J Magn Reson Imaging* 2021;54:e27326–75 CrossRef Medline
38. Ridley B, Marchi A, Wirsich J, et al. **Brain sodium MRI in human epilepsy: Disturbances of ionic homeostasis reflect the organization of pathological regions.** *Neuroimage* 2017;157:173–83 CrossRef Medline
39. Thulborn KR, Lu A, Atkinson IC, et al. **Residual tumor volume, cell volume fraction, and tumor cell kill during fractionated chemoradiation therapy of human glioblastoma using quantitative sodium MR imaging.** *Clin Cancer Res* 2019;25:1226–32 CrossRef Medline
40. Wiggins GC, Brown R, Lakshmanan K. **High-performance radiofrequency coils for (23)Na MRI: brain and musculoskeletal applications.** *NMR Biomed* 2016;29:96–106 CrossRef Medline
41. Wilcox M, Wright SM, McDougall M. **A review of non-1H RF receive arrays in magnetic resonance imaging and spectroscopy.** *IEEE Open J Eng Med Biol* 2020;1:290–300 CrossRef
42. Lee RF, Giaquinto R, Constantinides C, et al. **A broadband phased-array system for direct phosphorus and sodium metabolic MRI on a clinical scanner.** *Magn Reson Med* 2000;43:269–77 CrossRef Medline
43. Zamecnik J. **The extracellular space and matrix of gliomas.** *Acta Neuropathol* 2005;110:435–42 CrossRef Medline
44. Amara S, Tiriveedhi V. **Inflammatory role of high salt level in tumor microenvironment (review).** *Int J Oncol* 2017;50:1477–81 CrossRef Medline
45. Leslie TK, James AD, Zaccagna F, et al. **Sodium homeostasis in the tumour microenvironment.** *Biochim Biophys Acta Rev Cancer* 2019;1872:188304 CrossRef Medline
46. Ouwerkerk R, Bleich KB, Gillen JS, et al. **Tissue sodium concentration in human brain tumors as measured with ^{23}Na MR imaging.** *Radiology* 2003;227:529–37 CrossRef Medline
47. Bartha R, Megyesi JF, Watling CJ. **Low-grade glioma: correlation of short echo time 1H-MR spectroscopy with ^{23}Na MR imaging.** *AJNR Am J Neuroradiol* 2008;29:464–70 CrossRef Medline
48. Nagel AM, Bock M, Hartmann C, et al. **The potential of relaxation-weighted sodium magnetic resonance imaging as demonstrated on brain tumors.** *Invest Radio* 2011;46:539–47 CrossRef Medline
49. Thulborn KR, Davis D, Adams H, et al. **Quantitative tissue sodium concentration mapping of the growth of focal cerebral tumors with sodium magnetic resonance imaging.** *Magn Reson Med* 1999;41:351–59 CrossRef Medline
50. Schepkin VD, Ross BD, Chenevert TL, et al. **Sodium magnetic resonance imaging of chemotherapeutic response in a rat glioma.** *Magn Reson Med* 2005;53:85–92 CrossRef Medline
51. Thulborn KR, Lu A, Atkinson IC, et al. **Quantitative sodium MR imaging and sodium bioscales for the management of brain tumors.** *Neuroimaging Clin N Am* 2009;19:615–24 CrossRef Medline
52. Kuhn SA, Mueller U, Hanisch UK, et al. **Glioblastoma cells express functional cell membrane receptors activated by daily used medical drugs.** *J Cancer Res Clin Oncol* 2009;135:1729–45 CrossRef Medline
53. Cong D, Zhu W, Kuo JS, et al. **Ion transporters in brain tumors.** *Curr Med Chem* 2015;22:1171–81 CrossRef Medline
54. McLean LA, Roscoe J, Jorgensen NK, et al. **Malignant gliomas display altered pH regulation by NHE1 compared with nontransformed astrocytes.** *Am J Physiol Cell Physiol* 2000;278:C676–88 CrossRef Medline
55. Zhu W, Carney KE, Pigott VM, et al. **Glioma-mediated microglial activation promotes glioma proliferation and migration: roles of Na+/H+ exchanger isoform 1**. *Carcinogenesis* 2016;37:839–51 CrossRef Medline
56. Guan X, Hasan MN, Begum G, et al. **Blockade of Na/H exchanger stimulates glioma tumor immunogenicity and enhances combinatorial TMZ and anti-PD-1 therapy.** *Cell Death Dis* 2018;9:1010 CrossRef Medline
57. Stock C, Pedersen SF. **Roles of pH and the Na(+)/H(+) exchanger NHE1 in cancer: From cell biology and animal models to an emerging translational perspective?** *Semin Cancer Biol* 2017;43:5–16 CrossRef Medline
58. Cong D, Zhu W, Shi Y, et al. **Upregulation of NHE1 protein expression enables glioblastoma cells to escape TMZ-mediated toxicity via increased H(+) extrusion, cell migration and survival**. *Carcinogenesis* 2014;35:2014–24 CrossRef Medline
59. Biller A, Badde S, Nagel A, et al. **Improved brain tumor classification by sodium MR imaging: prediction of IDH mutation status and tumor progression.** *AJNR Am J Neuroradiol* 2016;37:66–73 CrossRef Medline
60. Hashimoto T, Ikehira H, Fukuda H, et al. **In vivo sodium-23 MRI in brain tumors: evaluation of preliminary clinical experience.** *Am J Physiol Imaging* 1991;6:74–80
61. Regnery S, Behl NG, Platt T, et al. **Ultra-high-field sodium MRI as biomarker for tumor extent, grade and IDH mutation status in glioma patients.** *Neuroimage Clin* 2020;28:102427 CrossRef Medline
62. Xing Z, Yang X, She D, et al. **Noninvasive assessment of IDH mutational status in World Health Organization grade II and III astrocytomas using DWI and DSC-PWI combined with conventional MR imaging.** *AJNR Am J Neuroradiol* 2017;38:1138–44 CrossRef Medline
63. Li Y, Shan X, Wu Z, et al. **IDH1 mutation is associated with a higher preoperative seizure incidence in low-grade glioma: a systematic review and meta-analysis.** *Seizure* 2018;55:76–82 CrossRef Medline
64. Ozer B, Bui Y, Markovic D, et al. **NCMP-01: seizure control after initial presentation in IDH mutated glioma patients.** *Neuro Oncol* 2017;19(Supple 6):vi135–36 CrossRef
65. Laymon CM, Oborski MJ, Lee VK, et al. **Combined imaging biomarkers for therapy evaluation in glioblastoma multiforme:**

correlating sodium MRI and F-18 FLT PET on a voxel-wise basis. *Magn Reson Imaging* 2012;30:1268–78 CrossRef Medline
66. Haneder S, Giordano FA, Konstandin S, et al. **^{23}Na-MRI of recurrent glioblastoma multiforme after intraoperative radiotherapy: technical note.** *Neuroradiology* 2015;57:321–26 CrossRef Medline
67. Schepkin VD. **Sodium MRI of glioma in animal models at ultrahigh magnetic fields.** *NMR Biomed* 2016;29:175–86 CrossRef Medline
68. Winter PM, Poptani H, Bansal N. **Effects of chemotherapy by 1,3-bis(2-chloroethyl)-1-nitrosourea on single-quantum- and triple-quantum-filtered ^{23}Na and ^{31}P nuclear magnetic resonance of the subcutaneously implanted 9L glioma.** *Cancer Res* 2001;61:2002–07 Medline
69. Dijkstra K, Hofmeijer J, van Gils SA, et al. **A biophysical model for cytotoxic cell swelling.** *J Neurosci* 2016;36:11881–90 CrossRef Medline
70. Dani KA, Warach S. **Metabolic imaging of ischemic stroke: the present and future.** *AJNR Am J Neuroradiol* 2014;35:S37–43 CrossRef Medline
71. Thulborn KR, Gindin TS, Davis D, et al. **Comprehensive MR imaging protocol for stroke management: tissue sodium concentration as a measure of tissue viability in nonhuman primate studies and in clinical studies.** *Radiology* 1999;213:156–66 CrossRef Medline
72. Wang Y, Hu W, Perez-Trepichio AD, et al. **Brain tissue sodium is a ticking clock telling time after arterial occlusion in rat focal cerebral ischemia.** *Stroke* 2000;31:1386–91; discussion 92 CrossRef Medline
73. Hussain MS, Stobbe RW, Bhagat YA, et al. **Sodium imaging intensity increases with time after human ischemic stroke.** *Ann Neurol* 2009;66:55–62 CrossRef Medline
74. Neumaier-Probst E, Konstandin S, Ssozi J, et al. **A double-tuned (1) H/(23) Na resonator allows (1) H-guided (23)Na-MRI in ischemic stroke patients in one session.** *Int J Stroke* 2015;10:56–61 CrossRef Medline
75. Shen JM, Xia XW, Kang WG, et al. **The use of MRI apparent diffusion coefficient (ADC) in monitoring the development of brain infarction.** *BMC Med Imaging* 2011;11:2 CrossRef Medline
76. Tsang A, Stobbe RW, Asdaghi N, et al. **Relationship between sodium intensity and perfusion deficits in acute ischemic stroke.** *J Magn Reson Imaging* 2011;33:41–47 CrossRef Medline
77. Cressman JR Jr, Ullah G, Ziburkus J, et al. **The influence of sodium and potassium dynamics on excitability, seizures, and the stability of persistent states, I: single neuron dynamics.** *J Comput Neurosci* 2009;26:159–70 CrossRef Medline
78. Kunz WS, Kudin AP, Vielhaber S, et al. **Mitochondrial complex I deficiency in the epileptic focus of patients with temporal lobe epilepsy.** *Ann Neurol* 2000;48:766–73 Medline
79. Folbergrová J, Kunz WS. **Mitochondrial dysfunction in epilepsy.** *Mitochondrion* 2012;12:35–40 CrossRef Medline
80. Dietzel I, Heinemann U, Hofmeier G, et al. **Stimulus-induced changes in extracellular Na+ and Cl- concentration in relation to changes in the size of the extracellular space**. *Exp Brain Res* 1982;46:73–84 CrossRef Medline
81. Antonio LL, Anderson ML, Angamo EA, et al. **In vitro seizure-like events and changes in ionic concentration.** *J Neurosci Methods* 2016;260:33–44 CrossRef
82. Patel DC, Tewari BP, Chaunsali L, et al. **Neuron-glia interactions in the pathophysiology of epilepsy.** *Nat Rev Neurosci* 2019;20:282–97 CrossRef Medline
83. Wang Y, Majors A, Najm I, et al. **Postictal alteration of sodium content and apparent diffusion coefficient in epileptic rat brain induced by kainic acid.** *Epilepsia* 1996;37:1000–06 CrossRef Medline

A Combined Radiomics and Machine Learning Approach to Overcome the Clinicoradiologic Paradox in Multiple Sclerosis

G. Pontillo, S. Tommasin, R. Cuocolo, M. Petracca, N. Petsas, L. Ugga, A. Carotenuto, C. Pozzilli, R. Iodice, R. Lanzillo, M. Quarantelli, V. Brescia Morra, E. Tedeschi, P. Pantano, and S. Cocozza

ABSTRACT

BACKGROUND AND PURPOSE: Conventional MR imaging explains only a fraction of the clinical outcome variance in multiple sclerosis. We aimed to evaluate machine learning models for disability prediction on the basis of radiomic, volumetric, and connectivity features derived from routine brain MR images.

MATERIALS AND METHODS: In this retrospective cross-sectional study, 3T brain MR imaging studies of patients with multiple sclerosis, including 3D T1-weighted and T2-weighted FLAIR sequences, were selected from 2 institutions. T1-weighted images were processed to obtain volume, connectivity score (inferred from the T2 lesion location), and texture features for an atlas-based set of GM regions. The site 1 cohort was randomly split into training ($n = 400$) and test ($n = 100$) sets, while the site 2 cohort ($n = 104$) constituted the external test set. After feature selection of clinicodemographic and MR imaging–derived variables, different machine learning algorithms predicting disability as measured with the Expanded Disability Status Scale were trained and cross-validated on the training cohort and evaluated on the test sets. The effect of different algorithms on model performance was tested using the 1-way repeated-measures ANOVA.

RESULTS: The selection procedure identified the 9 most informative variables, including age and secondary-progressive course and a subset of radiomic features extracted from the prefrontal cortex, subcortical GM, and cerebellum. The machine learning models predicted disability with high accuracy (r approaching 0.80) and excellent intra- and intersite generalizability ($r \geq 0.73$). The machine learning algorithm had no relevant effect on the performance.

CONCLUSIONS: The multidimensional analysis of brain MR images, including radiomic features and clinicodemographic data, is highly informative of the clinical status of patients with multiple sclerosis, representing a promising approach to bridge the gap between conventional imaging and disability.

ABBREVIATIONS: DD = disease duration; EDSS = Expanded Disability Status Scale; IQR = interquartile range; MAE = mean absolute error; ML = machine learning; MS = multiple sclerosis; WBV = whole-brain volume

MR imaging is firmly established as a fundamental tool for the diagnosis[1] and monitoring[2] of multiple sclerosis (MS), with MR imaging features commonly used as surrogate markers of disease activity in both clinical trials[3] and routine clinical practice.[4] However, conventional MR imaging measures (ie, the number, volume, and gadolinium enhancement of WM lesions) explain only a small fraction of the diversity of clinical outcomes in MS,[5] with this mismatch traditionally referred to as the "clinicoradiologic paradox."[6] The reasons for this apparent dissociation are manifold, embracing the difficulty to both define and measure clinical disability and the inability of conventional MR imaging to exhaustively characterize CNS structural and functional modifications in MS.[6] From a clinical standpoint, the Expanded Disability Status Scale (EDSS) score remains the most widely used outcome measure to assess MS-related disability in clinical trials.[7] From a neuroimaging perspective, however, many research studies have attempted to address these blind spots, leveraging advanced MR imaging techniques to identify clinically relevant disease biomarkers

Received November 7, 2020; accepted after revision July 12, 2021.

From the Departments of Advanced Biomedical Sciences (G.P., L.U., E.T., S.C.), Electrical Engineering and Information Technology (G.P., M.Q.), Clinical Medicine and Surgery (R.C.), Laboratory of Augmented Reality for Health Monitoring (R.C.), Department of Electrical Engineering and Information Technology, and Department of Neurosciences and Reproductive and Odontostomatological Sciences (M.P., A.C., R.I., R.L., V.B.M.), University of Naples "Federico II," Naples, Italy; Department of Human Neuroscience (S.T., C.P., P.P.), Sapienza University of Rome, Rome, Italy; Istituto di Ricovero e Cura a Carattere Scientifico Istituto Neurologico Mediterraneo (N.P., P.P.), Pozzilli, Italy; and Institute of Biostructure and Bioimaging (M.Q.), National Research Council, Naples, Italy.

Please address correspondence to Renato Cuocolo, MD, PhD, Department of Clinical Medicine and Surgery, University of Naples "Federico II," Naples, Italy; e-mail: renato.cuocolo@unina.it; @renatocuocolo

Indicates article with online supplemental data.

http://dx.doi.org/10.3174/ajnr.A7274

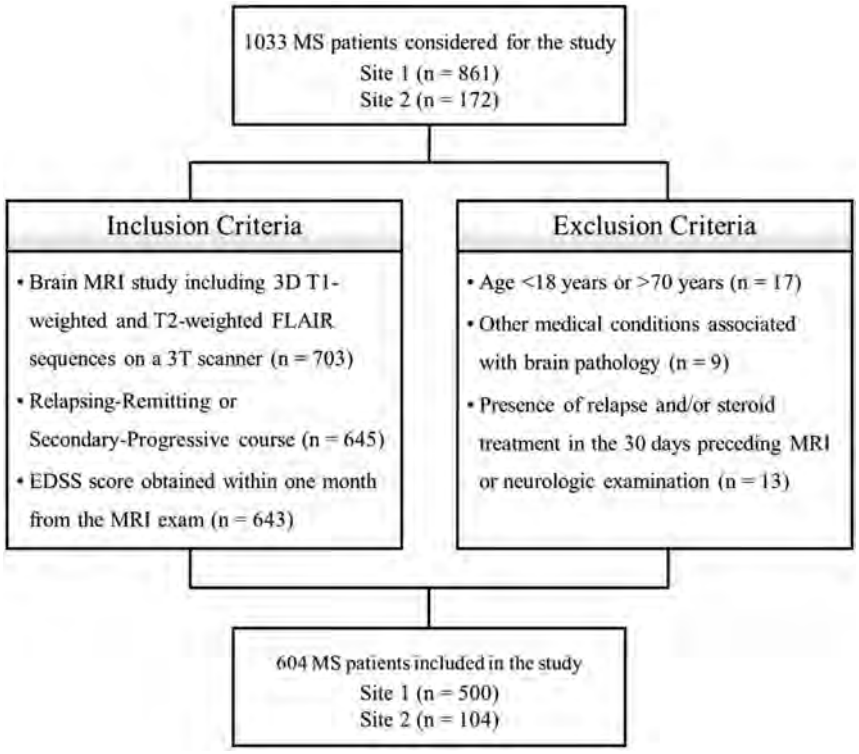

FIG 1. Flow diagram showing inclusion and exclusion criteria.

(eg, brain global and regional atrophy,[8] spinal atrophy,[9] cortical lesions,[10] microstructural damage of normal-appearing white matter, normal-appearing white matter,[11] and GM[12] changes of structural and functional brain networks[13]) that have the potential to bridge the gap between MR imaging and disability in MS and are progressively being integrated into clinical scenarios.

Of note, technical advances and the implementation of imaging guidelines[2,14] have led to the widespread availability of good-quality clinical scans, including isotropic sequences suitable for volumetric quantifications.[8] Furthermore, new promising connectomic approaches have shifted the emphasis from the sole quantification of total lesion burden to the functional consequences of WM damage in terms of brain network economy,[13] which can also be coarsely inferred from macroscopic T2 lesions.[15] Finally, the diffusion of radiomics has considerably augmented the amount of potentially meaningful information extractable from clinical images,[16] with machine learning (ML) methods providing the means for more flexible modeling of high-dimensional neuroimaging data sets compared with traditional statistical approaches.[17]

Given this background, we aimed to conceptually address the "clinicoradiologic paradox" in MS by evaluating machine learning models for EDSS score prediction on the basis of a systematic mapping of textural, volumetric, and macrostructural disconnection features derived from routine brain MR images. The results were validated by external testing on a separate data set obtained from a second institution.

MATERIALS AND METHODS

Subjects

In this retrospective cross-sectional study, brain MR imaging studies of consecutive patients with an MS diagnosis revised according to the 2010 McDonald criteria[18] and a relapsing-remitting or secondary-progressive[19] course including 3D T1-weighted and T2-weighted FLAIR sequences were selected from the radiologic databases of 2 institutions: the MS Center of the University of Naples "Federico II" (site 1) and the Human Neuroscience Department of the University of Rome "Sapienza" (site 2). All studies were performed between October 2006 and January 2020. Clinical disability was estimated using EDSS scores obtained within 1 month of the MR imaging. Exclusion criteria were as follows: younger than 18 years of age or older than 70 years of age; other pre-existing major systemic, psychiatric, or neurologic disorders; and the presence of a relapse and/or steroid treatment in the 30 days preceding the MR imaging (Fig 1).

The study was conducted in compliance with the ethical standards and approved by the local Ethics Committees, and written informed consent was obtained from all subjects according to the Declaration of Helsinki.

MR Imaging Data Acquisition

All MR images were acquired with a 3T scanner and included a 3D T1-weighted sequence (≤1-mm isotropic resolution) for volumetric analyses and a T2-weighted FLAIR sequence for quantifying total demyelinating lesion volume. Details about sequence parameters are provided in the Online Supplemental Data.

MR Imaging Data Processing

A flow chart summarizing the data-processing pipeline is available in Fig 2, while a complete description of all processing steps is provided in the Online Supplemental Data.

Volumetric Analysis. Demyelinating lesions were automatically segmented on FLAIR images using the Lesion Segmentation Tool (LST), Version 3.0.0 (www.statistical-modelling.de/lst.html) for SPM (http://www.fil.ion.ucl.ac.uk/spm/software/spm12). Lesion probability maps were used to fill lesions in T1-weighted images for subsequent processing steps and binarized to compute total lesion volume.

Filled T1-weighted volumes underwent the segmentation pipeline implemented in the Computational Anatomy Toolbox (CAT12.6; http://www.neuro.uni-jena.de/cat) in SPM to obtain an atlas-based parcellation into 114 brain regions defined according to the CAT12-adapted version of the Automated Anatomical

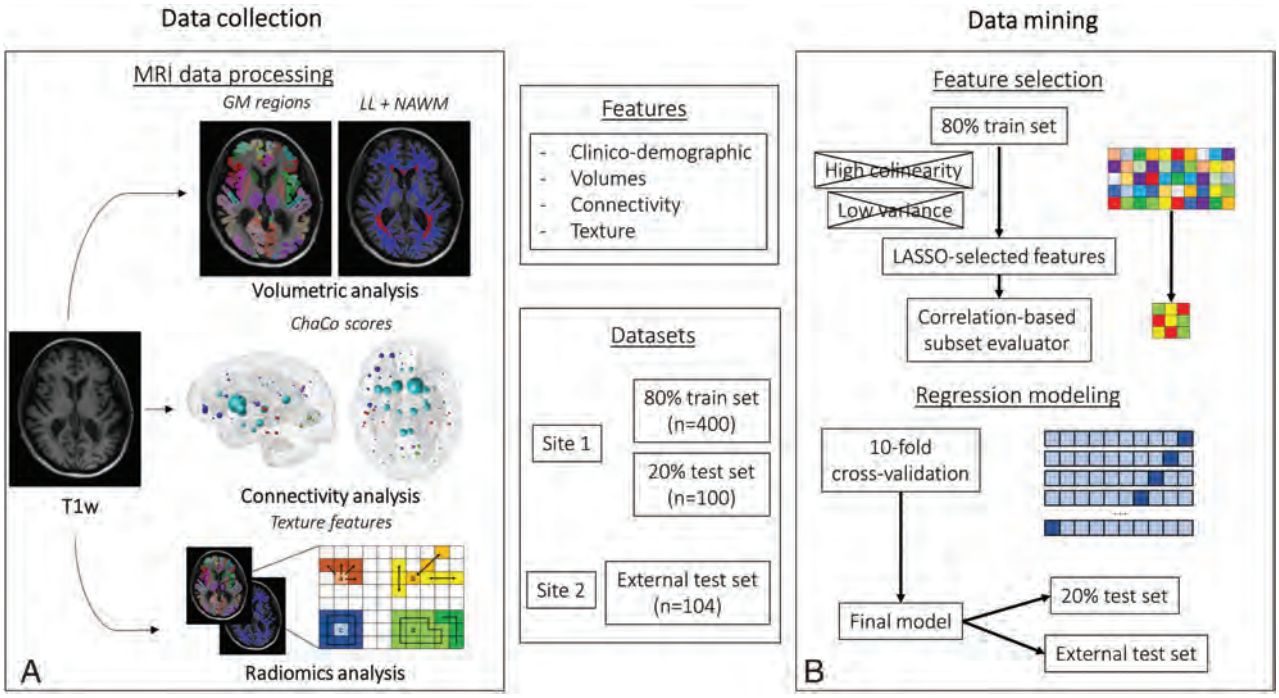

FIG 2. Workflow summarizing the main MR imaging data-processing and data-mining steps. Image illustrates the data set composition as well as the major steps performed for feature extraction, feature selection, and regression modeling. LL indicates lesion load; NAWM, normal-appearing white matter; ChaCo, change in connectivity; T1w, T1-weighted imaging.

Labeling atlas (https://github.com/muschellij2/aal).[20] Furthermore, whole-brain volume (WBV), GM subregion ROIs (and corresponding volumes), and normal-appearing white matter masks were also derived from the segmentation procedure.

Finally, total intracranial volume was estimated using CAT12, and brain volumes (both WBV and GM regions) were transformed into *z* scores while adjusting for age, sex, and estimated total intracranial volume.

Connectivity Analysis. Subject-wise, for each of the 116 GM cortical/subcortical regions defined in the Automated Anatomical Labeling atlas,[20] a change in the connectivity score was computed using the Network Modification (NeMo) tool,[15] representing an estimate of local structural disconnection caused by WM tract disruption, as inferred from the location and load of WM lesions.

Radiomics Analysis. First-order and texture features were extracted from each segmentation-derived ROI (normal-appearing white matter and 114 GM regions) from the unfilled T1-weighted volumes using PyRadiomics, Version 3.0.[21] Before the extraction, the images underwent standard preprocessing steps. An exhaustive description of the features obtainable by PyRadiomics is available in the official documentation (https://pyradiomics.readthedocs.io/en/latest/features.html).

Radiomics feature stability with respect to the MR imaging processing pipeline was tested on a subset of 30 randomly selected subjects, and only features with excellent stability (intraclass correlation coefficient ≥ 0.90) were retained for subsequent analyses.

Machine Learning

ML analyses were performed using the Weka data mining platform (Version 3.8.3; http://old-www.cms.waikato.ac.nz/~ml/weka/)[22] and scikit-learn Python package (https://scikit-learn.org/stable/index.html).[23] Given the nature of the EDSS score, regression algorithms were used to develop predictive models, with several algorithms (ie, ridge regression, support-vector machine, random forest, and Gaussian process) investigated to assess differences in performance due to model architecture. A description of the ML algorithms is provided in the Online Supplemental Data.

The site 1 cohort was randomly split into training (80% of subjects) and test (20% of subjects) sets for model tuning and testing, respectively, while the site 2 cohort was exclusively used as an external test set. After data-preprocessing (details in the Online Supplemental Data), clinicodemographic (age, sex, disease duration [DD], disease course), textural, and other MR imaging–derived (T2 lesion volume, WBV, and change in connectivity scores for each GM region) variables underwent multiple feature-selection steps on the training set. First, low variance (0.01 threshold) and highly colinear (>0.8) features were removed. Then, LASSO regression (https://www.lasso.io/), using the EDSS score as the dependent variable, was used to remove features whose coefficients shrank to zero. Finally, the Weka correlation–based subset evaluator was used to identify the best feature subset for EDSS prediction.

The resulting data set was used to train the 4 ML regression algorithms, whose tuning and initial performance evaluation were performed using 10-fold cross-validation in the training cohort (80% of site 1 data). Each final model was then assessed on the previously unseen cases of both the internal (remaining 20% of site 1 data) and external (site 2 data) test sets.

Table 1: Clinicodemographic characteristics of the studied population, along with MR imaging–derived global brain volumes[a]

	Site 1 ($n = 500$)	Site 2 ($n = 104$)	*P* Value (Site 1 vs Site 2)
Age (mean) (yr)	37.5 (SD, 10.9)	38.3 (SD, 9.8)	.49
Female sex (No.) (%)	349 (69.8)	80 (76.9)	.16
Secondary-progressive course (No.) (%)	72 (14.4)	20 (19.2)	.23
DD (mean) (yr)	9.3 (SD, 8.1)	9.2 (SD, 8.5)	.83
EDSS (median) (IQR)	2.5 (2.0–4.0)	2.0 (1.5–4.0)	.03
TLV (mean) (mL)	10.6 (SD, 13.4)	7.2 (SD, 8.6)	.05
WBV (mean) (mL)	1026.1 (SD, 116.3)	1042.6 (SD, 117.4)	.48

Note:—TLV indicates total lesion volume.
[a] Between-group differences regarding MR imaging measures are adjusted for age, sex, and estimated total intracranial volume.

As an ancillary analysis, the models were retrained using clinicodemographic features exclusively, to indirectly assess the incremental benefit provided by imaging-derived measures.

Statistical Analysis

Statistical analyses were performed using the Statistical Package for the Social Sciences (SPSS, Version 25.0; IBM) with a significance level $\alpha = .05$. Between-site differences in terms of clinicodemographic variables were tested using the Student *t* test (age and disease duration), Fisher exact test (sex and disease course), and median test (EDSS), respectively. The effect of different ML algorithms on model performance was tested using 1-way repeated measures ANOVA with absolute errors as the dependent variable, including post hoc tests to compare each pair of predictive models, Bonferroni-corrected for controlling the family-wise error rate.

RESULTS

Subjects

A total of 500 patients with MS were selected from site 1 (428 relapsing-remitting, 72 secondary-progressive; mean age, 37.5 [SD, 10.9] years; male/female ratio = 151:349; mean disease duration = 9.3 [SD, 8.1] years). After the data set split, 400 subjects from site 1 constituted the training set, and 100 subjects, the internal test set. From site 2, one hundred four demographically and clinically comparable patients (84 relapsing-remitting, 20 secondary-progressive; mean age, 38.3 [SD, 9.8] years; male/female ratio = 24:80; mean disease duration = 9.2 [SD, 8.5] years) were included in the external test set.

The median EDSS score was 2.5 (interquartile range [IQR] = 2.0–4.0) and 2.0 (IQR = 1.5–4.0) for patients from sites 1 and 2, respectively ($P = .03$). In the overall study population, patients with secondary-progressive MS showed a higher EDSS score (median, 5.5; IQR = 4.5–6.0) than those with relapsing-remitting MS (median, 2.5; IQR = 2.0–3.5) ($P < .001$, accounting for age, sex, and disease duration). Demographic and clinical variables of all subjects included in the study are reported in Table 1.

MR Imaging Data Analyses and ML Predictive Models

For each participant, MR imaging–derived global (T2 lesion volume and WBV, also reported in Table 1) and regional (114 GM regions) brain volumes were computed, along with the change in connectivity scores corresponding to the 116 GM parcels of the Automated Anatomical Labeling atlas.

Furthermore, a total of 125,580 radiomics features were extracted from the 115 segmentation-derived ROIs (normal-appearing white matter and 144 GM regions), of which 43 were excluded as having nonexcellent reproducibility.

The feature-selection procedure, performed on the training cohort, identified 4907 low-variance and 99,312 highly colinear features. At LASSO regression, 21 features were selected, further reduced to 9 by the subset evaluator. These consisted of age and secondary-progressive course in addition to a subset of radiomic features (details in Table 2), which were then used to train the ML algorithms for EDSS score prediction. The trained model hyperparameters and ridge regression feature weights are available in the Online Supplemental Data.

Correlation coefficients (*r*) of the final models predicting EDSS scores in the 10-fold cross-validation in the training cohort ranged from 0.79 ($R^2 = 0.62$, mean absolute error [MAE] = 0.66) for the random forest model to 0.80 ($R = 0.64$, MAE = 0.65) for ridge regression. On the internal test set, performances ranged from $r = 0.73$ ($R = 0.54$, MAE = 0.87) for Gaussian process regression to $r = 0.74$ ($R^2 = 0.55$, MAE = 0.72) for ridge regression, while in the external test set, they ranged from $r = 0.755$ ($R = 0.570$, MAE = 1.155) for ridge regression to $r = 0.799$ ($R^2 = 0.638$, MAE = 1.247) for Gaussian process regression (Table 3).

There was a significant effect of the ML algorithm on the model performance in both the internal [$F(1.82, 180.39) = 7.94$] ($P = .001$) and external [$F(1.70, 175.52) = 5.25$] ($P = .009$) test sets. In particular, on the internal test set, Gaussian process regression performed significantly worse than all other algorithms (Bonferroni-corrected $P \leq .01$), while support-vector machine regression performed significantly better than Gaussian process regression on the external test set (Bonferroni-corrected $P < .001$). Details of the pair-wise comparisons between different model performances are reported in the Online Supplemental Data.

As for the ancillary analysis, while it was clear that clinical features substantially contribute to EDSS prediction, with ridge regression and support-vector machine regression yielding the best overall results on the external test set ($r = 813$, MAE = 1.005 and $r = 0.814$, MAE = 0.945, respectively), models using these alone were much less consistent across the 3 data sets, with performance varying greatly on the basis of algorithm architecture (Online Supplemental Data).

DISCUSSION

In this study, we proved that predictive models based on textural features extracted from routine brain MR images, along with basic clinicodemographic data, correlate with clinical disability in patients with MS with high accuracy and intra- and intersite generalizability.

Since its earliest days, MR imaging research in MS has had the objective of unraveling the relationship between neuroradiologic

Table 2: Selected radiomics features[a]

Anatomic Label	Feature Class	Class Characteristics	Feature	Feature Characteristics
Right frontal superior orbital cortex	First order	Describes the distribution of voxel intensities	Median	The median gray level intensity
Left amygdala	Gray level co-occurrence matrix	Quantifies how often pairs of pixels with specific values occur in a specified spatial range	Correlation	Measures the linear dependency of gray level values to their respective voxels in the matrix
Left caudate nucleus	Gray level co-occurrence matrix	Quantifies how often pairs of pixels with specific values occur in a specified spatial range	Informational measure of correlation 1	Quantifies the complexity of the texture
Right thalamus	First order	Describes the distribution of voxel intensities	Energy	Measures the magnitude of voxel values
Left cerebellar lobule VIII	Gray level dependence matrix	Quantifies gray level dependencies (ie, the number of connected voxels within a set distance that are dependent on the center voxel)	Small dependence low gray level emphasis	Measures the joint distribution of small dependence with higher gray-level values
Cerebellar vermis (lobules IV–V)	Gray level size-zone matrix	Quantifies gray level zones (ie, the number of connected voxels sharing the same intensity value)	Size-zone non-uniformity	Measures the variability of size-zone volumes
Left cerebellar crus	First order	Describes the distribution of voxel intensities	Median	Median gray level intensity

[a] Characteristics of each selected feature and relative class according to PyRadiomics official documentation (https://pyradiomics.readthedocs.io/en/latest/features.html) are presented, along with the anatomic location (according to Tzourio-Mazoyer et al[20]) of the corresponding ROI.

Table 3: Machine learning predictive models[a]

	Ridge Regression			Gaussian Process			Support-Vector Machine			Random Forest			
Cohort	*r*	R^2	MAE	*r*	R^2	MAE	*r*	R^2	MAE	*r*	R^2	MAE	*P* Value
Training	0.797	0.636	0.651	0.795	0.632	0.814	0.797	0.635	0.710	0.790	0.624	0.656	–
Internal test	0.741	0.549	0.725	0.733	0.537	0.874	0.734	0.538	0.754	0.734	0.539	0.740	.001[a]
External test	0.755	0.570	1.155	0.799	0.638	1.247	0.794	0.631	1.112	0.775	0.600	1.162	.009[b]

Note:—– indicates not available.
[a] $F(1.82, 180.39) = 7.94$. Partial $\eta^2 = 0.07$. *df* corrected using Greenhouse-Geisser estimates of sphericity ($\varepsilon = 0.61$).
[b] $F(1.70, 175.52) = 5.25$. Partial $\eta^2 = 0.05$. *df* corrected using Greenhouse-Geisser estimates of sphericity ($\varepsilon = 0.57$).

imaging and clinical status.[24] Indeed, several studies investigated the association between conventional MR imaging markers of MS pathology and EDSS, reporting correlation coefficients ranging from 0.15 to 0.60[24] and nurturing the concept of a "clinicoradiologic paradox."[6] Through the years, many of the confounders sustaining this apparent contradiction have been addressed, with emphasis on a more specific characterization of CNS structural and functional modifications through advanced MR imaging techniques and a finer assessment of MS-related disability, including the evaluation of cognitive performance.[5]

Most interesting, a more recent study has dealt with this classic issue using a multivariate statistical analysis of local intensity patterns on conventional MR images of a small homogeneous sample of patients with MS, leading to promising results.[25] The potential of ML in the analysis of MR imaging data in MS is also highlighted by another recent study using models based on FLAIR images and demographic information for the prediction of 2-year clinical disability and achieving a mean squared error of 3 (corresponding to a mean EDSS score error of 1.7).[26] Furthermore, studies with a large number of subjects demonstrated the clinical relevance of automatic volumetric quantifications, systematically mapping brain anatomy at both global and regional levels on clinical MR images of patients with MS.[27,28]

In our work, we revisited the conventional MR imaging/clinical disability dissociation problem in the light of recent developments in the fields of radiomics and ML modeling, exploring the informative value of volumetric, macrostructural disconnection and textural features derived from routine MR images of a large multisite cohort of patients with MS. We found that ML models based on radiomics features extracted from specific brain regions, along with basic clinicodemographic data, are highly predictive of the EDSS score (*r* approaching 0.80, about 64% of shared variance),

demonstrating excellent intra- and intersite generalizability ($r \geq 0.73$, about 53% of shared variance). Of note, the ML algorithm had little effect on the predictive performance, with similar prediction errors across models, indicating substantial model-independence of our findings. Also, as per our ancillary analysis, while clinicodemographic variables alone were highly informative of patients' clinical status, the inclusion of radiomics features in the models substantially increased the generalizability and stability across different ML algorithms, supporting the additional value of a holistic approach including a variety of data types/sources.

Although a meaningful comparison of effect sizes among studies is hindered by the variability of study design, sample size, and statistical methods, our study seemingly provides a sensible improvement compared with earlier works,[6] with sample width and external validation across different sites further strengthening our results.

Most interesting, our findings confirm that signal intensity patterns as assessed by the quantitative texture analysis of conventional brain MR images encode clinically relevant information,[25] apparently outperforming measures like volume or macrostructural disconnection in terms of shared variance with clinical disability. Indeed, textural features may capture subtle modifications of brain tissue microstructure, which are known to correlate with clinical status in patients with MS.[12] Furthermore, the systematic mapping of different brain regions through atlas-based automatic segmentation of T1-weighted volumes may enhance radiomics analysis by adding anatomic specificity, with most informative features in our models extracted from areas whose pathologic modifications are known to impact the clinico-cognitive performance (ie, prefrontal cortex,[29] deep gray matter,[27] and cerebellum[30]). Conversely, a simpler shape feature like volume, as well as the coarse estimation of GM structural disconnection as inferred by T2 lesion location, may represent less pathologically specific disease markers, therefore providing a minor contribution to explaining MS-related disability.

To date, few studies have explored the potential of radiomics in MS, mainly focusing on the analysis of WM lesions for diagnostic classification purposes,[31,32] with alterations of brain tissue microstructure mostly characterized through advanced MR imaging techniques,[33,34] which provide more neurobiologically interpretable results but require dedicated acquisitions that are difficult to implement in large-scale population studies. Nevertheless, the systematic radiomics analysis of conventional brain MR images may hide a huge unused potential, promising to exploit the maximum clinically meaningful information contained in neuroradiologic images, taking full advantage of a massive amount of clinical MR imaging data collected through the years.

Some limitations of the current study should be acknowledged. First, using EDSS as a measure of clinical severity has several shortcomings, including incomplete coverage of CNS domains, nonlinearity, low sensitivity, and inter- and intraobserver variability.[35] However, despite these limitations and the availability of alternative rating scales, the EDSS is still considered the reference method to assess MS-related disability in both clinical trials and routine, therefore being more scalable to real-world scenarios.[35] Furthermore, it is known that radiomics features may have instability due to variations in scanner and image-acquisition parameters.[36] Nevertheless, this issue may be mitigated by the combined evaluation of basic clinicodemographic variables and other MR imaging–derived metrics with proved robustness (eg, automatic volumetric quantifications[8]) as suggested by the excellent generalizability of our models across different sequences and scanners. Finally, our work paves the way for future studies exploiting the proposed methodologic framework to predict longitudinal clinical outcomes, possibly providing a tool for effective prognostic stratification of patients with MS in clinical practice.

CONCLUSIONS

We demonstrated that the multidimensional analysis of routine brain MR images, including the systematic investigation of textural features in conjunction with basic clinicodemographic data, is highly informative of the clinical status of patients with MS. In the era of big data, this approach may represent a way of filling the gap between conventional imaging and clinical disability in MS.

Disclosures: Maria Petracca—*UNRELATED*: *Travel/Accommodations/Meeting Expenses Unrelated to Activities Listed*: travel sponsorship from Novartis. Nikolaos Petsas—*UNRELATED*: *Consultancy*: Istituto di Ricovero e Cura a Carattere Scientifico Istituto Neurologico Mediterraneo, Pozzilli, Italy; *Employment*: Sapienza University of Rome, Italy; *Grants/Grants Pending*: Onlus Sant'Andrea, Rome, Italy.* Carlo Pozzilli—*UNRELATED*: *Board Membership*: Merck, Biogen, Novartis, Bristol Myers Squibb, Almirall, Sanofi, Roche; *Consultancy*: Novartis; *Grants/Grants Pending*: Merck, Roche, Biogen*; *Payment for Lectures Including Service on Speakers Bureaus*: Almirall, Bayer, Biogen, Genzyme, Merck Serono, Novartis, Roche and Teva; *Payment for Manuscript Preparation*: Merck, Biogen, Roche; *Payment for Development of Educational Presentations*: Multiple Sclerosis Paradigm. Vincenzo Brescia Morra—*UNRELATED*: *Consultancy*: Biogen, Teva Pharmaceutical Industries, Genzyme, Merck, Novartis and Almirall; *Payment for Lectures Including Service on Speakers Bureaus*: Biogen, Teva Pharmaceutical Industries, Genzyme, Merck, Novartis, and Almirall. Patrizia Pantano—*UNRELATED*: *Grants/Grants Pending*: Fondazione Italiana Sclerosi Multipla, Sapienza University.* Sirio Cocozza—*UNRELATED*: *Board Membership*: Amicus Therapeutics, *Comments*: fees for Advisory Board; *Payment for Lectures Including Service on Speakers Bureaus*: Sanofi, Amicus, *Comments*: fees for speaking. *Money paid to the institution.

REFERENCES

1. Rovira A, Wattjes MP, Tintore M, et al; MAGNIMS Study Group. **Evidence-based guidelines: MAGNIMS consensus guidelines on the use of MRI in multiple sclerosis: clinical implementation in the diagnostic process.** *Nat Rev Neurol* 2015;11:471–82 CrossRef Medline
2. Wattjes MP, Rovira A, Miller D, et al. **Evidence-based guidelines: MAGNIMS consensus guidelines on the use of MRI in multiple sclerosis: establishing disease prognosis and monitoring patients.** *Nat Rev Neurol* 2015;11:597–606 CrossRef Medline
3. van Munster CE, Uitdehaag BM. **Outcome measures in clinical trials for multiple sclerosis.** *CNS drugs* 2017;31:217–36 CrossRef Medline
4. Giovannoni G, Turner B, Gnanapavan S, et al. **Is it time to target no evident disease activity (NEDA) in multiple sclerosis?** *Mult Scler Relat Disord* 2015;4:329–33 CrossRef Medline
5. Chard D, Trip SA. **Resolving the clinico-radiological paradox in multiple sclerosis.** *F1000Res* 2017;6:1828 CrossRef Medline
6. Barkhof F. **The clinico-radiological paradox in multiple sclerosis revisited.** *Curr Opin Neurol* 2002;15:239–45 CrossRef Medline
7. Uitdehaag BM. **Disability outcome measures in Phase III clinical trials in multiple sclerosis.** *CNS Drugs* 2018;32:543–58 CrossRef Medline
8. Storelli L, Rocca MA, Pagani E, et al; MAGNIMS Study Group. **Measurement of whole-brain and gray matter atrophy in multiple sclerosis: assessment with MR imaging.** *Radiology* 2018;288:554–64 CrossRef Medline

9. Kearney H, Miller DH, Ciccarelli O. **Spinal cord MRI in multiple sclerosis–diagnostic, prognostic and clinical value.** *Nat Rev Neurol* 2015;11:327–38 CrossRef Medline
10. Calabrese M, Filippi M, Gallo P. **Cortical lesions in multiple sclerosis.** *Nat Rev Neurol* 2010;6:438–44 CrossRef Medline
11. Moll NM, Rietsch AM, Thomas S, et al. **Multiple sclerosis normal-appearing white matter: pathology-imaging correlations.** *Ann Neurol* 2011;70:764–73 CrossRef Medline
12. Pontillo G, Cocozza S, Lanzillo R, et al. **Determinants of deep gray matter atrophy in multiple sclerosis: a multimodal MRI study.** *AJNR Am J Neuroradiol* 2019;40:99–106 CrossRef Medline
13. Tewarie P, Steenwijk MD, Tijms BM, et al. **Disruption of structural and functional networks in long-standing multiple sclerosis.** *Hum Brain Mapp* 2014;35:5946–61 CrossRef Medline
14. Traboulsee A, Simon JH, Stone L, et al. **Revised Recommendations of the Consortium of MS Centers Task Force for a Standardized MRI Protocol and Clinical Guidelines for the Diagnosis and Follow-Up of Multiple Sclerosis.** *AJNR Am J Neuroradiol* 2016;37:394–401 CrossRef Medline
15. Kuceyeski A, Maruta J, Relkin N, et al. **The Network Modification (NeMo) tool: elucidating the effect of white matter integrity changes on cortical and subcortical structural connectivity.** *Brain Connect* 2013;3:451–63 CrossRef Medline
16. Gillies RJ, Kinahan PE, Hricak H. **Radiomics: images are more than pictures, they are data.** *Radiology* 2016;278:563–77 CrossRef Medline
17. Abraham A, Pedregosa F, Eickenberg M, et al. **Machine learning for neuroimaging with scikit-learn.** *Front Neuroinform* 2014;8:14 CrossRef Medline
18. Polman CH, Reingold SC, Banwell B, et al. **Diagnostic criteria for multiple sclerosis: 2010 revisions to the McDonald criteria.** *Ann Neurol* 2011;69:292–302 CrossRef Medline
19. Lublin FD. **New multiple sclerosis phenotypic classification.** *Eur Neurol* 2014;72 (Suppl 1):1–5 CrossRef Medline
20. Tzourio-Mazoyer N, Landeau B, Papathanassiou D, et al. **Automated anatomical labeling of activations in SPM using a macroscopic anatomical parcellation of the MNI MRI single-subject brain.** *Neuroimage* 2002;15:273–89 CrossRef Medline
21. van Griethuysen JJ, Fedorov A, Parmar C, et al. **Computational radiomics system to decode the radiographic phenotype.** *Cancer Res* 2017;77:e104–07 CrossRef Medline
22. Frank E, Hall M, Trigg L, et al. **Data mining in bioinformatics using Weka.** *Bioinformatics* 2004;20:2479–81 CrossRef Medline
23. Pedregosa F, Varoquaux G, Gramfort A, et al. **Scikit-learn: machine learning in Python.** *J Mach Learn Res* 2011;12:2825–30
24. Barkhof F. **MRI in multiple sclerosis: correlation with Expanded Disability Status Scale (EDSS).** *Mult Scler* 1999;5:283–86 CrossRef Medline
25. Hackmack K, Weygandt M, Wuerfel J, et al. **Can we overcome the 'clinico-radiological paradox' in multiple sclerosis?** *J Neurol* 2012;259:2151–60 CrossRef Medline
26. Roca P, Attye A, Colas L, et al; OFSEP Investigators; Steering Committee; Investigators; Imaging Group. **Artificial intelligence to predict clinical disability in patients with multiple sclerosis using FLAIR MRI.** *Diagn Interv Imaging* 2020;101:795–802 CrossRef Medline
27. Eshaghi A, Prados F, Brownlee WJ, et al; MAGNIMS Study Group, **Deep gray matter volume loss drives disability worsening in multiple sclerosis.** *Ann Neurol* 2018;83:210–22 CrossRef Medline
28. Azevedo CJ, Cen SY, Khadka S, et al. **Thalamic atrophy in multiple sclerosis: a magnetic resonance imaging marker of neurodegeneration throughout disease.** *Ann Neurol* 2018;83:223–24. CrossRef Medline
29. Feinstein A, Roy P, Lobaugh N, et al. **Structural brain abnormalities in multiple sclerosis patients with major depression.** *Neurology* 2004;62:586–90 CrossRef Medline
30. Cocozza S, Petracca M, Mormina E, et al. **Cerebellar lobule atrophy and disability in progressive MS.** *J Neurol Neurosurg Psychiatry* 2017;88:1065–72 CrossRef Medline
31. Liu Y, Dong D, Zhang L, et al. **Radiomics in multiple sclerosis and neuromyelitis optica spectrum disorder.** *Eur Radiol* 2019;29:4670–77 CrossRef Medline
32. Michoux N, Guillet A, Rommel D, et al. **Texture analysis of T2-weighted MR images to assess acute inflammation in brain MS lesions.** *PLoS One* 2015;10:e0145497 CrossRef Medline
33. Zivadinov R, Tavazzi E, Bergsland N, et al. **Brain iron at quantitative MRI is associated with disability in multiple sclerosis.** *Radiology* 2018;289:487–96 CrossRef Medline
34. Chen JT, Collins DL, Atkins HL, et al; Canadian MS/BMT Study Group. **Magnetization transfer ratio evolution with demyelination and remyelination in multiple sclerosis lesions.** *Ann Neurol* 2008;63:254–62 CrossRef Medline
35. Meyer-Moock S, Feng YS, Maeurer M, et al. **Systematic literature review and validity evaluation of the Expanded Disability Status Scale (EDSS) and the Multiple Sclerosis Functional Composite (MSFC) in patients with multiple sclerosis.** *BMC Neurol* 2014;14:58 CrossRef Medline
36. Bologna M, Corino V, Mainardi L. **Technical note: virtual phantom analyses for preprocessing evaluation and detection of a robust feature set for MRI-radiomics of the brain.** *Medical Phys* 2019;46:5116–23 CrossRef Medline

Imaging Features of Symptomatic MCA Stenosis in Patients of Different Ages: A Vessel Wall MR Imaging Study

H. Kang, J. Liang, Y. Zhang, Z. Li, X. Yang, and B. Sui

ABSTRACT

BACKGROUND AND PURPOSE: The prevalence of intracranial artery stenosis is high in Asian people. This study aimed to investigate whether there are differences in the imaging features of symptomatic MCA stenosis in patients of different ages using vessel wall MR imaging.

MATERIALS AND METHODS: We retrospectively reviewed the data of consecutive patients with unilateral MCA stenosis based on a prospectively established vessel wall MR imaging data base between January 2017 and December 2018. According to age, the patients were divided into the young group (18–45 years of age) and the middle-aged and elderly group (older than 45 years of age).

RESULTS: Overall, 131 patients with unilateral MCA stenosis were included (45.8% in the young group and 54.2% in the middle-aged and elderly group). Middle-aged and elderly patients had a higher prevalence of hypertension ($P = .01$) and diabetes ($P = .05$). The lesion length ($P < .0001$), proportion of circular involvement ($P = .006$), and proportion of circular enhancement ($P = .03$) were higher in the young group than in the middle-aged and elderly group. The analysis of the atherosclerotic subgroup showed that compared with middle-aged and elderly patients, young patients had longer lesions ($P = .002$). The atherosclerotic-versus-nonatherosclerotic subgroup analysis showed that the maximal wall thickness in the patients with atherosclerosis was larger than that of patients without it ($P = .002$).

CONCLUSIONS: Compared with the middle-aged and elderly group, young patients with MCA stenosis tended to have longer lesions and more circular wall involvement and circular enhancement, which may indicate the differences in underlying vascular pathophysiologic and developmental mechanisms in symptomatic MCA stenosis.

ABBREVIATIONS: AS = atherosclerosis; HR VW-MRI = high-resolution vessel wall MR imaging; MOP = middle-aged and elderly; NWI = normalized wall index; RI = remodeling index; SI = signal intensity

Ischemic stroke is an important cause of death and disability in adults. The incidence rate of ischemic stroke in young people has increased by 40% in the 2020s compared with the 2010s.[1,2]

Intracranial artery stenosis is an important cause of ischemic stroke and is more commonly found in Asian people. Although atherosclerosis (AS) is still considered the most common reason, the etiology of intracranial artery stenosis, especially in young people, is more complex and diverse, often making the clinical diagnosis difficult and uncertain.

Traditional imaging technologies, including CT angiography, MR angiography, and digital subtraction angiography, can provide information only on lumen stenosis, which has limited value in the etiologic differential diagnosis. In recent years, high-resolution vessel wall MR imaging (HR VW-MR imaging) has been increasingly applied in clinical practice. The technique has proved to be an optimal and reliable method to display intracranial vessel wall features. By directly visualizing the structure of the vessel wall and identifying the characteristics of lesions, HR-VW-MR imaging has shown great potential and application prospects in the evaluation of patients with intracranial artery stenosis.[3-9] It has been proposed that different vessel wall imaging

Received February 23, 2021; accepted after revision June 11.

From the Beijing Neurosurgical Institute (H.K., Y.Z., X.Y.), Beijing Tiantan Hospital, Capital Medical University, Beijing, China; Shijingshan Teaching Hospital of Capital Medical University (J.L.), Beijing Shijingshan Hospital, Beijing, China; and Tiantan Neuroimaging Center for Excellence (Z.L., B.S.), China National Clinical Research Center for Neurological Diseases, Beijing Tiantan Hospital, Capital Medical University, Beijing, China.

H. Kang and J. Liang share first authorship.

This work was supported by Beijing Municipal Natural Science Foundation (grant No. 7212028)

Please address correspondence to Binbin Sui, MD, Tiantan Neuroimaging Center of Excellence, Beijing Tiantan Hospital, Capital Medical University, Beijing, China, No.119 South Fourth Ring West Rd, Fengtai District, Beijing, 100050, China; e-mail: reneesui@163.com

http://dx.doi.org/10.3174/ajnr.A7268

features can be found in various diseases, including dissection, vasculitis, and Moyamoya disease,[10-12] and they can provide important information for clinical assessment.

Although it was reported that AS is still the most common cause of intracranial artery stenosis in young patients, multiple etiologies other than AS should be considered. It is generally believed that AS is more commonly found in older patients. With similar findings of artery stenosis by conventional MRA, different HR VW-MR imaging manifestations due to various stenosis mechanisms may be found in young and elderly groups. One previous study has shown that concentric wall thickening and enhancement on HR VW-MR imaging were found more commonly in patients younger than 35 years of age than in patients 35–45 years of age.[13] However, it is still unclear whether there are different HR VW-MR imaging features in patients of different ages, and there is no comparison study of HR VW-MR imaging features between young and middle-aged and elderly (MOP) patients. In this study, using HR VW-MR imaging, we sought to identify differences in the imaging features of stenosed MCA lesions of atherosclerosis and nonatherosclerotic disease in patients of different ages.

MATERIALS AND METHODS

Participants

We retrospectively reviewed the data of consecutive patients with unilateral MCA stenosis based on a prospectively established HR VW-MR imaging data base between January 2017 and December 2018. Our ethics committee approved this retrospective study, and the requirement for written informed consent was waived due to its retrospective nature. Consecutive patients with ipsilateral MCA stenosis were included. The inclusion criteria were as follows: 1) symptomatic patients who had an ischemic stroke or TIA, 2) unilateral MCA stenosis confirmed by CT angiography or MRA, or 3) the stenosed MCA ipsilateral to the ischemic lesion or responsible for the TIA and defined as the culprit (index) vessel by the neurologist and neuroradiologist. Patients were excluded for the following reasons: 1) definite cardiogenic embolism, such as a history of atrial fibrillation confirmed by electrocardiogram or a Holter monitor within 1 month or a recent history of myocardial infarction, atrial septal defect, or left atrial/ventricular thrombosis confirmed by echocardiography; 2) extracranial carotid stenosis of >50%;[14] unstable plaques of the extracranial carotid artery that met 3 of the following 4 criteria: stenosis >70%, mainly hypoechoic on ultrasound images, superficial irregularity, and ulceration; 3) definite Moyamoya disease; 4) ipsilateral or bilateral MCA occlusion or bilateral MCA stenosis; or 5) poor MR image quality or lack of clinical data. The clinical data (including age, sex, smoking history, hypertension, diabetes, hyperlipidemia, and homocysteine) and the HR VW-MR imaging characteristics were reviewed and analyzed. According to age, the patients were divided into the young group (18–45 years of age) and the MOP group (older than 45 years of age).

MR Imaging Protocol

MR imaging was performed using 3T MR imaging scanners (Trio Tim, Siemens; Discovery 750, GE Healthcare; and Ingenia CX, Philips Healthcare) with a 32-channel head coil. The MR imaging protocol included 3D TOF-MRA, 3D T1WI (sampling perfection with application-optimized contrasts by using different flip angle evolution [SPACE sequence, Siemens]/Cube [GE Healthcare]/volume isotropic turbo spin-echo acquisition [VISTA]), 3D T2/PDWI proton-density weighted imaging (PDWI) (SPACE/CUBE/VISTA), 3D T1 MPRAGE, and contrast-enhanced 3D T1WI (SPACE/CUBE/VISTA). Postcontrast T1-weighted images were acquired 3 minutes after gadolinium injection (0.1 mmol/kg of gadopentetate dimeglumine, Magnevist; Bayer HealthCare Pharmaceuticals) using parameters identical to those of the precontrast T1-weighted images. The parameters of the imaging sequences are listed in the Online Supplemental Data.

Image Analysis

All MR images were transferred to a dedicated postprocessing workstation for analysis with Vessel Explorer software (Version 1.1; TsingHua Imaging Co). HR VW-MR imaging data were analyzed by 2 experienced neuroradiologists (J.L. and B.S.) independently, who were blinded to the clinical data. Differences between the 2 observers were solved by consensus.

The vessel centerline of the MCA was extracted automatically on TOF-MRA and copied to the precontrast 3D T1-weighted images. Then, oblique sagittal precontrast T1-weighted images were reconstructed perpendicular to the M1 segment of the relevant MCA with a reconstructed section thickness of 0.7 mm. The analysis plane was set as the maximal lumen narrowing site. The reference site was defined as the nearest lesion-free segment proximal or distal to the lumen narrowing site. Precontrast T1-weighted images were used for the main analysis, including the measurements of lumen and wall thickness at the analysis and reference planes, assessment of the wall thickening and involvement pattern, remodeling patterns, and the surface morphology. A 3D T1 MPRAGE sequence was used to identify intralesion hemorrhages. Postcontrast T1-weighted images were used for the enhancement assessment. 3D T2-weighted and proton-density weighted images were used as supplementary images if there was obscurity of the vessel wall on T1-weighted images.

The maximum wall thickness and lesion length were measured in the circumferential plane and along the longitudinal axis of the artery, respectively (Fig 1*A*). The degree of stenosis was calculated as follows: degree of stenosis = (1 − Lumen Area at the Maximal Lumen Narrowing Site/Reference Lumen Area) × 100%.[15,16] The normalized wall index (NWI) was calculated as follows: NWI = Wall Area/(Lumen Area + Wall Area).[17] The wall thickening, involvement pattern, and remodeling patterns of the index MCA were analyzed on precontrast T1-weighted images, as was the surface morphology. In the circumferential plane, the wall of the MCA was divided into 4 quadrants: namely, the superior wall, the inferior wall, the ventral wall, and the dorsal wall (Fig 1*B*); and circular involvement was defined as lesions involving all 4 quadrants. The pattern of wall thickening was classified as concentric or eccentric (Fig 1*C*, *-D*). Concentric stenosis was identified if the thinnest part of the vessel wall was estimated to have a thickness no less than 50% of the thickest point on all image slices or a stenosis without wall thickening.[6] Eccentric stenosis was diagnosed if the thinnest part of the vessel wall was estimated to have a thickness of <50% of the thickest point.[15] The remodeling index (RI)

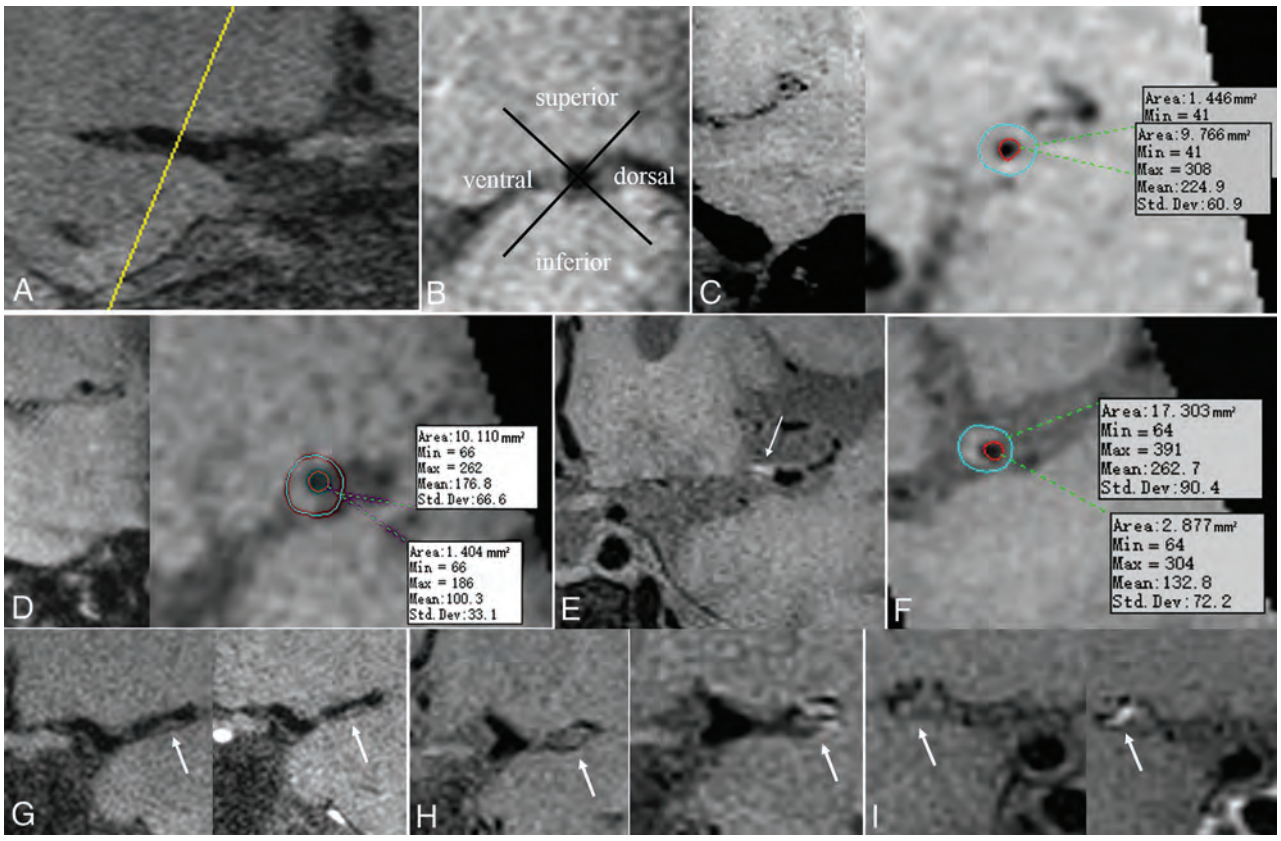

FIG 1. *A*, Normal MCA. *B*, Enlarged view perpendicular to the lumen section. The wall of the MCA is divided into 4 quadrants: namely, the upper wall, the lower wall, the ventral wall, and the dorsal wall. *C*, Annular thickening of the vessel wall, ie, concentricity. *D*, Eccentric thickening of the vessel wall. *E*, Local T1 hyperintensity in the M1 segment of the left MCA. *F*, An enlarged cross-section of the blood vessel at the lesion shows eccentric wall thickening and T1 hyperintensity. Degree of lesion enhancement: grade 0 (*G*); grade I (*H*); grade II (*I*). Min indicates minimum; Max, maximum, Std. Dev., standard deviation.

was calculated as follows: RI = Lumen Area at the Maximal Lumen Narrowing Site / Reference Lumen Area. RI ≥ 1.05 was considered positive remodeling, RI ≤ 0.95 was considered negative remodeling, and 0.95 < RI < 1.05 nonremodeling.[18]

Intralesion hemorrhage[19] was defined as high signal intensity (SI) in MCA lesions on 3D T1 MPRAGE images, with an SI of >150% of the adjacent brain parenchyma (Fig 1*E, -F*).[20] On post-contrast T1-weighted images, the degree of lesion enhancement was defined using the following grading criteria: grade 0, the degree of enhancement less than or equal to that of the adjacent normal arterial wall (Fig 1*G*); grade I, the degree of enhancement greater than grade 0 but lower than that of the pituitary funnel (Fig 1*H*); and grade II, the degree of enhancement greater than or equal to that of pituitary funnel enhancement (Fig 1*I*).[21]

Maaijwee et al[22] reported that traditional vascular risk factors in young adults, especially in patients between 35 and 50 years of age, have increased in prevalence, indicating a sharp rise. Therefore, we further conducted a subgroup analysis by dividing patients into the older than 35-year group and the 35-year-or-younger group. In addition, to clarify the difference in the characteristics of lesions between young and MOP patients with different degrees of stenosis, patients with stenosis of ≥50% and patients with stenosis of <50% were classified into different subgroups. We also performed subgroup analysis of confirmed atherosclerotic plaque cases. Atherosclerotic lesions were defined according to the following diagnostic criteria: The clinical diagnosis of AS required ≥2 vascular risk factors (hypertension, hyperlipidemia, diabetes mellitus, obesity, coronary artery disease, men older than 50 years of age, and women older than 60 years of age) and failure to meet the clinical criteria for CNS vasculitis or reversible cerebral vasoconstriction syndrome.[23] The typical HR-VW-MR imaging diagnosis of AS is based on eccentric, irregular, heterogeneous wall thickening with vessel wall enhancement and T2-weighted hyperintensity.[24] The diagnosis was confirmed by consensus of the neurologist, neurointerventional surgeon, and neuroradiologist. The clinical and imaging features of MCA AS were compared between young and MOP patients. The clinical and imaging features of intracranial atherosclerosis versus nonatherosclerosis were compared in the young group and the middle-aged and older group.

Statistical Analysis

The Statistical Package for the Social Sciences (SPSS 25.0; IBM) was used to analyze the differences between the 2 groups. The intraclass correlation coefficient was calculated to find the intraobserver and interobserver reproducibility in the measurements of high SI, vessel wall area, and luminal area. Continuous variables are expressed as mean (SD), and categoric variables were analyzed using the Pearson χ^2 test or Fisher exact test.

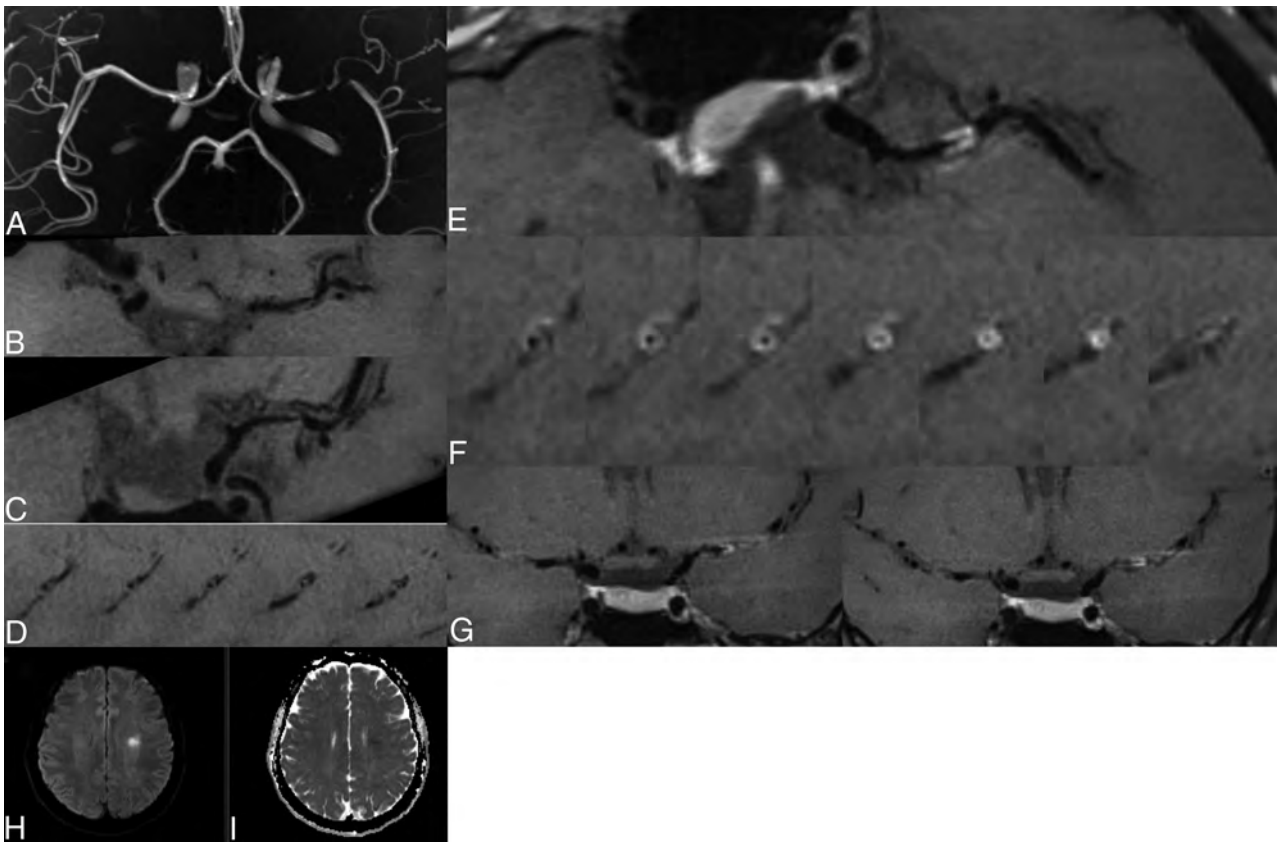

FIG 2. A 37-year-old man. Left MCA stenosis is shown on a 3D TOF-MRA MIP image (*A*). HR-VW-MR imaging shows an isointense signal lesion on precontrast T1 images at the stenosed segment of the left MCA, with an irregular surface (*B* and *C*). Oblique serial sagittal images demonstrate a concentric wall thickening lesion with circular wall involvement (*D*). Postcontrast T1 images show intense (grade II) concentric enhancement of the lesion (*E–G*). DWI shows a small patchy acute ischemic lesion in the left centrum semiovale, with restricted diffusion displayed (*H* and *I*).

Continuous variables were compared between the 2 groups by the independent-samples *t* test or the Mann-Whitney *U* test. The significance threshold was set at $P < .05$.

RESULTS

Demographic Data of Young and MOP Groups

In total, 131 patients with unilateral MCA stenosis were included from January 2017 to December 2018. The mean age of the patients was 47.1 (SD, 12.5) years, and 16.8% (22/131) were women. The young group included 60 patients (45.8%), and the MOP group included 71 patients (54.2%). The young group included 27 patients (45.0%) with TIA and 33 patients (55%) with infarction, and the MOP group included 20 patients (28.2%) with TIA and 51 patients (71.8%) with infarction. The median interval time between symptom onset and HR VW-MR imaging was 4.3 (SD, 3.3) days. One hundred and eleven (84.7%) patients had atherosclerotic disease, and 20 (15.3%) had nonatherosclerotic disease.

Intraobserver and Interobserver Reproducibility for Imaging Analysis

The intraobserver and interobserver reproducibility of measurements of high SI were 0.870 (95% CI, 0.773–0.969) and 0.936 (95% CI, 0.860–1.000), respectively. The intraobserver and interobserver reproducibility of measurements of the wall area were 0.854 (95% CI, 0.744–0.964) and 0.920 (95% CI, 0.838–1.000), respectively. The intraobserver and interobserver reproducibility of measurements of the luminal area were 0.838 (95% CI, 0.731–0.946) and 0.918 (95% CI, 0.846–0.990), respectively.

Comparison of Clinical and Imaging Features between the Young and MOP Groups

The clinical and imaging features were compared between the young and MOP groups in the Online Supplemental Data. MOP patients had a higher prevalence of hypertension (70.4% versus 41.7%, $P = .01$) and diabetes (29.6% versus 15.0%, $P = .05$) than young patients. The proportions of circular wall involvement (40.0% versus 19.7%, $P = .006$) and circular enhancement (68.1% versus 45.5%, $P = .03$) were higher in the young group than in the MOP group (Figs 2 and 3). Lesions were significantly longer in the young group than in the MOP group (8.47 versus 6.23 mm, $P < .0001$). The proportion of eccentric thickening was slightly higher in the MOP group (85.9%) than in young patients (80.0%), but this difference was not statistically significant ($P = .37$). No significant differences were found in other parameters between the 2 groups.

Comparison of Clinical and Imaging Features of Atherosclerotic Plaques between Young and MOP Patients

In total, 111 cases (84.7%) were confirmed as peri-interventional plaques (47 cases in the young group and 64 cases in the MOP

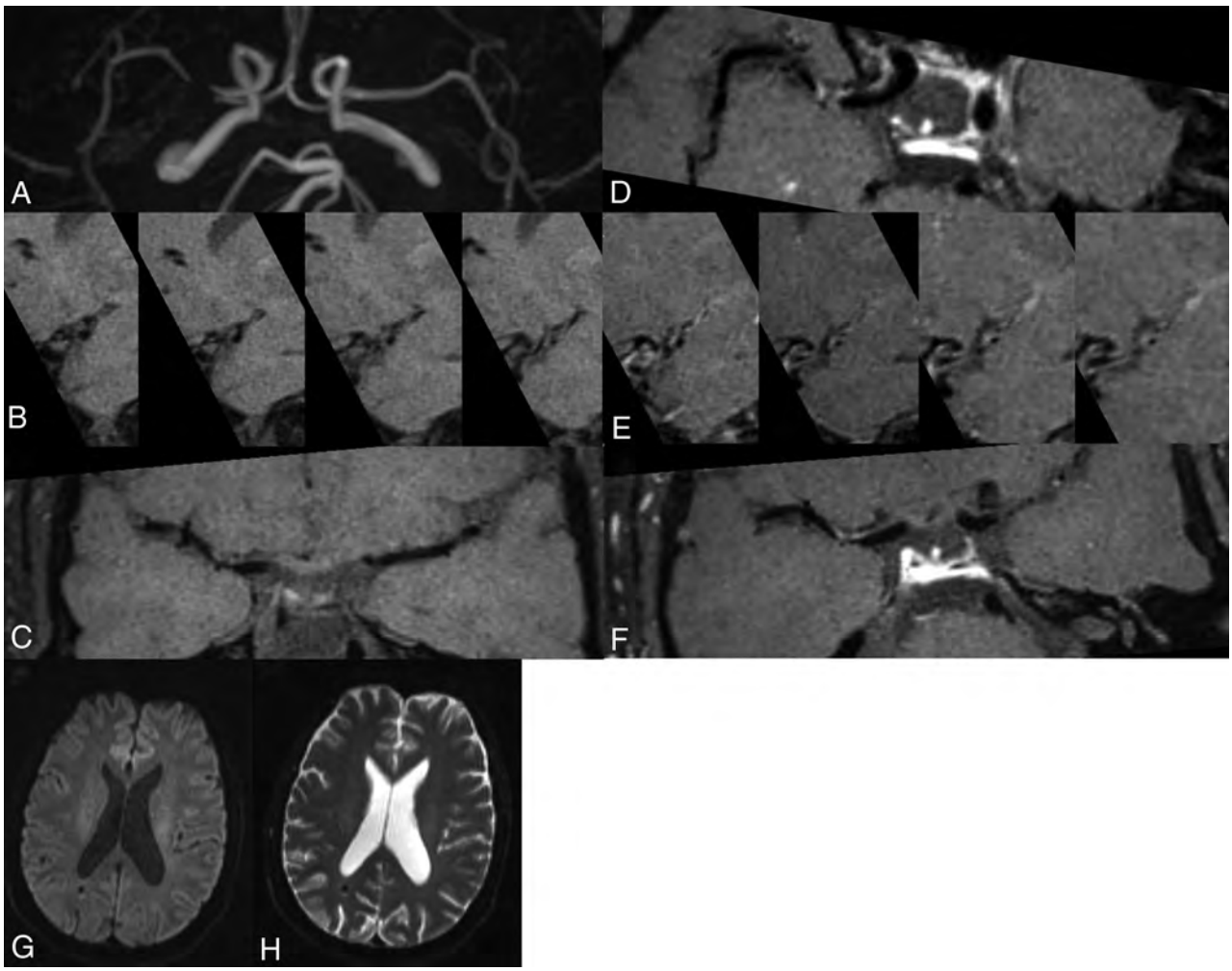

FIG 3. A 37-year-old woman. Right MCA stenosis is shown on a 3D TOF-MRA MIP image (*A*). HR-VW-MR imaging shows an isointense signal lesion on precontrast T1 images at the stenosed segment of the right MCA, with a relatively regular surface (*B*). Oblique sagittal serial images demonstrate an eccentric wall thickening lesion with mainly ventral and superior wall involvement (*C*). Postcontrast T1 images show moderate (grade I) eccentric enhancement of the lesion (*D–F*). DWI shows that there was no abnormally restricted lesion (*G–H*).

group) (Online Supplemental Data). The subgroup analysis showed that MOP patients had a higher prevalence (75.0% versus 44.7%, $P = .001$) of hypertension than young patients. Lesions were longer in the young group than in the MOP group (8.25 versus 6.28 mm, $P = .002$). The prevalence of intraplaque hemorrhage was higher in the MOP group (20.3%) than in the young group (44.7%), but no significant difference was found between two groups ($P = .09$).

Comparison of Intracranial Atherosclerotic versus Non-Atherosclerotic Disease in the Young Group and Middle-Aged and Older Group

The atherosclerosis-versus-nonatherosclerosis subgroup analysis only showed that the wall maximal thickness in the patients with AS was larger than that of patients without atherosclerosis (1.72 versus 1.42 mm, $P = .002$). The patients with AS had a higher prevalence of hypertension (62.2% versus 30.0%, $P = .007$), diabetes (26.1% versus 5.0%, $P = .04$), hyperlipidemia (63.1% versus 35.3%, $P = .02$), and smoking (78.4% versus 50.0%, $P = .008$) than the patients without it (Online Supplemental Data).

Comparison of Clinical and Imaging Features in Different Age/Stenosis Subgroups

In our subgroup analysis of patients with a degree of stenosis of >50%, the rates of hypertension (75.8% versus 43.3%, $P = .009$) and diabetes (30.3% versus 10.0%, $P = .05$) were higher in the MOP group than in the young group, while the lesions were longer in the young group than in the MOP group (8.90 versus 6.57 mm, $P = .002$) (Online Supplemental Data).

In our subgroup analysis of patients with a degree of stenosis of <50%, the rate of hypertension (65.8% versus 40.0%, $P = .03$) and the degree of stenosis (34.7% versus 26.6%, $P = .04$) were higher in the MOP group than in the young group. Moreover, the lesions were longer in the young group than in the MOP group (8.40 versus 5.95 mm, $P = .02$) (Online Supplemental Data).

Comparison of Clinical and Imaging Features between Patients 35 Years of Age or Younger and Patients 35–45 Years of Age

Our subgroup analysis by age within the young group revealed that patients 35 years of age or younger had a smaller proportion

of constrictive remodeling (36.0% versus 71.4%, $P = .02$), less circular wall involvement (20.0% versus 54.3%, $P = .005$), and a higher remodeling ratio (1.05 versus 0.85, $P = .004$) than patients 35–45 years of age (Online Supplemental Data).

DISCUSSION

In recent years, the incidence of stroke in young adults has markedly increased.[20] Approximately 10% of ischemic strokes occur in young patients.[22] The risk factors and etiologic features of ischemic stroke in young adults are considered very different from those of older patients with stroke with traditional vascular risk factors such as hypertension, hypercholesterolemia, diabetes mellitus, and obesity.[25] One study reported that the high incidence of traditional vascular risk factors among young people showed the same trend as the increasing incidence of ischemic stroke.[20] Our results showed that the MOP group had a higher prevalence of hypertension ($P = .01$) and diabetes ($P = .05$) than the young patients. The atherosclerosis-versus-nonatherosclerosis subgroup analysis showed that the patients with AS had a higher prevalence of hypertension ($P = .007$), diabetes ($P = .04$), hyperlipidemia ($P = .02$), and smoking ($P = .008$) than the patients without atherosclerosis. No significant difference was found between people 35 years of age and younger and people 35–45 years of age in these traditional risk factors ($P > .05$). These findings indicate that traditional risk factors are still mainly prevalent among elderly individuals with atherosclerosis. However, only the incidence of diabetes was collected in the current study. Uncontrolled diabetes is thought to be an important contributor to intracranial plaque. It is necessary to include the analysis of hemoglobin A1C in future studies.

In our subgroup analysis of people with <50% stenosis, the degree of stenosis was higher in the MOP group than in the young group (34.7% versus 26.6%, $P = .04$). This finding might suggest that in cases of mild stenosis, the progression and degree of MCA stenosis in MOP patients may be faster and more severe due to the effects of traditional risk factors. The stenosis degree was <50% in 68 patients (30 in the young group, 38 in the MOP group), which suggests that mild and moderate stenosis can be symptomatic. Along with stenosis degree, MCA lesion features on HR VW-MR imaging should considered when assessing MCA stenosis.

HR VW-MR imaging plays a very important role in the evaluation of intracranial artery stenosis. Many features of vessel wall lesions, including the wall thickening morphology, surface status, lesion burden, and the degree and pattern of lesion enhancement, can be analyzed. These detailed features of the involved arterial wall are helpful to establish diagnoses and differential diagnoses of vascular diseases, as well as to evaluate the severity and stability of the lesions. In the current study, we did not find a statistically significant difference in NWI, wall thickening pattern, remodeling pattern, wall maximal thickness, or surface morphology between young and MOP patients (all $P > .05$). These results might indicate that these parameters were similar in symptomatic MCA stenosis irrespective of age. However, we found that the wall maximal thickness of the patients with AS was larger than that of the patients without it ($P = .002$). One possible reason is that many patients with atherosclerosis have eccentric thickening of the vessel wall, so the maximum thickness of the vessel wall is larger than that of the nonatherosclerotic vessel wall.

Eccentric wall thickening was found more often in patients 35 years of age and younger than in patients 35–45 years of age (88.0% versus 74.3%, $P = .19$), and the patients 35 years of age and younger had a lower proportion of constrictive remodeling than patients 35–45 years of age (36.0% versus 71.4%, $P = .02$). These results were not in agreement with previous studies, in which concentric wall lesions were more frequently reported in patients younger than 35 years of age.[6,23,26,27] This difference could be explained by the higher incidence of CNS vasculitis in younger patients in those studies. Smooth, homogeneous, concentric arterial wall thickening and enhancement on HR-VW-MR imaging are considered features of CNS vasculitis. However, previous studies have shown that vasculitis sometimes also results in eccentric wall abnormality.[28,29] This makes the diagnosis of CNS vasculitis more difficult in clinical practice. Our results might indicate that with multiple different risk factors, concentric wall thickening, whether due to vasculitis or not, could be present in patients 35–45 years of age. The incidence of vasculitis in different age groups needs to be confirmed in future studies.

Wall enhancement reflects an inflammatory reaction or the increased permeability of the endothelium, with contrast leakage from the lumen into the arterial wall. Obvious enhancement often presents in the active or unstable phase of the disease. The enhancement degree was not significantly different between different age groups. Because all patients in this study were symptomatic, it could be expected that more than half of them had intense enhancement (grade II) in both the young and MOP groups. The enhancement pattern is another factor that may be related to the vascular physiopathologic mechanism. Circular enhancement was more prevalent in the young group than in the MOP group (68.1% versus 45.5%, $P = .03$). This result could be expected because circular involvement was also more prevalent in young patients. Whether circular wall involvement and enhancement can be taken as a feature of non-AS vascular disease or whether a larger circumferential burden is required should be further investigated.

One interesting result of our study is that the lesions were significantly longer in the young group than in the MOP group (8.47 versus 6.23 mm, $P < .0001$), while the NWI was not found to be significantly different between the 2 groups. Similar results were also found in subgroups with different degrees of stenosis. Most of the previous HR VW-MR imaging studies have focused on circumferential plane analysis of intracranial artery lesions, while less attention has been paid to the length of the lesion. However, lesion length is an important factor that reflects the longitudinal burden of the lesions, which might affect the distal blood supply of the stenosed artery. One possible explanation for this phenomenon might be the different developmental mechanisms in younger-versus-MOP patients. The anatomic and pathologic factors related to MCA lesion length remain unclear. Younger patients with a degree of wall thickening and stenosis similar to those in older patients might need longer involvement of the MCA to cause clinical symptoms. Another reason for the lesion length difference is the various possible diseases in younger patients. Arterial dissection, for example, could involve a longer lesion length than AS disease. Intracranial artery dissection is still considered relatively rare but is an important cause of intracranial

stenosis and ischemic stroke, especially in young adults.[30,31] Patients younger than 45 years of age with intracranial artery dissections have approximately 20% of strokes and 2% of all ischemic strokes.[22] The differences and significance of lesion length in various artery diseases should be investigated in future studies.

Our study included an AS subgroup analysis between young and symptomatic MOP patients. The young patients had a lower prevalence of hypertension (44.7% versus 75.0%, $P = .001$) and longer plaque length (8.25 versus 6.28 mm, $P = .002$) than the MOP patients. The difference between hypertension prevalences indicated that early AS in young patients might be caused by various risk factors. The plaque length results showed a larger longitudinal burden of the involved MCA in young patients. They also suggested that the underlying mechanisms might be different for AS plaques between young and symptomatic MOP patients. Although there are similar medical treatment strategies for AS stenosis, it is worth studying whether this imaging feature difference is related to different outcomes in patients of different ages. Moreover, whether plaque length influences the effect of angioplasty should also be investigated. Further longitudinal studies will provide more valuable information about the clinical significance of this feature.

There are some limitations to our study. First, the retrospective design of this single-center study might have led to selection bias. Some results differed from previous findings, which might be due to the differences between the patients in different studies. The proportion of male patients in this study was relatively high, limiting its generalizability. Second, the imaging data were obtained from 3 different machines, so it was difficult to avoid vendor effects when performing parameter analysis, especially for the measurements of maximal wall thickness and lesion length. Another limitation of the study is the lack of follow-up data, which would be very helpful in the differential diagnosis of various diseases that are difficult to diagnose. Additionally, the dynamic change in vessel wall features would help us to understand the pathologic mechanisms of different vascular diseases.

CONCLUSIONS

Compared with the MOP group, young patients had longer lesions, more circular wall involvement, and more circular enhancement, which may result from the various vascular physiopathologic mechanisms in symptomatic patients of different ages with MCA stenosis.

REFERENCES

1. Bejot Y, Bailly H, Durier J, et al. **Epidemiology of stroke in Europe and trends for the 21st century.** *Presse Med* 2016;45:e391–98 CrossRef Medline
2. Feigin VL, Roth GA, Naghavi MG, et al; Global Burden of Diseases, Injuries and Risk Factors Study 2013 and Stroke Experts Writing Group. **Global burden of stroke and risk factors in 188 countries, during 1990-2013: a systematic analysis for the global burden of disease study 2013.** *Lancet Neurol* 2016;15:913–24 PMC CrossRef Medline
3. Bodle JD, Feldmann E, Swartz RH, et al. **High-resolution magnetic resonance imaging: an emerging tool for evaluating intracranial arterial disease.** *Stroke* 2013;44:287–92 CrossRef Medline
4. Li ML, Xu WH, Song L, et al. **Atherosclerosis of middle cerebral artery: evaluation with high-resolution MR imaging at 3T.** *Atherosclerosis* 2009;204:447–52 CrossRef Medline
5. Majidi S, Sein J, Watanabe M, et al. **Intracranial-derived atherosclerosis assessment: an in vitro comparison between virtual histology by intravascular ultrasonography, 7T MRI, and histopathologic findings.** *AJNR Am J Neuroradiol* 2013;34:2259–64 CrossRef Medline
6. Swartz RH, Bhuta SS, Farb RI, et al. **Intracranial arterial wall imaging using high-resolution 3-Tesla contrast-enhanced MRI.** *Neurology* 2009;72:627–34 CrossRef Medline
7. Turan TN, Rumboldt Z, Granholm AC, et al. **Intracranial atherosclerosis: correlation between in-vivo 3T high resolution MRI and pathology.** *Atherosclerosis* 2014;237:460–63 CrossRef Medline
8. Chen XY, Wong KS, Lam WW, et al. **High signal on T1 sequence of magnetic resonance imaging confirmed to be intraplaque haemorrhage by histology in middle cerebral artery.** *Int J Stroke* 2014;9:E19 CrossRef Medline
9. van der Kolk AG, Zwanenburg JJ, Denswil NP, et al. **Imaging the intracranial atherosclerotic vessel wall using 7T MRI: initial comparison with histopathology.** *AJNR Am J Neuroradiol* 2015;36:694–701 CrossRef Medline
10. Nakamura Y, Yamaguchi Y, Makita N, et al. **Clinical and radiological characteristics of intracranial artery dissection using recently proposed diagnostic criteria.** *J Stroke Cerebrovasc Dis* 2019;28:1691–1702 CrossRef Medline
11. Mandell DM, Mossa-Basha M, Qiao Y, et al; Vessel Wall Imaging Study Group of the American Society of Neuroradiology. **Intracranial vessel wall MRI: principles and expert consensus recommendations of the American Society of Neuroradiology.** *AJNR Am J Neuroradiol* 2017;38:218–29 CrossRef Medline
12. Ryoo S, Cha J, Kim SJ, et al. **High-resolution magnetic resonance wall imaging findings of Moyamoya disease.** *Stroke* 2014;45:2457–60 CrossRef Medline
13. Xu YY, Li ML, Gao S, et al. **Etiology of intracranial stenosis in young patients: a high-resolution magnetic resonance imaging study.** *Ann Transl Med* 2017;5:319 CrossRef Medline
14. Kim DK, Verdoorn JT, Gunderson TM, et al. **Comparison of noncontrast vessel wall imaging and 3D time-of-flight MRA for atherosclerotic stenosis and plaque characterization within intracranial arteries.** *J Neuroradiol* 2020;47:266–71 CrossRef Medline
15. Xu WH, Li ML, Gao S, et al. **In vivo high-resolution MR imaging of symptomatic and asymptomatic middle cerebral artery atherosclerotic stenosis.** *Atherosclerosis* 2010;212:507–11 CrossRef Medline
16. Varnava AM, Mills PG, Davies MJ. **Relationship between coronary artery remodeling and plaque vulnerability.** *Circulation* 2002;105:939–43 CrossRef Medline
17. Harteveld AA, Denswil NP, Van Hecke W, et al. **Ex vivo vessel wall thickness measurements of the human circle of Willis using 7T MRI.** *Atherosclerosis* 2018;273:106–14 CrossRef Medline
18. Zhang D, Chen Y, Chen H, et al. **A high-resolution MRI study of relationship between remodeling patterns and ischemic stroke in patients with atherosclerotic middle cerebral artery stenosis.** *Front Aging Neurosci* 2017;9:140 CrossRef Medline
19. Ter-Karapetyan A, Triphan SM, Jobst BJ, et al. **Towards quantitative perfusion MRI of the lung in COPD: the problem of short-term repeatability.** *PLoS One* 2018;13:e0208587CrossRef Medline
20. Xu WH, Li ML, Gao S, et al. **Middle cerebral artery intraplaque hemorrhage: prevalence and clinical relevance.** *Ann Neurol* 2012;71:195–98 CrossRef Medline
21. Qiao Y, Zeiler S, Mirbagheri S, et al. **Intracranial plaque enhancement in patients with cerebrovascular events on high-spatial-resolution MR images.** *Radiology* 2014;271:534–42 CrossRef Medline
22. Maaijwee NA, Rutten-Jacobs LC, Schaapsmeerders P, et al. **Ischaemic stroke in young adults: risk factors and long-term consequences.** *Nat Rev Neurol* 2014;10:315–25 CrossRef Medline

23. Mossa-Basha M, Hwang WD, De Havenon A, et al. **Multicontrast high-resolution vessel wall magnetic resonance imaging and its value in differentiating intracranial vasculopathic processes.** *Stroke* 2015;46:1567–73 CrossRef Medline
24. Tan H, Chen X, Maingard J, et al. **Intracranial vessel wall imaging with magnetic resonance imaging: current techniques and applications.** *World Neurosurg* 2018;112:186–98 CrossRef Medline
25. O'Donnell MJ, Xavier D, Liu L, et al; INTERSTROKE investigators. **Risk factors for ischaemic and intracerebral haemorrhagic stroke in 22 countries (the INTERSTROKE study): a case-control study.** *Lancet* 2010;376:112–23 CrossRef Medline
26. Mandell DM, Matouk CC, Farb RI, et al. **Vessel wall MRI to differentiate between reversible cerebral vasoconstriction syndrome and central nervous system vasculitis: preliminary results.** *Stroke* 2012;43:860–62 CrossRef Medline
27. Ahn SH, Lee J, Kim YJ, et al. **Isolated MCA disease in patients without significant atherosclerotic risk factors: a high-resolution magnetic resonance imaging study.** *Stroke* 2015;46:697–703 CrossRef Medline
28. Obusez EC, Hui F, Hajj-Ali RA, et al. **High-resolution MRI vessel wall imaging: spatial and temporal patterns of reversible cerebral vasoconstriction syndrome and central nervous system vasculitis.** *AJNR Am J Neuroradiol* 2014;35:1527–32 CrossRef Medline
29. Van Rooij JL, Rutgers DR, Spliet WG, et al. **Vessel wall enhancement on MRI in the diagnosis of primary central nervous system vasculitis.** *Int J Stroke* 2018;13:NP24–27 CrossRef Medline
30. Sikkema T, Uyttenboogaart M, Eshghi O, et al. **Intracranial artery dissection.** *Eur J Neurol* 2014;21:820–26 CrossRef Medline
31. Li S, Yan B, Kaye A, et al. **Prognosis of intracranial dissection relates to site and presenting features.** *J Clin Neurosci* 2011;18:789–93 CrossRef Medline

The First Examination of Diagnostic Performance of Automated Measurement of the Callosal Angle in 1856 Elderly Patients and Volunteers Indicates That 12.4% of Exams Met the Criteria for Possible Normal Pressure Hydrocephalus

M. Borzage, A. Saunders, J. Hughes, J.G. McComb, S. Blüml, and K.S. King

ABSTRACT

BACKGROUND AND PURPOSE: Many patients with dementia may have comorbid or misdiagnosed normal pressure hydrocephalus, a treatable neurologic disorder. The callosal angle is a validated biomarker for normal pressure hydrocephalus with 93% diagnostic accuracy. Our purpose was to develop and evaluate an algorithm for automatically computing callosal angles from MR images of the brain.

MATERIALS AND METHODS: This article reports the results of analyzing callosal angles from 1856 subjects with 5264 MR images from the Open Access Series of Imaging Studies and the Alzheimer's Disease Neuroimaging Initiative databases. Measurement variability was examined between 2 neuroradiologists ($n = 50$) and between manual and automatic measurements ($n = 281$); from differences in simulated head orientation; and from real-world changes in patients with multiple examinations ($n = 906$). We evaluated the effectiveness of the automatic callosal angle to differentiate normal pressure hydrocephalus from Alzheimer disease in a simulated cohort.

RESULTS: The algorithm identified that 12.4% of subjects from these carefully screened cohorts had callosal angles of $<90°$, a published threshold for possible normal pressure hydrocephalus. The intraclass correlation coefficient was 0.97 for agreement between neuroradiologists and 0.90 for agreement between manual and automatic measurement. The method was robust to different head orientations. The median coefficient of variation for repeat examinations was 4.2% (Q1 = 3.1%, Q3 = 5.8%). The simulated classification of normal pressure hydrocephalus versus Alzheimer using the automatic callosal angle had an accuracy, sensitivity, and specificity of 0.87 each.

CONCLUSIONS: In even the most pristine research databases, analyses of the callosal angle indicate that some patients may have normal pressure hydrocephalus. The automatic callosal angle measurement can rapidly and objectively screen for normal pressure hydrocephalus in patients who would otherwise be misdiagnosed.

ABBREVIATIONS: AD = Alzheimer disease; ADNI = Alzheimer's Disease Neuroimaging Initiative; CA = callosal angle; DESH = disproportionately enlarged subarachnoid space hydrocephalus; ICC = intraclass correlation coefficient; NPH = normal pressure hydrocephalus; OASIS = Open Access Series of Imaging Studies

Normal pressure hydrocephalus (NPH) is a treatable form of dementia that can be difficult to diagnose.[1] Clinical features of NPH are gait disturbance, postural instability, cognitive deterioration, and urinary incontinence or urgency, but these features are frustratingly nonspecific in elderly patients.[2] Classic neuroimaging findings show differences from the atrophy routinely

Received March 5, 2021; accepted after revision July 3.

From the Fetal and Neonatal Institute, Division of Neonatology (M.B.), Department of Radiology (A.S., S.B.), and Division of Neurosurgery (J.G.M.), Children's Hospital Los Angeles, Los Angeles, California; Department of Pediatrics (M.B.), and Neurological Surgery (J.G.M.), Keck School of Medicine, University of Southern California, Los Angeles, California; Rudi Schulte Research Institute (M.B., A.S., S.B., K.S.K.), Santa Barbara, California; and Department of Neuroradiology (J.H., K.S.K.), Barrow Neurological Institute, Phoenix, Arizona.

This work was supported by the Rudi Schulte Research Institute.

Data used in preparation of this article were obtained from the Alzheimer's Disease Neuroimaging Initiative database (adni.loni.usc.edu). Thus, the investigators within the Alzheimer's Disease Neuroimaging Initiative contributed to the design and implementation of Alzheimer's Disease Neuroimaging Initiative and/or provided data but did not participate in the analysis or writing of this report. A complete listing of Alzheimer's Disease Neuroimaging Initiative investigators can be found at http://adni.loni.usc.edu/wp-content/uploads/how_to_apply/ADNI_Acknowledgement_List.pdf.

Data collection and sharing for this project were funded, in part, by the Alzheimer Disease Neuroimaging Initiative (National Institutes of Health Grant U01 AG024904) and Department of Defense Alzheimer Disease Neuroimaging Initiative (Department of Defense award number W81XWH-12–2-0012). The Alzheimer's Disease Neuroimaging Initiative is funded by the National Institute on Aging, the National Institute of Biomedical Imaging and Bioengineering, and through generous contributions from the following: AbbVie; Alzheimer's Association; Alzheimer's Drug Discovery Foundation; Araclon Biotech; BioClinica; Biogen; Bristol-Myers Squibb; CereSpir; Cogstate; Eisai; Elan Pharmaceuticals; Eli Lilly and Company; EuroImmun; F. Hoffmann-La Roche Ltd and its affiliated company Genentech; Fujirebio; GE Healthcare; IXICO Ltd; Janssen Alzheimer Immunotherapy Research & Development; Johnson & Johnson Pharmaceutical Research & Development LLC; Lumosity; Lundbeck; Merck & Co; Meso Scale Diagnostics, LLC; NeuroRx Research; NeuroTrack Technologies; Novartis Pharmaceuticals Corporation; Pfizer; Piramal Imaging; Servier; Takeda Pharmaceutical Company; and Transition Therapeutics. The Canadian Institutes of Health Research is providing funds to support the Alzheimer Disease Neuroimaging Initiative clinical sites in Canada. Private sector contributions are facilitated by the Foundation for the National Institutes of Health (www.fnih.org). The grantee organization is the Northern California Institute for Research and Education, and the study is coordinated by the Alzheimer's Therapeutic Research Institute at the University of Southern California. Alzheimer Disease Neuroimaging Initiative data are disseminated by the Laboratory for Neuro Imaging at the University of Southern California.

Data were provided, in part, by OASIS. OASIS-3: Principal Investigators: T. Benzinger, D. Marcus, J. Morris; NIH P50 AG00561, P30 NS09857781, P01 AG026276, P01 AG003991, R01 AG043434, UL1 TR000448, R01 EB009352. AV-45 doses were provided by Avid Radiopharmaceuticals, a wholly owned subsidiary of Eli Lilly.

observed in senescent adults. Specialized physiologic imaging of water diffusion, CSF flow, or cerebrovascular reactivity may help with diagnosing NPH,[3,4] but each method requires acquiring additional prospective images that are not commonly included in clinical assessments. Lumbar drain trials have diagnostic utility but are invasive;[5] noninvasive biomarkers with strong evidence of therapeutic benefits are preferred before attempting treatment by shunting, which has an 11% risk of serious adverse events.[4,6]

Fortunately, numerous putative NPH imaging biomarkers exist including the following: anatomic assessments of the relative size and shape of the ventricles and subarachnoid spaces; disproportionately enlarged subarachnoid space hydrocephalus (DESH);[7] volume-based assessments of CSF and ratios versus intracranial volume;[8] distance-based assessment of the ventricles versus intracranial width, ie, the Evans index;[3] and angle-based measurements of the parietal portion of the lateral ventricles, ie, the callosal angle (CA).[9] Measurement of the CA, at times used in concert with the Evans index, is a validated biomarker for NPH, with diagnostic accuracies of 93%, 77.8%, and 88.9% for threshold angles of 90°, 90.8°, and 100°, respectively, as validated in studies of 102, 90, and 318 patients, respectively.[10-12]

With an abundance of useful biomarkers, deploying them into clinical practice entails manipulation of the images using 3D software, which requires an investment of precious time by the interpreting radiologist. Since NPH may not be among the most likely differential diagnoses for an elderly patient, manually measuring these biomarkers for screening purposes is impractical. An alternative approach is to perform automated analysis of images to measure these biomarkers and present results to radiologists to interpret. The advantages of such an approach are that the measurement eliminates the need to perform manual assessment and removes observer variability. For these putative imaging biomarkers, automated solutions exist for calculating the DESH,[13] Evans index,[14] and CSF volumes and ratios,[15] but to the best of our knowledge, measurements of the CA have not yet been automated. Therefore, our objective was to automate CA measurements and then do the following: 1) assess the agreement between 2 neuroradiologists measuring the CA and between manual and automatic measurements; 2) evaluate the variation of automated CA under both simulated and real-world conditions; 3) use the algorithm to analyze MR images to identify patients with possible NPH in studies with different scanners, vendors, and imaging parameters; and 4) characterize the performance of the automated measurement for the differentiation of NPH from other dementia.

MATERIALS AND METHODS

Subjects

We included data from 2 imaging databases: the Open Access Series of Imaging Studies (OASIS),[16,17] ($n = 1015$ subjects, 567 women, 448 men) and the Alzheimer Disease Neuroimaging Initiative (ADNI),[18] ($n = 841$ subjects, 354 women, 487 men). The mean ages of the subjects at the time of their MR imaging were 68.5 (SD, 9.3) and 75.3 (SD, 6.9) years, respectively. OASIS subjects included groups for cognitively normal and any stage of cognitive decline in aging. New OASIS subjects underwent a clinical assessment, which included a family history of Alzheimer disease (AD), medical history, physical examination, neurologic evaluation, and MR imaging. Stages of cognitive decline were determined using the Clinical Dementia Rating Scale,[19] and patients were excluded if the primary cause of dementia was not AD. ADNI subjects included groups for cognitively healthy, early mild cognitive impairment, late mild cognitive impairment, and AD. New ADNI subjects in all groups were excluded for NPH during an initial screening visit, which included neuropsychological testing and MR imaging.

Neuroimaging

OASIS neuroimaging was performed on 1.5T (Vision) and 3T (TIM Trio, BioGraph mMR) Siemens clinical scanners. The images were T1-weighted MPRAGE (TE = 4.0 ms, TR = 9.7 ms, TI = 20 ms, slice thickness = 1.25 mm, matrix = 256 × 256). ADNI neuroimaging was performed on 1.5T (Signa Excite, Signa HDxt) and 3T (Discovery, Signa Premier) GE Healthcare, 1.5 T (Intera) and 3T (Achieva, Ingenia) Philips Healthcare, and 1.5T (Avanto, Espree, Sonata, Symphony) and 3T (Allegra, Prisma, Skyra, Trio/TIM, Verio, Vida) Siemens clinical scanners. The images were T1-weighted MPRAGE with variations in protocol depending on the scanner and software (TE = 2.86–4.61 ms, TR = 2300–3000 ms, TI = 853–1000 ms, slice thickness = 1.2 mm, matrix 192–256 × 192–256).

Manual CA Measurement

Two board-certified neuroradiologists (K.S.K., J.H.) acquired manual CA measurements using established methods:[9,10] identifying a midsagittal section, creating a reference plane through the anterior commissure and posterior commissure, creating a coronal reference plane perpendicular to the bicommissural plane at the level of the posterior commissure, drawing 2 straight lines along the medial walls of the left and right lateral ventricles on the coronal image, and calculating the angle between the lines.

Automated CA Measurement

Images were preprocessed with FreeSurfer (http://surfer.nmr.mgh.harvard.edu) to align to a standard orientation and extract the ventricles.[20] The extracted ventricles included the left and right lateral ventricles, choroid plexus, and the third ventricle. CA measurements were calculated in Matlab (R2020A; MathWorks). The algorithm applied to the ventricles creates an axial reference plane by using the centroid of the ventricles and the most distal points on the left and right anterior horns; makes a coronal reference plane perpendicular to the axial plane; pitches the coronal reference plane backward to make it oblique; slices the ventricles; and computes the angle between the medial walls of the lateral ventricles. See the algorithm details in Fig 1.

Parameter Optimization

Radiologists use the anterior/posterior commissure plane as a reference plane when performing manual CA measurements. This bicommissural plane is more difficult to reliably compute with automated methods than the centroid and distal points of

Please address correspondence to A. Saunders, MS, Children's Hospital of Los Angeles, Department of Radiology, 4650 Sunset Blvd., Los Angeles, CA 90027; e-mail: saundera@usc.edu

Indicates open access to non-subscribers at www.ajnr.org

http://dx.doi.org/10.3174/ajnr.A7294

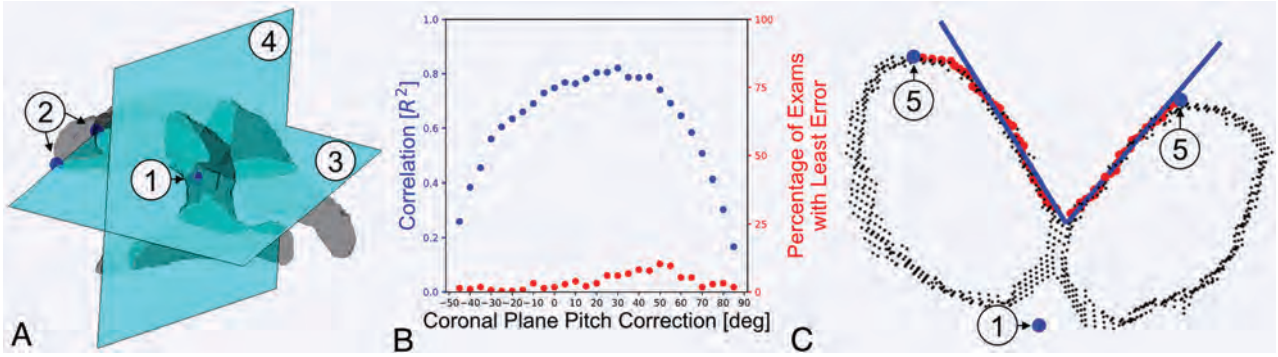

FIG 1. CA algorithm. CA measurements are automatically calculated with the following approach. *A*, Ventricles are segmented in FreeSurfer, and 3 reference points are calculated: the centroid of the extracted ventricles (1) and the most anterior points to the left and right of the centroid (2). These 3 points are used to calculate the axial reference plane (3) and the coronal reference plane (4), shown here without pitch correction. *B*, The coronal plane pitch correction is optimized by finding the angle that maximizes the correlation of manual and automated CA measurements (30°). For each pitch correction, the percentage of examinations with the least error is also shown. *C*, The pitch-corrected coronal section is analyzed by finding the most superior point to the left and right of the centroid (5). A greedy pathfinding algorithm connects the 2 superior reference points (5) to identify the medial walls of the lateral ventricles (*red points*). The inferior 20% and superior 20% of *red points* are excluded, selecting the middle 60% for angle calculation; this was found empirically to exclude the portions of the ventricle walls with higher curvature. A first-order polynomial fit produces the fit lines (*blue lines*), and the angle between them is calculated.

the left and right lateral ventricles. However, using our different reference planes would lead to systematic bias in the automatically measured CA. To reduce this bias, we identified the key difference in the reference planes as a coronal pitch. Thus, we systematically varied the pitch in the coronal plane with angles from −45° to 85° in increments of 5°. At each angle of pitch, we remeasured the CA for all subjects for whom we had manual CA measurements and determined the pitch that minimized error between the manual and automated CAs. For the optimized angle, we used the linear trend from the correlation of manual and automatic CAs to adjust all subsequent automatic CA measurements.

Assessing Measurement Variability

We performed 3 different assessments of measurement variability: 1) We used Bland-Altman analysis to ascertain the limits of agreement between CAs manually measured by both neuroradiologists ($n = 50$) and between 1 neuroradiologist's manual CA measurements and linearly corrected automatic CA measurements ($n = 281$). 2) We performed a Monte Carlo simulation to assess potential sources of variability due to misalignment and localization errors during image acquisition and FreeSurfer preprocessing. We selected 24 subjects and reoriented their heads multiple times. Each head was randomly translated in three directions (SD 8 mm in each direction) and randomly rotated in three directions (SD 10°, 3°, and 6° for pitch, roll, and yaw, respectively). After reorienting their heads, we automatically computed the CA. Leverage plots were used to determine the sensitivity of each angle measurement to these translations and rotations (not shown). 3) We computed the coefficient of variation of subjects who had ≥3 MRIs to assess real-world intrapatient variability. Our assumption was that these repeat scans would include real-world variability in image quality, patient orientation, scanner drift, and ventricle morphology. For each subject, we automatically measured the CA for each repeat scan and computed the coefficient of variation of the angles.

Simulated Effectiveness of the CA to Differentiate NPH and AD

We performed a Monte Carlo simulation to examine the effectiveness of the automatic CA measurement to differentiate NPH and AD. We simulated CAs for 1 million patients. Each patient was randomly assigned to NPH or AD with equal likelihood. Ground truth CAs were generated from a Gaussian distribution for patients from the NPH (mean 66° [SD, 14°]) and AD (mean 104° [SD, 15°]) cohorts as given by Ishii et al.[10] Measurement error due to automatic CA calculation was randomly added to each angle: This error was determined by the distribution of error in our comparison of manual and linearly corrected automatic measurements. We calculated the probability that the random angle belonged to the NPH or AD group and used the higher probability to classify the patient as having NPH or AD. When the probabilities were within 5% of each other, we classified the patient as indeterminate. Classification performance was quantified using accuracy, sensitivity, and specificity.

Analysis of NPH and AD Prevalence and Comorbidity

We estimated the probability of comorbid or misdiagnosed NPH in the evaluated databases and clinical practice. We used literature values for prevalence and diagnostic accuracies of NPH and AD in a relevant population. This analysis used the following assumptions: Our relevant population is cognitively impaired patients 65 years of age and older; all patients in this cognitively impaired population have either NPH (NPH+AD–), AD (NPH–AD+), or comorbid NPH and AD (NPH+AD+); the biologic processes and thus the probabilities of having NPH or AD are independent.

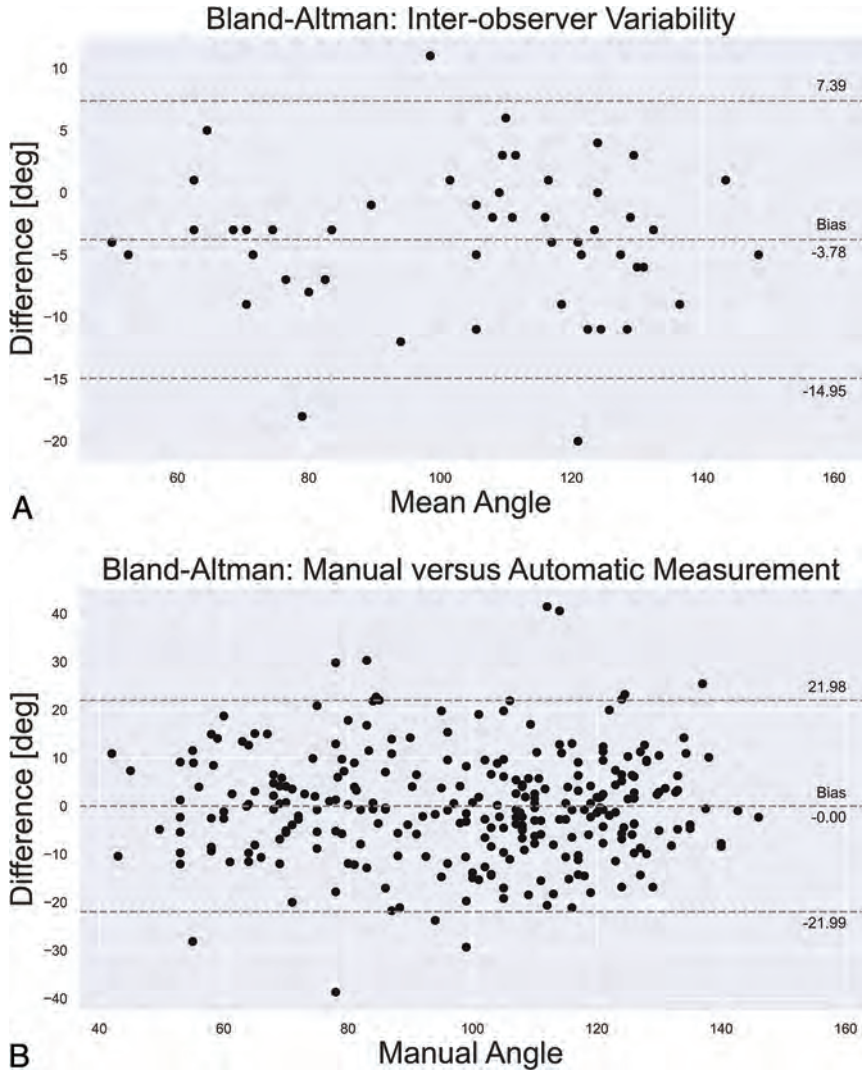

FIG 2. Measurement variability. *A*, We found a slight bias (−3.78°) with 95% limits of agreement of −14.95° to +7.39° between 2 radiologists. This translates to an intraclass correlation coefficient of 0.97, demonstrating good reproducibility of the callosal angle biomarker between 2 readers. *B*, Comparison of manual and linearly corrected automatic CA measurements for $n = 281$ images had 95% limits of agreement of about ±22° and an ICC of 0.90. We observed lower agreement between manual and automatic measurements than between the 2 neuroradiologists, which highlights the impact of differences in measurement methods.

RESULTS

Figure 1 demonstrates the automatic CA measurement algorithm and determination of correction factors. Figure 1*B* shows the comparison of manual and automatic CA measurements ($n = 281$) to optimize the coronal reference plane pitch. The highest correlation was found when adjusting the pitch of the automatic coronal reference plane back (ie, the most superior part of the plane moved posterior) by 30°, and the highest percentage of examinations with the least error between manual and automatic measurements occurred at a 50° pitch correction. We selected the best correlation (30°) for our optimization; the correlation protects against large measurement errors by minimizing the squared error, whereas the percentage of examinations with the fewest errors does not. However, the correlation and percentage of examinations with the fewest errors changed only modestly, with pitch corrections ranging from 25° to 50°, meaning that pitch correction is relatively insensitive over this range. At a 30° pitch correction, the intraclass correlation coefficient (ICC) was 0.87, the coefficient of determination was $R^2 = 0.82$, the median absolute error was 8.1° (Q1 = 3.4°, Q3 = 13.2°), and the line of fit was *Manual CA* = *Automatic CA* × 1.27 − 3.93. The pitch correction and linear correction factors were applied to all subsequent automated CA measurements.

The Bland-Altman analysis of the 2 neuroradiologists' manual measurements (Fig 2*A*) had a bias of −3.78° with 95% limits of agreement of −14.95° to +7.39°, a median absolute error of 4° (Q1 = 3°, Q3 = 7°), an ICC of 0.97, and coefficient of determination of $R^2 = 0.95$. Bland-Altman analysis of the manual and linearly corrected automatic measurements (Fig 2*B*) had no bias, with 95% limits of agreement of about ±22°, median absolute error of 6.5° (Q1 = 2.9°, Q3 = 12.0°), an ICC of 0.90, and coefficient of determination $R^2 = 0.82$. For the Monte Carlo analysis of head position sensitivity, we re-oriented each subject's head (mean, $n = 1122$ [SD, 381] times). The automatically measured CA was sensitive to initial orientation, with significant change in the CA measurements due to pitch, roll, and yaw rotations ($P < .001$, $P = .028$, and $P = .004$ respectively) and left-right translation ($P < .001$), but not anterior-posterior or superior-inferior translations ($P = .222$, $P = .350$, respectively). However, the parameter estimates for these significant factors indicate that the effects are negligible: Estimates for pitch, roll, and yaw rotations are −0.006°, 0.004°, and −0.003°, respectively, and left-right translation is −0.001°, indicating that a 1° of pitch, roll, or yaw corresponds to a CA change of ≤0.006°, and a 1-mm translation corresponds to a CA change of ≤0.001°. For the real-world intrapatient variability analysis, we identified $n = 906$ subjects ($n = 213$ OASIS, $n = 693$ ADNI), each with between 3 and 8 repeat MRIs. For these subjects, we determined that the median coefficient of variation was 4.2% (Q1 = 3.1%, Q3 = 5.8%). The median time between repeat examinations was 214 days (Q1 = 183 days, Q3 = 396 days). See Fig 3 for details on the distribution of the coefficient of variation in these subjects. A visual inspection of all automatic measurements (A.S., with 3 years' experience) found that 52 angles (1%) had fit lines that deviated from the expected placement.

When applying the algorithm to all available images, we computed 5264 CA measurements. The median CA was 113°

(Q1 = 101°, Q3 = 123°) (Fig 4). This asymmetric distribution had a skewness of −1.048 (acute) and excess kurtosis of 0.456. In this distribution, 12.4%, 13.0%, and 23.5% of subjects had CAs narrower than suggested thresholds for possible NPH of 90°, 90.8°, and 100°, respectively.

For the Monte Carlo analysis of classification using the automatic CA measurement, we calculated the accuracy, sensitivity, and specificity to all be 0.87. The percentage of indeterminate measurements was 5.4%. For the analysis of NPH and AD comorbidity, we used literature values for the following: the prevalence of NPH of 2.9% (mean of 3 studies),[21-23] the prevalence of AD of 11.7%,[24] and the diagnostic accuracy for AD of 77%.[25] Thus, if a patient is diagnosed with AD, the probabilities of the true disease processes are 96.3% NPH–AD+, 2.8% NPH+AD+ (comorbid), and 0.9% NPH+AD– (misdiagnosed). We calculated the sum of the latter 2 values and estimate that 3.7% of patients diagnosed with AD actually were NPH+.

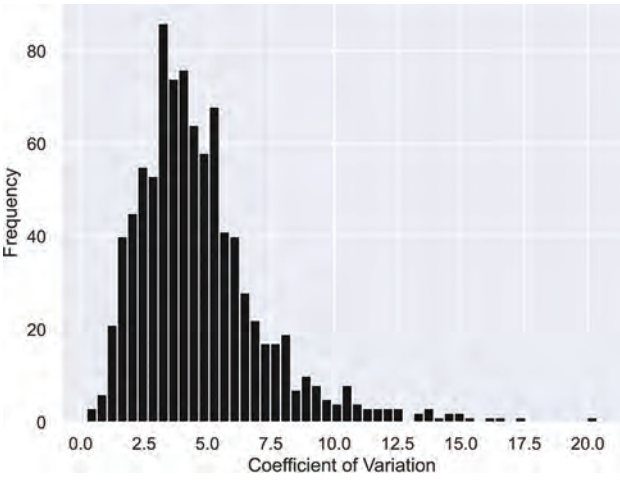

FIG 3. Histogram of coefficients of variation for 906 patients. The variation of automatic CA measurements is calculated for patients with 3–8 separate MR imaging acquisitions. The median coefficient of variation is 4.2%. This is noteworthy because it means that the CA measurement is highly reproducible in a large, real-world sample of MR imaging examinations.

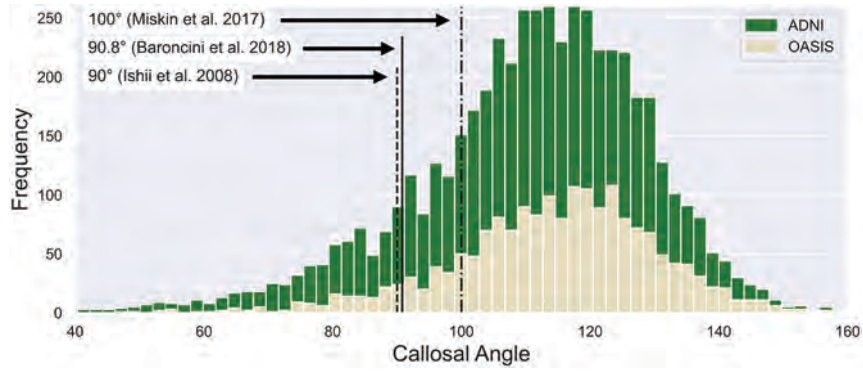

FIG 4. Histogram of automatically measured CAs. Angles are measured from 5264 MR images from 1856 patients. The median CA is 113° (Q1 = 101°, Q3 = 123°). The distribution has an acute skewness of −1.048 and excess kurtosis of 0.456. Suggested thresholds for suspected normal pressure hydrocephalus of 90°, 90.8°, and 100° are shown, and we note that 12.4%, 13.0%, and 23.5% of images have CAs narrower than the corresponding cutoffs.

DISCUSSION

To the best of our understanding, this is the first automated CA measurement and the largest number of CA measurements made. Thus, the distribution of the CA provides a revised and expanded population for comparing individual CA measurements. Obtaining these results through manual CA measurements would be extremely time-consuming and prone to observer variability, which highlights the suboptimal reliability of manual CA measurement. Modest differences in the selection of the bicommissural plane, the anterior-posterior position of the coronal reference plane, and lines that best parallel the medial walls of the lateral ventricles contribute to different measurements of the CA.

One of our most noteworthy findings was that at least 12.4% of the images we measured met the CA criteria for possible NPH.[10] The estimated rate of NPH is 2.1%–3.9% in adults older than 65 years of age.[21-23] Our estimate of comorbid or misdiagnosed NPH among patients diagnosed with AD was 3.7%, which is consistent with the reported value of 3.9%.[26] If the databases we examined contain patients with NPH who are classified as neurotypical or diagnosed with other dementias, it suggests that other analyses using these databases may be skewed by a substantial fraction of the overall sample. Perhaps even more important, if these patients do have NPH or another hydrocephalus indicated by a narrowed CA, their dementias may be treatable.

The Monte Carlo analysis of NPH classification performance allowed us to compute the accuracy, sensitivity, and specificity (all 0.87) of our automated approach, which were lower than results from Ishii et al[10] (0.93, 0.97, and 0.88, respectively). Despite mild performance decreases when using the automatic CA measurement, the potential for rapid evaluation is substantial and may be particularly valuable in cases in which NPH findings are incidental.

The automated measurement is deterministic, eliminating observer variability and establishing a more structured reporting framework between radiologists and clinicians for the CA biomarkers. The benefit of the robust approach we selected was demonstrated in both intrapatient variability analyses. The Monte Carlo analysis demonstrated that our approach is robust to the initial position and orientation of the brains of our subjects; thus, even if FreeSurfer fails to correctly align the heads or subjects have an abnormal orientation of their ventricles, the effect on the CA measurements would be small (<1°) across the entire range of rotations and translations tested. This finding appears to be sufficient to handle most scenarios in which the head is even crudely oriented. The real-world analysis demonstrated a median coefficient of variation of 4.2%, representing errors which are 8.7–13.6 times smaller than the putative differences between the mean CA in patients with NPH (66°) and AD (104°).[10] It is reasonable to expect that in a clinical radiology practice, these automatic CA measurements

would provide highly repeatable quantitation to support distinguishing NPH from atrophy in patients with a clinical suspicion of movement disorders and dementia.

The systematic bias between the automatic and manually computed CA is likely due to different methods for selecting axial reference planes. The automatic method identifies landmarks from the segmented surface representations of the lateral ventricles, while the clinical method uses the anterior/posterior commissures. The finding that a 30° pitch correction improves agreement with manual measurement is consistent with the typical angle of the bicommissural plane relative to the axial plane, and measurement of the angle in the posterior area of the lateral ventricles may better capture pathologically narrow angles as the ventricles expand upward on both sides of the falx cerebri.[27] We chose reference points for the automated method to be reliable but still comparable with those used in manual CA measurements. The centroid of the ventricles represents a global average that is inherently robust, and the anterior horns have less anatomic variability than the posterior extrema or superior extrema, which we speculate may be altered by NPH. Furthermore, the reference points were selected to be reproducible across a wide range of image qualities and modalities, which we suspect includes CT. CT is commonly included in primary imaging studies for dementia work-up; adapting the automatic CA method for use in CT is a promising future option to reach additional patients who may not have undergone MRI.

Limitations

A limitation of the field of NPH research, and thus this article, is the lack of treatment-responsive patients with NPH in a public database. Such a database would enable us to directly assess the accuracy, specificity, and sensitivity of our measures in identifying NPH. Thus, future objectives for those studying NPH, including our group, should include collecting neuroimaging of shunt-responsive patients with NPH. Meanwhile, our algorithm can flag potential cases of a narrowed CA, which can then be verified by a trained reader as we have done in this study. We chose to demonstrate the utility of our efforts on making a CA algorithm that is pragmatic to use by providing secondary analyses of subjects in large existing databases. There are areas of possible improvement in our algorithm: The automated CA measurement had some performance disadvantages when evaluated against manual observations. There may be an opportunity to adjust the algorithm to be more robust to irregular variations in the segmented ventricles, but these errors were infrequent. There are also other imaging biomarkers that might benefit patients with NPH, which we did not use (eg, the Evans Index), an area with potential for future investigation. One minor limitation of our study is that we performed manual measurements on 281 of our total 5264 images (5.3%). This limitation is due to the substantial time requirement for a neuroradiologist to perform CA measurements, which highlights the need for automated tools if CA or other quantitative biomarkers are to be routinely measured.

CONCLUSIONS

NPH is a treatable dementia that is commonly misdiagnosed due to the poor specificity of its neurologic symptoms. CA measurements are an established tool to assess the risk for NPH, but manual measurement is time-consuming. We developed an algorithm for automated CA measurement, applied it to 5264 T1-weighted MRIs, and compared its performance with manual CA measurements. We found that agreement between manual and automatic measurements (ICC = 0.90) was lower than the agreement between 2 neuroradiologists (ICC = 0.97). Intrapatient variability was evaluated in subjects with ≥3 longitudinal imaging examinations; the median coefficient of variation was 4.2%, indicating reliable automatic measurement. Although NPH was an exclusion criterion from these databases, 12.4% of the automatic CA measurements met the criteria for possible NPH. We believe automatic CA measurements can rapidly and objectively assess NPH in patients who would otherwise be misdiagnosed with other dementias, and can create opportunities for successful treatment of dementia.

Disclosures: Kevin S. King—*RELATED*: *Grant*: Rudi Schulte Research Institute, *Comments*: My work on this project was conducted with support of the nonprofit Rudi Schulte Research Institute. The Rudi Schulte Research Institute is a trust established to support hydrocephalus-related research by issuing competitive fellowships in response to submitted research proposals.

REFERENCES

1. Bradley WG. **Normal pressure hydrocephalus: new concepts on etiology and diagnosis.** *AJNR Am J Neuroradiol* 2000;21:1586–90 Medline
2. Hakim S, Adams RD. **The special clinical problem of symptomatic hydrocephalus with normal cerebrospinal fluid pressure: observations on cerebrospinal fluid hydrodynamics.** *J Neurol Sci* 1965;2:307–27 CrossRef Medline
3. Ng SE, Low A, Tang KK, et al. **Idiopathic normal pressure hydrocephalus: correlating magnetic resonance imaging biomarkers with clinical response.** *Ann Acad Med Singap* 2009;38:803–08 Medline
4. Halperin JJ, Kurlan R, Schwalb JM, et al. **Practice guideline: Idiopathic normal pressure hydrocephalus: response to shunting and predictors of response.** *Neurology* 2015;85:2063–71 CrossRef Medline
5. Thakur SK, Serulle Y, Miskin NP, et al. **Lumbar puncture test in normal pressure hydrocephalus: does the volume of CSF removed affect the response to tap?** *AJNR Am J Neuroradiol* 2017;38:1456–60 CrossRef Medline
6. Damasceno BP. **Normal pressure hydrocephalus: diagnostic and predictive evaluation.** *Dement Neuropsychol* 2009;3:8–15 CrossRef Medline
7. Craven CL, Toma AK, Mostafa T, et al. **The predictive value of DESH for shunt responsiveness in idiopathic normal pressure hydrocephalus.** *J Clin Neurosci* 2016;34:294– 98 CrossRef Medline
8. Palm WM, Walchenbach R, Bruinsma B, et al. **Intracranial compartment volumes in normal pressure hydrocephalus: volumetric assessment versus outcome.** *AJNR Am J Neuroradiol* 2006;27:76–79 Medline
9. Virhammar J, Laurell K, Cesarini KG, et al. **The callosal angle measured on MRI as a predictor of outcome in idiopathic normal-pressure hydrocephalus.** *J Neurosurg* 2014;120:178–84 CrossRef Medline
10. Ishii K, Kanda T, Harada A, et al. **Clinical impact of the callosal angle in the diagnosis of idiopathic normal pressure hydrocephalus.** *Eur Radiol* 2008;18:2678–83 CrossRef Medline
11. Baroncini M, Balédent O, Ardi CE, et al. **Ventriculomegaly in the elderly: who needs a shunt? A MRI study on 90 patients.** *Acta Neurochir Suppl* 2018;126:221–28 CrossRef Medline
12. Miskin N, Patel H, Franceschi AM, et al. **Diagnosis of normal-pressure hydrocephalus: use of traditional measures in the era of volumetric MR imaging.** *Radiology* 2017;285:197–205 CrossRef Medline
13. Gunter NB, Schwarz CG, Graff-Radford J, et al. **Automated detection of imaging features of disproportionately enlarged subarachnoid space hydrocephalus using machine learning methods.** *NeuroImage Clin* 2019;21:101605 CrossRef Medline

14. Takahashi N, Kinoshita T, Ohmura T, et al. **Automated method to compute Evans index for diagnosis of idiopathic normal pressure hydrocephalus on brain CT images.** In: Amato SG, Petrick NA, eds. *Medical Imaging 2017: Computer-Aided Diagnosis*. Vol 10134. International Society for Optics and Photonics; 2017:101342C CrossRef
15. Szczepek E, Czerwosz LT, Nowiński K, et al. **Analysis of intracranial volume ratios by means of cerebrospinal fluid deployment indicators.** *Folia Neuropathol* 2015;53:121–27 CrossRef Medline
16. LaMontagne PJ, Benzinger TL, Morris JC, et al. **OASIS-3: longitudinal neuroimaging, clinical, and cognitive dataset for normal aging and Alzheimer disease.** *medRxiv* 2019. https://www.medrxiv.org/content/10.1101/2019.12.13.19014902v1.full.pdf. Accessed December 16, 2020
17. Marcus DS, Fotenos AF, Csernansky JG, et al. **Open access series of imaging studies: longitudinal MRI data in nondemented and demented older adults.** *J Cogn Neurosci* 2010;22:2677–84 CrossRef Medline
18. Jack CR, Bernstein MA, Fox NC, et al. **The Alzheimer's Disease Neuroimaging Initiative (ADNI): MRI methods.** *J Magn Reson Imaging* 2008;27:685–91 CrossRef Medline
19. Morris JC. **Clinical dementia rating: a reliable and valid diagnostic and staging measure for dementia of the Alzheimer type.** *Int Psychogeriatr* 1997;9(Suppl 1):173–76 CrossRef Medline
20. Fischl B. **FreeSurfer.** *Neuroimage* 2012;62:774–81 CrossRef Medline
21. Hiraoka K, Meguro K, Mori E. **Prevalence of idiopathic normal-pressure hydrocephalus in the elderly population of a Japanese rural community.** *Neurol Med Chir (Tokyo)* 2008;48:197–200 CrossRef Medline
22. Jaraj D, Rabiei K, Marlow T, et al. **Prevalence of idiopathic normal-pressure hydrocephalus.** *Neurology* 2014;82:1449–54 CrossRef Medline
23. Andersson J, Rosell M, Kockum K, et al. **Prevalence of idiopathic normal pressure hydrocephalus: a prospective, population-based study.** *PLoS One* 2019;14:e0217705 CrossRef Medline
24. Hebert LE, Weuve J, Scherr PA, et al. **Alzheimer disease in the United States (2010–2050) estimated using the 2010 census.** *Neurology* 2013;80:1778–83 CrossRef Medline
25. Sabbagh MN, Lue L-F, Fayard D, et al. **Increasing precision of clinical diagnosis of Alzheimer's disease using a combined algorithm incorporating clinical and novel biomarker data.** *Neurol Ther* 2017;6:83–95 CrossRef Medline
26. Silverberg G, Mayo M, Saul T, et al. **Elevated cerebrospinal fluid pressure in patients with Alzheimer's disease.** *Fluids Barriers CNS* 2006;3:7 CrossRef
27. Jinkins JR. **Clinical manifestations of hydrocephalus caused by impingement of the corpus callosum on the falx: an MR study in 40 patients.** *AJNR Am J Neuroradiol* 1991;12:331–40 Medline

SWI Susceptibility Vessel Sign in Patients Undergoing Mechanical Thrombectomy for Acute Ischemic Stroke

N.F. Belachew, T. Dobrocky, E.B. Aleman, T.R. Meinel, A. Hakim, J. Vynckier, M. Arnold, D.J. Seiffge, R. Wiest, P. Mordasini, J. Gralla, U. Fischer, E.I. Piechowiak, and J. Kaesmacher

ABSTRACT

BACKGROUND AND PURPOSE: The frequency and clinical significance of the susceptibility vessel sign in patients with acute ischemic stroke remains unclear. We aimed to assess its prevalence in patients with acute ischemic stroke undergoing mechanical thrombectomy and to analyze its association with interventional and clinical outcome parameters in that group.

MATERIALS AND METHODS: Six hundred seventy-six patients with acute ischemic stroke and admission MR imaging were reviewed retrospectively. Of those, 577 met the eligibility criteria for further analysis. Imaging was performed using a 1.5T or 3T MR imaging scanner. Associations between baseline variables, interventional and clinical outcome parameters, and susceptibility vessel sign were determined with multivariable logistic regression models. Results are shown as adjusted ORs with 95% CIs.

RESULTS: The susceptibility vessel sign was present in 87.5% ($n = 505$) of patients and associated with tandem occlusion (adjusted OR, 3.3; 95% CI, 1.1–10.0; $P = .032$) as well as successful reperfusion, defined as an expanded TICI score of ≥2b (adjusted OR, 2.4; 95% CI, 1.28–4.6; $P = .007$). The susceptibility vessel sign was independently associated with functional independence (mRS ≤ 2: adjusted OR, 2.1; 95% CI, 1.1–4.0; $P = .028$) and lower mortality (adjusted OR, 0.4; 95% CI, 0.2–0.7; $P = .003$) at 90 days, even after adjusting for successful reperfusion. The susceptibility vessel sign did not influence the number of passes performed during mechanical thrombectomy, the first-pass reperfusion, or the risk of peri- or postinterventional complications.

CONCLUSIONS: The susceptibility vessel sign is an MR imaging phenomenon frequently observed in patients with acute ischemic stroke and is associated with successful reperfusion after mechanical thrombectomy. However, superior clinical functional outcome and lower mortality noted in patients showing the susceptibility vessel sign could not be entirely attributed to higher reperfusion rates.

ABBREVIATIONS: AIS = acute ischemic stroke; aOR = adjusted OR; MT = mechanical thrombectomy; SVS = susceptibility vessel sign

SWI is an MR imaging sequence particularly sensitive to compounds that distort the local magnetic field and therefore allow the detection of very small amounts of blood products and calcium. Due to the paramagnetic property of deoxygenated hemoglobin in trapped blood cells, it can also be used to locate thrombus material in occluded vessels after acute ischemic stroke (AIS), which may be seen as a distinct loss of signal within the affected vessel.[1] While this phenomenon was first described as the "gradient recalled echo susceptibility vessel sign (GRE SVS)" in T2*-weighted imaging,[2,3] the clot-detection rate has proved to be significantly higher with SWI, which provides better spatial resolution and is therefore superior in visualizing blood-degradation products.[4] However, not all thromboembolic vessel occlusions are visible on SWI. Their detectability depends on the composition of the clot, making erythrocyte-rich thrombi more likely to result in an occlusion that is apparent on SWI.[5,6] While mechanical thrombectomy (MT) has proved effective in treating large-vessel occlusion in patients with AIS,[7] data on the prevalence of the SVS in these patients are inconsistent.[2-4,8-12] Although thrombus composition is known to influence the success of MT,[13-17] it is unclear whether the SVS is associated with successful reperfusion and good clinical outcome.[2,9-12,18,19] Our aim was to assess the

Received February 3, 2021; accepted after revision May 27.

From the Departments of Diagnostic and Interventional Neuroradiology (N.F.B., T.D., E.B.A., A.H., R.W., P.M., J.G., E.I.P., J.K.), Neurology (T.R.M., J.V., M.A., D.J.S., U.F.), and Diagnostic, Interventional and Pediatric Radiology (J.K.), Inselspital, Bern University Hospital, and University of Bern, Bern, Switzerland.

E.I. Piechowiak and J. Kaesmacher have shared last author position.

Please address correspondence to Nebiyat Filate Belachew, MD, Department of Diagnostic and Interventional Neuroradiology, Inselspital, Freiburgstr 18, CH-3010, Switzerland; e-mail: nebiyatfilate.belachew@insel.ch; @NFBelachew

Indicates open access to non-subscribers at www.ajnr.org

Indicates article with online supplemental data.

http://dx.doi.org/10.3174/ajnr.A7281

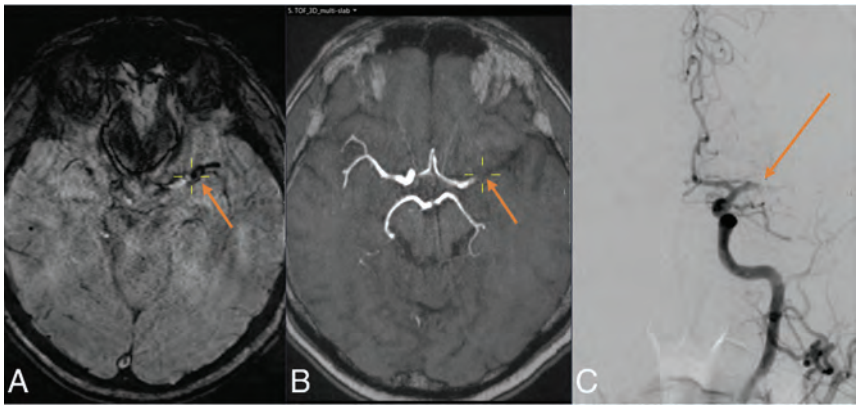

FIG 1. A 70-year-old male patient with acute ischemic stroke. The SVS is visible on SWI (*A*) as a distinct, circumscribed signal loss along the main trunk of the left MCA, representing the occlusive thrombus. Complete occlusion of the left MCA main trunk (M1 segment) is also seen on the arterial TOF sequence (*B*) and on DSA (*C*). *Yellow crosshairs* are centered on the proximal end of the vessel occlusion on SWI (*A*) and arterial TOF (*B*). The *arrow* points to the proximal end of the vessel occlusion on SWI, arterial TOF and DSA.

prevalence of the SVS in patients with AIS undergoing MT and to analyze its association with interventional and clinical outcome parameters.

MATERIALS AND METHODS

Inclusion Criteria

Clinical and radiologic data were gathered from the records of patients with AIS who underwent MT at our hospital between January 2010 and December 2018. The inclusion criteria were as follows: 1) a final clinical diagnosis of AIS; 2) SWI performed on admission; 3) symptomatic occlusion of at least one intracranial artery on angiography; and 4) the patient having undergone endovascular treatment in the form of MT. SWI quality was classified as "excellent" (if there were no artifacts), "good" (if there were minor artifacts), "poor" (if there were major artifacts, but the SVS was assessable), or "very poor" (if the SVS was not assessable due to major artifacts). The SVS was considered "technically undeterminable" if the thrombus was masked due to its proximity to the skull base or being overlaid with other pathologies (eg, hemorrhage). Patients with very poor-quality SWI or a technically undeterminable SVS status were excluded.

Most patients with stroke admitted to our institution are scanned using MR imaging. However, the final decision on whether to perform MR imaging or CT is made by the neuroradiologists and neurologists in charge on a case-by-case basis depending on clinical aspects and contraindications. SWI was an inherent part of our stroke MR imaging protocol throughout this study, except when the neuroradiologists were confident that it would yield inconclusive results on the basis of the sequences performed beforehand (ie, due to the presence of foreign objects or motion artifacts). This study was approved by the local ethics committee.

Analysis of Clinical Information

Demographics, baseline characteristics, and clinical data such as age, sex, history of stroke, medication before AIS (antiplatelet treatments, anticoagulants, or statins), and cardiovascular risk factors such as hypertension, diabetes mellitus, dyslipidemia, and smoking habits were collected. In addition, we recorded the systolic and diastolic blood pressures on admission, the glucose levels on admission, the NIHSS score on admission, and stroke subtypes according to the Trial of Org 10172 in Acute Stroke Treatment (TOAST) classification.[20] Also, IV thrombolysis before imaging (transfer patients) and before MT, time from symptom onset/last seen well to admission, time from symptom onset/last seen well to IV thrombolysis, time from symptom onset/last seen well to MT, and time from groin puncture to reperfusion were registered.

Technical Information on MR Imaging

Imaging was performed on a 1.5T or 3T MR imaging scanner (1.5T: Magnetom Avanto or Magnetom Aera; 3T: Magnetom Verio; Siemens). Magnetom Avanto 1.5T SWI and 1.5T Magnetom Aera SWI were performed with the following parameters: TR, 49 ms; TE, 40 ms; flip angle, 15.0°; section thickness, 1.6, 1.8, or 2.0 mm; and intersection gap, 0 mm. Magnetom Verio 3T SWI was performed with the following parameters: TR, 27 ms; TE, 20 ms; flip angle, 15.0°; section thickness, 2.0 mm; and intersection gap, 0 mm.

Imaging Analysis

The presence of SVS was evaluated retrospectively by 2 independent neuroradiologists (N.F.B. and E.B.A.) with 5 and 4 years of experience, respectively. Except for knowing which side was symptomatic, the raters were blinded to all clinical information and outcome parameters, and they were not involved in any patient treatment. SWI was classified as SVS+ if a distinct signal loss corresponding to an occluded and symptomatic intracranial artery could be identified (Fig 1). Applying the definition used by Kang et al,[9] we determined the SVS to be present even if its diameter was the same as or smaller than the diameter of the contralateral artery. However, the SVS was only classified as SVS+ if no alternative explanations for the signal loss were observed (ie, neighboring vein, petechial hemorrhage, or microcalcification in the neighboring parenchyma). SWIs in which the SVS was not present though a symptomatic vessel occlusion was apparent were categorized as SVS– (Fig 2). MR imaging field strength and time from symptom onset/last seen well to imaging were documented for each case. Additionally, the DWI-ASPECTS was evaluated.

DSA and MT

The primary site of occlusion was determined on conventional angiography. Tandem occlusions were also noted. However, only intracranial occlusions were considered for SVS evaluation. MT was performed by skilled interventional neuroradiologists

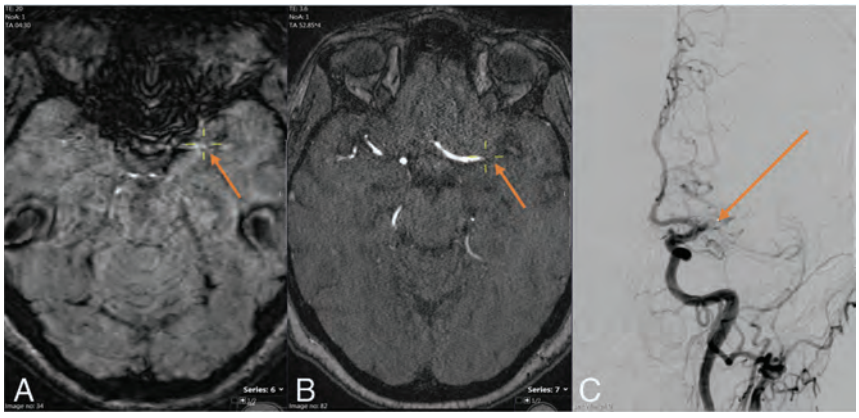

FIG 2. A 48-year-old female patient with acute ischemic stroke. SWI shows no SVS (*A*). Complete proximal occlusion of the left MCA main trunk (M1 segment) is seen on the arterial TOF sequence (*B*) and on DSA (*C*). *Yellow crosshairs* are centered on the proximal end of the vessel occlusion on SWI (*A*) and arterial TOF (*B*). The *arrow* points to the proximal end of the vessel occlusion on SWI, arterial TOF, and DSA.

according to the current clinical practice guidelines and institutional protocols. The expanded TICI score[21] was documented after the first pass and at the end of MT. Also, the total number of passes performed during MT was recorded. First-pass reperfusion and overall reperfusion were deemed successful if the expanded TICI was 2b or better. DSA was screened for embolization into previously unaffected (ie, new) territories and for peri-interventional complications (vasospasm, dissection, and perforation) by a research fellow with 3 years of experience.

Outcome

The clinical outcome was assessed by evaluating the NIHSS 24 hours after treatment as well as the mRS and mortality 90 days after treatment. The NIHSS was evaluated by the attending neurologist, whereas the mRS was evaluated by a neurologist or a study nurse, in person or by a telephone call. Early neurologic recovery was defined as a decrease in the NIHSS score 24 hours after treatment compared with admission, whereas functional independence was defined as mRS $\leq$ 2. Symptomatic intracranial hemorrhage within 48 hours after MT was assessed according to the European Cooperative Acute Stroke Study (ECASS II).[22]

Statistical Analysis

Data analysis was performed using the SPSS Software (Version 25.0; IBM). Continuous variables were compared using the Mann-Whitney *U* test, whereas categoric variables were compared using the χ^2 test. Multivariable binary logistic regression analyses were performed to determine the association between baseline parameters, tandem occlusion, and successful reperfusion, as well as functional independence and mortality at 90 days with the SVS. Adjustment was performed for all cofactors with $P < .15$ (sex, diabetes mellitus, prestroke mRS >2, antiplatelet therapy, diastolic blood pressure, admission glucose, admission NIHSS, primary site of occlusion, tandem occlusion, and DWI-ASPECTS) as well as for additional cofactors that are known or suspected to influence the variables of interest (ie, age, sex, bridging therapy, stroke subtype, and symptomatic intracranial hemorrhage). Sensitivity analyses excluding patients with prestroke mRS > 2 were performed for functional independence and mortality at 90 days. Interrater reliability was determined by calculating the Cohen κ. Results with 2-tailed *P* values < .05 were considered statistically significant and are shown as median comparisons with respective *P* values or as an adjusted OR (aOR) with 95% CIs.

RESULTS

From January 2010 to December 2018, one thousand three hundred seventeen patients underwent MT for AIS at our hospital. In 676 patients, an MR imaging was acquired on admission, and SWI was available for 614 of them. SVS status was assessable in 93.4% patients ($n = 577$; 37 were excluded due to very poor-quality SWI or technically undeterminable SVS status) of whom 87.5% ($n = 505/577$) were categorized as SVS+. An overview of the patient-selection process can be found in the Online Supplemental Data. SVS prevalence tended to be higher among patients who had received IV thrombolysis before MR imaging, but this difference was not statistically significant (87.5% versus 78.6%; $P = .076$). Patients for whom the SVS was assessable did not differ significantly from patients with an unassessable SVS with regard to demographics and key outcome parameters (Online Supplemental Data). However, AIS patients with an admission CT instead of an admission MR imaging had significantly higher admission NIHSS scores, higher NIHSS scores at 24 hours, lower reperfusion rates, lower rates of functional independence at 90 days, and higher mortality rates at 90 days (Online Supplemental Data). Interrater reliability for SVS classification was strong ($\kappa = 0.873$, $P < .001$). The results for both the SVS– and the SVS+ group are listed in the Online Supplemental Data.

The SVS– group had a higher percentage of female patients (62.5% versus 49.7%; $P = .042$), more patients diagnosed with diabetes mellitus before stroke (27.8% versus 12.7%; $P = .001$), more patients with prestroke dependency (mRS > 2: 16.7% versus 7.1%; $P = .005$), and higher DWI-ASPECTS (8 versus 8; $P = .006$). Vessel occlusions in the anterior circulation tended to be seen more often in the ICA and proximal MCA (M1) for the SVS+ group and more often in the distal MCA (M2 and M3) for the SVS– group (ICA = 8.3% versus 16.4%; M1 = 50.0% versus 53.1%; M2 = 25.0% versus 21.4%; M3 = 0.6% versus 1.4%; $P = .013$). By contrast, the SVS+ group had more tandem occlusions (19.2% versus 5.6%; $P = .004$). None of the other baseline characteristics differed between the 2 groups.

In a multivariable logistic regression model, diabetes mellitus before stroke (aOR, 0.431; 95% CI, 0.204–0.912; $P = .028$) and prestroke dependency (mRS > 2: aOR, 0.390; 95% CI, 0.174–0.875; $P = .022$) were associated with SVS– after adjusting for all factors with $P < .15$ (Online Supplemental Data). Although the SVS– group had a higher percentage of female patients, the same

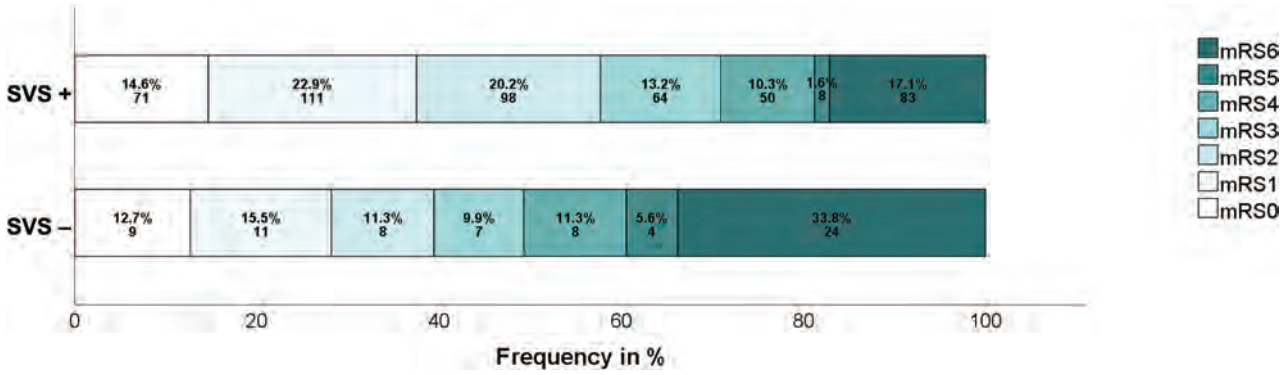

FIG 3. Distribution of the mRS according to SVS status. Data are expressed as percentages and total values. Prestroke mRS > 2 for SVS+ versus SVS–: 7.1% versus 16.7% ($P = .005$). Functional independence (mRS ≤ 2) for SVS+ versus SVS– at 90 days: 59.7% versus 40.6% ($P = .004$).

model showed no association between sex and SVS status (aOR, 0.680; 95% CI, 0.373–1.239; $P = .208$).

In a second model in which we compared patients on the basis of the presence of tandem pathology and adjusted for all covariates with $P < .15$ (Online Supplemental Data), tandem occlusions were associated with SVS+ intracranial vessel occlusions (aOR, 3.328; 95% CI, 1.112–9.965; $P = .032$).

Association between the SVS and Reperfusion

Patients with SVS+ intracranial vessel occlusions had a higher rate of successful reperfusion after MT (84.6% versus 72.2%; $P = .009$). Notably, the presence of the SVS had no influence on the number of passes performed during MT (1 versus 1; $P = .552$), the first-pass reperfusion (58.6% versus 52.9%; $P = .382$), or the likelihood of peri- or postinterventional complications (symptomatic intracranial hemorrhage: 4.2% versus 5.6%, $P = 0591$; embolization into previously unaffected [ie, new] territories: 4.2% versus 1.4%, $P = .250$; peri-interventional complications: 14.3% versus 16.7%, $P = .592$). In a third logistic regression model adjusted for all covariates with $P < .15$ (Online Supplemental Data) as well as for age, bridging therapy, and stroke subtype, SVS+ was associated with successful reperfusion after MT (expanded TICI score ≥ 2b: aOR, 2.864; 95% CI, 1.442–5.691; $P = .003$). This observation did not change regardless of whose rating (rater 1 or 2) was used for analysis (Online Supplemental Data).

Association between the SVS and Clinical Outcome

The SVS+ group showed superior early recovery 24 hours after treatment (NIHSS improvement: −4 versus −2; $P = .001$) and a better clinical outcome 90 days after treatment (mRS ≤ 2: 55.4% versus 38.9%; $P = .004$). Mortality was higher in the SVS– group (33.3% versus 16.4%; $P = .001$). Figure 3 shows the mRS distribution according to SVS status. In two separate multivariable regression models adjusted for the effects of all cofactors with $P < .15$ (Online Supplemental Data) as well as clinical predictors of good outcome (age, stroke subtype, bridging therapy, successful reperfusion, and symptomatic ICH), SVS+ was associated with a lower mRS score (mRS ≤ 2: aOR, 2.062; 95% CI, 1.034–4.115; $P = .040$) and lower mortality (aOR, 0.351; 95% CI, 0.167–0.738; $P = .006$) 90 days after treatment. These observations did not change regardless of the whose rating (rater 1 or 2) was used for analysis (Online Supplemental Data). A sensitivity analysis that excluded patients with prestroke mRS > 2 and was adjusted for the first-line retrieval technique did not change these findings either (Online Supplemental Data).

DISCUSSION

The main findings of this study are the following: The SVS was present in 87.5% ($n = 505$) of patients treated with MT for intracranial vessel occlusion and was associated with tandem occlusion as well as successful reperfusion. It was independently associated with functional independence and lower mortality rates 90 days after treatment, even after adjusting for successful reperfusion and showed no association with the number of passes performed during MT, the first-pass reperfusion, or the peri- and postinterventional complication rate.

While earlier studies included only a small number of patients,[2,3,8,9,18] more recent ones have examined the SVS in larger study populations.[10-12] However, because several important questions remain, larger studies are required.[12]

Early publications reported an overall SVS prevalence of ~ 50%[2,3,8] in patients with AIS, whereas more recent studies have indicated that the prevalence is around 70%.[9-12,18] Our findings suggest that the prevalence may be even higher. There are several possible explanations for these differences: 1) Sample size among the studies examining SVS varied widely, and small test populations may be prone to statistical inaccuracies that limit validity.[11,12,23] 2) The eligibility criteria for MR imaging may differ between institutions and hospitals, leading to selection bias. For instance, whereas some hospitals scan patients regardless of special monitoring, others prefer CT when such monitoring is required. However, the SVS distribution may be different in patients whose condition is critical. 3) We only included patients who had undergone MT; consequently, patients who showed spontaneous reperfusion or had sufficient reperfusion after IV thrombolysis were excluded. Despite some evidence to the contrary,[2,3] most studies suggested that SVS+ intracranial vessel occlusions (particularly in the ICA and MCA) are less amenable to IV thrombolysis.[8,24,25] Therefore, it is possible that the overall prevalence is lower if MR imaging is always performed before IV thrombolysis. 4) The comparability of SVS studies is often limited

owing to differing inclusion criteria (eg, ICA/M1 occlusions only[8] versus other occlusion patterns[3]). 5) Not all studies adopted the same definition of SVS. Whereas some defined it as a signal loss within the margins of an acutely occluded vessel,[9] others considered the SVS to be present only if the diameter of the signal loss exceeded that of the contralateral vessel.[3] 6) The sensitivity for SVS may differ depending on the sequence (T2* gradient recalled-echo versus SWI[4]) and the particular MR imaging scanner used (ie, its field strength and manufacturer). The slightly longer acquisition time for SWI compared with T2* gradient recalled-echo sequences might be justified by the higher spatial resolution of SWI, which provides better visualization of blood-degradation products in distal or small thrombi and has proved to increase SVS sensitivity.[4] 7) Indications for MT and access to MR imaging have evolved considerably since the SVS was first reported in 2000.[1] Thus, study populations may differ significantly between current and earlier studies.

MT is more effective with erythrocyte-rich than with fibrin-rich thrombi.[14,26,27] Because erythrocyte-rich clots are more likely to result in an SVS+ intracranial vessel occlusion,[5] SVS may also predict successful reperfusion after MT. If so, it could function as a noninvasive surrogate marker for thrombus composition. Although many studies have addressed this question, only one found an association between the SVS status and reperfusion success after MT.[9-12,18] Other than the present study, Darcourt et al[11,17] were the only investigators to report a significant relationship between SVS+ intracranial vessel occlusions and successful reperfusion after MT. This report raises the question of why earlier studies found no association. Some of the previously mentioned factors (ie, differing SVS definitions and variations in the sensitivity of SVS detection) may play a role. In addition, Bourcier et al[10] have suggested that first-line MT techniques may affect reperfusion success in AIS patients with SVS. This hypothesis is currently being investigated prospectively (adaptatiVe Endovascular Strategy to the CloT MRI in Large Intracranial Vessel Occlusion [VECTOR] trial; ClinicalTrials.gov Identifier: NCT04139486). Future studies could also investigate whether certain stent-based retrieval techniques are superior to others in terms of reperfusion and/or peri- and postinterventional complication rates. Although our observations suggest that SVS+ thrombi are easier to retrieve via MT than SVS– clots, most data so far suggest that they are less amenable to intravenous thrombolysis. Future studies may examine the risks and benefits of bridging therapy in patients with AIS, depending on the SVS status.

Few data are available on the association of SVS status with clinical outcome after MT. Bourcier et al[18] reported lower NIHSS scores 24 hours after treatment and lower mRS scores 90 days after treatment in SVS+ patients but were not able to confirm the finding in a later study with a larger study population.[10] Darcourt et al[11] reported that SVS+ intracranial vessel occlusions were associated with early neurologic recovery. To our knowledge, no other studies have examined clinical outcome in relation to the SVS after thrombectomy. Our data show superior early neurologic recovery when the SVS was present. Furthermore, SVS+ was associated with better functional outcome and survival 90 days after treatment. Because these findings did not change after factoring in reperfusion success, other factors must have contributed to cause worse outcomes in patients in whom the SVS was absent. We hypothesized that atypical thrombi (septic[28] or neoplastic[29,30]), which are likely to contain few erythrocytes[31] and develop after a preceding illness, could be part of the explanation. However, in an additional sensitivity analysis, clinical outcome remained worse for the SVS–group when patients with prestroke dependency (mRS $>$ 2) were excluded.

Taking into account that SVS–was also associated with the diagnosis of diabetes mellitus before stroke, further studies on the overall health of patients with SVS–intracranial vessel occlusions are needed to identify underlying, non-stroke-related diseases that may affect thrombus composition[32] and could explain prestroke dependency, worse outcome, and/or higher mortality rates. According to our data, the occlusion site, for which we adjusted in all our statistical analyses, did not influence reperfusion success or clinical outcome. However, Aoki et al[23] have suggested differences in outcome for the proximal-versus-distal M1 SVS. Further studies are needed to determine whether the conclusions drawn about SVS as a potential imaging biomarker depend on the affected vessel segment and/or circulation (ie, anterior versus posterior).

The number of passes performed during MT is a good indicator of the difficulty of clot removal. Although Bourcier et al[10] provided data on how often $>$2 passes were performed, none of the other studies examining the association between SVS status and reperfusion after MT have addressed this question.[9,11,12,18] Our data suggest that there is no difference between patients with SVS+ and SVS– in this regard. However, the number of passes performed is at the discretion of the neurointerventionalist in charge and may vary depending on his or her experience and the applicable standards as well as clinical and environmental factors. Although all MTs evaluated in this study were performed by skilled experts, comparability with future studies from different institutions might be limited as a consequence. Further research is necessary to establish reliable guidelines on appropriate MT strategies and the safe number of passes, depending on clinical aspects and imaging characteristics of the occlusive clot.

We hypothesized that intracranial vessel occlusions caused by thromboembolic incidents originating from arteriosclerotic plaques or dissections of the carotid arteries tend to contain a higher number of trapped erythrocytes with deoxygenated hemoglobin (deoxyhemoglobin, intracellular methemoglobin, or hemosiderin) and, thus, are more likely to be SVS+. Our data support that assumption; 96.0% of patients with severe stenosis or dissection of the carotid arteries had an SVS+ intracranial vessel occlusion. However, we found no association between SVS status and stroke subtypes according to the TOAST classification. Although there are some data indicating that SVS+ is associated with a cardioembolic stroke cause,[3,9] an equal number of studies have found no association between SVS status and stroke subtype whatsoever.[8,10] Some contraindications to MR imaging (pacemakers, implantable cardioverter-defibrillators, and other metal implants) may have altered the distribution of stroke subtypes in our patient cohort because patients with certain pre-existing medical conditions (eg, heart disease) could have been excluded disproportionately. Advances in the development and increasing use of MR imaging–compatible medical devices could allow the

inclusion of those patients in future studies. The initial SVS status of intracranial vessel occlusions that resolved without MT may have some diagnostic value with regard to etiology.[3,9] Further research on how spontaneous reperfusion and the efficiency of IV thrombolysis relate to SVS status is required before the potential of SVS as an imaging biomarker for stroke subtype can be evaluated reliably.

Limitations

This was a retrospective single-center study, which may limit generalizability. Patients who were not eligible for MR imaging or showed an undeterminable SVS were excluded, possibly causing selection bias. A previous study has shown that baseline criteria and reperfusion outcome of patients with stroke may differ depending on initial imaging technique.[33] Because most studies examining SVS in patients with AIS used T2* gradient recalled-echo sequences, comparability with our study is limited. Although the SVS may give some indication about clot histology, clot composition, which may also impact reperfusion success, was not quantified. The SVS– and SVS+ groups could not be compared with regard to thrombus length and clot burden because the thrombus could only be visualized in patients who showed the SVS. There was no adjustment for occlusions that crossed vessel sections and affected multiple branches (ie, M1–M2), though this aspect might impact first-pass reperfusion and overall reperfusion. Good collateral circulation has been associated with better reperfusion,[34] but because contralateral angiography was not performed systematically, we were not able to adjust for this factor. We also did not check for early re-occlusion. Future studies could evaluate whether SVS status affects the sustainability of any achieved reperfusion. First-pass expanded TICI, the NIHSS score 24 hours after treatment, and clinical outcome at 90 days could not be assessed for every patient because angiography was not always performed after the first pass and a few patients were lost to follow-up. The resulting data gaps constitute another source of potential selection bias.

CONCLUSIONS

The SVS is an MR imaging phenomenon frequently observed in patients with AIS, which is associated with successful reperfusion and superior clinical outcome after MT. Our study shows the potential benefits of assessing the SVS in the acute stroke setting. Knowledge of SVS status may influence treatment decisions, improve follow-up care, and refine the assessment of prognosis. Future research will need to assess the diagnostic value of SVS regarding clot composition and patient comorbidities, which may help explain the differences in reperfusion success and clinical outcome observed in this study. However, decisions regarding imaging technique should be made on a case-by-case basis, depending on availability and the patient's clinical condition. Future studies will have to evaluate the overall clinical value of SVS assessment before it can be considered in the diagnostic process.

ACKNOWLEDGMENTS

We thank Susan Kaplan for editorial assistance.

Disclosures: Marcel Arnold—*RELATED*: *Grant*: Swiss National Science Foundation, Swiss Heart Foundation, *Comments*: research grants*; *Consulting Fee or Honorarium*: Bayer HealthCare AG, Bristol Myers Squibb, Covidien, Medtronic, AstraZeneca, Amgen, Daiichi Sankyo, Nestlé Health Science, and Portola, *Comments*: speaker honoraria for scientific lectures or honoraria for scientific advisory boards. Roland Wiest—*RELATED*: *Grant*: Innosuisse grant 43087.1 IP-LS*; *UNRELATED*: *Expert Testimony*: Bayer HealthCare AG*; *Grants/Grants Pending*: Sinergia CRSII5_180365.* Pasquale Mordasini—*UNRELATED*: *Consultancy*: Consultant for Medtronic, Cerenovus, MicroVention, Phenox, Siemens*; *Grants/Grants Pending*: scientific grants from Siemens, iSchemaView*; *Payment for Lectures Including Service on Speakers Bureaus*: speaker at educational courses for Medtronic.* Jan Gralla—*RELATED*: *Grant*: Swiss National Foundation, *Comments*: Swiss National Science Foundation SNF grant for MRI in stroke*; *UNRELATED*: *Board Membership*: Penumbra, *Comments*: Clinical Event Committee member of the Promise Study (Penumbra), Consultancy*; *Consultancy*: Medtronic, *Comments*: Global Principal Investigator of STAR and Swift Direct (Medtronic), Consultancy.* Urs Fischer—*UNRELATED*: *Consultancy*: Medtronic, Stryker*; *Grants/Grants Pending*: Swiss National Science Foundation, Medtronic, *Comments*: SWIFT DIRECT, BEYOND SWIFT, ELAN, SWITCH.* Johannes Kaesmacher—*UNRELATED*: *Grants/Grants Pending*: SAMW/Bangerter Foundation.* *Money paid to institution.

REFERENCES

1. Flacke S, Urbach H, Keller E, et al. **Middle cerebral artery (MCA) susceptibility sign at susceptibility-based perfusion MR imaging: clinical importance and comparison with hyperdense MCA sign at CT.** *Radiology* 2000;215:476–82 CrossRef Medline
2. Schellinger PD, Chalela JA, Kang DW, et al. **Diagnostic and prognostic value of early MR imaging vessel signs in hyperacute patients with stroke imaged <3 hours and treated with recombinant tissue plasminogen activator**. *AJNR Am J Neuroradiol* 2005;26:618–24 Medline
3. Cho KH, Kim JS, Kwon SU, et al. **Significance of susceptibility vessel sign on T2*-weighted gradient echo imaging for identification of stroke subtypes.** *Stroke* 2005;36:2379–83 CrossRef Medline
4. Allibert R, Billon Grand C, Vuillier F, et al. **Advantages of susceptibility-weighted magnetic resonance sequences in the visualization of intravascular thrombi in acute ischemic stroke.** *Int J Stroke* 2014;9:980–84 CrossRef Medline
5. Kim SK, Yoon W, Kim TS, et al. **Histologic analysis of retrieved clots in acute ischemic stroke: correlation with stroke etiology and gradient-echo MRI.** *AJNR Am J Neuroradiol* 2015;36:1756–62 CrossRef Medline
6. Liebeskind DS, Sanossian N, Yong WH, et al. **CT and MRI early vessel signs reflect clot composition in acute stroke.** *Stroke* 2011;42:1237–43 CrossRef Medline
7. Powers WJ, Derdeyn CP, Biller J, et al; American Heart Association Stroke Council. **2015 American Heart Association/American Stroke Association Focused Update of the 2013 Guidelines for the Early Management of Patients with Acute Ischemic Stroke Regarding Endovascular Treatment: a Guideline for Healthcare Professionals from the American Heart Association/American Stroke Association.** *Stroke* 2015;46:3020–35 CrossRef Medline
8. Kimura K, Iguchi Y, Shibazaki K, et al. **M1 susceptibility vessel sign on T2* as a strong predictor for no early recanalization after IV-t-PA in acute ischemic stroke.** *Stroke* 2009;40:3130–32 CrossRef Medline
9. Kang DW, Jeong HG, Kim DY, et al. **Prediction of stroke subtype and recanalization using susceptibility vessel sign on susceptibility-weighted magnetic resonance imaging.** *Stroke* 2017;48:1554–59 CrossRef Medline
10. Bourcier R, Mazighi M, Labreuche J, et al; ASTER Trial Investigators. **Susceptibility vessel sign in the ASTER trial: Higher recanalization rate and more favourable clinical outcome after first line stent retriever compared to contact aspiration.** *J Stroke* 2018;20:268–76 CrossRef Medline
11. Darcourt J, Withayasuk P, Vukasinovic I, et al. **Predictive value of susceptibility vessel sign for arterial recanalization and clinical improvement in ischemic stroke.** *Stroke* 2019;50:512–15 CrossRef Medline

12. Soize S, Batista AL, Rodriguez Regent C, et al. **Susceptibility vessel sign on T2* magnetic resonance imaging and recanalization results of mechanical thrombectomy with stent retrievers: a multicentre cohort study.** *Eur J Neurol* 2015;22:967–72 CrossRef Medline
13. Van Der Marel K, Chueh J-Y, Brooks OW, et al. **Quantitative assessment of device-clot interaction for stent retriever thrombectomy.** *J Neurointerv Surg* 2016;8:1278–82 CrossRef Medline
14. Yuki I, Kan I, Vinters HV, et al. **The impact of thromboemboli histology on the performance of a mechanical thrombectomy device.** *AJNR Am J Neuroradiol* 2012;33:643–48 CrossRef Medline
15. Dobrocky T, Piechowiak E, Cianfoni A, et al. **Thrombectomy of calcified emboli in stroke: Does histology of thrombi influence the effectiveness of thrombectomy?** *J Neurointerv Surg* 2018;10:345–50 CrossRef Medline
16. Duffy S, Mccarthy R, Farrell M, et al. **Per-pass analysis of thrombus composition in patients with acute ischemic stroke undergoing mechanical thrombectomy.** *Stroke* 2019;50:1156–63 CrossRef Medline
17. Darcourt J, Garcia C, Phuong DM, et al. **Absence of susceptibility vessel sign is associated with aspiration-resistant fibrin/platelet-rich thrombi.** *Int J Stroke* 2021 Jan 12. [Epub ahead of print] CrossRef Medline
18. Bourcier R, Volpi S, Guyomarch B, et al. **Susceptibility vessel sign on MRI predicts favorable clinical outcome in patients with anterior circulation acute stroke treated with mechanical thrombectomy.** *AJNR Am J Neuroradiol* 2015;36:2346–53 CrossRef Medline
19. Liu M, Li L, Li G. **The different clinical value of susceptibility vessel sign in acute ischemic patients with stroke under different interventional therapy: a systematic review and meta-analysis.** *J Clin Neurosci* 2019;62:72–79 CrossRef Medline
20. Adams HP, Bendixen BH, Kappelle LJ, et al. **Classification of subtype of acute ischemic stroke: definitions for use in a multicenter clinical trial–TOAST.** Trial of Org 10172 in Acute Stroke Treatment. *Stroke* 1993;24:35–41 CrossRef Medline
21. Liebeskind DS, Bracard S, Guillemin F, et al; HERMES Collaborators. **ETICI reperfusion: defining success in endovascular stroke therapy.** *J Neurointerv Surg* 2019;11:433–38 CrossRef Medline
22. Hacke W, Kaste M, Fieschi C, et al. **Randomised double-blind placebo-controlled trial of thrombolytic therapy with intravenous alteplase in acute ischaemic stroke (ECASS II)**: S**econd European-Australasian Acute Stroke Study Investigators.** *Lancet* 1998;352:1245–51 CrossRef Medline
23. Lapergue B, Blanc R, Gory B, et al; ASTER Trial Investigators. **Effect of endovascular contact aspiration vs stent retriever on revascularization in patients with acute ischemic stroke and large vessel occlusion: the ASTER randomized clinical trial.** *JAMA* 2017;318:443–52 CrossRef Medline
24. Aoki J, Kimura K, Shibazaki K, et al. **Location of the susceptibility vessel sign on T2*-weighted MRI and early recanalization within 1 hour after tissue plasminogen activator administration.** *Cerebrovasc Dis Extra* 2013;3:111–20 CrossRef Medline
25. Kimura K, Sakamoto Y, Aoki J, et al. **Clinical and MRI predictors of no early recanalization within 1 hour after tissue-type plasminogen activator administration.** *Stroke* 2011;42:3150–55 CrossRef Medline
26. Hashimoto T, Hayakawa M, Funatsu N, et al. **Histopathologic analysis of retrieved thrombi associated with successful reperfusion after acute stroke thrombectomy.** *Stroke* 2016;47:3035–37 CrossRef Medline
27. Gunning GM, Mcardle K, Mirza M, et al. **Clot friction variation with fibrin content; implications for resistance to thrombectomy.** *J Neurointerv Surg* 2018;10:34–38 CrossRef Medline
28. Ruttmann E, Willeit J, Ulmer H, et al. **Neurological outcome of septic cardioembolic stroke after infective endocarditis.** *Stroke* 2006;37:2094–99 CrossRef Medline
29. Kneihsl M, Enzinger C, Wünsch G, et al. **Poor short-term outcome in patients with ischaemic stroke and active cancer.** *J Neurol* 2016;263:150–56 CrossRef Medline
30. Aarnio K, Joensuu H, Haapaniemi E, et al. **Cancer in young adults with ischemic stroke.** *Stroke* 2015;46:1601–06 CrossRef Medline
31. Fu CH, Chen CH, Lin YH, et al. **Fibrin and platelet-rich composition in retrieved thrombi hallmarks stroke with active cancer.** *Stroke* 2020;51:3723–27 CrossRef Medline
32. Ye G, Gao Q, Qi P, et al. **The role of diabetes mellitus on the thrombus composition in patients with acute ischemic stroke.** *Interv Neuroradiol* 2020;26:329–36 CrossRef Medline
33. Meinel TR, Kaesmacher J, Mosimann PJ, et al. **Association of initial imaging modality and futile recanalization after thrombectomy.** *Neurology* 2020;95:e2331–42 CrossRef Medline
34. Bang OY, Saver JL, Kim SJ, et al. **Collateral flow predicts response to endovascular therapy for acute ischemic stroke.** *Stroke* 2011;42:693–99 CrossRef Medline

Impact of Implementing an Elaborated CT Perfusion Protocol for Aneurysmal SAH on Functional Outcome: CTP Protocol for SAH

V. Malinova, K. Döring, M.-N. Psychogios, V. Rohde, and D. Mielke

ABSTRACT

BACKGROUND AND PURPOSE: The acute phase of aneurysmal SAH is characterized by a plethora of impending complications with the potential to worsen patients' outcomes. The aim of this study was to evaluate whether an elaborated CTP-based imaging protocol during the acute aneurysmal SAH phase is able to prevent delayed infarctions and contribute to a better outcome.

MATERIALS AND METHODS: In 2012, an elaborated CTP-based protocol was implemented for the management of patients with aneurysmal SAH. Retrospective analysis of patients with aneurysmal SAH treated from 2010 to 2013 was performed, comparing the patients treated before (group one, 2010–2011) with those treated after the protocol implementation (group two, 2012–2013) with regard to delayed infarctions and outcome according to the mRS at 3-months' follow-up.

RESULTS: A total of 133 patients were enrolled, of whom 57 were included in group 1, and 76, in group 2. There were no significant differences between the groups concerning baseline characteristics. In the multivariate analysis, independent predictors of a good outcome (mRS $\leq$ 2) were younger age ($P < .001$), lower World Federation of Neurosurgical Societies grade ($P < .001$), absence of delayed infarction ($P = .01$), and management according to the CTP protocol ($P = .01$). Larger or multiple infarctions occurred significantly more often in group 1 compared with group 2 (88% versus 33% of all delayed infarctions, $P = .03$). The outcome in group 2 was significantly better compared with group 1 ($P = .005$).

CONCLUSIONS: The findings suggest that implementation of an elaborated CTP protocol is associated with a better outcome. An earlier initiation of further diagnostics and treatment with prevention of large territorial and/or multiple infarctions might have led to this finding.

ABBREVIATIONS: aSAH = aneurysmal subarachnoid hemorrhage; DCI = delayed cerebral ischemia; DIND = delayed ischemic neurologic deficits; ERT = endovascular rescue therapy; TCD = transcranial Doppler sonography; WFNS = World Federation of Neurosurgical Societies

Aneurysmal SAH (aSAH) is a potentially lethal cerebrovascular disease due to primary and secondary brain function disturbances requiring elaborated treatment protocols in cerebrovascular centers with a thorough expertise in this field.[1] In particular, the first 2 weeks after aneurysm rupture represent the most critical phase of aSAH, associated with impending complications with the risk of substantially worsening the functional outcome.[2,3] The focus of most diagnostic and therapeutic measures in the acute phase after aSAH is preservation of sufficient cerebral perfusion with the aim of prevention of secondary brain injury. CTP has been increasingly implemented in imaging protocols for early prediction and detection of delayed cerebral ischemia (DCI) after aSAH.[4-9] Nevertheless, there is a substantial heterogeneity in the CTP protocols used in different centers, not allowing general conclusions concerning the beneficial role of CTP protocols for the management of patients with aSAH in clinical practice. Despite the increased use of CTP, its actual diagnostic and prognostic value has not yet been completely determined. In 2012, an interdisciplinary imaging protocol was drawn up (neurosurgery and neuroradiology) at our institution (University Medical Center Göttingen) to facilitate a uniform management of patients with aSAH in the acute phase after ictus. Before 2012, CTP was performed only on an individual basis. The aim of this study was to investigate whether an elaborated CTP-based imaging protocol during the acute aSAH phase contributes to earlier identification of patients at risk for developing DCI and prevention of delayed infarction. Our hypothesis was that an elaborated CTP-based protocol would lead to a lower incidence of delayed infarction or to smaller infarctions and therefore would result in a better clinical outcome.

Received March 25, 2021; accepted after revision July 3.

From the Departments of Neurosurgery (V.M., V.R., D.M.) and Neuroradiology (K.D., M.-N.P.), Georg-August-University, Göttingen, Germany; and Department of Neuroradiology (M.-N.P.), Clinic of Radiology and Nuclear Medicine, University Medicine Basel, Basel, Switzerland.

Please address correspondence to Vesna Malinova, MD, Department of Neurosurgery, Georg-August-University, Robert-Koch-Str 40, 37075 Göttingen, Germany; e-mail: vesna.malinova@gmail.com

http://dx.doi.org/10.3174/ajnr.A7279

MATERIALS AND METHODS

Patient Population

This study was conducted according to the principles of the Declaration of Helsinki.[10] The study (No. 16/9/20) was approved by the local Ethics Committee of University Medicine Göttingen. A patient's consent for treatment was obtained according to the individual institutional guidelines. Due to the retrospective analysis of the data for this study, additional informed consent was deemed unnecessary.

A consecutive cohort of patients with aSAH treated at our department in a 4-year period was retrospectively analyzed. The inclusion criterion was complete data availability concerning the baseline characteristics, the ischemic complications, and the functional outcome. Patients treated before 2010 could not be included because of unavailability of complete data. Because the CTP protocol was implemented in 2012, group 1, in which CTP was performed on an individual basis, consisted of all patients treated between January 2010 and December 2011. Group 2, in which the CTP protocol was applied, consisted of the patients treated between January 2012 and December 2013. While management of patients with SAH using the CTP protocol was continued after December 2013, we decided to compare similar study periods to avoid data distortion during statistical analysis and eliminate possible confounders. Both groups were compared regarding the detection and management of ischemic complications as well as functional outcome.

All patients were admitted to the intensive care unit, where they were treated for at least 14 days after the bleeding. Aneurysm occlusion was performed within 48 hours after rupture by either microsurgical clipping or endovascular coiling. Patients who were admitted later were excluded. A CT scan was performed 4 hours after aneurysm treatment. Any infarction seen on that CT scan was considered treatment-associated and not related to DCI. Nimodipine was routinely administered orally or intravenously for 14 days in every patient. A neurologic assessment was performed 3 times per day (once in every shift) in all patients who were neither comatose nor sedated. Normotension and normovolemia were initially targeted in all patients. Blood flow velocities within the MCA were measured by transcranial Doppler sonography (TCD) daily for 14 days in all patients. In case of suspected DCI either clinically or radiologically, hypertension was initiated with a target systolic arterial pressure of 160–180 mm Hg. In case of refractory vasospasm with perfusion deficits, endovascular rescue therapy (ERT) was indicated, consisting of either dilation (proximal vasospasm), intra-arterial nimodipine administration (distal vasospasm), or both. The baseline characteristics were extracted from the patients' medical records. The functional outcome at 3 months' follow-up was documented during the follow-up examination of the patients in the neurosurgical outpatient department.

CTP Protocol

In 2012, a CTP-based imaging protocol was elaborated for the management of patients with aSAH.[5] CT combined with CTA and CTP was performed routinely in all comatose/sedated patients on days 3–5 after the bleeding event. Additionally, CT, CTA, and CTP were performed in cases of delayed ischemic neurologic deficits (DIND) or TCD vasospasm and in case of an increase in the velocity acceleration of blood flow of >50 cm/s within 24 hours (Fig 1). The CTP parameters were analyzed qualitatively and quantitatively using cutoff values that have been previously published elsewhere.[6] Whole-brain volume CTP data were generated on a 128-section multidetector CT scanner (Definition AS+; Siemens). The acquisition of images was initiated 4 seconds after a bolus of contrast medium, iopamidol (Imeron 400; Bracco) was injected (36 mL of contrast medium with a flow rate of 6 mL/s followed by 36 mL of saline solution with a flow rate of 6 mL/s). For CTP, we used the following parameters: tube settings = 80 kV; 200 effective mAs; rotation time = 0.6 seconds; maximum pitch = 0.5; collimation = 32 × 1.2 mm; scan time = 45.0 seconds; scan length = 84 mm; volume CT dose index = 218.99 mGy; dose-length product = 2505 mGy × cm; effective dose = 5.3 mSv.

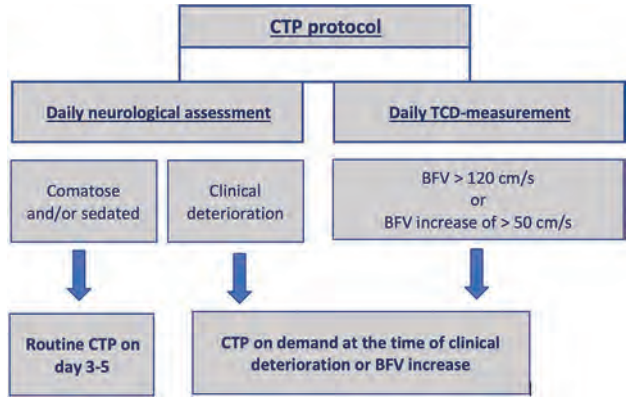

FIG 1. Flow chart of the CTP protocol. BFV indicates blood flow velocity.

CTP was used to detect "tissue at risk," to diagnose hemodynamically relevant vasospasm, and to initiate treatment (ie, induced hypertension). In case of refractory hemodynamically relevant severe vasospasm, ERT was additionally performed.

Definition of Primary End Points

TCD vasospasm was defined as an increase in blood flow velocity of >120 cm/s. DIND were defined as new focal or global neurologic deterioration in unsedated or comatose patients if other possible causes could be excluded. Delayed infarction was defined as newly diagnosed infarction on CT after excluding treatment-associated infarction. The incidence of delayed infarction as well as the extent of infarction (small infarctions versus large territorial and/or multiple infarctions) was evaluated. The functional outcome was assessed according to the mRS 3 months after ictus. Good outcome was considered mRS ≤ 2. The effective radiation exposure was calculated by summing the radiation doses of every examination performed with ionizing radiation and was converted to millisieverts. The effective dose for the DSA was calculated by applying the following equation: Effective Dose (mSv) = DAP (dose-area product) (mGy × cm^2) × Conversion Factor (mSv/mGy × cm^2). We applied a commonly used conversion factor for DSA of 0.087 mSv (Gy × cm^2)-1: https://www.iaea.org/resources/rpop/health-professionals/interventional-procedures/radiation-doses-in-interventional-fluoroscopy#5. The effective dose of CTP can differ depending on the scanner parameters.

Table 1: Baseline characteristics in both patient groups

Characteristics	Group 1	Group 2	*P* Value
No. of patients	57	76	
Mean age (range) (yr)	53.3 (SD, 15.2) (21–84)	54.4 (SD, 12.9) (29–86)	.64
Sex			
Male (%)	21/57 (36.8%)	21/76 (27.6%)	.26
Female (%)	36/57 (63.2%)	55/76 (72.4%)	
WFNS grade			
I–III (%)	28/57 (49.1%)	42/76 (55.3%)	.48
IV–V (%)	29/57 (50.9%)	34/76 (44.7%)	.41
Mean (95% CI)	3.1 (2.7–3.6)	2.9 (2.5–3.2)	
Fisher grade			
1–2 (%)	7/57 (12.3%)	8/76 (10.5%)	.75
3–4 (%)	50/57 (87.7%)	68/76 (89.5%)	.97
Mean (95% CI)	3.4 (3.2–3.6)	3.4 (3.3–3.6)	
Multiple aneurysms	12/57 (21.1%)	18/76 (23.7%)	.72
Aneurysm location			
Anterior incl. posterior communicating artery	46/57 (80.7%)	64/76 (84.2%)	.59
Posterior	11/57 (19.3%)	12/76 (15.8%)	
Aneurysm treatment			
Clipping	34/57 (59.6%)	44/76 (57.9%)	.84
Coiling	23/57 (40.4%)	32/76 (42.1%)	

Note:—incl. indicates including.

Thus, we calculated the effective dose of CTP on the scanner at our department of neuroradiology by means of the CT Expo software (http://sascrad.com/information/downloads/).[11]

Statistical Analysis

The statistical analyses were performed by means of GraphPad Prism software (Version 8; GraphPad Software). The normality of the data was evaluated using data-distribution tests. Nonparametric tests (Mann-Whitney *U* test) were applied for the analysis of nonnormally distributed data, and a *t* test was used for normally distributed data. For the presentation of baseline data, descriptive statistics and frequency distribution analysis were performed. Multivariate linear regression analysis was performed to identify independent predictors.

RESULTS

A total of 133 patients were enrolled in the study, of whom 57 patients were included in group 1 and 76 patients in group 2. The mean age of the patients was 53.9 (SD, 18.8) years (range, 21–86 years); 68.4% (91/133) of all included patients were women. A good World Federation of Neurosurgical Societies (WFNS) grade (I–III) was found in 52.6% (70/133), and a good Fisher grade (1–2), in 11.3% (15/133) of the patient population. The baseline characteristics of both patient groups are summarized in Table 1, showing no significant differences between the patient populations.

Imaging Findings

Several differences could be detected between the groups with regard to the radiologic examinations performed. Expectedly, CTP was significantly more frequently performed in group 2 compared with group 1 (mean number of CTPs in group 2 = 1.3 [SD, 1.2], ranging from 0 to 5 compared with 0.5 [SD, 0.9], ranging from 0 to 4 in group 1; Mann-Whitney *U* test, $P < .001$). CTA was also more frequently performed in group 2 compared with group 1 (mean number of CTAs = 1.9 [SD, 1.1], ranging from 0 to 5 in group 2 compared with 1.1 [SD, 0.8], ranging from 0–3 in group 1; Mann-Whitney *U* test; $P < .001$). The first CTP was, on average, performed on day 8 after bleeding (mean, 8.2 [SD, 3.5] days, ranging from 2 to 14 days) in group 1 and on day 4 (mean, 4.1 [SD, 2.3] days, ranging from 3 to 12 days) in group 2. Diagnostic DSA was, however, more frequently performed in group 1 than in group 2 (mean number of DSAs in group 1 = 1.2 [SD, 0.7], ranging from 0 to 3 compared with 0.8 [SD, 0.6], ranging from 0 to 2 in group 2; Mann-Whitney *U* test, $P = .0005$). Most interesting, nonenhanced CT scans were also significantly more frequently performed in group 1 compared with group 2 (mean number of CT scans = 5.5 [SD, 3.7], ranging from 1 to 25 in group 1 compared with 4.4 [SD, 1.9] ranging from 2 to 10 in group 2; Mann-Whitney *U* test, $P = .03$). Despite these differences, we found no significant difference in the mean cumulative radiation exposure (25.5 [SD, 14.3] mSv in group 1 versus 25.8 [SD, 19.2] mSv in group 2; Mann-Whitney *U* test, $P = .92$) between the 2 groups. The mean calculated effective dose for DSA in our study was 7.8 (SD, 2.4) mSv. The calculated effective dose for CTP in our study was 5.3 mSv.

Primary End Points

TCD vasospasm was detected in 58% (33/57) in group 1 and in 51% (39/76) in group 2 (Fisher exact test, $P = .46$). DIND developed in 8.8% (5/57) of the patients in group 1 compared with 19.7% (15/76) of the patients in group 2 (Fisher exact test, $P = .09$). The incidence of ischemic complications is shown in Fig 2. Induced hypertension was performed in 50.9% of the patients in group 1 and in 51.3% of the patients in group 2. ERT for the treatment of refractory, severe vasospasm was significantly more often performed in group 2 (ERT in group 2 in 15.8% [12/76 patients] and in 8.8% [5/57 patients] in group 1; Mann-Whitney *U* test, $P = .004$). In group 1, four patients underwent angioplasty alone and 1 patient had a combination of angioplasty and nimodipine. In group 2, five patients had angioplasty, 3 patients received intra-arterial nimodipine alone, and 4 patients had both. In those with DIND, only 1 of the 5 patients underwent ERT in group 1, which improved after ERT. In group 2, six patients with DIND underwent ERT, of whom 5 patients improved after ERT and 1 patient had permanent deficits despite ERT. Delayed infarction was detected in 19.3% (11/57) in group 1 and in 15.8% (12/76) in group 2 (Fisher exact test, $P = .64$).

Considering the extent of infarction, large territorial and/or multiple infarctions were statistically significantly more frequently detected in group 1 (88.8% of all delayed infarctions) compared with group 2 (33.3% of all delayed infarctions, Fisher exact test, $P = .03$) (Fig 3). In group two, 58% of patients undergoing ERT

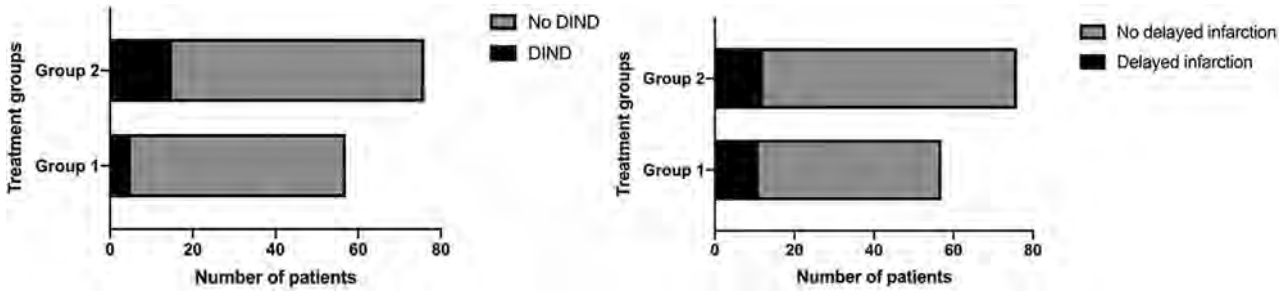

FIG 2. Incidence of vasospasm and ischemic complications in both groups, showing no significant difference for either DIND or delayed infarction.

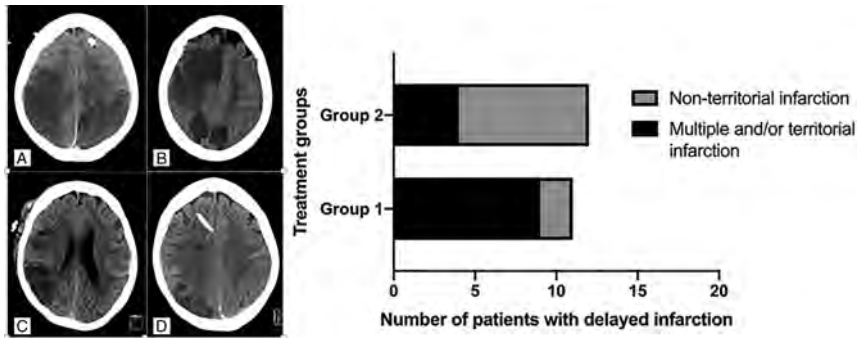

FIG 3. Examples of large territorial and multiple infarctions (*A* and *B*) and smaller infarctions affecting only a part of a vessel territory (*C* and *D*).

had no infarction and 42% developed delayed infarction despite ERT, of whom only 1 patient had multiple territorial infarctions. In group one, 60% of the patients undergoing ERT developed multiple and/or territorial delayed infarction and 40% had no infarction. The functional outcome of the patients in group 2 (median mRS at 3 months = 1, interquartile range = 0–3.8) was statistically significantly better compared with the patients in group 1 (median mRS at 3 months = 3, interquartile range = 0–6; Mann-Whitney *U* test, $P = .005$) (Fig 4). In the multivariate analysis, independent predictors of good functional outcome were younger age ($P < .001$), lower WFNS grade ($P < .001$), the absence of delayed infarction ($P < .001$), and treatment according to the CTP protocol ($P < .001$). The results of the multivariate analysis are summarized in Table 2. A lower WFNS grade ($P = .01$) and treatment according to the CTP protocol ($P = .03$) were the only independent predictors of large territorial and/or multiple infarctions in a multivariate analysis, including well-known predictors in the analysis such as Fisher grading, WFNS grading, DIND, ERT, and CTP protocol (Table 3).

DISCUSSION

The case fatality of aSAH has decreased by 17% during the past 3 decades, and the functional outcome of the survivors of aSAH is continuously improving due to advances in diagnostics and treatment of impending complications after the bleeding.[3,12] Because aSAH affects younger patients compared with other stroke types, the aspired goal is to increase the proportion of patients reaching full functional recovery with no or minimal long-term disability. Pursuing the goal of early DCI prediction and detection, which, if left untreated, results in infarctions and long-term disability, we implemented, in 2012, an elaborated CTP-based protocol in addition to the institutional standards for aSAH management.[5,13] In the present study, we have evaluated the impact of that CTP-based protocol on functional outcome, comparing 2-year treatment periods before and after the adoption of the protocol. We have chosen the same 2-year interval before and after the protocol implementation to reduce bias introduced by a longer study period (eg, technical advancements in ERT, experience of the neuroradiologist and neurosurgeon), thereby accepting lower patient numbers. The data consistency could be confirmed by comparing the baseline characteristics and excluding significant differences between the 2 patient groups.

Ischemic Complications and Functional Outcome with and without CTP Protocol

The proportion of patients reaching a better outcome was significantly higher in the patient group treated according to the predefined protocol. Several previously published studies reported on the early prediction of functional outcome after aSAH by CTP, which allowed the possibility of influencing the outcome by initiating further measures for preventing permanent neurologic disability.[14-16] Delayed infarction is one of the strongest contributors to permanent disability after aSAH, which was earlier shown to be predictable by early CTP.[17-21] Although the incidence of delayed infarction in our study was higher in the patient group treated without a predefined protocol, the difference was not statistically significant. However, the proportion of large, territorial, and/or multiple infarctions was significantly higher among the patients treated before the protocol implementation, possibly explaining the worse outcome in this patient group. Additionally, ERTs were significantly more frequently indicated after the protocol adoption. A more reliable identification of patients requiring ERT might be the reason for preventing large territorial and/or multiple infarctions in the patient group treated according to the predefined CTP protocol and, hence, might have contributed to a better outcome in this treatment group.

Similar results were recently published by Omoto et al,[22] who reported that CTP routinely performed between days 5 and 9 after ictus was an effective measure for indicating ERT. However, the number of patients receiving ERT in our study was too small to allow conclusions concerning its effectiveness. Furthermore, the role of ERT has not yet been ultimately defined, and indication criteria are yet to be established. Expectedly, we found different practices when indicating further radiologic examinations by comparing both treatment groups. While CTP and CTA were more frequently scheduled after the CTP protocol implementation, the number of diagnostic DSA and CT scans significantly decreased, indicating a more targeted indication for DSA in patients who might require ERT as well. When we took into account the invasiveness of DSA and the mostly higher radiation exposure associated with DSA compared with CTP, this approach seems to be more targeted to the management of patients with aSAH by acquiring direct information about the cerebral perfusion and not only cerebral vasospasm. Although DSA remains the criterion standard, the combination of CTA and CTP has been shown to be a valid noninvasive alternative to DSA for the diagnosis of vasospasm.[23-25]

The differences in the use of radiologic examinations, however, might also be the reason why the calculated cumulative radiation exposure did not significantly differ between treatment groups, despite the increased use of CTP. CTP is associated with relevant radiation exposure, which has to be considered while elaborating CTP-based treatment protocols. Effective radiation doses ranging from 3.8 to 22.1 mSv have been calculated for CTP, varying depending on the tube voltage.[26] A meticulous risk-stratification of patients is necessary to allow a more targeted indication for performing CTP.[27] While the value of TCD for detection of cerebral vasospasm is well-established, its role in diagnosing symptomatic vasospasm is rather controversial.[28,29] TCD alone (blood flow velocity $>$ 120 cm/s) has a low sensitivity of only 63% for identifying patients at risk for developing DCI.[29] Therefore, a combination including additional imaging such as CTP is useful to facilitate a more reliable identification of patients at risk for DCI.[5] A clinical evaluation and TCD were used to better identify patients at risk for DCI in whom CTP was indicated, and routine CTP was performed only in comatose and/or sedated patients. Ditz et al[21] followed a similar approach, analyzing CTPs performed in unconscious patients with aSAH and found that CTP could identify DCI-related hypoperfusion but could not prevent all delayed infarctions in this population. The CTP protocol could not prevent all delayed infarctions in our study but was associated with smaller infarctions compared with the patient population treated before the protocol adoption. The findings of our study support the concept of elaborating imaging protocols in patients with aSAH, providing direct information about cerebral perfusion and allowing a more targeted treatment-planning, which ideally might result in a better outcome. Further evaluation of CTP protocols with regard to the indication for further diagnostics and treatment is needed, applying a prospective study design to better use the information about cerebral perfusion gathered by CTP.

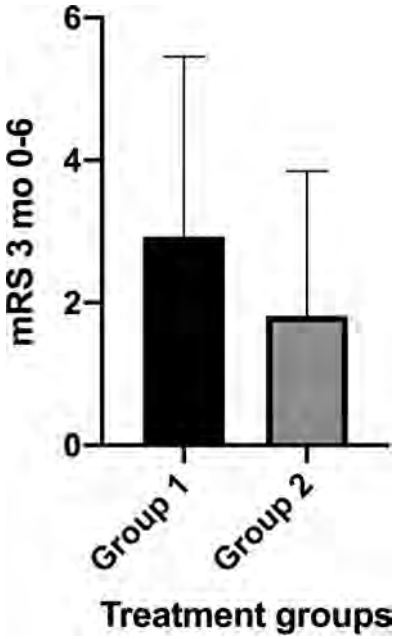

FIG 4. Comparison of functional outcome (mRS at 3 months' follow-up) showing significantly better functional outcome in group 2 compared with group 1 (Mann-Whitney *U* test, $P = .0005$).

Table 2: Multivariate analysis for prediction of functional outcome at 3 months' follow-up

Variables	Estimate	SD (95% CI)	*t*	*P* Value
Age	0.05746	0.01000 (0.03766–0.07725)	5.743	<.001[a]
WFNS grade	0.5963	0.09633 (0.4057–0.7869)	6.191	<.001[a]
Fisher grade	0.2520	0.2206 (−0.1850–0.6890)	1.142	.25
Delayed infarction	1.827	0.3828 (1.070–2.585)	4.773	<.001[a]
CTP protocol	−0.9287	0.2728 (−1.469–0.3889)	3.406	<.001[b]
ERT	−0.6650	0.4308 (−1.517–0.1876)	1.544	.12

[a] Highly significant, multivariate regression analysis.
[b] Moderately significant, multivariate regression analysis.

Table 3: Multivariate analysis for prediction of delayed, large territorial and/or multiple infarctions

Variables	Estimate	SD (95% CI)	*t*	*P* Value
CT protocol	−0.1070	0.0512 (−0.2084–0.0055)	2.088	.03[a]
WFNS grade	0.5963	0.09633 (0.4057–0.7869)	6.191	.01[a]
Fisher grade	0.0080	0.0412 (0.0896–0.0735)	0.1956	.84
DIND	0.0637	0.0733 (−0.0814–0.2089)	0.8692	.38
ERT	−0.6650	0.4308 (−1.517-0.1876)	1.544	.12

[a] Significant, multivariate regression analysis.

Limitations of the Study

A limitation of the study is the retrospective nature, with the resulting shortcomings leading to the small number of included patients because of incomplete data availability before 2010. Due to the retrospective data acquisition, we cannot exclude individual decision-making for performing ERT in some patients. The effectiveness of ERT is considered a confounder because the indication for ERT was

consistently based on the CTP findings in group 2, whereas the decision to perform ERT in group 1 was made individually and CTP was only performed sporadically. The improvement of ERT techniques across time might have impacted the functional outcome as well. Cognitive impairment was not considered during the evaluation of patients' outcomes, another limitation of the study.

CONCLUSIONS

The findings of the study suggest that implementation of an elaborated CTP protocol is associated with a better outcome. An earlier identification of patients with impending DCI and early initiation of further diagnosis and treatment, with prevention of large territorial and/or multiple infarctions, might have led to this finding. An elaborated CTP protocol might be a suitable measure for a more reliable ERT indication, which has to be addressed in a prospective study.

Disclosures: Veit Rohde—*UNRELATED*: *Other*: Advisory board for BBraun Ausculap, Tuttlingen, Germany, until 2018, *Comments*: payment of travel expenses. *Expert Testimony*: Deutsche Forschungsgesellschaft (DFG), ongoing, *Comments*: no payment; *Payment for Lectures Including Service on Speakers Bureaus*: Ulrich, Ulm, Germany, until 2018, *Comments*: €500. Dorothee Mielke—*UNRELATED*: *Board Membership*: Advisory Board Member for Medtronic; *Consultancy*: review doctoral thesis/professor at the Universities of Oslo and Geneva.

REFERENCES

1. Muehlschlegel S. **Subarachnoid hemorrhage.** *Continuum (Minneap Minn)* 2018;24:1623–57 CrossRef Medline
2. Vergouwen MD, Etminan N, Ilodigwe D, et al. **Lower incidence of cerebral infarction correlates with improved functional outcome after aneurysmal subarachnoid hemorrhage.** *J Cereb Blood Flow Metab* 2011;31:1545–53 CrossRef Medline
3. Pegoli M, Mandrekar J, Rabinstein AA, et al. **Predictors of excellent functional outcome in aneurysmal subarachnoid hemorrhage.** *J Neurosurg* 2015;122:414–18 CrossRef Medline
4. Etminan N, Beseoglu K, Heiroth HJ, et al. **Early perfusion computerized tomography imaging as a radiographic surrogate for delayed cerebral ischemia and functional outcome after subarachnoid hemorrhage.** *Stroke* 2013;44:1260–66 CrossRef Medline
5. Malinova V, Dolatowski K, Schramm P, et al. **Early whole-brain CT perfusion for the detection of patients at risk for delayed cerebral ischemia after subarachnoid hemorrhage.** *JNS* 2016;125:128–36 CrossRef
6. Malinova V, Tsogkas I, Behme D, et al. **Defining cutoff values for early prediction of delayed cerebral ischemia after subarachnoid hemorrhage by CT perfusion.** *Neurosurg Rev* 2020;43:581–87 CrossRef Medline
7. Sun H, Li W, Ma J, et al. **CT perfusion diagnoses delayed cerebral ischemia in the early stage of the time-window after aneurysmal subarachnoid hemorrhage.** *J Neuroradiol* 2017;44:313–18 CrossRef Medline
8. Duan Y, Xu H, Li R, et al. **Computed tomography perfusion deficits during the baseline period in aneurysmal subarachnoid hemorrhage are predictive of delayed cerebral ischemia.** *J Stroke Cerebrovasc Dis* 2017;26:162–68 CrossRef Medline
9. Fragata I, Alves M, Papoila AL, et al. **Computed tomography perfusion as a predictor of delayed cerebral ischemia and functional outcome in spontaneous subarachnoid hemorrhage: a single center experience.** *Neuroradiol J* 2019;32:179–88 CrossRef Medline
10. Williams JR. **The Declaration of Helsinki and public health.** *Bull World Health Organ* 2008;86:650–52 CrossRef Medline
11. Stamm G, Nagel HD. **CT-expo- a new software for dose evaluation of CT: RöFo-advances in the area of X-rays and imaging.** *Fortschr Röntgenstr* 2002;174:1570–76 CrossRef Medline
12. Lovelock CE, Rinkel GJ, Rothwell PM. **Time trends in outcome of subarachnoid hemorrhage: population-based study and systematic review.** *Neurology* 2010;74:1494–1501 CrossRef Medline
13. Mielke D, Malinova V, Moerer O, et al. **Does the subspecialty of an intensive care unit (ICU) have an impact on outcome in patients suffering from aneurysmal subarachnoid hemorrhage?** *Neurosurg Rev* 2019;42:147–53 CrossRef Medline
14. Mathys C, Martens D, Reichelt DC, et al. **Long-term impact of perfusion CT data after subarachnoid hemorrhage.** *Neuroradiology* 2013;55:1323–31 CrossRef Medline
15. Huenges Wajer IM, Cremers CH, van Zandvoort MJ, et al. **CT perfusion on admission and cognitive functioning 3 months after aneurysmal subarachnoid hemorrhage.** *J Neurol* 2015;262:623–28 CrossRef Medline
16. Tanabe J, Nakahara I, Matsumoto S, et al. **Cortical blood flow insufficiency scores with computed tomography perfusion can predict outcomes in aneurysmal subarachnoid hemorrhage patients: a cohort study.** *Neurocrit Care* 2021;34:946–55 CrossRef Medline
17. Pham M, Johnson A, Bartsch AJ, et al. **CT perfusion predicts secondary infarction after aneurysmal subarachnoid hemorrhage.** *Neurology* 2007;69:762–65 CrossRef Medline
18. Dong L, Zhou Y, Wang M, et al. **Whole-brain CT perfusion on admission predicts delayed cerebral ischemia following aneurysmal subarachnoid hemorrhage.** *Eur J Radiol* 2019;116:165–73 CrossRef Medline
19. Sanelli PC, Anumula N, Johnson CE, et al. **Evaluating CT perfusion using outcome measures of delayed cerebral ischemia in aneurysmal subarachnoid hemorrhage.** *AJNR Am J Neuroradiol* 2013;34:292–98 CrossRef Medline
20. Westermaier T, Pham M, Stetter C, et al. **Value of transcranial Doppler, perfusion-CT and neurological evaluation to forecast secondary ischemia after aneurysmal subarachnoid hemorrhage.** *Neurocrit Care* 2014;20:406–12 CrossRef Medline
21. Ditz C, Hartlieb M, Neumann A, et al. **Routine use of perfusion computed tomography for the detection of delayed cerebral ischemia in unconscious patients after aneurysmal subarachnoid hemorrhage.** *Acta Neurochir (Wien)* 2021;163:151–60 CrossRef Medline
22. Omoto K, Nakagawa I, Nishimura F, et al. **Computed tomography perfusion imaging after aneurysmal subarachnoid hemorrhage can detect cerebral vasospasm and predict delayed cerebral ischemia after endovascular treatment.** *Surg Neurol Int* 2020;11:233 CrossRef Medline
23. Stecco A, Fabbiano F, Amatuzzo P, et al. **Computed tomography perfusion and computed tomography angiography in vasospasm after subarachnoid hemorrhage.** *J Neurosurg Sci* 2018;62:397–405 CrossRef Medline
24. Greenberg ED, Gold R, Reichman M, et al. **Diagnostic accuracy of CT angiography and CT perfusion for cerebral vasospasm: a meta-analysis.** *AJNR Am J Neuroradiol* 2010;31:1853–60 CrossRef Medline
25. Wintermark M, Ko NU, Smith WS, et al. **Vasospasm after subarachnoid hemorrhage: utility of perfusion CT and CT angiography on diagnosis and management.** *AJNR Am J Neuroradiol* 2006;27:26–34 Medline
26. Ringelstein A, Lechel U, Fahrendorf DM, et al. **Radiation exposure in perfusion CT of the brain.** *J Comput Assist Tomogr* 2014;38:25–28 CrossRef Medline
27. De Rooij NK, Greving JP, Rinkel GJ, et al. **Early prediction of delayed cerebral ischemia after subarachnoid hemorrhage: development and validation of a practical risk chart.** *Stroke* 2013;44:1288–94 CrossRef Medline
28. Matamoros CES, Samaniego EA, Sam K, et al. **Prediction of symptomatic vasospasm in patients with aneurysmal subarachnoid hemorrhage using early transcranial Doppler.** *J Vasc Interv Neurol* 2020;11:19–26 Medline
29. Carrera E, Schmidt JM, Oddo M, et al. **Transcranial Doppler for predicting delayed cerebral ischemia after subarachnoid hemorrhage.** *Neurosurgery* 2009;65:316–23 CrossRef Medline

Spiral 2D T2-Weighted TSE Brain MR Imaging: Initial Clinical Experience

E. Sartoretti, S. Sartoretti-Schefer, L. van Smoorenburg, C.A. Binkert, A. Gutzeit, M. Wyss, and T. Sartoretti

ABSTRACT

BACKGROUND AND PURPOSE: Spiral MR imaging may enable improved image quality and higher scan speeds than Cartesian trajectories. We sought to compare a novel spiral 2D T2-weighted TSE sequence with a conventional Cartesian and an artifact-robust, non-Cartesian sequence named MultiVane for routine clinical brain MR imaging.

MATERIALS AND METHODS: Thirty-one patients were scanned with all 3 sequences (Cartesian, 4 minutes 14 seconds; MultiVane, 2 minutes 49 seconds; spiral, 2 minutes 12 seconds) on a standard clinical 1.5T MR scanner. Three readers described the presence and location of abnormalities and lesions and graded images qualitatively in terms of overall image quality, the presence of motion and pulsation artifacts, gray-white matter differentiation, lesion conspicuity, and subjective preference. Image quality was objectivized by measuring the SNR and the coefficients of variation for CSF, GM, and WM.

RESULTS: Spiral achieved a scan time reduction of 51.9% and 21.9% compared with Cartesian and MultiVane, respectively. The number and location of lesions were identical among all sequences. As for the qualitative analysis, interreader agreement was high (Krippendorff $\alpha > .75$). Spiral and MultiVane both outperformed the Cartesian sequence in terms of overall image quality, the presence of motion artifacts, and subjective preference ($P < .001$). In terms of the presence of pulsation artifacts, gray-white matter differentiation, and lesion conspicuity, all 3 sequences performed similarly well ($P > .15$). Spiral and MultiVane outperformed the Cartesian sequence in coefficient of variation WM and SNR ($P < .01$).

CONCLUSIONS: Spiral 2D T2WI TSE is feasible for routine structural brain MR imaging and offers high-quality, artifact-robust brain imaging in short scan times.

ABBREVIATIONS: CV = coefficient of variation; SENSE = sensitivity encoding

T2WI sequences are essential components of every clinical MR imaging protocol. Specifically, the T2 contrast is particularly useful to analyze brain anatomy, CSF spaces, and parenchymal lesions.

Currently, most clinical institutions rely on axially acquired cartesian 2D T2WI TSE sequences.[1] These sequences offer a relatively short scan time (especially when accelerated by means of parallel imaging[2] or compressed sensing[3]) and achieve a reliable and accurate depiction of the brain. Alternatively, especially in pediatric and elderly patients, certain institutions rely on sequences with a non-Cartesian sampling scheme, such as PROPELLER.[4,5] With PROPELLER, multiple echo-trains of TSE are acquired in a rotating, partially overlapping fashion rather than in a rectilinear fashion as in Cartesian imaging.[5] While sequences with this sampling scheme offer central *k*-space oversampling and thus increased robustness toward artifacts, they require a considerable increase in scan time compared with their Cartesian counterparts in case of fully matching scan parameters.[5] Thus, a sequence offering both artifact robustness and an intrinsically short scan time is highly desirable for clinical T2-weighted brain MR imaging.

Despite requiring high technological standards both in terms of scanner hardware and software, spiral MR imaging sequences have recently been implemented for clinical MR imaging. Sequences with spiral *k*-space sampling have inherently reduced gradient moments, central *k*-space oversampling, and a nondedicated phase-encoding direction, thus rendering them less susceptible to artifacts. Furthermore, the efficiency of *k*-space sampling

Received June 5, 2021; accepted after revision July 23.

From the Institute of Radiology (E.S., S.S.-S., L.v.S., C.A.B., T.S.), Kantonsspital Winterthur, Winterthur, Switzerland; Faculty of Medicine (E.S., T.S.), University of Zürich, Zürich, Switzerland; Department of Radiology (A.G.), Paracelsus Medical University, Salzburg, Austria; Philips Healthcare (M.W.), Zürich, Switzerland; and Department of Radiology and Nuclear Medicine (T.S.), Maastricht University Medical Center, Maastricht University, Maastricht, the Netherlands.

Please address correspondence to Sabine Sartoretti-Schefer, MD, Institute of Radiology, Kantonsspital Winterthur, Brauerstr 15, 8401 Winterthur, Switzerland; e-mail: sabine.sartoretti@ksw.ch

Indicates article with online supplemental data.

http://dx.doi.org/10.3174/ajnr.A7299

Table 1: Sequence parameters

Parameter	Cartesian T2WI TSE	MultiVane T2WI TSE	Spiral T2WI TSE
Technique	2D TSE	2D TSE	2D TSE
FOV AP/FH/RL (mm)	230 × 230 × 149	230 × 230 × 149	230 × 230 × 149
Acquired voxel size (mm^3)	0.7 × 0.7 × 4.0	0.7 × 0.7 × 4.0	0.7 × 0.7 × 4.0
Reconstructed voxel size (mm^3)	0.45 × 0.45 × 4.0	0.45 × 0.45 × 4.0	0.45 × 0.45 × 4.0
No. of slices	30	30	30
TR (ms)	5300	5300	5300
TE equivalent (ms)	90	90	90
Flip angle	90°	90°	90°
Refocusing flip angle	180°	180°	180°
TSE factor	28	30	8
Spiral acq window	–	–	Spiral in-out, 11.4 ms
Parallel imaging	No	SENSE 1.5	No
NSA	2	1	2
Receiver bandwidth (Hz/pixel)	560	290	114
SAR (W/kg)	<1.9	<2.0	<1.6
dB/dT (T/s)	52	33	72
Acquisition time (min:sec)	04:14	02:49	02:12

Note:—NSA indicates number of signal averages; acq, acquisition; SAR, specific absorption rate; dB/dT, ratio between the amount of change in amplitude of the magnetic field (dB) and the time it takes to make that change (dt); T/s, Tesla/second; AP/FH/RL, anterior-posterior/foot-head/right-left; –, scan parameter does not exist for this sequence.

is high in spiral MR imaging due to the longer acquisition duration per shot.[6] Recent clinical feasibility studies have thus shown the value of spiral MR imaging for T1-weighted spin-echo/gradient recalled-echo brain and spine imaging as well as for intracranial vessel imaging.[6-13]

Here we expand on previous endeavors by presenting, for the first time, initial clinical results of a spiral TSE technique for routine clinical 2D T2-weighted TSE brain MR imaging. We hypothesized that this sequence would offer both short scan times and artifact robustness, thus combining the best features of conventional Cartesian imaging and non-Cartesian imaging. To this extent, we prospectively compared the novel spiral 2D T2WI TSE sequence with a conventional Cartesian 2D T2WI TSE sequence and a (non-Cartesian) PROPELLER-like sampled 2D T2WI TSE sequence in patients.

MATERIALS AND METHODS

Study Design and Subjects

This institutional review board-approved intraindividual comparison study was performed between January and May 2021. All participants gave general written informed consent. We prospectively acquired all 3 sequences in 31 consecutive patients (mean age, 57 years; age range, 18–85 years; 16 men, 15 woman) who were referred to our department for brain MR imaging due to various clinical indications. Exclusion criteria were as follows: general contraindication to MR imaging (ie, metallic implants and so forth), younger than 18 years of age, and pregnancy. The final main diagnoses were the following: chronic lacunar infarcts ($n = 1$), periventricular heterotopia ($n = 1$), territorial infarcts ($n = 6$), metastases ($n = 1$), microangiopathy ($n = 9$), multiple sclerosis demyelinating lesions ($n = 1$), periventricular leukomalacia ($n = 1$), subdural hematoma ($n = 1$), dilated Virchow-Robin spaces ($n = 7$), and normal findings ($n = 3$).

MR Imaging

Imaging was performed on a standard clinical 1.5T scanner (Ingenia; Philips Healthcare) with a 16-channel head coil. The combination of spiral with TSE was enabled with the Compressed SENSE 2.0 WIP software, Release 5.7 (Philips Healthcare). As part of the routine clinical protocol, the following additional sequences were acquired besides the 2D T2WI TSE scans: a sagittal 3D FLAIR sequence, a precontrast sagittal 3D T1WI turbo field echo sequence, a diffusion-weighted transverse sequence, a susceptibility-weighted transverse sequence, and, in selected cases, a sagittal postcontrast 3D T1 black-blood TSE sequence or a postcontrast sagittal 3D T1 m-Dixon turbo field echo sequence.

The 3 2D T2WI TSE sequences (Table 1) were acquired in random order. The performance of the spiral sequence was benchmarked against 2 commercially available sequences used routinely at our institution: A conventional Cartesian 2D T2WI TSE sequence and a MultiVane 2D T2WI TSE sequence using PROPELLER-like, non-Cartesian *k*-space sampling. Sequence parameters of the Cartesian and MultiVane sequences were chosen on the basis of long-standing and well-established clinical protocols.[10] The sequence parameters of the spiral sequence were selected on the basis of the initial optimization of this sequence by the vendor and in-house by means of volunteer tests. Most important, the sequence parameters were kept as constant as possible among all 3 sequences.[9-11] However, due to institutional scan time constraints, MultiVane was accelerated with sensitivity encoding (SENSE), and the number of signal averages was adapted to shorten the scan time.

The spiral sequence uses an in-plane spiral in-out readout scheme (spiral acquisition window, 11.4 ms; scan duration, 2 minutes 12 seconds). Blurring due to off-resonance was corrected during reconstruction on the basis of a magnetic field map acquired before the spiral scans.[11] This study was performed on the standard product configuration without additional enhancement. Eddy current calibration of B_0 eddy currents and linear and cross-term eddy currents was performed as part of the standard system tuning procedure. Compensation of those eddy current contributions was performed in run-time as part of the vendor's product-acquisition software.[14]

Qualitative Analysis

Image analysis was performed independently by 3 readers (a board-certified neuroradiologist with 30 years of experience and 2 trainees, each with 3 years of experience in medical imaging) in a blinded and randomized manner.

First, as outlined elsewhere,[15] for each sequence and patient, the readers recorded the presence, number, and localization of abnormalities and lesions. In case of discrepancies among the 3 sequences or among the readers, the lesions were evaluated on all available imaging sequences in consensus to detect potential false-positive and false-negative findings.[15]

Second, as suggested elsewhere,[16-19] all images were graded one-by-one in the following categories using 4-point Likert scales: overall image quality (1, nondiagnostic; 2, limited but interpretable; 3, minimally limited; and 4, optimal quality), the presence of motion and pulsation artifacts (1, severe image artifacts; 2, moderate artifacts; 3, mild artifacts; 4, no artifacts), gray-white matter differentiation (1, indistinguishable gray-white sharpness; 2, very blurry gray-white sharpness; 3, slightly blurry gray-white sharpness; 4, well-defined gray-white sharpness), and lesion conspicuity (1, a lesion whose borders are barely distinguishable from background brain; 2, a lesion with very blurry margins; 3, a lesion with slightly blurry margins; 4, sharp lesion margins). Additionally, readers were asked to record any other artifacts or anything unusual that appeared to them during the readout.

Last, for each patient, all 3 sequences were presented side-by-side, and the readers were asked to order the sequences according to their subjective preference. Specifically, a score of 3 was given to the best sequence; a score of 2, to the second-best sequence; and a score of 1, for the worst sequence. Scores could be used more than once if sequences were judged equivalent.[20]

Quantitative Analysis

As secondary end points, we used ROI-based analyses to objectify image quality and image appearance.[9,16] For each patient, ROIs were drawn on representative images from each sequence. ROIs were positioned within the frontal WM, the GM of the caudate head, and in the lateral ventricles (CSF) at the level of foramen of Monro.[17] All ROIs were the same size and had identical positioning between sequences.[16] From each ROI, the mean signal intensity and SD of the signal intensity were extracted. ROI placement was performed twice, and the average values of both measurements were considered representative for further analysis.[9] As suggested in the literature,[9,17,21] we then computed the SNR and the coefficient of variations (CVs) for WM, GM, and CSF as follows:

$$SNR = \frac{1}{2}\left[\frac{mean(Signal_{WM})}{SD(Signal_{WM})} + \frac{mean(Signal_{GM})}{SD(Signal_{GM})}\right],$$

$$CV\ for\ Tissue\ a\ (CV_a) = \frac{SD(Signal_a)}{mean(Signal_a)}.$$

Statistical Analysis

Data distribution was initially checked with histograms, boxplots, and quantile-quantile plots. Differences in qualitative metrics were initially checked with Friedman tests followed by post hoc Wilcoxon signed rank tests. Interreader agreement of qualitative scores was quantified with Krippendorff α coefficients (0, no agreement, 1, perfect agreement). Differences in quantitative metrics were initially checked with 1-way repeated-measures ANOVAs followed by post hoc paired t tests. P values were corrected for multiple comparisons with the Holm method. P values $< .05$ were considered significant. All statistical analyses were performed in the R programming language (http://www.r-project.org/).

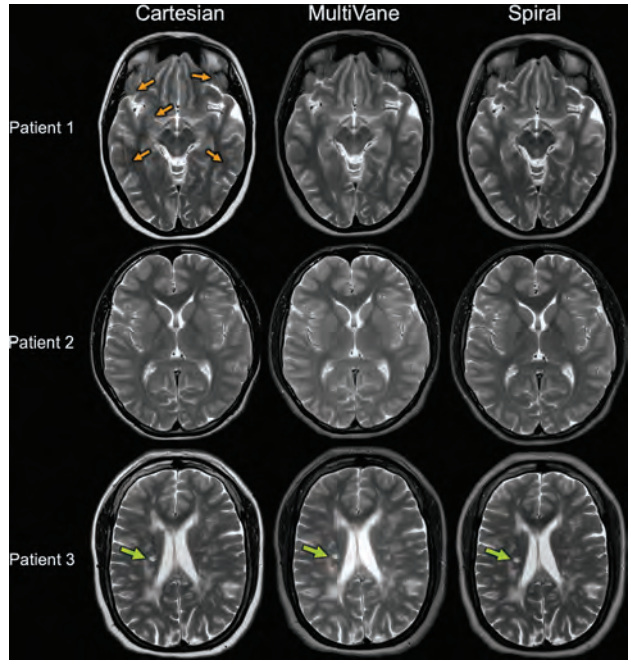

FIGURE. Representative images from 3 different patients (1 patient per row). In patient 1, ghosting artifacts from bulk motion appear on Cartesian images (*orange arrows*) but not on MultiVane or spiral images. In patient 2, no artifacts were present and thus an excellent visualization could be achieved for all 3 sequences. In patient 3, a small focal multiple sclerosis lesion is visualized clearly on all 3 sequences (*green arrow*).

RESULTS

Representative image examples are shown in the Figure and the Online Supplemental Material. With a scan time of 02:12 minutes, spiral achieved a scan time reduction of 51.9% and 21.9% compared with Cartesian and MultiVane, respectively.

In terms of the presence, number, and location of lesions, there were no differences among the 3 sequences. All readers recorded the same pathologic and abnormal findings on all 3 sequences. Besides motion and pulsation artifacts, no other types of artifacts were recorded.

Concerning the qualitative metrics (Table 2 and Online Supplemental Material), interreader agreement was high ($\alpha =$ .755 for presence of pulsation artifacts; $\alpha =$ .98 for presence of motion artifacts). Spiral and MultiVane both outperformed the Cartesian sequence in terms of overall image quality and the presence of motion artifacts ($P < .001$ for all readers and both metrics). Between spiral and MultiVane, there were no significant differences in these 2 metrics ($P > .4$ for all readers and both

Table 2: Detailed overview of qualitative and quantitative data

	Cartesian	MultiVane	Spiral
Overall image quality[a]	3; (2,3)/3; (2.5,3)/3; (3,3)	4; (4,4)/4; (4,4)/4; (4,4)	4; (4,4)/4; (4,4)/4; (4,4)
Presence of motion artifacts[a]	3; (2,3)/3; (2,3)/3; (3,3)	4; (4,4)/4; (4,4)/4; (4,4)	4; (4,4)/4; (4,4)/4; (4,4)
Presence of pulsation artifacts[a]	4; (4,4)/4; (3.5,4)/4; (4,4)	4; (3,4)/4; (3,4)/4; (3,4)	4; (4,4)/4; (4,4)/4; (4,4)
GWM differentiation[a]	3; (3,4)/3; (3,4)/3; (3,4)	4; (3,4)/4; (3,4)/4; (3,4)	4; (3,4)/4; (3,4)/4; (3,4)
Lesion conspicuity[a]	4; (3.75,4)/4; (3.75,4)/4; (3.75,4)	4; (4,4)/4; (4,4)/4; (4,4)	4; (4,4)/4; (4,4)/4; (4,4)
Subjective preference (No. of times score 1/No. of times score 2/No. of times score 3)	Reader 1: (6/22/3) Reader 2: (7/21/3) Reader 3: (8/20/3)	Reader 1: (0/5/25) Reader 2: (0/6/25) Reader 3: (0/6/25)	Reader 1: (0/5/26) Reader 2: (0/5/26) Reader 3: (0/5/26)
CV_{CSF}[b]	0.026 (0.02)	0.023 (0.019)	0.021 (0.014)
CV_{GM}[b]	0.109 (0.053)	0.096 (0.035)	0.087 (0.025)
CV_{WM}[b]	0.07 (0.027)	0.053 (0.019)	0.053 (0.02)
SNR[b]	13.36 (3.4)	16.1 (3.3)	16.6 (3.9)

Note:—GWM indicates gray-white matter; IQR, interquartile range.
[a] Qualitative data are shown as median; (IQR) for readers 1/2/3.
[b] Quantitative data are presented as mean (SD).

metrics). In terms of the presence of pulsation artifacts and gray-white matter differentiation, all 3 sequences performed similarly well ($P > .15$ for each reader). Finally, for lesion conspicuity, there were also no significant differences among the 3 sequences ($P > .45$ for each reader). Readers indicated a higher subjective preference for spiral and MultiVane compared with the Cartesian sequence ($P < .001$ for all readers) without significant differences between spiral and MultiVane ($P > .5$ for all readers).

Concerning the quantitative metrics (Table 2 and Online Supplemental Material), there were no significant differences among the 3 sequences for the metrics CV_{CSF} and CV_{GM} ($P > .12$ for both metrics). However, both spiral and MultiVane outperformed the Cartesian sequence in the metrics CV_{WM} and SNR ($P < .01$ for both sequences and metrics). Between spiral and MultiVane, there were, however, no differences in terms of CV_{WM} and SNR ($P > .5$ for both metrics).

DISCUSSION

In this study, we compared a novel spiral 2D T2WI TSE sequence with its conventional Cartesian counterpart and an artifact-robust, PROPELLER-like sampled sequence named MultiVane. We showed that the spiral sequence outperforms the Cartesian sequence and performs equally as well as the MultiVane sequence in terms of subjective and objective image quality. Concerning the exact frequency and nature of artifacts, all 3 sequences exhibited only motion and pulsation artifacts. However, the spiral and MultiVane both had significantly fewer motion artifacts than the Cartesian sequence, while all 3 sequences had only minor pulsation artifacts in select cases. Thus, the spiral sequence enables high-quality, artifact-robust imaging on a level with the MultiVane sequence, yet at a shorter scan time.

Spiral MR imaging has several benefits over Cartesian *k*-space sampling. Due to the longer acquisition duration per shot, scan efficiency is high and the scan time can, thus, be very short. Furthermore, spiral trajectories show inherently reduced gradient moments, central *k*-space oversampling, and a nondedicated phase-encoding direction. These traits render spiral sequences more robust toward artifacts. Thus, with spiral MR imaging, rapid and artifact-robust imaging can be achieved.[6] Accordingly, promising clinical results have been reported for anatomic spiral T1WI spin-echo and gradient recalled-echo imaging. While the technical details of spiral TSE and T2WI imaging have been described previously,[22,23] to the best of our knowledge, this is the first study investigating the value of a spiral TSE technique as implemented for 2D T2-weighted TSE brain MR imaging in patients on a standard clinical MR imaging scanner and clinical routine.

Currently, most institutions rely on Cartesian or PROPELLER-like sampled sequences (such as MultiVane) for clinical T2-weighted brain MR imaging. While PROPELLER sequences have become a popular choice for anatomic brain imaging due to their increased robustness predominantly toward motion artifacts, scan time is generally increased compared with conventional Cartesian TSE imaging.[5,24,25]

A standard rectilinear sequence requires (M/L) excitations to fill a *k*-space of matrix size M with acquisitions of echo-train length L. For PROPELLER imaging, at least $(\pi/2) \times$ (M/L) excitations are needed for an equivalent sequence, thus leading to approximately 60% increase in scan time compared with Cartesian imaging.[5] With parallel imaging or compressed sensing acceleration, the increase in scan time can be reduced. Specifically, as in the clinical routine at our institution, our MultiVane sequence also used SENSE 1.5 and 1 signal average, explaining why MultiVane had a shorter scan time than the Cartesian sequence. Hypothetically, if the MultiVane sequence had been acquired without SENSE and with 2 signal averages, as in the case of the Cartesian and spiral sequences, scan time would have increased by a factor of 2.5, which would have resulted in a 66% increase in scan time compared with the Cartesian sequence.

With spiral MR imaging, however, the dilemma of artifact robustness and scan speed can be resolved. Specifically, our spiral sequence offers exceptionally short scan times as well as both motion and pulsation artifact robustness, thus combining the best features of conventional Cartesian imaging and non-Cartesian (PROPELLER-like) imaging. In this context, the spiral sequence achieved a scan time reduction of nearly 50% compared with the Cartesian sequence. Most important, while not investigated in this study, scan time for the spiral sequence may be shortened even further with parallel imaging or compressed sensing techniques.

A further important aspect of the current study concerns the exact choice and configuration of the sequences. While 2D TSE techniques are widely considered the reference standard for clinical brain MRI,[1] 3D and multiband TSE techniques have also been proposed for clinical T2-weighted brain imaging. While not investigated in this study, our spiral TSE technique is highly adaptable and may be combined with these approaches.[22,26,27] Furthermore, with high-field imaging being popular for brain MR imaging, our spiral sequence can also be acquired at 3T. Thus, our spiral sequence had lower specific absorption rate values than its counterparts, an advantage at 3T. However, the spiral sequence is more susceptible to off-resonance B_0 effects, which are more pronounced at 3T. Thus, a future study assessing the clinical value of our spiral TSE technique at 3T would be of interest.

One limitation of our study was the limited sample size: Because the spiral sequence could not be run with standard clinical software, the scanner console had to be rebooted before each spiral acquisition (to load a patch). This step limited our ability to acquire the sequence in further patients. Second, it may have not been possible to fully blind readers toward sequence details because the spiral sequence has a distinct appearance. Third, scan parameters were not fully identical among all sequences, possibly representing a source of bias, especially for the quantitative image analysis. Last, we are aware that while formula-based approaches for estimation of quantitative metrics are widely used, they are inherently limited, and more sophisticated methods may yield more accurate estimations.[9]

CONCLUSIONS

We show that a spiral 2D T2WI TSE sequence enables high-quality, artifact-robust brain MR imaging in clinical routine at short scan times. This sequence may, thus, represent a promising option for improved and rapid clinical T2-weighted brain MR imaging.

Disclosure forms provided by the authors are available with the full text and PDF of this article at www.ajnr.org.

REFERENCES

1. Kaufmann TJ, Smits M, Boxerman J, et al. **Consensus recommendations for a standardized brain tumor imaging protocol for clinical trials in brain metastases.** *Neuro Oncol* 2020;22:757–72 CrossRef Medline
2. Pruessmann KP, Weiger M, Scheidegger MB, et al. **SENSE: sensitivity encoding for fast MRI.** *Magn Reson Med* 1999;42:952–62 Medline
3. Lustig M, Donoho D, Pauly JM. **Sparse MRI: the application of compressed sensing for rapid MR imaging.** *Magn Reson Med* 2007;58:1182–95 CrossRef Medline
4. Pipe JG. **Motion correction with PROPELLER MRI: application to head motion and free-breathing cardiac imaging.** *Magn Reson Med* 1999;42:963–69
5. Ohgiya Y, Suyama J, Seino N, et al. **MRI of the neck at 3 Tesla using the periodically rotated overlapping parallel lines with enhanced reconstruction (PROPELLER) (BLADE) sequence compared with T2-weighted fast spin-echo sequence.** *J Magn Reson Imaging* 2010;32:1061–67 CrossRef Medline
6. Ooi MB, Li Z, Robison RK, et al. **Spiral T1 spin-echo for routine postcontrast brain MRI exams: a multicenter multireader clinical evaluation.** *AJNR Am J Neuroradiol* 2020;41:238–45 CrossRef Medline
7. Sartoretti T, van Smoorenburg L, Sartoretti E, et al. **Ultrafast intracranial vessel imaging with non-Cartesian spiral 3-dimensional time-of-flight magnetic resonance angiography at 1.5 T: an in vitro and clinical study in healthy volunteers.** *Invest Radiol* 2020;55:293–303 CrossRef Medline
8. Sartoretti T, Sartoretti E, Schwenk Á, et al. **Clinical feasibility of ultrafast intracranial vessel imaging with non-Cartesian spiral 3D time-of-flight MR angiography at 1.5T: an intra-individual comparison study.** *PLoS One* 2020;15:e0232372 CrossRef Medline
9. Sartoretti T, Sartoretti E, van Smoorenburg L, et al. **Spiral 3-dimensional T1-weighted turbo field echo: increased speed for magnetization-prepared gradient echo brain magnetic resonance imaging.** *Invest Radio* 2020;55:775–84 CrossRef Medline
10. Sartoretti E, Sartoretti T, van Smoorenburg L, et al. **Qualitative and quantitative analysis of a spiral gradient echo sequence for contrast-enhanced fat-suppressed T1-weighted spine magnetic resonance imaging.** *Invest Radiol* 2021;56:517–24 CrossRef Medline
11. Li Z, Hu HH, Miller JH, et al. **A spiral spin-echo MR imaging technique for improved flow artifact suppression in T1-weighted postcontrast brain imaging: a comparison with Cartesian turbo spin-echo.** *AJNR Am J Neuroradiol* 2016;37:642–47 CrossRef Medline
12. Greve T, Sollmann N, Hock A, et al. **Highly accelerated time-of-flight magnetic resonance angiography using spiral imaging improves conspicuity of intracranial arterial branches while reducing scan time.** *Eur Radiol* 2020;30:855–65 CrossRef Medline
13. Greve T, Sollmann N, Hock A, et al. **Novel ultrafast spiral head MR angiography compared to standard MR and CT angiography.** *J Neuroimaging* 2020;31:45–56 CrossRef Medline
14. Robison RK, Li Z, Wang D, et al. **Correction of B.** *Magn Reson Med* 2019;81:2501–13 CrossRef Medline
15. Herrmann J, Gassenmaier S, Nickel D, et al. **Diagnostic confidence and feasibility of a deep learning accelerated HASTE sequence of the abdomen in a single breath-hold.** *Invest Radiol* 2021;56:313–19 CrossRef Medline
16. Vranic JE, Cross NM, Wang Y, et al. **Compressed sensing-sensitivity encoding (CS-SENSE) accelerated brain imaging: reduced scan time without reduced image quality.** *AJNR Am J Neuroradiol* 2019;40:92–98 CrossRef Medline
17. Kim HG, Choi JW, Yoon SH, et al. **Image quality assessment of silent T.** *Br J Radiol* 2018;91:20170680 CrossRef Medline
18. Sartoretti E, Wyss M, Eichenberger B, et al. **Rapid T2-weighted turbo spin echo MultiVane brain MRI using compressed SENSE: a qualitative analysis.** *Clin Radiol* 2021;76:786.e15–22 CrossRef Medline
19. Ngamsombat C, Gonçalves Filho AL, Longo MG, et al. **Evaluation of ultrafast wave-controlled aliasing in parallel imaging 3D-FLAIR in the visualization and volumetric estimation of cerebral white matter lesions.** *AJNR Am J Neuroradiol* 2021;42:1584–90 CrossRef Medline
20. Jensen CT, Liu X, Tamm EP, et al. **Image quality assessment of abdominal CT by use of new deep learning image reconstruction: initial experience.** *AJR Am J Roentgenol* 2020;215:50–57 CrossRef Medline
21. Zhu X, Ye J, Bao Z, et al. **Benefits of silent DWI MRI in success rate, image quality, and the need for secondary sedation during brain imaging of children of 3-36 months of age.** *Acad Radiol* 2020;27:543–49 CrossRef Medline
22. Li Z, Wang D, Robison RK, et al. **Sliding-slab three-dimensional TSE imaging with a spiral-in/out readout.** *Magn Reson Med* 2016;75:729–38 CrossRef Medline
23. Li Z, Karis JP, Pipe JG. **A 2D spiral turbo-spin-echo technique.** *Magn Reson Med* 2018;80:1989–96 CrossRef Medline
24. Nyberg E, Sandhu GS, Jesberger J, et al. **Comparison of brain MR images at 1.5T using BLADE and rectilinear techniques for**

patients who move during data acquisition. *AJNR Am J Neuroradiol* 2012;33:77–82 CrossRef Medline

25. Corcuera-Solano I, Doshi A, Pawha PS, et al. **Quiet PROPELLER MRI techniques match the quality of conventional PROPELLER brain imaging techniques.** *AJNR Am J Neuroradiol* 2015;36:1124–27 CrossRef Medline
26. Li Z, Pipe JG, Ooi MB, et al. **Improving the image quality of 3D FLAIR with a spiral MRI technique.** *Magn Reson Med* 2020;83:170–77 CrossRef Medline
27. Sun C, Yang Y, Cai X, et al. **Non-Cartesian slice-GRAPPA and slice-SPIRiT reconstruction methods for multiband spiral cardiac MRI.** *Magn Reson Med* 2020;83:1235–49 CrossRef Medline

A Thrombectomy Model Based on Ex Vivo Whole Human Brains

Y. Liu, J.L.A. Larco, S.I. Madhani, A.H. Shahid, R.A. Quinton, R. Kadirvel, D.F. Kallmes, W. Brinjikji, and L.E. Savastano

ABSTRACT

BACKGROUND AND PURPOSE: The persistent challenges in thrombectomy for large-vessel occlusion, such as suboptimal complete recanalization and first-pass effect imply an insufficient understanding of the artery-clot-device interaction. In this study, we present a thrombectomy model using fresh human brains, which can capture the artery-clot-device interaction through concurrent transmural and angiographic visualizations.

MATERIALS AND METHODS: Fresh nonfrozen whole adult human brains were collected and connected to a customized pump system tuned to deliver saline flow at a physiologic flow rate and pressure. Angiography was performed to verify the flow in the anterior-posterior and vertebrobasilar circulations and collaterals. Large-vessel occlusion was simulated by embolizing a radiopaque clot analog. Thrombectomy was tested, and the artery-clot-device interactions were recorded by transmural and angiographic videos.

RESULTS: Baseline cerebral angiography revealed excellent penetration of contrast in the anterior-posterior and vertebrobasilar circulations without notable arterial cutoffs and with robust collaterals. Small branches (<0.5 mm) and perforating arteries were consistently opacified with good patency. Three device passes were performed to achieve recanalization, with failure modes including elongation, fragmentation, and distal embolization.

CONCLUSIONS: This model enables concurrent transmural and angiographic analysis of artery-clot-device interaction in a human brain and provides critical insights into the action mechanism and failure modes of current and upcoming thrombectomy devices.

ABBREVIATIONS: LVO = large-vessel occlusion; VA = vertebral artery

Thrombectomy has been the standard of care for stroke with large-vessel occlusion (LVO), but clinical challenges such as suboptimal rates of first-pass effect and overall complete recanalization persist even after years of experience and development of new thrombectomy devices.[1,2] Such challenges imply the need for improved next-generation devices optimized in more realistic thrombectomy models. Historically, preclinical testing of thrombectomy devices has relied heavily on benchtop models. Although phantoms reproduce the gross arterial geometry and enable easy and reproducible testing of devices, they have oversimplified vascular anatomy and have much stiffer vessel walls compared with the human cerebral vasculature.[3,4] Animal models have also been used to evaluate device performance; however, the visualization of device-clot-artery interaction is limited by fluoroscopy, and the arteries do not accurately represent the complex anatomy and hemodynamic conditions of human brains.[5] A thrombectomy model that can realistically mimic the mechanical properties, anatomy, and blood flow of human cerebral vasculature is an unmet need.

In this study, we present a thrombectomy model using ex vivo whole human brains with unmodified cerebral vasculature and realistic flow conditions. This model allows concurrent direct optical and fluoroscopic examinations of the device-clot-artery interactions. The preparation of the brains and recreation of LVO will be described, followed by thrombectomy testing for model validation.

MATERIALS AND METHODS

Brain Preparation

The reparation method of the brains has been previously disclosed.[6] Briefly, after local institutional review board approval

Received April 30, 2021; accepted after revision July 8.

From the Departments of Radiology (Y.L., R.K., D.F.K., W.B.) and Neurosurgery (J.L.A.L., S.I.M., A.H.S., L.E.S.) and Division of Anatomic Pathology (R.A.Q.), Mayo Clinic, Rochester, Minnesota.

This work was supported by the National Institutes of Health National Institute of Neurological Disorders and Stroke (NS105853).

Please address correspondence to Luis E. Savastano, MD, PhD, Department of Neurosurgery, Mayo Clinic, 200 First St SW, Rochester, MN 55905; e-mail: Savastano.Luis@mayo.edu; @SavastanoLuisMD

Indicates open access to non-subscribers at www.ajnr.org
Indicates article with supplemental online videos.

http://dx.doi.org/10.3174/ajnr.A7291

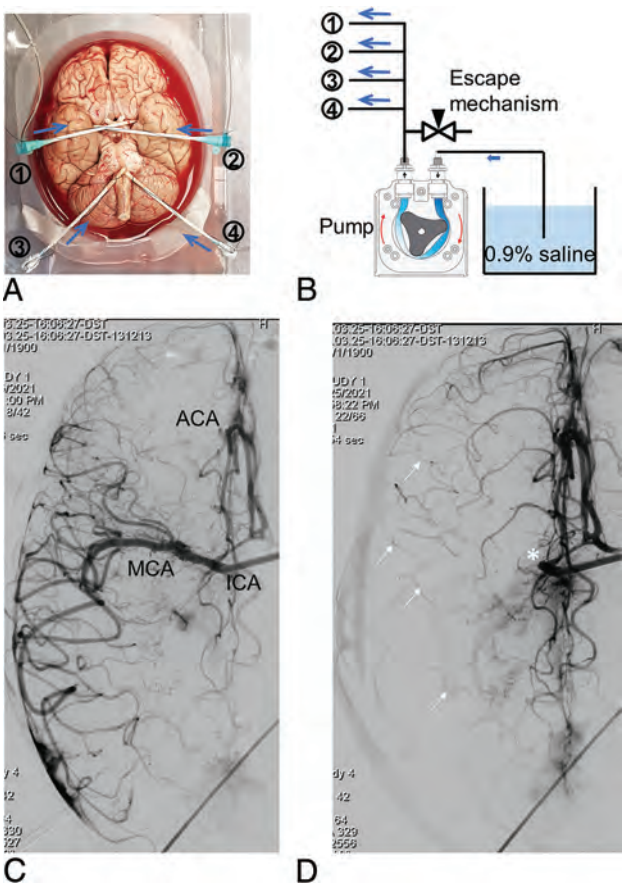

FIG 1. Ex vivo brain model flow setup and cerebral angiography. The bilateral ICAs and VAs of a fresh human cadaver brain were cannulated with sheaths to deliver saline solution and contrast (*blue arrows*) and catheters (*A*). The sheaths were connected to a pump system and connected in parallel to an escape system, including a reservoir of saline hung at a height that mimics the back pressure, equivalent to the peripheral arterial resistance, that releases the cerebral pressure when an occlusion is created (*B*). DSA of the right ICA in the late arterial phase in a pure ventrocaudal projection shows good opacification of the right MCA candelabra, right anterior cerebral artery (ACA), with cross-filling into the left ACA through a patent anterior communicating artery (*C*). Occlusion of the proximal right MCA (*asterisk*) enhances the visualization of robust leptomeningeal collaterals (*arrows*) from the ACA into cortical MCA branches (*D*). MCA indicates middle cerebral artery.

(20–002582), fresh nonfrozen whole adult human brains were collected during research-consented hospital postmortem examinations within 24 hours of the patient's death, and craniotomy was carefully performed to minimize damage to the brain and cerebral vessels. Brains with a history of head trauma, neurosurgical procedures, and stroke were excluded from this study. The arachnoid was then removed to expose the circle of Willis, including the anterior and posterior circulations. Postmortem clots were then removed by manual aspiration. The ICAs and vertebral arteries (VAs) were then cannulated with 8F or 9F femoral sheaths and tied with sutures (Fig 1*A*). The sheaths were then connected to a customized pump system to deliver 0.9% saline into the brain (Fig 1*B*). The saline allows direct observation of the interactions between the clot, artery, and thrombectomy devices. The pump system was calibrated to deliver physiologically representative flow rates to the ICAs and VAs, and the pressure was tuned by adjusting the downstream flow resistance to recreate physiologic pressure.[6] The flow rates were calibrated to infuse about 300 mL/min for each ICA and 160 mL/min for each vertebral artery. Then, using an 014 pressure-sensing guidewire (ComboWire XT; Philips Healthcare), we obtained intra-arterial pressures with a diastolic pressure around 80 mm Hg and a systolic pressure of about 100 mm Hg. Outward pressure can be replicated by submerging the brain in a saline tank, and the saline height above the brain can be adjusted to match the intracranial pressure (5 to 20 cm of water). Baseline cerebral angiographies of the ICA and vertebrobasilar circulations were performed in anteroposterior and lateral projections by injecting 10 mL of contrast (iohexol, Omnipaque 300; GE Healthcare) in the sheath.

Recreation of Large-Vessel Occlusion

A fibrin-rich clot analog was made by mixing human plasma and red blood cells at a volume ratio of 19:2.[4] To increase radiopacity, 0.5 g of barium sulfate powder was added per 10 mL of blood mixture. Higher amounts of barium sulfate can further increase the radiopacity but will make the clot analog more fragment-prone.[4] Coagulation was induced by adding 1 mL of 5% calcium chloride and 10 μL of 10 U/mL thrombin per 10 mL of blood mixture.[7] To simulate LVO, we loaded clot analogs into a syringe and embolized them to the brain via a 0.088-inch guide catheter (Neuron MAX; Penumbra) under physiologic pressure. This clot analog was selected to challenge current thrombectomy devices because fibrin-rich clots have been reported to be associated with more device passes, longer procedure times, and less favorable patient outcomes.[8] Clot analogs with different histology and tensile properties can also be made by mixing human plasma and red blood cells with different volume ratios.[7,9]

Thrombectomy Testing

Thrombectomy was performed with a 6F catheter (Sofia Plus; MicroVention) using the direct-aspiration technique or in combination with a stent retriever (Solitaire; Medtronic) using the Solumbra technique. These 2 techniques were selected because they are most often used for thrombectomy on the basis of a survey of neurointerventionalists.[10] The aspiration catheter was navigated to the clot face over a 0.014-inch guidewire (Synchro; Stryker) and a 0.027-inch microcatheter (Phenom; Medtronic) under roadmap guidance. Aspiration was provided by a vacuum pump (Gomco 405; Allied Healthcare).

RESULTS

Brain Model

After a learning curve of about 8 brains (if the operator has extensive experience in cerebrovascular anatomic dissections), it is possible to consistently have an operational testing platform that replicates physiologic hemodynamic conditions and allows real-time visualization of the device-clot interaction in about 75% of all harvested brains. About one-fourth of the brains could not be used due to a variety of reasons including the following: 1) major leaks due to perforating vessel avulsion during the extraction process from the skull base or cortical damage with M4 branch transection with the bone saw (easy to see after connecting the arteries

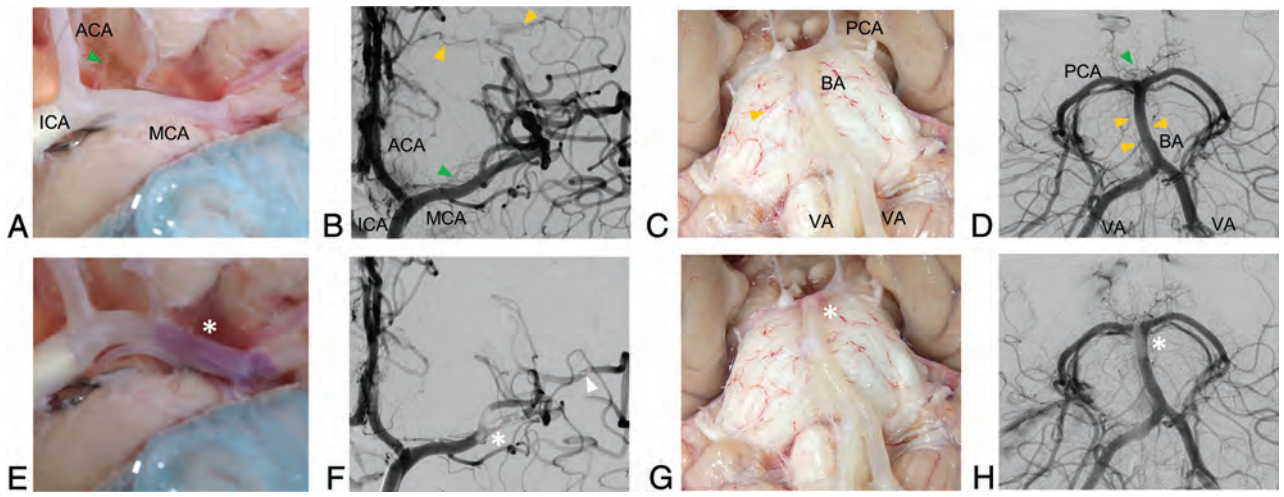

FIG 2. Concurrent direct transmural observation and DSA of the brain model pre- and post-LVO. Baseline transmural and angiographic visualization of the anterior circulation model (*A* and *B*) includes ICA, MCA, anterior cerebral artery (ACA), lenticulostriate arteries (*green triangle*), and leptomeningeal cortical collaterals (*yellow triangles*). The posterior circulation model (*C* and *D*) includes the vertebral arteries, the basilar artery with bifurcation into the posterior cerebral arteries, the thalamoperforating arteries (*green triangle*), and the pontine arteries (*yellow triangles*). Embolization of a radiopaque clot analog (*asterisks*, *E–H*) generally results in MCA bifurcation occlusion involving the lenticulostriate vessels (*E* and *F*) and occasionally results in concurrent distal MCA branch occlusion (*triangle* in *F*) and occlusion of the basilar artery apex (*G* and *H*).

to the flow system); 2) thick circumferential atherosclerotic plaques that prevent transmural visualization; 3) the length of the paraclinoid ICA and V4 segment of the VA being too short to allow cannulization by the sheaths. About 10–15 thrombectomy passes can be tested for each brain (about 5 in each anterior circulation and 5 in the basilar artery), but that changes depending on the type of clot and device used. After the brain is harvested, preparation and testing need to be done in about 6 hours before the brain decays.

Baseline Cerebral Angiography

Cerebral angiography revealed excellent penetration of contrast in the ICA and the vertebrobasilar circulation both in the arterial and capillary phases without notable arterial cutoffs and occasional minimal extravasation. Small branches (<0.5 mm) and perforating arteries were consistently opacified by radiopaque contrast with good patency (Fig 1*C*). Interhemispheric collateral flow through the circle of Willis was identified. Robust leptomeningeal collaterals were also identified by creating a proximal MCA occlusion and following contrast flow from the anterior cerebral artery to the cortical MCA branches in the late arterial phase (Fig 1*D*).

Concurrent Fluoroscopic and Transmural Visualization of Embolic Large-Vessel Occlusion

Direct transmural visualization concurrent with angiography was feasible for both the ICA and the vertebrobasilar circulation (Figs 2*A–D*). The anterior circulation model provided visualization of the intracranial ICA system, including the lenticulostriate vessels and cortical leptomeningeal collaterals (Figs 2*A*, *-B*). The posterior circulation model revealed the vertebrobasilar system including the thalamoperforating and pontine arteries (Figs 2*C*, *-D*). Embolization of the radiopaque clot analog could be visualized in real-time by fluoroscopy (Online Video 1). Postembolization cerebral transluminal observation and angiography demonstrated LVO at the MCA bifurcation (Figs 1*E*, *-F*) and the basilar artery apex (Figs 1*G*, *-H*), which remained stable under physiologic flow and pressure. In the anterior circulation, postembolization contrast filling defects included the lenticulostriate arteries and distal cortical MCA branches, likely due to partial clot fragmentation and downstream migration (Fig 1*F*). In the posterior circulation, postembolization contrast filling defects included the pontine arteries and the thalamoperforating arteries (Fig 1*H*).

Concurrent Fluoroscopic and Optical Visualization of the Recanalization Procedure

The model allowed concurrent fluoroscopic and optical visualization through the arterial wall of the thrombectomy, greatly enhancing the analysis of device-clot interaction. For example, for an occlusion at the basilar apex, 3 device passes were performed to recanalize the parent artery. In the first pass (Online Video 2), the aspiration catheter was navigated to the clot face, and vacuum was then activated. Vacuum and device withdrawal are needed to overcome the resistance forces including the vessel wall friction and hydrodynamic forces in the antegrade direction. The clot corked the catheter tip and started to be pulled back with an initial length of L_0 (Fig 3*A*). During pulling, the tensional load stretched the clot to a length of L_1 (Fig 3*B*). As the clot was further pulled to enter the smaller VA, the increased resistance forces surpassed the device-clot integration force resulting in clot disengagement from the catheter (Fig 3*C*). The clot was then pushed downstream by the flow, resulting in a recurrent occlusion at the basilar artery apex. In the second pass (Online Video 3), as the clot was pulled into the VA, the tensional load elongated and weakened the clot and eventually caused clot fragmentation with distal embolization to the basilar artery apex. In the third pass (Online Video 4), the remaining clot fragment remained corked at the catheter tip and was pulled out without disengagement or fragmentation. Compared with the previous 2 passes, the clot fragment in the third pass had a smaller surface area and,

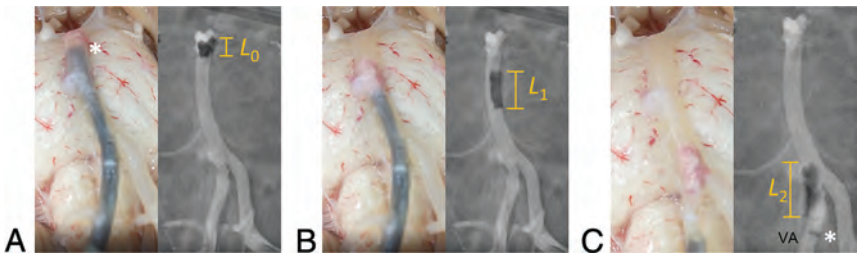

FIG 3. Concurrent transmural and angiographic visualization of a direct-aspiration thrombectomy for an embolic occlusion at the basilar apex. The aspiration catheter was navigated to the clot face, and the clot with an initial length of L_0 was corked by vacuum at the catheter tip (*asterisk*) (*A*). Device pullout elongated the clot to a length of L_1 and disengaged the clot from the basilar apex (*B*). As the clot was pulled from the basilar artery into the right VA, it further elongated (L_2) and was stripped away from the catheter tip (*asterisk* in *C*).

therefore, smaller frictional and hydrodynamic shear forces fighting against the catheter pull, leading to a smaller tensional load within the clot.

DISCUSSION

In this article, we introduced a human cadaveric model for cerebrovascular research with concurrent transmural and angiographic visualization and demonstrated its value for testing in LVO. Compared with our previous work in which thrombectomy testing in ex vivo brains was transmurally observed,[6] the angiographic study presented here included baseline cerebrovascular anatomy in cadavers and the changes during and after thrombectomy, revealing important features such as the presence of leptomeningeal collaterals and the capacity to assess the patency of small branches and perforating arteries. In addition, the previously published model was able to only assess recanalization in the arterial segments exposed at the base of the brain (mostly the distal VA, basilar artery, and P1 and the ICA terminus with the proximal M1 and A1). The present model here introduced provides a much broader area of analysis, practically including the whole brain and the cerebral vasculature down to the cortical branches. In addition to a more clinically relevant and accurate scoring of the recanalization procedure, it may enable the testing of miniaturized thrombectomy devices in the removal of thrombi from distal branches to eloquent brain areas.

In addition to the human brain model herein described, another 3 main categories of thrombectomy models have been reported and reviewed in the literature: benchtop phantoms,[11] in vivo animal models,[12] and emerging computational models.[13] Benchtop phantoms leverage recent advances in high-resolution medical imaging and 3D printing techniques to replicate patient-specific anatomy in a consistent fashion. This feature is advantageous in early device testing and benchmarking of different devices. Hemodynamics in the benchtop phantoms can also be customized to replicate physiologic conditions. Transparent phantoms also allow direct visualization of the device-clot interaction, though the "vascular" walls are much stiffer than human arteries (or totally rigid), lack submillimeter arteries, and do not adhere well to the clots.[11] Animal models have been extensively used and are critical to test device safety. These models provide a more realistic device-artery-clot interaction, but it can only be visualized using fluoroscopy, with a limited resolution and frame rate. In addition, the blood flow in animal models is usually slower than that of the human cerebrum, resulting in an underestimation of hemodynamic force and events of distal embolization, and the 3D anatomic configuration is much simpler than the human cerebral vasculature. Finally, computational models may be promising to generate a realistic "virtual patient" model with characteristics otherwise difficult to be simultaneously mimicked in phantoms and animals such as anatomic tortuosity, hemodynamics, and vessel wall properties. However, the development of a realistic and validated biomechanical model continues to be a persisting challenge.

First, this model has the unmodified geometric complexity of the human cerebral vasculature, including a patent circle of Willis, small branches and perforating arteries, and functional leptomeningeal collaterals. These anatomic features are extremely important because the models used to date are mostly artificial benchtop phantoms that do not have submillimeter arteries.[11] Animal models (eg, swine) do not fully emulate the human cerebral vasculature distribution or wall characteristics.[3] Residual occlusion in small branching and perforating arteries is believed to be one of the reasons for poor neurologic outcome despite apparently "complete" recanalization, and this model may be of benefit to better characterize this problem and develop solutions.[14]

Second, the human brain model provides a realistic mechanical response of the arteries to the mechanical load of devices. This is critical to accurately test arterial deformation, stretching, collapse under vacuum, and even arterial injury such as perforation. Recently, mechanical thrombectomy devices were recalled from the market after multiple events of fatal catastrophic arterial ruptures.[15] By comparison, benchtop phantoms have much stiffer and stronger walls, preventing arterial deformation, traction, and even injury, and the friction encountered is not realistic.[3,11] Animal models do provide a more realistic environment and enable gross analysis of arterial injury, but recent publications have shown that human arteries differ both in architecture and mechanical strength compared with the extracranial arteries of animals,[5] and the analysis of the response continues to be limited by the resolution and frame rate of fluoroscopy.

Third, this model allows concurrent fluoroscopy and direct transluminal observation of artery-clot-device interaction to understand the action mechanism and failure modes of thrombectomy devices. Neurointerventionalists are blind to the arterial wall response under vacuum and/or device pull; therefore, a model that "opens a window" for direct visualization has a large potential in research and improvement of technology. In this study, we have demonstrated that pulling back of thrombectomy devices can cause elongation, thinning, weakening, and possible fracturing of the clot, leading to distal embolization and residual occlusion. Although such a phenomenon has been reported in

benchtop models,[16] fidelity of this brain model is higher, and analysis is more comprehensive due to the more realistic vessel wall properties, including friction and strength. In addition, the realistic mechanical properties of the vessel wall make this model unique to reveal failure modes of device-artery interaction such as vessel traction and vessel collapse as shown previously.[14] Pulling back the catheter with weak clot-catheter integration results in residual occlusions or iatrogenic embolization and is likely the main cause of low first-pass recanalization. We think that future aspiration technologies should aim to ingest clots in situ, proximal-to-distal, and at low vacuum power to prevent vessel collapse.

Although only embolic LVOs were presented in this study, we believe that this model can be adapted to recreate other neurovascular conditions, including medium and distal vessel occlusions (and test the performance of novel miniaturized thrombectomy devices), brain aneurysms, and intracranial atherosclerotic diseases.

We do acknowledge some limitations with this model that must be considered to extrapolate results to our patients. First, saline was used to enable direct transmural observation of the thrombectomy procedure, but the viscosity is lower than that of blood. Blood can be used to replicate the hydrodynamics, though this will limit direct transmural observation. Ideally, other colorless and transparent fluids that can simultaneously mimic the viscosity and friction of blood can be used, though such fluid has not been reported in the literature. Second, the brain is ex vivo, and biologic activities such as vasospasm and vascular tone cannot be captured. Third, the model as presented in this article does not include the tortuous path of the ICA through the skull base, though this feature could be implemented if needed by using appropriately shaped sheaths. Fourth, the degree of arterial deformation in this model could be potentially more pronounced given the absence of enclosing calvaria and skull base; therefore, extrapolation to patients needs to be considered with care. Last, variance among different brains is inevitable (for example in the size and shape of the circle of Willis), somehow limiting the reproducibility of results, and necessitates testing multiple brains to minimize bias. Overall, this is a proof-of-concept study, and further validation against clinical experience and other thrombectomy models are warranted.

CONCLUSIONS

The whole-human brain model with concurrent transmural and angiographic visualization of recanalization provides unsurpassed fidelity of the human cerebrovascular system and enables accurate analysis of artery-clot-device interaction in thrombectomy.

Disclosures: Yang Liu—*UNRELATED*: *Stock/Stock Options*: Endovascular Engineering. Ram Kadirvel—*RELATED*: *Grant*: National Institutes of Health, *Comments*: National Institutes of Health NS076491.* David F. Kallmes—*UNRELATED*: *Board Membership*: Triticum,* *Comments*: Advisory Board; *Consultancy*: NoNO, Vesalio, Minnetronix,* *Comments*: Data and Safety Monitoring Board; *Grants/Grants Pending*: Balt, MicroVention, Medtronic, Neurogami, Monarch Medical, Insera Therapeutics, MIVI Neurovascular,* *Comments*: research support; *Patents (Planned, Pending, or Issued)*: Balloon-Guide technology, Spine Augmentation technology*; *Royalties*: Balloon Guide Technology; *Stock/Stock Options:* Marblehead Medical, Conway Medical Center, Superior Medical Experts. Luis E. Savastano—*UNRELATED*: *Board Membership*: President of Endovascular Engineering; *Employment*: Chief Medical Officer of VerAvanti; *Stock/Stock Options:* VerAvanti and Endovascular Engineering. *Money paid to the institution.

REFERENCES

1. Kleine JF, Wunderlich S, Zimmer C, et al. **Time to redefine success? TICI 3 versus TICI 2b recanalization in middle cerebral artery occlusion treated with thrombectomy.** *J NeuroIntervent Surg* 2017;9:117–21 CrossRef
2. Abbasi M, Liu Y, Fitzgerald S, et al. **Systematic review and meta-analysis of current rates of first pass effect by thrombectomy technique and associations with clinical outcomes.** *J Neurointerv Surg* 2021;13:212–16 CrossRef Medline
3. Liu Y, Abbasi M, Arturo Larco JL, et al. **Preclinical testing platforms for mechanical thrombectomy in stroke: a review on phantoms, in-vivo animal, and cadaveric models.** *J Neurointerv Surg* 2021;13:816–22 CrossRef Medline
4. Reddy A, Liu Y, Cockrum J, et al. **Construction of a comprehensive endovascular test bed for research and device development in mechanical thrombectomy in stroke.** *J Neurosurg* 2020;134:1190–97 CrossRef Medline
5. Ding Y, Fitzgerald S, Liu Y, et al. **A novel rabbit thromboembolic occlusion model.** *J Neurointerv Surg* 2021 Feb 11. [Epub ahead of print] CrossRef Medline
6. Gebrezgiabhier D, Liu Y, Reddy AS, et al. **A human brain test bed for research in large vessel occlusion stroke.** *J Neurosurg* 2021 Jan 22. [Epub ahead of print] CrossRef Medline
7. Fitzgerald S, Liu Y, Dai D, et al. **Novel human acute ischemic stroke blood clot analogues for in-vitro thrombectomy testing.** *AJNR Am J Neuroradiol* 2021;42:1250–57 CrossRef Medline
8. Jolugbo P, Ariëns RA. **Thrombus composition and efficacy of thrombolysis and thrombectomy in acute ischemic stroke.** *Stroke* 2021;52:1131–42 CrossRef Medline
9. Liu Y, Reddy AS, Cockrum J, et al. **Standardized fabrication method of human-derived emboli with histologic and mechanical quantification for stroke research.** *J Stroke Cerebrovasc Dis* 2020;29:105205 CrossRef Medline
10. Fargen KM, Arthur AS, Spiotta AM, et al. **A survey of neurointerventionalists on thrombectomy practices for emergent large vessel occlusions.** *J Neurointerv Surg* 2017;9:142–46 CrossRef Medline
11. Waqas M, Mokin M, Lim J, et al. **Design and physical properties of 3-dimensional printed models used for neurointervention: a systematic review of the literature.** *Neurosurgery* 2020;87:E445–53 CrossRef Medline
12. Herrmann AM, Meckel S, Gounis MJ, et al. **Large animals in neurointerventional research: a systematic review on models, techniques and their application in endovascular procedures for stroke, aneurysms and vascular malformations.** *J Cereb Blood Flow Metab* 2019;39:375–94 CrossRef Medline
13. Konduri PR, Marquering HA, van Bavel EE, et al; INSIST Investigators. **In-silico trials for treatment of acute ischemic stroke.** *Front Neurol* 2020;11:558125 CrossRef Medline
14. Liu Y, Gebrezgiabhier D, Reddy AS, et al. **Failure modes and effects analysis of mechanical thrombectomy for stroke discovered in human brains.** *J Neurosurg* 2021 June 4. [Epub ahead of print] CrossRef Medline
15. Majidi S, Bageac DV, Fayed I, et al. **JET 7 XTRA Flex reperfusion catheter-related complications during endovascular thrombectomy.** *J Neurointerv Surg* 2021;13:352–56 CrossRef Medline
16. Liu Y, Zheng Y, Reddy AS, et al. **Analysis of human emboli and thrombectomy forces in large vessel occlusion stroke.** *J Neurosurg* 2020;134:893–901 CrossRef Medline

Evaluation of Outcome Prediction of Flow Diversion for Intracranial Aneurysms

S. Hadad, F. Mut, R. Kadirvel, Y.-H. Ding, D. Kallmes, and J.R. Cebral

ABSTRACT

BACKGROUND AND PURPOSE: Identifying and predicting which aneurysms are likely to quickly occlude and which ones are likely to remain open following treatment with flow-diverting devices is important to develop optimal patient management strategies. The purpose of this study was to evaluate predictions based on computational fluid dynamics models using the elastase rabbit aneurysm model.

MATERIALS AND METHODS: A series of 13 aneurysms created in rabbits were treated with flow diverters, and outcomes were angiographically assessed at 8 weeks' follow-up. Computational fluid dynamics models were constructed from pretreatment 3D rotational angiograms and Doppler ultrasound flow velocity measurements. Postimplantation mean aneurysm inflow rate and flow velocity were used to prospectively predict aneurysm occlusion blinded to the actual outcomes. Specifically, if both variables were below their corresponding thresholds, fast occlusion was predicted, while if one of them was above the threshold, slow or incomplete occlusion was predicted.

RESULTS: Of the 13 aneurysms included, 8 were incompletely occluded 8 weeks after treatment, and 5 were completely occluded. A total of 10 computational fluid dynamics–based predictions agreed with the angiographic outcome, reaching 77% accuracy, 80% sensitivity, and 75% specificity. Posttreatment mean velocity alone was able to achieve the same predictive power as the combination of inflow rate and velocity.

CONCLUSIONS: Subject-specific computational fluid dynamics models of the hemodynamic conditions created immediately after implantation of flow-diverting devices in experimental aneurysms created in rabbits are capable of prospectively predicting, with a reasonable accuracy, which aneurysms will completely occlude and which ones will remain incompletely occluded.

ABBREVIATIONS: CFD = computational fluid dynamics; DUS = Doppler ultrasound; FD = flow-diverting (diverter); Q = inflow rate; VEL = velocity

Treatment of intracranial aneurysms with flow-diverting (FD) devices has been gaining popularity as a viable alternative to coiling or clipping, especially for complex aneurysms with wide necks.[1] Many complex aneurysms have been successfully treated with an increasing variety of flow diverters.[2] However, aneurysms are not immediately excluded from the circulation, and numerous aneurysms remain patent for a long time after treatment; approximately 25% remain incompletely occluded after 6 months.[3,4] Thus, understanding and identifying which aneurysms are likely to quickly occlude and which ones are likely to remain incompletely occluded is important for personalized management-planning and to avoid or minimize retreatment of these aneurysms.

Computational fluid dynamics (CFD) has been previously proposed in several studies as a predictive tool for flow-diversion treatment of intracranial aneurysms.[5-10] Similarly, alteration of the mean aneurysm flow amplitude, estimated from high-frame-rate dynamic DSA, has also been proposed as an outcome predictor for FD treatment.[11] Therefore, the objective of this study was to evaluate the predictive power of previously reported subject-specific CFD models[12] by performing a prospective analysis of aneurysm occlusion after FD treatment using elastase rabbit models.

Received January 12, 2021; accepted after revision June 10.

From the Departments of Bioengineering and Mechanical Engineering (S.H., F.M., J.R.C.), George Mason University, Fairfax, Virginia; and Department of Interventional Neuroradiology (R.K., Y.-H.D., D.K.), Mayo Clinic, Rochester, Minnesota.

This work was supported by the National Institutes of Health, grant No. R01NS076491.

Please address correspondence to Sara Hadad, MSc, Bioengineering Department, Volgenau School of Engineering, George Mason University, 4400 University Dr, MSN 1J7, Fairfax, VA 22030; e-mail: shadad@gmu.edu

http://dx.doi.org/10.3174/ajnr.A7263

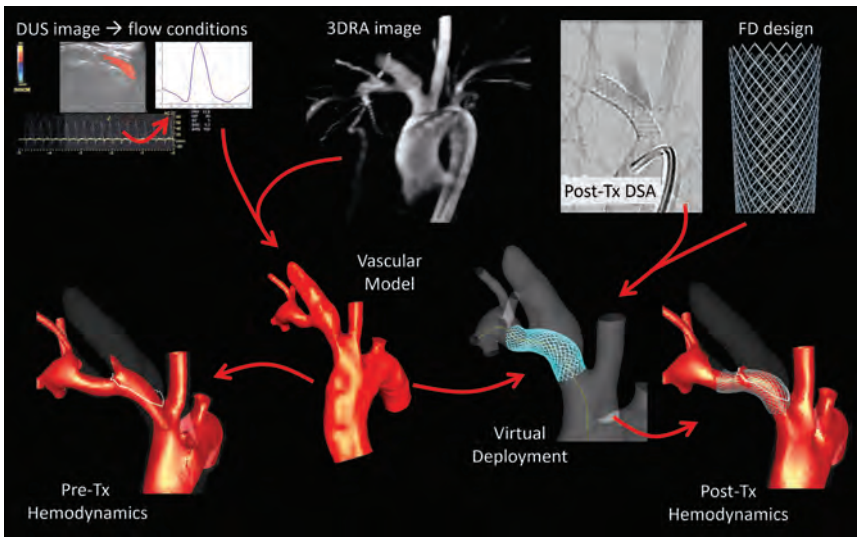

FIG 1. Subject-specific, multimodal image–based CFD modeling methodology. A subject-specific vascular model constructed from a 3D rotational angiography (3DRA) image, flow conditions derived from Doppler ultrasound images, and an FD model constructed from device-design data and virtually deployed into vascular model guided by 2D-DSA. Pre- and posttreatment hemodynamics characterized by corresponding CFD simulations and inflow jets visualized with velocity isosurfaces. Tx indicates Treatment; Pre-Tx, Pretreatment; Post-Tx, Posttreatment.

MATERIALS AND METHODS

Animal Models and Imaging Data

A total of 13 aneurysms were experimentally created in rabbits using elastase and carotid ligation techniques previously developed and used to evaluate flow diverters.[13] The aneurysms were allowed to progress for 4 weeks and then were treated by implantation of a flow-diverting device, the Pipeline Embolization Device (PED; Medtronic). Vessel diameter at the aneurysm neck and device sizes are given in the Online Supplemental Data. A 3D rotational angiography image was acquired immediately before the implantation of the flow diverter, and 2D-DSA sequences were acquired both immediately prior to and immediately after implantation. Doppler ultrasound was used to measure the pretreatment blood flow velocity in the parent artery proximal and distal to the aneurysm. Aneurysm occlusion was subsequently evaluated using DSA sequences acquired 8 weeks after the implantation of the flow-diverting device.

Hemodynamics Modeling

Subject-specific CFD models were created from the 3D rotational angiography images using a previously described methodology,[14] illustrated in Fig 1. Briefly, 3D vascular segmentations were used to create anatomic models of the aneurysm and parent artery. Blood flow was mathematically modeled by the unsteady incompressible Navier-Stokes equations, which were numerically solved using a finite element code.[15] Pulsatile flow conditions were derived from the Doppler ultrasound acquired in the parent artery proximal to the aneurysm. The velocity waveforms were digitized and converted to flow-rate curves by multiplying by the vessel cross-sectional area and were used to prescribe inflow boundary conditions. Outflow boundary conditions consistent with a flow division proportional to the vessel cross-sectional area to the power 3/2 (the Murray law) were applied. Vascular walls were approximated as rigid, and no-slip boundary conditions were applied at the walls. Simulations were performed for 2 cardiac cycles, and flow fields from the second cycle were used to characterize the aneurysm hemodynamic environment.

FD Modeling

As in previous studies,[6,14] models of the flow-diverting device were created and virtually deployed within the vascular models (Fig 1). For this purpose, the skeleton of the parent artery was first reconstructed from the vascular model, and a cylindrical structure was expanded within the vascular model until it contacted the wall or reached the device diameter. The device design (48 wires of 32-μm thickness braided into 24 cells with a braid angle of 150°) was then mapped onto the deployed cylindrical surface, taking into account the foreshortening effects due to device oversizing.[16] 2D-DSA images acquired immediately postimplantation (Online Supplemental Data) were used to verify that the position of the virtual FD within the vascular model was consistent with the actual FD depicted in the DSA images. The computational mesh was then adaptively refined to resolve the device wires, and a new flow solution corresponding to the immediate posttreatment conditions was obtained using an immersed boundary method on unstructured grids.[17]

Outcome Prediction and Evaluation

In a previous study,[12] a series of 36 aneurysms created in rabbits was used to compare the hemodynamics between aneurysms that were completely occluded at ≤4 weeks (fast-occlusion group) and aneurysms that remained incompletely occluded at 8 weeks (slow- or incomplete-occlusion group). In that study, it was found that the posttreatment mean aneurysm velocity (VEL) and the mean aneurysm inflow rate (Q) were significantly lower in the fast-occlusion group than in the incomplete-occlusion group (VEL, $P = .05$; Q, $P = .02$). Receiver operating characteristic curve analysis suggested that these variables could be used to discriminate between aneurysms in these 2 groups, with a discriminatory power given by the corresponding areas under the receiver operating characteristic curve of 0.83 (VEL) and 0.90 (Q), respectively. The optimal threshold for each of these 2 variables was determined from the point along the receiver operating characteristic curve closest to the upper-left corner (ie, the threshold that maximizes specificity and sensitivity). The values of these thresholds were 0.161 cm/s for VEL, and 0.041 mL/s for Q.

Outcome predictions were made for the 13 aneurysms in the current series on the basis of these previously determined thresholds. Specifically, if both the posttreatment VEL and Q were below the corresponding thresholds, the aneurysm was assigned

Table 1: Posttreatment hemodynamic variables, predictions, outcomes, and agreement

Subject	Q (mL/s)	VEL (cm/s)	Prediction	Outcome	Agreement
1	0.055	0.391	I	I	A
2	0.013	0.127	C	I	D
3	0.048	0.532	I	I	A
4	0.013	0.112	C	I	D
5	0.018	0.179	I	I	A
6	0.053	0.362	I	I	A
7	0.031	0.344	I	I	A
8	0.094	0.664	I	I	A
9	0.011	0.108	C	C	A
10	0.007	0.156	C	C	A
11	0.021	0.102	C	C	A
12	0.100	0.831	I	C	D
13	0.025	0.156	C	C	A

Note:—I indicates incomplete occlusion; C, complete occlusion; A, agreement; D, disagreement.

Table 2: Summary of agreement between predictions and outcomes

	Outcomes		
Predictions	Complete	Incomplete	Total
Complete	4	2	6
Incomplete	1	6	7
Total	5	8	13

to the fast-occlusion group. Alternatively, if either of these 2 variables were above their thresholds, the aneurysm was assigned to the incomplete-occlusion group. All predictions were made prospectively, blinded to the actual outcome.

On the basis of DSA sequences acquired at 8 weeks after treatment with an FD, the outcomes were assessed as complete occlusion (no filling of the aneurysm and no remnant) or incomplete occlusion (persistent filling of the aneurysm or small remnant). Note that because all outcomes were assessed at 8 weeks, a small remnant at 8 weeks would most likely have placed the aneurysm in the slow-occlusion group of the previous study (not in the fast-occlusion group in which complete occlusion was required at ≤4 weeks). Finally, the outcomes were compared against the predictions on the basis of the immediate posttreatment CFD analyses.

RESULTS

The main results of the study are summarized in Table 1. This table lists the values of the hemodynamic variables used to predict outcomes, namely the mean aneurysm Q and mean aneurysm VEL, both corresponding to the hemodynamic conditions immediately after FD implantation. The table also shows, for each aneurysm, the prospective prediction based on both Q and VEL, the actual outcome at 8 weeks, and whether they agreed or disagreed. For completeness, the pre- and posttreatment values of these variable and their relative change are listed in the Online Supplemental Data.

Of the 13 aneurysms treated, 8 (62%) were angiographically classified as incompletely occluded at 8 weeks, and 5 (38%), as completely occluded. Sample DSA images acquired immediately before and after treatment and at 8 weeks, follow-up are shown in the Online Supplemental Data for each aneurysm.

A summary of the agreement between predictions and outcomes is presented in Table 2. Of the 13 predictions, 10 agreed with the actual outcomes, corresponding to an overall accuracy of 77%, a sensitivity of 80%, and a specificity of 75%. In 3 cases (23%), the predictions disagreed with the outcomes. Two of these disagreements corresponded to false-negatives (ie, predicted complete occlusions but aneurysms were incompletely occluded at follow-up), and one, to a false-positive (ie, predicted incomplete occlusion but the aneurysm was completely occluded at follow-up).

Examples of an aneurysm predicted and confirmed to be completely occluded at follow-up and another predicted and confirmed to be incompletely occluded are presented in Fig 2. In the first case, it can be seen that the aneurysm had a strong inflow jet before treatment, but this jet was effectively blocked by the FD device, resulting in low-inflow and low-velocity patterns after treatment. In the second case, the FD device did not sufficiently reduce the inflow and mean velocity, and the aneurysm remained incompletely occluded at follow-up.

DISCUSSION

Predicting whether an aneurysm will immediately occlude after treatment with an FD device or whether it will remain incompletely occluded is important to plan the best management strategy for each individual patient. For example, it could help support decisions about using multiple devices to achieve the desired hemodynamic environment, choosing a different FD device or endovascular approach, closely monitoring patients who may need retreatment, or determining when to discontinue dual antiplatelet therapy.

The use of image-based CFD models to predict FD outcomes has been proposed in several studies that demonstrated hemodynamic differences between completely and incompletely occluded aneurysms.[5-10] Furthermore, similar trends have been reported for intrasaccular FDs for the treatment of bifurcation aneurysms that are problematic for endoluminal devices.[18] The current work focused on validating CFD-based predictions in experimental aneurysms created in rabbits. The study was restricted to endoluminal FDs, and hemodynamic variables previously identified as the principal distinguishing characteristics between fast occlusion and incomplete occlusion after treatment were used to predict outcomes. The same variables were also identified as potential discriminators between fast and incomplete occlusions after FD treatment of human aneurysms, with similar areas under the curve.[19] Therefore, it is reasonable to expect that the results of the current study will generalize to human aneurysms and be consistent with recent reports relating posttreatment flow velocity and FD outcome in humans.[20]

Our results indicate that the combination of Q and mean VEL immediately after FD implantation is indeed capable of predicting outcomes with an accuracy of 77%. Specifically, aneurysms with low Q and low mean VEL after treatment (below their corresponding thresholds) are predicted to occlude completely, while

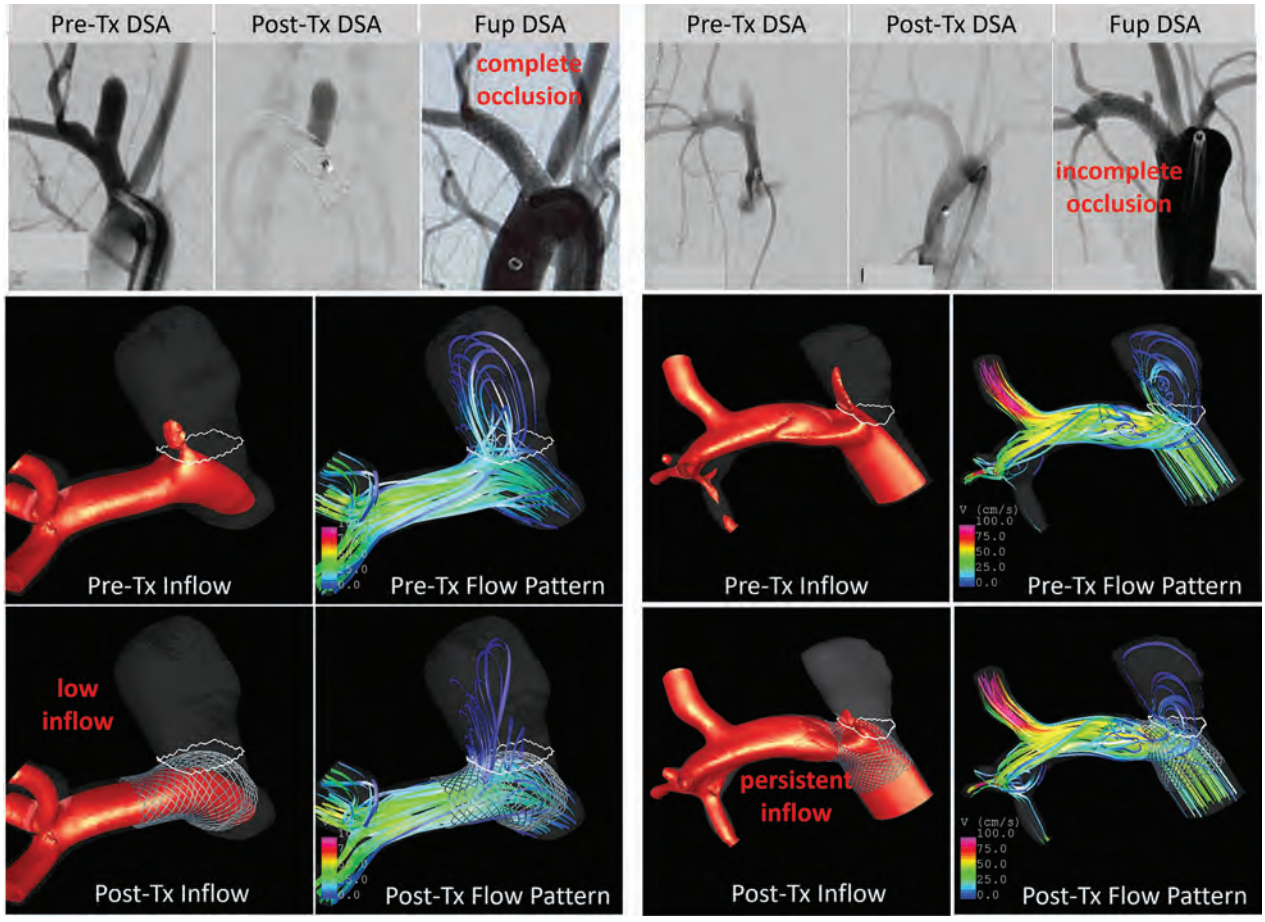

FIG 2. Examples of a completely occluded (left, subject 11) and an incompletely occluded (right, subject 7) aneurysm after treatment with FD devices. In both cases, prospective CFD predictions coincided with the angiographic outcomes at 8 weeks. Visualizations show the inflow jet (isovelocity surfaces) and flow pattern (streamlines) before and after treatment. Substantial reduction of the inflow and flow velocities is observed in the completely occluded aneurysm, but persistent posttreatment inflow and flow velocity can be seen in the incompletely occluded aneurysm. The *circled white line* show neck area of the aneurysm. Tx indicates Treatment; Fup,follow up; Fup DSA, Follow up DSA.

aneurysms with either a large Q or large mean VEL are predicted to remain incompletely occluded at 8 weeks. Most interesting, if the predictive variables (Q and VEL) were considered separately, VEL was able to correctly predict the same 77% of cases, while Q alone was capable of correctly predicting only 62% of the cases. This finding suggests that the posttreatment mean aneurysm VEL may be a better predictor than the mean aneurysm inflow Q; however, in the current sample, these 2 variables were not independent (regression analysis showed a linear correlation with an R^2 value of 0.91), explaining why the VEL + Q combination was not better than the VEL alone. Further studies with more cases are needed to determine whether the combination of these 2 variables can be better than the mean VEL alone in general.

Recently, Paliwal et al[21] constructed machine learning models based on 16 morphologic, hemodynamic, and device parameters and applied them to a retrospective cohort of 84 aneurysms treated with FDs and obtained a 90% accuracy in an internal 20-fold cross-validation. In another study, Sindeev et al[22] analyzed the flow changes in 3 aneurysms treated with FDs with known outcomes using CFD and phase-contrast MR imaging and concluded that CFD could be used to predict outcomes. Previously, Pereira et al[11] studied a prospective series of 24 patients treated with FDs and calculated the mean aneurysm flow amplitude ratio from dynamic DSA images and concluded that this variable could predict complete or incomplete occlusion at 12 months with an accuracy of 86%, sensitivity of 88%, and specificity of 73%. In comparison, we achieved an accuracy of 77%, sensitivity of 80%, and specificity of 75% when validating the predictions in a prospective manner blinded to the outcomes and in an external data set of 13 rabbit models.

Some of these previous studies have proposed the change in hemodynamic variables such as the mean aneurysm VEL from pretreatment to posttreatment as potential predictors of outcomes.[9,13] In our previous study,[14] changes in hemodynamic variables were slightly different between the complete and incomplete aneurysm occlusion groups; thus, it was not possible to use these changes for outcome prediction (ie, it was not possible to calculate corresponding thresholds to discriminate between the 2 groups). However, it was the posttreatment conditions (not their change from the pretreatment values) that were able to predict the outcomes. Large hemodynamic changes may facilitate fast occlusions, but they may not be sufficient if these changes do not produce hemodynamic conditions with values below the predictive thresholds.

In our study, 2 aneurysms had low-flow conditions after treatment according to the CFD models but remained incompletely occluded at follow-up. These false-negatives are difficult to understand and may indicate that though important, flow conditions may not be the only determining factor for aneurysm occlusion. Perhaps other biologic mechanisms not included in the current models such as individual responses to antiplatelet therapy, diminished fibrin activity, impaired endothelialization, and so forth may slow down the occlusion process. However, in one of these cases (subject 2), the distal parent artery was larger than the FD diameter (device undersized), and consequently, the device was not well-apposed to the wall. This result was confirmed with optical coherence tomography imaging at follow-up (Online Supplemental Data). In such cases, it is very difficult to predict the exact positioning of the FD in the vascular model, and it is possible that the virtual FD was more effective at disrupting the flow into the aneurysm than the actual device, explaining this false-negative.

One case with high-flow conditions after treatment (values above their thresholds) was completely occluded at follow-up (false-positive). Here, we need to remember that the thresholds were determined from a previous study in which one group of aneurysms was completely occluded at 4 weeks, while the other remained open at 8 weeks. Thus, in the current study, perhaps this false-positive case may have been incompletely occluded at 4 weeks but occluded before 8 weeks. These disagreements may also be due to limitations of the CFD models (see below), which could deviate from the actual in vivo hemodynamics in certain subjects. Nevertheless, our models were able to prospectively predict the outcomes correctly in 77% of the cases. This predictive power is consistent with those in previous studies based on DSA flow assessments[13] and with the previously determined areas under the curve.[14,21]

In our previous studies, we have found similar hemodynamic differences between complete and incomplete occlusions after FD treatment in rabbits[8,14] and in humans,[21] which, in the current study, were used as outcome predictors. Furthermore, we showed that in humans, individualized flow conditions derived from an empirical law relating the inflow rate and parent artery diameter were sufficient to distinguish between complete and incomplete occlusions,[21] suggesting that it may not be necessary to measure patient-specific flow rates in humans. Additionally, rabbit elastase models have been shown to appropriately mimic human intracranial aneurysms for studying aneurysm treatment.[23] Thus, it is to be expected that the proposed approach will also work in human aneurysms. The application of CFD modeling of FDs for easy use in the clinic can be simplified by 2 main aspects: 1) developing integrated vascular modeling tools that can be easily interfaced with angiography systems (to accelerate/simplify the manual part of the modeling process), and 2) performing steady-state simulations, which provide good estimates of the mean velocity and inflow rates (accelerating the automatic part of the process). These simplifications would allow CFD models to be created and run in a few minutes. On the other hand, if the hemodynamic variables identified here as good predictors of aneurysm occlusion could be reliably derived from other techniques, such as the mean aneurysm flow amplitude from cine DSA or 4D phase-contrast MR imaging, it may not be necessary to construct CFD models for all patients. However, these other techniques also have limitations that need to be carefully considered (eg, mean aneurysm flow amplitude is a 2D technique and may underestimate mean velocities in the aneurysm, where the flow has, in general, a complex 3D structure).

The current study has several limitations. The CFD modeling is based on several approximations such as Newtonian flows, rigid vessel walls, inflow rates derived from Doppler ultrasound measurements of flow velocities, and outflow boundary conditions based on the Murray law. However, previous studies showed that these models were able to reproduce in vivo velocity values at the aneurysm neck measured with Doppler ultrasound and overall flow patterns observed in DSA sequences.[16] The virtual FD deployment methodology takes into account foreshortening effects and is able to reasonably reproduce the geometry of the implanted device,[16] but it does not exactly reproduce the FD position and shape, which could be affected by operator-dependent maneuvers, which could locally compress or expand the device. The sample size was small for both the "training" set used to determine the predictive thresholds of hemodynamic variables, and the "testing" set used to compare the prospective predictions with actual outcomes. Only the PED device was used in this study; thus, the results are exclusively valid for this device. Only 1 device was implanted in each subject; the effects of multiple devices was not studied. Further studies with larger samples and human aneurysms should be performed to confirm our results and further characterize the predictive thresholds of hemodynamic variables (and perhaps develop multivariate models) and the predictive power of CFD models.

CONCLUSIONS

Subject-specific CFD models of the hemodynamic conditions created immediately after implantation of FD devices in experimental cerebral aneurysms created in rabbits are capable of prospectively predicting (with a reasonable accuracy) which aneurysms will quickly occlude and which ones will remain incompletely occluded for a longer time.

Disclosures: Sara Hadad—*RELATED*: *Grant*: National Institutes of Health, *Comments:* research grant.* Fernando Mut—*RELATED*: *Grant*: National Institutes of Health.* Ram Kadirvel—*RELATED*: *Grant*: National Institutes of Health, *Comments*: grant No. NS076491.* David Kallmes—*UNRELATED*: *Grants/Grants Pending*: Medtronic, MicroVention, NeuroSigma, NeuroGami Medical, *Comments*: preclinical research*; *Stock/Stock Options*: Superior Medical Experts, *Comments*: founder/owner. Juan R. Cebral—*RELATED*: *Grant*: National Institutes of Health, *Comments*: research grant*; *UNRELATED*: *Grants/Grants Pending*: National Institutes of Health, Philips Healthcare, *Comments*: research grants*; *Other*: Travis C. Valentine Memorial Fund. *Money paid to the institution.

REFERENCES

1. Pierot L, Biondi A. **Endovascular techniques for the management of wide-neck intracranial bifurcation aneurysms: a critical review of the literature.** *J Neuroradiol* 2016;43:167–75 CrossRef Medline
2. Lylyk P, Miranda C, Ceratto R, et al. **Curative endovascular reconstruction of cerebral aneurysms with the Pipeline Embolization Device: the Buenos Aires experience.** *Neurosurgery* 2009;64:632–42 CrossRef Medline

3. Brinjikji W, Murad MH, Lanzino G, et al. **Endovascular treatment of intracranial aneurysms with flow diverters: a meta-analysis.** *Stroke* 2013;44:442–47 CrossRef Medline
4. Kallmes DF, Brinjikji W, Cekirge S, et al. **Safety and efficacy of the Pipeline Embolization Device for treatment of intracranial aneurysms: a pooled analysis of 3 large studies.** *J Neurosurg* 2017;127:775–80 CrossRef Medline
5. Kulcsar Z, Augsburger L, Reymond P, et al. **Flow diversion treatment: intra-aneurismal blood flow velocity and WSS reduction are parameters to predict aneurysm thrombosis.** *Acta Neurochir (Wien)* 2012;154:1827–34 CrossRef Medline
6. Cebral JR, Mut F, Raschi M, et al. **Analysis of hemodynamics and aneurysm occlusion after flow-diverting treatment in rabbit models.** *AJNR Am J Neuroradiol* 2014;35:1567–73 CrossRef Medline
7. Paliwal N, Damiano RJ, Davies JM, et al. **Association between hemodynamic modifications and clinical outcome of intracranial aneurysms treated using flow diverters.** *Proc SPIE Int Soc Opt Eng* 2017;10135:101352F CrossRef
8. Ma D, Dargush GF, Natarajan SK, et al. **Computer modeling of deployment and mechanical expansion of neurovascular flow diverter in patient-specific intracranial aneurysms.** *J Biomech* 2012;45:2256–63 CrossRef Medline
9. Chong W, Zhang Y, Qian Y, et al. **Computational hemodynamics analysis of intracranial aneurysms treated with flow diverters: correlation with clinical outcomes.** *AJNR Am J Neuroradiol* 2014;35:136–42 CrossRef Medline
10. Huang Q, Xu J, Cheng J, et al. **Hemodynamic changes by flow diverters in rabbit aneurysm models: a computational fluid dynamic study based on micro-computed tomography reconstruction.** *Stroke* 2013;44:1936–41 CrossRef Medline
11. Pereira VM, Bonnefous O, Ouared R, et al. **A DSA-based method using contrast-motion estimation for the assessment of the intra-aneurysmal flow changes induced by flow-diverter stents.** *AJNR Am J Neuroradiol* 2013;34:808–15 CrossRef Medline
12. Chung B, Mut F, Kadirvel R, et al. **Hemodynamic analysis of fast and slow aneurysm occlusions by flow diversion in rabbits.** *J Neurointerv Surg* 2015;7:931–35 CrossRef Medline
13. Ding YH, Dai D, Schroeder D, et al. **Experimental testing of the dual-layer Woven EndoBridge device using an elastase-induced aneurysm model in rabbits.** *Interv Neuroradiol* 2016;22:299–303 CrossRef Medline
14. Cebral JR, Mut F, Raschi M, et al. **Strategy for analysis of flow diverting devices based on multi-modality image-based modeling.** *Int J Numer Method Biomed Eng* 2014;30:951–68 CrossRef Medline
15. Mut F, Löhner R, Chien A, et al. **Computational hemodynamics framework for the analysis of cerebral aneurysms.** *Int J Numer Method Biomed Eng* 2011;27:822–39 CrossRef Medline
16. Mut F, Cebral JR. **Effects of flow-diverting device oversizing on hemodynamics alteration in cerebral aneurysms.** *AJNR Am J Neuroradiol* 2012;33:2010–16 CrossRef Medline
17. Appanaboyina S, Mut F, Löhner R, et al. **Simulation of intracranial aneurysm stenting: techniques and challenges.** *Comput Methods Appl Mech Eng* 2009;198:3567–82 CrossRef
18. Cebral JR, Chung BJ, Mut F, et al. **Analysis of flow dynamics and outcomes of cerebral aneurysms treated with intrasaccular flow-diverting devices.** *AJNR Am J Neuroradiol* 2019;40:1511–16 CrossRef Medline
19. Mut F, Raschi M, Scrivano E, et al. **Association between hemodynamic conditions and occlusion times after flow diversion in cerebral aneurysms.** *J Neurointerv Surg* 2015;7:286–90 CrossRef Medline
20. Beppu M, Tsuji M, Ishida F, et al. **Computational fluid dynamics using a porous media setting predicts outcome after flow-diverter treatment.** *AJNR Am J Neuroradiol* 2020;41:2107–13 CrossRef Medline
21. Paliwal N, Jaiswal P, Tutino VM, et al. **Outcome prediction of intracranial aneurysm treatment by flow diverters using machine learning.** *Neurosurg Focus* 2018;45:E7 CrossRef Medline
22. Sindeev S, Arnold PG, Frolov S, et al. **Phase-contrast MRI versus numerical simulation to quantify hemodynamical changes in cerebral aneurysms after flow diverter treatment.** *PLoS One* 2018;13:e0190696 CrossRef Medline
23. Brinjikji W, Ding YH, Kallmes DF, et al. **From bench to bedside: utility of the rabbit elastase aneurysm model in preclinical studies of intracranial aneurysm treatment.** *J Neurointerv Surg* 2016;8:521–25 CrossRef Medline

Outcomes of Mechanical Thrombectomy in the Early (<6-hour) and Extended (≥6-hour) Time Window Based Solely on Noncontrast CT and CT Angiography: A Propensity Score–Matched Cohort Study

P. Hendrix, D. Chaudhary, V. Avula, V. Abedi, R. Zand, A. Noto, I. Melamed, O. Goren, C.M. Schirmer, and C.J. Griessenauer

ABSTRACT

BACKGROUND AND PURPOSE: Current stroke care recommendations for patient selection for mechanical thrombectomy in the extended time window demand advanced imaging to determine the stroke core volume and hypoperfusion mismatch, which may not be available at every center. We aimed to determine outcomes in patients selected for mechanical thrombectomy solely on the basis of noncontrast CT and CTA in the early (<6-hour) and extended (≥6-hour) time windows.

MATERIALS AND METHODS: Consecutive mechanical thrombectomies performed for acute large-vessel occlusion ischemic (ICA, M1, M2) stroke between February 2016 and August 2020 were retrospectively reviewed. Eligibility was based solely on demographics and noncontrast CT (ASPECTS) and CTA, due to the limited availability of perfusion imaging during the study period. Propensity score matching was performed to compare outcomes between time windows.

RESULTS: Of 417 mechanical thrombectomies performed, 337 met the inclusion criteria, resulting in 205 (60.8%) and 132 (39.2%) patients in the 0- to 6- and 6- to 24-hour time windows, respectively. The ASPECTS was higher in the early time window (9; interquartile range = 8–10) than the extended time window (9; interquartile range = 7–10; $P = .005$). Propensity score matching yielded 112 well-matched pairs. Equal rates of TICI 2b/3 revascularization and symptomatic intracranial hemorrhage were observed. A favorable functional outcome (mRS 0–2) at 90 days was numerically more frequent in the early window (45.5% versus 33.9%, $P = .091$). Mortality was numerically more frequent in the early window (25.9% versus 17.0%, $P = .096$).

CONCLUSIONS: Patients selected for mechanical thrombectomy in the extended time window solely on the basis of noncontrast CT and CTA still achieved decent rates of favorable 90-day functional outcomes, not statistically different from patients in the early time window.

ABBREVIATION: IQR = interquartile range

Randomized controlled trials demonstrated that mechanical thrombectomy for anterior circulation large-vessel occlusion strokes provides beneficial outcomes when performed within the early 6-hour time window.[1] Among these randomized controlled trials, the Solitaire with the Intention for Thrombectomy as Primary Endovascular Treatment (SWIFT PRIME) and Extending the Time for Thrombolysis in Emergency Neurological Deficits–Intra-Arterial (EXTEND-IA) trials enrolled patients on the basis of ischemic core imaging, whereas the Multicenter Randomized Clinical Trial of Endovascular Treatment for Acute Ischemic Stroke in the Netherlands (MR CLEAN) and Mechanical Thrombectomy After Intravenous Alteplase Versus Alteplase Alone After Stroke (THRACE) trials did not. The selection of patients with advanced imaging provided a more favorable absolute treatment benefit.[2-6] Nevertheless, due to the safety and efficacy demonstrated in MR CLEAN and THRACE, current guidelines do not recommend advanced imaging as long as the patient presents within the 6-hour time window with a CT-ASPECTS of ≥6 (class I).[7] The Endovascular Therapy Following Imaging Evaluation for Ischemic

Received May 22, 2021; accepted after revision June 29.

From the Department of Neurosurgery (P.H., I.M., O.G., C.M.S., C.J.G.), Department of Neurology (D.C., R.Z., A.N.), Geisinger Neuroscience Institute, and Department of Molecular and Functional Genomics (V. Avula, V. Abedi), Geisinger Health System, Danville, Pennsylvania; Department of Neurosurgery (P.H.), Saarland University Hospital, Homburg, Germany; Biocomplexity Institute (V. Abedi), Virginia Polytechnic Institute and State University, Blacksburg, Virginia; and Research Institute of Neurointervention (C.M.S., C.J.G.), and Department of Neurosurgery (C.J.G.), Christian Doppler University Hospital, Paracelsus Medical University, Salzburg, Austria.

P. Hendrix received salary support from Geisinger and Medtronic.

Previously presented as an abstract at: Annual Meeting of the Society of Neurointerventional Surgery, July 26–30, 2021; Colorado Springs, Colorado.

Please address correspondence to Christoph J. Griessenauer, MD, Department of Neurosurgery, Geisinger Health System, 100 N Academy Ave, Danville, PA 17822; e-mail: christoph.griessenauer@gmail.com

http://dx.doi.org/10.3174/ajnr.A7271

Stroke 3 (DEFUSE-3)[8] trial and Diffusion Weighted Imaging (DWI) or Computerized Tomography Perfusion (CTP) Assessment With Clinical Mismatch in the Triage of Wake Up and Late Presenting Strokes Undergoing Neurointervention with Trevo (DAWN)[9] trial generated class I evidence for mechanical thrombectomy in the extended 6- to 16-hour time window, while DAWN also expanded to the 16- to 24-hour time window (class IIa). Most important, enrollment in DEFUSE-3 and DAWN was also based on core imaging.[8,9] Therefore, to date, patient selection in the extended time window (6–24 hours) demands advanced imaging to determine the stroke core volume and hypoperfusion mismatch (CT perfusion or diffusion-weighted brain MR imaging).

Recently, Nogueira et al[10] compared outcomes between patients selected with noncontrast CT and CTA and patients who underwent CT perfusion in the early and extended time windows. They found that the CT perfusion acquisition was associated with better outcomes neither in the early nor extended time window. There is a lack of real-world data on patients selected solely on the basis of noncontrast CT and CTA for the extended time window. Here, we present mechanical thrombectomy outcomes in the early and extended time windows in patients evaluated solely on the basis of noncontrast CT and CTA.

MATERIALS AND METHODS

Consecutive mechanical thrombectomies performed for acute large-vessel occlusion ischemic stroke between February 2016 and August 2020 at comprehensive stroke centers Geisinger Medical Center and Geisinger Wyoming Valley Medical Center were retrospectively reviewed. Local institutional review board approval was obtained before the study initiation.

Patient Selection, Treatment, and Outcome Assessment

Patients were treated according to current American Heart Association/American Stroke Association guidelines except for the limited availability of perfusion imaging during the study period.[7,11] Each patient underwent a noncontrast CT scan followed by determination of the ASPECTS. Eligibility for mechanical thrombectomy was based on patient demographics, baseline NIHSS scores, time since symptom onset, and noncontrast CT, including CT-ASPECTS. Scores were obtained by the on-call stroke neurologist and treating neuroendovascular surgeon. None of the patients included underwent advanced imaging beyond noncontrast CT or CTA. Patients transferred from outside hospitals or affiliated primary stroke centers did not undergo additional noncontrast CT or CTA on presentation to the comprehensive stroke center, unless the neurologic status significantly declined during transport or outside imaging was insufficient to facilitate decision-making. Transferred patients were promptly directed to the angiography suite on the basis of imaging provided through the telestroke system. Eligibility for treatment was ultimately determined by the treating neuroendovascular surgeon and adjudicated by the stroke center quality framework. Successful revascularization (TICI 2b/3) was evaluated by the neuroendovascular surgeon. Symptomatic intracranial hemorrhage was assessed according to the Heidelberg Bleeding Classification.[12] Functional outcome at 90 days was determined using the mRS, with mRS 0–2 indicating a favorable functional outcome and mRS 6 indicating death.

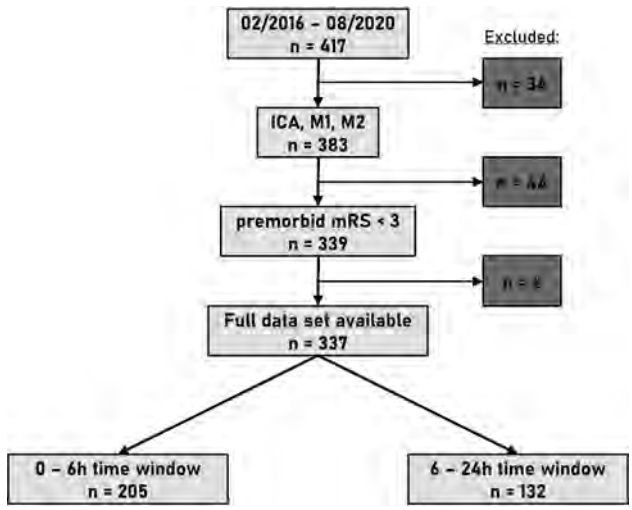

FIG 1. Flow sheet patient selection.

Statistical Analysis

Categoric variables are given as frequency and percentage. Continuous variables are stated as the median and interquartile range (IQR). Baseline characteristics were compared by means of the χ^2, Fisher exact, and Mann-Whitney *U* tests, as appropriate. Propensity score matching of 0- to 6- versus 6- to 24-hour time windows was performed using age, sex, baseline NIHSS, site of occlusion, and CT-ASPECTS as parameters. Matching was performed using the nearest neighbor method, without replacement and a caliper of 0.1. Subsequent outcome analyses were performed comparing pairs using the McNemar and Wilcoxon signed-rank test. *P* values of $<.05$ were considered statistically significant. SPSS, Version 25 (IBM) and R statistical and computing software, Version 4.03 (http://www.r-project.org/) were used to perform statistical analysis.

RESULTS

During the study period, February 2016 to August 2020, two hundred thirty-seven/417 (56.8%) mechanical thrombectomies were performed in transferred patients. In the early time window, transferred patients constituted 52.0% of all cases, whereas transferred patients even constituted 63.9% of all cases in the extended time window, thereby demonstrating the challenges of timely stroke management in a health care system that serves a large rural area. Of 417 mechanical thrombectomies performed during the study period, 383 had ICA or MCA (M1 or M2) segment large-vessel occlusions. Forty-four patients with premorbid mRS >2 and another 2 patients with missing data were excluded. The final dataset comprised 337 cases. Two hundred five (60.8%) were treated within the early 0- to 6-hour time window, and 132 (39.2%), in the extended 6- to 24-hour time window (Fig 1).

Prematch Comparison of Early-versus-Extended Time Windows

Baseline demographics between patients who underwent mechanical thrombectomy in the early ($n=205$) and extended

Table 1: Baseline characteristics

	Overall Cohort		
	0–6 Hours ($n = 205$)	6–24 Hours ($n = 132$)	*P* Value
Variable			
Age (median) (IQR) (yr)	72 (61–80)	75 (60–83)	.418
Female	104 (50.7%)	71 (53.4%)	.584
Baseline NIHSS (median) (IQR)	18 (14–24)	17 (11–22)	.045
Premorbid mRS (median) (IQR)	0 (0–1)	0 (0–1)	.600
Risk factors			
Arterial hypertension	157 (76.6%)	106 (80.3%)	.421
Type 2 diabetes	60 (29.3%)	38 (28.8%)	.924
Dyslipidemia	142 (69.3%)	95 (72.0%)	.596
Coronary artery disease	54 (26.3%)	34 (25.8%)	.905
Atrial fibrillation	90 (43.9%)	47 (35.6%)	.130
Chronic kidney disease	47 (22.9%)	37 (28.0%)	.290
Ischemic stroke	30 (14.6%)	15 (11.4%)	.389
Smoking (ever)	115 (56.1%)	70 (53.0%)	.581
Site of occlusion			
ICA	41 (20.0%)	34 (25.8%)	.427
M1	127 (62.0%)	78 (59.1%)	
M2	37 (18.0%)	20 (15.2%)	
CT-ASPECTS (median) (IQR)	9 (8–10)	9 (7–10)	.005
Transfer to CSC	104 (50.7%)	82 (62.1%)	.040
IV-tPA	117 (57.1%)	18 (13.6%)	<.001
Time to intervention (median) (IQR)	204 (158–263)	684 (476–919)	<.001
Primary aspiration	47 (22.9%)	36 (27.3%)	.366
TICI 2b/3 revascularization	193 (94.1%)	120 (90.9%)	.259
sICH	13 (6.3%)	12 (9.1%)	.347
Functional outcome			
mRS 0–2	90 (43.9%)	43 (32.6%)	.038
mRS 6	58 (28.3%)	25 (18.9%)	.052

Note:—CSC indicates comprehensive stroke center; sICH, symptomatic intracranial hemorrhage.

($n = 132$) time windows in the pre-propensity score–matched comparison were similar except for a higher baseline NIHSS score in the 0- to 6-hour time window ($P = .045$) (Table 1). CT-ASPECTS was lower in the 6- to 24-hour time window group ($P = .005$) (Fig 2). Rates of successful revascularization and symptomatic intracranial hemorrhage were similar. A favorable functional outcome was more frequently observed in the early time window ($P = .038$) (Fig 2). A trend toward more deaths was found in the group with the early time window ($P = .052$).

Propensity Matched Comparison of Early-versus-Extended Time Windows

Propensity score matching yielded 112 matched pairs. Standardized mean differences were <0.1. Additional balance measures are provided in Figs 3 and 4. Comparison of the 0- to 6-hour versus 6- to 24-hour groups demonstrated equal distribution of age, sex, baseline NIHSS score, occlusion site, and CT-ASPECTS (Table 2). Outcome analysis showed equal rates of TICI 2b/3 revascularization and symptomatic intracranial hemorrhage. A favorable functional outcome was numerically more frequent in the 0- to 6-hour group than the 6- to 24-hour group (45.5% versus 33.9%), but it was not statistically significant ($P = .091$). Likewise, death rates were numerically larger in the 0- to 6-hour group than in the 6- to 24-hour group (25.9% versus 17.0%) though they were not statistically significant ($P = .096$).

DISCUSSION

This retrospective cohort provides additional evidence from a real-world setting that clinical evaluation and noncontrast CT-ASPECTS in the extended time window are sufficient to achieve favorable outcome rates. Safety end points for symptomatic intracranial hemorrhage and death at 90 days were similar for both time windows. Likewise, successful revascularization was achieved in >90% regardless of the time windows. A favorable functional outcome was more frequently achieved in the early time window. This observation remained evident even after matching CT-ASPECTS variables, reflecting the predominant role of time in revascularization. However, still, 1 of 3 patients in the extended time window achieved a favorable functional outcome. These observations align with Santos et al,[13] who also analyzed a cohort selected solely by noncontrast CT and CTA. They compared 186 patients from the 0- to 6-hour window with 63 patients in the time window beyond 6 hours. While applying strict inclusion criteria (NIHSS > 11, CT-ASPECTS > 6, and premorbid mRS < 2 for the extended time window), the authors observed a favorable functional outcome in 57% and 65.1% in the 0- to 6-hour and beyond the 6-hour time windows, respectively. Mortality and symptomatic intracranial hemorrhage rates were equal across time windows.[13]

Advanced imaging such as CT perfusion or diffusion-weighted MR imaging allows the preselection of those patients with small cores with a higher likelihood of a beneficial outcome from mechanical thrombectomy. This effect becomes particularly apparent in the extended time window. Patients beyond 6 hours of symptom onset have comparatively small cores, but without intervention, they are not likely to withstand hypoperfusion resulting in cerebral infarction and neurologic decline. Albers[14] appropriately illustrated the role of timing and imaging on patient selection together with inherent absolute treatment effects when discussing the late window paradox. Albers postulated that patients who withstand the first 6 hours without significant infarctions (core volumes) have likely a favorable status due to good collateral supply. On the other hand, patients with poor collaterals are very likely to have significant infarctions even in the early time window. Early deteriorators are patients who do not benefit from mechanical thrombectomy despite timely treatment. Patients with poor collateral status and early infarctions are very unlikely to be candidates for mechanical thrombectomy in the extended time window. In contrast, patient selection in the early time window is likely to be more liberal. Therefore,

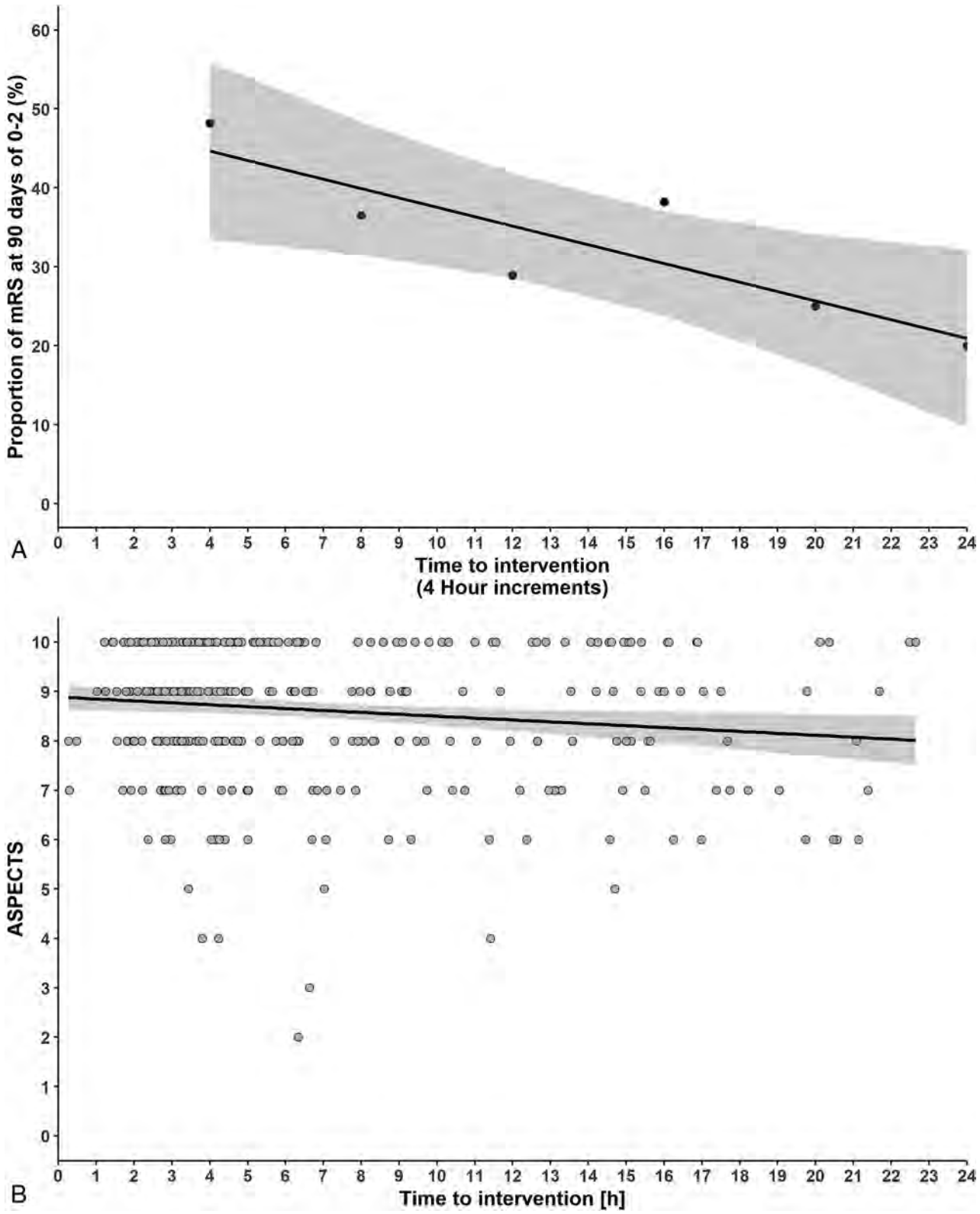

FIG 2. *A*, Mean proportion of favorable functional outcomes (mRS 0–2) per 4-hour interval of time since symptom onset to intervention, including a trendline. The trendline declines with time. *B*, CT-ASPECTS of all cases plotted across time from symptom onset to intervention. The trendline remains almost stable with time, representing patient selection based on favorable CT-ASPECTS.

patients selected in the extended time window have an a priori more favorable basis, translating into a relatively benign functional outcome of this particular subgroup.[14]

CT perfusion imaging performed within 6 hours of symptom onset may overestimate the infarct core.[15] Thus, CT perfusion imaging in the early time window requires careful interpretation.

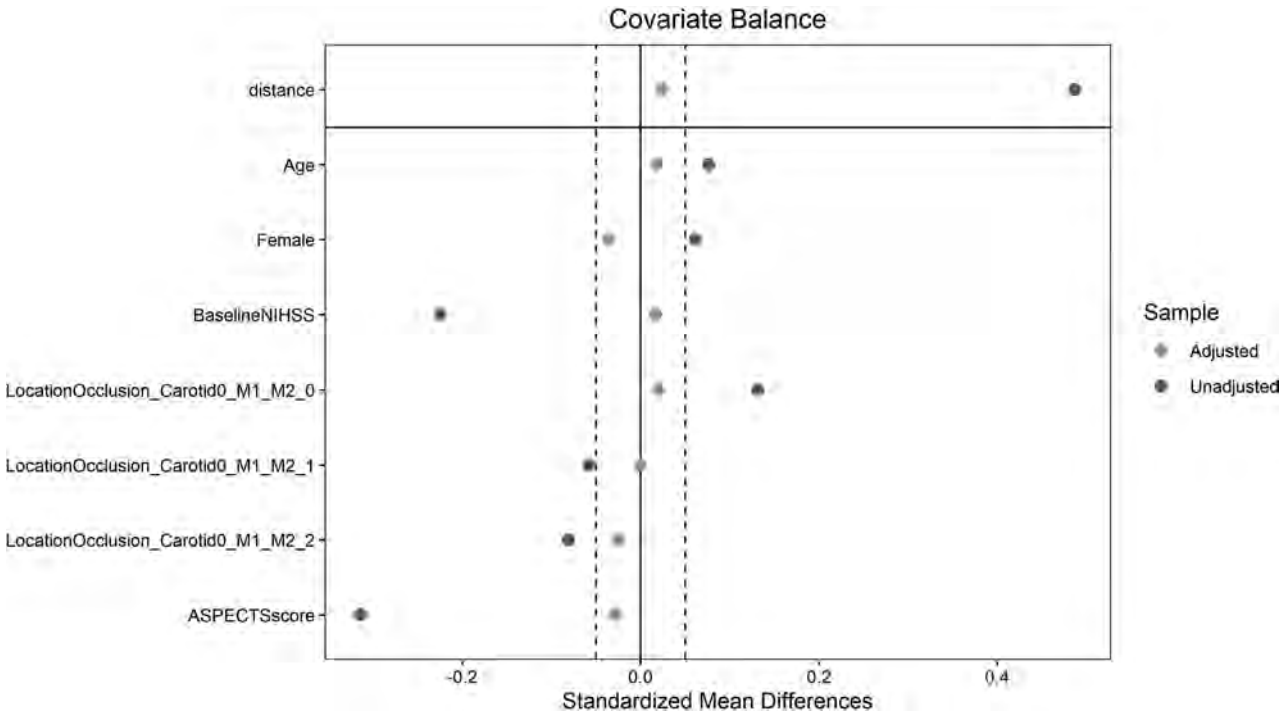

FIG 3. Standardized mean differences for covariates integrated into propensity score matching. Prematching (unadjusted) standardized mean differences and postmatching (adjusted) standardized mean differences are shown. Standardized mean difference < 0.1 indicates well-matched samples.

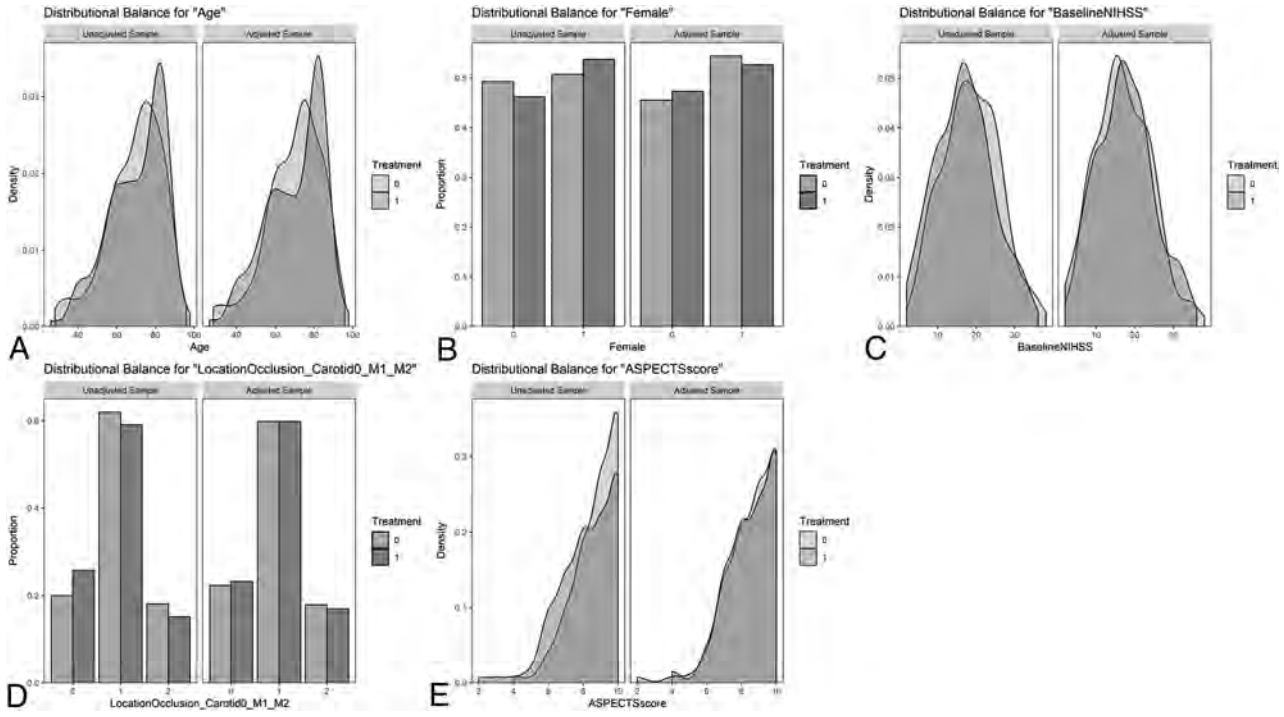

FIG 4. Unadjusted (unmatched) and adjusted (matched) group comparison for the early 0- to 6-hour time window (indicated by 0) and the extended 6- to 24-hour time window (indicated by 1). Density overlay for age, baseline NIHSS, and ASPECTS and equality of height of proportions for female sex and location demonstrate good comparability after propensity score matching.

For the extended time window, to date, only DEFUSE-3 and DAWN provide class I recommendations. In both trials, patients underwent advanced imaging to screen for core infarct volumes, and patient selection was based on predefined cutoffs.[8,9] Despite the awareness of stroke care inequities between urban and rural areas,[16] the current literature lacks a discussion on strategies for patients

Table 2: Propensity score–matched cohort

	Overall Cohort		
	0–6 Hours (n = 112)	6–24 Hours (n = 112)	P Value
Variable			
Age (median) (IQR) (yr)	73 (62–81)	75 (59–83)	.759
Female	61 (54.5%)	59 (52.7%)	.773
Baseline NIHSS (median) (IQR)	17 (12–22)	17 (12–22)	.985
Site of occlusion			
ICA	25 (22.3%)	26 (23.2%)	.991
M1	67 (59.8%)	67 (59.8%)	
M2	20 (17.9%)	19 (17.0%)	
CT-ASPECTS (median) (IQR)	9 (8–10)	9 (8–10)	.720
Time to intervention (median) (IQR) (hr)	210 (157–266)	691 (497–907)	<.001
TICI 2b/3 revascularization	106 (94.6%)	104 (92.9%)	.593
sICH	6 (5.4%)	7 (6.2%)	.782
Functional outcome			
mRS 0–2	51 (45.5%)	38 (33.9%)	.091
mRS 6	29 (25.9%)	19 (17.0%)	.096

eligible for mechanical thrombectomy requiring long-distance transfers. During the study period, February 2016 to August 2020, two hundred thirty-seven/417 (56.8%) mechanical thrombectomies were performed in transferred patients. Among the early time window, transferred patients constituted 52.0% of all cases, whereas transferred patients even constituted 63.9% of all cases among the extended time window. In our health care system, transfer times regularly exceed 1 hour due to the long distance despite an internal flight air ambulance system. To date, it is unknown whether transferred patients should undergo repeat imaging to update CT-ASPECTS and rule out hemorrhage or even undergo advanced imaging to estimate the infarct core and guide patient selection.

Furthermore, only a subset of affiliated rural hospitals are certified primary stroke centers capable of providing timely advanced imaging. Contrasting the ideal stroke care system incorporating timely transportation and timely availability of advanced imaging with a stroke care system, in large part, also covering rural areas highlights 2 aspects that require reiterated adjudication by stroke quality frameworks. First, suspending advanced imaging should guide patient selection in both the early and extended time windows. Second, delaying mechanical thrombectomy by repeat imaging unless there is severe neurologic decline may result in fatality due to herniation or hemorrhage.

Recently, Nogueira et al[10] found CT perfusion–based patient selection not superior to standardized noncontrast CT and CTA in terms of functional-outcome prediction. These observations, together with real-world data such as presented in the current study, challenge the demand for advanced imaging to guide patient selection and justify patient selection based purely on favorable CT-ASPECTS, even in the extended time window. The selection of patients with favorable CT-ASPECTS is shown in Fig 2. Notably, the selection of patients with large-vessel occlusion for mechanical thrombectomy using advanced imaging may increase the relative proportion of patients achieving functional independence but might compromise the absolute number of patients potentially benefitting from this treatment by excluding patients who might have benefitted.

Lowering the threshold for performing mechanical thrombectomy has also been debated for patients presenting with poor CT-ASPECTS such as CT-ASPECTS < 6. In this context, older age and large-core infarcts do not uniformly present a contraindication for mechanical thrombectomy. Instead, a subset of patients with large-core infarcts undergoing mechanical thrombectomy still achieve a favorable functional outcome.[17–21] Whether sparing of either the deep or superficial MCA territories provides a better outcome is still controversial.[22,23] Partial reperfusion of distinct areas such as the motor-eloquent cortical area appears to outweigh the degree of partial reperfusion.[24] It remains uncertain whether advanced imaging would identify these patients better or exclude patients who could benefit.

Mechanical thrombectomy beyond the 6-hour time window with patient selection based on advanced imaging appears cost-effective.[25,26] Providing timely interpretation of perfusion-based advanced imaging modalities has been challenging for every stroke center. It has led to the development of outsourced solutions and automated interpretation platforms. However, standardized cloud-based services to assess core and penumbra on CT or MR perfusion are associated with a substantial financial burden. This study shows that selection of patients with large-vessel occlusion strokes for thrombectomy with favorable CT-ASPECTS even in the extended time window is feasible, without using advanced imaging modalities.

In summary, absolute treatment effects become lower with less stringent preselection criteria. However, withholding mechanical thrombectomy due to lack of advanced imaging does not appear justifiable for those patients with favorable CT-ASPECTS irrespective of the time window. Additional investigation is required to determine the value of advanced imaging in patients in extended time windows and those with large-core infarcts on presentation.

Limitations

Its sample size and retrospective design limit this study. There is no randomization or comparative control group for the time-window groups. The study does not provide the number of patients that ultimately did not undergo mechanical thrombectomy, which, specifically for the late window, needs to be considered. Here, patient selection is based on the decision of the stroke care team. Finally, the study does not provide specific demographic, neurologic, or radiologic criteria (such as collateral scores), finally leading to a decision for or against mechanical thrombectomy in the late time window.

CONCLUSIONS

Patients selected for mechanical thrombectomy in the extended time window solely on the basis of noncontrast CT and CTA still

achieved decent rates of favorable 90-day functional outcomes not statistically different from those in patients in the early time window. However, additional investigation is required to determine the value of advanced imaging in the extended time window, specifically if advanced imaging is associated with further delay when serving patients from rural areas with long-distance transfers.

Disclosure forms provided by the authors are available with the full text and PDF of this article at www.ajnr.org.

REFERENCES

1. Goyal M, Menon BK, van Zwam WH, et al. **Endovascular thrombectomy after large-vessel ischaemic stroke: a meta-analysis of individual patient data from five randomised trials.** *Lancet* 2016;387:1723–31 CrossRef Medline
2. Saver JL, Goyal M, Bonafe A, et al. **Stent-retriever thrombectomy after intravenous t-PA vs. t-PA alone in stroke.** *N Engl J Med* 2015;372:2285–95 CrossRef Medline
3. Campbell BC, Mitchell PJ, Kleinig TJ, et al. **Endovascular therapy for ischemic stroke with perfusion-imaging selection.** *N Engl J Med* 2015;372:1009–18 CrossRef Medline
4. Berkhemer OA, Fransen PSS, Beumer D, et al; MR CLEAN Investigators. **A randomized trial of intraarterial treatment for acute ischemic stroke.** *N Engl J Med* 2015;372:11–20 CrossRef Medline
5. Bracard S, Ducrocq X, Mas JL, et al; THRACE Investigators. **Mechanical thrombectomy after intravenous alteplase versus alteplase alone after stroke (THRACE): a randomised controlled trial.** *Lancet Neurol* 2016;15:1138–47 CrossRef Medline
6. Goyal M, Menon BK, van Zwam WH, et al; HERMES Collaborators. **Endovascular thrombectomy after large-vessel ischaemic stroke: a meta-analysis of individual patient data from five randomised trials.** *Lancet* 2016;387:1723–31 CrossRef Medline
7. Powers WJ, Rabinstein AA, Ackerson T, et al. **Guidelines for the Early Management of Patients with Acute Ischemic Stroke: 2019 Update to the 2018 Guidelines for the Early Management of Acute Ischemic Stroke—a Guideline for Healthcare Professionals From the American Heart Association/American Stroke Association.** *Stroke* 2019;50:e344–418 CrossRef Medline
8. Albers GW, Marks MP, Kemp S, et al. **Thrombectomy for stroke at 6 to 16 hours with selection by perfusion imaging.** *N Engl J Med* 2018;378:708–18 CrossRef Medline
9. Nogueira RG, Jadhav AP, Haussen DC, et al. **Thrombectomy 6 to 24 hours after stroke with a mismatch between deficit and infarct.** *N Engl J Med* 2018;378:11–21 CrossRef Medline
10. Nogueira RG, Haussen DC, Liebeskind D, et al; Trevo Registry and DAWN Trial Investigators. **Stroke imaging selection modality and endovascular therapy outcomes in the early and extended time windows.** *Stroke* 2021;52:491–97 CrossRef Medline
11. Powers WJ, Derdeyn CP, Biller J, et al; American Heart Association Stroke Council. **2015 American Heart Association/American Stroke Association Focused Update of the 2013 Guidelines for the Early Management of Patients with Acute Ischemic Stroke Regarding Endovascular Treatment: a Guideline for Healthcare Professionals From the American Heart Association/American Stroke Association.** *Stroke* 2015;46:3020–35 CrossRef Medline
12. von Kummer R, Broderick JP, Campbell BC, et al. **The Heidelberg Bleeding Classification: classification of bleeding events after ischemic stroke and reperfusion therapy.** *Stroke* 2015;46:2981–86 CrossRef Medline
13. Santos T, Carvalho A, Cunha AA, et al. **NCCT and CTA-based imaging protocol for endovascular treatment selection in late presenting or wake-up strokes.** *J Neurointerv Surg* 2019;11:200–03 CrossRef Medline
14. Albers GW. **Late window paradox.** *Stroke* 2018;49:768–71 CrossRef Medline
15. Boned S, Padroni M, Rubiera M, et al. **Admission CT perfusion may overestimate initial infarct core: the ghost infarct core concept.** *J Neurointerv Surg* 2017;9:66–69 CrossRef Medline
16. Hammond G, Luke AA, Elson L, et al. **Urban-rural inequities in acute stroke care and in-hospital mortality.** *Stroke* 2020;51:2131–38 CrossRef Medline
17. Rebello LC, Bouslama M, Haussen DC, et al. **Endovascular treatment for patients with acute stroke who have a large ischemic core and large mismatch imaging profile.** *JAMA Neurol* 2017;74:34–40 CrossRef Medline
18. Deb-Chatterji M, Pinnschmidt H, Flottmann F, et al; GSR-ET Investigators. **Predictors of independent outcome of thrombectomy in stroke patients with large baseline infarcts in clinical practice: a multicenter analysis.** *J Neurointerv Surg* 2020;12:1064–68 CrossRef Medline
19. Kakita H, Yoshimura S, Uchida K, et al; RESCUE-Japan Registry 2 Investigators. **Impact of endovascular therapy in patients with large ischemic core: subanalysis of recovery by endovascular salvage for Cerebral Ultra-Acute Embolism Japan Registry 2.** *Stroke* 2019;50:901–08 CrossRef Medline
20. Ospel J, Kappelhof M, Groot AE, et al. **Combined effect of age and baseline Alberta Stroke Program Early Computed Tomography Score on post-thrombectomy clinical outcomes in the MR CLEAN Registry.** *Stroke* 2020;51:3742–45 CrossRef Medline
21. Kerleroux B, Janot K, Dargazanli C, et al; JENI Research Collaborative. **Perfusion imaging to select patients with large ischemic core for mechanical thrombectomy.** *J Stroke* 2020;22:225–33 CrossRef Medline
22. Gautheron V, Xie Y, Tisserand M, et al. **Outcome after reperfusion therapies in patients with large baseline diffusion-weighted imaging stroke lesions: a THRACE trial (Mechanical Thrombectomy After Intravenous Alteplase Versus Alteplase Alone After Stroke) subgroup analysis.** *Stroke* 2018;49:750–53 CrossRef Medline
23. Xing PF, Zhang YW, Zhang L, et al. **Higher baseline cortical score predicts good outcome in patients with low Alberta Stroke Program Early Computed Tomography Score treated with endovascular treatment.** *Neurosurgery* 2021;88:612–18 CrossRef Medline
24. Raychev R, Saber H, Saver JL, et al. **Impact of eloquent motor cortex-tissue reperfusion beyond the traditional thrombolysis in cerebral infarction (TICI) scoring after thrombectomy.** *J Neurointerv Surg* 2020 Dec 18. [Epub ahead of print] CrossRef Medline
25. Peultier A-C, Pandya A, Sharma R, et al. **Cost-effectiveness of mechanical thrombectomy more than 6 hours after symptom onset among patients with acute ischemic stroke.** *JAMA Netw Open* 2020;3:e2012476 CrossRef Medline
26. Peultier A-C, Redekop WK, Allen M, et al. **Exploring the cost-effectiveness of mechanical thrombectomy beyond 6 hours following advanced imaging in the United Kingdom.** *Stroke* 2019;50:3220–27 CrossRef Medline

Local Intra-arterial Thrombolysis during Mechanical Thrombectomy for Refractory Large-Vessel Occlusion: Adjunctive Chemical Enhancer of Thrombectomy

S.H. Baik, C. Jung, J.Y. Kim, D.-W. Shin, B.J. Kim, J. Kang, H.-J. Bae, and J.H. Kim

ABSTRACT

BACKGROUND AND PURPOSE: Data on adjunctive intra-arterial thrombolysis during mechanical thrombectomy for refractory thrombus are sparse. The aim of this study was to evaluate the efficacy and safety of local intra-arterial urokinase as an adjunct to mechanical thrombectomy for refractory large-vessel occlusion.

MATERIALS AND METHODS: We retrospectively evaluated patients with acute ischemic stroke who underwent mechanical thrombectomy for anterior circulation large-vessel occlusion between January 2016 and December 2019. Patients were divided into 2 groups based on the use of intra-arterial urokinase as an adjunctive therapy during mechanical thrombectomy for refractory thrombus: the urokinase and nonurokinase groups. Herein, refractory thrombus was defined as the target occlusion with minimal reperfusion (TICI 0 or 1) despite >3 attempts with conventional mechanical thrombectomy. The baseline characteristics, procedural outcomes, and clinical outcome were compared between the 2 groups.

RESULTS: One hundred fourteen cases of refractory thrombus were identified. A total of 45 and 69 patients were in the urokinase and the nonurokinase groups, respectively. The urokinase group compared with the nonurokinase group showed a higher rate of successful reperfusion (82.2% versus 63.8%, $P = .034$), with lower procedural times (54 versus 69 minutes, $P = .137$). The rates of good clinical outcome, distal embolism, and symptomatic intracranial hemorrhage were similar between the 2 groups. The use of intra-arterial urokinase (OR = 3.682; 95% CI, 1.156–11.730; $P = .027$) was an independent predictor of successful reperfusion.

CONCLUSIONS: The use of local intra-arterial urokinase as an adjunct to mechanical thrombectomy may be an effective and safe method that provides better recanalization than the conventional mechanical thrombectomy for refractory thrombus in patients with embolic large-vessel occlusion.

ABBREVIATIONS: CA = contact aspiration; IA = intra-arterial; ICH = intracerebral hemorrhage; IQR = interquartile range; LVO = large-vessel occlusion; MT = mechanical thrombectomy; mTICI = modified TICI; SR = stent retriever; sICH = symptomatic ICH; UK = urokinase

Successful reperfusion is one of the most powerful factors for determining good clinical outcome in patients undergoing mechanical thrombectomy (MT) to treat acute ischemic stroke due to large-vessel occlusion (LVO).[1,2] Therefore, many studies have focused on improving the efficacy of MT.[3]

Although satisfactory recanalization rates can be obtained via standard MT, about 10%–35% of patients fail to achieve sufficient recanalization.[4,5] In these refractory cases, various rescue treatments such as local intra-arterial fibrinolysis, suction aspiration, mechanical thrombus disruption, balloon angioplasty, and stent placement have been proposed.[6-8] However, the rates of effective recanalization following these rescue treatment methods remain low.

Intra-arterial (IA) thrombolysis has been studied mainly as a primary therapy in previous randomized clinical trials before the era of newer-generation MT devices. Recent observational studies on the concomitant use of IA tissue-type tPA or urokinase (UK) during MT have demonstrated promising results with improved reperfusion rates, shortened procedural times, and acceptable safety profiles.[9-14] However, to date, data are limited on the use of local IA thrombolysis as an adjunct to MT in response to multiple failed attempts of conventional thrombectomy as a treatment for refractory thrombus. The impact of local IA thrombolysis as an adjunctive therapy to MT for refractory thrombus in terms of recanalization and hemorrhagic complications remains largely unknown.

Received April 15, 2021; accepted after revision June 11.

From the Departments of Radiology (S.H.B., C.J., D.-W.S., J.H.K.,), and Neurology (J.Y.K., B.J.K., J.K., H.-J.B.), Seoul National University Bundang Hospital, Seongnam, Korea.

This study was supported by a grant (No.14-2020-033) from the Seoul National University Bundang Hospital Research Fund.

Please address correspondence to Cheolkyu Jung, MD, PhD, Department of Radiology, Seoul National University Bundang Hospital, 82, Gumi-ro 173beon-gil, Bundang-gu, Seongnam, 13620, Korea; e-mail: jck0097@gmail.com

Indicates article with online supplemental data.

http://dx.doi.org/10.3174/ajnr.A7264

We hypothesized that the use of local IA UK as an adjunct to MT may improve the recanalization rate in refractory thrombus. The aim of this study was to evaluate the efficacy and safety of using local IA UK as an adjunctive therapy to MT for treating refractory thrombus in patients with LVO with failed conventional MT.

MATERIALS AND METHODS

Patients

This study was approved by the local institutional review board of Seoul National University Bundang Hospital (No. B-2102–667–112); the requirement of written informed consent was waived due to the retrospective nature of this study.

A retrospective analysis was performed in all consecutive patients with acute ischemic stroke who underwent endovascular treatment between January 2016 and December 2019 at our center. The inclusion criteria for the study were as follows: 1) time from symptom onset to groin puncture ≤24 hours, 2) occlusion of the intracranial segment of the ICA or MCA (M1 or M2 segment) visible on CT or MR angiography, 3) baseline NIHSS score of ≥6 points, 4) stent retriever (SR) or contact aspiration (CA) thrombectomy as the primary treatment, and 5) refractory thrombus, defined as the target occlusion with minimal reperfusion (TICI 0 or 1) despite >3 attempts with conventional MT. The exclusion criteria of this study were as follows: 1) posterior circulation occlusion, 2) large-artery atherosclerosis as the cause of stroke, 3) other etiologies of stroke such as dissection or vasculitis, 4) tandem or multiple occlusions, and 5) IA UK as a rescue therapy (UK alone without additional MT) or treatment for distal embolism.

Generally, local IA UK is administered if standard thrombectomy yields no response (modified TICI [mTICI] scale 0 or 1) for ≥3 attempts. Hence, refractory thrombus is defined on the basis of the number of passes. In particular, for the purpose of our analysis, refractory thrombus did not include atherosclerosis-related occlusion lesions because these generally require multiple attempts of MT due to elastic recoil and thrombus buildup.

Endovascular Treatment

All included patients underwent MT ≥3 times and were treated with one of the following techniques: SR, CA alone, or CA combined with SR. Patients were divided into 2 groups based on the use of IA UK: 1) the UK group, which included patients who received adjunctive IA UK during MT of the primary occlusion, and 2) the non-UK SR group, which included those who did not receive IA UK. In the UK group, IA UK was adjunctively used only for refractory thrombus that did not respond to a conventional MT using CA or SR or combined techniques (mTICI 0 or 1), and additional MT was performed subsequently after injection of UK.

All procedures were performed by 3 experienced neurointerventionalists (C.J., S.H.B., and J.Y.K.) in a single tertiary care center. The endovascular procedure was typically performed via a femoral approach through an 8F or 9F sheath with the patient under local anesthesia or conscious sedation. An 8F or 9F balloon guide catheter was routinely used whenever possible. The specific thrombectomy devices used and intervention strategies were at the discretion of the operator. If successful reperfusion was not achieved with the initially selected first-line MT despite multiple attempts, rescue therapy was performed by switching to the other primary method.

IA UK has long been used as a stand-alone intra-arterial thrombolysis at our center. Local intra-arterial urokinase was performed through a microcatheter (0.021 or 0.027 inch). Initially, the microcatheter was navigated across the thrombus and placed just distal to the thrombus. After confirmation of antegrade contrast opacification beyond the occlusion site, UK injection was started. Next, the microcatheter was gradually withdrawn and positioned within the offending thrombus while injecting the UK. Then, the microcatheter was pulled back and placed proximal to the thrombus, and the small amount of UK remaining was injected gently. More proximal regional infusion was prohibited. After the completion of UK administration, additional mechanical thrombectomy followed after waiting 3–5 minutes. This method was used by all 3 operators. The details of the conventional MT technique were described previously.[15,16]

Data Collection and Outcome Measures

Clinical and radiologic data, including patient demographics, angiographic and radiologic findings, time intervals (ie, onset, puncture, reperfusion time), and clinical information, were prospectively collected. Two interventional neuroradiologists (C.J. and S.H.B.) independently evaluated all images. Discordance between the 2 readers was resolved by consensus. In patients with successful reperfusion, the procedure time was defined as the interval from puncture to final recanalization, whereas in patients with unsuccessful reperfusion, it was defined as the time interval from puncture to the last angiographic series. The reperfusion status was assessed on the final angiogram and was classified according to the mTICI scale. The primary outcome was the rate of successful reperfusion, which was defined with an mTICI score of 2b or 3. Complete reperfusion was defined as an mTICI grade of 3. Good clinical outcome was defined as a 3-month mRS score of 0–2. The angiographic findings such as time intervals, number of passes, and reperfusion status before and after the administration of IA UK were checked.

The safety outcomes included procedural complications (perforation and dissection) and hemorrhagic complications. An intracerebral hemorrhage (ICH) was classified on the basis of the second European-Australasian Acute Stroke Study classification, and symptomatic intracerebral hemorrhage (sICH) was defined as any hemorrhage associated with an increase in the NIHSS score by ≥4 within a 24-hour period.[17]

Statistical Analysis

The differences in the baseline characteristics and the procedural and clinical outcomes between the UK and non-UK groups were compared. The Pearson χ^2 test or Fisher exact test was used for categoric variables, and the Mann-Whitney *U* test, for continuous variables. Multivariable logistic regression was performed to evaluate the independent variables for successful reperfusion in patients with refractory thrombus. All statistical analyses were performed using SPSS for Windows (Version 20.0; IBM). A *P* value < .05 was considered statistically significant.

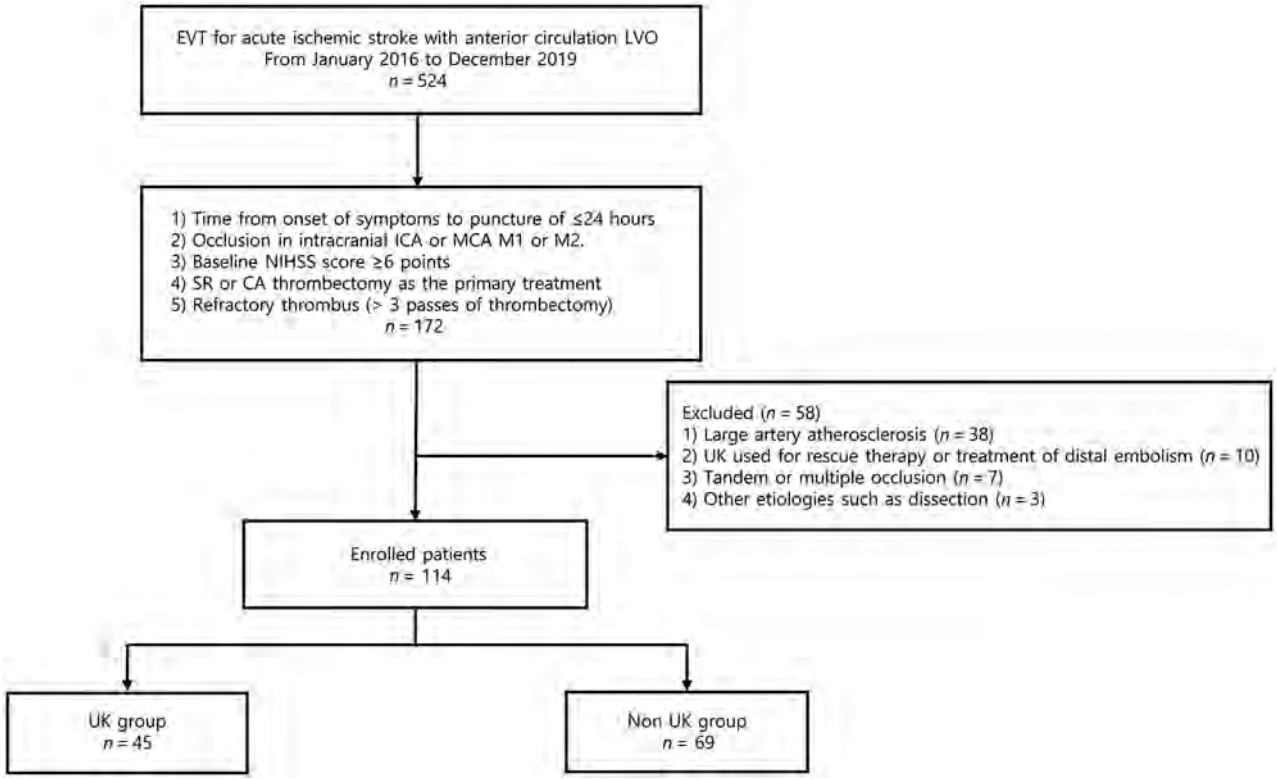

FIG 1. Flow chart of patient selection. EVT indicates endovascular treatment.

RESULTS

A flow chart depicting the patient recruitment process is shown in Fig 1. Between January 2016 and December 2019, a total of 524 patients with acute ischemic stroke with LVO in the anterior circulation underwent endovascular treatment within the first 24 hours after symptom onset. Of the 524 patients, 172 patients were identified as having refractory thrombus. Of these, 58 patients were excluded due to the following reasons: 1) large-artery atherosclerosis ($n = 38$); 2) use of UK for rescue therapy or treatment of distal embolism ($n = 10$); 3) tandem or multiple occlusions ($n = 7$); and 4) other etiologies of stroke, such as dissection ($n = 3$). Finally, 114 patients (median age, 75 years; interquartile range [IQR], 65–81 years; 56 men [49.1%]) with refractory thrombus qualified for the final analysis. Of the included 114 patients, 45 patients (39.5%) were included in the UK group and administered IA UK as an adjunct to MT, and the remaining 69 patients (60.5%) were included in the non-UK group and did not receive IA UK during MT.

The baseline characteristics of all patients and 2 subgroups are shown in Table 1. The median NIHSS score was 15 (IQR, 12–18). Seventy-seven (67.5%) patients were identified as having cardioembolism, and 17 (14.9%) patients had active cancer at the time of acute stroke. Forty-five patients (39.5%) had MCA M1 occlusions, and 29 patients (25.4%) received intravenous tPA before endovascular treatment. There were no significant differences in the baseline characteristics between the 2 groups.

The procedural and clinical outcomes are summarized in Tables 2 and 3. A total of 45 patients received adjunctive IA UK (median dose, 40,000; IQR, 20,000–60,000 IU) during MT to treat refractory thrombus despite conventional MT (before IA UK; median number of passes, 4; IQR, 3–5). IA UK was administered at a median of 244 minutes (IQR, 182–470 minutes) after symptom onset or after last seen well. The UK group showed a higher rate of successful reperfusion (82.2% versus 63.8%, $P = .034$) and complete reperfusion (35.6% versus 17.4%, $P = .044$) compared with the non-UK group. Additionally, the procedure time was shorter in the UK group (median, 54 versus 69 minutes; $P = .137$), with fewer rescue therapies, albeit without statistical significance (60.0% versus 73.9%, $P = .118$). After the injection of UK, final reperfusion was obtained after a mean of 15 minutes (range, 10–18 minutes), and 2 additional thrombectomies (range, 1–4) were performed on average. Furthermore, conversion to the other MT technique was performed in 10 (22.2%) patients. With respect to the number of passes, there were more patients who underwent MT with ≥8 passes in the non-UK group than in the UK group (13.3% versus 18.8%, $P = .441$). Among patients who had ≥8 MT passes, the non-UK group showed lower rates of successful reperfusion compared with the UK group (100.0% versus 30.8%, $P = .011$) (Fig 2).

Regarding procedural complications, the incidence of vessel perforation and dissection was comparable between the 2 groups (2.2% versus 1.4% and 2.2% versus 5.8%, respectively). Overall, vessel perforation occurred in 2 (1.8%) patients, and dissection occurred in 5 (4.4%) patients. sICH and SAH were not different between the 2 groups (11.1% versus 14.5%, $P = .602$, and 4.4% versus 7.2%, $P = .702$, respectively).

In a subgroup analysis, comparison of successful reperfusion rates according to the etiology of stroke is presented in the

Table 1: Baseline characteristics between the 2 groups[a]

	Total ($n = 114$)	UK Group (MT+UK+MT) ($n = 45$)	Non-UK Group (MT+MT) ($n = 69$)	*P* Value
Age[b]	75 (65–81)	74 (63–81)	75 (65–82)	.615
Male	56 (49.1)	21 (46.7)	35 (50.7)	.672
Risk factor				
Hypertension	59 (51.8)	23 (51.1)	36 (52.2)	.912
Diabetes	27 (23.7)	12 (26.7)	15 (21.7)	.545
Dyslipidemia	20 (17.5)	10 (22.2)	10 (14.5)	.289
Smoking	15 (13.2)	7 (15.6)	8 (11.6)	.541
Coronary artery disease	9 (7.9)	3 (6.7)	6 (8.7)	1.000
Atrial fibrillation	72 (63.2)	26 (57.8)	46 (66.7)	.336
TOAST				
LAA	0 (0.0)	0 (0.0)	0 (0.0)	
CA	77 (67.5)	29 (64.4)	48 (69.6)	.568
SUD	19 (16.7)	6 (13.3)	13 (18.8)	.441
Cancer-related stroke	17 (14.9)	9 (20.0)	8 (11.6)	.218
IV tPA	29 (25.4)	9 (20.0)	20 (29.0)	.282
Admission NIHSS[b]	15 (12–18)	15 (10–18)	15 (12–19)	.080
Baseline ASPECTS[b]	8 (7–9)	8 (7–9)	8 (7–9)	.328
Occlusion site				.182
ICA	42 (36.8)	12 (26.7)	30 (43.5)	
M1	45 (39.5)	20 (44.4)	25 (36.2)	
M2	27 (23.7)	13 (28.9)	14 (20.3)	

Note:—TOAST indicates Trial of Org 10172 in Acute Stroke Treatment[31]; LAA, large-artery atherosclerosis; CA, cardioembolism; SUD, stroke of undetermined etiology.

[a] Values in parentheses represent the number of patients (%).

[b] Data are median and numbers in parentheses are IQR.

Table 2: Procedural characteristics in the UK group

Characteristics	Quartile or No. (%)
Dose of IA UK (IU)	40,000 (20,000–60,000)
Dose of IA UK based on site	*P* value = .056[a]
ICA (IU)	60,000 (58,000–100,000)
M1 (IU)	40,000 (28,000–60,000)
M2 (IU)	40,000 (20,000–50,000)
UK to reperfusion time (min)	15 (10–18)
Rescue therapy after IA UK	10 (22.2)
No. of passes before IA UK	4 (3–5)
No. of passes after IA UK	2 (1–2)
Final reperfusion status	
0–1	2 (4.4)
2a	6 (13.3)
2b	21 (46.7)
3	16 (35.6)

[a] *P* value was calculated by the Kruskal-Wallis test.

Online Supplemental Data. Among patients who had cardioembolism or active cancer, the UK group showed a higher rate of successful reperfusion in the refractory thrombus group (86.2% versus 54.2%, $P = .004$; 77.8% versus 50.0%, $P = .335$, respectively); however, the latter did not reach statistical significance compared with the non-UK group.

Multivariate logistic regression analysis showed that the procedure time (OR = 0.98; 95% CI, 0.962–0.998; $P = .026$) and intra-arterial urokinase (OR = 3.682; 95% CI, 1.156–11.730; $P = .027$) were independent predictors of successful reperfusion in patients with multiple MT passes (≥3) when adjusted for age, intravenous tPA, baseline NIHSS, M2 occlusion, onset to puncture time, rescue therapy, distal embolism, and number of passes (Table 4).

DISCUSSION

The results of our study indicate that patients with embolic LVO with refractory thrombus who were treated with IA UK as an adjunct to MT showed a higher rate of successful reperfusion and a shorter procedure time compared with those who were not treated with IA UK. In addition, the adjunctive use of IA UK for refractory thrombus did not increase the risk of procedural and hemorrhagic complications. Moreover, the use of IA UK was shown to be an independent predictor of successful reperfusion in patients with embolic LVO with refractory thrombus after adjustment for multiple confounders.

Only a handful of retrospective studies to date have evaluated the safety and efficacy of IA thrombolysis before, after, or during MT for various purposes. Kaesmacher et al[12] recently reported that in selected patients, the use of IA UK during or after MT may not only be safe but may also improve angiographic reperfusion. However, this study included the use of IA UK not only as adjunctive therapy to MT (25%) but also as a rescue therapy (without additional MT) (15%), as a method to improve reperfusion (from TICI 2a or 2b) (53%) and treatment of emboli to new territory (7%). Zaidi et al[11] also recently reported that IA tPA could be used as a rescue treatment in patients who were refractory to SR therapy, showing a successful reperfusion in 61.2% of cases without increasing the incidence of sICH. Similarly, Heiferman et al[9] and Yi et al[10] showed that using adjuvant IA tPA injection combined with SR thrombectomy improved revascularization without increasing adverse effects. Our results are in line with these studies. However, our study included only refractory cases that did not respond to multiple attempts of conventional MT; herein, we demonstrated that the IA UK as an adjunct to MT increased the rate of successful and complete reperfusion and shortened the procedure time without increasing the rate of hemorrhagic complications compared with the non-IA UK group. To the best of our knowledge, this is the first report to explore the efficacy of IA UK as an adjunctive option to augment MT in the setting of embolic LVO with refractory thrombus.

The greatest concern of using IA UK is the risk of hemorrhage. The most severe complication of IA UK is sICH, which is known to occur in 10% of patients in the recombinant prourokinase group, as shown in the previous Prolyse in Acute Cerebral Thomboembolism (PROACT-II) trial,[18] and in 5.2% in those

Table 3: Procedural and clinical outcomes between the 2 groups[a]

	Total (n = 114)	UK Group (MT+UK+MT) (n = 45)	Non-UK Group (MT+MT) (n = 69)	P Value
Onset to puncture time (min)[b]	158 (110–413)	182 (122–412)	149 (102–420)	.561
Procedure time[b]	62 (42–93)	54 (39–88)	69 (49–113)	.137
Onset to reperfusion time[b]	253 (169–491)	254 (195–481)	231 (164–503)	.561
First-line technique				.533
SR	72 (63.2)	31 (68.9)	41 (59.4)	
CA	29 (25.4)	9 (20.0)	20 (29.0)	
Combined technique	13 (11.4)	5 (11.1)	8 (11.6)	
Rescue therapy	78 (68.4)	27 (60.0)	51 (73.9)	.118
Switch to SR	24 (21.1)	9 (20.0)	15 (21.7)	
Switch to CA	23 (20.2)	8 (17.8)	15 (21.7)	
Switch to SR+CA	34 (29.8)	10 (22.2)	24 (34.8)	
Total No. of passes[b]	5 (5–6)	6 (5–6)	6 (6–7)	.289
4–5 Passes	49 (43.0)	22 (48.9)	27 (39.1)	.304
6–7 Passes	46 (40.4)	17 (37.8)	29 (42.0)	.651
≥8 Passes	19 (16.7)	6 (13.3)	13 (18.8)	.441
Other adjuvant treatments	22 (19.3)	7 (15.6)	15 (21.7)	.414
Final reperfusion status				
2b–3	81 (71.1)	37 (82.2)	44 (63.8)	.034
3	28 (24.6)	16 (35.6)	12 (17.4)	.044
mRS at 90 days[b]	3 (2–5)	3 (1–4)	3 (2–5)	.352
mRS 0–2 at 90 days	41 (36.0)	17 (37.8)	24 (34.8)	.745
Mortality at 90 days	16 (14.0)	7 (15.6)	9 (13.0)	.706
Vessel perforation	2 (1.8)	1 (2.2)	1 (1.4)	1.000
Dissection	5 (4.4)	1 (2.2)	4 (5.8)	.647
ICH	15 (13.2)	5 (11.1)	10 (14.5)	.602
SAH	7 (6.1)	2 (4.4)	5 (7.2)	.702
HI1 or HI2	20 (17.5)	7 (15.6)	13 (18.8)	.652
PH1 or PH2	8 (7.0)	2 (4.4)	6 (8.7)	.476

Note:—HI indicates hemorrhagic infarction; PH, parenchymatous hematoma.
[a] Values in parentheses represent the number of patients (%).
[b] Data are medians and numbers in parentheses are IQR.

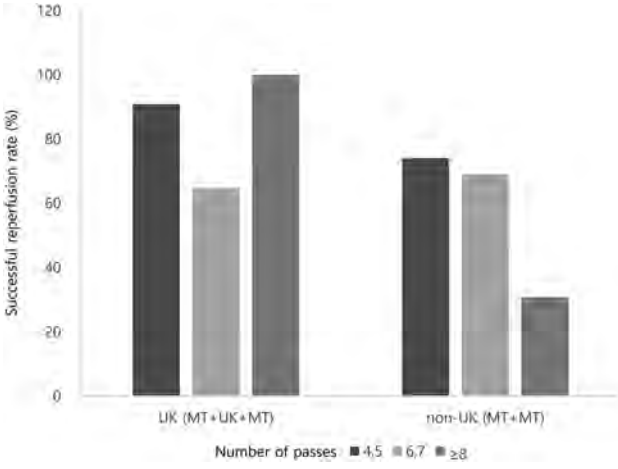

FIG 2. Comparison of successful reperfusion rates according to the total number of passes between the 2 groups.

receiving IA UK as an adjunct treatment to MT, as shown in a recent report.[12] However, our study shows that the occurrence of sICH was 11.1% in those with IA UK. However, the patients in our study consisted of only those who had refractory occlusion due to embolic thrombi, which is usually related to large clot burden, a long procedure time, and an increased number of passes. Thus, our patients were, at baseline, probably at higher risk of poor outcome. Despite these circumstances, we found that the occurrence of sICH was comparable between the UK and non-UK groups. This finding may be explained by an improvement in the procedural efficacy and perfusion, which minimizes infarction expansion, ultimately reducing the overall ICH risk.[19,20]

Despite significant improvements in the various endovascular techniques, some situations are not amenable to conventional methods, especially in the case of large and/or stubbornly rooted thrombi.[8] Recently, several studies reported a novel rescue technique using double SRs, showing safe and effective outcomes and thereby demonstrating it as a potential option for refractory LVO.[8,21,22] Besides, Chang et al[23] reported that rescue stent placement for failed MT achieved successful reperfusion in 64.6% of cases. Nonetheless, double-stent thrombectomy is a relatively complex technique that demands extensive technical experience as well as specific anatomic features, like arterial bifurcation.[21,22] In addition, the increased cost of 2 SRs is another disadvantage. Moreover, rescue permanent stent placement is preferable for refractory occlusion caused by atherosclerotic stenosis or arterial dissection rather than for embolic occlusion. In addition, a drawback of permanent stent placement is that it requires antiplatelet medication during or immediately after the treatment in patients with acute stroke.

Our results showed that the efficacy of reperfusion is better with the use of IA UK than without it in patients with refractory thrombus. There are several possible advantages to using local IA UK as an adjunct to MT in refractory thrombus. First, the local IA thrombolysis enhances the efficacy of thrombectomy by fibrin degradation which softens and increases the surface area of the clots enabling easier detachment.[24,25] Second, UK thrombolysis also decreases the surface area interaction with the vessel wall, which reduces friction/adhesion.[3] These theoretic advantages of combining IA UK and MT could help explain the improvement in reperfusion in patients with LVO with refractory thrombus.

Previous reports indicated that fibrin-rich thrombi are less responsive to SR thrombectomy and thrombolysis compared with red blood cell–rich thrombi.[26,27] Thrombi retrieved from active cancer usually show high fibrin/platelet and low erythrocyte fractions, whereas cardioembolic stroke is associated with red blood cell–rich thrombi.[28] In exploring the effect of IA UK on reperfusion of refractory LVO, according to stroke etiology, IA UK enhanced the reperfusion among patients with cardioembolism. Moreover, we found a trend toward higher successful reperfusion in patients with active cancer who received IA UK than in those who did not. This finding may be explained by the lysis effect of IA UK on dense fibrin fiber within the thrombi from active cancer, despite its resistance to lysibility compared with red blood cell–rich thrombi.[27] Our subgroup results implied that the use of local IA UK as an adjunct to MT could be a treatment option for refractory occlusion from cancer-related stroke as well as cardioembolism.

Table 4: Multivariable analysis of successful reperfusion in patients with multiple passes (≥4) of mechanical thrombectomy

	Successful Reperfusion (mTICI 2b/3)	
	Adjusted OR (95% CI)	*P* Value
Age	1.018 (0.971–1.066)	.463
IV tPA	0.773 (0.240–2.485)	.665
Baseline NIHSS	0.986 (0.881–1.104)	.806
ICA occlusion	1.287 (0.405–4.091)	.669
Onset to puncture time	0.999 (0.997–1.001)	.385
Procedure time	0.980 (0.962–0.998)	.026
Rescue therapy	0.816 (0.252–2.961)	.816
No. of passes	0.778 (0.538–1.125)	.182
Distal embolism	0.828 (0.248–2.765)	.759
Intra-arterial urokinase	3.682 (1.156–11.730)	.027

There were scarce and discrepant data for determining the optimal number of passes and the optimal timing of switching to the other rescue therapies during MT.[29] Some previous studies suggested ≥4 passes of thrombectomy as the maximum cutoff point before futile reperfusion,[25] while others found that patients who achieve successful reperfusion after ≥4 MT passes still had better outcomes compared with patients without reperfusion.[30] In our study, the UK group compared with the non-UK group showed not only fewer cases of an excessive number of passes (≥8 passes), but among those with an excessive number of passes, the rate of successful reperfusion was higher. Nevertheless, our findings should not be interpreted as suggestive of endless efforts to achieve favorable reperfusion. In our cohort, 33 cases still remained unsuccessful, even with the use of IA UK as an adjunct to MT. Furthermore, multiple attempts at MT could be associated with an increased procedure time and higher complication rates. Thus, we believe that the early use of adjunctive IA UK may be beneficial when thrombus is deemed not responsive to the standard MT.

To the best of our knowledge, there are limited data on the role of IA UK and its relation to a modern MT technique. Although several previous studies reported various techniques and doses of IA UK, it has mostly been used as a rescue therapy or for distal embolism.[12,14,18] Currently, there is no standardized protocol for dosing and administration of IA UK as an adjunct to MT for refractory thrombus. In our cohort, IA UK tends to be given in various doses, depending on the occlusion site; generally, if it is locally administrated, a lower dose (median, 40,000 IU) of IA UK seems to be sufficient to enhance the efficacy of thrombectomy, which is followed by a relatively short duration of action (median UK injection to reperfusion time, 15 minutes) (Fig 3). However, further research on the optimal protocol of IA UK is warranted.

There are several limitations to this study. First, due to the nonrandomized, retrospective design, there could be bias; the use of IA UK and the selection of the MT technique for refractory occlusion were at the discretion of the operator. Hence, the conclusion of improved reperfusion without an increase in the risk of hemorrhage should be interpreted cautiously. Second, the sample size may not have been large enough to show

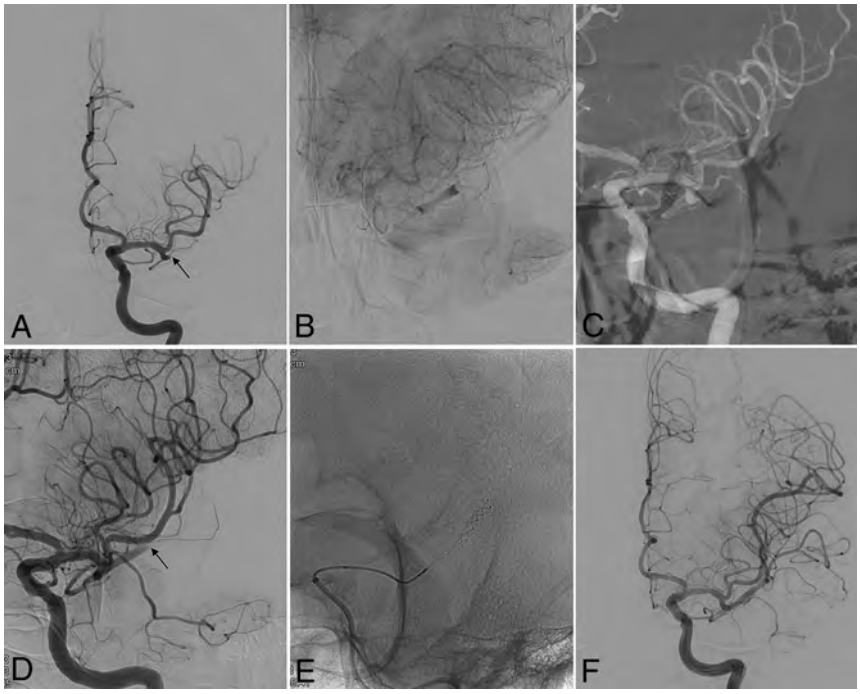

FIG 3. *A*, A-63-year-old male patient with acute stroke due to left MCA proximal M2 occlusion (*arrow*). *B*, Left ICA angiogram obtained after SR thrombectomy (twice) and CA thrombectomy (twice) (not shown) still shows complete occlusion at the left MCA M2 segment. *C*, Intra-arterial urokinase (40,000 IU) is injected through a 0.021-inch microcatheter from the distal-to-proximal portion of the thrombus. *D*, After completion of urokinase administration, additional SR thrombectomy followed (not shown). The angiographic morphology of the thrombus is changed, and minimal recanalization is achieved (*arrow*). *E* and *F*, After 1 more attempt of SR thrombectomy, complete recanalization is achieved.

statistical differences between the subgroups of this cohort. Another limitation could be the lack of histologic examination of the retrieved clots. The relationship between the thrombus composition and the efficacy of combining IA UK with MT could be a topic for future research.

CONCLUSIONS

The use of local IA UK as an adjunct to MT seems to be a safe and effective method for treating embolic LVO with refractory thrombus that is unresponsive to conventional MT. The use of adjunctive IA UK may provide enhanced reperfusion not only in patients with cardioembolism but also in those with cancer-related stroke. Further prospective studies are needed to verify this method.

Disclosures: Sung Hyun Baik—*RELATED*: *Grant*: Seoul National University Bundang Hospital, *Comments*: No. 14-2020-033.

REFERENCES

1. Liebeskind DS, Bracard S, Guillemin F, et al. HERMES Collaborators. **eTICI reperfusion: defining success in endovascular stroke therapy.** *J Neurointerv Surg* 2019;11:433–38 CrossRef Medline
2. Rizvi A, Seyedsaadat SM, Murad MH, et al. **Redefining 'success': a systematic review and meta-analysis comparing outcomes between incomplete and complete revascularization.** *J Neurointerv Surg* 2019;11:9–13 CrossRef Medline
3. Yoo AJ, Andersson T. **Thrombectomy in acute ischemic stroke: challenges to procedural success.** *J Stroke* 2017;19:121–30 CrossRef Medline
4. Kaesmacher J, Gralla J, Mosimann PJ, et al. **Reasons for reperfusion failures in stent-retriever-based thrombectomy: registry analysis and proposal of a classification system.** *AJNR Am J Neuroradiol* 2018;39:1848–53 CrossRef Medline
5. Leischner H, Flottmann F, Hanning U, et al. **Reasons for failed endovascular recanalization attempts in stroke patients.** *J Neurointerv Surg* 2019;11:439–42 CrossRef Medline
6. Gascou G, Lobotesis K, Machi P, et al. **Stent retrievers in acute ischemic stroke: complications and failures during the perioperative period.** *AJNR Am J Neuroradiol* 2014;35:734–40 CrossRef Medline
7. Kim BM. **Causes and solutions of endovascular treatment failure.** *J Stroke* 2017;19:131–42 CrossRef Medline
8. Xu H, Peng S, Quan T, et al. **Tandem stents thrombectomy as a rescue treatment for refractory large vessel occlusions.** *J Neurointerv Surg* 2021;13:33–38 CrossRef Medline
9. Heiferman DM, Li DD, Pecoraro NC, et al. **Intra-arterial alteplase thrombolysis during mechanical thrombectomy for acute ischemic stroke.** *J Stroke Cerebrovasc Dis* 2017;26:3004–08 CrossRef Medline
10. Yi TY, Chen WH, Wu YM, et al. **Adjuvant intra-arterial rt-PA injection at the initially deployed Solitaire stent enhances the efficacy of mechanical thrombectomy in acute ischemic stroke.** *J Neurol Sci* 2018;386:69–73 CrossRef Medline
11. Zaidi SF, Castonguay AC, Jumaa MA, et al. **Intraarterial thrombolysis as rescue therapy for large vessel occlusions.** *Stroke* 2019;50:1003–06 CrossRef Medline
12. Kaesmacher J, Bellwald S, Dobrocky T, et al. **Safety and efficacy of intra-arterial urokinase after failed, unsuccessful, or incomplete mechanical thrombectomy in anterior circulation large-vessel occlusion stroke.** *JAMA Neurol* 2020;77:318–26 CrossRef Medline
13. Anadani M, Ajinkya S, Alawieh A, et al. **Intra-arterial tissue plasminogen activator is a safe rescue therapy with mechanical thrombectomy.** *World Neurosurg* 2019;123:e604–e8 CrossRef Medline
14. Kaesmacher J, Meinel TR, Kurmann C, et al. **Safety and efficacy of intra-arterial fibrinolytics as adjunct to mechanical thrombectomy: a systematic review and meta-analysis of observational data.** *J Neurointerv Surg* 2021 Jan 29. [Epub ahead of print] CrossRef Medline
15. Yoon W, Jung MY, Jung SH, et al. **Subarachnoid hemorrhage in a multimodal approach heavily weighted toward mechanical thrombectomy with Solitaire stent in acute stroke.** *Stroke* 2013;44:414–19 CrossRef Medline
16. Turk AS, Frei D, Fiorella D, et al. **ADAPT FAST study: a direct aspiration first pass technique for acute stroke thrombectomy.** *J Neurointerv Surg* 2014;6:260–64 CrossRef Medline
17. Hacke W, Kaste M, Fieschi C, et al. **Randomised double-blind placebo-controlled trial of thrombolytic therapy with intravenous alteplase in acute ischaemic stroke (ECASS II): Second European-Australasian Acute Stroke Study Investigators.** *Lancet* 1998;352:1245–51 CrossRef Medline
18. Furlan A, Higashida R, Wechsler L, et al. **Intra-arterial prourokinase for acute ischemic stroke: the PROACT II study: a randomized controlled trial—Prolyse in Acute Cerebral Thromboembolism.** *JAMA* 1999;282:2003–11 CrossRef Medline
19. Lee YB, Yoon W, Lee YY, et al. **Predictors and impact of hemorrhagic transformations after endovascular thrombectomy in patients with acute large vessel occlusions.** *J Neurointerv Surg* 2019;11:469–73 CrossRef Medline
20. Tonetti DA, Desai SM, Casillo S, et al. **Successful reperfusion, rather than number of passes, predicts clinical outcome after mechanical thrombectomy.** *J Neurointerv Surg* 2020;12:548–51 CrossRef Medline
21. Aydin K, Barburoglu M, Oztop Cakmak O, et al. **Crossing Y-Solitaire thrombectomy as a rescue treatment for refractory acute occlusions of the middle cerebral artery.** *J Neurointerv Surg* 2019;11:246–50 CrossRef Medline
22. Crosa R, Spiotta AM, Negrotto M, et al. **"Y-stent retriever": a new rescue technique for refractory large-vessel occlusions?** *J Neurosurg* 2018;128:1349–53 CrossRef Medline
23. Chang Y, Kim BM, Bang OY, et al. **Rescue stenting for failed mechanical thrombectomy in acute ischemic stroke: a multicenter experience.** *Stroke* 2018;49:958–64 CrossRef Medline
24. Fischer U, Kaesmacher J, Molina CA, et al. **Primary thrombectomy in tPA (tissue-type plasminogen activator) eligible stroke patients with proximal intracranial occlusions.** *Stroke* 2018;49:265–69 CrossRef Medline
25. del Zoppo GJ, Pessin MS, Mori E, et al. **Thrombolytic intervention in acute thrombotic and embolic stroke.** *Semin Neurol* 1991;11:368–84 CrossRef Medline
26. Gunning GM, McArdle K, Mirza M, et al. **Clot friction variation with fibrin content; implications for resistance to thrombectomy.** *J Neurointerv Surg* 2018;10:34–38 CrossRef Medline
27. Staessens S, Denorme F, Francois O, et al. **Structural analysis of ischemic stroke thrombi: histological indications for therapy resistance.** *Haematologica* 2020;105:498–507 CrossRef Medline
28. Navi BB, Reiner AS, Kamel H, et al. **Risk of arterial thromboembolism in patients with cancer.** *J Am Coll Cardiol* 2017;70:926–38 CrossRef Medline
29. Baek JH, Kim BM, Heo JH, et al. **Number of stent retriever passes associated with futile recanalization in acute stroke.** *Stroke* 2018;49:2088–95 CrossRef Medline
30. Filioglo A, Cohen JE, Honig A, et al. **More than five stentriever passes: real benefit or futile recanalization?** *Neuroradiology* 2020;62:1335–40 CrossRef Medline
31. Adams HP, Jr., Bendixen BH, Kappelle LJ, et al. **Classification of subtype of acute ischemic stroke. Definitions for use in a multicenter clinical trial. TOAST. Trial of org 10172 in Acute Stroke Treatment.** *Stroke* 1993;24:35–41 CrossRef Medline

Evolution of MRI Findings in Patients with Idiopathic Intracranial Hypertension after Venous Sinus Stenting

N.F. Belachew, W. Almiri, R. Encinas, A. Hakim, S. Baschung, J. Kaesmacher, T. Dobrocky, C.J. Schankin, M. Abegg, E.I. Piechowiak, A. Raabe, J. Gralla, and P. Mordasini

ABSTRACT

BACKGROUND AND PURPOSE: The correlation between imaging findings and clinical status in patients with idiopathic intracranial hypertension is unclear. We aimed to examine the evolution of idiopathic intracranial hypertension–related MR imaging findings in patients treated with venous sinus stent placement.

MATERIALS AND METHODS: Thirteen patients with idiopathic intracranial hypertension (median age, 26.9 years) were assessed for changes in the CSF opening pressure, transstenotic pressure gradient, and symptoms after venous sinus stent placement. Optic nerve sheath diameter, posterior globe flattening and/or optic nerve protrusion, empty sella, the Meckel cave, tonsillar ectopia, the ventricles, the occipital emissary vein, and subcutaneous fat were evaluated on MR imaging before and 6 months after venous sinus stent placement. Data are expressed as percentages, medians, or correlation coefficients (r) with P values.

RESULTS: Although all patients showed significant reductions of the CSF opening pressure (31 versus 21 cm H_2O; $P = .005$) and transstenotic pressure gradient (22.5 versus 1.5 mm Hg; $P = .002$) and substantial improvement of clinical symptoms 6 months after venous sinus stent placement, a concomitant reduction was observed only for posterior globe involvement (61.5% versus 15.4%; $P = .001$), optic nerve sheath diameter (6.8 versus 6.1 mm; $P < .001$), and subcutaneous neck fat (8.9 versus 7.4 mm; $P = .001$). Strong correlations were observed between decreasing optic nerve sheath diameters and improving nausea/emesis (right optic nerve sheath diameter, $r = 0.592$, $P = .033$; left optic nerve sheath diameter, $r = 0.718$, $P = .006$), improvement of posterior globe involvement and decreasing papilledema ($r = 0.775$, $P = .003$), and decreasing occipital emissary vein diameter and decreasing headache frequency ($r = 0.74$, $P = .035$). Decreasing transstenotic pressure gradient at 6 months strongly correlated with decreasing empty sella ($r = 0.625$, $P = .022$) and regressing cerebellar ectopia ($r = 0.662$, $P = .019$).

CONCLUSIONS: Most imaging findings persist long after normalization of intracranial pressure and clinical improvement. However, MR imaging findings related to the optic nerve may reflect treatment success.

ABBREVIATIONS: IIH = idiopathic intracranial hypertension; VAS = visual analog scale

Idiopathic intracranial hypertension (IIH) is a disorder characterized by increased intracranial pressure that is not caused by a mass lesion, a meningeal process, or cerebral venous thrombosis.[1] The diagnosis requires a thorough neurologic and ophthalmologic examination, a diagnostic lumbar puncture, and neuroimaging.[1] Imaging is primarily performed to exclude pathologies that would provide an obvious alternative explanation for clinical and laboratory diagnostic findings.[1,2] However, several imaging findings, though not specific, may assist in establishing the diagnosis.[2,3] Neither IIH pathogenesis nor the evolution of imaging findings in patients with IIH is fully understood.[4,5] It is particularly unclear whether IIH-associated MR imaging findings provide any information on treatment success.[6-10] We, therefore, aimed to examine the evolution of IIH-related MR imaging findings in patients treated with venous sinus stent placement.

MATERIALS AND METHODS

Inclusion Criteria

All information was derived from medical record review, MR imaging analyses, and telephone interviews with patients diagnosed with

Received March 22, 2021; accepted after revision July 22.

From the Department of Diagnostic and Interventional Neuroradiology (N.F.B., W.A., R.E., A.H., J.K., T.D., E.I.P., J.G., P.M.), Department of Diagnostic, Interventional and Pediatric Radiology (J.K.), Department of Neurology (C.J.S.), Department of Ophthalmology (M.A.), and Department of Neurosurgery (A.R.), Inselspital, Bern University Hospital and University of Bern, Bern, Switzerland; and Faculty of Medicine (S.B.), University of Bern, Bern, Switzerland.

Please address correspondence to Nebiyat Filate Belachew, MD, Department of Diagnostic and Interventional Neuroradiology, Inselspital, Freiburgstrasse 18, CH-3010, Switzerland; e-mail: nebiyatfilate.belachew@insel.ch; @NFBelachew

Indicates open access to non-subscribers at www.ajnr.org

Indicates article with online supplemental data.

http://dx.doi.org/10.3174/ajnr.A7311

IIH who underwent venous sinus stent placement at our hospital between October 2016 and April 2020. Patients were included if they met the following criteria: 1) final diagnosis of IIH according to the modified Dandy criteria;[1] 2) confirmation of a functionally relevant venous sinus stenosis on DSA and venous sinus manometry; 3) treatment of venous sinus stenosis with venous sinus stent placement; and 4) MR imaging available before and after venous sinus stent placement. Venous sinus stent placement was performed if the condition was deemed refractory to conservative therapy by the treating physicians or treatment had to be stopped due to adverse effects. Venous sinus stenosis with a transstenotic pressure gradient of ≥4 mm Hg was considered functionally relevant. All 13 patients gave general consent. Ethics approval was obtained from the local ethics committee. All patients included in the current study had previously been examined to assess technical and clinical outcome parameters after venous sinus stent placement (clinical data currently under review).

Analysis of Clinical Information

Information on age, sex, arterial hypertension, diabetes mellitus, and obesity (including body mass index) was gathered for all patients. Initial IIH-related symptoms such as headache (intensity according to visual analog scale [VAS] of 0–10 and frequency per week), nausea and/or emesis, phono- and photophobia, tinnitus of any kind, diplopia, and other subjective visual disturbances (ie, transient visual obscuration, blurry vision) were documented. Clinical symptoms were listed as IIH-related only if treating physicians had confidently excluded alternative causes. The time from symptom onset to first treatment and the duration of conservative treatment were documented. Additionally, the CSF opening pressure and the presence of papilledema were recorded.

DSA, Venous Sinus Manometry, and Venous Sinus Stent Placement

Diagnostic DSA and venous sinus manometry were performed with the patient under local anesthesia. The transstenotic pressure gradient was measured as described by Fargen et al.[11] DSA and venous sinus manometry were repeated with the patient under general anesthesia directly before as well as immediately after venous sinus stent placement to compare the pre- and postinterventional transstenotic pressure gradient. Venous sinus stent placement was performed with the patient under general anesthesia according to institutional protocols and in accordance with the recommendations of Fargen et al.[12] Patients were preloaded with aspirin, 100 mg/day, and clopidogrel, 75 mg/day, 5 days before the intervention. Aspirin, 100 mg/day, was continued life-long, while clopidogrel was discontinued 6 months after venous sinus stent placement.

Six-Month Follow-up and Outcome

At the 6-month follow-up, DSA, venous sinus manometry, and diagnostic lumbar puncture for CSF opening pressure measurement were repeated with the patient under local anesthesia. In addition to chart review, patients were interviewed to assess symptoms before venous sinus stent placement as well as changes in all IIH-related symptoms and quality of life after venous sinus stent placement (Online Supplemental Data). The patients' statements were compared with the information in their medical records. The follow-up period (from venous sinus stent placement until the interview) was documented in months for each case. Ophthalmology reports were reviewed to assess the evolution or development of papilledema.

Technical Imaging Information

MR imaging was performed using a 1.5T or a 3T MR imaging scanner (1.5T: Magnetom Aera or Magnetom Avanto^{fit}; 3T: Magnetom Skyra^{fit}, Magnetom Prisma, Magnetom Verio, or Magentom Vida; Siemens). Measurements and evaluation of the Meckel cave, the optic nerve sheath diameter, posterior globe flattening, optic nerve protrusion, and empty sella were performed on a 3D isovoxel T2-weighted sampling perfection with application-optimized contrasts by using different flip angle evolution sequence (SPACE; Siemens). Tonsillar ectopia, subcutaneous fat in the scalp and the neck, and the occipital emissary vein were assessed on 3D T1-weighted MPRAGE sequences with contrast media. The acquisition parameters are provided in the Online Supplemental Data. If the relevant sequence was not available for evaluation or was inadequate due to artifacts, the neuroradiologist decided whether reliable assessment was possible on an alternative sequence.

Imaging Analysis

Posterior globe flattening and optic nerve protrusion were assessed by a senior neuroradiologist (A.H.) with 14 years of experience. All quantitative measurements were performed by 2 independent neuroradiologists (W.A. and R.E.) with 8 and 3.5 years of experience, respectively. All evaluations were performed on the latest scan before venous sinus stent placement and at 6-month follow-up. The only exception was patient 4 for whom the only follow-up MR imaging was from 6 days after venous sinus stent placement. Quantitative measurements were repeated 3 times by each neuroradiologist and acquired on different days to avoid recall bias. Posterior globe flattening and optic nerve protrusion were only assessed once on the baseline scan before venous sinus stent placement and the follow-up scan. All imaging data were evaluated in a randomized order. Neuroradiologists were blinded to the clinical conditions of the patients.

The width of the Meckel cave was measured bilaterally on coronal images parallel to the brainstem. The optic nerve sheath diameter was measured bilaterally on axial images perpendicular to the optic nerve. Optic globe involvement was assessed on multiplanar T2-SPACE reconstructions and categorized as normal convexity of the optic globe, posterior globe flattening, or optic nerve protrusion with or without posterior globe flattening. The empty sella was quantified on sagittal images after drawing a line between the tuberculum and dorsum sellae and measuring the maximal perpendicular distance to the superior margin of the pituitary gland. Tonsillar ectopia was quantified on paramedian sagittal images by measuring the shortest distance between the most inferior margins of the cerebellar tonsil and the opisthion-basion line. The maximal thickness of subcutaneous fat was measured on sagittal images perpendicular to the coronal suture (frontal) and posteriorly at the level of the dens axis (occipital). Ventricle size was determined on axial images perpendicular to

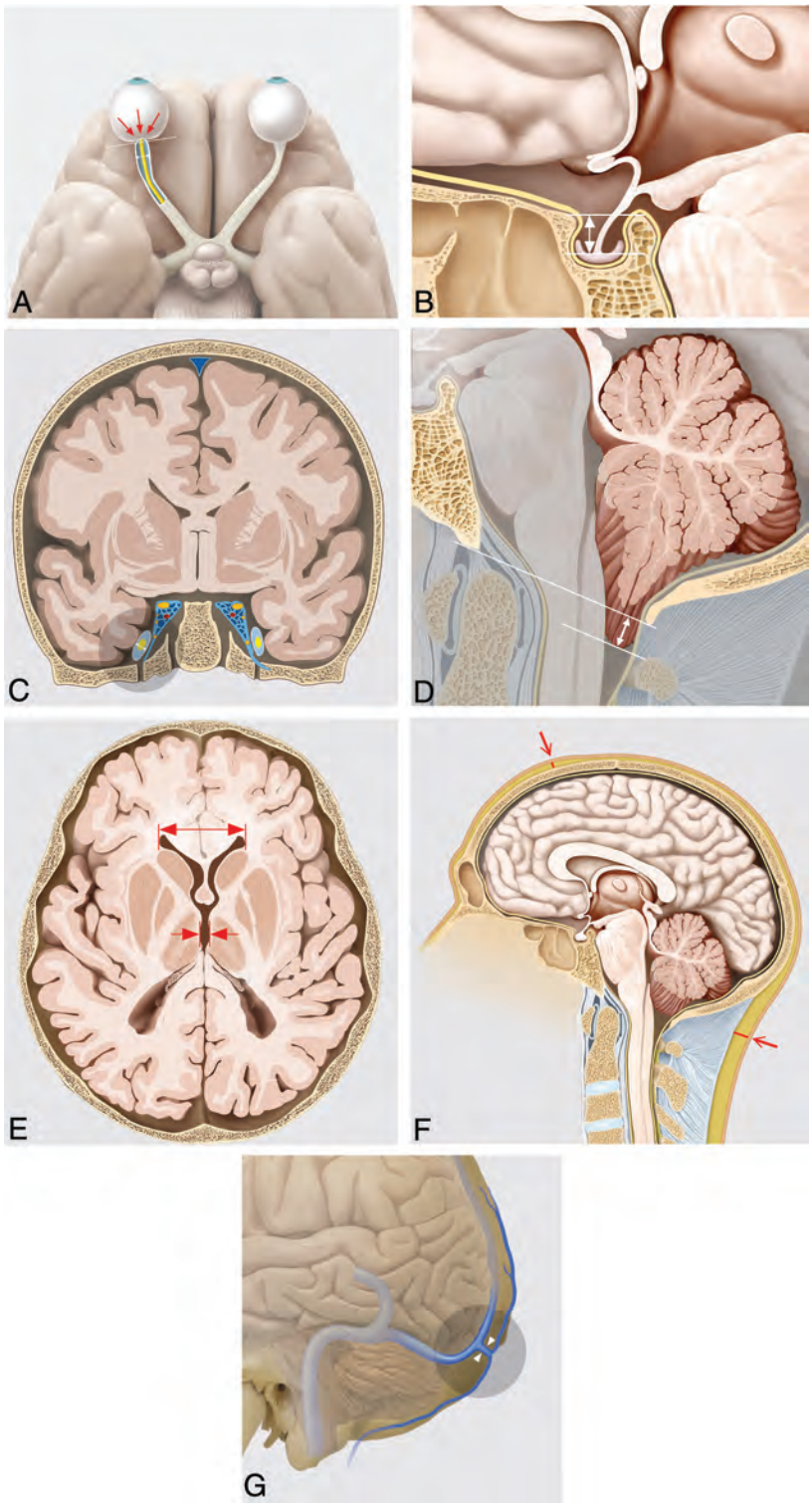

FIG 1. *A*, Posterior globe flattening (*white line*), optic nerve protrusion (*red arrows*), and distension of the optic nerve sheath diameter (*white line with arrowheads*) in the right eye. *B*, Measurement technique applied to quantify the empty sella (*white line with arrowheads*). *C*, Measurement of the Meckel cave: The *circled gray area* highlights the width measurement (*white line with arrowheads*) on the right side. *D*, Standard measurement to assess cerebellar ectopia (*white line with arrowheads*). *E*, Measurement of the distance between the anterior horns of the lateral ventricles (*red line with arrowhead*) as well as the diameter of the third ventricle corpus (*red arrows* pointing to perpendicular *red lines* delimiting the third ventricle corpus). *F*, Measurement of the frontal and occipital subcutaneous fat (*red lines*). *G*, Anatomic course of the occipital emissary vein.

the brainstem by measuring the distance between the anterior horns of the lateral ventricles and the maximal width of the third ventricle corpus at the same level. As suggested by Hedjoudje et al,[13] the occipital emissary vein was measured at its proximal osseous segment whenever it could be identified. Figure 1 illustrates all the MR imaging findings evaluated in this study.

Statistical Analysis

Data analyses were performed using SPSS Software (Version 25.0; IBM). Continuous parametric variables were compared using the *t* test for dependent variables, whereas nonparametric variables were compared using the Wilcoxon signed rank test. Mean values were used for statistical analyses of quantitative parameters with repeat measurements by 2 raters. Categoric variables were compared using the Fisher exact test. Results are shown as total values, medians with or without interquartile range (25%–75%), or median comparisons with *P* values for the test applied. Intra- and interobserver agreement was assessed by calculating the intraclass correlation coefficient. Correlation between IIH-related MR imaging findings and clinical improvement was assessed using the Spearman rank correlation coefficient.

RESULTS

Thirteen patients with IIH who underwent venous sinus stent placement for venous sinus stenosis at our hospital between October 2016 and April 2020 were included in this study. The mean age was 26.9 years (23.3–35.3 years of age). Patients' demographic characteristics and comorbidities are listed in Table 1. All except 1 patient ($n = 12/13$) received conservative therapy before venous sinus stent placement, and 1 patient ($n = 1/13$) additionally underwent surgical treatment (ventriculoperitoneal shunt). The mean duration of conservative therapy was 18.9 months (6–26 months), and the mean duration of the follow-up period was 16.6 months (7.8–32.2 months). Treatment and symptoms before venous sinus stent placement and at 6-month follow-

up are summarized in Table 2. Intracranial pressure values before and after venous sinus stent placement are summarized in Table 3.

Pressure Values before and after Venous Sinus Stent Placement

CSF opening pressure (31 versus 21 cm H_2O; $P = .005$) and the transstenotic pressure gradient with the patient under local anesthesia and general anesthesia were significantly lower after venous sinus stent placement compared with before (22.5 versus 1.5 mm Hg, $P = .002$; and 9 versus 1 mm Hg, $P = .002$). Reductions of CSF opening pressure (−9.25 cm H_2O), transstenotic pressure gradient under local anesthesia (−8 mm Hg), and transstenotic pressure gradient under general anesthesia (−19 mm Hg) were substantial.

Headache before and after Venous Sinus Stent Placement

Six of 11 patients in this study reported experiencing >1 type of headache. All patients initially had IIH-related headaches, which showed complete resolution 6 months after venous sinus stent placement (intensity according to the VAS: 7 versus 0, $P = .005$; and frequency per week: 7 versus 0, $P = .003$).

Other IIH-Related Symptoms before and after Venous Sinus Stent Placement

Other than headaches, visual disturbances ($n = 9/13$; 69.2%) and tinnitus ($n = 8/13$; 61.5%) were the most common IIH-related symptoms. Papilledema was documented in 9/13 patients. All patients who agreed to be interviewed ($n = 11/13$) reported a substantial impairment of their daily life due to IIH-related symptoms before venous sinus stent placement. Mean symptom duration before any treatment was 23.6 months (7.3–52.1 months). The mean duration of conservative therapy was 18.9 months (6.0–26.0 months). All patients who had nausea/emesis ($n = 8/8$), photophobia/phonophobia ($n = 3/3$), or diplopia ($n = 3/3$) showed substantial improvement or complete resolution 6 months after venous sinus stent placement. Almost all patients with tinnitus (6/8; 75.0%) or visual disturbances other than diplopia (8/9; 88.9%) showed substantial improvement or complete resolution. For all except 1 patient (who was lost to ophthalmologic follow-up), substantial or complete resolution of papilledema was documented after venous sinus stent placement ($n = 8/9$). All patients with available follow-up reported a substantial improvement in the quality of life ($n = 11/11$) after venous sinus stent placement.

Table 1: Demographics and comorbidities[a]

	Data Available for % (No.)	
Age	100% (13/13)	26.9 (23.3–35.3)
Sex (female) (%)	100% (13/13)	100% (13)
Comorbidities		
Diabetes mellitus	100% (13/13)	15.4% (2)
Arterial hypertension	100% (13/13)	23.1% (3)
Body mass index	100% (13/13)	28.9 (25.6–36.2)
Obesity	100% (13/13)	
None		15.4% (2)
Moderate		38.5% (5)
Severe		46.2% (6)

[a] Data are expressed as percentages (No.) or median (interquartile range [25%–75%]).

Table 2: Therapy and symptoms before and after venous sinus stent placement[a]

Before Venous Sinus Stent Placement			After Venous Sinus Stent Placement		
	Data Available (%) (No.)			Data Available (%) (No.)	
Headache intensity (VAS)	84.6% (11/13)	7 (5.5–9.0)	Headache intensity (VAS)	84.6% (11/13)	0 (0–0)
			Headache intensity improvement (VAS)	84.6% (11/13)	−7 (−9 to −4.5)
Headache, frequency (per wk)	84.6% (11/13)	7 (4.5–7)	Headache frequency (per wk)	84.6% (11/13)	0 (0–0)
≤1		15.4% (2)	≤1		84.6% (11)
2–4		0.0% (0/0)	2–4		0.0% (0)
>4		69.2% (9)	>4		0.0% (0)
Patients with >1 type of headache	84.6% (11/13)	46.2% (6)	Headache frequency improvement (per wk)	84.6% (11/13)	−7 (−7 to −4.5)
Nausea/emesis	100% (13/13)	61.5% (8)	Nausea/emesis IMP-AF	100% (8/8)	100% (8)
Photophobia/phonophobia	100% (13/13)	23.1% (3)	Photophobia/phonophobia IMP-AF	100% (3/3)	100% (3)
Tinnitus	100% (13/13)	61.5% (8)	Tinnitus IMP-AF	100% (8/8)	75.0% (6)
Diplopia	100% (13/13)	23.1% (3)	Diplopia IMP-AF	100% (3/3)	100% (3)
Visual disturbances	100% (13/13)	69.2% (9)	Visual disturbances IMP-AF	100% (9/9)	88.9% (8)
Papilledema	100% (13/13)	69.2% (9)	Papilledema IMP-AF	88.9% (8/9)	88.9% (8)
Daily life impairment	84.6% (11/13)	84.6% (11)	Daily life quality IMP-AF	100% (11/11)	100% (11/11)
Symptom duration (mo)	100% (15/15)	23.6 (7.3–52.1)	Follow-up period (mo)	100% (13/13)	16.6 (7.8–32.2)
Other therapy					
Conservative therapy	100% (13/13)	92.3% (12)			
Duration of conservative therapy (in months)	100% (15/15)	18.9 (6–26)			
Surgical therapy	100% (15/15)	7.7% (1)			

Note:—HA indicates headache; IMP-AF, improvement among affected.

[a] Data are expressed as percentages (No.) or median (interquartile range [25%–75%]).

Table 3: Pressure values before and after venous sinus stent placement[a]

Before			After		
	Data Available (%) (No.)			Data Available (%) (No.)	
CSF opening pressure (cm H_2O)	84.6% (11/13)	31 (23–38)	CSF opening pressure (cm H_2O)	76.9% (10/13)	21 (18.75–29.25)
			CSF opening pressure improvement (mm Hg)	76.9% (10/13)	−9.25 (−20.7 to −5.7)
Transstenotic pressure gradient in GA (mm Hg)	100% (13/13)	9 (5–15)	Transstenotic pressure gradient in GA (mm Hg)	100% (13/13)	1 (0–2)
			Transstenotic pressure gradient improvement (in mm Hg)	100% (13/13)	−8 (−15 to −3.5)
Transstenotic pressure gradient on diagnosis in LA (mm Hg)	92.3% (12/13)	22.5 (13.25– 26.25)	Transstenotic pressure gradient at 6-mo follow-up in LA (mm Hg)	92.3% (12/13)	1.5 (0.25– 5)
			Transstenotic pressure gradient improvement at 6-mo follow-up (mm Hg)	92.3% (12/13)	−19 (−21.75 to −13.25)

Note:—LA indicates local anesthesia; GA, general anesthesia.
[a] Data are expressed as percentages (No.) or median (interquartile range [25%–75%]).

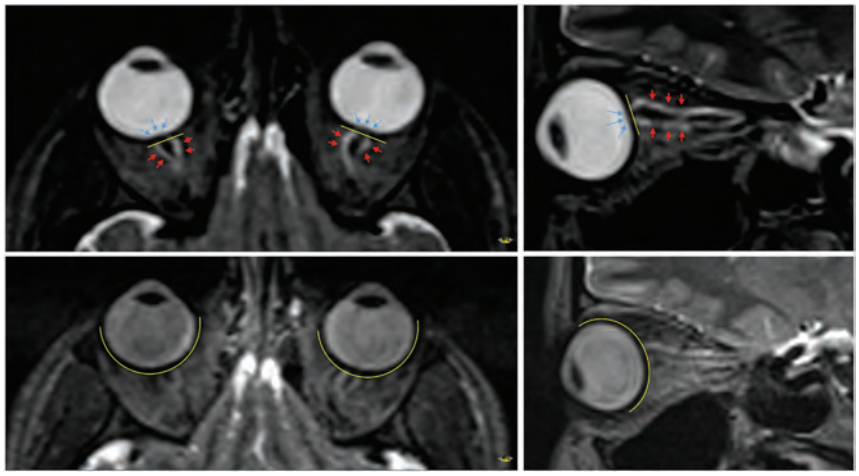

FIG 2. Axial reformation of both eye globes as well as sagittal reformation of the left eye globe along the axis of the optic nerve before (*upper images*) and after (*lower images*) stent placement. Before venous sinus stent placement, there is flattening of the posterior sclera (*yellow line*) with intraocular protrusion of the optic nerve (*blue arrows*) and distension of the optic nerve sheath diameter due to increased perineural fluid (*red arrows*). None of these 3 signs are seen after venous sinus stent placement.

IIH-Related MR Imaging Findings before and after a Venous Sinus Stent Placement

Inter- and intrarater agreement was excellent (intraclass correlation coefficient for raters 1 and 2: 0.968; intraclass correlation coefficient for repeat measurements for rater 1 = 0.998 and rater 2 = 0.968). No differences between measurements at baseline and after venous sinus stent placement were seen for the sella (4.9 versus 4.9 mm, $P = .753$), tonsillar ectopia (−1.1 versus −0.67 mm, $P = .600$), the lateral ventricles (31.5 versus 32.2 mm, $P = .124$), the diameter of the proximal occipital emissary vein (1.6 versus 1.6 mm, $P = .790$), or the subcutaneous fat in the scalp (4.1 versus 4.1 mm, $P = .834$). The occipital emissary vein was identified in 11/13 patients (84.6%) before and after venous sinus stent placement. The width of the Meckel cave tended to decrease, whereas the diameter of the third ventricle corpus had increased on the follow-up scan, though these findings were not statistically significant (4.5 versus 4.2 mm, $P = .096$; 3.7 versus 4.5 mm, $P = .075$). Measurements for optic nerve sheath diameter (6.8 versus 6.1 mm, $P < .001$) and subcutaneous fat in the neck (8.9 versus 7.4 mm, $P = .001$) were the only 2 quantitative parameters to have decreased on 6-month follow-up imaging. Optic globe involvement improved after venous sinus stent placement (normal convexity of the optic globe: 38.5% versus 84.6%; posterior globe flattening: 30.8% versus 15.4%; and posterior globe flattening with optic nerve protrusion: 30.8% versus 0%; $P = .001$). Figure 2 exemplifies the improvement in orbital findings after venous sinus stent placement. Changes of quantitative measurements at 6 months did not differ when patients showing improvement of all IIH-related symptoms were compared with patients who had at least 1 persistent symptom. All MR imaging findings evaluated before and after venous sinus stent placement, including the number of MRIs suitable for assessment, are listed in Table 4.

Correlation between Evolution of IIH-Related MR Imaging Findings and Development of Intracranial Pressure Values and IIH-Related Symptoms after Venous Sinus Stent Placement

Decreasing empty sella height measurements as well as regressing cerebellar ectopia at 6 months correlated strongly with transstenotic pressure gradient improvement with the patient under general

Table 4: IIH-related MR imaging findings before venous sinus stent placement and at 6-month follow-up[a]

MR Imaging Findings	Evaluation Possible (%) (No.)	Before Venous Sinus Stent Placement	At 6-Month Follow-Up	*P* Values
Meckel cave (mm)	100% (26/26)	4.3 (4.0–4.9)	4.1 (3.4–5.1)	.096
Empty sella (mm)	100% (13/13)	4.9 (3.5–6.9)	4.9 (3.2–7.0)	.753
Tonsillar ectopia (mm)	100% (13/13)	−1.1 (−1.9 to −1.9)	−0.67 (−1.3 to −0.9)	.600
Lateral ventricles (mm)	100% (13/13)	31.5 (29.4–34.6)	32.2 (29.7–34.6)	.124
Third ventricle corpus (mm)	100% (13/13)	3.7 (3.2–4.2)	4.5 (3.5–5.2)	.075
Optic nerve sheath diameter (mm)	100% (26/26)	6.8 (6.2–7.3)	6.1 (5.9–6.5)	.000
Optic nerve protrusion (%)	100% (26/26)			
Posterior globe involvement (%)	100% (26/26)			.001
Normal convexity of the optic globe		38.5% (10)	84.6% (22)	
Posterior globe flattening		30.8% (8)	15.4% (4)	
Posterior globe flattening with optic nerve protrusion		30.8% (8)	0.0% (0)	
Extracranial findings				
Proximal emissary vein (mm)	84.6% (11/13)	1.6 (0.6–2.3)	1.6 (0.6–2.4)	.790
Subcutaneous fat thickness in the scalp (mm)	100% (13/13)	4.1 (3.8–4.3)	4.1 (3.5–4.6)	.834
Subcutaneous fat thickness in the neck (mm)	100% (13/13)	8.9 (7.3–11.2)	7.4 (5.9–8.3)	.001

[a] Data are expressed as percentages (No.) or median (interquartile range [25%–75%]).

anesthesia immediately after stent placement (empty sella: $r = 0.625$, $P = .022$; cerebellar ectopia: $r = 0.567$, $P = .043$) and improvement of the transstenotic pressure gradient with the patient under local anesthesia 6 months after stent placement (empty sella: $r = 0.620$, $P = .032$; cerebellar ectopia: $r = 0.662$, $P = .019$). Decreasing optic nerve sheath diameter on the right side moderately correlated with improvement of transstenotic pressure gradient assessed directly after venous sinus stent placement with the patient under general anesthesia ($r = 0.570$; $P = .042$). Correlations between changes in IIH-related MR imaging findings and improvement of intracranial pressure values after venous sinus stent placement are summarized in the Online Supplemental Data.

Decreasing optic nerve sheath diameters on both sides correlated with improvement in nausea/emesis (right optic nerve sheath diameter: $r = 0.592$, $P = .033$; left optic nerve sheath diameter: $r = 0.718$, $P = .006$). Improvement of posterior globe flattening and/or nerve protrusion correlated strongly with improvement of papilledema ($r = 0.775$; $P = .003$). Decreasing empty sella height measurements at 6 months strongly correlated with less improvement of headache intensity assessed with the VAS ($r = -0.661$, $P = .027$). Decreasing optic nerve sheath diameter on the left side also correlated strongly with less improvement of headache intensity (VAS) ($r = -0.606$, $P = .048$). Decreasing diameter of the proximal occipital emissary vein correlated strongly with decreasing headache frequency ($r = 0.741$; $P = .035$). Online Supplemental Data show an overview of clinicoradiologic correlation results.

DISCUSSION

The main findings of this study are as follows: 1) Posterior globe flattening and optic nerve protrusion improved at 6-month follow-up, in line with the favorable clinical outcome observed in all patients. 2) In the same period, there was a reduction of optic nerve sheath diameter, and 3) subcutaneous fat in the neck. 4) However, optic nerve sheath diameter remained above the physiologic threshold of 5 mm 6 months after normalization of the CSF opening pressure and the transstenotic pressure gradient. 5) The other MR imaging findings evaluated did not differ at 6 months from those before treatment. 6) Strong correlations were observed between decreasing optic nerve sheath diameter and improving nausea/emesis, improvement of posterior globe involvement, and decreasing papilledema, decreasing empty sella and improving transstenotic pressure gradient, regressing cerebellar ectopia and improving transstenotic pressure gradient, as well as decreasing diameter of the proximal occipital emissary vein and decreasing headache frequency.

Previous studies have shown the high specificity of IIH-associated MR imaging findings, particularly if >2 of them can be identified concurrently.[3,14] However, data regarding the correlation between IIH-associated MR imaging findings and clinical symptoms are scarce.[6-10] As with CSF analysis, neuroimaging is primarily performed to exclude other diseases affecting the CNS.[1,2] IIH-related symptoms are diverse and mainly nonspecific. Thus, they are often difficult to quantify.[4] Consequently, the assessment of treatment success in patients with IIH requires thorough multidisciplinary monitoring and minimally invasive

procedures such as diagnostic lumbar puncture. Neuroimaging may offer a noninvasive alternative, which could depict treatment success in terms of a decrease of intracranial pressure and the improvement of clinical symptoms.

The results regarding the correlation of orbital MR imaging findings with IIH-related visual symptoms are conflicting.[6,8,10,15] Our data suggest that they resolve with the normalization of intracranial pressure and the improvement in IIH-related symptoms. However, the optic nerve sheath diameter remained above the threshold of 5 mm,[16] which indicates that even orbital findings do not simply vanish 6 months after successful treatment. Our findings differing from those in previous studies may be attributed to the lack of standardized protocols for the assessment of IIH-related MR imaging findings. Measurements may also differ depending on the MR imaging sequences used for evaluation.[17] Automated analysis software packages, which are likely to yield more accurate results than manual measurement techniques, may help solve this problem.[15] Similar to Wong et al,[6] our data suggest that the extent of posterior globe involvement on MR imaging reliably reflects the severity of papilledema. Strong correlation between decreasing optic nerve sheath diameter and relief of nausea may indicate that optic nerve involvement plays a role in the pathogenesis of nausea in patients with IIH.

The significant reduction of subcutaneous fat in the neck 6 months after successful treatment is probably associated with lifestyle changes and an increase in daily activity. However, monitoring of weight loss should be a more effective way of assessing treatment success in this regard.

Despite substantial improvement of clinical symptoms and a significant reduction in intracranial pressure, the other imaging findings did not show any relevant changes. Possible explanations include the following: 1) 2D measurement parameters may not reflect the 3D neuromorphologic changes observed in patients with IIH. 2) IIH-associated MR imaging findings could precede symptom manifestation of IIH, and resolution might be delayed despite clinical improvement. Thus, a 6-month follow-up period may be too short to observe a normalization. 3) Independent factors (ie, genetics) could influence the pace of neuromorphologic recovery. 4) Additional, unrecognized medical conditions may induce neuromorphologic changes similar to IIH (eg, tonsillar ectopia in adult Chiari malformation[18]).

The association between IIH-related MR imaging findings in the pituitary gland/stalk and clinical outcome is unclear.[6-8,10] In this study, the evaluation of the empty sella sign was quantified through repeat measurements intended to increase generalizability and avoid any rater bias. However, many of the above-mentioned problems may also affect our measurements.

None of the patients in our study showed tonsillar ectopia of >5 mm, though Aiken et al[18] found pathologic tonsillar ectopia in 20.9% patients. Given the low sensitivity of this finding,[3] future studies will be needed to determine whether patients with IIH and tonsillar ectopia of >5 mm show resolution after successful treatment. Despite strong correlations between improvement of the transstenotic pressure gradient and decreasing empty sella height as well as resolution of cerebellar ectopia, the marginal differences observed at 6 months suggest that neither of these MR imaging findings show sufficient variation to act as imaging biomarkers for intracranial pressure in clinical routine.

Data on whether IIH is associated with an enlargement or narrowing of the Meckel cave are conflicting.[9,19] Both possibilities may be plausible, depending on the intracranial distribution of CSF pressure. Bialer et al[9] found enlargement, defined as "prominent or increased fluid signal expanding the Meckel cave but not distorting the contours," more often in patients with IIH than in controls, but they did not provide a quantifiable threshold. Degnan and Levy[19] found narrowing of the mediolateral diameter on axial images and suggested a threshold of 4.5 mm. In the present study, median values before and after venous sinus stent placement were below that threshold. However, the width tended to decrease after successful treatment. Assuming that this change occurred in response to the decrease of intracranial pressure, our results suggest that IIH is associated with enlargement of the Meckel cave. Future studies might examine whether patients with IIH share a common feature that is associated with a narrow Meckel cave, but not directly related to IIH.

Slit-like ventricles were reported in some of the earliest studies examining IIH-associated MR imaging findings. However, their incidence is low, and several studies failed to confirm that slit-like ventricles are observed significantly more often in patients with IIH than in controls.[3] Our data suggest that the third ventricle, which tended to be larger at 6-month follow-up, might be more susceptible to changes in intracranial pressure than the lateral ventricles. This possibility could be explained by its central position and overall configuration. The use of automated volume-measuring software might improve the accuracy and reliability of ventricle size assessment.[20]

Hedjoudje et al[13] have suggested that occipital emissary veins are more prominent and frequent in patients with IIH. In support of their findings, we were able to identify the proximal occipital emissary vein in nearly all patients with IIH. However, the median diameter was smaller than that found by Hedjoudje et al and had not changed at 6-month follow-up, suggesting poor reflection of treatment success. On the other hand, a strong correlation between the decreasing proximal occipital emissary vein diameter on imaging and decreasing headache frequency may indicate that unlike the other findings, the occipital emissary vein could reflect the frequency of symptom occurrence. The determination of a reliable threshold in terms of pathologic dilation could increase its diagnostic value. However, applicability in clinical routine is restricted because the occipital emissary vein is not an anatomic structure that can always be identified on imaging.

Our results suggest that IIH-associated MR imaging findings unrelated to the optic nerve have limited value in the assessment of treatment success. The lack of relevant change in most MR imaging findings after 6 months despite evident treatment success may not only suggest that they outlast the symptomatic period but could also indicate that they precede it.[21] Given the increasing rate of obesity and the widespread use of diagnostic neuroimaging worldwide, the number of patients with suspected IIH and the actual incidence of IIH are likely to rise.[22] Future research may focus on developing imaging scores with high sensitivity and specificity capable of justifying minimally invasive procedures (lumbar puncture or venous sinus manometry) in patients with few or

nonspecific symptoms. Detection of IIH in the presymptomatic patients or even in the early phase would allow swift treatment, which might influence the course of disease favorably.

Limitations

Generalizability is limited due to the retrospective, monocentric design of this study. The small number of patients included ($n = 13$) may have caused sampling error. We exclusively examined patients with IIH treated with venous sinus stent placement; however, the evolution of IIH-related MR imaging findings might differ between patients who received conservative or surgical treatment. Clinical data were incomplete because 2 patients were not available for interview and 1 patient was lost to ophthalmologic follow-up. Only 2 patients showed persistence of at least 1 IIH-related symptom after venous sinus stent placement. Thus, this study provides no data regarding the evolution of IIH-related MR imaging findings in patients who had an unfavorable outcome. There was no healthy control cohort, which could have helped to establish a physiologic variation range for IIH-associated MR imaging findings. There was only a 6-day follow-up MR imaging for patient 4. This patient was also the only one showing improvement but not complete resolution of posterior globe involvement; this issue may, therefore, have been due to the short follow-up period. Venous sinus stenosis is the most sensitive MR imaging finding associated with IIH.[3] However, due to device-related artifacts in the ROI, it was not possible to evaluate IIH stenosis reliably on follow-up MR imaging after venous sinus stent placement.

CONCLUSIONS

Most IIH-related MR imaging findings persist long after normalization of intracranial pressure and clinical improvement. However, MR imaging findings related to the optic nerve may reflect treatment success.

ACKNOWLEDGMENTS

We thank Susan Kaplan for editorial assistance.

Disclosures: Johannes Kaesmacher—*UNRELATED*: *Grants/Grants Pending*: SAMW/Bangerter Foundation, Clinical Trials Unit, Bern. Christoph J. Schankin—*UNRELATED*: *Consultancy*: Novartis, Eli Lilly, Teva Pharmaceuticals, Allergan, Almirall, MindMed; *Employment*: Zynnon; *Expert Testimony*: Teva Pharmaceuticals; *Grants/Grants Pending*: Novartis; *Payment for Lectures Including Service on Speakers Bureaus*: Novartis, Eli Lilly, Teva Pharmaceuticals, Allergan, Almirall, Amgen, MindMed, Grünenthal; *Payment for Development of Educational Presentations*: Eli Lilly; *Stock/Stock Options*: Zynnon; *Travel/Accommodations/Meeting Expenses Unrelated to Activities Listed*: Teva Pharmaceuticals. Andreas Raabe—*UNRELATED*: *Employment*: Inselspital, Neurochirurgische Universitätsklinik. Jan Gralla—*UNRELATED*: *Grants/Grants Pending*: Medtronic, *Comments*: stroke trials: Global Principal Investigator of STAR and SWIFT DIRECT (Medtronic), Consultancy*; *Other*: Swiss National Foundation, *Comments*: Swiss National Foundation grant for MRI in stroke.* *Money paid to the institution.

REFERENCES

1. Friedman DI, Liu GT, Digre KB. **Revised diagnostic criteria for the pseudotumor cerebri syndrome in adults and children.** *Neurology* 2013;81:1159–65 CrossRef Medline
2. Holbrook J, Saindane AM. **Imaging of intracranial pressure disorders.** *Neurosurgery* 2017;80:341–54 CrossRef Medline
3. Kwee RM, Kwee TC. **Systematic review and meta-analysis of MRI signs for diagnosis of idiopathic intracranial hypertension.** *Eur J Radiol* 2019;116:106–15 CrossRef Medline
4. Markey KA, Mollan SP, Jensen RH, et al. **Understanding idiopathic intracranial hypertension: mechanisms, management, and future directions.** *Lancet Neurol* 2016;15:78–91 CrossRef Medline
5. Mollan SP, Ali F, Hassan-Smith G, et al. **Evolving evidence in adult idiopathic intracranial hypertension: pathophysiology and management.** *J Neurol Neurosurg Psychiatry* 2016;87:982–92 CrossRef Medline
6. Wong H, Sanghera K, Neufeld A, et al. **Clinico-radiological correlation of magnetic resonance imaging findings in patients with idiopathic intracranial hypertension.** *Neuroradiology* 2020;62:49–53 CrossRef Medline
7. Zagardo MT, Cail WS, Kelman SE, et al. **Reversible empty sella in idiopathic intracranial hypertension: an indicator of successful therapy?** *AJNR Am J Neuroradiol* 1996;17:1953–56 Medline
8. Saindane AM, Bruce BB, Riggeal BD, et al. **Association of MRI findings and visual outcome in idiopathic intracranial hypertension.** *AJR Am J Roentgenol* 2013;201:412–18 CrossRef Medline
9. Bialer OY, Rueda MP, Bruce BB, et al. **Meningoceles in idiopathic intracranial hypertension.** *Am J Roentgenol* 2014;202:608–13 CrossRef Medline
10. Batur Caglayan HZ, Ucar M, Hasanreisoglu M, et al. **Magnetic resonance imaging of idiopathic intracranial hypertension: before and after treatment.** *J Neuroophthalmol* 2019;39:324–29 CrossRef Medline
11. Fargen KM, Spiotta AM, Hyer M, et al. **Comparison of venous sinus manometry gradients obtained while awake and under general anesthesia before venous sinus stenting.** *J Neurointerv Surg* 2017;9:990–93 CrossRef Medline
12. Fargen KM, Liu K, Garner RM, et al. **Recommendations for the selection and treatment of patients with idiopathic intracranial hypertension for venous sinus stenting.** *J Neurointerv Surg* 2018;10:1203–08 CrossRef Medline
13. Hedjoudje A, Piveteau A, Gonzalez-Campo C, et al. **The occipital emissary vein: a possible marker for pseudotumor cerebri.** *AJNR Am J Neuroradiol* 2019;40:973–78 CrossRef
14. Mallery RM, Rehmani OF, Woo JH, et al. **Utility of magnetic resonance imaging features for improving the diagnosis of idiopathic intracranial hypertension without papilledema.** *J Neuroophthalmol* 2019;39:299–307 CrossRef Medline
15. Alperin N, Bagci AM, Lam BL, et al. **Automated quantitation of the posterior scleral flattening and optic nerve protrusion by MRI in idiopathic intracranial hypertension.** *AJNR Am J Neuroradiol* 2013;34:2354–59 CrossRef Medline
16. Caffery TS, Perret JN, Musso MW, et al. **Optic nerve sheath diameter and lumbar puncture opening pressure in nontrauma patients suspected of elevated intracranial pressure.** *Am J Emerg Med* 2014;32:1513–15 CrossRef Medline
17. Golden E, Krivochenitser R, Mathews N, et al. **Contrast-enhanced 3D-FLAIR imaging of the optic nerve and optic nerve head: novel neuroimaging findings of idiopathic intracranial hypertension.** *AJNR Am J Neuroradiol* 2019;40:334–39 CrossRef Medline
18. Aiken AH, Hoots JA, Saindane AM, et al. **Incidence of cerebellar tonsillar ectopia in idiopathic intracranial hypertension: a mimic of the Chiari I malformation.** *AJNR Am J Neuroradiol* 2012;33:1901–06 CrossRef Medline
19. Degnan AJ, Levy LM. **Narrowing of Meckel's cave and cavernous sinus and enlargement of the optic nerve sheath in pseudotumor cerebri.** *J Comput Assist Tomogr* 2011;35:308–12 CrossRef Medline
20. Yepes-Calderon F, Nelson MD, McComb JG. **Automatically measuring brain ventricular volume within PACS using artificial intelligence.** *PLoS One* 2018;13:e0193152–14 CrossRef Medline
21. Chan W, Green AL, Mishra A, et al. **Transverse venous sinus stenosis in idiopathic intracranial hypertension: a prospective pilot study.** *Can J Ophthalmol* 2020;55:401–05 CrossRef Medline
22. Kilgore KP, Lee MS, Leavitt JA, et al. **Re-evaluating the incidence of idiopathic intracranial hypertension in an era of increasing obesity.** *Ophthalmology* 2017;124:697–700 CrossRef Medline

Dual-Energy Parathyroid 4D-CT: Improved Discrimination of Parathyroid Lesions from Thyroid Tissue Using Noncontrast 40-keV Virtual Monoenergetic Images

P.M. Bunch, A.A. Pavlina, M.E. Lipford, and J.R. Sachs

ABSTRACT

BACKGROUND AND PURPOSE: In parathyroid CT, a noncontrast phase aids discrimination of parathyroid lesions (not iodine-containing) from thyroid tissue (iodine-containing). When thyroid iodine is pathologically diminished, this differentiation is difficult with standard CT. Because the attenuation of an element is maximal near its K-edge (iodine = 33.2 keV), we hypothesized that dual-energy CT 40-keV virtual monoenergetic images will accentuate thyroid iodine relative to standard images, improving the differentiation of thyroid from parathyroid lesions. Our purpose was to test this hypothesis through quantitative assessment of Hounsfield unit attenuation and contrast-to-noise on dual-energy CT standard (70-keV) and 40-keV noncontrast images.

MATERIALS AND METHODS: For this retrospective study including 20 dual-energy parathyroid CTs, we used an ROI-based analysis to assess the attenuation of thyroid tissue, parathyroid lesions, and sternocleidomastoid muscle as well as corresponding contrast-to-noise on standard and 40- keV noncontrast images. Wilcoxon signed rank tests were performed to compare differences between 70 and 40 keV.

RESULTS: Absolute and percentage increases in attenuation at 40 keV were significantly greater for thyroid gland than for parathyroid lesions and sternocleidomastoid muscle ($P < .001$ for all). Significant increases in the contrast-to-noise of thyroid relative to parathyroid lesions (median increase, 0.8; $P < .001$) and relative to sternocleidomastoid muscle (median increase, 1.3; $P < .001$) were observed at 40 keV relative to 70 keV.

CONCLUSIONS: Forty-kiloelectron volt virtual monoenergetic images facilitate discrimination of parathyroid lesions from thyroid tissue by significantly increasing thyroid attenuation and associated contrast-to-noise. These findings are particularly relevant for parathyroid lesions that exhibit isoattenuation to the thyroid on parathyroid CT arterial and venous phases and could, therefore, be missed without the noncontrast phase.

ABBREVIATIONS: CNR = contrast-to-noise ratio; DECT = dual-energy CT; IQR = interquartile range; VMI = virtual monoenergetic images

Parathyroid 4D-CT is a powerful tool for localizing abnormal parathyroid tissue in the setting of primary hyperparathyroidism.[1] Localization of a single adenoma facilitates minimally invasive parathyroidectomy and its associated benefits,[2,3] whereas localization of multigland disease aids bilateral neck exploration. The optimal number of CT phases is undetermined, but the most commonly used protocol involves 3 CT acquisitions of the neck and upper chest, including noncontrast, arterial, and venous phases.[4]

Parathyroid lesions, exophytic thyroid nodules, and lymph nodes may appear morphologically identical on CT.[5] Although the classic postcontrast enhancement pattern of parathyroid adenomas is well-described (hyperattenuating relative to thyroid on arterial phase images; hypoattenuating [washout] relative to thyroid on venous phase images), a challenge for the radiologist is that this classic pattern is seen in only 20% of adenomas.[6] Moreover, it is estimated that up to 25% of parathyroid lesions could be missed without the noncontrast CT phase.[6] Parathyroid lesions are always lower in attenuation than the normal, iodine-containing thyroid gland on noncontrast images.[1] However, another challenge for the radiologist is that thyroid disease and primary hyperparathyroidism frequently coexist,[7,8] and chronic thyroid disease (eg, Hashimoto disease) can result in abnormal hypoattenuation of the thyroid gland related to diminished iodine content (Fig 1).[1] In such cases, using the noncontrast images to differentiate parathyroid lesions from the abnormally hypoattenuating thyroid gland is more difficult.

Numerous applications of dual-energy CT (DECT) have been described for neuroradiology practice.[9] Low-keV (eg, 40 keV)

Received January 15, 2021; accepted after revision June 8.

From the Department of Radiology, Wake Forest School of Medicine, Winston Salem, North Carolina.

A scientific abstract related to the work represented in this article was presented at: Annual Meeting of the American Society of Neuroradiology, May 22–26. 2021; Virtual.

Please address correspondence to Paul M. Bunch, MD, Department of Radiology, Wake Forest School of Medicine, Medical Center Boulevard, Winston Salem, NC 27157; e-mail: paul.m.bunch@gmail.com; @pbunchmd

http://dx.doi.org/10.3174/ajnr.A7265

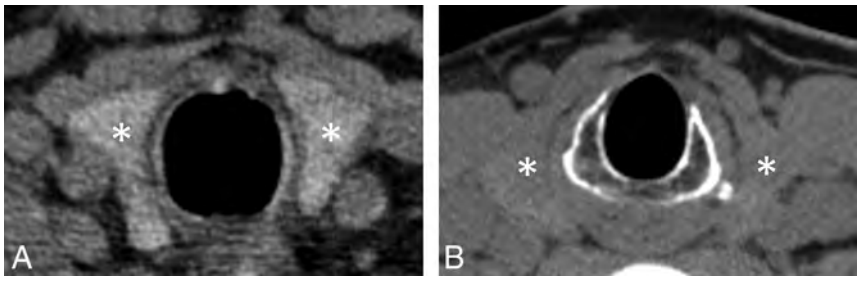

FIG 1. Axial, noncontrast, single-energy CT image (*A*) obtained in a patient with normal thyroid function demonstrates the normal hyperattenuating appearance of the thyroid gland (*asterisks*, *A*) relative to adjacent soft tissue. When present, this normal hyperattenuating appearance enables differentiation of parathyroid lesions adjacent to the thyroid gland from exophytic thyroid tissue. In contrast, the axial noncontrast single-energy CT image (*B*) obtained in a patient with long-standing Hashimoto disease demonstrates an iodine-deficient thyroid gland (*asterisks*, *B*), appearing nearly isodense to muscle, which renders differentiation of parathyroid lesions from exophytic thyroid tissue more difficult.

virtual monoenergetic imaging is an application of dual-energy CT that can be used to accentuate the conspicuity of enhancing masses on neck CT[10] as well as to increase arterial attenuation and the contrast-to-noise ratio (CNR) on CT angiography of the head and neck.[11] These applications of low-kiloelectron volt virtual monochromatic images (VMI) related to iodinated contrast media are possible because the CT attenuation of an element is maximal at or slightly above the K-edge of the element, and the K-edge of iodine is 33.2 keV.[9,12] It would, therefore, be expected that low-kiloelectron volt VMI could also be used to accentuate the attenuation of native thyroid iodine on noncontrast images (Fig 2), though formal investigation is warranted.

We hypothesized that 40-keV VMI will increase the conspicuity of thyroid tissue relative to nonthyroid tissue (eg, parathyroid lesions, muscle) on the noncontrast phase of a DECT parathyroid 4D-CT protocol, thereby facilitating discrimination of parathyroid lesions from exophytic thyroid tissue. The purpose of this study was to test our hypothesis through the quantitative assessment of Hounsfield unit attenuation and CNR on standard (70-keV) noncontrast VMI and 40-keV noncontrast VMI.

MATERIALS AND METHODS

Subjects

For this retrospective, Health Insurance Portability and Accountability Act–compliant, institutional review board–approved study, all parathyroid 4D-CT examinations performed at our institution between March 2020 and November 2020 were retrospectively reviewed ($n = 35$). Inclusion criteria were the following: 1) DECT acquisition used, 2) parathyroidectomy performed, 3) largest pathologically-proved parathyroid lesion measured at least 1 cm in the long axis, and 4) no prior thyroidectomy. Examinations not meeting all inclusion criteria were excluded.

Medical Record Review

The following data were obtained from the electronic medical record for the study cohort: age, sex, medical history of hypothyroidism, parathyroid surgery operative notes, and pathology reports for parathyroid surgical specimens.

Image Acquisition

All parathyroid 4D-CT examinations were performed on a Revolution Apex CT system (GE Healthcare) using a dual-energy acquisition. The CT acquisition parameters were as follows: 80-/140-kV(peak) simultaneous acquisition, 250–445 mA, 0.516:1 pitch, 0.5-second rotation time, 40-mm detector coverage, 2.5-mm helical section thickness, and 2.5-mm interval for each of 3 CT phases (noncontrast, 30-second postcontrast, and 60-second postcontrast). Multiplanar reconstructions of each CT phase were generated, including 0.625-mm axial 70-keV VMI and 0.625-mm axial 40-keV VMI of the noncontrast phase (reconstruction method: adaptive statistical iterative reconstruction V, 20%; convolution kernel: standard; display FOV: 22 cm for 70- and 40- keV image sets). The volume CT dose index for each CT phase ranged between 14 and 24 mGy (32-cm phantom). For comparison, a recently reported single-energy protocol performed at 140 kV(p) resulted in a volume CT dose index range of 19 to 24 mGy (32-cm phantom).[1]

Image Analysis

2D circular ROIs were drawn by a neuroradiology fellow on the 0.625-mm axial 70- and 40-keV images using our institution's PACS. An attending neuroradiologist with 4 years' experience interpreting parathyroid 4D-CT reviewed and verified all ROIs placed by the neuroradiology fellow, optimizing ROI size and position if needed. The image sets were linked so that identical ROIs could be drawn in the same location on both the 70- and 40-keV image sets. In each patient, ROIs were placed in the right and left lobes of the thyroid gland, within the right and left sternocleidomastoid muscles, within the subcutaneous fat of the midline posterior neck, and within the largest pathologically-proved parathyroid lesion (adenoma or hyperplasia). Care was taken with the placement of all ROIs to avoid confounding structures, such as thyroid nodules and blood vessels. The ROI size for the thyroid lobes and sternocleidomastoid muscles was 0.5 cm^2. ROI size for subcutaneous fat was 2.0 cm^2 in most ($n = 18$) patients, though by necessity, it was 1.0 cm^2 in 2 very thin patients. The ROI size for parathyroid lesions ranged between 0.1 and 0.83 cm^2 (median, 0.20 cm^2). The mean Hounsfield unit attenuation (SD) was recorded for each ROI.

Absolute differences in Hounsfield unit attenuation and percentage change were calculated for thyroid gland, parathyroid lesions, and sternocleidomastoid muscles at 40 keV compared with 70 keV.

The CNR of the thyroid gland relative to pathologically-proved parathyroid lesions ($CNR_{thy/par}$) of at least 1 cm was calculated using the following formula: $(ROI_{thy} - ROI_{par})/SD$, where ROI_{thy} is the mean Hounsfield unit attenuation of the thyroid lobes, ROI_{par} is the mean Hounsfield unit attenuation of the parathyroid lesion, and SD is the Hounsfield unit attenuation SD of subcutaneous fat.

The CNR of the thyroid gland relative to the sternocleidomastoid muscles ($CNR_{thy/scm}$) was calculated for each patient using the

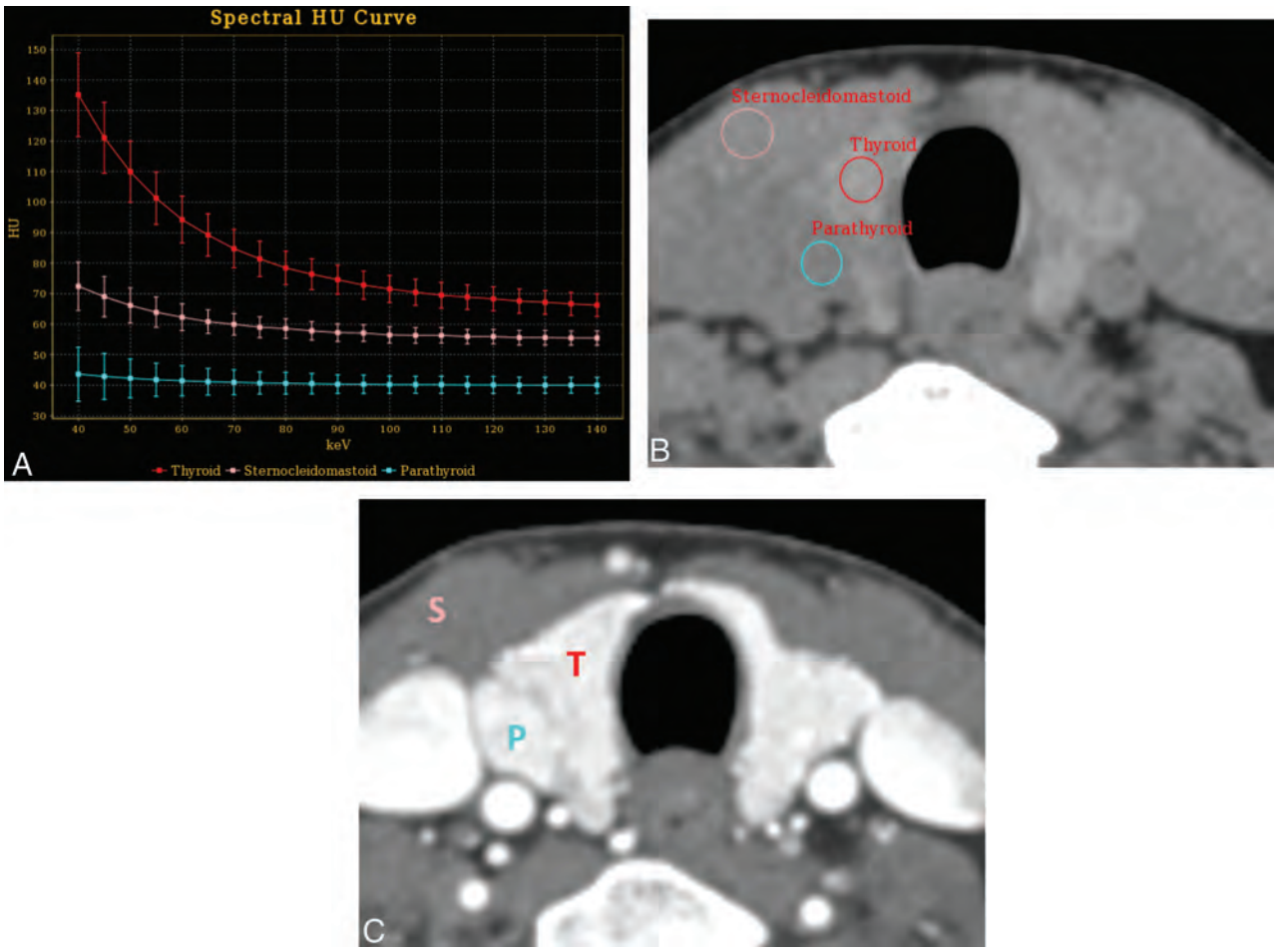

FIG 2. Virtual monoenergetic spectral curves (*A*) demonstrate noncontrast Hounsfield unit attenuation as a function of kiloelectron volts for the thyroid gland (red), sternocleidomastoid muscle (pink), and pathologically-proved parathyroid adenoma (blue) generated from ROIs placed on an axial noncontrast 70-keV virtual monoenergetic image (*B*) in a 56-year-old woman with primary hyperparathyroidism. The noncontrast Hounsfield unit attenuation difference between thyroid and the other tissues of interest is maximal at 40 keV. Corresponding axial arterial phase CT image (*C*) is also provided for comparison. T indicates thyroid; S, sternocleidomastoid; P, parathyroid.

Table 1: Characteristics of the study group

Characteristics	
Age (median) (range) (yr)	63 (33–81)
Sex	
Male	9
Female	11
Operative findings	
Single-gland disease	16
Multigland disease	4
Concurrent hypothyroidism	
Yes	3
No	17

following formula: $(ROI_{thy} - ROI_{scm})/SD$, where ROI_{scm} is the mean Hounsfield unit attenuation of the sternocleidomastoid muscles.

Statistical Analysis

Descriptive analyses were performed using absolute and relative frequencies for categoric variables and median and interquartile range (IQR) for continuous variables, respectively. The Wilcoxon signed rank test was used to compare differences in Hounsfield unit attenuation, CNR, and image noise between the 70- and 40-keV images. All analyses were performed with Excel 2016 (Microsoft) and Matlab (MathWorks). A P value $< .05$ indicated a statistically significant difference.

RESULTS

Subjects

Of the 35 parathyroid 4D-CT examinations reviewed, 3 examinations were excluded because a DECT acquisition was not used, 8 were excluded because the patient had not yet undergone parathyroidectomy, 2 were excluded because the largest pathologically-proved parathyroid lesion did not meet the 1-cm minimum size threshold of this study, and 2 were excluded due to prior thyroidectomy. This process yielded 20 parathyroid 4D-CT examinations in the study cohort. Characteristics of the study group are summarized in Table 1.

Histopathologic analysis of the surgical specimens from these 20 patients revealed a total of 28 pathologically-proved parathyroid lesions, 26 (93%) of which were identified and described on preoperative CT. The 2 parathyroid lesions not identified on preoperative CT both measured <1 cm in maximum dimension and occurred in 2 different patients with multiglandular disease. In

Table 2: Summary of differences in Hounsfield unit attenuation, contrast-to-noise, and image noise at 70 and 40 keV

	40 keV (Median) (IQR)	70 keV (Median) (IQR)	Difference (40-70 keV) (Median) (IQR)	*P*	Comparison (*P*)
Hounsfield unit attenuation					
Thyroid					
Absolute (HU)	158 (133–264)	84 (74–113)	+67 (55–142)	<.001	Par
				<.001	SCM
% Change			+89% (66–123)	<.001	Par
				<.001	SCM
Parathyroid					
Absolute (HU)	42 (29–59)	32 (22–41)	+9 (4–17)	<.001	Thy
				.22	SCM
% Change			+29% (13–58)	<.001	Thy
				.09	SCM
Sternocleidomastoid					
Absolute (HU)	67 (63–75)	57 (54–59)	+11 (10–16)	<.001	Thy
				.22	Par
% Change			+22% (17–28)	<.001	Thy
				.09	Par
Contrast-to-noise					
Thy/Par	4.7 (3.3–6.0)	3.8 (2.4–4.8)	+0.8 (0.2–1.2)	<.001	
Thy/SCM	3.6 (1.7–5.0)	2.3 (0.9–3.1)	+1.3 (0.7–1.9)	<.001	
Image noise (HU)	32 (23–37)	16 (12–19)	+14 (11–20)	<.001	

Note:—Thy indicates thyroid; Par, parathyroid; SCM, sternocleidomastoid.

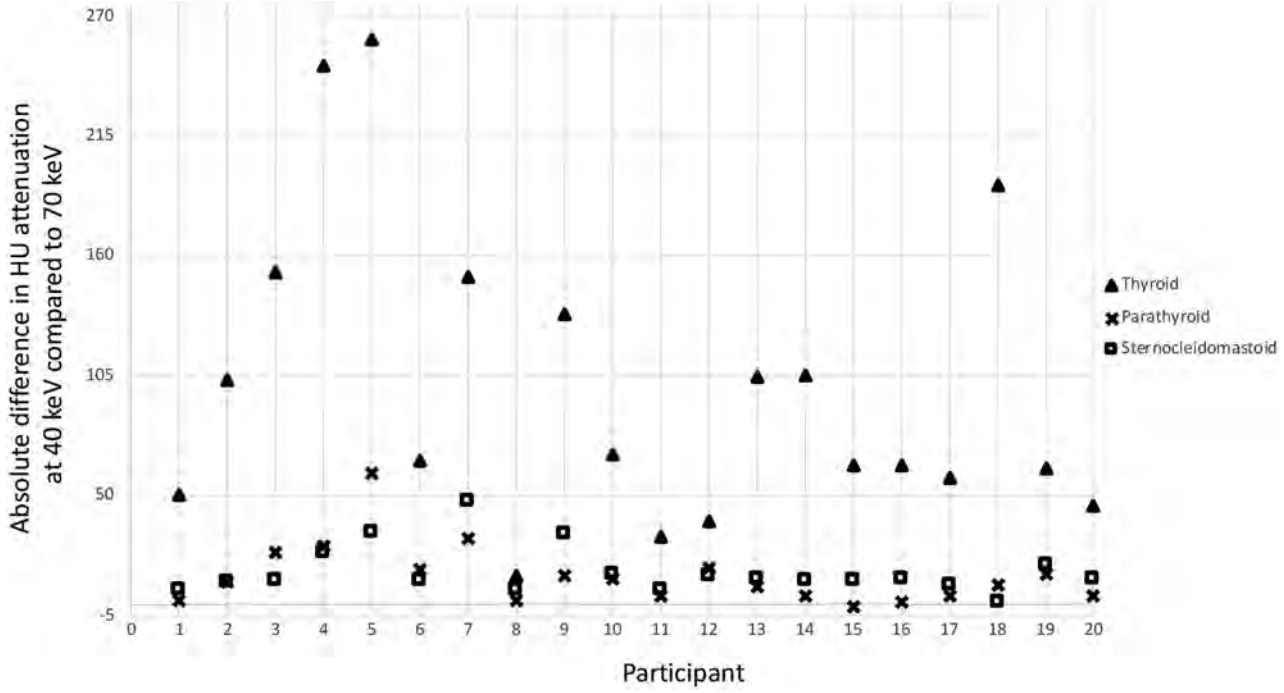

FIG 3. Dot plot demonstrates the absolute difference in Hounsfield unit attenuation between 40 keV and 70 keV for thyroid gland (*triangle*), parathyroid lesions (*X*), and sternocleidomastoid muscles (*square*) in each of the 20 study participants.

one of these patients, 2 of 3 proved parathyroid lesions were described on preoperative CT, and 3 of 4 proved parathyroid lesions were described on preoperative CT in the other.

Image Analysis

Quantitative data related to Hounsfield unit attenuation and percentage change, CNR, and image noise are summarized in Table 2.

Attenuation and Percentage Change. Thyroid gland, parathyroid lesion, and sternocleidomastoid muscle Hounsfield unit attenuation increased at 40 keV compared with 70 keV in 20/20 (100%) patients, 19/20 (95%) patients, and 20/20 (100%) patients, respectively. For all 20 patients, the absolute Hounsfield unit increase (Fig 3) and percentage Hounsfield unit increase at 40 keV relative to 70 keV was greater for thyroid than for parathyroid lesions and for the sternocleidomastoid muscles. One parathyroid lesion

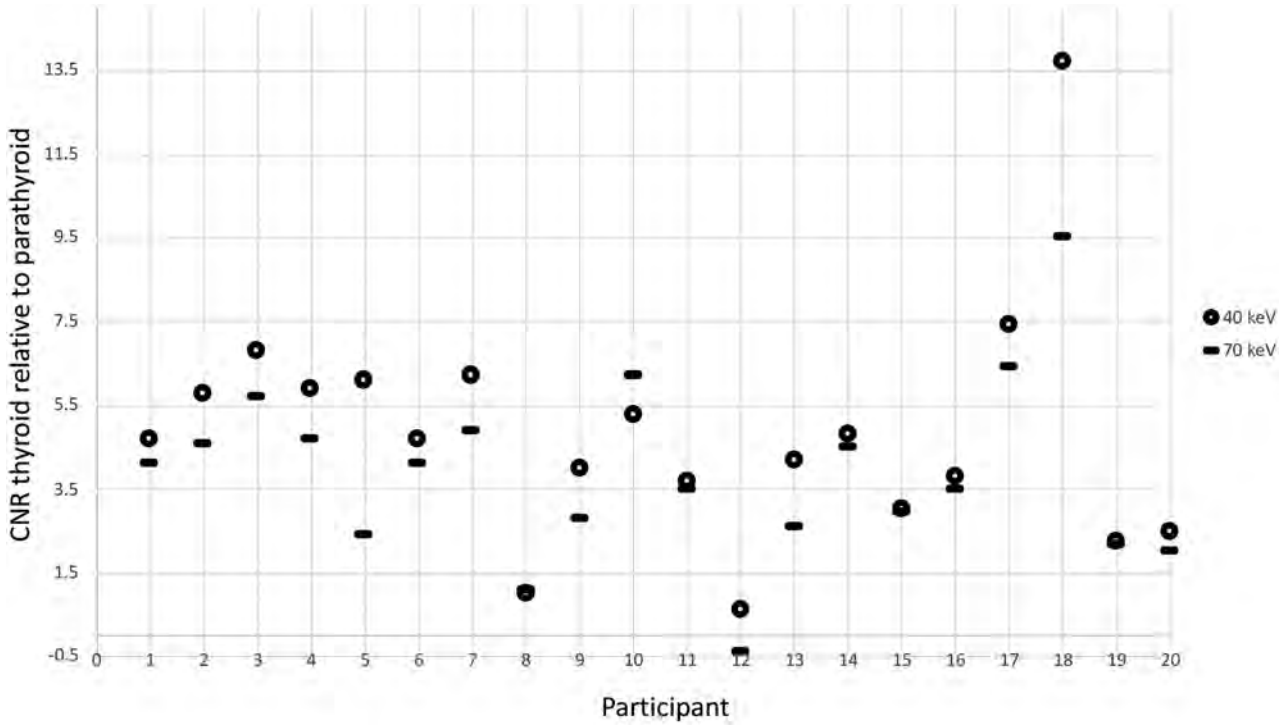

FIG 4. Dot plot demonstrates contrast-to-noise ratios between the thyroid gland and pathologically-proved parathyroid lesions at 40 keV (*circle*) and 70 keV (*line*) for each of the 20 study participants.

(participant No. 15, Fig 3) demonstrated a 5% decrease in Hounsfield unit attenuation at 40 keV compared with 70 keV.

The median absolute difference in Hounsfield unit attenuation at 40 keV compared with 70 keV was +67 HU (IQR, 55–142 HU) for the thyroid gland, +9 HU (IQR, 4–17 HU) for parathyroid lesions, and +11 HU (IQR, 10–16 HU) for the sternocleidomastoid muscles. The observed differences in absolute Hounsfield unit attenuation increase for thyroid compared with parathyroid lesions ($P < .001$) and sternocleidomastoid muscles ($P < .001$) were statistically significant. There was no significant difference in the absolute Hounsfield unit increase between parathyroid lesions and sternocleidomastoid muscles ($P = .22$).

The median percentage difference in Hounsfield unit attenuation at 40 keV compared with 70 keV was +89% (IQR, +66% to +123%) for the thyroid gland, +29% (IQR, +13% to +58%) for parathyroid lesions, and +22% (IQR, +17% to +28%) for the sternocleidomastoid muscles. The observed differences in the percentage increase in Hounsfield unit attenuation for thyroid compared with parathyroid lesions ($P < .001$) and sternocleidomastoid muscles ($P < .001$) were statistically significant. There was no significant difference in the percentage increase in Hounsfield unit attenuation between parathyroid lesions and sternocleidomastoid muscles ($P = .09$).

Contrast-to-Noise. The CNR of the thyroid gland relative to parathyroid lesions ($CNR_{thy/par}$) increased on 40-keV VMI compared with standard 70-keV VMI in 18/20 (90%) patients (Fig 4). The median $CNR_{thy/par}$ at 40 keV was 4.7 (IQR, 3.3–6.0) compared with 3.8 (IQR, 2.4–4.8) at 70 keV, and the median increase in $CNR_{thy/par}$ at 40 keV compared with 70 keV was 0.8 (IQR, 0.2–1.2; $P < .001$). $CNR_{thy/par}$ decreased at 40 keV relative to 70 keV in participants Nos. 8 and 10 (Fig 4), one of whom (participant No. 8) had a minimal increase in thyroid attenuation at 40 keV and known hypothyroidism. In the other (participant No. 10), the observed percentage increase in thyroid attenuation at 40 keV relative to 70 keV was similar (rather than disproportionate) to the percentage increase in parathyroid lesion attenuation.

The CNR of the thyroid gland relative to the sternocleidomastoid muscles ($CNR_{thy/scm}$) increased on 40-keV VMI compared with standard 70-keV VMI in 20/20 (100%) patients. The median $CNR_{thy/scm}$ at 40 keV was 3.6 (IQR, 1.7–5.0) compared with 2.3 (IQR, 0.9–3.1) at 70 keV, and the median increase in $CNR_{thy/scm}$ at 40 keV compared with 70 keV was 1.3 (IQR, 0.7–1.9; $P < .001$).

Image Noise. Image noise, defined as the Hounsfield unit attenuation SD of subcutaneous fat for the purposes of this study, increased at 40 keV compared with 70 keV in 20/20 (100%) patients. The median image noise at 40 keV was 32 HU (IQR, 23–37 HU) compared with 16 HU (IQR, 12–19 HU) at 70 keV, and the median noise increase at 40 keV compared with 70 keV was 14 HU (IQR, 11–20 HU; $P < .001$).

DISCUSSION

Numerous applications of DECT have been described in head and neck imaging.[10,13-21] Previously published studies of dual-energy parathyroid CT have primarily focused on the potential for radiation dose reduction using virtual noncontrast images to eliminate the standard noncontrast phase[22,23] and on describing quantitative dual-energy characteristics of parathyroid adenomas, thyroid parenchyma, and lymph nodes on postcontrast phases.[24,25] The authors are aware of 1 previous study that evaluated dual-energy

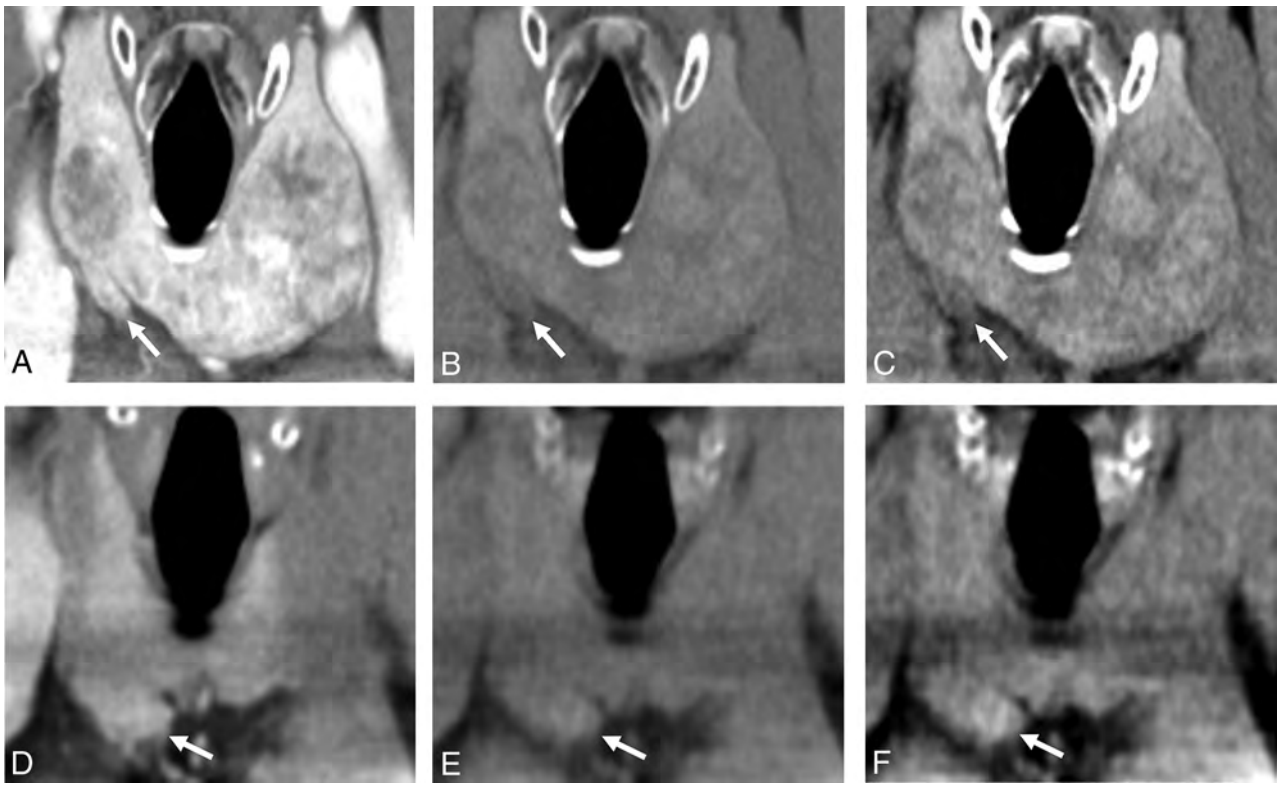

FIG 5. Coronal arterial phase (*A*), noncontrast 70-keV (*B*), and noncontrast 40-keV (*C*) images demonstrate a pathologically-proved right inferior parathyroid adenoma (*arrows*). Because the parathyroid adenoma appears isodense to the adjacent thyroid gland on the arterial phase image, it is uncertain whether the finding represents a parathyroid lesion or exophytic thyroid tissue. The parathyroid adenoma appears slightly hypoattenuating to the thyroid parenchyma on the standard (70-keV) noncontrast image; however, this attenuation difference is accentuated on the 40-keV image, indicating that the finding represents a parathyroid lesion rather than exophytic thyroid tissue. In contrast, coronal arterial phase (*D*), noncontrast 70-keV (*E*), and noncontrast 40-keV (*F*) images from a different patient demonstrate exophytic thyroid tissue (*arrows*) arising from the lower pole of the right thyroid lobe. On the arterial phase image alone, it is uncertain whether the finding represents exophytic thyroid tissue or a right inferior parathyroid lesion. Although the finding is isodense relative to the thyroid gland on the 70-keV noncontrast image, some uncertainty persists because of the nearly isoattenuating appearance of the thyroid gland relative to adjacent muscle, suggesting decreased iodine content from chronic thyroid disease. The 40-keV noncontrast image demonstrates substantially increased attenuation of the finding comparable with the increased attenuation of the remainder of the thyroid gland, indicating that the finding of interest represents exophytic thyroid tissue rather than a parathyroid lesion. In this patient, a biochemical cure was achieved with removal of a pathologically-proved parathyroid adenoma identified elsewhere in the neck (not shown), confirming that the finding depicted in images *D*, *E*, and *F* is indeed not a parathyroid lesion. Section thickness (2 mm), window level (40 HU), and window width (400 HU) are identical for all 6 images.

noncontrast parathyroid CT images obtained on a dual-source system using 90-keV, 150-keV, and mixed images (dual-energy composition factor, 0.8), but 40-keV VMI were not specifically evaluated in this previous investigation.[25]

Our study compared the conspicuity of thyroid tissue relative to pathologically-proved parathyroid lesions and muscle on 40-keV noncontrast VMI and standard 70-keV noncontrast VMI obtained on a fast-kiloelectron volt switching system and found statistically significant increase in CNR at 40 keV compared with the 70 keV standard. These findings support our hypothesis that noncontrast 40-keV VMI facilitate the differentiation of parathyroid lesions from exophytic thyroid tissue by accentuating the attenuation of iodine within thyroid tissue that is absent from parathyroid tissue (Fig 5). Although the attenuation of thyroid, parathyroid, and muscle generally increased at 40 keV relative to 70 keV, the increase in attenuation of the thyroid gland was disproportionately greater in most subjects because of the proximity to the K-edge (33.2 keV) of iodine. Although the cause of the observed 5% decrease in Hounsfield unit attenuation of 1 parathyroid adenoma at 40 keV compared with 70 keV is uncertain, this finding may relate to intralesional fat deposition,[1] given that the attenuation of fat is known to decrease at low kiloelectron volts.[12]

Localization confidence is highly desirable in parathyroid imaging. Not uncommonly, multiple parathyroid imaging studies are requested in an attempt to maximize the surgeon's confidence in localization through concordant imaging results. The degree of diagnostic confidence or lack thereof carries implications for the operative plan, and in certain high-risk scenarios (eg, the reoperative neck), it may determine whether an operation is offered at all.[1] Although radiologists' confidence was not directly tested in this study, it has been our clinical experience in interpreting dual-energy parathyroid CT that noncontrast 40-keV VMI facilitate more confident differentiation of parathyroid lesions from exophytic thyroid tissue. Some authors have advocated for omitting the true noncontrast phase as nonessential.[23,26,27] However, in our experience, the true noncontrast phase is indispensable because it improves sensitivity by enabling detection of parathyroid lesions

that would be otherwise overlooked (eg, abutting and isoattenuating to thyroid on contrast-enhanced phases), and it decreases false-positive candidate lesions by facilitating accurate characterization of exophytic thyroid tissue on the basis of intrinsic iodine content. To minimize adverse effects of the additional 40-keV VMI series on workflow, the 40-keV VMI are automatically generated and sent to the PACS at our institution, thus requiring no manual processing by the radiologist.

There are limitations to this study. First, a small number of patients were included in the cohort, which relates to our recent implementation of dual-energy parathyroid 4D-CT and our requirement that only data from pathologically-proved parathyroid lesions be used. Second, all parathyroid 4D-CTs were acquired with a single vendor's DECT system so that our findings are not necessarily generalizable to other vendors' DECT systems, though the underlying physical principles should be the same. This study investigated the potential value of noncontrast 40-keV VMI for the focused task of determining whether a tissue of interest is likely to be thyroid, and it was not intended to be a comprehensive assessment of image quality.

Note that image noise, as estimated by the Hounsfield unit attenuation SD of subcutaneous fat, was significantly higher at 40 keV. This phenomenon of increased noise on 40-keV VMI has also been observed in a DECT phantom study[28] and is in keeping with the progressive increase in image noise observed on low-kiloelectron volt VMI described in a previous study of neck DECT examinations also performed using a fast-kiloelectron volt switching system.[29] In the future, image noise in 40- keV VMI could likely be decreased with the addition of noise-reducing reconstruction algorithms;[30] however, such algorithms were not a part of the current study. Furthermore, it is possible that additional gains in CNR could be achieved at a kiloelectron volt intermediate between 40 and 70 keV by balancing the benefit of the disproportionate increase in thyroid iodine attenuation at a low kiloelectron volt against the cost of increased noise. Although in our clinical experience the noncontrast 40-keV VMI increased the radiologist's interpretation confidence, the overall assessment should continue to incorporate other candidate parathyroid lesion features (eg, morphology, enhancement characteristics, polar vessel sign). Finally, whether there is a positive impact of 40-keV VMI on interpretation accuracy remains undetermined.

CONCLUSIONS

Compared with standard (70-keV VMI) noncontrast images, 40-keV VMI significantly increase Hounsfield unit attenuation and CNR of thyroid tissue relative to parathyroid lesions and sternocleidomastoid muscle. Therefore, 40-keV VMI facilitate differentiation of parathyroid lesions from exophytic thyroid tissue on noncontrast images, which is particularly useful for the subset of parathyroid lesions that exhibit isoattenuation to thyroid parenchyma on the arterial and venous phases of a parathyroid 4D-CT protocol and could be missed without the noncontrast CT phase.

REFERENCES

1. Bunch PM, Randolph GW, Brooks JA, et al. **Parathyroid 4D CT: what the surgeon wants to know.** *Radiographics* 2020;40:1383–94 CrossRef Medline
2. Perrier N, Parangi S. **Minimally invasive single gland parathyroid exploration.** In: Randolph G, ed. *Surgery of the Thyroid and Parathyroid Glands*. 2nd ed. Elsevier 2012; 580–89
3. Minisola S, Cipriani C, Diacinti D, et al. **Imaging of the parathyroid glands in primary hyperparathyroidism.** *Eur J Endocrinol* 2016;174: D1–8 CrossRef Medline
4. Hoang JK, Williams K, Gaillard F, et al. **Parathyroid 4D-CT: multi-institutional international survey of use and trends.** *Otolaryngol Head Neck Surg* 2016;155:956–60 CrossRef Medline
5. Bunch PM, Kelly HR. **Preoperative imaging techniques in primary hyperparathyroidism: a review.** *JAMA Otolaryngol Head Neck Surg* 2018;144:929–37 CrossRef Medline
6. Bahl M, Sepahdari AR, Sosa JA, et al. **Parathyroid adenomas and hyperplasia on four-dimensional CT scans: three patterns of enhancement relative to the thyroid gland justify a three-phase protocol.** *Radiology* 2015;277:454–62 CrossRef Medline
7. Bentrem DJ, Angelos P, Talamonti MS, et al. **Is preoperative investigation of the thyroid justified in patients undergoing parathyroidectomy for hyperparathyroidism?** *Thyroid* 2002;12:1109–12 CrossRef Medline
8. Jovanovic MD, Zivaljevic VR, Diklic AD, et al. **Surgical treatment of concomitant thyroid and parathyroid disorders: analysis of 4882 cases.** *Eur Arch Otorhinolaryngol* 2017;274:997–1004 CrossRef Medline
9. Sachs JR, West TG, Lack CM, et al. **How to incorporate dual-energy computed tomography into your neuroradiology practice: questions and answers.** *J Comput Assist Tomogr* 2018;42:824–30 CrossRef Medline
10. Forghani R, Kelly HR, Curtin HD. **Applications of dual-energy computed tomography for the evaluation of head and neck squamous cell carcinoma.** *Neuroimaging Clin N Am* 2017;27:445–59 CrossRef Medline
11. Neuhaus V, Große Hokamp N, Abdullayev N, et al. **Comparison of virtual monoenergetic and polyenergetic images reconstructed from dual-layer detector CT angiography of the head and neck.** *Eur Radiol* 2018;28:1102–10 CrossRef Medline
12. Potter CA, Sodickson AD. **Dual-energy CT in emergency neuroimaging: added value and novel applications.** *Radiographics* 2016;36:2186–98 CrossRef Medline
13. Vogl TJ, Schulz B, Bauer RW, et al. **Dual-energy CT applications in head and neck imaging.** *AJR Am J Roentgenol* 2012;199:S34–39 CrossRef Medline
14. Tawfik AM, Razek AA, Kerl JM, et al. **Comparison of dual-energy CT-derived iodine content and iodine overlay of normal, inflammatory and metastatic squamous cell carcinoma cervical lymph nodes.** *Eur Radiol* 2014;24:574–80 CrossRef Medline
15. Liu X, Ouyang D, Li H, et al. **Papillary thyroid cancer: dual-energy spectral CT quantitative parameters for preoperative diagnosis of metastasis to the cervical lymph nodes.** *Radiology* 2015;275:167–76 CrossRef Medline
16. Yamauchi H, Buehler M, Goodsitt MM, et al. **Dual-energy CT-based differentiation of benign posttreatment changes from primary or recurrent malignancy of the head and neck: comparison of spectral Hounsfield units at 40 and 70 keV and iodine concentration.** *AJR Am J Roentgenol* 2016;206:580–87 CrossRef
17. Kuno H, Sakamaki K, Fujii S, et al. **Comparison of MR imaging and dual-energy CT for the evaluation of cartilage invasion by laryngeal and hypopharyngeal squamous cell carcinoma.** *AJNR Am J Neuroradiol* 2018;39:524–31 CrossRef Medline
18. Forghani R, Chatterjee A, Reinhold C, et al. **Head and neck squamous cell carcinoma: prediction of cervical lymph node metastasis by dual-energy CT texture analysis with machine learning.** *Eur Radiol* 2019;29:6172–81 CrossRef Medline

19. Lee DH, Lee YH, Seo HS, et al. **Dual-energy CT iodine quantification for characterizing focal thyroid lesions.** *Head Neck* 2019;41:1024–31 CrossRef Medline
20. Timmer VCML, Kroonenburgh AMJLV, Henneman WJP, et al. **Detection of bone marrow edema in the head and neck with dual-energy CT: ready for clinical use?** *AJR Am J Roentgenol* 2020;214:893–99 CrossRef Medline
21. Sachs JR, Lack CM, West TG, et al. **Unique characteristics of intravitreal silicone oil on dual-energy computed tomography.** *J Comput Assist Tomogr* 2020;44:370–73 CrossRef Medline
22. Roskies M, Liu X, Hier MP, et al. **3-phase dual-energy CT scan as a feasible salvage imaging modality for the identification of non-localizing parathyroid adenomas: a prospective study.** *J Otolaryngol Head Neck Surg* 2015;44:44 CrossRef Medline
23. Leiva-Salinas C, Flors L, Durst CR, et al. **Detection of parathyroid adenomas using a monophasic dual-energy computed tomography acquisition: diagnostic performance and potential radiation dose reduction.** *Neuroradiology* 2016;58:1135–41 CrossRef Medline
24. Forghani R, Roskies M, Liu X, et al. **Dual-energy CT characteristics of parathyroid adenomas on 25-and 55-second 4D-CT acquisitions: preliminary experience.** *J Comput Assist Tomogr* 2016;40:806–14 CrossRef Medline
25. Woisetschläger M, Gimm O, Johansson K, et al. **Dual energy 4D-CT of parathyroid adenomas not clearly localized by sestamibi scintigraphy and ultrasonography: a retrospective study.** *Eur J Radiol* 2020;124:108821 CrossRef Medline
26. Raghavan P, Durst CR, Ornan DA, et al. **Dynamic CT for parathyroid disease: are multiple phases necessary?** *AJNR Am J Neuroradiol* 2014;35:1959–64 CrossRef Medline
27. Morón F, Delumpa A, Chetta J, et al. **Single phase computed tomography is equivalent to dual phase method for localizing hyperfunctioning parathyroid glands in patients with primary hyperparathyroidism: a retrospective review.** *PeerJ* 2017;5:e3586 CrossRef Medline
28. Matsumoto K, Jinzaki M, Tanami Y, et al. **Virtual monochromatic spectral imaging with fast kilovoltage switching: improved image quality as compared with that obtained with conventional 120-kVp CT.** *Radiology* 2011;259:257–62 CrossRef Medline
29. Lam S, Gupta R, Levental M, et al. **Optimal virtual monochromatic images for evaluation of normal tissues and head and neck cancer using dual-energy CT.** *AJNR Am J Neuroradiol* 2015;36:1518–24 CrossRef Medline
30. Jensen CT, Liu X, Tamm EP, et al. **Image quality assessment of abdominal CT by use of new deep learning image reconstruction: initial experience.** *AJR Am J Roentgenol* 2020;215:50–57 CrossRef Medline

Intraindividual Comparison between the Contrast-Enhanced Golden-Angle Radial Sparse Parallel Sequence and the Conventional Fat-Suppressed Contrast-Enhanced T1-Weighted Spin-Echo Sequence for Head and Neck MRI

S.-J. Hur, Y. Choi, J. Yoon, J. Jang, N.-Y. Shin, K.-J. Ahn, and B.-S. Kim

ABSTRACT

BACKGROUND AND PURPOSE: The golden-angle radial sparse parallel-volumetric interpolated breath-hold (GRASP-VIBE) sequence is a recently introduced imaging technique with high resolution. This study compared the image quality between conventional fat-suppressed T1-weighted TSE and GRASP-VIBE after gadolinium enhancement in the head and neck region.

MATERIALS AND METHODS: Data from 65 patients with clinical indications for head and neck MR imaging between September 2020 and January 2021 were retrospectively reviewed. Two radiologists assessed the overall image quality, overall artifacts, and image conspicuities in the oropharynx, hypopharynx, and cervical lymph nodes according to 5-point scores (best score: 5). Interobserver agreement was assessed using weighted κ statistics. The SNR and contrast-to-noise ratio were calculated and compared between the 2 sequences using a paired Wilcoxon signed rank test.

RESULTS: The analysis included 52 patients (mean age, 60 [SD, 14] years; male, 71.2% [37/52]) who were mostly diagnosed with head and neck malignancies (94.3% [50/52]). κ statistics ranged from slight agreement in cervical lymph node conspicuity ($\kappa = 0.18$) to substantial agreement in oropharyngeal mucosal conspicuity ($\kappa = 0.80$) (κ range, 0.18–0.80). Moreover, GRASP-VIBE demonstrated significantly higher mean scores in overall image quality (4.68 [SD, 0.41] versus 3.66 [SD, 0.73]), artifacts (4.47 [SD, 0.48] versus 3.58 [SD, 0.71]), oropharyngeal mucosal conspicuity (4.85 [SD, 0.41] versus 4.11 [SD, 0.79]), hypopharyngeal mucosal conspicuity (4.84 [SD, 0.34] versus 3.58 [SD, 0.81]), and cervical lymph node conspicuity (4.79 [SD, 0.32] versus 4.08 [SD, 0.64]) than fat-suppressed T1-weighted TSE (all, $P < .001$). Furthermore, GRASP-VIBE demonstrated a higher SNR (22.8 [SD, 11.5] versus 11.3 [SD, 5.6], $P < .001$) and contrast-to-noise ratio (4.7 [SD, 5.4] versus 2.3 [SD, 2.7], $P = .059$) than fat-suppressed T1-weighted TSE.

CONCLUSIONS: GRASP-VIBE provided better image quality with fewer artifacts than conventional fat-suppressed T1-weighted TSE for the head and neck regions.

ABBREVIATIONS: CNR = contrast-to-noise ratio; GRASP-VIBE = golden-angle radial sparse parallel-volumetric interpolated breath-hold; T1-TSE = fat-suppressed T1-weighted TSE

MR imaging is an integral imaging technique for detailed anatomic assessment of complex head and neck regions. In particular, conventional gadolinium-enhanced fat-suppressed T1-weighted TSE (T1-TSE) is widely used in routine clinical settings.[1-3] However, the image quality of T1-TSE in the lower neck region is often degraded by artifacts caused by pulsation, respiratory motion, and wide magnetic susceptibility variations.[4-6] Therefore, conventional T1-TSE has its limitations when considering the need for detailed assessment of small, complex structures in the head and neck region.

The golden-angle radial sparse parallel-volumetric interpolated breath-hold (GRASP-VIBE) sequence is a recently introduced imaging technique that combines radial 3D T1-weighted spoiled gradient-echo (VIBE, Siemens; THRIVE, Philips Healthcare; LAVA, GE Healthcare), parallel imaging, and compressed sensing reconstruction for dynamic contrast-enhanced MR imaging. GRASP-VIBE continuously acquires radial spokes throughout the scan with contrast agent injection. Then, multiple phases of dynamic 3D T1-weighted images are reconstructed from highly

Received April 1, 2021; accepted after revision July 25.

From the Department of Radiology, Seoul St. Mary's Hospital, College of Medicine, The Catholic University of Korea, Seoul, Korea.

This research was supported by the Basic Science Research Program through the National Research Foundation of Korea funded by the Ministry of Education (2021R1I1A1A01040285).

Please address correspondence to Yangsean Choi, MD, Department of Radiology, Seoul St. Mary's Hospital, The Catholic University of Korea, College of Medicine, Seoul, Korea, 222 Banpo-daero, Seocho-gu, Seoul (06591), Korea; e-mail: phillipchoi007@gmail.com

http://dx.doi.org/10.3174/ajnr.A7285

Table 1: Detailed acquisition parameters of the 2 sequences

Sequence	GRASP-VIBE	T1-TSE
FOV	200 × 200	200 × 200
Matrix	224 × 224	384 × 230
Section thickness (mm)	4	4
Gap (mm)	0	1
No. of slices	26	32
In-plane resolution (mm)	1.04 × 1.04	0.52 × 0.52
Echo-train	1	4
Flip angle	12°	160°
TR/TE (ms)	4.1/1.9	690/12
Bandwidth (Hz/px)	496 Hz/px	310 Hz/px
No. of excitations	1	1
Fat-suppression technique	Chemical shift selective	Dixon
Scanning type	Gradient-echo	TSE
Scan time (min/sec)	4/46	2/6
No. of dynamic acquisitions (temporal resolution) (sec)	95 (2.5)	NA
Acquisition type	3D	2D

Note:—NA indicates not applicable.

Table 2: Baseline characteristics of included patients[a]

Variable	*N* = 52
Age (mean) (yr)	60 (SD, 14)
Sex	
Male	37 (71.2)
Female	15 (28.8)
Diagnosis	
Head and neck malignancies	50 (94.3)
Buccal	1 (1.9)
Floor of mouth	1 (1.9)
Vocal cord	10 (19.2)
Supraglottis	1 (1.9)
Hypopharynx	7 (13.5)
Salivary gland	6 (11.5)
Tongue	13 (25.0)
Tonsil	10 (19.2)
Other malignancies	3 (5.7)
Primary lesion visible	
Yes	10 (19.2)
No	42 (80.8)
Postoperative state	
Yes	45 (86.5)
No	7 (13.5)

[a] All values are presented as No. (%) unless otherwise specified.

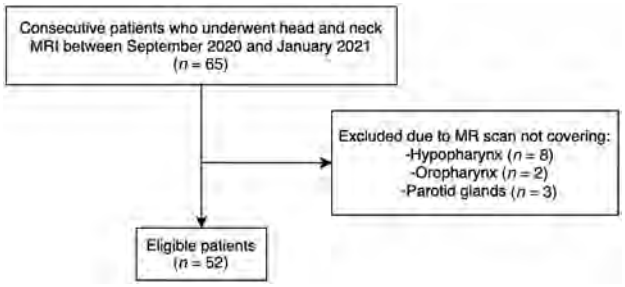

FIG 1. Flow chart of the patient-selection process.

undersampled radial spokes using iterative reconstruction. Because the continuous golden-angle sampling conserves the sampling uniformity of the *k*-space at any time point, any number of successive radial spokes are combined to make dynamic images, enabling various temporal resolutions and time points. Furthermore, GRASP-VIBE gives a static 3D image after combination of all the radial spokes, which can be used as an enhanced 3D T1-weighted image. Also, because GRASP uses a radial trajectory where the center of the *k*-space is sampled every TR, it is more motion-robust at high spatial and temporal resolutions.[7] Excellent GRASP-derived images have already been demonstrated with fewer motion and pulsation artifacts in prior liver,[8] prostate,[9] and breast[10] studies.

A similar study by Wu et al[11] applied a radial-volumetric interpolated breath-hold examination (VIBE) in the head and neck and found that radial VIBE was a viable motion-robust improvement over the conventional fat-suppressed T1-TSE.[11] Our study attempted to apply a more novel GRASP-VIBE technique in the head and neck with a larger sample size and variable clinical indications, including preoperative staging and postoperative assessment, thereby reflecting a more comprehensive clinical setting.

We hypothesized that GRASP-VIBE would yield better images of the head and neck than conventional T1-TSE and that GRASP-VIBE would be a promising alternative imaging technique to T1-TSE. Therefore, the purpose of the current study was to qualitatively and quantitatively compare the image qualities of GRASP-VIBE and conventional T1-TSE sequences.

MATERIALS AND METHODS

Patients

This single-center retrospective cohort study was approved by our institutional review board, and the requirement for informed consent was waived. Between September 2020 and January 2021, data from 65 consecutive patients who had undergone head and neck MR imaging for various clinical indications were reviewed. The inclusion criteria were as follows: 1) availability of simultaneously acquired gadolinium-enhanced GRASP-VIBE and T1-TSE sequences; 2) MR imaging scan area covering the nasopharynx to the subglottic region; and 3) visible left parotid glands and masseter muscles.

GRASP-VIBE Acquisition

GRASP-VIBE sequence data were acquired using a fat-saturated T1-weighted radial 3D gradient recalled-echo sequence.[7] GRASP-VIBE samples were characterized by a *k*-space with a stack-of-stars scheme, in which radial spokes are stacked along the partition direction. An angle increase of 111.25° in consecutive spokes yields approximately uniform *k*-space coverage during acquisition.[12] Moreover, compressed-sensing reconstruction was applied to minimize streaking artifacts caused by data undersampling in the radial acquisition. For this study, a 2.5-second temporal resolution (ie, 21 spokes/frame and a static image of 2427 radial views) was used.

MR Imaging Acquisition

All MR imaging examinations were performed using 3T scanners with 64-channel head and neck coils (Magnetom Vida; Siemens). Gadoteridol (ProHance; Bracco Diagnostics) had been intravenously administered at a rate of 1–2 mL/s (0.01 mmol/kg of

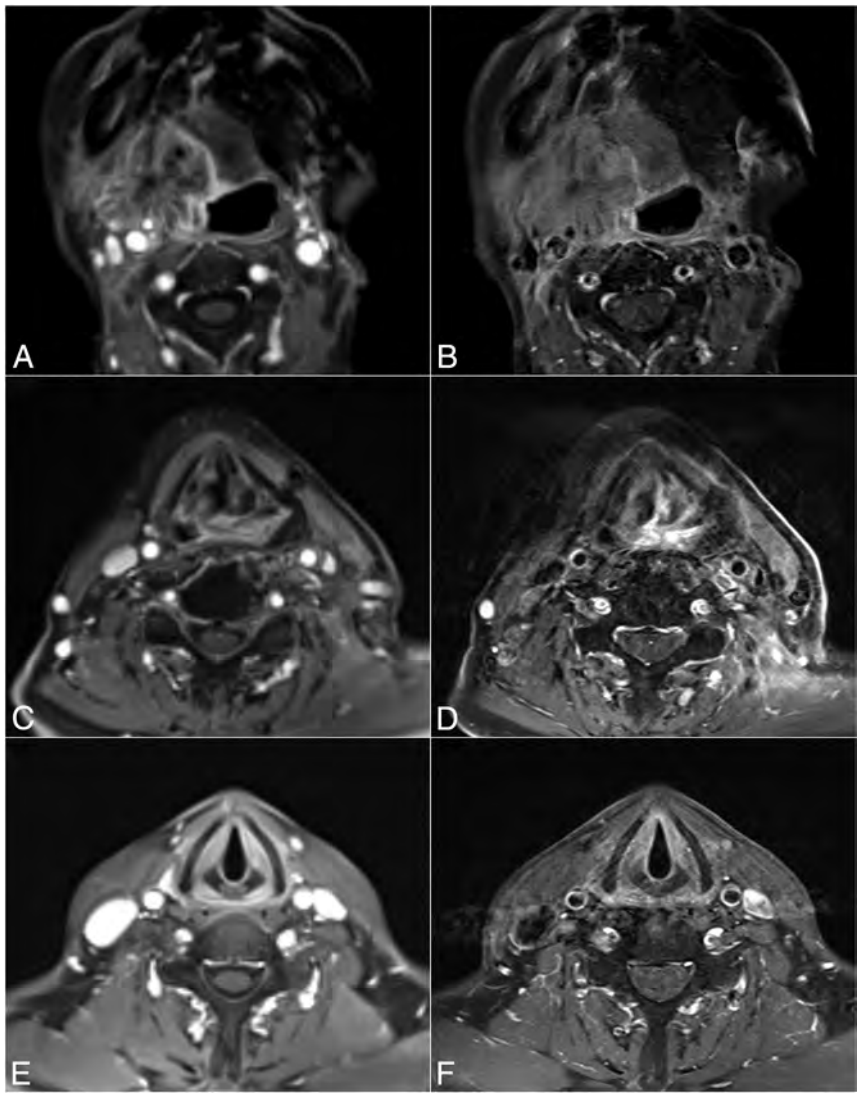

FIG 2. A 55-year-old female patient with a history of recurrent squamous cell carcinoma of the tongue (*top row*); the lesion is better delineated in GRASP-VIBE (*A*) than in T1-TSE (*B*). A 76-year-old male patient with a history of left hypopharyngeal cancer with transoral robotic surgery (*middle row*). Compared with GRASP-VIBE (*C*), a significant respiratory motion artifact is observed in T1-TSE (*D*). A 70-year-old male patient with a history of left vocal cord squamous cell carcinoma in situ and laser cordectomy (*bottom row*). Compared with GRASP-VIBE (*E*), there is a noticeable pulsation artifact from blood vessels in T1-TSE (*F*).

body weight). Approximately 5 seconds after gadoteridol administration, GRASP-VIBE was acquired. T1-TSE was acquired approximately 4–5 minutes after gadoteridol administration. The acquisition times for the GRASP-VIBE and T1-TSE were 4 minutes 46 seconds and 2 minutes 6 seconds, respectively. The details of the GRASP-VIBE and T1-TSE acquisition parameters are summarized in Table 1. All images were acquired under free-breathing conditions.

Qualitative Image Analysis

Two radiologist raters (raters 1 and 2 with 2 and 8 years of experience in head and neck radiology, respectively) independently reviewed the MR images. The raters were blinded to the patient's clinical information during the review. The qualitative assessment included overall image quality, overall artifacts, and image conspicuities of the oropharyngeal, hypopharyngeal, and cervical lymphatic channels. All assessments were graded using a 5-point scoring system. For assessment of overall image quality and overall artifacts, scores were graded as 5 = best, 4 = good, 3 = adequate, 2 = poor, and 1 = nondiagnostic. The artifacts under evaluation included respiratory motion artifacts, pulsation artifacts of nearby blood vessels, and susceptibility artifacts in the oral cavity. For the assessment of mucosa conspicuities, scores were graded as 5 = sharp margin, 4 = minimal blurring, 3 = moderate blurring, 2 = substantial blurring, and 1 = nondiagnostic due to severe blurring.

Quantitative Image Analysis

For quantitative analysis, the first rater (R1) drew circular ROIs with areas ranging from 10 to 30 mm^2 on the left parotid glands and masseter muscles. All ROIs were then reviewed by the second rater (R2). Image analyses were performed using an in-house PACS at a designated workstation. From the ROIs, the SNR and contrast-to-noise ratio (CNR) were calculated using the following formulas:[13-15]

$$SNR = \frac{SI_{Parotid\ \ gland}}{SD_{Masseter\ \ muscle}},$$

$$CNR = \frac{(SI_{Parotid\ \ gland} - SI_{Masseter\ \ muscle})}{SD_{Masseter\ \ muscle}}.$$

$SI_{Parotid\ gland}$ is the mean signal intensity of the parotid glands, and $SI_{Masseter\ muscle}$ and $SD_{Masseter\ muscle}$ indicate the mean signal intensity and SD of the masseter muscles, respectively. All signal intensities and SDs were calculated within the ROIs.

Statistical Analyses

Interobserver agreement in the image-quality assessment for each category was assessed using weighted κ coefficients. The image-assessment scores as well as the SNR and CNR between GRASP-VIBE and T1-TSE were compared using a paired Wilcoxon rank sum test. Statistical significance was 2-sided and was set at $P < .05$. All statistical analyses were performed with R statistical and computing software, Version 4.10.1 (http://www.r-project.org/).

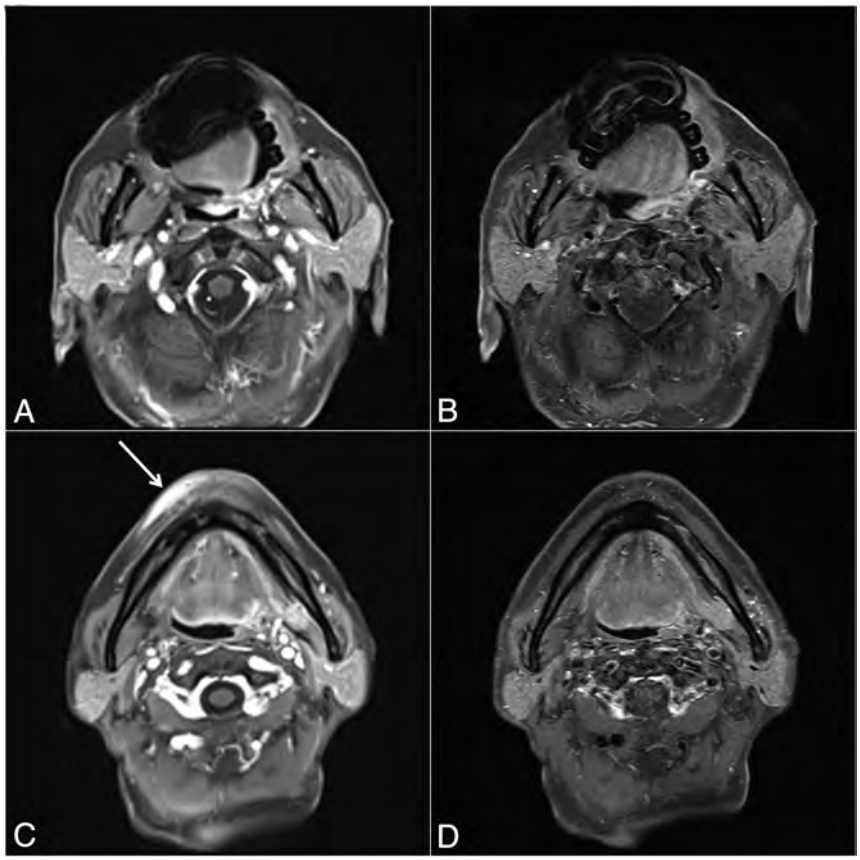

FIG 3. A 73-year-old male patient with a history of oropharyngeal squamous cell carcinoma of the right tonsil; the susceptibility artifacts due to dental amalgam are more prominent in GRASP-VIBE (*A*) than in T1-TSE (*B*). In right submental region of the same patient, fat suppression is weaker in GRASP-VIBE (*C*) than in T1-TSE (*D*).

RESULTS

Clinical Characteristics of Patients

Among the initial 65 patients, 13 patients were excluded because their scans did not cover the hypopharynx ($n = 8$), oropharynx ($n = 2$), and parotid glands and masseter muscles ($n = 3$). After exclusion, 52 eligible patients remained for analysis (Fig 1). The baseline characteristics of eligible patients are summarized in Table 2. Among the 52 patients (mean age, 60 [SD, 14] years; 37 men and 15 women), 50 had head and neck malignancies, including tongue cancer (13, 25%), vocal cord cancer (10, 19.2%), supraglottic cancer (1, 1.9%), tonsil cancer (10, 19.2%), hypopharynx cancer (7, 13.5%), salivary gland cancer (6, 11.5%), buccal cancer (1, 1.9%), and floor of mouth cancer (1, 1.9%); and 3 had other malignancies (5.7%). Forty-five patients (86.5%) were examined during postoperative follow-up, and malignant lesions were visible in 10 patients (19.2%). Representative MR imaging comparing the 2 sequences is illustrated in Figs 2 and 3.

Qualitative Assessment

The results of the qualitative assessment of the 2 sequences are summarized in Table 3 and graphically depicted in Fig 4. The mean quality scores were significantly higher in GRASP-VIBE than in T1-TSE in all assessments, including overall image quality, overall artifacts, and image conspicuities of the oropharyngeal, hypopharyngeal, and cervical lymph nodes (all, $P < .001$).

Interobserver agreement was variable, as measured by κ statistics; the agreement was substantial for the assessment of oropharyngeal mucosa conspicuity ($\kappa = 0.80$, for GRASP-VIBE; $\kappa = 0.5$, for T1-TSE), whereas it was slight-to-moderate for the assessment of cervical lymph node conspicuity ($\kappa = 0.18$ for GRASP-VIBE; $\kappa = 0.34$ for T1-TSE).

Quantitative Assessment

The boxplots of the SNR and CNR of GRASP-VIBE and T1-TSE are depicted in Fig 5. The mean SNR of GRASP-VIBE (22.8 [SD, 11.5]) was significantly higher than that of T1-TSE (11.3 [SD, 5.6]) ($P < .001$). The mean CNR of GRASP-VIBE (4.7 [SD, 5.4]) was also higher than that of T1-TSE (2.3 [SD, 2.7]), but without statistical significance ($P = .059$).

DISCUSSION

In the current study, overall image quality, overall artifacts, and image conspicuities at different anatomic locations of the head and neck were compared between GRASP-VIBE and T1-TSE. Furthermore, the SNR and CNR of both sequences were quantitatively compared. GRASP-VIBE provided significantly better image quality and a higher SNR compared with the conventional T1-TSE sequence. Therefore, GRASP-VIBE could be a superior alternative to conventional T1-TSE for the assessment of the head and neck region.

Compared with T1-TSE, GRASP-VIBE showed higher scores in all qualitative assessments, including overall image quality, overall artifacts, and image conspicuities of the oropharyngeal, hypopharyngeal, and cervical lymphatic channels. GRASP-VIBE showed significantly higher scores, especially in terms of artifacts and hypopharyngeal mucosa conspicuity. This finding is due to pulsation and respiratory motion artifacts inherently associated with the T1-TSE sequence, which mainly affect the lower neck region and, in turn, degrade the image quality of the hypopharyngeal region.

In this regard, the findings of our study are clinically relevant for imaging assessment of hypopharyngeal and laryngeal head and neck cancers, whose MR imaging scans are often critically affected by pulsation artifacts from adjacent carotid arteries and jugular veins as well as respiratory motion artifacts from involuntary movement due to free breathing or swallowing. Minimizing such artifacts would be beneficial for the accurate evaluation of not only the primary lesions but also recurrences in postoperative

Table 3: Qualitative evaluations and κ values for overall image quality, overall artifacts, and anatomic conspicuities of GRASP-VIBE and T1-TSE

	GRASP-VIBE			T1-TSE			
	Scores (mean)	κ	*P* Value[a]	Scores (mean)	κ	*P* Value[a]	*P* Value[b]
Overall image quality							
Rater A	4.74 (SD, 0.49)	0.29	.003	3.81 (SD, 0.68)	0.594	<.001	
Rater B	4.62 (SD, 0.53)			3.51 (SD, 0.91)			
Average of two raters	4.68 (SD, 0.41)			3.66 (SD, 0.73)			<.001
Overall artifacts		0.21	.041		0.542	<.001	
Rater A	4.26 (SD, 0.68)			3.60 (SD, 0.60)			
Rater B	4.68 (SD, 0.51)			3.55 (SD, 0.97)			
Average of two raters	4.47 (SD, 0.48)			3.58 (SD, 0.71)			<.001
Oropharyngeal mucosal conspicuity		0.80	<.001		0.5	<.001	
Rater A	4.87 (SD, 0.39)			4.15 (SD, 0.74)			
Rater B	4.83 (SD, 0.47)			4.04 (SD, 1.06)			
Average of two raters	4.85 (SD, 0.41)			4.11 (SD, 0.79)			<.001
Hypopharyngeal mucosal conspicuity		0.30	.016		0.422	.002	
Rater A	4.89 (SD, 0.32)			3.58 (SD, 0.84)			
Rater B	4.79 (SD, 0.49)			3.57 (SD, 1.05)			
Average of two raters	4.84 (SD, 0.34)			3.58 (SD, 0.81)			<.001
Cervical lymph node conspicuity		0.18	.072		0.34	.001	
Rater A	4.64 (SD, 0.48)			4.34 (SD, 0.65)			
Rater B	4.94 (SD, 0.30)			3.81 (SD, 0.83)			
Average of two raters	4.79 (SD, 0.32)			4.08 (SD, 0.64)			<.001

[a] *P* value for κ.
[b] *P* values for paired Wilcoxon rank sum tests comparing the scores of the 2 sequences.

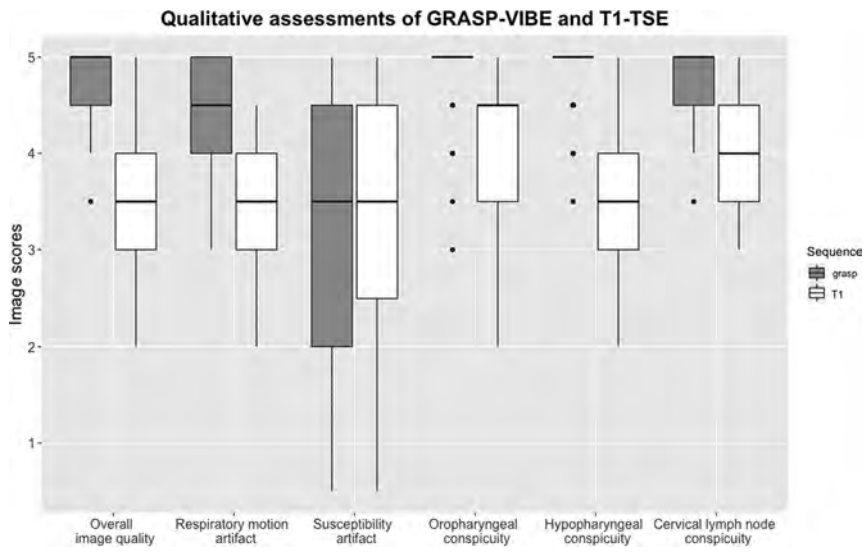

FIG 4. Boxplots of qualitative assessments for GRASP-VIBE and T1-TSE.

follow-up MR imaging, in which anatomic complexities become more challenging in the head and neck region.

Our findings are consistent with those in a previous similar study by Wu et al,[11] who compared radial VIBE with conventional T1-TSE and found that radial VIBE was more motion-robust. The motion-robust benefit of radial VIBE has been documented in other anatomic regions as well, such as the abdomen[16] and prostate.[9] The added value of the present study is the application of a novel GRASP-VIBE technique and its direct intraindividual comparison with the conventional T1-TSE for head and neck MR imaging in routine clinical settings.

The potential benefit of GRASP-VIBE over T1-TSE lies in its 3D reconstruction capability for coronal and sagittal images. While the protocol of the current study involved only GRASP-VIBE for high temporal resolution, GRASP-VIBE can also be acquired with high spatial resolution. Finally, the functional application of GRASP-VIBE in evaluating tumor angiogenesis has also been previously investigated in lung cancer,[17] rectal cancer,[18] and parotid neoplasms,[19] proving its 4D imaging characteristics.

The GRASP-VIBE sequence has a few weaknesses compared with T1-TSE. GRASP-VIBE is more prone to susceptibility artifacts than T1-TSE because the gradient recalled-echo sequence has no 180° refocusing pulse, which limits correction for large and fixed magnetic field inhomogeneities induced by metallic implants.[20] In head and neck MR imaging, significant susceptibility artifacts are often seen in the oral cavity due to dental amalgams; we found that fat suppression in GRASP-VIBE was weaker in submental regions due to local signal loss caused by severe susceptibility change and local magnetic inhomogeneity in the oral cavity. However, the fat-saturation techniques for GRASP-VIBE and T1-TSE were different—chemical shift selective and Dixon, respectively—which might have contributed to the difference in fat-suppression effects. Furthermore, the radial sampling of *k*-space in GRASP-VIBE inherently leads to undersampling of peripheral *k*-spaces, resulting in the edge smoothing of

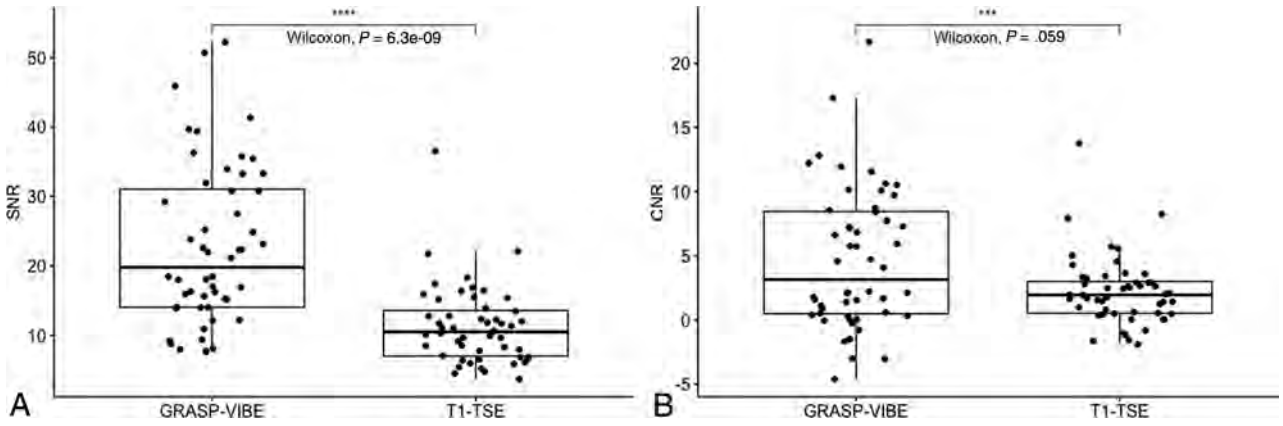

FIG 5. Boxplots of SNR (*A*) and CNR (*B*) of GRASP-VIBE and T1-TSE.

images.[21] Nonetheless, reduction of significant motion artifacts would compensate for such smoothing around the borders of structures.

This study had several limitations that need to be addressed. First, the 2 raters were not blinded to the names of the sequences during image analysis, possibly causing selection bias. However, the 2 sequences demonstrated obvious differences in image texture, and blinding would have had a limited role. Additionally, there was an interval of approximately 4–5 minutes between the GRASP-VIBE and T1-TSE sequences, which might have affected the extent and degree of tissue contrast enhancement. Finally, interobserver agreement was variable across qualitative assessment categories, possibly due to the differences in the experience of the raters (2 versus 8 years in head and neck radiology).

CONCLUSIONS

In qualitative image assessment, GRASP-VIBE demonstrated better image quality, fewer artifacts, and better image conspicuities than conventional contrast-enhanced T1-TSE. GRASP-VIBE also provided a significantly higher SNR than T1-TSE. Therefore, the results of the current study are consistent with our hypothesis that GRASP-VIBE is a promising alternative to T1-TSE for the evaluation of head and neck MR imaging.

ACKNOWLEDGMENTS

The authors sincerely appreciate the technical support and advice provided by Hyun-Soo Lee, PhD (MR research collaboration scientist, Siemens Healthineers).

REFERENCES

1. Barakos JA, Dillon WP, Chew WM. **Orbit, skull base, and pharynx: contrast-enhanced fat suppression MR imaging.** *Radiology* 1991;179:191–98 CrossRef Medline
2. Hirsch JA, Loevner LA, Yousem DM, et al. **Gadolinium-enhanced fat-suppressed T1-weighted imaging of the head and neck: comparison of gradient and conventional SE sequences.** *J Comput Assist Tomogr* 1998;22:771–76 CrossRef Medline
3. Ross MR, Schomer DF, Chappell P, et al. **MR imaging of head and neck tumors: comparison of T1-weighted contrast-enhanced fat-suppressed images with conventional T2-weighted and fast spin-echo T2-weighted images.** *Am J Roentgenol* 1994;163:173–78 CrossRef Medline
4. Kataoka M, Ueda H, Koyama T, et al. **Contrast-enhanced volumetric interpolated breath-hold examination compared with spin-echo T1-weighted imaging of head and neck tumors.** *AJR Am J Roentgenol* 2005;184:313–19 CrossRef Medline
5. Castelijns JA, Gerritsen GJ, Kaiser MC, et al. **Invasion of laryngeal cartilage by cancer: comparison of CT and MR imaging.** *Radiology* 1988;167:199–206 CrossRef Medline
6. Becker M, Zbären P, Laeng H, et al. **Neoplastic invasion of the laryngeal cartilage: comparison of MR imaging and CT with histopathologic correlation.** *Radiology* 1995;194:661–69 CrossRef Medline
7. Feng L, Grimm R, Block KT, et al. **Golden-angle radial sparse parallel MRI: combination of compressed sensing, parallel imaging, and golden-angle radial sampling for fast and flexible dynamic volumetric MRI.** *Magn Reson Med* 2014;72:707–17 CrossRef Medline
8. Chandarana H, Feng L, Block TK, et al. **Free-breathing contrast-enhanced multiphase MRI of the liver using a combination of compressed sensing, parallel imaging, and golden-angle radial sampling.** *Invest Radiol* 2013;48:10–16 CrossRef Medline
9. Rosenkrantz AB, Geppert C, Grimm R, et al. **Dynamic contrast-enhanced MRI of the prostate with high spatiotemporal resolution using compressed sensing, parallel imaging, and continuous golden-angle radial sampling: preliminary experience.** *J Magn Reson Imaging* 2015;41:1365–73 CrossRef Medline
10. Heacock L, Gao Y, Heller SL, et al. **Comparison of conventional DCE-MRI and a novel golden-angle radial multicoil compressed sensing method for the evaluation of breast lesion conspicuity.** *J Magn Reson Imaging* 2017;45:1746–52 CrossRef Medline
11. Wu X, Raz E, Block TK, et al. **Contrast-enhanced radial 3D fat-suppressed T1-weighted gradient-recalled echo sequence versus conventional fat-suppressed contrast-enhanced T1-weighted studies of the head and neck.** *Am J Roentgenol* 2014;203:883–89 CrossRef Medline
12. Winkelmann S, Schaeffter T, Koehler T, et al. **An optimal radial profile order based on the golden ratio for time-resolved MRI.** *IEEE Trans Med Imaging* 2007;26:68–76 CrossRef Medline
13. Ikeda H, Ohno Y, Murayama K, et al. **Compressed sensing and parallel imaging accelerated T2 FSE sequence for head and neck MR imaging: comparison of its utility in routine clinical practice.** *Eur J Radiol* 2021;135:109501 CrossRef Medline
14. Vranic JE, Cross NM, Wang Y, et al. **Compressed sensing-sensitivity encoding (CS-SENSe) accelerated brain imaging: reduced scan time without reduced image quality.** *AJNR Am J Neuroradiol* 2019;40:92–98 CrossRef Medline
15. Toledano-Massiah S, Sayadi A, De Boer R, et al. **Accuracy of the compressed sensing accelerated 3D-FLAIR sequence for the detection of MS plaques at 3T.** *AJNR Am J Neuroradiol* 2018;39:454–58 CrossRef Medline

16. Seo N, Park SJ, Kim B, et al. **Feasibility of free-breathing dynamic contrast-enhanced MRI of the abdomen: a comparison between CAIPIRINHA-VIBE, radial-VIBE with KWIC reconstruction and conventional VIBE.** *Br J Radiol* 2016;89:1–7 CrossRef Medline
17. Chen L, Zeng X, Wu Y, et al. **A study of the correlation of perfusion parameters in high-resolution GRASP MRI with microvascular density in lung cancer.** *J Magn Reson Imaging* 2019;49:1186–94 CrossRef Medline
18. Attenberger UI, Liu J, Riffel P, et al. **Quantitative perfusion analysis of the rectum using golden-angle radial sparse parallel magnetic resonance imaging: initial experience and comparison to time-resolved angiography with interleaved stochastic trajectories.** *Invest Radiol* 2017;52:715–24 CrossRef Medline
19. Mogen JL, Block KT, Bansal NK, et al. **Dynamic contrast-enhanced MRI to differentiate parotid neoplasms using golden-angle radial sparse parallel imaging.** *AJNR Am J Neuroradiol* 2019;40:1029–36 CrossRef Medline
20. Lee MJ, Kim S, Lee SA, et al. **Overcoming artifacts from metallic orthopedic implants at high-field-strength MR imaging and multidetector CT.** *Radiographics* 2007;27:791–803 CrossRef Medline
21. Huang SY, Seethamraju RT, Patel P, et al. **Body MR imaging: artifacts, k-space, and solutions.** *Radiographics* 2015;35:1439–60 CrossRef Medline

Measuring 3D Cochlear Duct Length on MRI: Is It Accurate and Reliable?

M.B. Eser, B. Atalay, M.B. Dogan, N. Gündüz, and M.T. Kalcioglu

ABSTRACT

BACKGROUND AND PURPOSE: Prior studies have evaluated cochlear length using CT to select the most suitable cochlear implants and obtain patient-specific anatomy. This study aimed to test the accuracy and reliability of cochlear lateral wall length measurements using 3D MR imaging.

MATERIALS AND METHODS: Two observers measured the cochlear lateral wall length of 35 patients (21 men) with postlingual hearing loss using CT and MR imaging. The intraclass correlation coefficient (with 95% confidence intervals) was used to evaluate intraobserver and interobserver reliability for the 3D cochlear measurements.

RESULTS: The mean age of the participants was 39.85 (SD, 16.60) years. Observer 1 measured the mean lateral wall length as 41.52 (SD, 2.25) mm on CT and 41.44 (SD, 2.18) mm on MR imaging, with a mean difference of 0.08 mm (95% CI, −0.11 to 0.27 mm), while observer 2 measured the mean lateral wall length as 41.74 (SD, 2.69) mm on CT and 42.34 (SD, 2.53) mm on MR imaging, with a mean difference of −0.59 mm (95% CI, −1.00 to −0.20 mm). An intraclass correlation coefficient value of 0.90 (95% CI, 0.84–0.94) for CT and 0.69 (95% CI, 0.46–0.82) for MR imaging was obtained for the interobserver reliability for the full-turn cochlear lateral wall length.

CONCLUSIONS: CT-based 3D cochlear measurements show excellent intraobserver and interobserver reliability, while MR imaging–based lateral wall length measurements have good-to-excellent intraobserver reliability and moderate interobserver reliability. These results corroborate the use of CT for 3D cochlear measurements as a reference method and demonstrate MR imaging to be an alternative acquisition technique with comparably reliable results.

ABBREVIATIONS: ICC = intraclass correlation coefficient; LWL = lateral wall length

Across the years, there has been an increase in the proportion of the global population with postlingual profound hearing loss, especially in developed countries.[1] An effective surgical treatment for patients with profound hearing loss is a cochlear implant.[2] As a result, the number of patients requiring presurgical imaging has also amplified.[3,4] CT has been the reference method for evaluating bony structures and cochlear length measurements.

In the last 25 years, many studies have evaluated cochlear length using CT and conebeam CT[3,4] aimed at selecting the most suitable cochlear implants and obtaining patient-specific anatomy and tonotopy.[5-9] The most common methods for cochlear length measurements include the *A*-value (the widest diameter of the cochlear basal turn) and measuring the cochlear circumference over 3D reconstruction.[3,4] The current literature proposes that accurate measurements may help in developing custom-made cochlear implant designs per the patient's specific anatomy and tonotopy.[2] However, the radiation exposure in these CT-based measurements is a consideration; therefore, it is desirable to use alternate imaging methods like MR imaging to make these measurements.[10]

This study aimed to test the accuracy and reliability of MR imaging–based 3D cochlear length measurements that were previously performed by CT. A secondary aim was to test the effect of the observer's experience on these measurements.

MATERIALS AND METHODS

This retrospective diagnostic accuracy study was conducted at the Istanbul Medeniyet University, Goztepe Prof. Dr. Suleyman Yalcin City Hospital, between January 1, 2014, and December 31,

Received April 21, 2021; accepted after revision July 25.

From the Departments of Radiology (M.B.E., B.A., M.B.D., N.G.) and Otorhinolaryngology-Head and Neck Surgery (M.T.K.), Faculty of Medicine, Istanbul Medeniyet University, Goztepe Prof. Dr. Suleyman Yalcin City Hospital, Istanbul, Turkey.

The data that support the findings of this study are available on request from the corresponding author.

Paper previously presented at: Annual Scientific Meeting of the European Society of Head and Neck Radiology, September 2–4, 2021; Virtual, Vienna, Austria.

Please address correspondence to Mehmet Bilgin Eser, MD, Department of Radiology, Istanbul Medeniyet University Faculty of Medicine, Goztepe Prof. Dr. Suleyman Yalcin City Hospital, Istanbul, Turkey; e-mail: bilgineser@hotmail.com; @MehmetBilginEs1

http://dx.doi.org/10.3174/ajnr.A7287

Table 1: Internal acoustic canal 3D FIESTA-C protocol

	3D FIESTA-C
Plane	Axial + coronal + sagittal oblique
Fat suppression	+
TR (ms)	6.9
TE (ms)	Min
Flip angle	55°
Section thickness (mm)	1
FOV (mm)	320 × 320
Bandwidth (Hz)	90
Matrix (mm × mm)	256 × 192

Note:—Min indicates 2.6–12 ms.

2020. Ethics approval was obtained from the local University Ethics Committee, and the committee waived the need for informed consent due to the retrospective nature of the study. The Standards for Reporting of Diagnostic Accuracy Studies (STARD) guideline was followed during the conduct and documentation of the study.[11]

Study Participants

Patients with postlingual hearing loss who underwent cochlear implant surgery in our university hospital were recruited for the study based on the following inclusion and exclusion criteria.

Inclusion Criteria

1. Patients for whom both MRI and CT imaging were performed in our hospital
2. Patients whose round window niche (the cochlear outer wall and apical turn end point) could be clearly distinguished on imaging
3. Patients who did not have a congenital anomaly of the inner ear as seen on the CT and MRI.

Exclusion Criteria

1. Patients who were operated on at our hospital, but imaging was performed at another center
2. The image quality of the scans was inadequate for measurement
3. Cochlear calcifications that did not allow measurement of the lateral cochlear wall.

Protocols for CT and MR Imaging

CT was performed per the temporal bone algorithm using a Optima CT660 scanner (GE Healthcare); all patients were scanned supine. The FOV was adjusted to include the entire temporal bone, data were collected with a 512 × 512 matrix detector, and the section thickness was 0.625 mm.

MR imaging was performed using the Optima 450w 1.5T scanner (GE Healthcare). For this study, the FIESTA-C (Siemens) equivalent, the CISS sequence, was performed in the 3 in-plane acquisitions, namely axial, coronal, and oblique sagittal, through the internal auditory canal (details about this sequence are presented in Table 1). Cochlear lateral wall length measurements were made per the reconstructed coronal FIESTA-C acquisition.

Recording and Processing of the Demographic and Imaging Data

Demographic data of the study participants were recorded. CT and MR images of the patients were blinded and transferred to a Mac OS X (10.15.7; Apple) computer; raw imaging data were registered with the PACS software. Measurements were made with a 3D MPR application.

Two observers performed and recorded their CT and MR imaging measurements independently: Observer 1 had performed cochlear measurements on 387 cases before participating in the study; observer 2 had no prestudy experience of cochlear measurement and was given 1 hour of training with sample cases. First, they measured the cochlea on the CT images, followed by measurement on MR imaging at a gap of 2 weeks to avoid recognition bias.

For CT measurements, the procedure described by Eser et al[12] was used to measure the length of the cochlear duct starting from the cochlear view, following the full-turn cochlea, and covering the lateral cochlear wall. The observers selected each point as the outermost coordinate to avoid partial volume effects and beam-hardening artifacts (Fig 1). The MR imaging measurement method was modified to obtain the round window niche and follow the hyperintense cochlear fluid boundary (Fig 2). Unlike the previous study, the hook of the apical turn was not included for both CT and MR imaging measurements.[12]

Statistical Analysis

Gaussian distribution of the outcome data was evaluated using the Kolmogorov-Smirnov test, and Gaussian-distributed data were presented as mean (SD). A paired *t* test was used to determine the mean difference. Intraobserver and interobserver reliability for CT and MR imaging was evaluated using the intraclass correlation coefficient (ICC) (with 95% confidence intervals) as described by Koo and Li[13] (2-way mixed-effects, absolute agreement, single measurement). If the ICC value was 0.49 and below, the reliability was considered weak. ICCs ranging from 0.50 to 0.74 represented moderate reliability, between 0.75 and 0.89 represented good reliability, and >0.90 meant excellent reliability. A P value < .05 was used to determine statistical significance. All data were evaluated using SPSS for Mac OS X (Version 22.0; IBM).

RESULTS

Demographic Data of the Participants

The study included 35 patients (all whites), of which 70% ($n = 21$) were men. The average age of all participants was 39.85 (SD, 16.60) years, while the mean age of male participants was 36.71 (SD, 15.02) years, and it was 44.57 (SD, 18.26) years for the female participants. Measurements on CT and MR images of 1 patient's left ear could not be made due to calcifications secondary to chronic otitis media, so this ear was excluded. MR imaging of another 2 patients was excluded due to motion artifacts. Therefore, interobserver reliability analyses were performed on 69 ears for CT and 65 ears for MR imaging, while 65 ears were evaluated during intraobserver reliability analyses.

Cochlear Length Measurement and Intraobserver Reliability Results

Observer 1 measured the mean cochlear lateral wall length (LWL) as 41.52 (SD, 2.25) mm on CT and 41.44 (SD, 2.18) mm on MR imaging, with a mean difference for the full-turn cochlear length

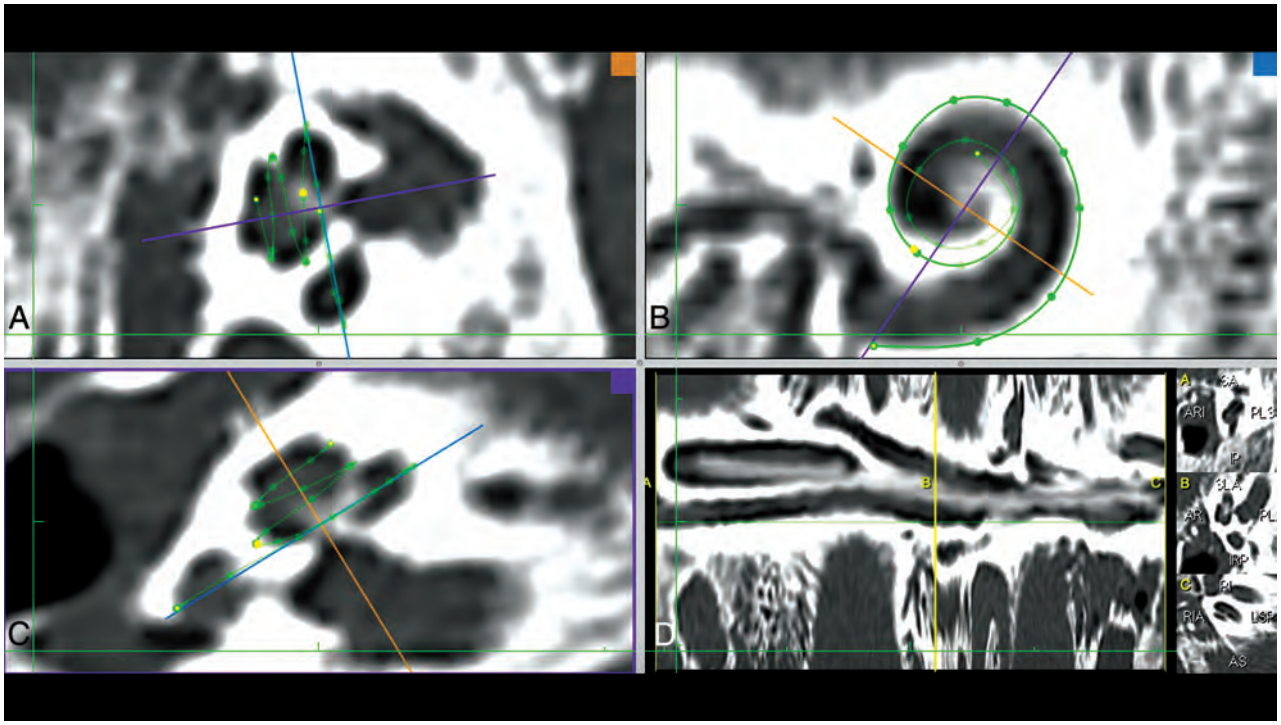

FIG 1. Screenshot of the CT postprocessing software used in the study. *A* and *C*, Planes perpendicular to the modiolus are formed. *B*, The cochlear view is shown; in this plane, the basal turn can be fully traced and the bone structure of the round window is visualized as a *thin line* parallel to the *purple line*. The *purple line* also indicates the *A*-value measured from the niche to the opposite cochlear wall and the diameter of the cochlear basal turn. *C*, The round window niche is distinguished as a hypodense area below the measuring point. *D*, The measurement screen.

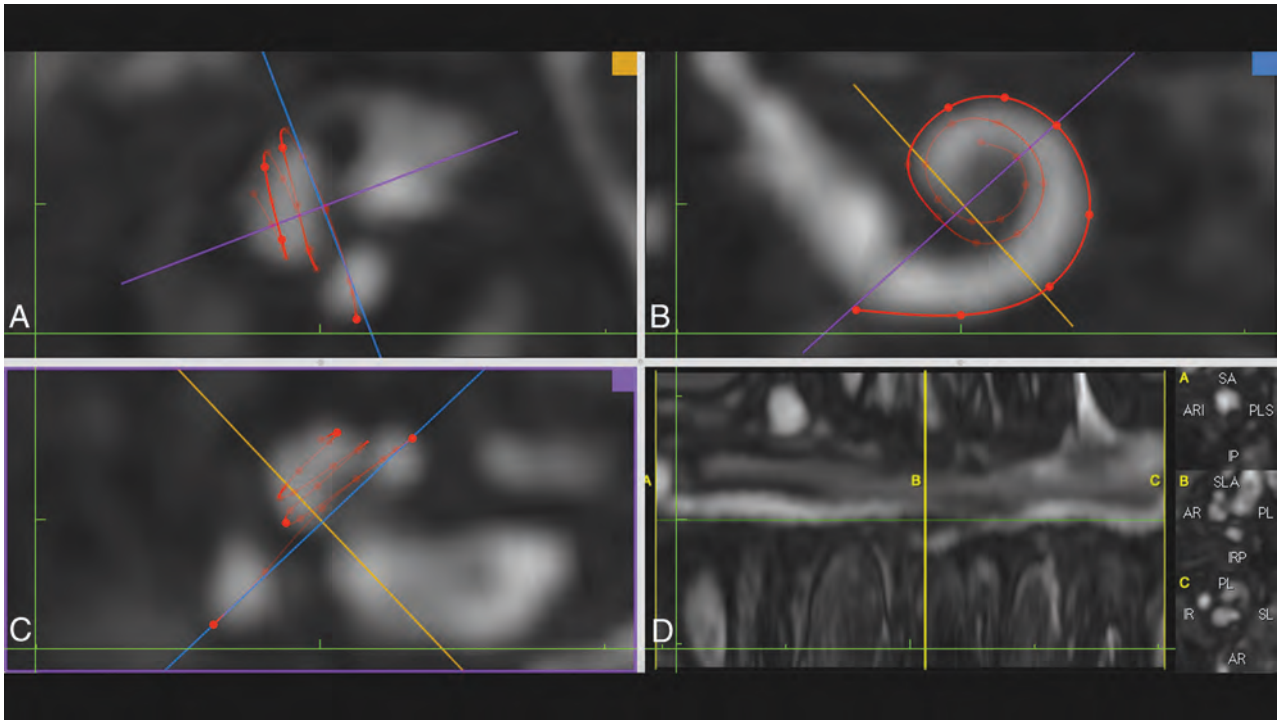

FIG 2. Screenshot of the MR imaging postprocessing software. *A* and *C*, Planes perpendicular to modiolus are formed. *B*, The cochlear view is shown; in this plane, the basal turn can be fully traced and the bone structure of the round window is viewed as a *thin hypointense line* parallel to the *purple line*. *C*, The round window niche is not distinguished, and bone and air are shown as hypointense on the FIESTA-C MR imaging sequence. *D*, The measurement screen.

Table 2: Intraobserver accuracy and reliability of observer 1's cochlear LWL measurements between CT and MR imaging

	CT (mean) (95% CI)	MRI (mean) (95% CI)	ICC (95% CI)	*P* Value
Cochlea basal turn length (mm)	22.95 (SD, 1.21) (22.65–23.25)	23.37 (SD, 1.12) (23.09–23.65)	0.70 (0.48–0.82)	<.001[a]
Cochlea 2 turn length (mm)	35.92 (SD, 1.98) (35.43–36.41)	36.27 (SD, 1.77) (35.83–36.71)	0.85 (0.75–0.91)	<.001[a]
Cochlea lateral wall length (mm)	41.52 (SD, 2.25) (40.96–42.08)	41.44 (SD, 2.18) (40.90–41.98)	0.94 (0.90–0.96)	<.001[a]

[a] The *P* value is statistically significant.

Table 3: Intraobserver accuracy and reliability of observer 2's cochlear LWL measurements between CT and MR imaging

	CT (mean) (95% CI)	MRI (mean) (95% CI)	ICC (95% CI)	*P* Value
Cochlea basal turn length (mm)	22.57 (SD, 1.21) (22.28–22.88)	22.91 (SD, 1.18) (22.61–23.20)	0.69 (0.52–0.80)	<.001[a]
Cochlea 2 turn length (mm)	35.51 (SD, 2.17) (34.98–36.05)	36.37 (SD, 2.08) (35.85–36.88)	0.79 (0.66–0.87)	<.001[a]
Cochlea lateral wall length (mm)	41.74 (SD, 2.69) (41.07–42.40)	42.34 (SD, 2.53) (41.71–42.97)	0.86 (0.73–0.92)	<.001[a]

[a] The *P* value is statistically significant.

Table 4: Interobserver reliability of 2 observers

	CT ICC (95% CI)	*P* Value	MRI ICC (95% CI)	*P* Value
Cochlea basal turn length	0.86 (0.73–0.92)	<.001[a]	0.72 (0.45–0.85)	<.001[a]
Cochlea 2 turn length	0.87 (0.79–0.92)	<.001[a]	0.77 (0.64–0.85)	<.001[a]
Cochlea lateral wall length	0.90 (0.84–0.94)	<.001[a]	0.69 (0.46–0.82)	<.001[a]

[a] The *P* value is statistically significant.

between these 2 observations as 0.08 mm (95% CI, −0.11−0.27 mm). The average cochlear LWLs and ICC results (with 95% confidence intervals) for observer 1 are presented in Table 2.

Observer 2 measured the mean cochlear LWL as 41.74 (SD, 2.69) mm on CT and 42.34 (SD, 2.53) mm on MR imaging, with a mean difference of −0.59 mm (95% CI, −1.00 to −0.20 mm) between these observations for the full-turn cochlear length. The average measurement and ICC results (with 95% confidence intervals) for observer 2 are given in Table 3.

Interobserver Reliability Results

An ICC value of 0.90 (95% CI, 0.84−0.94) for CT and 0.69 (95% CI, 0.46−0.82) for MR imaging was obtained for the interobserver reliability for the full-turn cochlear LWL. The reliability between the 2 observers as assessed by ICCs is given in Table 4.

DISCUSSION

This study tested the accuracy and reliability of measuring cochlear length using a 3D reconstruction on CT and MR imaging. High intraobserver and interobserver reliability was observed for CT-based measurements, whereas good-to-excellent intraobserver reliability and moderate-to-good interobserver reliability was observed for MR imaging to measure cochlear LWL.

Accuracy and Reliability of 3D Cochlear Length Measurements

Intraobserver accuracy of an experienced observer's CT measurements (observer 1) with MR imaging measurements was the following: There was moderate reliability for the basal turn length, good reliability for the 2-turn length, and excellent reliability for the full-turn cochlear length. There have been limited studies evaluating MR imaging for similar objectives.[14,15] One of these studies measured the intraobserver and interobserver reliability of the *A*-value, while the other study used the spiral ganglion as the measurement target, and only 1 observer performed the measurements. Multiple studies have been performed with CT,[3] and most measured the *A*-value and rarely dealt with the reproducibility of the method. Schurzig et al[16] revealed the superiority of 3D measurements over spiral formulas. Likewise, Eser et al[12] evaluated 3D CT measurements and reported good-to-excellent intraobserver reliability in their study (ICC = 0.87).

Our results show that the cochlear lateral wall length measurements are accurate when done by an experienced observer. The second observer had no experience in temporal bone imaging, except for 3 years of radiology experience and was given only 1 hour of training before measurements. A short training period was chosen as per the study hypothesis, which was that even with a short training period, there would be high accuracy and reliability. This hypothesis was proved for CT-based measurements: Good-to-excellent reliability was seen between the 2 observers. A probable reason is that the bony anatomic structures can be visualized easily with high-resolution CT (Fig 3). On the contrary, the section thickness is higher in MR imaging, making it more difficult to detect anatomic bone landmarks. However, while the interobserver reliability was moderate-to-good with MR imaging, our results demonstrate high (good-to-excellent) intraobserver reliability with MR imaging.

Although Observer 1's mean MR imaging measurements were similar to the CT measurements, the second observer's MR imaging measurements were longer than the CT measurements, a probable reason being the basic difference between the 2 imaging techniques.[12,14] The structure visualized on CT was the hyperdense bony cortex surrounding the cochlea, while on MR imaging, it was the hyperintense fluid in the cochlea. These may cause a partial volume artifact for both imaging modalities.[12] Therefore, the cochlea can be observed slightly shorter than its actual size with CT and is slightly longer than its actual length with MR imaging. Second, the anatomic landmarks required for measurement are probably more clearly differentiated on CT.[17] For instance, the round window niche is an anatomic landmark that has been used unanimously in previous studies as the

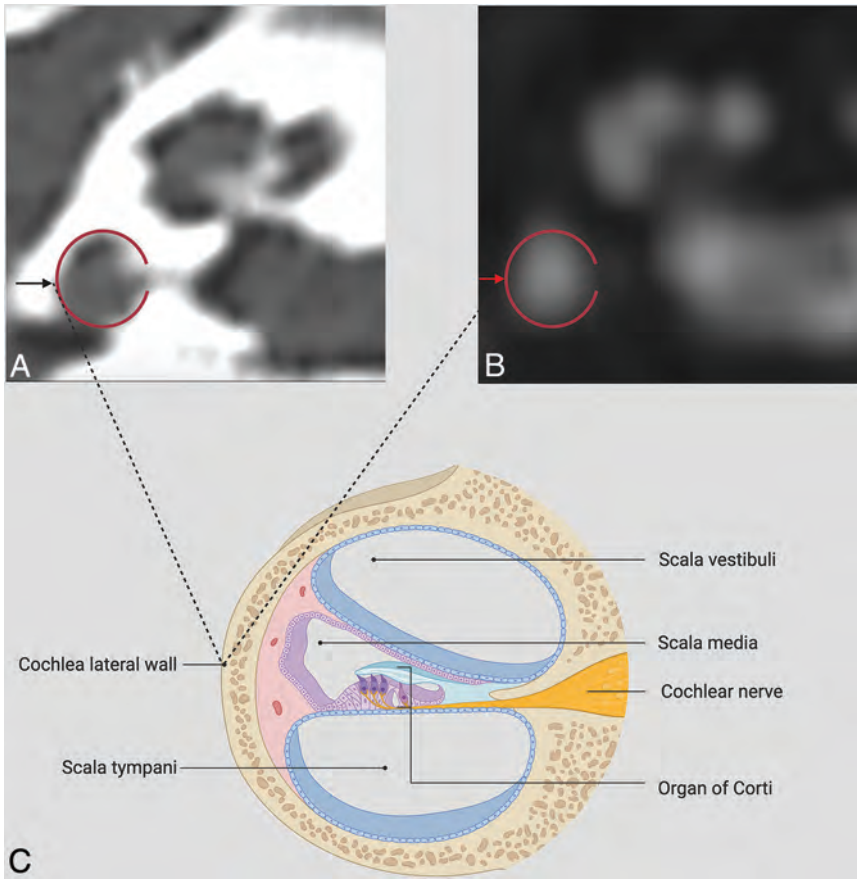

FIG 3. CT (*A*) and MR imaging (*B*) of the cochlea of the same patient. The *red ring* seen in these images shows the lateral wall of the cochlea. The *black arrow* seen on the CT (*A*) image and the *red arrow* seen on the MR imaging (*B*) image indicate the outermost point of the lateral cochlear wall. The lateral cochlear wall, the target point of measurement, and other anatomic structures are summarized in a schematic view (*C*). Created with BioRender.com.

starting point for CT measurement and can be easily detected in the cochlear view.[18] In this study, both observers faced difficulty in finding the round window niche because it is made of a thin bone structure and was hardly differentiated on MR imaging due to the hyperintense fluid signal of the inner ear.

The final challenge that reduces interobserver reliability is the difficulty in deciding the cochlea apical end point. In 2013, Erixon and Rask-Andersen[19] included the hook segment in the measurement and found an approximately 1-mm variation in the cochlear apical turn between the 2 observers. Moreover, the measurements were taken with a highly sensitive micrometer made from the plastic casts of cochleae obtained from cadavers. Despite an increase in the interobserver reliability with this choice, we decided to exclude the hook segment in the apical turn, contrary to previous studies.

Last, it is important to consider how measurements are affected by the observer's experience. As hypothesized, the experienced observer's intraobserver reliability reached an ICC value of 0.94, while the inexperienced observer had an ICC of 0.86, which was still highly acceptable. Furthermore, the interobserver reliability was better for CT-based measurements (ICC = 0.90), while it was moderate (ICC = 0.69) for MR imaging due to the aforementioned reasons. These results suggest that MR imaging measurements are affected more negatively by the observer's experience than CT measurements.

Is the Difference in Interobserver Reliability Clinically Significant?

On evaluating paired *t* test results across the intraobserver and interobserver reliability, we observed that the highest difference achieved in the 2 observers' MR imaging measurements was for the full-turn cochlear length (−0.90 [SD, 1.71] mm; 95% CI, −1.31 to −0.47 mm). This result shows that there was a negligible difference (on average, 1 mm) between the 2 observers. Considering that cochlear implant lengths are currently produced at 2-mm intervals, this difference is not clinically essential in cochlear implant selection.[20] In a recent meta-analysis, Atalay et al[3] reported a similar difference (0.61 [SD, 0.54] mm) in the organ of Corti length between people from the general population and patients with acquired hearing loss and stated that this difference was not significant with the same reasoning. However, Schurzig et al[16] compared the accuracy of spiral formulas. For the same *A*-value, they found the organ of Corti length varying from 29.2 (SD, 2.30) mm to 43.4 (SD, 3.40) mm. Considering that 2 mm is important in this implant selection, it is far from an acceptable margin of error.[3,9,16,20] Therefore, CT measurements should preferably be considered in the selection of cochlear implants, and MR imaging may be used as a second-line alternative.

How Do the Technical Differences between CT and MR Imaging Influence the 3D Cochlear Length Measurements?

Imaging technology is improving progressively. The most commonly used imaging method for pre-cochlear implant evaluation is multidetector CT, followed by conebeam CT.[3] In a recent study, 0.25-mm isotropic-voxel resolution was achieved with ultra-high-resolution CT in clinical images.[21] However, with MR imaging, the section thickness cannot go below 0.60-mm isotropic-voxel resolution, even with 3D sequences. Although this voxel size difference does not seem very large, 3D CT images have approximately 14 times higher spatial resolution than MRI[21]; this spatial resolution difference is probably responsible for the high interobserver reliability with CT. Although significant improvements have been made recently for bone imaging with MR imaging, such as zero TE, to reduce these technical differences, CT is more useful clinically.[22,23] Nevertheless, if MR imaging sequences developed in the future can show the bone structure in detail, pre-cochlear implant imaging of patients can be performed with MR imaging only, significantly

avoiding unnecessary radiation exposure. Extensive and comprehensive studies are needed to obtain a higher spatial resolution with MR imaging that allows detailed imaging of the bone structure.

Last, it is necessary to discuss the MR imaging sequences and magnets exclusively. Besides the 3D FIESTA-C and CISS sequences used frequently for imaging the internal auditory canal, cochlea, and labyrinth, 3D FSE sequences are also used.[24-28] The 3D T2 FSE sequences (Cube, GE Healthcare; sampling perfection with application-optimized contrasts by using different flip angle evolutions [SPACE], Siemens; driven equilibrium radiofrequency reset pulse [DRIVE]) can eliminate banding artifacts and have fewer flow and susceptibility artifacts.[28] Also, the use of 3T magnets provides a high signal-to-noise ratio and better spatial resolution than 1.5T, with shorter acquisition times.[24,25] However, more artifacts are encountered along with these advantages, especially with gradient recalled-echo sequences (banding and susceptibility artifacts). These artifacts may obscure fine anatomic detail of the cochlea and labyrinth.

Limitations

Our study has some limitations. Although the CT and MR imaging devices used in the study are currently the most used device technologies, ultra-high-resolution CT and 3T-magnet MR imaging devices are also available. Other researchers may repeat this study using currently available higher resolution isotropic 3D T2 sequences (Cube, SPACE, DRIVE) acquired at 3T. Studies with these new devices are likely to provide a greater interobserver reliability for MR imaging. If MR imaging scans were obtained in the cochlear view plane, the distortion-caused artifacts could be reduced, increasing the interobserver reliability. Another limitation is the difference in the level of experience between the 2 observers. However, to avoid this, we tested the effect of experience on measurements; high reliability in CT measurements showed us that the observer experience has a minimal effect on CT-based evaluations. Nevertheless, comparing MR imaging measurements of observers with comparable professional experience will help appreciate the true potential of MR imaging measurements.

CONCLUSIONS

This study showed that the 3D cochlear length measurements made with CT had excellent intraobserver and interobserver reliability, while MR imaging–based measurements also demonstrated good-to-excellent intraobserver reliability for full-turn cochlear measurement and moderate interobserver reliability. These results corroborate the importance of CT imaging in 3D cochlear measurements as a reference method, and MR imaging may be used as an alternative imaging technique that offers comparably reliable results.

ACKNOWLEDGMENT

Figure 3 was created with BioRender.com.

REFERENCES

1. Roth TN, Hanebuth D, Probst R. **Prevalence of age-related hearing loss in Europe: a review.** *Eur Arch Otorhinolaryngol* 2011;268:1101–07 CrossRef Medline
2. Roche JP, Hansen MR. **On the horizon: cochlear implant technology.** *Otolaryngol Clin North Am* 2015;48:1097–116 CrossRef Medline
3. Atalay B, Eser MB, Kalcioglu MT, et al. **Comprehensive analysis of factors affecting cochlear size: a systematic review and meta-analysis.** *Laryngoscope* 2021 Mar 25. [Epub ahead of print] CrossRef Medline
4. Koch RW, Ladak HM, Elfarnawany M, et al. **Measuring cochlear duct length: a historical analysis of methods and results.** *J Otolaryngol Head Neck Surg* 2017;46:1–11 CrossRef Medline
5. Mistrík P, Jolly C. **Optimal electrode length to match patient specific cochlear anatomy.** *Eur Ann Otorhinolaryngol Head Neck Dis* 2016;133(Suppl 1):S68–71 CrossRef Medline
6. Kjer HM, Fagertun J, Wimmer W, et al. **Patient-specific estimation of detailed cochlear shape from clinical CT images.** *Int J Comput Assist Radiology Surg* 2018;13:389–96 CrossRef Medline
7. Timm ME, Majdani O, Weller T, et al. **Patient specific selection of lateral wall cochlear implant electrodes based on anatomical indication ranges.** *PLoS One* 2018;13:e0206435 CrossRef Medline
8. Schurzig D, Timm ME, Batsoulis C, et al. **A novel method for clinical cochlear duct length estimation toward patient-specific cochlear implant selection.** *OTO Open* 2018;2:2473974X1880023 CrossRef Medline
9. Eser MB, Atalay B, Kalcıoğlu MT. **Comment on "The Effect of Cochlear Size on Cochlear Implantation Outcomes."** *Biomed Res Int* 2020;2020:5674547 CrossRef Medline
10. Helal RA, Jacob R, Elshinnawy MA, et al. **Cone-beam CT versus multidetector CT in postoperative cochlear implant imaging: evaluation of image quality and radiation dose.** *AJNR Am J Neuroradiol* 2021;42:362–67 CrossRef Medline
11. Bossuyt PM, Reitsma JB, Bruns DE, et al. STARD Group. **STARD 2015: an updated list of essential items for reporting diagnostic accuracy studies.** *Radiology* 2015;277:826–69 CrossRef Medline
12. Eser MB, Atalay B, Kalcıoğlu MT. **Is cochlear length related to congenital sensorineural hearing loss: preliminary data.** *J Int Adv Otol* 2021;17:1–8 CrossRef Medline
13. Koo TK, Li MY. **A guideline of selecting and reporting intraclass correlation coefficients for reliability research.** *J Chiropr Med* 2016;15:155–63 CrossRef Medline
14. Connor SE, Bell DJ, O'Gorman R, et al. **CT and MR imaging cochlear distance measurements may predict cochlear implant length required for a 360° insertion.** *AJNR Am J Neuroradiol* 2009;30:1425–30 CrossRef Medline
15. Sobrinho FP, Lazarini PR, Yoo HJ, et al. **A method for measuring the length of the cochlea through magnetic resonance imaging.** *Braz J Otorhinolaryngol* 2009;75:261–67 CrossRef Medline
16. Schurzig D, Timm ME, Lexow GJ, et al. **Cochlear helix and duct length identification: evaluation of different curve fitting techniques.** *Cochlear Implants Int* 2018;19:268–83 CrossRef Medline
17. Widmann G, Dejaco D, Luger A, et al. **Pre- and post-operative imaging of cochlear implants: a pictorial review.** *Insights Imaging* 2020;11:93 CrossRef Medline
18. Verbist BM, Frijns JH, Geleijns J, et al. **Multisection CT as a valuable tool in the postoperative assessment of cochlear implant patients.** *AJNR Am J Neuroradiol* 2005;26:424–29 Medline
19. Erixon E, Rask-Andersen H. **How to predict cochlear length before cochlear implantation surgery.** *Acta Otolaryngol* 2013;133:1258–65 CrossRef Medline
20. Dhanasingh A. **Cochlear duct length along the outer wall vs organ of corti: which one is relevant for the electrode array length selection and frequency mapping using Greenwood function?** *World J Otorhinolaryngol Head Neck Surg* 2019;5:117–21 CrossRef Medline
21. Heutink F, Koch V, Verbist B, et al. **Multi-scale deep learning framework for cochlea localization, segmentation and analysis on clinical ultra-high-resolution CT images.** *Computer Comput Methods Programs Biomed* 2020;191:105387 CrossRef Medline
22. Lu A, Gorny KR, Ho ML. **Zero TE MRI for craniofacial bone imaging.** *AJNR Am J Neuroradiol* 2019;40:1562–66 CrossRef Medline
23. Delso G, Wiesinger F, Sacolick LI, et al. **Clinical evaluation of zero-echo-time MR imaging for the segmentation of the skull.** *J Nucl Med* 2015;56:417–22 CrossRef Medline
24. Byun JS, Kim HJ, Yim YJ, et al. **MR imaging of the internal auditory canal and inner ear at 3T: comparison between 3D driven**

equilibrium and 3D balanced fast field echo sequences. *Korean J Radiology* 2008;9:212–18 CrossRef Medline

25. Naganawa S, Koshikawa T, Fukatsu H, et al. **MR cisternography of the cerebellopontine angle: comparison of three-dimensional fast asymmetrical spin-echo and three-dimensional constructive interference in the steady-state sequences.** *AJNR Am J Neuroradiol* 2001;22:1179–85 Medline
26. Jung NY, Moon WJ, Lee MH, et al. **Magnetic resonance cisternography: comparison between 3-dimensional driven equilibrium with sensitivity encoding and 3-dimensional balanced fast-field echo sequences with sensitivity encoding.** *J Comput Assist Tomogr* 2007;31:588–91 CrossRef Medline
27. Schmalbrock P. **Comparison of three-dimensional fast spin echo and gradient echo sequences for high-resolution temporal bone imaging.** *J Magn Reson Imaging* 2000;12:814–25 Medline
28. Benson JC, Carlson ML, Lane JI. **MRI of the internal auditory canal, labyrinth, and middle ear: how we do it.** *Radiology* 2020;297:252–65 CrossRef Medline

Protuberant Fibro-Osseous Lesion of the Temporal Bone: "Bullough Bump"—Multimodality Imaging Case Series and Literature Review

N. Shekhrajka, D.R. Shatzkes, K.E. Dean, M.C. Smithgall, and G. Moonis

ABSTRACT

SUMMARY: A handful of cases of protuberant fibro-osseous lesions of the temporal bones have been described in the literature to date, with primary focus on the pathologic features. Here we review 3 cases of pathology-proved protuberant fibro-osseous lesions of the temporal bone and include a literature review with a focus on the imaging features. While rare, these lesions have near-pathognomonic imaging features defined by a location at the cortex of the outer table of the temporal bone at the occipitomastoid suture, lack of involvement of the underlying marrow, variable mineralization, and MR signal characteristics atypical of a chondroid lesion. One case in this series was FDG-avid and had occasional mitotic features, possibly reflecting an aggressive variant. Neuroradiologists should be familiar with this benign diagnosis to aid in timely identification and avoid unnecessary additional imaging.

ABBREVIATIONS: FD = fibrous dysplasia; PFOLT = protuberant fibro-osseous lesion of the temporal bone

Protuberant fibro-osseous lesion of the temporal bone (PFOLT) was originally described by Selesnick et al,[1] in 1999. They presented 2 unique-but-identical cases of right-sided retroauricular exophytic fibro-osseous lesions in young patients emanating from the outer cortex of the bone near the occipitomastoid suture line. Almost 11 years later, Sia et al[2] reported 2 similar cases in 2010, and they proposed naming the lesion "Bullough lesion/bump" after Professor Peter Bullough, who described the pathologic features in the original case report in 1999. To date, 10 similar cases have been reported in the literature. These lesions have near-pathognomonic imaging features, defined by a location at the outer table cortex of the temporal bone at the occipitomastoid suture, lack of involvement of the underlying marrow, variable mineralization, and MR signal characteristics atypical of a chondroid lesion. The goal of this article is to report a multi-institutional series of this lesion, to discuss the clinical characteristics and unique imaging features of the lesion, and to review the existing cases in the literature.

Received March 24, 2021; accepted after revision July 9.

From the Department of Radiology (N.S.), Copenhagen University Hospital, Copenhagen, Denmark; Department of Radiology (D.R.S.), Donald and Barbara Zucker School of Medicine at Hofstra/Northwell, Lenox Hill Hospital, New York, New York; Department of Radiology (K.E.D.), Weill Cornell Medicine, New York, New York; and Department of Pathology (M.C.S.), Anatomic and Clinical Pathology, and Department of Radiology (G.M.), Columbia University Irving Medical Center, New York, New York.;

Please address correspondence to Gul Moonis, MD, Department of Radiology, Columbia University Irving Medical Center, 630 W 168th Street, New York, NY 10032; e-mail: gm2640@cumc.columbia.edu; @gmoonis

http://dx.doi.org/10.3174/ajnr.A7298

Case Series

Institutional review board approval was waived and not required for this retrospective case series. Three cases were identified from 3 different institutions in New York City between 2015 and 2020.

Demographic information was obtained from the electronic medical record, including age, clinical presentation, imaging findings, and histopathologic diagnosis.

Case 1. A 39-year-old previously healthy woman presented with a painless mass in the right retroauricular region, which had been slowly growing for the last 5 years. No other contributory history was noted. On physical examination, a nontender mass was palpated in the right retroauricular region without changes in the overlying skin. The mass was hard in consistency, and the overlying skin was freely mobile. No other findings were observed on the clinical examination. Neurologic examination findings were normal, as were hematologic and audiologic parameters.

On skull radiographs, bony thickening of the right retroauricular region with a small exophytic sclerotic/mineralized lesion was noted (Fig 1). Noncontrast CT of the head demonstrated a 3.5 × 1.1 cm, well-defined, broad-based, protuberant calcified mass with ground-glass density in the retroauricular region emanating from the outer cortex of the right temporal bone near the occipitomastoid suture (Fig 2). There was a stalk-like attachment to the outer cortex, with some irregularity of the otherwise intact underlying cortex. No intracranial extension was seen. There was elevation of the overlying scalp. Given the imaging features, the initial differential diagnoses of the lesion included osteoma, osteoblastoma, parosteal osteosarcoma, and periosteal chondrosarcoma. MR imaging

of the brain with and without contrast showed a T1- and T2-hypointense (to muscle), mildly enhancing, broad-based, postauricular lesion emanating from the outer table of the right temporal bone. There was a more pronounced peripheral rim of enhancement noted (Fig 3). There were no signal changes in the underlying bone, nor was there intramedullary or intracranial extension.

The lesion was excised without any postoperative complications. The temporalis muscle was found to be partially adherent to the lesion intraoperatively. A calcified peduncular attachment of the lesion to the outer table was noted, which was resected. Microscopically, there were numerous rounded ossified bodies composed of either woven or lamellar bone within a bland fibrous stroma. Atypia, mitotic activity, or osteoblastic rimming were not identified (Fig 4).

The patient has been followed for 4 years without any evidence of tumor recurrence.

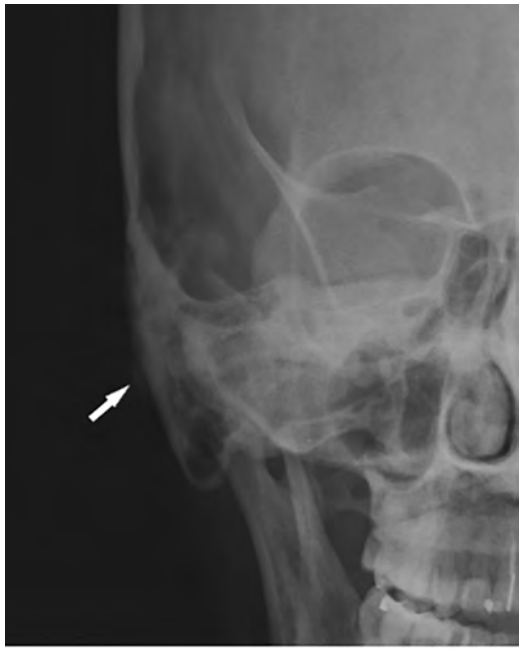

FIG 1. Case 1. Plain radiographs of the skull show a small, exophytic sclerotic/mineralized lesion with bony thickening of the right retroauricular cortex (*white arrow*).

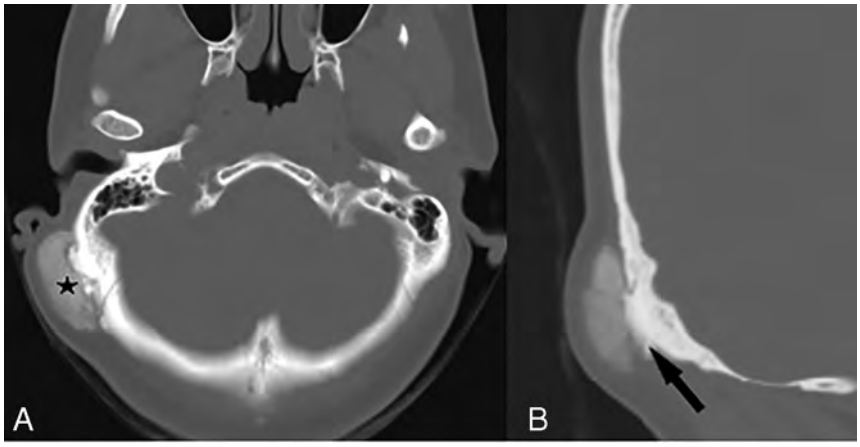

FIG 2. Case 1. Axial (*A*) and coronal (*B*) noncontrast CT images through the temporal bone show a well-defined, exophytic, protuberant calcified mass with ground-glass density (*star*) in the retroauricular region, seen emanating from the outer cortex of the right temporal bone near the occipitomastoid suture causing elevation of the overlying scalp without intramedullary or intracranial extension. A broad-based stalk-like attachment to the occipitomastoid suture is noted (*arrow*).

Case 2. An 18-year-old man presented with a lump behind the left ear noted by his father 2 years earlier. His father thought that the lump was slowly growing. He had no pain, hearing loss, or history of trauma, and the patient was otherwise healthy. Physical examination showed a 3 × 2 cm left retroauricular bony protuberance over the mastoid area (Fig 5). The remainder of the head and neck examination had normal findings.

He initially underwent noncontrast head CT, which demonstrated a well-marginated calcific mass with a sclerotic stalk within the occipitomastoid suture and a larger exophytic component containing punctate areas of osseous and/or calcific density (Fig 6). The initial differential diagnosis included osteochondroma, parosteal osteosarcoma, or chondrosarcoma. MR imaging of the skull base was then performed, demonstrating immediate T1 signal intensity, very low T2 signal intensity (to muscle), and mild heterogeneous contrast enhancement (Fig 7). The low T2 signal intensity was thought incompatible with a chondroid lesion, and the differential was revised to a Bullough lesion versus parosteal osteosarcoma.

A 3-cm fibro-osseous mass with a mushroom-like shape was excised from the outer cortex of the left temporal bone. Histologic analysis revealed rounded or ovoid areas of calcification within a background of bland fibrous stroma, compatible with a Bullough lesion. The postoperative course was uncomplicated, and there has been no recurrence 5 years following resection.

Case 3. A 25-year-old woman with a history of retinopathy of prematurity and chronic daily headaches presented with a hard, palpable mass behind her right ear. The patient reported that she initially noticed the mass 2 months prior, and it was slowly growing since that time. The patient denied changes to her existing headaches or other new symptoms. On examination, the lesion was nonmobile, firm, and approximately 2 cm in size.

A head CT at that time identified an irregularly calcified, protuberant mass arising from the outer cortex of the right temporal bone overlying the occipitomastoid suture with no continuity with the medullary cavity (Fig 8). On review of existing head CTs from 2007, 2010, and 2011 (all acquired for headaches), it was noted that the mass had substantially increased in size, now measuring 2.9 × 1.5 × 2.3 cm, compared with 0.6 × 0.3 × 0.5 cm in 2007 (Fig 9). In addition to being smaller, the lesion previously appeared solidly calcified in 2007, suggestive of a peripheral

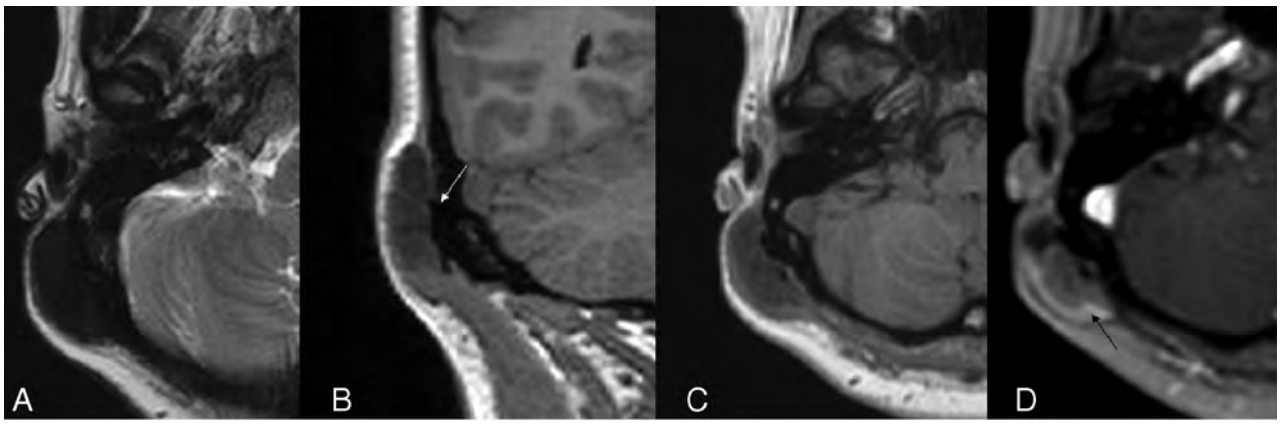

FIG 3. Case 1. MR images with and without contrast. Axial T2 (*A*), coronal and axial T1 (*B* and *C*), and postgadolinium axial (*D*) T1-weighted images show a T1- and T2-hypointense (to muscle), mildly enhancing broad-based, exophytic postauricular lesion emanating from the outer table of the right temporal bone (*arrow* in *B*). There is no signal change in the underlying bone and no intramedullary or intracranial extension. A thin, peripheral rim of enhancement is seen (*arrow* in *D*).

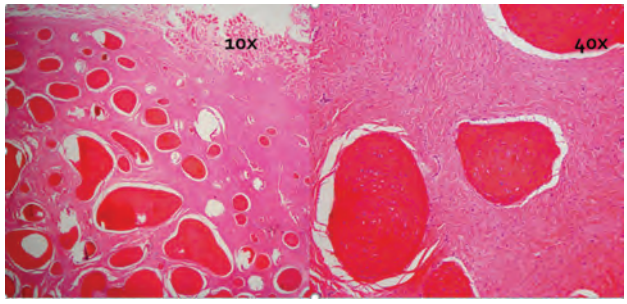

FIG 4. Case 1. Histology under low-power (10×) and high-power (40×) fields. Note numerous rounded ossified bodies composed of either woven or lamellar bone within a bland fibrous stroma. No atypia, mitotic activity or osteoblastic rimming are identified.

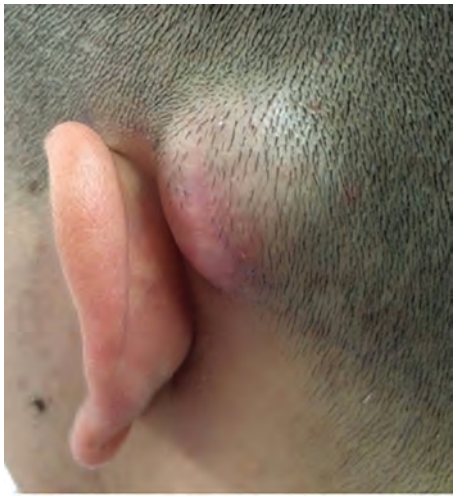

FIG 5. Case 2. On clinical examination, a 3 × 2 cm left retroauricular bony protuberance over the mastoid area is noted.

ivory osteoma. With growth, that initial solidly calcified component appeared as a bony stalk with surrounding more irregular calcifications. A subsequent brain MR imaging with and without contrast demonstrated a predominantly T2-hypointense mass with an enhancing rim (Fig 10). The leading differential diagnosis was an osteochondroma. Given the interval growth, the patient was referred to neurosurgery, and a PET/CT was acquired. The lesion was found to be FDG-avid (Fig 11).

The patient underwent a right temporal craniectomy with mesh cranioplasty and an excision of a 3.3 cm, tan-white, rubbery, fibro-osseous mass. On histologic analysis, the tumor was composed of spindle cells with fascicular architecture and entrapped islands of bone. Findings were most consistent with a Bullough lesion (Fig 12). Of note, occasional mitotic features were observed, a finding that differs from those in other reported cases of Bullough lesions. The patient did well postoperatively without any clinical or imaging findings or recurrence for 18 months.

Literature Review

To date, 10 cases of PFOLT have been reported in the literature.[1-7] The cases have varied in age (10–70 years; mean, 37.5 years) and have been seen predominantly in females (female/male ratio, 7:3) and on the right side (right/left ratio, 8:2). All patients presented with a firm retroauricular mass that had been slowly enlarging for many years (range, 1–15 years), except for case 2 from the original case reports by Selesnick et al,[1] in which the patient discovered the mass 5 days before presentation. On examination, the lesion presented as a nontender, firm or hard, immobile, exophytic, retroauricular mass with smooth surfaces and without overlying skin or soft-tissue abnormalities. In only 1 pediatric case reported by Jiang et al[5] was the mass tender to touch. No lymphadenopathy was noted. The findings of the remainder of the regional and systemic physical examination were unremarkable. No comorbidities were reported in any of the cases, except in case 2 by Lee et al,[4] whose patient had a history of hepatitis B, and the pediatric case reported by Jiang et al with a family history of polycystic kidney disease. No history of preceding trauma had been reported before the appearance of the mass, except in case 2 by Lee et al, whose patient had a history of a fall in childhood with the appearance of a bean-sized lesion slowly growing for years in the same location as the subsequent

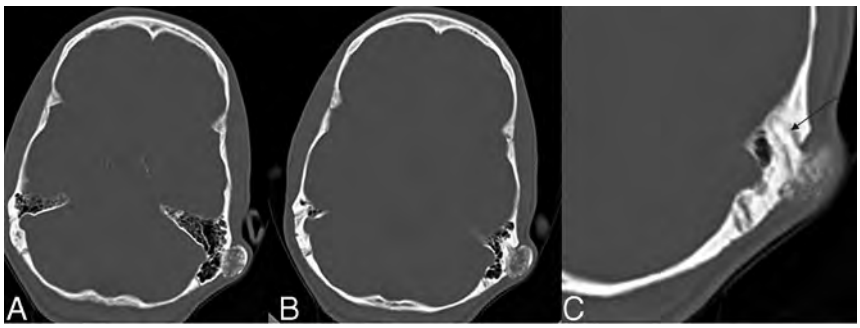

FIG 6. Case 2. Axial noncontrast CT images through the temporal bones (*A* and *B*) show a well-marginated exophytic mass based along the lateral mastoid cortex with a densely calcified rim and a central heterogeneously calcified component. Magnified axial CT image (*C*) shows a densely calcified stalk (*black arrow*) that extends into the occipitomastoid suture.

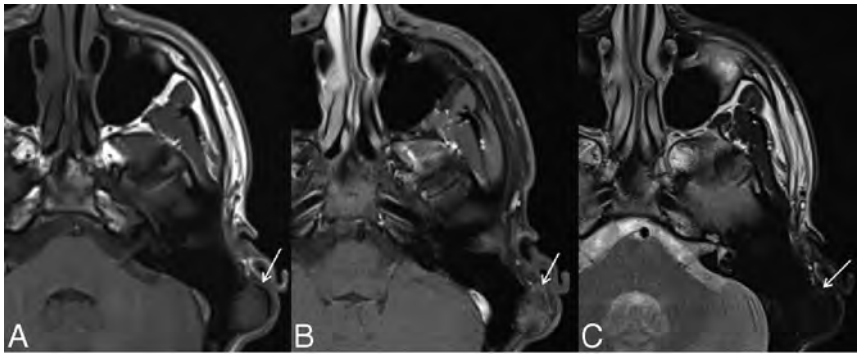

FIG 7. Case 2. MR images with and without contrast. Axial T1 (*A*), axial T1 postgadolinium fat-saturated (*B*), and axial T2-weighted (*C*) images show a thin peripheral signal void (*arrow* in *A*) and central intermediate signal intensity on noncontrast T1WI with mild heterogeneous enhancement (*arrow* in *B*) and diffusely low T2 signal intensity (*arrow* in *C*).

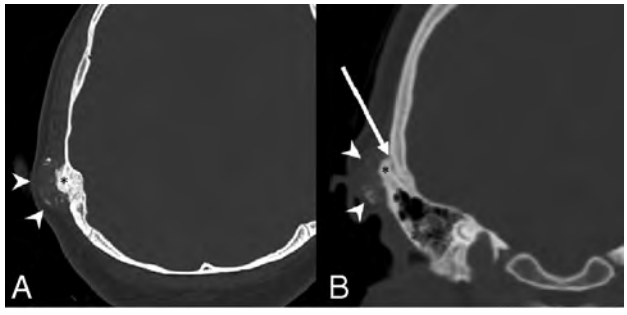

FIG 8. Case 3. Axial and coronal noncontrast CT images (*A* and *B*) demonstrate an irregularly calcified mass (*white arrowheads*) centered over the right temporal outer cortex at the level of the occipitomastoid suture (*white arrow*). Note the solidly calcified bony stalk (*black asterisk*). No gross destruction of the outer table cortex is seen, and there is no intraosseous or intracranial extension. The lesion uplifts the overlying scalp.

Bullough lesion. In the case described by Jiang et al, the mass was first noticed when the patient had a minor trauma.

Two patients underwent plain skull radiographs, which showed a wide-based retroauricular bony exostosis with a speckled appearance in 1 case and spiculated margins and a somewhat sunburst appearance in the other.[2,5] All the reported patients underwent CT of the head without contrast. On imaging, the size of the mass ranged from 1.7 to 5.5 cm.[4,6] A well-defined, heterogeneous, broad-based, exophytic, retroauricular mass, emanating from the outer cortex of the temporal bone and in close relationship to the occipitomastoid suture was seen in all cases. The lesion consisted of varying degrees of mineralization, ranging from small punctate foci of calcification to coarse calcification, interposed within a more lucent ground-glass matrix. The underlying cortex was intact, without intramedullary or intracranial extension, but elevation of the overlying scalp soft tissue was reported in all cases. No involvement of the mastoid air cells was reported. Sia et al[2] also noticed an irregular contour of the underlying cortex in 1 case and some remodeling of the underlying cortex in another case, but with an intact bony cortex without intramedullary or intracranial extension in both cases. In 2 cases, a pedunculated attachment of the lesion to the underlying bone was reported.[6,7] None of these patients were evaluated by MR imaging.

In all cases, the lesion was surgically excised and sent for histologic examination. On microscopy, the lesion characteristically showed a mixture of ovoid-to-spherical bone islands of various sizes composed of either woven or lamellar bone and embedded in a dense fibrocollagenous stroma. Direct continuity between collagen from bone and the surrounding fibrous stroma has been identified.[2,6] Immunohistochemical stains for CD34, desmin, S-100 protein, smooth-muscle actin, epithelial membrane antigen, carcinoembryonic antigen, progesterone receptor, signal transducer and activator of transcription 6, and pancytokeratin were negative, with a negligible Ki-67 proliferation index.[2,4] β-catenin staining did not show nuclear localization, which would be suggestive of aberrant Wnt/β-catenin signaling, and only showed weak cytoplasmic positivity in the peripheral merging areas of osseous islands in 1 case.[4] In addition, mouse double minute 2 homolog was tested in 1 case and was not amplified, which would be seen in certain low-grade osteosarcomas. Overall, these results are consistent with a fibro-osseous lesion without muscle, nerve, vascular, or epithelial differentiation. No mitotic activity or cellular atypia has been reported. No evidence of guanine nucleotide stimulatory protein (*GNAS*) mutation, which is characteristically present in fibrous dysplasia, has been found.[4]

DISCUSSION

This case series describes the clinical, pathologic, and radiologic features in 3 cases of PFOLT. Most existing publications on this

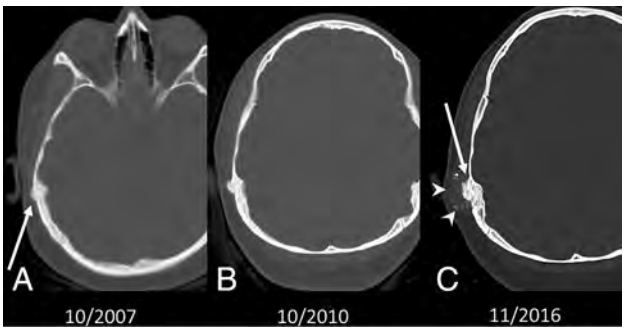

FIG 9. Case 3. Axial noncontrast CT images across time demonstrating the slow, interval growth of the retroauricular mass along the outer cortex of the right temporal bone. Also note that the lesion was initially a solidly calcified bony stalk, imaging similar to a peripheral ivory osteoma (*white arrow* in *A*). As the lesion grew, the ossification was less solid at the periphery and more irregular (*white arrowheads* in *C*) with persistence of the initial bony stalk (*arrow* in *C*).

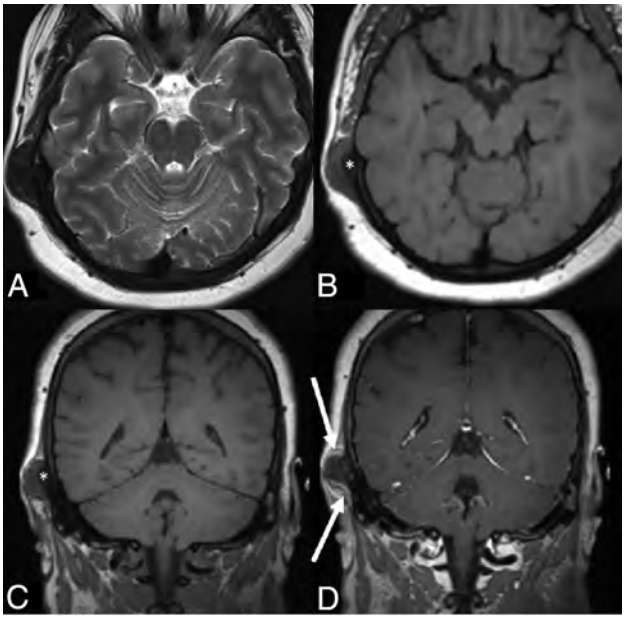

FIG 10. Case 3. MR images with and without contrast. Axial T2-weighted image (*A*) demonstrates the homogeneous T2-hypointense signal of the lesion. The lesion is predominantly T1-hypointense on the axial and coronal noncontrast T1-weighted images (*B* and *C*), particularly centrally, corresponding to the more densely calcified bony stalk (*white asterisk*). A largely peripheral cap of enhancement (*white arrows*) is noted on the coronal, postcontrast T1-weighted image.

topic have been in the pathology, otolaryngology, and neurosurgery literature. We believe this imaging-focused series is the first one in the radiology literature with multimodality imaging appearances, including plain film, CT, MR imaging, and PET. Given the distinctive imaging features, familiarity of radiologists with this entity may allow an earlier prospective diagnosis.

On CT, PFOLTs are well-marginated, protuberant, calcified masses in the retroauricular region, emanating from the outer cortex near or from the occipitomastoid suture. The degree of calcification ranges from ground-glass (case 1) to more a heterogeneous speckled appearance (cases 2 and 3). Stalk-like attachment to the outer cortex is intermittently identified. The lesion is distinct from the marrow with no marrow continuity with the parent bone. No abnormal osseous density in the adjacent medullary cavity is present. On MR imaging, the lesions are markedly hypointense on T2-weighted images with mild heterogeneous enhancement. There is no extension of this lesion into the overlying scalp or surrounding soft tissues. In 2 cases, peripheral rimlike enhancement was noted on MR imaging.

Case 3 demonstrated an interval increase in size and PET avidity. Also of note, occasional mitotic figures were observed in this case on histology. Although the lesion is considered benign, case 3 suggests a more aggressive variant.

The imaging differential diagnosis of PFOLT includes fibrous dysplasia (FD), ossifying fibroma, osteoma, osteochondroma, surface osteosarcoma, and periosteal chondrosarcoma.

FD is a fibro-osseous lesion with approximately 110 reported cases involving the temporal bone.[4,8,9] FD, unlike PFOLT, is usually nonprotuberant and shows growth during childhood but becomes static after puberty.[5,10] Protuberant variants of FD, so-called "fibrous dysplasia protuberans," are extremely rare, and only a few cases of this entity have been reported.[11,12] FD is usually associated with a mutation in the *GNAS1* gene,[13,14] whereas this mutation has not been found in PFOLT,[4] suggesting a different molecular pathogenesis of PFOLT. On imaging, FD is a poorly defined, nonprotuberant, intraosseous- or intramedullary-based lesion with bone expansion and disruption of the bony architecture with a ground-glass matrix. Histologically, FD contains curvilinear trabeculae of woven or occasionally lamellar bone, with inconspicuous osteoblastic rimming embedded within bland fibrous stroma. Ossifying fibroma is also an intramedullary-based, expansile, ground-glass lesion but is more localized, round or ovoid, with thin sharply circumscribed borders.[15] Only a handful of cases of ossifying fibroma have been described in the temporal bone.[16,17]

Osteoma is a benign osteoblastic tumor composed of well-differentiated mature osseous tissue resembling dense cortical bone, though cancellous bone may be seen.[18] The most common sites are the frontal and ethmoid sinuses; however, in the temporal bone, the external auditory canal is the most common site of origin, followed by the mastoid and squamous portion.[18] Histologically, it shows an admixture of lamellar and woven bone with Haversian-like canals, while a minority are composed of trabecular bone. Only a few cases of mastoid osteoma have been reported, and these can be pedunculated or sessile well-demarcated hyperdense masses arising from the lateral mastoid cortex without a predilection for the occipitomastoid suture.[19-24]

Osteochondroma is the most common benign tumor of bone but is uncommon in the head and neck.[25] On CT, the lesion is composed of cortical and medullary bone protruding from and continuous with the underlying bone with an overlying cartilage cap. There is pathognomonic cortical and marrow continuity of the lesion and the parent bone. MR imaging is the best radiologic technique for visualizing the effect of the lesion on surrounding structures and evaluating the hyaline cartilage cap.[25] Microscopically, these lesions contain an outer fibrous periosteal layer and a cartilage cap with underlying ossification, which is continuous with the cortex and marrow space.

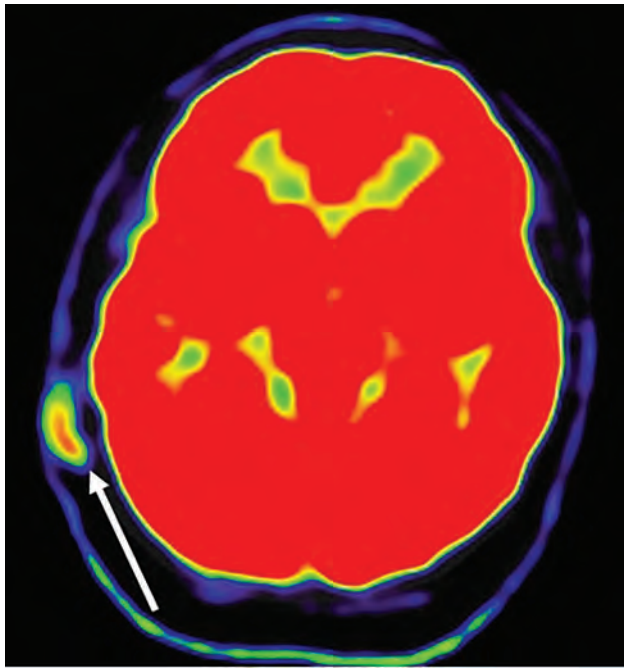

FIG 11. Case 3. FDG-PET image demonstrates FDG-avidity of the lesion (*white arrow*), consistent with the occasional mitotic features at histology.

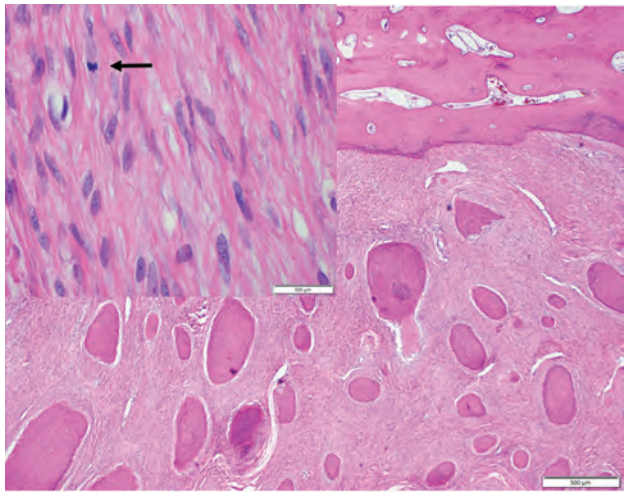

FIG 12. Case 3. Histology under a low-power field demonstrates numerous round ossified bodies within a proliferation of bland spindle cells. The fibrous stroma shows occasional mitotic figures (*arrow* in inset); however, no atypia is identified.

Osteosarcoma is a primary malignant bone tumor in which neoplastic cells produce osteoid. Surface osteosarcomas are rare variants of osteosarcoma that include parosteal osteosarcoma, periosteal osteosarcoma, and high-grade surface osteosarcoma.[26,27] The parosteal subtype, which was first referred to as "juxtacortical osteosarcoma," is the most frequently encountered one. These tumors are rare in the temporal bone and have been identified in the mastoid segment and glenoid fossa.[28] On CT, they present as aggressive soft-tissue masses with calcification, cortical thickening, periosteal new bone formation, and invasion of the surrounding soft tissue.[29,30] On MR imaging, the lesion is hyperintense on T2-weighted images with enhancement.[29] Histologically, these lesions demonstrate broad, woven bone trabeculae embedded in fibrous stroma and molecularly demonstrate CDK4a and use double minute 2 homolog amplification.[31]

Periosteal chondrosarcoma is a rare malignant cartilaginous tumor arising from the bony surfaces of the long bone and is extremely rare in craniofacial bones. On CT, the tumor is juxtacortical with thickening or erosion of the underlying cortex and contains calcific densities characteristic of cartilage tumors.[32] On MR imaging, the lesion is T2-hyperintense with enhancement of the periphery and septations. Low signal and punctate foci of mineralization can be seen on both T1- and T2-weighted sequences.[32] Histologically, these are atypical chondroid lesions with secondary calcification and ossification eroding the outer cortex, without invading the bone marrow.

As noted above, a PFOLT has distinct radiographic and histologic features that help differentiate it from these other lesions. This includes a relationship to the occipitomastoid suture, lack of continuity with the underlying medullary cavity, lack of a cartilage cap, lack of a periosteal reaction, and lack of T2-hyperintensity on MR imaging. Morphologically, a PFOLT shows a mixture of ovoid-to-spherical bone islands of various sizes composed of either woven or lamellar bone and embedded in a dense fibrocollagenous stroma.

CONCLUSIONS

We have described the multimodality imaging appearance of a Bullough lesion in 3 cases, with distinct imaging features that can help suggest the correct diagnosis.

Disclosures: Gul Moonis—*UNRELATED*: *Royalties*: Wolters Kluwer, *Comments*: US $140 in 2020.

REFERENCES

1. Selesnick SH, Desloge RB, Bullough PG. **Protuberant fibro-osseous lesions of the temporal bone: a unique clinicopathologic diagnosis.** *Am J Otol* 1999;20:394–96 Medline
2. Sia SF, Davidson AS, Soper JR, et al. **Protuberant fibro-osseous lesion of the temporal bone: "Bullough lesion."** *Am J Surg Pathol* 2010;34:1217–23 CrossRef Medline
3. Nagarajan K, Jothiramalingam SB. **3D CT appearance of exophytic mastoid fibro-osseous lesion.** *Indian J Otol* 2013;19:143 CrossRef
4. Lee M, Song JS, Chun SM, et al. **Protuberant fibro-osseous lesions of the temporal bone: two additional case reports.** *Am J Surg Pathol* 2014;38:1510–05 CrossRef Medline
5. Jiang B, Mushlin H, Zhang L, et al. **Bullough's bump: unusual protuberant fibro-osseous tumor of the temporal bone: case report.** *J Neurosurg Pediatr* 2018;21:107–11 CrossRef Medline
6. Sturdà C, Rapisarda A, Gessi M, et al. **Bullough's lesion: an unexpected diagnosis after the resection of a slowly growing osseous-like retroauricular bump: case report and review of the literature.** *World Neurosurg* 2019;122:372–75 CrossRef Medline
7. Maroun CA, Khalifeh I, Faddoul DS, et al. **A patient with a protuberant fibro-osseous lesion of the temporal bone.** *J Craniofac Surg* 2019;30:e453–54 CrossRef Medline
8. Kim YH, Song JJ, Choi HG, et al. **Role of surgical management in temporal bone fibrous dysplasia.** *Acta Otolaryngol* 2009;129:1374–79 CrossRef Medline

9. Silu M, Gupta G. **External auditory canal stenosis due to isolated fibrous dysplasia of temporal bone: a case report.** *Int J Otorhinolaryngol Head Neck Surg* 2019;6:204 CrossRef
10. Kushchayeva YS, Kushchayev SV, Glushko TY, et al. **Fibrous dysplasia for radiologists: beyond ground glass bone matrix.** *Insights Imaging* 2018;9:1035–56 CrossRef Medline
11. Dorfman HD, Ishida T, Tsuneyoshi M. **Exophytic variant of fibrous dysplasia (fibrous dysplasia protuberans).** *Hum Pathol* 1994;25:1234–37 CrossRef Medline
12. Hamadani M, Awab A, Rashid A, et al. **Fibrous dysplasia protuberans in a patient with McCune-Albright syndrome.** *J Coll Physicians Surg Pak* 2006;16:376–77 Medline
13. Weinstein LS, Shenker A, Gejman PV, et al. **Activating mutations of the stimulatory G protein in the McCune-Albright syndrome.** *N Engl J Med* 1991;325:1688–95 CrossRef Medline
14. Lee SE, Lee EH, Park H, et al. **The diagnostic utility of the *GNAS* mutation in patients with fibrous dysplasia: meta-analysis of 168 sporadic cases.** *Hum Pathol* 2012;43:1234–42 CrossRef Medline
15. Khoury NJ, Naffaa LN, Shabb NS, et al. **Juvenile ossifying fibroma: CT and MR findings.** *Eur Radiol* 2002;12(Suppl 3):S109–13 CrossRef Medline
16. Levine PA, Wiggins R, Archibald RW, et al. **Ossifying fibroma of the head and neck: involvement of the temporal bone- and unusual and challenging site.** *Laryngoscope* 1981;91:720–25 CrossRef Medline
17. Vlachou S, Terzakis G, Doundoulakis G, et al. **Ossifying fibroma of the temporal bone.** *J Laryngol Otol* 2001;115:654–56 CrossRef Medline
18. Jeong J, Choi YJ, Hong CE, et al. **Giant osteoma in the mastoid of the temporal bone: complete excision of a rare tumor.** *Otol Neurotol* 2018;39:e894–96 CrossRef Medline
19. Singh RK, Goyal A, Kumar A, et al. **Mastoid osteoma of temporal bone: a rare case report.** *J Clin Diagn Res* 2017;11:MD01–2 CrossRef Medline
20. Kandakure VT, Lahane VJ, Mishra S. **Osteoma of mastoid bone; a rare presentation—case report.** *Indian J Otolaryngol Head Neck Surg* 2019;71:1030–32 CrossRef Medline
21. Park SJ, Kim YH. **A case of giant osteoma developed from the mastoid cortical bone.** *Korean J Audiol* 2012;16:95–98 CrossRef Medline
22. Cheng J, Garcia R, Smouha E. **Mastoid osteoma: a case report and review of the literature.** *Ear Nose Throat J* 2013;92:E7–9 Medline
23. Viswanatha B. **Characteristics of osteoma of the temporal bone in young adolescents.** *Ear Nose Throat J* 2011;90:72–79 CrossRef Medline
24. Lee RE, Balkany TJ. **Giant mastoid osteoma with postoperative high-frequency sensorineural hearing loss.** *Ear Nose Throat J* 2008;87:23–25 CrossRef Medline
25. Murphey MD, Choi JJ, Kransdorf MJ, et al. **Imaging of osteochondroma: variants and complications with radiologic-pathologic correlation.** *Radiographics* 2000;20:1407–34 CrossRef Medline
26. Nouri H, Ben Maitigue M, Abid L, et al. **Surface osteosarcoma: clinical features and therapeutic implications.** *J Bone Oncol* 2015;4:115–23 CrossRef Medline
27. Raymond AK. **Surface osteosarcoma.** *Clin Orthop Relat Res* 1991;140–48 Medline
28. Tan JH, Miyakoshi A, Mafee MF. **Imaging of fibro-osseous lesions of the temporal bone.** *Oper Tech Otolaryngol Head Neck Surg* 2014;25:96–109 CrossRef
29. Murphey MD, Jelinek JS, Temple HT, et al. **Imaging of periosteal osteosarcoma: radiologic-pathologic comparison.** *Radiology* 2004;233:129–38 CrossRef Medline
30. Villemure-Poliquin N, Trudel M, Labonté S, et al. **Low-grade surface osteosarcoma of the temporal bone in paediatric patients: a case report and literature review.** *Clin Med Insights Pediatr* 2019;13:1179556519855381 CrossRef Medline
31. Yoshida A, Ushiku T, Motoi T, et al. **Immunohistochemical analysis of MDM2 and CDK4 distinguishes low-grade osteosarcoma from benign mimics.** *Mod Pathol* 2010;23:1279–88 CrossRef Medline
32. Chaabane S, Bouaziz MC, Drissi C, et al. **Periosteal chondrosarcoma.** *AJR Am J Roentgenol* 2009;192:W1–6 CrossRef Medline

Pulsatility Attenuation along the Carotid Siphon in Pseudoxanthoma Elasticum

J.W. Bartstra, R.J. van Tuijl, P.A. de Jong, W.P.T.M. Mali, I.C. van der Schaaf, Y.M. Ruigrok, G.J.E. Rinkel, B.K. Velthuis, W. Spiering, and J.J.M. Zwanenburg

ABSTRACT

SUMMARY: We compared velocity pulsatility, distensibility, and pulsatility attenuation along the intracranial ICA and MCA between 50 patients with pseudoxanthoma elasticum and 40 controls. Patients with pseudoxanthoma elasticum had higher pulsatility and lower distensibility at all measured locations, except for a similar distensibility at C4. The pulsatility attenuation over the siphon was similar between patients with pseudoxanthoma elasticum and controls. This finding suggests that other disease mechanisms are the main contributors to increased intracranial pulsatility in pseudoxanthoma elasticum.

ABBREVIATIONS: PI = pulsatility index; PXE = pseudoxanthoma elasticum; SVD = small-vessel disease; 2D-PC = 2D phase-contrast

The curved shape combined with distensibility of the carotid siphon attenuates arterial pulsatility and protects the cerebral vasculature.[1,2] Calcification and stiffening in the siphon may reduce pulsatility attenuation and cause increased intracranial arterial pulsatility. Arterial calcifications occur in atherosclerotic plaques in the intimal arterial wall.[3] Medial arterial calcifications in the medial layer and internal elastic lamina contribute to arterial stiffening.[4] Extracranial arterial stiffness increases intracranial pulsatility because it hampers attenuation of the pulse pressure to the microvascular bed,[3] but reduced attenuation along the siphon has been studied less.

Pseudoxanthoma elasticum (PXE) is a rare disorder with severe calcifications in the skin, eyes, and internal elastic lamina of the arteries of the arms, legs, and carotid siphon.[5] PXE results in increased arterial stiffness, peripheral arterial disease, stroke, and small-vessel disease (SVD).[6,7] Carotid siphon calcification is associated with increased arterial flow pulsatility, and both calcification and pulsatility are associated with SVD.

To investigate whether patients with PXE have reduced pulsatility attenuation along the carotid siphon, we compared velocity pulsatility and distensibility along the ICA and MCA and pulsatility attenuation over the siphon between patients with PXE and controls.

Received May 12, 2021; accepted after revision July 12.

From the Departments of Radiology (J.W.B., R.J.v.T., P.A.d.J., W.P.T.M.M., I.C.v.d.S., B.K.V., J.J.M.Z.), and Neurology and Neurosurgery (Y.M.R., G.J.E.R.), Rudolf Magnus Institute of Neuroscience, Utrecht, the Netherlands; and Department of Vascular Medicine (W.S.), University Medical Center Utrecht, Utrecht University, Utrecht, the Netherlands.

J.W. Bartstra and R.J. van Tuijl shared first authorship.

Please address correspondence to Rick J. van Tuijl, MSc, University Medical Center Utrecht, PO Box 85500, Heidelberglaan 100, 3584 CX Utrecht, The Netherlands; e-mail: r.j.vantuijl@umcutrecht.nl

http://dx.doi.org/10.3174/ajnr.A7288

MATERIALS AND METHODS

Data Availability

Anonymized data will be shared on reasonable request to the corresponding author.

Participants

Fifty patients with PXE and 40 age- and sex-matched controls were included. Controls were either families or acquaintances of patients with PXE, excluding first-/second-degree relatives. Exclusion criteria were younger than 18 years of age, estimated glomerular filtration rate of <30 mL/min/1.73m^2, a cardiac device, or claustrophobia. The study was approved by University Medical Center Utrecht institutional review board. All participants gave written informed consent.

MR Imaging Acquisition

All participants were scanned on a 3T MR imaging unit with a 32-channel head coil (Philips Healthcare). 2D phase-contrast (2D-PC) MR imaging with retrospective cardiac gating was acquired separately for both sides proximal to the cavernous segment (C4) and distal to the carotid siphon at the ophthalmic (C6)[8] and MCA M1 segment, using the following imaging parameters: FOV = 250 × 250 mm^2, reconstructed spatial resolution = 0.25 × 0.25 × 3 mm^3, acquired temporal resolution = 64 ms, and unidirectional through-plane velocity encoding sensitivities of 100 cm/s for C4 and MCA and 150 cm/s for C6 to avoid phase wraps. The flow acquisitions provided time-resolved measurements of the blood

Baseline characteristics patients with PXE and controls[a]

Characteristic	PXE ($n = 49$)	Controls ($n = 40$)	*P* Value
Age (yr)	57 (SD, 12)	58 (SD, 11)	.49
Male sex (No.) (%)	24 (49%)	20 (50%)	.92
Systolic BP (mm Hg)	136 (SD, 20)	133 (SD, 15)	.59
Diastolic BP (mm Hg)	77 (SD, 12)	79 (SD, 10)	.33
Statin use (No.) (%)	25 (51%)	5 (13%)	<.01
LDL cholesterol (mmol/L)	2.8 (SD, 0.91)	3.6 (SD, 0.83)	<.01
Hypercholesterolemia (No.) (%)	42 (86%)	37 (93%)	.31
Current smoking (No.) (%)	6 (12%)	4 (11%)	.84
Pulsatility measurements			
ICA C4 (No.)	93	79	
PI	1.12 (0.98–1.22)	0.94 (0.81–1.08)	<.01
Distensibility (mm Hg^{-1})	0.18 (0.16–0.24)	0.21 (0.17–0.25)	.14
Mean velocity (cm/s)	22.8 (17.9–29.5)	18.9 (15.4–23.7)	<.01
ICA C6 (No.)	70	34	
PI	0.96 (0.89–1.09)	0.83 (0.75–0.94)	<.01
Distensibility (mm Hg^{-1})	0.33 (0.27–0.43)	0.57 (0.45–0.63)	<.01
Mean velocity (cm/s)	32.5 (28.2–37.8)	29.7 (24.9–37.7)	.08
MCA (No.)	95	77	
PI	0.92 (0.82–1.05)	0.79 (0.67–0.87)	<.01
Distensibility (mm Hg^{-1})	0.30 (0.25–0.40)	0.48 (0.42–0.57)	<.01
Mean velocity (cm/s)	36.6 (32.0–42.2)	38.3 (33.8–48.7)	.05
Pulsatility attenuation			
C4 to C6	−0.09 (−0.13 to −0.06)	−0.11 (−0.16 to −0.08)	.03
C6 to MCA	−0.06 (−0.09 to −0.02)	−0.05 (−0.14–0.00)	.59
C4 to MCA	−0.16 (−0.21 to −0.11)	−0.16 (−0.24 to −0.11)	.48

Note:—BP indicates blood pressure; C4, cavernous ICA segment; C6, ophthalmic ICA segment; LDL, low-density lipoprotein.

[a] Data are means and median and interquartile range or No. (%).

flow velocity and volumetric flow rates over the cardiac cycle. Flow measurements of sufficient quality were included.[1]

Data Processing

Semiautomated analysis of the 2D-PC acquisitions was performed with scanner software (software release R5.1.7; Philips Healthcare).[1] ROIs were automatically created with a mouse click without any manual correction. The automated ROI selection was repeated in 5 random subjects to test reproducibility. The velocity curve was obtained from mean ROI values of each cardiac phase. The minimum, maximum, and mean blood flow velocities from this curve (V_{min}, V_{max}, and V_{mean}) in centimeters/second were used to calculate the pulsatility index (PI) = $(V_{max}–V_{min})/V_{mean}$). Arterial distensibility, defined as $(A_{max}–A_{min})/A_{mean})/\Delta P) \times 100$, was calculated from each area curve, where A indicates ROI areas and ΔP is the systolic-diastolic pressure measured before MR imaging.[2] Pulsatility attenuation was calculated by subtracting the PI of the proximal from the distal segment.

Statistical Analysis

Descriptive data were presented as mean for normal and median (interquartile range) for non-normally distributed variables and number (percentage) for categoric variables. Because PI measurements for the left and right were not significantly different, no stratification per side was performed. Differences between the PXE and control groups were tested with the Student *t* test, Mann-Whitney *U* test, or χ^2 test when appropriate. Analysis was performed in R Studio, Version 1.1.456 (http://rstudio.org/download/desktop). A *P* value < .05 was regarded as statistically significant.

RESULTS

Baseline

Fifty patients with PXE (57 [SD, 12] years of age, 49% men) and 40 controls (58 [SD, 11] years of age, 50% men) were enrolled between January 2017 and May 2018 (baseline characteristics are in the Table). One patient with PXE had an ophthalmic artery aneurysm and was excluded.

Pulsatility Index, Distensibility, and Pulsatility Attenuation

Repeat automated ROI selection in 5 subjects demonstrated no changes in measurements. The PI decreased from C4 to C6 and from C6 to the MCA in both patients with PXE and controls (Table). Patients with PXE had a higher PI at all locations. Distensibility was significantly lower in PXE at C6 ($P < .01$) and the MCA ($P < .01$), but not at C4, where the ICA passes through the skull base (Table and Figure). In patients with PXE, pulsatility attenuation was less between C4 and C6 than in controls ($P = .03$), but the effective attenuation between C4 and the MCA was similar ($P = .48$) (Table).

DISCUSSION

This study shows that the siphon seems to function normally in PXE. Although patients with PXE have a higher PI and lower distensibility, pulsatility attenuation between C4 and MCA was similar compared with controls.

The current finding is different from that in patients with PXE with SVD, in whom pulsatility increased over the carotid siphon compared with a decrease in controls.[9] Although both small studies, these findings suggest that the hemodynamics in patients with SVD are not a representative model for the PXE phenotype. This possibility may be because patients with SVD have combined atherosclerotic intimal disease and medial arterial calcifications, whereas patients with PXE have relatively isolated medial arterial calcifications.[6]

Velocity pulsatility is affected by upstream arterial elasticity and downstream vascular or microvascular resistance.[10] Other factors include age, sex, and local constraints to arterial distensibility, such as the bony carotid canal and calcified lesions.[1,11] The distensibility proximal to the cavernous segment (C4) is affected by the skull base; therefore, no conclusion can be drawn regarding the distensibility or stiffness of the artery at this location. Variation in the configuration of the circle of Willis between C6 and the MCA may also affect pulsatility attenuation and blood flow.[12]

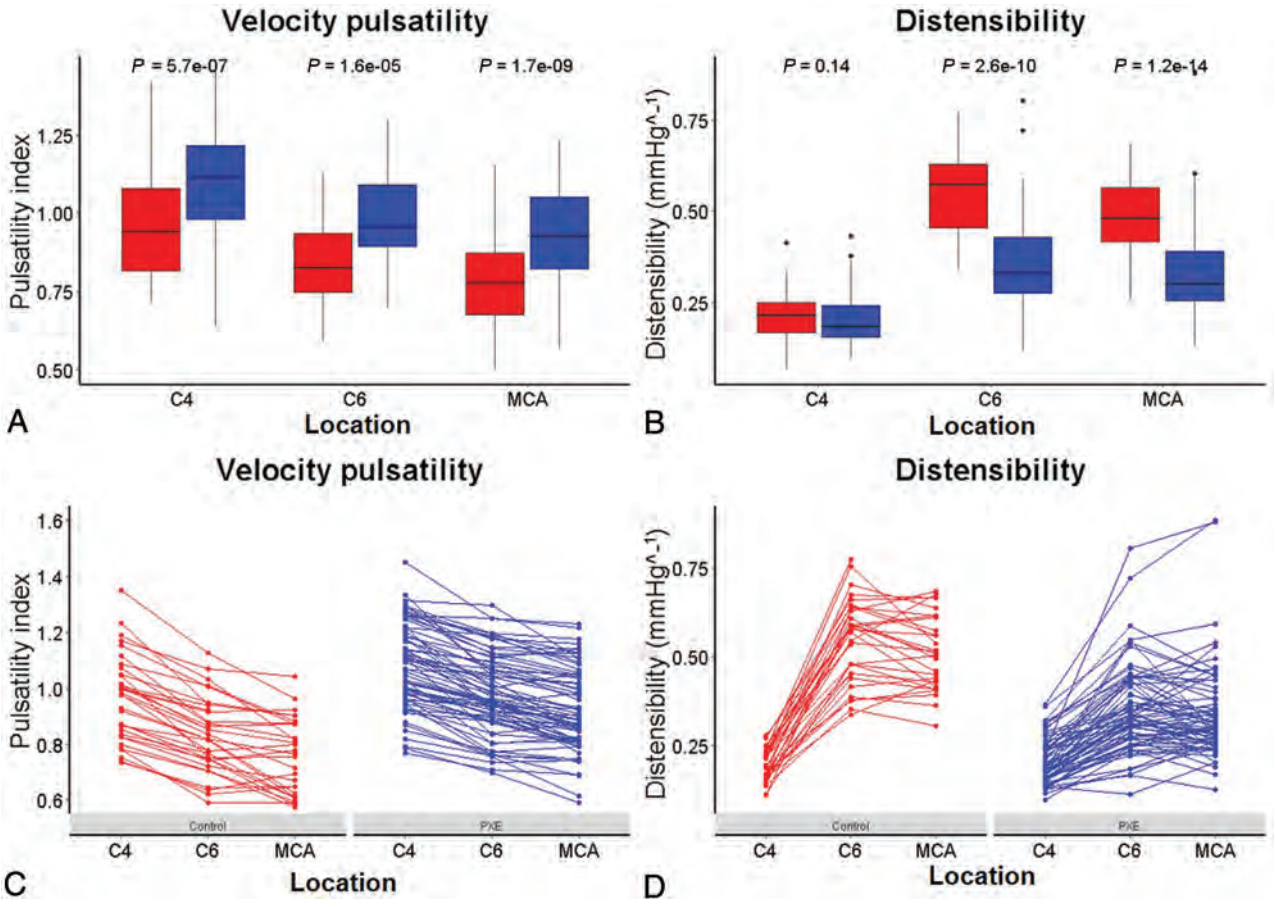

FIGURE. PI and distensibility in controls (red) and patients with PXE (blue). Differences in PI (*A*) and distensibility (*B*) in controls and patients with PXE at different locations (2 ICA segments and the MCA). Lower images show spaghetti plots of PI (*C*) and distensibility (*D*) to visualize consistency in behavior for the individual measurements.

A strong point is the relatively high number of patients for a rare disease such as PXE. A limitation is the high drop-out rate of measurements in the diverging C6 segments due to planning difficulties; however, the PI values are in the same range as described previously.[1] The order of the 2D-PC scans was the same for all patients. Although physiologic variations may occur during scanning (eg, blood pressure and heart rate fluctuation), they would be similar for both groups. We observed a similar pattern along the ICA in a study using 4D-phase conventional angiography, which does not have this physiologic variation.

Statin use is associated with increased calcification of atherosclerotic plaques in the coronary and carotid arteries.[13] Although the statin effect on medial artery calcifications in patients with PXE is unknown, we cannot exclude a possible role of statins in arterial calcification.[9]

CONCLUSIONS

Despite lower distensibility and higher pulsatility in patients with PXE, there was no overall difference in pulsatility attenuation between patients with PXE and controls. This finding suggests that extracranial calcification and stiffness may contribute more to increased intracranial arterial pulsatility in PXE than carotid siphon dysfunction.

Disclosure forms provided by the authors are available with the full text and PDF of this article at www.ajnr.org.

REFERENCES

1. van Tuijl RJ, Ruigrok YM, Velthuis BK, et al. **Velocity pulsatility and arterial distensibility along the internal carotid artery.** *J Am Heart Assoc* 2020;9:e016883 CrossRef Medline
2. O'Rourke MF, Staessen JA, Vlachopoulos C, et al. **Clinical applications of arterial stiffness; definitions and reference values.** *Am J Hypertens* 2002;15:426–44 CrossRef Medline
3. Bartstra JW, van den Beukel TC, Van Hecke W, et al. **Intracranial arterial calcification: prevalence, risk factors, and consequences—JACC Review Topic of the Week.** *J Am Coll Cardiol* 2020;76:1595–1604 CrossRef Medline
4. Lanzer P, Boehm M, Sorribas V, et al. **Medial vascular calcification revisited: review and perspectives.** *Eur Heart J* 2014;35:1515–25 CrossRef Medline
5. Plomp AS, Toonstra J, Bergen AA, et al. **Proposal for updating the pseudoxanthoma elasticum classification system and a review of the clinical findings.** *Am J Med Genet A* 2010;152A:1049–58 CrossRef Medline
6. Vos A, Kranenburg G, de Jong PA, et al. **The amount of calcifications in pseudoxanthoma elasticum patients is underestimated in computed tomographic imaging; a post-mortem correlation of histological and computed tomographic findings in two cases.** *Insights Imaging* 2018;9:493–98 CrossRef Medline
7. Kauw F, Kranenburg G, Kappelle LJ, et al. **Cerebral disease in a nationwide Dutch pseudoxanthoma elasticum cohort with a**

systematic review of the literature. *J Neurol Sci* 2017;373:167–72 CrossRef Medline
8. Bouthillier A, Van Loveren HR, Keller JT. **Segments of the internal carotid artery: a new classification.** *Neurosurgery* 1996;38:425–33 CrossRef Medline
9. van Tuijl RJ, Ruigrok YM, Geurts LJ, et al. **Does the internal carotid artery attenuate blood-flow pulsatility in small vessel disease? A 7T 4D-flow MRI study.** In: Proceedings of the *Annual Meeting & Exhibition of the International Society for Magnetic Resonance in Medicine and the Society for MR Radiographers & Technologists*, May 15–20, 2021; Virtual. Abstract No. 2930
10. Mitchell GF, Van Buchem MA, Sigurdsson S, et al. **Arterial stiffness, pressure and flow pulsatility and brain structure and function: the Age, Gene/Environment Susceptibility-Reykjavik Study.** *Brain* 2011;134:3398–3407 CrossRef Medline
11. Lefferts WK, DeBlois JP, Augustine JA, et al. **Age, sex, and the vascular contributors to cerebral pulsatility and pulsatile damping.** *J Appl Physiol* 2020;129:1092–1101 CrossRef Medline
12. Vrselja Z, Brkic H, Curic G. **Penetrating arteries of the cerebral white matter: the importance of vascular territories of delivering arteries and completeness of circle of Willis.** *Int J Stroke* 2016;11:NP36–37 CrossRef Medline
13. Mujaj B, Bos D, Selwaness M, et al. **Statin use is associated with carotid plaque composition: the Rotterdam Study.** *Int J Cardiol* 2018;260:213–18 CrossRef Medline

A Uniform Description of Perioperative Brain MRI Findings in Infants with Severe Congenital Heart Disease: Results of a European Collaboration

R. Stegeman, M. Feldmann, N.H.P. Claessens, N.J.G. Jansen, J.M.P.J. Breur, L.S. de Vries, T. Logeswaran, B. Reich, W. Knirsch, R. Kottke, C. Hagmann, B. Latal, J. Simpson, K. Pushparajah, A.F. Bonthrone, C.J. Kelly, S. Arulkumaran, M.A. Rutherford, S.J. Counsell, and M.J.N.L. Benders, for the European Association Brain in Congenital Heart Disease Consortium

ABSTRACT

BACKGROUND AND PURPOSE: A uniform description of brain MR imaging findings in infants with severe congenital heart disease to assess risk factors, predict outcome, and compare centers is lacking. Our objective was to uniformly describe the spectrum of perioperative brain MR imaging findings in infants with congenital heart disease.

MATERIALS AND METHODS: Prospective observational studies were performed at 3 European centers between 2009 and 2019. Brain MR imaging was performed preoperatively and/or postoperatively in infants with transposition of the great arteries, single-ventricle physiology, or left ventricular outflow tract obstruction undergoing cardiac surgery within the first 6 weeks of life. Brain injury was assessed on T1, T2, DWI, SWI, and MRV. A subsample of images was assessed jointly to reach a consensus.

RESULTS: A total of 348 MR imaging scans (180 preoperatively, 168 postoperatively, 146 pre- and postoperatively) were obtained in 202 infants. Preoperative, new postoperative, and cumulative postoperative white matter injury was identified in 25%, 30%, and 36%; arterial ischemic stroke, in 6%, 10%, and 14%; hypoxic-ischemic watershed injury in 2%, 1%, and 1%; intraparenchymal cerebral hemorrhage, in 0%, 4%, and 5%; cerebellar hemorrhage, in 6%, 2%, and 6%; intraventricular hemorrhage, in 14%, 6%, and 13%; subdural hemorrhage, in 29%, 17%, and 29%; and cerebral sinovenous thrombosis, in 0%, 10%, and 10%, respectively.

CONCLUSIONS: A broad spectrum of perioperative brain MR imaging findings was found in infants with severe congenital heart disease. We propose an MR imaging protocol including T1-, T2-, diffusion-, and susceptibility-weighted imaging, and MRV to identify ischemic, hemorrhagic, and thrombotic lesions observed in this patient group.

ABBREVIATIONS: AIS = arterial ischemic stroke; CHD = severe congenital heart disease; CSVT = cerebral sinovenous thrombosis; IVH = intraventricular hemorrhage; KCL = St. Thomas' Hospital London; LVOTO = left ventricular outflow tract obstruction; SVP = single ventricle physiology; TGA = transposition of the great arteries; UCZ = University Children's Hospital Zurich; WKZ = Wilhelmina Children's Hospital Utrecht; WMI = white matter injury

The incidence of patients with severe congenital heart disease (CHD), presenting as severely ill and requiring expert cardiologic care in the neonatal period or early infancy is around 3/1000 live births.[1] Mortality among infants has declined in recent decades, and 90% of children with CHD now survive into adulthood.[2,3]

Received April 6, 2021; accepted after revision July 19.

From the Departments of Neonatology (R.S., N.H.P.C., L.S.d.V., M.J.N.L.B.), Pediatric Intensive Care (R.S., N.H.P.C., N.J.G.J.), and Pediatric Cardiology (R.S., N.H.P.C., J.M.P.J.B.), Wilhelmina Children's Hospital, UMC Utrecht, Utrecht, the Netherlands; Utrecht Brain Center (R.S., L.S.d.V., M.J.N.L.B.), UMC Utrecht, Utrecht University, Utrecht, the Netherlands; Child Development Center (M.F., B.L.), Division of Pediatric Cardiology (W.K.), Pediatric Heart Center, Department of Diagnostic Imaging (R.K.), and Department of Neonatology and Pediatric Intensive Care (C.H.), University Children's Hospital Zurich, Zurich, Switzerland; Department of Pediatrics (N.J.G.J.), Beatrix Children's Hospital, UMC Groningen, Groningen, the Netherlands; Pediatric Heart Center (T.L., B.R.), University Hospital Giessen, Justus-Liebig-University Giessen, Giessen, Germany; Department of Pediatric Cardiology (J.S., K.P.), Evelina Children's Hospital London, London, UK; and Centre for the Developing Brain (K.P., A.F.B., C.J.K., S.A., M.A.R., S.J.C.), School of Biomedical Engineering and Imaging Sciences, King's College London, London, UK.

R. Stegeman and M. Feldmann shared first authorship.

S.J. Counsell and M.J.N.L. Benders shared last authorship.

This research was funded by a Consolidator Grant of the European Society of Pediatric Research. It was also funded by the Hartekind Foundation and Vrienden van het Wilhelmina Kinderziekenhuis Foundation; the Medical Research Council UK (MR/L011530/1); the British Heart Foundation (FS/15/55/31649); the Action Medical Research (GN2630); the Wellcome Engineering and Physical Sciences Research Council Center for Medical Engineering at King's College London (WT 203148/Z/16/Z); and the Mäxi Foundation, the Anna Müller Grocholski Foundation, and the EMDO Foundation Zurich.

Paper previously presented, in part, as abstracts at: Annual Scientific Sessions of the Cardiac Neurodevelopmental Outcome Collaborative, October 11–13, 2019; Toronto, Ontario, Canada; and Congress of the European Academy of Pediatric Societies, October 16–19, 2020; Virtual.

Please address correspondence to M.J.N.L. Benders, MD, PhD, Department of Neonatology, UMC Utrecht, KE 04.123.1, PO Box 85909, 3508 AB, Utrecht, the Netherlands; e-mail: M.Benders@umcutrecht.nl

Indicates open access to non-subscribers at www.ajnr.org

Indicates article with online supplemental data.

http://dx.doi.org/10.3174/ajnr.A7328

However, neurodevelopmental sequelae are a frequent long-term complication.[4]

Consequently, in an endeavor to elucidate the underlying mechanisms of impaired neurodevelopment, a number of studies have reported performance of brain MR imaging before and after open heart surgery in infants with CHD. A combined pattern of abnormal brain development and acquired brain injury has been found.[5-7] The most frequently reported lesions on perioperative MR imaging include white matter injury (WMI) and focal strokes.[8-11] In addition, other findings such as hypoxic-ischemic watershed injury, intraparenchymal hemorrhage, and cerebral sinovenous thrombosis (CSVT) have also been reported.[12-15]

The prevalence of brain lesions varies considerably across studies.[11,13,16-26] The large variability in the prevalence of brain lesions might reflect differences in inclusion criteria and practices among centers, but also a lack of a standardization in scoring and reporting of perioperative brain MR imaging findings in infants with CHD.[26]

A standardized description of perioperative brain MR imaging findings is important to accurately characterize the risks and patterns of brain lesions in infants with CHD. It facilitates the combination of data across centers to assess differences in medical care to determine lesion severity in relation to risk factors and subsequent neurodevelopmental outcome and enables neuroprotective approaches to be evaluated. The aim of this study was to describe the spectrum and prevalence of perioperative brain MR imaging findings in infants with CHD in a consistent manner, in terms of number, location, signal intensity, size, and volume across 3 European centers.

MATERIALS AND METHODS

Study Design and Population

Three prospective observational cohort studies were combined. Infants with severe CHD who underwent corrective or palliative cardiac surgery during the first 6 weeks of life in the respective centers at Wilhelmina Children's Hospital Utrecht (WKZ, 2016–2019), University Children's Hospital Zurich (UCZ, 2009–2019), and St. Thomas' Hospital London (KCL, 2014–2019) were eligible for inclusion. We considered cardiac surgery to include both median and lateral thoracotomies, with or without use of cardiopulmonary bypass. Brain MR imaging was performed pre- and/or postoperatively per clinical (WKZ) or research study (UCZ, KCL) protocol. Severe CHD types included transposition of the great arteries, single-ventricle physiology, or left ventricular outflow tract obstruction (such as aortic arch coarctation, hypoplasia with/without coarctation, interruption, valve stenosis, or hypoplastic left-heart complex). Infants with known or suspected genetic or syndromic disorders and other types of CHD were excluded. Clinical characteristics of the infants were collected prospectively at each center and subsequently combined. The respective institutional ethics research committees approved the studies (WKZ, No. 16–093; UCZ, KEK StV-23/619/04; KCL, 07/H0707/105). Parental informed consent was obtained for the use of clinically obtained data for research purposes (WKZ) or before study enrollment (UCZ, KCL). All methods were performed in accordance with relevant guidelines and regulations. The de-identified data will be made available upon reasonable request.

Brain MR Imaging Protocols

MR images were acquired on a 3T scanner (Philips Healthcare, Best, the Netherlands) using a 32-channel head coil in WKZ, a neonate-specific 32-channel head coil at KCL, and a 3T Signa HDxt (GE Healthcare) scanner with an 8-channel head coil in UCZ. Infants were swaddled in a vacuum cushion and received noise-protecting earplugs, and vital functions were monitored. In WKZ, infants were scanned in natural sleep or, if necessary, sedated with oral chloral hydrate (50 mg/kg) during MR imaging or received continuous sedation when mechanically ventilated.[26] In UCZ, infants underwent MR imaging in natural sleep when clinically stable. In KCL, MR imaging was performed in natural sleep. MR imaging protocols included T1, T2, DWI and SWI, and MRV.[11,24,27] In UCZ, SWI and MRV were acquired when there was suspicion of hemorrhage on conventional imaging or sinovenous thrombosis needed to be confirmed. Details of MR imaging protocols are available in the Online Supplemental Data.

Describing Perioperative Brain MR Imaging Findings

The system of describing perioperative brain MR imaging findings was determined jointly by the European Association Brain in Congenital Heart Disease Consortium and was based on the injury scoring sheet by Beca et al.[19] This adapted template was used in joint European MR imaging reviewing sessions to find a consensus on terminology, definitions, and scoring of brain MR imaging findings in infants with CHD. This uniform European description was then applied to score MR images of each cohort according to the scoring sheet presented in the Online Supplemental Data. All MR imaging findings were described irrespective of the potential pathologic significance and consequences for neurodevelopmental outcome. Type, number, size, volume, location, and signal intensity of brain MR imaging findings were examined. Postoperative brain findings were classified as new if preoperative MR imaging showed no corresponding findings, findings were in a different location, and/or there was an increase in size or number compared with the preoperative findings. Cumulative postoperative brain MR imaging findings included all infants with CHD with a postoperative MR imaging irrespective of the availability of a preoperative MR imaging.

WMI was defined as single or multiple lesions in the white matter without restriction of maximum lesion size, with high signal intensity on T1 and usually corresponding low signal intensity on T2.[24] Lesion sizes in each subject were measured on the T1 image in the plane showing the largest diameter, and largest lesion size was reported. Absolute WMI volume in cubic millimeters was segmented and calculated on 3D T1 images using ITK-SNAP (www.itksnap.org) (KCL) or 3D Slicer (http://www.slicer.org) (WKZ, UCZ).[28,29] Total brain volumes were automatically calculated on T2 images using neonatal-specific segmentation pipelines and were used to report the relative WMI burden (WMI volume/total brain volume).[30,31] Absolute WMI volume was not assessed in 7/45 (16%) infants with preoperative WMI and in 8/60 (13%) with postoperative WMI, due to motion corruption on 3D T1 images. The relative WMI burden could not be assessed in 15/45 (33%) infants with preoperative WMI and in 15/60 (25%) infants with postoperative WMI as a result of movement artifacts on either the

3D T1-weighted images (WMI volume segmentation) or the T2-weighted images (total brain volume segmentation).

Arterial ischemic stroke (AIS) was defined as a homogeneous area of altered signal intensity on T1- and T2-weighted images with a specific arterial distribution involving cortical gray matter and/or the basal ganglia/thalamus.[24,26] AIS was classified on the basis of the involved arterial territory: anterior, middle, or posterior cerebral artery or perforator branch (involving the basal ganglia/thalamus). Middle cerebral artery strokes were subcategorized as main, anterior, middle, posterior, or cortical branch.[32] Corticospinal tracts were involved when the corona radiata, and/or the posterior limb of the internal capsule, and/or the cerebral peduncle were affected. Hypoxic-ischemic watershed injury was defined as diffuse ischemia in intervascular borderzones among arterial territories.[26] Restricted diffusion, indicating recently acquired ischemic lesions, was assessed by high signal intensity on DWI and/or low signal on ADC images.

Hemorrhages (intraparenchymal cerebral/cerebellar, intraventricular [IVH], and subdural) were assessed using SWI, if available. For the intraparenchymal supratentorial hemorrhages, we included lesions of any size when the lesion was hypointense on the SWI. Cerebellar hemorrhages are single or multiple hemorrhages located within the cerebellum.[24] The size of cerebellar hemorrhages was quantified by measuring the largest diameter in millimeters on the SWI. IVH grade I was defined as bleeding restricted to the germinal matrix or choroid plexus; grade II, as extension of blood into the ventricles without enlargement; grade III, as ventricles enlarged by accumulated blood; and grade IV, periventricular hemorrhagic infarction, was defined when IVH was accompanied by periventricular hemorrhagic necrosis.[26,33]

CSVT was defined as MRV proved with T1 correlation (in WKZ/KCL) or high suspicion on T1/T2 (UCZ).[15]

Examples of brain findings on preoperative MR imaging sequences in infants with severe congenital heart disease are shown in the Online Supplemental Data.

RESULTS

Study Participants

A total of 202 infants with severe CHD (131 males, 65%) with a median gestational age of 39.0 weeks (interquartile range, 38.3–40.0 weeks) and a median birth weight of 3200 g (interquartile range, 2940–3648 g) (z score interquartile range −0.16, −0.77–0.48) were enrolled at 3 European centers and met the inclusion criteria. Details of demographic and clinical characteristics are presented in the Online Supplemental Data.

Preoperative Brain MR Imaging Findings

Preoperative MR imaging was performed in 180 infants with CHD at a median age of 6 days (interquartile range, 3–8 days) and postmenstrual age of 39.7 weeks (interquartile range, 38.9–40.9 weeks). WMI was found in 45 infants (25%); AIS, in 11 (6%); hypoxic-ischemic watershed injury, in 3 (2%); cerebellar hemorrhage, in 10 (6%); and IVH, in 25 (14%). We also observed subdural hemorrhage in 53 patients (29%). Details of preoperative brain MR imaging findings are described in the Online Supplemental Data. Preoperatively, no lesions, 1 type of lesion, or ≥2 types of lesions were observed in 110 (61%), 50 (28%), and 20 (11%) infants with CHD, respectively (Figure).

Postoperative Brain MR Imaging Findings (New Lesions)

New postoperative brain MR imaging findings were assessed in 146 infants with CHD and serial pre- and postoperative MR images. New WMI was found in 43 infants (30%); AIS, in 15 (10%); cerebellar hemorrhage, in 3 (2%); IVH, in 8 (6%); and subdural hemorrhage, in 25 (17%). Intraparenchymal cerebral hemorrhage ($n = 6$, 4%) and CSVT ($n = 15$, 10%) were exclusively observed postoperatively (Online Supplemental Data). Postoperatively, no new lesions, 1 type of new lesion, or ≥2 types of new lesion were shown in 83 (57%), 42 (29%), and 21 (14%) infants, respectively (Figure).

Postoperative Brain MR Imaging Findings (Also Including Infants without Preoperative MR Imaging)

Cumulative postoperative brain MR imaging findings were assessed in 168 infants with CHD at a median age of 22 days (interquartile range, 15–29 days), median postmenstrual age of 42.7 weeks (interquartile range, 41.2–43.8 weeks), and a median of 10 days (7–15) after surgery. WMI was observed in 60 infants (36%); AIS, in 24 (14%); hypoxic-ischemic watershed injury, in 2 (1%); intraparenchymal cerebral hemorrhage, in 8 (5%); cerebellar hemorrhage, in 10 (6%); IVH, in 22 (13%); subdural hemorrhage, in 48 (29%); and CSVT, in 17 (10%). Details of postoperative brain MR imaging findings are described in the Online Supplemental Data. Postoperatively, no cumulative lesions, 1 type of cumulative lesion, or ≥2 types of cumulative lesion were present in 75 (45%), 60 (36%), and 33 (20%) infants, respectively (Figure).

New Postoperative Brain Lesions in Infants with and without Preoperative Brain Lesions

Forty-eight percent of infants with preoperative brain lesions showed new lesions on postoperative MR imaging. Thirty-nine percent of infants without preoperative brain lesions had new lesions on postoperative MR imaging. In 51 infants (35%), no brain lesions were observed on either preoperative and postoperative MR imaging (Online Supplemental Data).

DISCUSSION

The aims of this European collaborative study were to standardize the description and consistently report perioperative brain MR imaging findings in infants with CHD. We report results from the largest combined cohort of infants with severe CHD thus far and found a broad spectrum of ischemic, hemorrhagic, and thrombotic brain lesions. WMI was the most prevalent lesion type, and WMI and AIS were common on both pre- and postoperative MR imaging. Cerebellar, intraventricular, and subdural hemorrhages were mainly observed preoperatively. Intraparenchymal cerebral hemorrhages and CSVT were exclusively detected on postoperative MR imaging.

WMI was the predominant finding on both pre- and postoperative MR imaging as reported previously.[8,9,11,13,19,24] The distribution of WMI that we observed matched the pattern previously reported. Kelly et al[24] and Guo et al[34] found WMI to be widespread throughout the whole brain, including some cases with involvement of the corona radiata. Total WMI volume on pre-

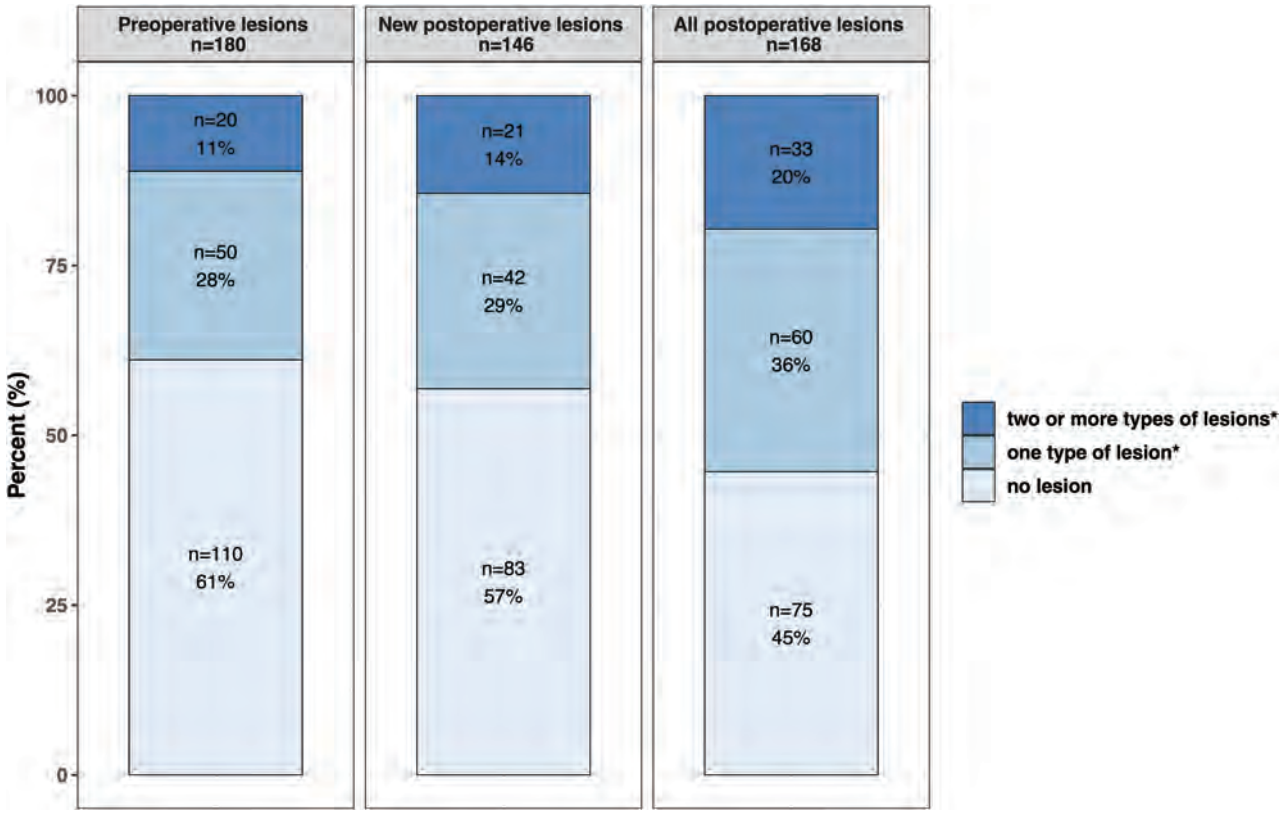

FIGURE. Proportion of infants with CHD with any kind of brain lesions. Any lesion included white matter injury, arterial ischemic stroke, hypoxic-ischemic watershed injury, intraparenchymal cerebral hemorrhage, cerebellar hemorrhage, intraventricular hemorrhage, and cerebral sinovenous thrombosis. Subdural hemorrhage was recorded but was not considered brain injury, being extra-axial and given its frequent occurrence in the healthy neonatal population.

and postoperative MR imaging in our European cohorts was in a similar range as reported recently in a multicenter analysis, suggesting that our findings might reflect the general pattern of WMI in neonates with CHD.[34] The mechanisms underpinning WMI are not entirely clear, but it is possible that focal ischemic injury such as a single, large white matter lesion may have a thromboembolic origin, while multifocal WMI is probably caused by acute or chronic hypoxia-ischemia in infants with CHD. In a recent study by Claessens et al,[26] focal injury (stroke, single white matter lesion) was more frequently seen after balloon atrial septostomy and associated with intraoperative, selective cerebral perfusion, while multifocal injury (watershed, WMI) was associated with low cardiac output syndrome. In our cohort, we recognize that thromboembolic strokes possibly caused single, large ischemic lesions, often confirmed on DWI or T1 as high signal, that exclusively affected the white matter.

AIS was identified more frequently on postoperative MR imaging compared with preoperative MR imaging, while hypoxic-ischemic watershed injury was rare, as reported previously.[10,12,13] A wide spectrum of AIS was observed with different arterial distributions, sizes, and ages of lesions as indicated by diffusion restriction, which was in line with previous results by Chen et al.[10] Most interesting, the middle cerebral artery branches were most frequently affected preoperatively, while the specific subtype of focal perforator strokes in the basal ganglia/thalamus region, including the posterior and middle cerebral artery branches, were most common on postoperative MR imaging. Preoperative AIS may be associated with balloon atrial septostomy, while selective cerebral perfusion has previously been associated with deep gray matter infarctions postoperatively.[17,26,35] AIS with diffusion restriction and without clear signal intensity alterations on T1- and T2-weighted images, indicative of recent injury, was more often observed on pre- compared with postoperative MR imaging, presumably because preoperative AIS was still visible on postoperative conventional T1- and T2-weighted images, while DWI and ADC had pseudonormalized. These findings show that infants with CHD are vulnerable to AIS at different time points from birth to the postoperative period. Thromboembolic events or cerebral hypoperfusion by low cardiac output might contribute to the observed patterns and timing of AIS.[10,26]

Cerebellar hemorrhages, low-grade IVH, and subdural hemorrhages were mainly present on preoperative MR imaging, while intraparenchymal cerebral hemorrhages and CSVT were exclusively observed on postoperative MR imaging, findings possibly indicating differences in the underlying etiology.[13-15,24,36-38] Subdural hemorrhage has been observed at a similar rate in asymptomatic term-born infants that underwent instrumental vaginal delivery and in other CHD populations and may be explained by a tendency toward more frequent use of instrumental vaginal delivery in labor complicated by CHD as suggested by CJ Kelly et al.[24,37-40] Perioperative disturbances in cerebral autoregulation and coagulation could be responsible for postoperative

hemorrhages and thromboses such as CSVT.[41] Previous studies have highlighted the importance of SWI to assess intraparenchymal hemosiderin foci because signal abnormalities are not always identified on conventional T1- or T2-weighted images.[13,14] CSVT was found less often postoperatively compared with the study by Claessens et al,[15] which might be explained by differences in the proportions of CHD types and differences or interim changes in anticoagulatory and perioperative approaches.[41] In both studies, the transverse sinus was most affected.[15]

Variability in brain lesions between our and other cohorts may be due to differences in the proportions of CHD types studied, clinical approaches such as age at surgery, and MR imaging protocols including section thickness, in-plane resolution, and timing of imaging. A larger interval between birth and the operation is associated with an increased incidence of preoperative WMI in infants with transposition of the great arteries, while hypoxic-ischemic brain injury is more often present on postoperative MR imaging after neonatal compared with postneonatal or infant heart surgery.[8,18,42] Longer times between the operation and postoperative MR imaging could impair the sensitivity of DWI and ADC to detect transient ischemic lesions.[12,13]

This study has some limitations: Infants in UCZ and KCL were scanned as part of a research study and only after parental consent was given, with the risk of selection bias in types of CHD, while infants at WKZ were scanned as part of standard clinical care. Differences in the timing of pre- and postoperative MR imaging, the operation, and image resolution may affect the sensitivity to detect small brain lesions. SWI and MRV were not performed routinely at UCZ, which might have impaired the sensitivity to detect small parenchymal hemorrhages and CSVT and led to an underestimation of respective prevalence. It was not possible to determine which portion of newly detected postoperative brain lesions actually occurred between the day of preoperative MR imaging and the day of the operation. Quantification methods of WMI volume and total brain volume differed among sites, though these were only used to determine the burden of WMI in relation to the total brain volume.

CONCLUSIONS

A broad spectrum of pre- and postoperative brain MR imaging findings was found in infants with severe CHD. An MR imaging protocol including T1-, T2-, DWI/ADC, SWI, and MRV is required to identify ischemic, hemorrhagic, and thrombotic lesions. Applying this standardized consensus description of perioperative brain MR imaging findings will enable future studies to determine lesion type, location, and extent in relation to outcome, identify risk factors across and among centers, and evaluate neuroprotective strategies in individuals with severe CHD.

ACKNOWLEDGMENTS

We are indebted to the families who supported this study. The authors would like to thank Julia Gunn and her colleagues from the Royal Children's Hospital Melbourne for kindly providing their MR imaging scoring sheet as a template for our uniform description of perioperative brain MR imaging findings. WKZ: We thank the Congenital Heart Disease LifeSpan Research group, which includes staff from the Departments of Obstetrics, Pediatric Heart Center, Pediatric Intensive Care, Neonatology, and Radiology. KCL: We thank the staff from the St. Thomas' Neonatal Intensive Care Unit; the Evelina Children's London Hospital Fetal and Paediatric Cardiology Departments; the Evelina London Paediatric Intensive Care Unit; the Centre for the Developing Brain at King's College London; our research radiographers; and our neonatal scanning team. UCZ: We thank Dr Ruth O'Gorman Tuura for the setup and technical supervision of the MR imaging protocol and Drs Oliver Kretschmar and Dave Hitendu for comments on the manuscript. We thank the staff from the Center for Magnetic Resonance Research; the Pediatric Heart Center; the Department of Intensive Care Medicine and Neonatology; and the Department of Diagnostic Imaging at the University Children's Hospital Zurich.

Disclosures: Raymond Stegeman—*RELATED*: *Grant*: European Society of Pediatric Research Grant, *Grant*: ZonMw CRUCIAL-TRIAL, Stichting Hartekind*, *Comments*: Linda de Vries—*RELATED*: *Grant*: European Society of Pediatric Research; *UNRELATED*: *Employment*: University Medical Centre Utrecht; *Payment for Lectures Including Service on Speakers Bureaus*, *Comments*: I teach a cranial ultrasound course every year in London*; *Royalties*: I am a co-author of 2 books and an associate editor of another book: 1) Govaert P, de Vries L. *An Atlas of Neonatal Brain Sonography*, 2nd ed. (CDM 182–183), Mac Keith Press. ISBN: 978-1-898683-56-8, July 2010; 2) Hellström-Westas L, de Vries LS, Rosen I. *An Atlas of Amplitude-Integrated EEGs in the Newborn*. 2nd ed. Informa Health, London; August 2008; ISBN 9781841846491; 3) Inder TE, Darras BT, de Vries LS, de Plessis AJ, Neil JJ, Perlman JM. *Volpe's Neurology of the Newborn*. 6th ed.* Walter Knirsch—*RELATED*: *Grant*: European Society of Pediatric Research; *Support for Travel to Meetings for the Study or Other Purposes*, *Comments*: travel costs. John Simpson—*Grant*: European Society of Pediatric Research; *UNRELATED*: *Consultancy*: Philips Healthcare, *Comments*: I have undertaken consultant work for Philips related to fetal cardiac imaging, nothing about brain imaging; *Payment for Lectures Including Service on Speakers Bureaus*: Canon Medical Systems, *Comments*: I received honorariums for lecturing on fetal cardiology. Christopher J. Kelly—*RELATED*: *Grant*: European Society of Pediatric Research, British Heart Foundation.* Sophie Arulkumaran—*RELATED*: *Grant*: European Society of Pediatric Research, British Heart Foundation (FS/15/55/31649).* Serena J. Counsell—*RELATED*: *Grant*: European Society of Pediatric Research, Medical Research Council Action for Medical Research, British Heart Foundation*; *UNRELATED*: *Consultancy*: IXICO Ltd.* Manon Benders—*RELATED*: *Grant*: European Society of Pediatric Research, ZonMw CRUCIAL-TRIAL, Stichting Hartekind*; *UNRELATED*: *Consultancy*: Chiesi stem cells.* *Money paid to the institution.

REFERENCES

1. Hoffman JI, Kaplan S. **The incidence of congenital heart disease.** *J Am Coll Cardiol* 2002;39:1890–900 CrossRef Medline
2. Moons P, Bovijn L, Budts W, et al. **Temporal trends in survival to adulthood among patients born with congenital heart disease from 1970 to 1992 in Belgium.** *Circulation* 2010;122:2264–72 CrossRef Medline
3. GBD 2017 Congenital Heart Disease Collaborators. **Global, regional, and national burden of congenital heart disease, 1990-2017: a systematic analysis for the Global Burden of Disease Study 2017.** *Lancet Child Adolesc Heal* 2020;4:185–200
4. Liamlahi R, Latal B. **Neurodevelopmental outcome of children with congenital heart disease.** *Handb Clin Neurol* 2019;162:329–45 CrossRef Medline
5. Miller SP, McQuillen PS, Hamrick S, et al. **Abnormal brain development in newborns with congenital heart disease.** *N Engl J Med* 2007 Nov;357:1928–38 CrossRef
6. Newburger JW, Bellinger DC. **Brain injury in congenital heart disease.** *Circulation*. 2006;113:183–85 CrossRef
7. Johnston MV. **Congenital heart disease and brain injury.** *N Engl J Med* 2007;357:1971–73 CrossRef Medline

8. Galli KK, Zimmerman RA, Jarvik GP, et al. **Periventricular leukomalacia is common after neonatal cardiac surgery.** *J Thorac Cardiovasc Surg* 2004;127:692–704 CrossRef Medline
9. Beca J, Gunn J, Coleman L, et al. **Pre-operative brain injury in newborn infants with transposition of the great arteries occurs at rates similar to other complex congenital heart disease and is not related to balloon atrial septostomy.** *J Am Coll Cardiol* 2009;53:1807–11 CrossRef Medline
10. Chen J, Zimmerman RA, Jarvik GP, et al. **Perioperative stroke in infants undergoing open heart operations for congenital heart disease.** *Ann Thorac Surg* 2009;88:823–29 CrossRef Medline
11. Bertholdt S, Latal B, Liamlahi R, et al; Research Group Heart and Brain. **Cerebral lesions on magnetic resonance imaging correlate with preoperative neurological status in neonates undergoing cardiopulmonary bypass surgery.** *Eur J Cardiothorac Surg* 2014;45:625–32 CrossRef Medline
12. Liu AY, Zimmerman RA, Haselgrove JC, et al. **Diffusion-weighted imaging in the evaluation of watershed hypoxic-ischemic brain injury in pediatric patients.** *Neuroradiology* 2001;43:918–26 CrossRef Medline
13. Mahle WT, Tavani F, Zimmerman RA, et al. **An MRI study of neurological injury before and after congenital heart surgery.** *Circulation* 2002;106:I109–14 Medline
14. Soul JS, Robertson RL, Wypij D, et al. **Subtle hemorrhagic brain injury is associated with neurodevelopmental impairment in infants with repaired congenital heart disease.** *J Thorac Cardiovasc Surg* 2009;138:374–81 CrossRef Medline
15. Claessens NHP, Algra SO, Jansen NJ, et al. **Clinical and neuroimaging characteristics of cerebral sinovenous thrombosis in neonates undergoing cardiac surgery.** *J Thorac Cardiovasc Surg* 2018;155:1150–58 CrossRef Medline
16. Licht DJ, Shera DM, Clancy RR, et al. **Brain maturation is delayed in infants with complex congenital heart defects.** *J Thorac Cardiovasc Surg* 2009;137:529–36; discussion 536–37 CrossRef Medline
17. McQuillen PS, Barkovich AJ, Hamrick SE, et al. **Temporal and anatomic risk profile of brain injury with neonatal repair of congenital heart defects.** *Stroke* 2007;38:736–41 CrossRef Medline
18. Petit CJ, Rome JJ, Wernovsky G, et al. **Preoperative brain injury in transposition of the great arteries is associated with oxygenation and time to surgery, not balloon atrial septostomy.** *Circulation* 2009;119:709–16 CrossRef Medline
19. Beca J, Gunn JK, Coleman L, et al. **New white matter brain injury after infant heart surgery is associated with diagnostic group and the use of circulatory arrest.** *Circulation* 2013;127:971–79 CrossRef Medline
20. Dimitropoulos A, McQuillen PS, Sethi V, et al. **Brain injury and development in newborns with critical congenital heart disease.** *Neurology* 2013;81:241–48 CrossRef Medline
21. Algra SO, Haas F, Poskitt KJ, et al. **Minimizing the risk of preoperative brain injury in neonates with aortic arch obstruction.** *J Pediatr* 2014;165:1116–22 CrossRef Medline
22. Claessens NH, Algra SO, Ouwehand TL, et al; CHD Lifespan Study Group Utrecht. **Perioperative neonatal brain injury is associated with worse school-age neurodevelopment in children with critical congenital heart disease.** *Dev Med Child Neurol* 2018;60:1052–58 CrossRef Medline
23. Peyvandi S, Chau V, Guo T, et al. **Neonatal brain injury and timing of neurodevelopmental assessment in patients with congenital heart disease.** *J Am Coll Cardiol* 2018;71:1986–96 CrossRef Medline
24. Kelly CJ, Arulkumaran S, Pereira CT, et al. **Neuroimaging findings in newborns with congenital heart disease prior to surgery: an observational study.** *Arch Dis Child* 2019;104:1042–48 CrossRef Medline
25. Lim JM, Porayette P, Marini D, et al. **Associations between age at arterial switch operation, brain growth, and development in infants with transposition of the great arteries.** *Circulation* 2019;139:2728–38 CrossRef Medline
26. Claessens NH, Chau V, de Vries LS, et al. **Brain injury in infants with critical congenital heart disease: insights from two clinical cohorts with different practice approaches.** *J Pediatr* 2019;215:75–82.e2 CrossRef Medline
27. Claessens NH, Khalili N, Isgum I, et al. **Brain and CSF volumes in fetuses and neonates with antenatal diagnosis of critical congenital heart disease: a longitudinal MRI Study.** *AJNR Am J Neuroradiol* 2019;40:885–91 CrossRef Medline
28. Yushkevich PA, Piven J, Hazlett HC, et al. **User-guided 3D active contour segmentation of anatomical structures: significantly improved efficiency and reliability.** *Neuroimage* 2006;31:1116–28 CrossRef Medline
29. Fedorov A, Beichel R, Kalpathy-Cramer J, et al. **3D slicer as an image computing platform for the quantitative imaging network.** *Magn Reson Imaging* 2012;30:1323–41 CrossRef Medline
30. Moeskops P, Viergever MA, Mendrik AM, et al. **Automatic segmentation of MR brain images with a convolutional neural network.** *IEEE Trans Med Imaging* 2016;35:1252–61 CrossRef Medline
31. Makropoulos A, Robinson EC, Schuh A, et al. **The developing human connectome project: a minimal processing pipeline for neonatal cortical surface reconstruction.** *Neuroimage* 2018;173:88–112 CrossRef Medline
32. Wagenaar N, Martinez-Biarge M, van der Aa NE, et al. **Neurodevelopment after perinatal arterial ischemic stroke.** *Pediatrics* 2018;142:e20174164 CrossRef Medline
33. Papile LA, Burstein J, Burstein R, et al. **Incidence and evolution of subependymal and intraventricular hemorrhage: a study of infants with birth weights less than 1,500 gm.** *J Pediatr* 1978;92:529–34 CrossRef Medline
34. Guo T, Chau V, Peyvandi S, et al. **White matter injury in term neonates with congenital heart diseases: topology and comparison with preterm newborns.** *Neuroimage* 2019;185:742–49 CrossRef Medline
35. Algra SO, Jansen NJ, van der Tweel I, et al. **Neurological injury after neonatal cardiac surgery: a randomized, controlled trial of 2 perfusion techniques.** *Circulation* 2014;129:224–33 CrossRef Medline
36. Block AJ, McQuillen PS, Chau V, et al. **Clinically silent preoperative brain injuries do not worsen with surgery in neonates with congenital heart disease.** *J Thorac Cardiovasc Surg* 2010;140:550–57 CrossRef Medline
37. Kelly P, Hayman R, Shekerdemian LS, et al. **Subdural hemorrhage and hypoxia in infants with congenital heart disease.** *Pediatrics* 2014;134:e773v81 CrossRef Medline
38. Looney CB, Smith JK, Merck LH, et al. **Intracranial hemorrhage in asymptomatic neonates: prevalence on MR images and relationship to obstetric and neonatal risk factors.** *Radiology* 2007;242:535–41 CrossRef Medline
39. Whitby EH, Griffiths PD, Rutter S, et al. **Frequency and natural history of subdural haemorrhages in babies and relation to obstetric factors.** *Lancet* 2004;363:846–51 CrossRef Medline
40. Tavani F, Zimmerman RA, Clancy RR, et al. **Incidental intracranial hemorrhage after uncomplicated birth: MRI before and after neonatal heart surgery.** *Neuroradiology* 2003;45:253–58 CrossRef Medline
41. Hunt R, Hoffman CM, Emani S, et al. **Elevated preoperative von Willebrand factor is associated with perioperative thrombosis in infants and neonates with congenital heart disease.** *J Thromb Haemost* 2017;15:2306–16 CrossRef Medline
42. Kinney HC, Panigrahy A, Newburger JW, et al. **Hypoxic-ischemic brain injury in infants with congenital heart disease dying after cardiac surgery.** *Acta Neuropathol* 2005;110:563–78 CrossRef Medline

DWI in Brains of Fetuses with Congenital Heart Disease: A Case-Control MR Imaging Study

J.-Y. Ren, H. Ji, M. Zhu, and S.-Z. Dong

ABSTRACT

BACKGROUND AND PURPOSE: Abnormal ADC values are seen in ischemic brain lesions such as acute or chronic hypoxia. We aimed to assess whether ADC values in the developing brain measured by in utero DWI were different in fetuses with congenital heart disease compared with healthy controls.

MATERIALS AND METHODS: In utero DWI was performed in 50 fetuses with congenital heart disease and 100 healthy controls at a similar gestational age. Pair-wise ADC values of the ROIs were manually delineated on each side of the frontal and periatrial WM and in the basal ganglia, thalamus, and cerebellar hemisphere, as well as a single measurement in the pons.

RESULTS: Fetuses with congenital heart disease had significantly lower ADC values in frontal and periatrial WM and the pons than controls (all $P < .05$) in the early stages of pregnancy. However, ADC values in the thalamus were higher for fetuses with congenital heart disease than for controls (gestational age, ≥26 weeks). For ADC values in the cerebellar hemisphere, there was no obvious significance between cases and controls ($P = .07$) in the late stages of pregnancy. Basal ganglia ADC values were consistently not significantly different between the 2 groups during the early and late stages of pregnancy ($P = .47$; .21).

CONCLUSIONS: Abnormal brain diffusivity can be detected using in utero DWI in fetuses with congenital heart disease. Abnormal ADC values found at a mean gestational age of 26 weeks suggest structural changes, which may provide an early indicator of the impact of congenital heart disease on the developing brain.

ABBREVIATIONS: CHD = congenital heart disease; GA = gestational age; HLHS = hypoplastic left-heart syndrome; TGA = transposition of the great arteries; TOF = tetralogy of Fallot

Congenital heart disease (CHD) is the most common congenital disability, affecting up about 0.6%–1.2% of live births and even more so in fetuses.[1] Although most children with CHD can survive, neurologic impairment has been recognized as the most common complication of heart deficits after birth.[2] Several studies have documented that certain congenital cardiac defects with altered circulation cause disturbances in brain oxygen and substrate deficiency, further reducing brain growth and maturation. In addition, these studies have indicated that fetuses with CHD may have delayed brain maturation in utero.[3,4] Therefore, prenatal evaluation of the brain structure and function of fetuses with CHD is essential and may contribute to decision-making in the postnatal management.

DWI is MR imaging that uses the objective measurements of ADC values to detect water proton motion and diffusivity in cerebral tissues. Compared with the conventional MR imaging sequences, DWI is capable of detecting subtle alterations in brain diffusion associated with early brain hypoxic damage.[5,6] Currently, fetal brain DWI has been used as a quantitative MR imaging method to assess the correlations of ADC with gestational age (GA) in various brain regions of healthy fetuses. However, it is not clear whether ADC could quantitatively evaluate early changes in brain development due to certain nonneurologic extra-CNS fetal pathologic conditions, especially for fetuses with CHD.[7]

This study aimed to investigate whether there were any differences in cerebral diffusion between fetuses with CHD and healthy controls using ADC values of in utero DWI in the early and late stages of pregnancy.

Received March 23, 2021; accepted after revision June 23.

From the Department of Radiology, Shanghai Children's Medical Center, School of Medicine, Shanghai Jiao Tong University, Shanghai, P.R. China.

J.-Y. Ren and H. Ji contributed equally to this work.

This work was supported by the National Natural Science Foundation of China (81971582,81571628), Natural Science Foundation of Shanghai (19ZR1476700), and the Shanghai Pujiang Program (2019PJD030).

Abstract previously presented, in part, as an oral presentation at: Annual Meeting of the European Congress of Radiology, February 27 to March 3, 2019; Vienna, Austria.

Please address correspondence to Su-Zhen Dong, MD, PhD, Department of Radiology, Shanghai Children's Medical Center, School of Medicine, Shanghai Jiao Tong University, No.1678 Dong Fang Rd, Shanghai 200127; e-mail: dongsuzhen@126.com

http://dx.doi.org/10.3174/ajnr.A7267

MATERIALS AND METHODS

Overall Population

Our study was authorized by the ethics commission of our hospital. All pregnant mothers involved in the study provided written informed consent before the examination for use of their clinical data for research purposes. All MR imaging studies were retrieved from our fetal MR imaging data base from August 2018 to June 2020. MR imaging was performed between 20 and 36 weeks of gestation (median GA, 26 weeks). GA was determined from the first day of the mother's last menstrual period and was confirmed by the results of an early second-trimester obstetric sonography. All fetal brain MR images were assessed by 2 pediatric radiologists (S.-Z.D. and M.Z.), who had 15 years of experience in fetal brain MR imaging, and a pediatric neuroradiologist (J.-Y.R.) with 3 years of experience in fetal brain MR imaging, to confirm a normal appearance. The fetuses with CHD were compared with a group of the healthy controls of similar GA. The subjects were subdivided on the basis of GA, with GA $<$ 26 weeks (20 − 25.9 weeks) in one group and GA $\geq$ 26 weeks (26 − 36 weeks) in a second group.

Healthy Control Population

The brain MR imaging of the fetuses that served as the control group were included after careful retrospective examination by the 2 experienced radiologists confirmed a normal brain appearance. Only singleton pregnancies eligible for fetal brain MR imaging in our hospital were included. Indications for fetal MR imaging consisted of extra-CNS abnormalities detected by sonography.

CHD Study Population

The cases of CHD were retrieved from the same fetal MR imaging data base. The inclusion criteria for retrieval were a single pregnancy and postnatally confirmed tetralogy of Fallot (TOF), double-outlet right ventricle, transposition of the great arteries (TGA), and hypoplastic left-heart syndrome (HLHS).

Exclusion Criteria

Exclusion criteria for the entire population were as follows: multiple pregnancies, fetal malformation or chromosomal abnormalities; associated arrhythmias; perinatal infection; fetal anemia; maternal conditions that might affect fetal hemodynamics such as pregestational diabetes, thyroid disease, or preeclampsia; any brain abnormality detected on conventional sequences; and cases in which DWI was not successfully performed or was nondiagnostic due to motion artifact degradation.

MR Imaging Protocol

All fetal brain MR imaging was performed using an Achieva 1.5T MR imaging scanner with a 60-mT/m gradient and a 16-channel SENSE-XL-Torso coil (Philips Healthcare), and imaging included steady-state free precession, T2WI single-shot turbo spin-echo, T1WI, and DWI. The following parameters were used for the steady-state free precession: TR, 3.6 ms; TE, 1.8 ms; matrix, 216 × 218; FOV, 260 × 325 mm^2; reverse corner, 80°; section thickness, 2–4 mm; spacing, −2–0 mm. The parameters for the single-shot turbo spin-echo sequence included TR/TE, 12,000/120 ms; matrix, 236 × 220; FOV, 260 × 355 mm^2; reverse angle, 90°; section thickness, 2 mm with 0-mm spacing. The DWI sequence was performed in the transverse plane using b-values of 0 and 700 mm^2s^{-1}. The maximal b-value of 700 was chosen to increase the SNR of the immature brain for demonstrating optimal contrast in the fetal brain. We used the following parameters: TR, 2494 ms; TE, 96 ms; section thickness, 4 mm; FOV, 280 × 320 mm^2; matrix, 188 × 125; spacing, 0 mm; flip angle, 90°. The scan time of the DWI sequence was 60 seconds. The total acquisition time was 15–25 minutes.

Pregnant women were in the supine or the left-sided position. No maternal or fetal sedation was used during the MR imaging examinations. First, the middle and lower abdomen of pregnant women was scanned in the coronal plane. This was followed by a focused multiplanar scan of the fetal brain. Subsequently, the fetal chest and abdomen were scanned in the axial, sagittal, and coronal planes. The repeat data acquisition or breath-holding of pregnant women at the end of expiration or both were used to reduce fetal motion artifacts to improve the success of the in utero DWI sequence.

Imaging Analysis

The DWI data were transmitted to a workstation (ADW4.4; GE Healthcare, USA). The ADC measurements were manually drawn in 11 circular, different ROIs. Pair-wise ADC measurements were obtained in the frontal and periatrial WM of each cerebral hemisphere and in the basal ganglia, thalami, and cerebellar hemispheres, as well as a single measurement in the pons. These measurements are based on ROI locations reported in previous literature.[8] The ROIs were manually traced. They varied in size depending on the brain region and GA. The sizes of ROIs ranged from 20 to 60 mm^2. The frontal WM ROIs were drawn anterior to the frontal horns on the inferior section. Both frontal WM and periatrial WM ROIs extended across the cerebral mantle, spanning the germinal matrix zone and the cortex, including the intermediate zone and the subplate. The periatrial WM ROIs were ovoid and placed midway between the anterior and posterior margins of the ventricular atrium. The width of the brain was multiplied by a constant factor, and the resulting products were used as the area of the periatrial WM ROIs.[9] For each ROI, a mean ADC value (SD) (10^{-3} mm^2/s) was obtained. ADC values from both sides of the brain were averaged for each anatomic location described above. Examples of ROI positioning are shown in Fig 1.

Manual ADC measurements of all cases were performed by the same pediatric neuroradiologist with 3 years of fetal brain MR imaging experience (observer 1, J.-Y.R.) after a training session. A subgroup of 30 randomly selected subjects was re-analyzed by the same operator after a 2-month interval, blinded to the initial results, to investigate intraobserver reproducibility. A different subgroup of 30 fetal brains was analyzed by a pediatric radiologist with 15 years of fetal brain MR imaging experience (observer 2, S.-Z.D.) to study interobserver reliability.

Statistical Analysis

The first step of our delineation consisted of comparison of ADC values in the ROIs marked in each hemisphere (right versus left) using a Student paired *t* test. The mean ADC value was presented graphically with quadratic curve fitting. For each ROI, the mean ADC value was plotted against the GA, and the relationship was assessed by linear regression between the CHD group and controls. Statistical comparisons between the control population and

fetuses with CHD adjusted for GA were analyzed using the nonparametric Mann-Whitney *U* test. The intraclass correlation coefficient was calculated to convey the association within and between observers for ADC measurements. A *P* value $< .05$ was considered statistically significant. All analyses were calculated by SPSS 22.0 software (IBM).

RESULTS

Study Cohort

For the CHD group, we retrospectively identified 55 singleton pregnancies eligible for inclusion in our study, which fulfilled the inclusion criteria for the CHD group. Five of the 55 fetuses in CHD group were further excluded from this study because the anatomic structures on the DWI sequence were not clear ventricular system and clear brain parenchyma; to accurately measure the ADC values. The subtypes of the cardiac lesions are summarized in Table 1.

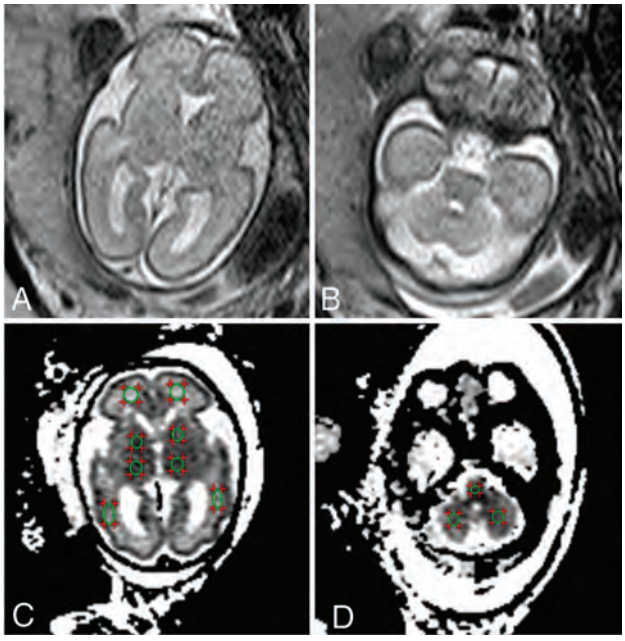

FIG 1. ADC map in a fetus at 26 weeks' GA showing ROIs in the different regions. *A* and *B*, T2WI. *C* and *D*, The same GA, DWI. Pair-wise ADC values of the ROIs are manually delineated on each side of the frontal WM, periatrial WM, basal ganglia, thalamus, and cerebellar hemisphere, as well as a single measurement in the pons.

Table 1: Clinical characteristics of our cohort[a]

	Control ($n = 100$)	CHD ($n = 50$)	*P* Value[b]
GA at MR imaging (mean) (wk)	26.6 (SD, 3.9)	26.1 (SD, 3.5)	.45
Maternal age (mean) (yr)	31.6 (SD, 5.0)	33.1 (SD, 4.0)	.65
Sex (No.) (%)			
Male	46 (46.0%)	26 (52.0%)	
Female	54 (54.0%)	24 (48.0%)	
Cardiac lesion			
TOF	NA	20 (40.0%)	
Double-outlet right ventricle	NA	10 (20.0%)	
TGA	NA	15 (30.0%)	
HLHS	NA	5 (10.0%)	

Note:—NA indicates not applicable.
[a] Data are presented as number (%) unless otherwise noted.
[b] By Wilcoxon rank sum test.

In the control group, indications for fetal brain MR imaging included the following: limitations of fetal sonography: maternal abdominal wall edema ($n = 10$), uterine myomas ($n = 10$), oligohydramnios ($n = 20$), unfavorable fetal lie ($n = 15$); extra-CNS abnormalities: bilateral cleft lip ($n = 12$), mild hydronephrosis ($n = 20$), congenital cystic adenomatoid malformation ($n = 3$), intestinal duplication ($n = 3$), ovarian cyst ($n = 5$), and hepatic cyst ($n = 2$).

Finally, data from 50 cases in the CHD group (range, 20 – 36 weeks; 25 fetuses in each of GA group: 20- to 25.9-week and 26- to 36-week groups) and 100 cases in the control group (range, 20 – 36 weeks; 50 fetuses in each of the corresponding 2 groups) were enrolled in the MR imaging analysis. The mean GA of the CHD group was 26.1 (SD, 3.5) weeks, similar to that in the control population (GA, 26.6 [SD, 3.9] weeks). The clinical characteristics of our cohort are shown in Table 1.

ADC Measurements

The intraobserver analysis showed excellent reproducibility of all intracranial volumes when observer 1 re-analyzed a subgroup of 30 randomly selected subjects after 2 months (all intraclass correlation coefficients > 0.90). Interobserver (observer 2) correlation coefficients were calculated for each mean ADC value of the frontal WM (0.80), periatrial WM (0.81), basal ganglia (0.82), thalamus (0.88), cerebellar hemisphere (0.87), and pons (0.86).

By means of a paired *t* test, the ADC values of the left and right sides were not significantly different, so the ADC values of each anatomic position of the hemispheres could be averaged. A significant negative correlation was observed between advancing GA and ADC measurements obtained in the periatrial WM, basal ganglia, thalamus, cerebellar hemisphere, and pons (CHD group: $R^2 = 0.19$, 0.24, 0.37, 0.20, and 0.23; control group: $R^2 = 0.47$, 0.31, 0.65, 0.54, and 0.41, respectively), while in the frontal WM, the ADC values revealed no statistical correlation with GA in the 2 groups ($P = .38$ and 0.94, respectively) (Fig 2).

T-test analysis indicated that fetuses with CHD had significantly lower ADC values in the frontal WM, periatrial WM, and pons than controls (all $P < .05$, respectively) in the early stages of pregnancy (GA $<$ 26 weeks), while they were not significantly different in the periatrial WM and pons between the CHD and control groups in the late stages of pregnancy (GA $\geq$26 weeks). Only frontal WM ADC values were significantly lower in cases of both early (GA $<$ 26 weeks) and late CHD (GA $\geq$ 26 weeks) (all $P < .05$). Although the CHD group with GA $<$ 26 weeks had slighter lower ADC values in the thalamus than controls ($P = .22$), the ADC values in the thalamus were significantly higher in fetuses with CHD than in the control population ($P < .05$) in the late stages of pregnancy (GA $\geq$26 weeks). As for the cerebellar hemisphere, there was a strong trend toward not reaching significance between cases and controls ($P = .07$) in late stages of pregnancy (GA $\geq$ 26 weeks). Basal ganglia ADC values ($P = .47$; 0.21) were consistently

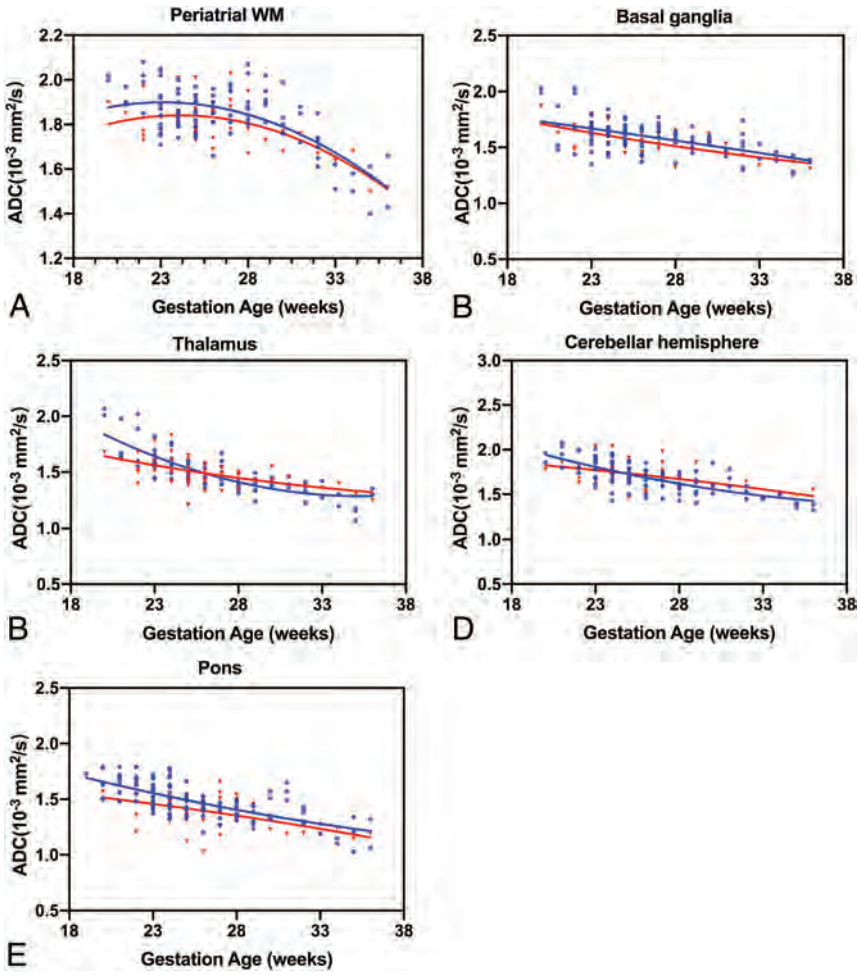

FIG 2. ADC values versus GA for all ROIs. Fetuses with CHD are referenced with *red triangles*, and *blue circles* indicate healthy controls. Periatrial WM (*A*), basal ganglia (*B*), thalamus (*C*), cerebellar hemisphere (*D*), pons (*E*).

not significantly different between the 2 groups in the early and late stages of pregnancy (Fig 3 and Table 2).

For the CHD and control groups, the mean ADC values of the supratentorial WM regions (frontal WM, periatrial WM) were consistently higher than those of the infratentorial regions (cerebellar hemisphere, pons), and the mean ADC values of the deep gray matter (basal ganglia, thalamus) were consistently similar to each other during the early and late stages of pregnancy, as shown in Table 2.

DISCUSSION

We used fetal DWI to show abnormal diffusion in different regions of the brain in fetuses with CHD compared with controls. These results reinforce the previous studies reporting that some congenital cardiac lesions can affect the development of the fetal brain in utero.[10,11] We observed regional differences in ADC during gestation, likely reflecting differences in fetal brain development because of many factors such as changes in the tissue cellularity and water content, neuronal maturation, neuronal remodeling and pruning, axonal sprouting, glial proliferation, and so forth. Our results suggest that during the early stage of neurodevelopment in fetuses with CHD, abnormal diffusivity in different brain areas may represent a difference in the structural organization of axons or glia. Our study also suggested that ADC values as measured by DWI could be a feasible method of evaluating brain injury in fetuses with certain CHDs.

Although sonography has always been the preferred imaging method for prenatal examination, MR imaging has obvious advantages over sonography in the display of neurologic maturation and abnormalities.[12] While conventional MR imaging sequences (T1WI and T2WI) are desirable to assess morphologic anomalies, DWI can detect microstructural brain changes preceding changes on conventional MR images and has a potential role in detecting and characterizing diffuse injuries of the fetal brain.[13] In this study, none of the CHD fetuses showed morphologic brain abnormalities, but the difference in ADC values deviating from the control group suggests abnormal brain axonal density.

Our results in the group with GA $<$ 26 weeks are similar to those in previously published fetal DWI studies.[8,9] Higher ADC values of supratentorial WM regions (frontal WM, periatrial WM) can be interpreted because of the presence of immature migrant cells, an increase in cellular density, and a loose tissular organization with larger extracellular spaces within the WM. The lower ADC values of the cerebellum, pons, and thalamus maybe due to earlier maturation and myelination. In the group with GA $\geq$ 26 weeks, our results corroborate previous abnormal ADC values in a smaller cohort of 3 fetuses with CHD with a mean GA of 34 weeks, reported by Berman et al,[14] who found that the ADC values of the thalamus in the CHD group were significantly higher than those in the control group; however, the values in the basal ganglia were not significantly different. Schönberg et al[15] also described ADC values in 8 fetuses affected by CHD with a mean GA of 32.5 weeks and found an increase in ADC values in all regions of the WM as well as in the basal ganglia, comparable with values found in healthy fetuses. In fetuses with CHD of $<$26 weeks' GA, our results showed a significant reduction in the ADC values of the WM and pons compared with the control group.

Several reasons could explain the difference among these studies. First, because of the characteristics of fetal brain development, most published fetal studies on this topic have been conducted in the third trimester.[16] However, many key steps of brain development have been completed by midgestation (GA, 21 – 26 weeks),

such as neuronal migration and dendritic formation, synapse formation, and oligodendrocyte maturation.[17] Therefore, our cohort study with an average GA of 26 weeks was chosen to determine the timing of intrauterine brain structural changes associated with CHD. Some studies have demonstrated that in normal deep WM areas, ADC values initially tend to increase from 20 gestational weeks up to a peak around 30 weeks.[8,9] Due to the decrease in water content and the beginning of higher-order maturation, this increase is rapidly followed by a subsequent decrease in ADC values in most brain areas after 30 weeks.[18] Therefore, in the early stages of pregnancy (GA < 26 weeks), the reduced mean ADC values in the WM of the CHD group probably represent delayed maturation.

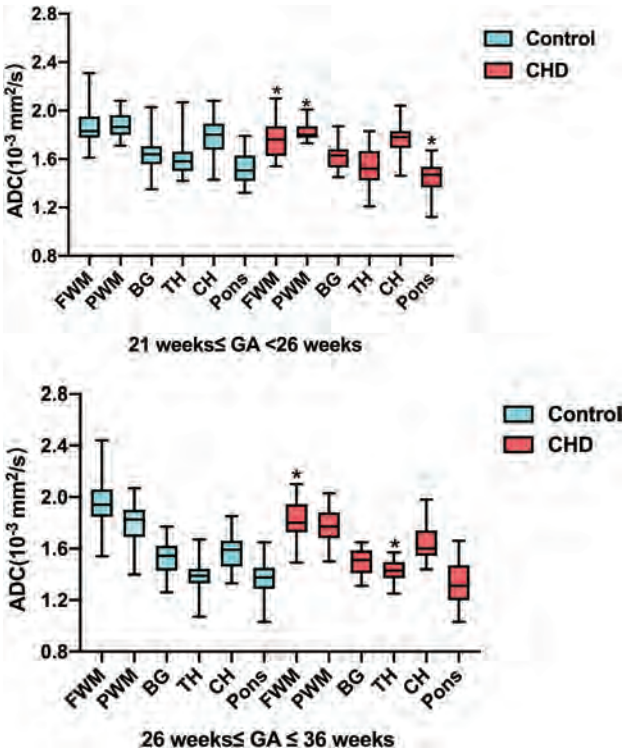

FIG 3. Box-and-whisker plots representing the distribution of ADC measurements across the fetal brain anatomic structures and pregnancy trimesters. *Asterisks* indicate significant differences between the CHD (red) and control (blue) groups for the same structure. BG indicates basal ganglia; TH, thalamus; CH, cerebellar hemisphere; FWM, frontal WM; PWM, periatrial WM.

Another source of the difference is that the types of CHD included in the cohort study were diverse. Of note, these previous findings[14,15] in regional tissue development were associated with a more specific type of complex CHD: HLHS. However, other CHD types with decreased oxygen delivery to the brain can also be associated with prenatal neurologic injury. Good examples of CHD types with decreased oxygenation of the brain are TGA and TOF. In TGA,[19] the aorta arises from the right ventricle and the fetal brain receives deoxygenated blood returning from the systemic circulation stream. In fetuses with TOF,[20] the presence of a large ventricular septal defect leads to mixing of blood in the left and right ventricles, which results in consecutively low oxygen saturation in the cerebral arteries. Moreover, Donofrio et al[21] evaluated cerebral blood flow perfusion changes in fetuses with CHD using head circumference and the cerebral-to-placental resistance ratio and found that fetuses with TGA were less affected than those with HLHS. These results indicate that diverse cardiac lesions are likely to have different brain effects. In addition, there is also a large difference in sample size.

Our results are aligned with Arthurs at al that showed that a significant decline was found for ADC values in the frontal WM compared with healthy fetuses, suggesting a high susceptibility to frontal chronic hypoxic-ischemic insult with pronounced abnormalities in frontal WM perfusion in fetuses with CHD.[22] We hypothesized that this phenomenon may represent chronic damage and WM gliosis from a decline in ADC values due to hypercellularity. A previous study[23] concluded that the thalamus, in particular, was more sensitive to hypoxia changes, consistent with our results that the CHD group had higher ADC values during the later stages of pregnancy. In our study, we did not observe abnormal diffusivity in the basal ganglia. We also found that although the CHD group with GA < 26 weeks had lower ADC values in the pons than in controls, there was not a significant difference between the 2 groups in the later stages of pregnancy (GA ≥ 26 weeks). The higher cognitive functions of the frontal lobes are protected by a compensatory mechanism such as the "brain-sparing" effect during an earlier pregnancy.[24] However, under chronic circumstances or a later pregnancy, perfusion redistribution aims to protect more elementary brain regions such as the basal ganglia and pons supplied by the middle and posterior cerebral arteries. Therefore, our data indicate that different regions of the brain differ in the sensitivity to hypoxic-ischemic injury during the development process.

There are some limitations to this study. Our sample size was limited, resulting in a failure to perform a more detailed classification analysis according

Table 2: ADC values in the CHD and control groups in different brain areas[a]

	Unit	Control (n = 100) (mean)	CHD (n = 50) (mean)	P Value
GA <26 wk (No.)		50	25	
Frontal WM	(10^{-3} mm^2/s)	1.87 (SD, 0.15)	1.77 (SD, 0.14)	.01[b]
Periatrial WM	(10^{-3} mm^2/s)	1.88 (SD, 0.10)	1.83 (SD, 0.08)	.04[b]
Basal ganglia	(10^{-3} mm^2/s)	1.65 (SD, 0.15)	1.62 (SD, 0.11)	.47
Thalamus	(10^{-3} mm^2/s)	1.61 (SD, 0.16)	1.55 (SD, 0.15)	.22
CH	(10^{-3} mm^2/s)	1.79 (SD, 0.15)	1.77 (SD, 0.12)	.40
Pons	(10^{-3} mm^2/s)	1.53 (SD, 0.13)	1.44 (SD, 0.13)	.03[b]
GA ≥26 wk (No.)		50	25	
Frontal WM	(10^{-3} mm^2/s)	1.94 (SD, 0.18)	1.82 (SD, 0.15)	.006[b]
Periatrial WM	(10^{-3} mm^2/s)	1.80 (SD, 0.16)	1.78 (SD, 0.13)	.41
Basal ganglia	(10^{-3} mm^2/s)	1.53 (SD, 0.13)	1.50 (SD, 0.10)	.21
Thalamus	(10^{-3} mm^2/s)	1.39 (SD, 0.11)	1.44 (SD, 0.08)	.04[b]
CH	(10^{-3} mm^2/s)	1.58 (SD, 0.13)	1.65 (SD, 0.13)	.07
Pons	(10^{-3} mm^2/s)	1.37 (SD, 0.13)	1.34 (SD, 0.15)	.38

Note:—CH indicates cerebellar hemisphere.
[a] Data are presented as means.
[b] P <.05.

to the characteristics of the types of CHD. Second, postpartum imaging follow-up studies and long-term standardized neuropsychological evaluations are required to determine the value of DWI for the prenatal diagnosis of fetuses with CHD. Because our study included fetuses with severe CHD, most of whom required corrective surgery during infancy, certain cognitive delays or involved disabilities that are only diagnosed during school age make follow-up difficult.

CONCLUSIONS

The ADC value of fetuses with CHD was significantly decreased in different brain areas during the early and late stages of pregnancy compared with healthy controls. This study suggests that abnormal brain diffusivity detected by fetal brain DWI could be a feasible early marker of axonal development from midgestation, which may lead to brain growth failure during the third trimester. This technique could aid in recognizing a possible detrimental effect of CHD on developing brain tissue. However, the prognostic value of ADC changes in postnatal development requires further study.

REFERENCES

1. Hansen T, Henriksen TB, Bach CC, et al. **Congenital heart defects and measures of prenatal brain growth: a systematic review.** *Pediatr Neurol* 2017;72:7–18 CrossRef Medline
2. Peyvandi S, Latal B, Miller SP, et al. **The neonatal brain in critical congenital heart disease: Insights and future directions.** *Neuroimage* 2019;185:776–82 CrossRef Medline
3. von Rhein M, Buchmann A, Hagmann C, et al. **Severe congenital heart defects are associated with global reduction of neonatal brain volumes.** *J Pediatr* 2015;167:1259–63 CrossRef Medline
4. Lie ML, Graham RH, Robson SC, et al. MERIDIAN Collaborative Group. **MRI for fetal developmental brain abnormalities: perspectives from the pregnant patient.** *Qual Health Res* 2018;28:1295–1307 CrossRef Medline
5. Le Bihan D. **Apparent diffusion coefficient and beyond: what diffusion MR imaging can tell us about tissue structure.** *Radiology* 2013;268:318–22 CrossRef Medline
6. Sartor A, Arthurs O, Alberti C, et al. **Apparent diffusion coefficient measurements of the fetal brain during the third trimester of pregnancy: how reliable are they in clinical practice?** *Prenat Diagn* 2014;34:357–66 CrossRef Medline
7. Cartry C, Viallon V, Hornoy P, et al. **Diffusion-weighted MR imaging of the normal fetal brain: marker of fetal brain maturation.** *J Radiol* 2010;91:561–66 CrossRef Medline
8. Schneider JF, Confort-Gouny S, Le Fur Y, et al. **Diffusion-weighted imaging in normal fetal brain maturation.** *Eur Radiol* 2007;17:2422–29 CrossRef Medline
9. Schneider MM, Berman JI, Baumer FM, et al. **Normative apparent diffusion coefficient values in the developing fetal brain.** *AJNR Am J Neuroradiol* 2009;30:1799–1803 CrossRef Medline
10. Claessens NH, Khalili N, Isgum I, et al. **Brain and CSF volumes in fetuses and neonates with antenatal diagnosis of critical congenital heart disease: a longitudinal MRI study.** *AJNR Am J Neuroradiol* 2019;40:885–91 CrossRef Medline
11. Mebius MJ, Kooi EM, Bilardo CM, et al. **Brain injury and neurodevelopmental outcome in congenital heart disease: a systematic review.** *Pediatrics* 2017;140:e20164055 CrossRef Medline
12. Griffiths PD, Bradburn M, Campbell MJ, et al. **Use of MRI in the diagnosis of fetal brain abnormalities in utero (MERIDIAN): a multicentre, prospective cohort study.** *Lancet* 2017;389:538–46 CrossRef Medline
13. Arthurs OJ, Thayyil S, Pauliah SS, et al. **Diagnostic accuracy and limitations of post-mortem MRI for neurological abnormalities in fetuses and children.** *Clin Radiol* 2015;70:872–80 CrossRef Medline
14. Berman JI, Hamrick SE, McQuillen PS, et al. **Diffusion-weighted imaging in fetuses with severe congenital heart defects.** *AJNR Am J Neuroradiol* 2011;32:E21–22 CrossRef Medline
15. Schönberg N, Weisstanner C, Wiest R, et al. **The influence of various cerebral and extracerebral pathologies on apparent diffusion coefficient values in the fetal brain.** *J Neuroimaging* 2020;30:477–85 CrossRef Medline
16. Clouchoux C, Du Plessis AJ, Bouyssi-Kobar M, et al. **Delayed cortical development in fetuses with complex congenital heart disease.** *Cereb Cortex* 2013;23:2932–43 CrossRef Medline
17. Kostović I, Jovanov-Milosević N. **The development of cerebral connections during the first 20-45 weeks' gestation.** *Semin Fetal Neonatal Med* 2006;11:415–22 CrossRef Medline
18. Han R, Huang L, Sun Z, et al. **Assessment of apparent diffusion coefficient of normal fetal brain development from gestational age week 24 up to term age: a preliminary study.** *Fetal Diagn Ther* 2015;37:102–07 CrossRef Medline
19. Alsaied T, Tseng S, King E, et al. **Effect of fetal hemodynamics on growth in fetuses with single ventricle or transposition of the great arteries.** *Ultrasound Obstet Gynecol* 2018;52:479–87 CrossRef Medline
20. Schellen C, Ernst S, Gruber GM, et al. **Fetal MRI detects early alterations of brain development in Tetralogy of Fallot.** *Am J Obstet Gynecol* 2015;213:392.e1-7 CrossRef Medline
21. Donofrio MT, Bremer YA, Schieken RM, et al. **Autoregulation of cerebral blood flow in fetuses with congenital heart disease: the brain sparing effect.** *Pediatr Cardiol* 2003;24:436–43 CrossRef Medline
22. Arthurs OJ, Rega A, Guimiot F, et al**. Diffusion-weighted magnetic resonance imaging of the fetal brain in intrauterine growth restriction.** *Ultrasound Obstet Gynecol* 2017;50:79–87 CrossRef Medline
23. Papadopoulou I, Langan D, Sebire NJ, et al. **Diffusion-weighted post-mortem magnetic resonance imaging of the human fetal brain in situ.** *Eur J Radiol* 2016;85:1167–73 CrossRef Medline
24. Cohen E, Baerts W, van Bel F. **Brain-sparing in intrauterine growth restriction: considerations for the neonatologist.** *Neonatology* 2015;108:269–76 CrossRef Medline

Grading of Pediatric Intracranial Tumors: Are Intravoxel Incoherent Motion and Diffusional Kurtosis Imaging Superior to Conventional DWI?

D. She, S. Lin, W. Guo, Y. Zhang, Z. Zhang, and D. Cao

ABSTRACT

BACKGROUND AND PURPOSE: An accurate evaluation of the World Health Organization grade is critical in pediatric intracranial tumors. Our aim was to explore the correlations between parameters derived from conventional DWI, intravoxel incoherent motion, and diffusional kurtosis imaging with histopathologic features to evaluate the accuracy of diffusion parameters for grading of pediatric intracranial tumors.

MATERIALS AND METHODS: Fifty-four pediatric patients with histologically proved intracranial tumors who underwent conventional DWI, intravoxel incoherent motion, and diffusional kurtosis imaging were recruited. The conventional DWI (ADC), intravoxel incoherent motion (pure diffusion coefficient [D], pseudodiffusion coefficient [D*], perfusion fraction [f], diffusional kurtosis imaging [K], and diffusion coefficient [Dk]) parameters in the solid component of tumors were measured. The cellularity, Ki-67, and microvessel density were measured. These parameters were compared between the low- and high-grade pediatric intracranial tumors using the Mann-Whitney *U* test. Spearman correlations and receiver operating characteristic analysis were performed.

RESULTS: The ADC, D, and Dk values were lower, whereas the K value was higher in high-grade pediatric intracranial tumors than in low-grade tumors (all, $P < .001$). The K value showed positive correlations ($r = 0.674$–0.802; all, $P < .05$), while ADC, D, and Dk showed negative correlations with cellularity and Ki-67 ($r = -0.548$ to -0.740; all, $P < .05$). The areas under the curve of ADC_{VOI}, D_{VOI}, Dk_{VOI}, and K_{VOI} were 0.901, 0.894, 0.863, and 0.885, respectively, for differentiating high- from low-grade pediatric intracranial tumors. The area under the curve difference in grading pediatric intracranial tumors was not significant (all, $P > .05$).

CONCLUSIONS: Intravoxel incoherent motion– and diffusional kurtosis imaging–derived parameters have similar performance compared with conventional DWI in predicting pediatric intracranial tumor grade. The diffusion metrics may potentially reflect tumor cellularity and Ki-67 in pediatric intracranial tumors.

ABBREVIATIONS: AUC = area under the curve; D = true diffusion coefficient; D* = pseudodiffusion coefficient; Dk = the corrected ADC without Gaussian bias; DKI = diffusional kurtosis imaging; f = perfusion fraction; IVIM = intravoxel incoherent motion; K = diffusional kurtosis; MVD = microvessel density; PIT = pediatric intracranial tumor; WHO = World Health Organization

Pediatric intracranial tumors (PITs) are the second most common cancers with the highest mortality among children.[1] In contrast to adults, the pathologic types of intracranial tumors are widely heterogeneous in children.[2] Preoperative accurate evaluation of the World Health Organization (WHO) grade is critical for choosing the appropriate therapeutic treatment and evaluating prognosis in PIT. Conventional MR imaging, such as T2-weighted and T1-weighted MR imaging without and with contrast, is usually used to assess the location, morphology, and extension of PITs.[3] However, differentiating high- and low-grade PITs remains challenging owing to the overlap of conventional MRI manifestation of these 2 tumors. Conventional DWI based on the monoexponential model could noninvasively provide additional functional

Received April 1, 2021; accepted after revision June 23.

From the Departments of Radiology (D.S., S.L., W.G., D.C.) and Pathology (Y.Z.), Fujian Key Laboratory of Precision Medicine for Cancer, and Key Laboratory of Radiation Biology of Fujian Higher Education Institutions (D.C.), First Affiliated Hospital of Fujian Medical University, Fuzhou, China; and Siemens Healthcare Ltd (Z.Z.), Shanghai, China.

This study was supported by the Funding Project of Medical Innovation of Fujian Province (No. 2019-CX-23); the Joint Project of Health and Education of Fujian Province (No. 2019-WJ-10); the Leading Project of the Department of Science and Technology of Fujian Province (No. 2020Y0025); the National Natural Science Foundation of China (No. 82071869); the Joint Funds of the Innovation of Science and Technology, Fujian Province (No. 2019Y9115); and the Startup Fund for Scientific Research, Fujian Medical University (No. 2018QH1048).

Dejun She and Shan Lin contributed equally to this study.

Please address correspondence to Dairong Cao, MD, Department of Radiology, First Affiliated Hospital of Fujian Medical University, 20 Cha-Zhong Rd, Fuzhou, Fujian 350005, China; e-mail: dairongcao@163.com

Indicates open access to non-subscribers at www.ajnr.org

Indicates article with online supplemental data.

http://dx.doi.org/10.3174/ajnr.A7270

information within the tumor.[4] Conventional DWI with ADC values has been reported to be useful in characterizing tumor cellularity and predicting the PIT grade.[4-7] However, the ADC value calculated using the monoexponential model may not accurately reflect the water molecular diffusion behavior due to the influence of capillary microcirculation and complex cellular microstructural barriers within the tumor.

Previous researchers have suggested that several advanced MR diffusion techniques, including intravoxel incoherent motion (IVIM) and diffusional kurtosis imaging (DKI), might provide a more accurate illumination of water molecular diffusion behavior.[8-10] IVIM with a biexponential model, introduced by Le Bihan[8] and Le Bihan et al,[9] can be used to distinguish real water molecular diffusion from microcirculation with sufficiently low b-values. On the other hand, DKI with a non-Gaussian model, proposed by Jensen et al,[10] could more accurately characterize the microstructural complexity of tumors with high b-values. Several investigations have demonstrated that IVIM and DKI have a higher accuracy for reflecting tumor biology and predicting tumor grades in glioma,[11,12] meningioma,[13] and sinonasal malignancies.[14] Because conventional DWI, IVIM, and DKI may reflect different information about tissue properties, investigating their roles in the grading of PIT should be valuable. However, only a few studies with small sample sizes have investigated the promising potential of IVIM in grading of PIT.[15,16] So far, no comparison of the 3 different diffusion models in predicting tumor biology and grades in PIT has been made. Thus, this study aimed to explore the correlations of metrics derived from conventional DWI, IVIM, and DKI with histopathologic features to compare the accuracy of conventional DWI, IVIM, and DKI for PIT grading.

MATERIALS AND METHODS

Patients

This retrospective study was approved by our institutional review board, and the informed consent requirement was waived due to the retrospective nature of this study. Between July 2017 and August 2020, a total of 56 consecutive pediatric patients with intracranial tumors were enrolled on the basis of the following inclusion criteria: 1) intracranial tumors histologically proved by surgery/biopsy, 2) preoperative MR imaging performed (without any previous treatment), and 3) available IVIM and DKI sequences. The exclusion criterion was the solid component of tumor being unavailable for analysis ($<10\ mm^2$, $n = 2$). Ultimately, 54 patients (40 boys and 14 girls; mean age, 9.35 [SD, 3.84] years; range, 8 months to 18 years) with 28 high-grade (WHO grades III and IV) and 26 low-grade (WHO grades I and II) tumors were included in this study.

MR Imaging Techniques

All patients underwent MR imaging examinations with a 3T MR imaging scanner (Magnetom Skyra; Siemens) using a 20-channel head/neck coil. Routine MR imaging was performed, including axial T2WI, SWI, and pre- and postcontrast T1WI.

Multiple b-value DWI was performed using a single-shot echo-planar imaging sequence in the axial plane. The detailed imaging parameters were as follows: TR/TE = 5000 ms/78 ms, FOV = 220 × 220 mm, acquisition matrix = 150 × 135, parallel acceleration factor = 2, section thickness = 5 mm, gap = 1 mm, and acquisition time = 8 minutes 25 seconds. Thirteen different b-values (b = 0, 50, 100, 150, 200, 300, 400, 600, 700, 800, 1000, 1400, and 2000 s/mm^2 with 2, 2, 2, 2, 2, 2, 2, 2, 2, 3, 3, 4, 4 signal averages, respectively) were applied in all 3 orthogonal diffusion directions.

Image Processing and Analysis

In the conventional DWI model, the DWI data-fitting was performed on the basis of the following equation: $S_b/S_0 = \exp(-b\cdot \times \mathrm{ADC})$, Where S_b and S_0 are the signal intensities at a specific b-value and at $b = 0$ s/mm^2, respectively. The ADC map was calculated from 2 b-values (0 and 1000 s/mm^2). For the IVIM model, the corresponding parameters, including D, D*, and f, were derived from the following equation using the following 11 b-values (b = 0, 50, 100, 150, 200, 300, 400, 600, 700, 800, and 1000 s/mm^2): $S_b/S_0 = (1-f) \times \exp(-b \times D) + f \times \exp[-b \times (D + D^*)]$. Where S_b and S_0 are the signal intensities at a specific b-value and at $b = 0$ s/mm^2, respectively. D is the true diffusion coefficient, D* is the pseudodiffusion coefficient, and f is the perfusion fraction. For the DKI model, diffusion signal intensities of 4 b-values (b = 0, 700, 1400, and 2000 s/mm^2) were fitted with the following equation: $S_b/S_0 = \exp(-b \times Dk + b^2 \times Dk^2 \times K/6)$. Where S_b and S_0 are the signal intensities at a specific b-value and at b=0 s/mm^2, respectively. Dk is the corrected ADC without Gaussian bias, and K is the diffusional kurtosis. ADC, IVIM, and DKI processing were performed using a prototype software (Diffusion Toolbox; Siemens), which generated quantitative parametric maps, including the ADC and D, D*, f, Dk, and K maps.

The quantitative parametric maps were independently analyzed by 2 blinded pediatric neuroradiologists (S.L. and W.G., with 3 and 5 years of experience in neuroradiology, respectively) unaware of the clinicopathologic data. For each patient, both reviewers placed 1 polygonal ROI (mean ROI = 643.20 [SD, 526.64] mm^2; range, 16.13–2181.77 mm^2) along the outer margin of the solid component of the tumors on the section where the lesion was the largest of the corresponding parametric maps. Consequently, the mean ADC_{ROI}, D_{ROI}, D^*_{ROI}, f_{ROI}, Dk_{ROI}, and K_{ROI} values of a single section were calculated. Moreover, 1 polygonal VOI (mean VOI = 41,441.50 [SD, 51,160.96] mm^3; range, 756.37–298,406.35 mm^3) was also drawn along the outer margin of the solid component of the tumors on the corresponding parameter maps to calculate the quantitative parameters for the whole lesion, which were referred as ADC_{VOI}, D_{VOI}, D^*_{VOI}, f_{VOI}, Dk_{VOI}, and K_{VOI}. Attention was paid to exclude the areas of necrosis, edema, cyst, hemorrhage, calcification, or apparent blood vessel. The measurements made by 2 neuroradiologists were used to evaluate the interreader repeatability. The measurements were made repeatedly by W.G. with a minimum washout period of 1 month to assess the intrareader repeatability.

In addition, the conventional MR imaging characteristics of each tumor were recorded by 1 blinded pediatric neuroradiologist (D.C., with 30 years of experience in neuroradiology), including tumor location, cystic degeneration, hemorrhage, necrosis, enhancement characteristics of the solid component, peritumoral edema, and tumor margin.

Histopathologic Evaluation

All PITs were classified according to the 2016 WHO Classification of Tumors of the Central Nervous System.[17]

Table 1: Comparison of demographic and conventional MR imaging characteristics between low- and high-grade PITs

Characteristics	Low-Grade Tumor	High-Grade Tumor	*P* Value
Demography			
Age (mean) (yr)	9.71 (SD, 3.66)	9.02 (SD, 4.11)	.51
Male sex (No.) (%)	17 (65.4%)	23 (82.1%)	.16
Location (No.)			.13
Cerebral hemisphere	9	5	
Cerebellum	12	11	
Basal ganglia/brain stem	3	3	
Other	2	9	
Conventional MR imaging			
Cystic degeneration (No.) (%)	16 (61.5%)	13 (46.4%)	.27
Hemorrhage (No.) (%)	5 (19.2%)	10 (35.7%)	.18
Necrosis (No.) (%)	5 (19.2%)	14 (50.0%)	.02
Enhancement (No.) (%)	21 (80.8%)	25 (89.3%)	.62
Peritumoral edema (No.) (%)	10 (38.5%)	15 (53.6%)	.27
Clear margin (No.) (%)	14 (53.8%)	13 (46.4%)	.59

Table 2: The inter- and intrarater repeatability for quantitative MR imaging parameters

Parameters	ICC (95% CI)	
	Interreader	Intrareader
Conventional DWI parameters		
ADC_{ROI} ($\times 10^{-3}$ mm^2/s)	0.917 (0.862–0.951)	0.918 (0.863–0.951)
ADC_{VOI} ($\times 10^{-3}$ mm^2/s)	0.928 (0.879–0.957)	0.927 (0.878–0.957)
IVIM parameters		
D_{ROI} ($\times 1^{-3}$ mm^2/s)	0.920 (0.867–0.953)	0.918 (0.862-0.951)
D_{VOI} ($\times 10^{-3}$ mm^2/s)	0.929 (0.880–0.958)	0.927 (0.876–0.957)
D^*_{ROI} ($\times 10^{-3}$ mm^2/s)	0.771 (0.636–0.860)	0.807 (0.690–0.883)
D^*_{VOI} ($\times 10^{-3}$ mm^2/s)	0.921 (0.869–0.954)	0.905 (0.842–0.944)
f_{ROI} (%)	0.886 (0.812–0.932)	0.957 (0.926–0.975)
f_{VOI} (%)	0.934 (0.890–0.961)	0.898 (0.830–0.939)
DKI parameters		
Dk_{ROI} ($\times 10^{-3}$ mm^2/s)	0.928 (0.879-0.958)	0.926 (0.876-0.957)
Dk_{VOI} ($\times 10^{-3}$ mm^2/s)	0.935 (0.891–0.962)	0.926 (0.876-0.957)
K_{ROI}	0.982 (0.967–0.990)	0.984 (0.971–0.991)
K_{VOI}	0.983 (0.972–0.990)	0.984 (0.933–0.977)

Note:—ICC indicates intraclass correlation coefficient.

Thirty-five histopathologic specimens (35/54, 64.8%) were retrospectively reviewed by an experienced pathologist (Y.Z.) for this study. All histologic parameters were calculated from 5 arbitrarily selected high-power fields (original magnification ×200; area, 0.583 mm^2). Tumor cellularity was determined using the number of tumor cell nuclei from the total tissue area.[4] The mean tumor cell counts for 5 high-power fields were calculated. The Ki-67 index was evaluated using a previous method.[15] Briefly, the specimens were immunostained with a commercial Ki-67 monoclonal antihuman antibody (MIB-1; Santa Cruz Biotechnology). The Ki-67 was determined using the percentage of tumor cell nuclei labeled with the Ki-67 monoclonal antibody from all tumor cell nuclei. The highest value for Ki-67 for 5 high-power fields was recorded. Microvessel density (MVD) was calculated as previously described.[18] The specimens were immunostained with a commercial anti-CD31 antibody (Abcam). The MVD was determined using the percentage of anti-CD31 immunostained vascular area from the total tissue area. The mean MVD value for 5 high-power fields was calculated.

Statistical Analysis

All data of PITs were presented as means (SDs), medians, and interquartile range, or number of cases and ratio, as appropriate. The inter- and intrareader repeatability was evaluated using the intraclass correlation coefficient with corresponding 95% CIs. Intraclass correlation coefficient values of >0.75 indicated good agreement. Comparisons of diffusion parameters, histologic parameters, and age between high- and low-grade tumor groups were made with the Mann-Whitney *U* test. Comparisons of sex and conventional MR imaging characteristics were made with the χ^2 test. The Spearman correlations were performed to assess correlations between diffusion parameters and histologic features (correlation coefficient ρ [r] $\leq$ 0.3, very weak to negligible; 0.31–0.5, weak; 0.51–0.7, moderate; 0.71–0.9, strong; 0.91–1.0, very strong). Receiver operating characteristic curve analyses were performed to assess the diagnostic performance and determine the optimal cutoff value of each diffusion parameter for tumor grading. The area under the curves (AUCs) among 9 parameters were compared using the DeLong method with a Bonferroni correction. The corrected *P* value was obtained by multiplying uncorrected *P* values by 36 (9 comparisons). The AUC, Youden index, sensitivity, specificity, positive likelihood ratio, and negative likelihood ratio were calculated. Statistical analyses were performed with commercial software programs (SPSS Version, 22.0, IBM; MedCalc, Version 15.0, MedCalc Software). *P* values < .05 were considered statistically significant.

RESULTS

The comparative results of demographic characteristics, tumor location, and conventional MR imaging characteristic between low- and high-grade PITs are summarized in Table 1. A high-grade PIT was more likely to demonstrate necrosis than a low-grade PIT (50% versus 19.2%, *P* <.05). No differences in other conventional MR imaging characteristics, age, and sex were observed between these 2 groups.

The quantitative MR imaging parameters of each pediatric brain tumor type are shown in the Online Supplemental Data. As shown in Table 2, inter- and intrareader agreement was good for the measurements of conventional DWI, IVIM, and DKI parameters (intraclass correlation coefficient = 0.771–0.984). The comparative results of histologic and quantitative MR imaging

Table 3: Comparison of histopathologic and quantitative MR imaging parameters between low- and high-grade PITs[a]

Parameters	Low-Grade Tumor	High-Grade Tumor	*P* Value
Conventional DWI parameters			
ADC_{ROI} ($\times10^{-3}$ mm^2/s)	1.563 (1.275–1.732)	0.834 (0.735–1.269)	<.001
ADC_{VOI} ($\times10^{-3}$ mm^2/s)	1.498 (1.254–1.692)	0.834 (0.725–1.118)	<.001
IVIM parameters			
D_{ROI} ($\times10^{-3}$ mm^2/s)	1.515 (1.233–1.724)	0.788 (0.660–1.246)	<.001
D_{VOI} ($\times10^{-3}$ mm^2/s)	1.459 (1.224–1.677)	0.800 (0.668–1.081)	<.001
D^*_{ROI} ($\times10^{-3}$ mm^2/s)	82.962 (65.868–96.610)	87.105 (72.954–107.516)	.36
D^*_{VOI} ($\times10^{-3}$ mm^2/s)	81.562 (71.791–92.899)	81.271 (76.037–92.996)	.43
f_{ROI} (%) (mean)	5.479 (SD, 2.603)	6.789 (SD, 2.773)	.08
f_{VOI} (%) (mean)	5.721 (SD, 2.183)	6.701 (SD, 2.852)	.17
DKI parameters			
Dk_{ROI} ($\times10^{-3}$ mm^2/s)	1.899 (1.443–2.062)	1.053 (0.916–1.466)	<.001
Dk_{VOI} ($\times10^{-3}$ mm^2/s)	1.719 (1.440–2.004)	1.044 (0.835–1.353)	<.001
K_{ROI} (mean)	0.483 (SD, 0.155)	0.887 (SD, 0.329)	<.001
K_{VOI} (mean)	0.500 (SD, 0.157)	0.912 (SD, 0.288)	<.001
Histopathology (19 missing)			
Cellularity (mean) (cells/mm^2)	2003 (SD, 769)	3175 (SD, 1161)	.001
Ki-67 (%)	2.315 (0.945–5.310)	40.680 (21.195–66.310)	<.001
MVD (%)	8.280 (4.340–15.400)	10.140 (8.345–19.995)	.12

[a] Data are expressed as mean (SD) or medians (lower quartile-upper quartile).

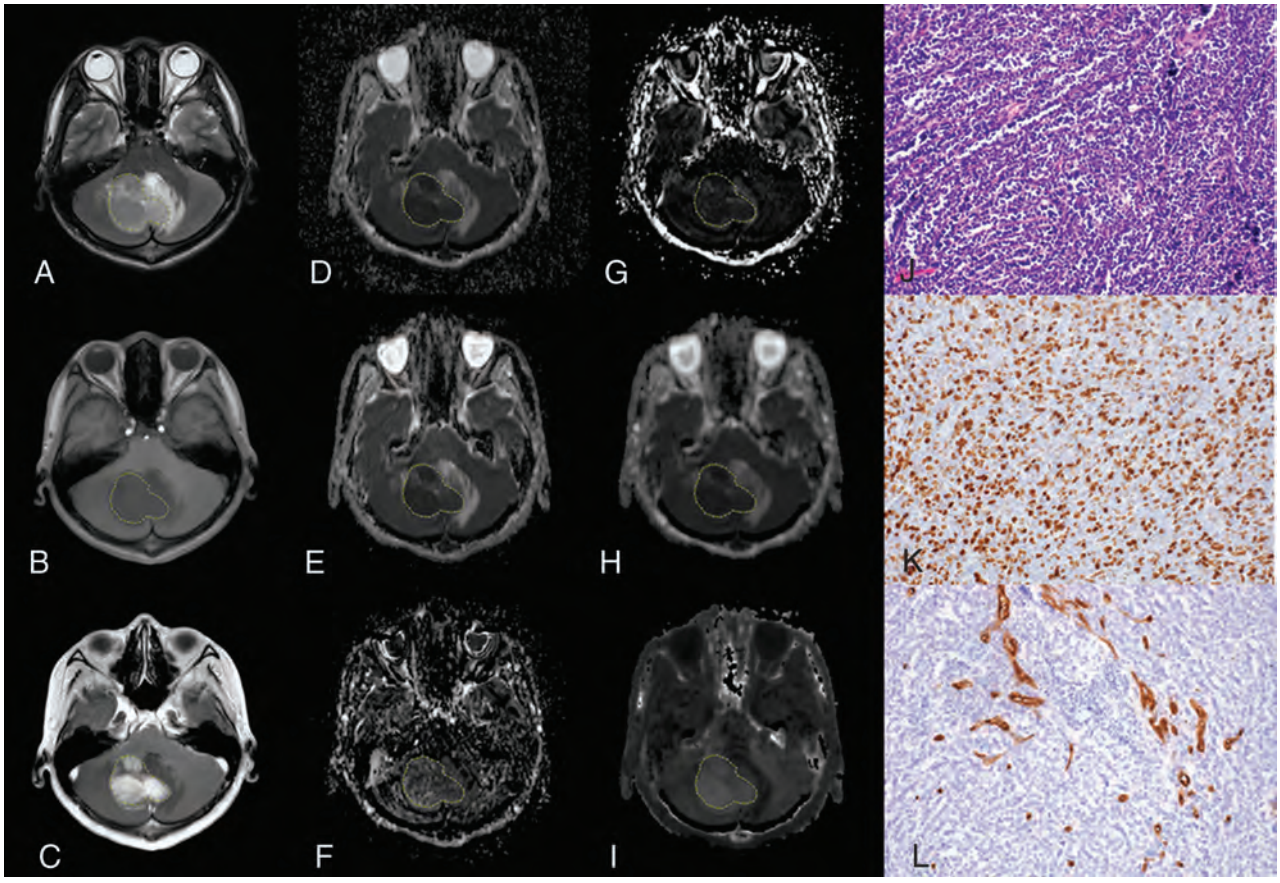

FIG 1. A 15-year-old boy with medulloblastoma in the cerebellum (WHO grade IV). The lesion shows hyperintensity on the T2-weighted image (*A*), hypointensity on the T1-weighted image (*B*), and enhancement on the postcontrast T1-weighted image (*C*). The lesion (VOI) demonstrates hypointensity on the ADC map (*D*), D map (*E*), and Dk map (*H*) and hyperintensity on the D* map (*F*), f map (*G*), and K map (*I*), with values of $0.647 \times 10^{-3} mm^2/s$, 0.594×10^{-3} mm^2/s, 0.778×10^{-3} mm^2/s, 87.228×10^{-3} mm^2/s, 6.312%, and 1.210, respectively. The pathologic diagnosis was medulloblastoma with a cellularity of 4927 cell/mm^2 (*J*), a Ki-67 index of 80% (*K*), and an MVD of 1.4% (*L*) (original magnification × 200).

parameters between low- and high-grade PITs are shown in Table 3. For the diffusion parameters, the ADC_{ROI}, ADC_{VOI}, D_{ROI}, D_{VOI}, Dk_{ROI}, and Dk_{VOI} values were significantly lower in high-grade tumors than in low-grade tumors (all, $P < .001$), whereas the K_{ROI} and K_{VOI} values of high-grade brain tumors were significantly higher than those in low-grade tumors

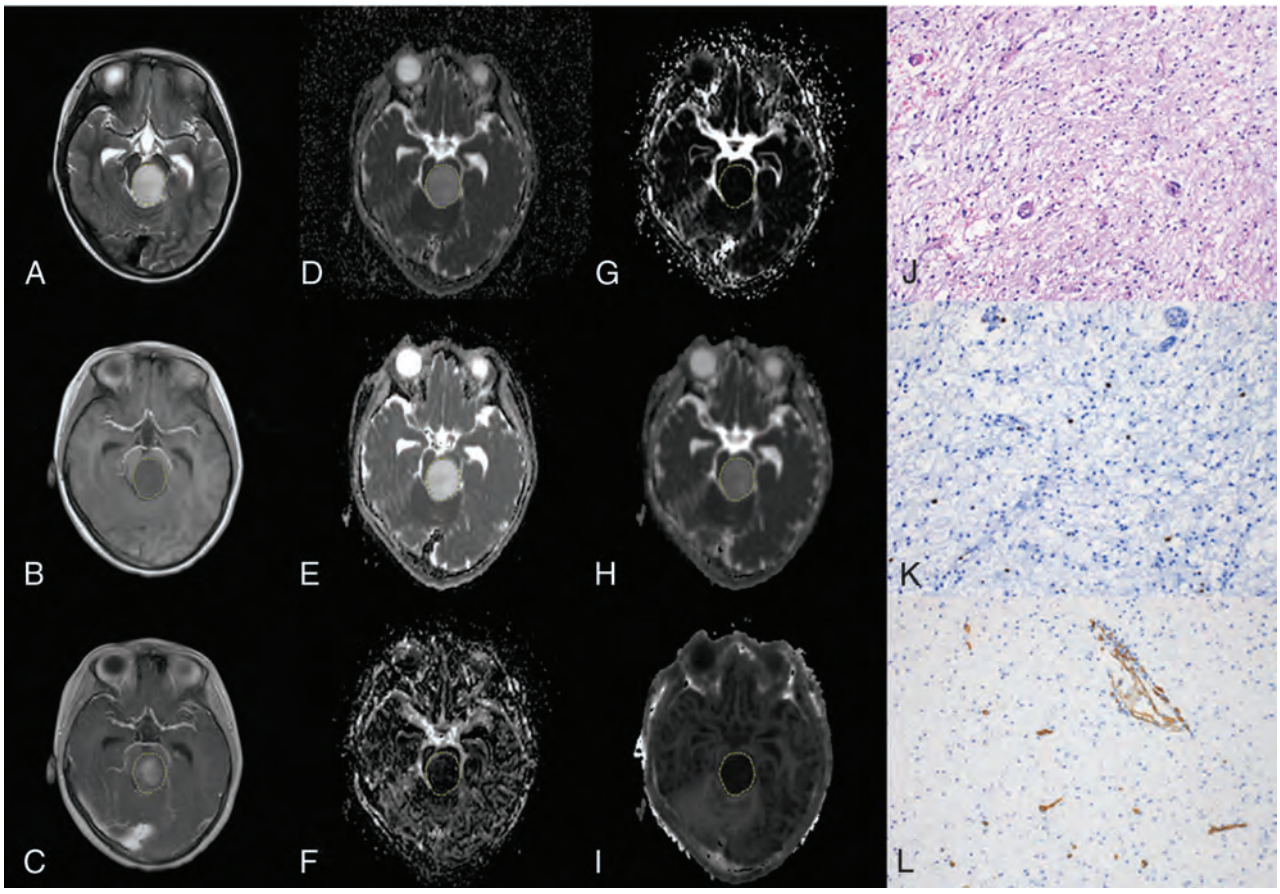

FIG 2. A 5-year-old boy with a diffuse astrocytoma in the brain stem (WHO grade II). The lesion shows hyperintensity on the T2-weighted image (*A*), hypointensity on the T1-weighted image (*B*), and enhancement on the postcontrast T1-weighted image (*C*). The lesion (VOI) demonstrates hyperintensity on the ADC map (*D*), D map (*E*), and Dk map (*H*) and hypointensity on the D* map (*F*), f map (*G*), and K map (*I*), with values of 1.528 $\times 10^{-3}$mm^2/s, 1.530 $\times 10^{-3}$ mm^2/s, 1.681 $\times 10^{-3}$ mm^2/s, 57.310 $\times 10^{-3}$ mm^2/s, 2.394%, and 0.315, respectively. The pathologic diagnosis was diffuse astrocytoma with a cellularity of 1917 cell/mm^2 (*J*), a Ki-67 index of 1.1% (*K*), and an MVD of 0.9% (*L*) (magnification, × 200).

Table 4: Correlation between histologic parameters and quantitative MR imaging parameters for all PITs

Parameters	Cellularity (*r*) (*P* Value) (Cells/mm^2)	Ki-67 (%) (*r*) (*P* Value)	MVD (%) (*r*) (*P* Value)
Conventional DWI parameters			
ADC_{ROI} ($\times 10^{-3}$ mm^2/s)	−0.651 ($P < .001$)	−0.717 ($P < .001$)	0.044 ($P = .80$)
ADC_{VOI} ($\times 10^{-3}$ mm^2/s)	−0.659 ($P < .001$)	−0.735 ($P < .001$)	−0.031 ($P = .86$)
IVIM parameters			
D_{ROI} ($\times 10^{-3}$ mm^2/s)	−0.657 ($P < .001$)	−0.714 ($P < .001$)	0.024 ($P = .89$)
D_{VOI} ($\times 10^{-3}$ mm^2/s)	−0.657 ($P < .001$)	−0.740 ($P < .001$)	−0.021 ($P = .91$)
D^*_{ROI} ($\times 10^{-3}$ mm^2/s)	−0.161 ($P = .36$)	−0.003 ($P = .99$)	0.082 ($P = .64$)
D^*_{VOI} ($\times 10^{-3}$ mm^2/s)	−0.029 ($P = .87$)	0.191 ($P = .27$)	0.273 ($P = .11$)
f_{ROI} (%)	0.099 ($P = .57$)	0.140 ($P = .42$)	0.105 ($P = .55$)
f_{VOI} (%)	0.096 ($P = .58$)	0.269 ($P = .12$)	0.163 ($P = .35$)
DKI parameters			
Dk_{ROI} ($\times 10^{-3}$ mm^2/s)	−0.548 ($P < .001$)	−0.625 ($P < .001$)	0.122 ($P = .49$)
Dk_{VOI} ($\times 10^{3}$ mm^2/s)	−0.601 ($P < .001$)	−0.704 ($P < .001$)	0.061 ($P = .73$)
K_{ROI}	0.677 ($P < .001$)	0.773 ($P < .001$)	−0.101 ($P = .56$)
K_{VOI}	0.674 ($P < .001$)	0.802 ($P < .001$)	−0.032 ($P = .86$)

($P < .001$) (Figs 1 and 2). The high-grade brain tumors tended to have higher f values, but the difference was not significant ($P > .05$). For the histologic parameters, the cellularity and Ki-67 were significantly higher in the high-grade group than in the low-grade group (all, $P < .05$) (Figs 1 and 2).

The correlation results between quantitative MR imaging parameters and histologic parameters are illustrated in Table 4. The cellularity and Ki-67 were inversely correlated with the ADC_{ROI}, ADC_{VOI}, D_{ROI}, D_{VOI}, Dk_{ROI}, and Dk_{VOI} values ($r = -0.548$ to -0.740; all, $P < .001$) and were positively associated with K_{ROI} and K_{VOI} values ($r = 0.674-0.802$; all, $P < .001$), respectively. The K_{VOI} value showed the strongest correlation with the Ki-67 index ($r = 0.802$, $P < .001$). The MVD was not significantly correlated with any diffusion parameters ($r = -0.101-0.273$; all, $P > .05$).

Table 5: Measurement of the quantitative MR imaging parameters and conventional MR imaging for differentiating high- and low-grade PITs

Parameters	Cutoff Value	Youden Index	Sensitivity (%)	Specificity (%)	+LR (%)	–LR (%)	AUC
ADC_{ROI}	1.238	0.558	75.0	80.8	3.90	0.31	0.826
ADC_{VOI}	1.163	0.703	85.7	84.6	5.57	0.17	0.901
D_{ROI}	1.034	0.563	67.9	88.5	5.88	0.36	0.830
D_{VOI}	1.119	0.668	82.1	84.9	5.34	0.21	0.894
Dk_{ROI}	1.648	0.585	89.3	69.2	2.90	0.15	0.799
DK_{VOI}	1.366	0.632	78.6	84.6	5.11	0.25	0.863
K_{ROI}	0.561	0.593	78.6	80.8	4.09	0.27	0.838
K_{VOI}	0.593	0.665	85.7	80.8	4.46	0.18	0.885
cMRI		0.304	48.3	82.1	2.70	0.63	0.652

Note:—cMRI indicates conventional MRI; LR, likelihood ratio.

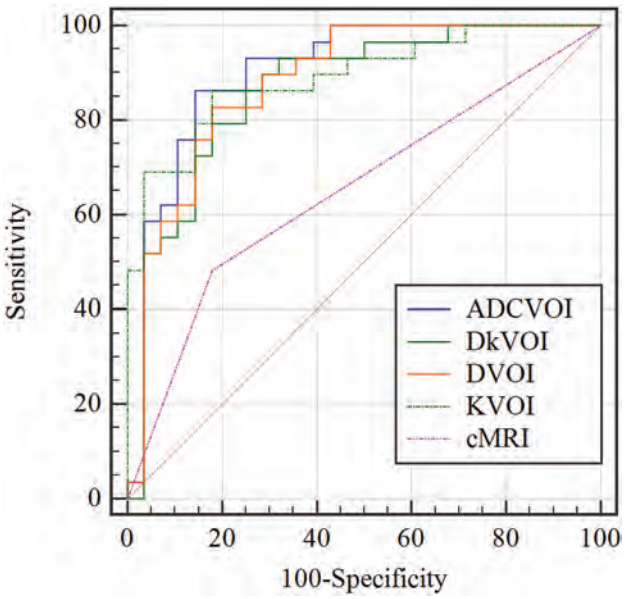

FIG 3. Receiver operating characteristic curves for ADC_{VOI}, D_{VOI}, Dk_{VOI}, K_{VOI}, and conventional MR imaging in distinguishing low- from high-grade pediatric intracranial tumors.

As demonstrated in Table 5 and Fig 3, according to receiver operating characteristic curve analysis, the ADC, D, Dk, and K values were useful in grading PITs (AUC = 0.799–0.901). The diagnostic performance of the quantitative diffusion parameters in grading PITs was superior to that of the conventional MRI (all, corrected $P < .05$). However, the diagnostic performance of quantitative diffusion parameters was similar (all, corrected $P > .05$, compared with each other).

DISCUSSION

An accurate assessment of the WHO grade and histologic features is particularly vital in PIT. In this study, with a relatively large sample size, the results showed that the DWI, IVIM, and DKI parameters were correlated with the cellularity or Ki-67 of PIT and were helpful in differentiating low- from high-grade PITs. However, IVIM- and DKI-derived parameters had similar diagnostic performance compared with conventional DWI.

Conventional MR imaging has been shown to be insufficient for differentiation of PIT, in part because location, cystic degeneration, necrosis, peritumoral edema, or enhancement may be seen with both high- and low-grade PITs.[3] In our study, high- and low-grade PITs have similar conventional MR imaging characteristics except necrosis. Even necrosis was not reliable for differentiating high- or low-grade PITs, which were not seen in half of the high-grade PITs (14/28, 50%) in this study. Consequently, advanced MR imaging techniques, such as diffusion imaging, that improve diagnostic performance of tumor grading remain valuable.

Our preliminary results showed that ADC, D, and Dk values were negatively correlated with cellularity and Ki-67. In comparison with ADC, D and Dk represent the pure molecular diffusion coefficient without microcirculation influence[8] and the corrected diffusion coefficient for non-Gaussian bias,[10] respectively. Therefore, it was not unusual that the negative correlation was found between quantitative diffusion metrics (D and Dk) and histologic features (cellularity and Ki-67) because high Ki-67 or cell density could reduce tumor stromal space and cause the restriction of water molecular diffusion (reflected by decreasing ADC, D, and Dk).[4] Our findings also agree with the results of an earlier IVIM study performed in a small number of pediatric patients, in which the D value was correlated with Ki-67 and the f value was correlated with MVD.[15] Additionally, we also found that the K value obtained from DKI was positively correlated with cellularity and Ki-67, a finding consistent with recent studies in adult intracranial tumors.[13,19] K is the deviation of water molecular diffusion from a Gaussian distribution, which might indicate the tissue heterogeneity.[10] These correlations may be attributed to a higher degree of heterogeneous cell membranes (reflected by cellularity and Ki-67) and complex intracellular microstructure (reflected by Ki-67). Furthermore, the K value had the strongest Ki-67-related correlation among all parameters, indicating that the K value could serve as a promising metric for predicting Ki-67 expression in PITs.

D* and f are both perfusion-related IVIM metrics that quantify the microcirculation perfusion of the tissue.[8] The f value represents the flowing blood volume fraction and has no correlation with cellularity and Ki-67, or even with MVD in this study. This result is in discordance with those of previous studies,[15,20] while consistent with another study.[21] Lima et al[20] found a positive correlation between f and MVD in a rat brain model, while Li et al[21] reported that the f value had no evident correlation with MVD in rabbit liver VX2 tumors. The reason for the discordance between the f value and capillary density is still unclear and may be attributed to the complex microcirculation environment, such as extravasation due to increased permeability in immature microvessels and higher vascular pressure, which may decrease the blood volume.[20] The heterogeneity of tumor included in this study might also account for this discordance. In addition, the D* value in our study had no correlation with histologic features due to the low SNR and the relatively weak reproducibility, in line with previous studies.[15]

Furthermore, we found that high-grade PITs had lower ADC, D, and Dk values but higher K values than low-grade tumors, in line with the recent studies.[11–13,15] In an earlier IVIM study performed in 17 pediatric intracranial tumors, lower ADC and D values were also seen in high-grade tumors.[15] The decrease of diffusion-related parameters (ADC, D, and Dk) in high-grade PITs reflected a higher cell density and increased mitotic activity (higher Ki-67), which were also shown in our study. The increase of the K value in high-grade PITs may be attributed to heterogeneous malignancies in childhood and complex microstructure in the tumors. Additionally, although the high-grade PIT tends to have higher f values, the difference was not significant, inconsistent with a previous study,[15] probably due to the differences in inclusion types and case sizes between the previous study and the present study. Specifically, some high-grade pediatric intracranial tumors, such as diffuse midline gliomas, showed a low microcapillary perfusion (mean $f_{VOI} = 4.20\%$). Most interesting, the diffusion parameters (ADC, D, and Dk) for ROIs were slightly higher than those for VOIs (the opposite of K) in low-grade PITs. The ROI method used in this study may be more prone to imaging noise, which may lead to the overestimation of diffusion parameters.[22]

Our preliminary study showed that ADC, D, Dk, and K had similar diagnostic performance for differentiating high- from low-grade PITs. We noticed that D_{ROI} had the highest specificity. This means that D removal of the perfusion portion could be conducive to revealing the cellular density within tumor[23-25] and could have a relatively better performance in diagnosing low-grade PITs. ADC_{VOI} achieved the highest Youden index, with a maximum AUC in a nonsignificant manner. Compared with IVIM and DKI, ADC was easily acquired with a shorter scanning time, had a low requirement for specific software, and was less prone to motion artifacts, which may be more applicable in pediatric patients. These preliminary findings suggest that ADC could serve as a useful and convenient marker in pediatric brain tumor grading.

This study had several limitations. First, our major limitation is the heterogeneity of the tumors studied. Larger numbers of individual tumor types are necessary to validate these preliminary findings across all tumor types. Second, the histopathologic analyses were available for only 35 (64.8%) cases due to the retrospective study. However, to our knowledge, the sample size in our study for histopathologic analyses was relatively large in the study of pediatric intracranial tumors. Third, conventional DWI, IVIM, and DKI parameters derived from regions of tumor may not correspond well to the histologic tissue samples for histologic analysis. Thus, a site-to-site MR imaging–guided biopsy may be needed to confirm our findings. Fourth, the diffusion encoding was performed using only 3 perpendicular directions in this study. More direction could be used to realize anisotropic diffusion via the diffusion tensor imaging in brain tissues and to increase spatial resolution. However, DWI averaged over 3 directions is usually applied during the clinical diagnostic procedure.

CONCLUSIONS

IVIM- and DKI-derived parameters have similar performance compared with conventional DWI in reflecting histologic features and predicting the PIT grade.

REFERENCES

1. Ward E, DeSantis C, Robbins A, et al. **Childhood and adolescent cancer statistics, 2014.** *CA Cancer J Clin* 2014;64:83–103 CrossRef Medline
2. Udaka YT, Packer RJ. **Pediatric brain tumors.** *Neurol Clin* 2018;36:533–56 CrossRef Medline
3. Cha S. **Update on brain tumor imaging: from anatomy to physiology.** *AJNR Am J Neuroradiol* 2006;27:475–87 Medline
4. Koral K, Mathis D, Gimi B, et al. **Common pediatric cerebellar tumors: correlation between cell densities and apparent diffusion coefficient metrics.** *Radiology* 2013;268:532–37 CrossRef Medline
5. Kralik SF, Taha A, Kamer AP, et al. **Diffusion imaging for tumor grading of supratentorial brain tumors in the first year of life.** *AJNR Am J Neuroradiol* 2014;35:815–23 CrossRef Medline
6. Bull JG, Saunders DE, Clark CA. **Discrimination of paediatric brain tumours using apparent diffusion coefficient histograms.** *Eur Radiol* 2012;22:447–57 CrossRef Medline
7. Al-Sharydah AM, Al-Arfaj HK, Saleh Al-Muhaish H, et al. **Can apparent diffusion coefficient values help distinguish between different types of pediatric brain tumors?** *Eur J Radiol Open* 2019;6:49–55 CrossRef Medline
8. Le Bihan D. **Intravoxel incoherent motion imaging using steady-state free precession.** *Magn Reson Med* 1988;7:346–51 CrossRef Medline
9. Le Bihan D, Breton E, Lallemand D, et al. **MR imaging of intravoxel incoherent motions: application to diffusion and perfusion in neurologic disorders.** *Radiology* 1986;161:401–07 CrossRef Medline
10. Jensen JH, Helpern JA, Ramani A, et al. **Diffusional kurtosis imaging: the quantification of non-Gaussian water diffusion by means of magnetic resonance imaging.** *Magn Reson Med* 2005;53:1432–40 CrossRef Medline
11. Bai Y, Lin Y, Tian J, et al. **Grading of gliomas by using monoexponential, biexponential, and stretched exponential diffusion-weighted MR imaging and diffusion kurtosis MR imaging.** *Radiology* 2016;278:496–504 CrossRef Medline
12. Goryawala MZ, Heros DO, Komotar RJ, et al. **Value of diffusion kurtosis imaging in assessing low-grade gliomas.** *J Magn Reson Imaging* 2018;48:1551–58 CrossRef Medline
13. Lin L, Bhawana R, Xue Y, et al. **Comparative analysis of diffusional kurtosis imaging, diffusion tensor imaging, and diffusion-weighted imaging in grading and assessing cellular proliferation of meningiomas.** *AJNR Am J Neuroradiol* 2018;39:1032–38 CrossRef Medline
14. Xiao Z, Zhong Y, Tang Z, et al. **Standard diffusion-weighted, diffusion kurtosis and intravoxel incoherent motion MR imaging of sinonasal malignancies: correlations with Ki-67 proliferation status.** *Eur Radiol* 2018;28:2923–33 CrossRef Medline
15. Kikuchi K, Hiwatashi A, Togao O, et al. **Intravoxel incoherent motion MR imaging of pediatric intracranial tumors: correlation with histology and diagnostic utility.** *AJNR Am J Neuroradiol Neuroradiol* 2019;40:878–84 CrossRef Medline
16. Burrowes D, Fangusaro JR, Nelson PC, et al. **Extended diffusion weighted magnetic resonance imaging with two-compartment and anomalous diffusion models for differentiation of low-grade and high-grade brain tumors in pediatric patients.** *Neuroradiology* 2017;59:803–11 CrossRef Medline
17. Louis DN, Perry A, Reifenberger G, et al. **The 2016 World Health Organization Classification of Tumors of the Central Nervous System: a summary.** *Acta Neuropathol* 2016;131:803–20 CrossRef Medline
18. Kikuchi K, Hiwatashi A, Togao O, et al. **Correlation between arterial spin-labeling perfusion and histopathological vascular density of pediatric intracranial tumors.** *J Neurooncol* 2017;135:561–69 CrossRef Medline
19. Zhao J, Wang YL, Li XB, et al. **Comparative analysis of the diffusion kurtosis imaging and diffusion tensor imaging in grading gliomas, predicting tumour cell proliferation and IDH-1 gene mutation status.** *J Neurooncol* 2019;141:195–203 CrossRef Medline
20. Lima M, Reynaud O, Tsurugizawa T, et al. **Characterization of glioma microcirculation and tissue features using intravoxel incoherent**

motion magnetic resonance imaging in a rat brain model. *Invest Radiol* 2014;49:485–90 CrossRef
21. Li JL, Ye WT, Liu ZY, et al. **Comparison of microvascular perfusion evaluation among IVIM-DWI, CT perfusion imaging and histological microvessel density in rabbit liver VX2 tumors.** *Magn Reson Imaging* 2018;46:64–69 CrossRef Medline
22. Iima M, Partridge SC, Le Bihan D. **Six DWI questions you always wanted to know but were afraid to ask: clinical relevance for breast diffusion MRI.** *Eur Radiol* 2020;30:2561–70 CrossRef Medline
23. Van Cauter S, Veraart J, Sijbers J, et al. **Gliomas: diffusion kurtosis MR imaging in grading.** *Radiology* 2012;263:492–501 CrossRef Medline
24. Raja R, Sinha N, Saini J, et al. **Assessment of tissue heterogeneity using diffusion tensor and diffusion kurtosis imaging for grading gliomas.** *Neuroradiology* 2016;58:1217–31 CrossRef Medline
25. Chen X, Lin L, Wu J, et al. **Histogram analysis in predicting the grade and histological subtype of meningiomas based on diffusion kurtosis imaging.** *Acta Radiol* 2020;61:1228–39 CrossRef Medline

Selective Motor Control is a Clinical Correlate of Brain Motor Tract Impairment in Children with Spastic Bilateral Cerebral Palsy

A. Vuong, E.G. Fowler, J. Matsumoto, L.A. Staudt, H. Yokota, and S.H. Joshi

ABSTRACT

BACKGROUND AND PURPOSE: Selective voluntary motor control is an important factor influencing gross motor function, interjoint coordination, and the outcome of hamstring-lengthening surgery in spastic cerebral palsy. Using DTI, we investigated whether selective voluntary motor control would show strong correlations with WM motor tract microstructure and whether selective voluntary motor control is more sensitive to global WM impairment than gross motor function.

MATERIALS AND METHODS: Children with spastic bilateral cerebral palsy born preterm and typically developing children were recruited. The Selective Control Assessment of the Lower Extremity (SCALE) and Gross Motor Function Measure (GMFM) were assessed in participants with cerebral palsy. Participants underwent brain MR imaging to collect DWI data. Tract-Based Spatial Statistics was used to analyze the WM for between-group differences and correlations with SCALE and GMFM. ROI analyses compared motor regions.

RESULTS: Twelve children with cerebral palsy (mean age, 11.5 years) and 12 typically developing children (mean age, 10.3 years) participated. Altered DTI outcomes were found throughout the whole brain for the cerebral palsy group. SCALE, developed to evaluate selective voluntary motor control in cerebral palsy, showed significant positive correlations with fractional anisotropy in more WM voxels throughout the whole brain and for motor regions, including the corticospinal tract and corpus callosum, compared with GMFM. A significant negative correlation between radial diffusivity and SCALE, but not GMFM, was found within the corpus callosum.

CONCLUSIONS: SCALE was a more sensitive clinical correlate of motor and whole-brain WM tract impairment in children with spastic bilateral cerebral palsy, suggesting greater anisotropy and myelination in these regions for those with higher selective voluntary motor control.

ABBREVIATIONS: AD = axial diffusivity; CC = corpus callosum; CerPed = cerebral peduncle; CP = cerebral palsy; CST = corticospinal tract; FA = fractional anisotropy; GMFCS = Gross Motor Function Classification System; GMFM = Gross Motor Function Measure; MD = mean diffusivity; PLIC = posterior limb of the internal capsule; RD = radial diffusivity; SCALE = Selective Control Assessment of the Lower Extremity; SCR = superior corona radiata; SVMC = selective voluntary motor control; TDC = typically developing children

Periventricular leukomalacia is an MR imaging finding associated with perinatal injury to the cerebral WM. Children born prematurely are at higher risk of neurologic sequelae, including spastic bilateral cerebral palsy (CP) associated with periventricular leukomalacia.[1-3] Within spastic bilateral CP, there is a wide range of clinical outcomes, and lower extremity function varies among individuals. The microstructural properties of cerebral WM and the neuronal organization associated with the range of motor impairments in spastic CP are not well-understood.[1,2]

Spastic CP is associated with damage to the corticospinal tract (CST) and other motor pathways that are responsible for selective voluntary motor control (SVMC). SVMC reflects the ability to perform isolated, skilled, and precise movements of a joint or limb with control of force and speed on request.[4] Impaired SVMC affects coordination between the lower extremity joints, resulting in coupling of the hip, knee, and ankle to varying degrees.[5] SVMC was

Received March 22, 2021; accepted after revision June 23.

From the Departments of Bioengineering (A.V., S.H.J.), Orthopaedic Surgery (A.V., E.G.F., L.A.S.), Pediatrics (J.M.), and Ahmanson-Lovelace Brain Mapping Center in the Department of Neurology (S.H.J.), University of California Los Angeles, Los Angeles, California; Center for Cerebral Palsy at UCLA/Orthopaedic Institute for Children (A.V., E.G.F., L.A.S.), Los Angeles, California; and Department of Diagnostic Radiology and Radiation (H.Y.), Chiba University Hospital, Chiba, Japan.

MR imaging data acquisition and gait assessments were funded by donations and grants from the UCLA Children's Discovery and Innovation Institute; Shapiro Family Foundation; United Cerebral Palsy of Los Angeles, Santa Barbara and Ventura Counties; Waters Foundation; California Community Foundation; Lena Longo Foundation; and UCLA Brain Mapping Center. No funders were involved in the preparation of this article.

Paper previously presented, in part, at: Annual Meeting of the American Academy for Cerebral Palsy and Developmental Medicine, September 18–21, 2019; Anaheim, California.

Please address correspondence to Andy Vuong, MS, Center for Cerebral Palsy at UCLA/OIC, 1000 Veteran Ave, 22-27 Rehabilitation Center, Los Angeles, CA 90095-1795; e-mail: avuong@mednet.ucla.edu

http://dx.doi.org/10.3174/ajnr.A7272

shown to have a strong influence on the gait and mobility characteristics of children with spastic CP.[6,7] In addition, it has been used as a prognostic factor for hamstring surgery[8] and selective posterior rhizotomy.[9] SVMC, as measured by the Selective Control Assessment of the Lower Extremity (SCALE)[4], had a larger causal effect on gross motor function compared with dynamic motor control (based on gait electromyography), strength, spasticity, contractures, and bony deformities.[7]

DTI is often used to assess microstructural WM differences in children with spastic bilateral CP.[1,2,10,11] This MR imaging technique provides image contrast based on the translational displacement or diffusion of water molecules in the brain.[12,13] DTI measures of fractional anisotropy (FA), radial diffusivity (RD), axial diffusivity (AD), and mean diffusivity (MD) provide details about tissue alterations associated with WM damage in CP.[12,13] In clinical populations and relative to normative values, lower FA has been interpreted as a local marker of the disruption of local tissue microstructural anisotropy, higher RD has corresponded with damaged myelination, lower AD has reflected axonal injury, and higher MD has indicated greater overall diffusivity within a region.[12-14] Together, these DTI outcomes reveal a holistic picture of microstructural differences in cerebral WM.

WM differences between children with spastic CP and typically developing children (TDC) have previously been found using DTI.[1,2,10,11] Motor function in children with spastic bilateral CP involves multiple regions of the brain beyond the CST and motor regions, including the commissural and association tracts and the visual, limbic, and sensory regions.[1,15] Therefore, methods and approaches that focus on a set of a priori regions ultimately limit the scope of analysis and may underestimate the global extent of WM differences.[12] In contrast, Tract-Based Spatial Statistics (TBSS; http://fsl.fmrib.ox.ac.uk/fsl/fslwiki/TBSS), a whole-brain voxel-based approach, is a comprehensive method to assess WM. Altered WM in spastic bilateral CP relative to TDC has been found using voxel-based approaches including TBSS.[1,2,10] In addition, correlations between DTI outcomes and a measure of mobility using the Gross Motor Function Classification System (GMFCS),[16] a categoric score, have been reported.[2,10] While prior DTI correlation analyses have used this mobility classification system to assess CP severity, none have used a motor performance measurement that includes SVMC.

To our knowledge, this is the first study to evaluate the relationships between a clinical measure of SVMC in spastic CP and DTI outcomes for motor regions of the brain. SVMC was assessed using SCALE.[4] Our primary hypothesis was the following: 1) SCALE would show a significant correlation with DTI outcomes in the motor tracts, particularly the CST; and 2) SCALE would be more sensitive to WM impairment than the Gross Motor Function Measure (GMFM),[17] a measure of gross motor function in spastic CP. Our secondary hypothesis was that significantly different DTI outcomes would be found for children with CP compared with a control group of TDC.

MATERIALS AND METHODS

Participants

This study was conducted in an outpatient clinical research center (Center for CP at UCLA/OIC and Ahmanson-Lovelace Brain Mapping Center). The institutional review board of the University of California Los Angeles provided ethics approval. Informed consent and assent for research were obtained from the children and their parents or guardians.

Inclusion criteria for all participants were the following: 1) between 5 and 18 years of age, 2) the ability to understand and follow verbal directions, and 3) the ability to lie still. Additional inclusion criteria for the CP group were the following: 1) a history of prematurity, 2) a diagnosis of spastic bilateral CP and periventricular leukomalacia as evidenced by MR imaging or sonography, and 3) the ability to walk with or without assistive devices.

Exclusion criteria for all participants were the presence of the following: 1) metal implants not verified as MR imaging–safe, 2) programmable implants including ventriculoperitoneal shunts and intrathecal baclofen pumps, and 3) dental braces. Additional exclusion criteria for children with CP were the following: 1) seizures not controlled by medication, 2) orthopedic surgery or neurosurgery within 1 year of starting the study, and 3) botulinum toxin or casting within 3 months of starting the study. Additional exclusion criteria for the TDC group were neurodevelopmental, neuromuscular, or neuropsychiatric diagnoses and visible abnormalities as observed on T1-weighted structural scans.

Clinical Assessments

The CP group was evaluated by experienced physical therapists using standardized protocols. GMFM dimensions D (standing) and E (walking, running, and jumping) were assessed.[17] The GMFM-66 Gross Motor Ability Estimator program was used to compute the final scores. SCALE was used to assess SVMC.[4] Specific isolated movement patterns at the hip, knee, ankle, subtalar, and toe joints were evaluated bilaterally. SCALE scores for each limb ranged from 0 (absent SVMC) to 10 (normal SVMC).[4] Left and right limb scores were summed for a total SCALE score with a maximum value of 20.

MR Imaging Protocols

Before MR imaging sessions, children viewed a slide presentation describing MR imaging procedures and practiced lying still for 10 minutes while listening to recordings of MR imaging sounds. Movies were provided during the MR imaging acquisition for children to view on request. All T1WI and DWI scans were acquired using a 32-channel coil on a 3T Magnetom Prisma MR imaging scanner (Siemens). T1-weighted MPRAGE images were obtained using TR = 2500 ms; TE = 1.8, 3.6, 5.39, and 7.18 ms; FOV = 256 × 256 mm^2; and isotropic voxel resolution = 0.8 × 0.8 × 0.8 mm^3. DWI scans were obtained using a single-shot, spin-echo, echo-planar acquisition with 6 reference images (b = 0 s/mm^2), 52 gradient directions (b = 1500 s/mm^2), TR = 3231 ms, TE = 89.6 ms, FOV = 210 × 210 mm^2, echo spacing = 0.69 ms, and isotropic voxel resolution = 1.5 × 1.5 × 1.5 mm^3.

Statistical Analysis

TBSS, a whole-brain voxel-based approach, was used to assess differences in DTI outcomes between the CP and TDC groups and correlations between DTI outcomes and SCALE and GMFM in the CP group. Whole-brain analyses of DTI outcomes FA, RD, AD, and MD were performed with TBSS

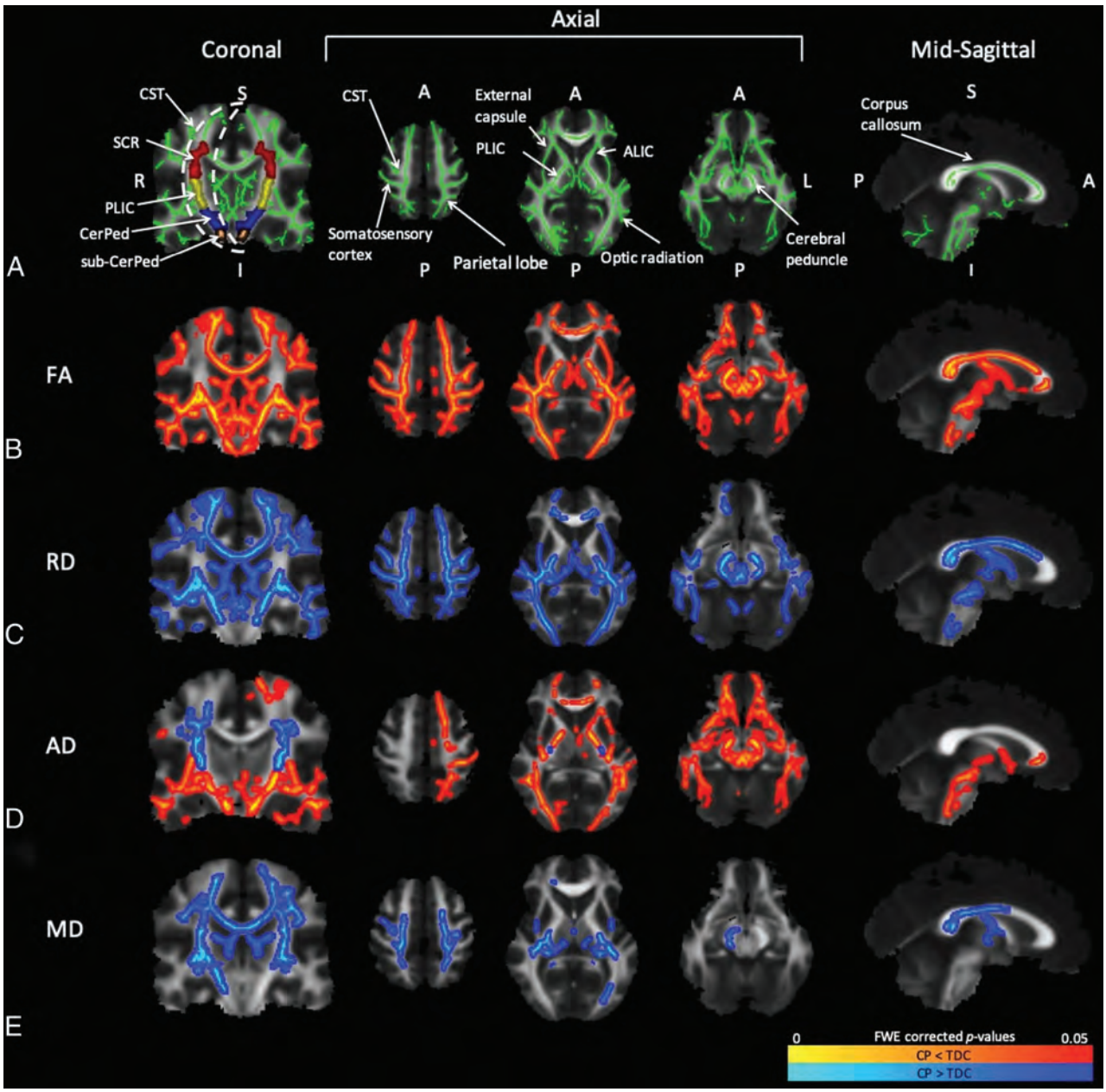

FIG 1. TBSS results show significant differences ($P < .05$) in DTI measures between the CP and TDC groups. Coronal slices were selected at the level of the CST. From left to right, axial slices were selected at the level of the motor cortex, PLIC, and CerPed, respectively. Mid-sagittal slices were selected at the level of the CC. *A*, The WM skeleton is shown in green with *arrows* labeling the CST, somatosensory cortex, parietal lobe, external capsule, PLIC, anterior limb of the internal capsule (ALIC), and corpus callosum. In the coronal view, ROIs for the SCR (red), PLIC (yellow), CerPed (blue), and sub-CerPed (orange) are shown. Significant differences between the CP and TDC groups are shown for FA (*B*), RD (*C*), AD (*D*), and MD (*E*). The hot colormaps denote whether a DTI measure for the CP group was less than (red-yellow) or greater than (blue-light blue) that in the TDC group. A indicates anterior; FWE, family-wise error; I, inferior; L, left; P, posterior; R, right; S, superior.

using the FMRIB (FSL) Diffusion Toolbox (http://fsl.fmrib.ox.ac.uk/fsl/fslwiki/FDT).[18] The mean WM skeleton used in this analysis was derived from and overlaid on the FMRIB58 standard-space FA template (https://fsl.fmrib.ox.ac.uk/fsl/fslwiki/FMRIB58_FA). Results were obtained after 5000 permutation-based randomized tests and corrected for multiple comparisons ($P < .05$) using the threshold-free cluster enhancement procedure.[19] Voxels with significant differences and correlations were projected separately onto the mean WM skeleton.

ROI analyses were performed to quantify voxels with significant findings within specific regions of the brain. Using the Johns Hopkins University ICBM-DTI-81 WM atlas labels (http://neuro.debian.net/pkgs/fsl-jhu-dti-whitematter-atlas.html),[20] we transferred ROIs to all images produced in the TBSS pipeline after nonlinear warping to the standard Montreal Neurological Institute 152 space and skeletonization. ROIs located along the descending pathways of the CST were parcellated bilaterally into the following regions (Fig 1*A*): 1) area inferior to the cerebral peduncle (sub-CerPed), 2) cerebral peduncle (CerPed), 3) posterior limb of the

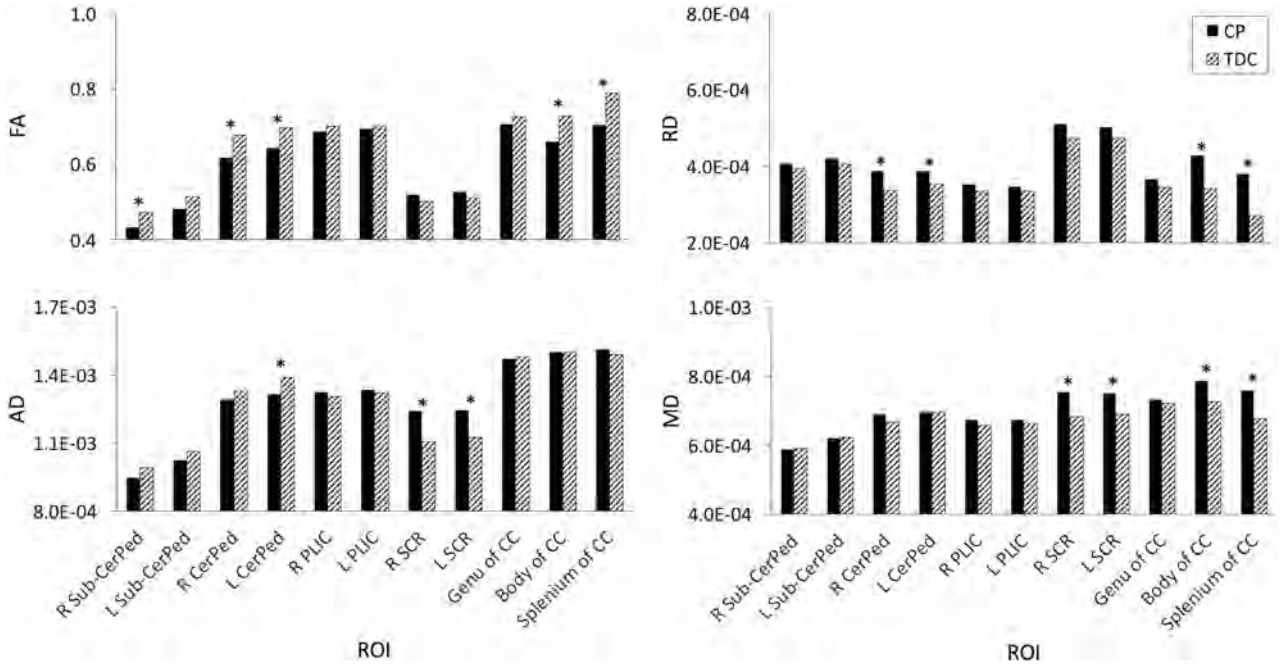

FIG 2. Mean differences in DTI measures between the CP and TDC groups within ROIs for the CST and CC. The *asterisk* indicates significant differences ($P < .05$). L indicates left; R, right.

internal capsule (PLIC), and 4) superior corona radiata (SCR). The sub-CerPed ROIs are labeled as CST in the Johns Hopkins University WM atlas labels. ROIs for the corpus callosum (CC) were the genu, body, and splenium.

To further compare the CP and TDC groups, we calculated means for FA, RD, AD, and MD in each ROI. Data were tested for normal distribution using the Shapiro-Wilk test.[21] Between-group differences were analyzed using *t* tests, assuming unequal variance (JMP Pro 14; SAS Institute). Corrections for multiple comparisons were made using the Benjamini-Hochberg false discovery rate.[22]

Significant correlations between DTI outcomes and clinical measures (SCALE and GMFM) within each ROI were quantified for the CP group by performing voxel counts in FSL (http://www.fmrib.ox.ac.uk/fsl). The percentages of significant voxels in relation to the total number of voxels within ROIs were calculated.

RESULTS

Twelve children with spastic bilateral CP (2 girls, 10 boys; mean age, 11.5 [SD, 2.8] years; age range, 7.3–16.6 years) participated. GMFCS levels were the following: I ($n = 3$), II ($n = 1$), III ($n = 7$), and IV ($n = 1$). Total SCALE scores ranged from 1 to 18. Twelve participants were recruited for the TDC group (12 boys; mean age, 10.3 [SD, 1.5] years; age range, 7.5–12.9 years).

Group Differences

The mean WM skeleton used for statistical comparisons of whole-brain WM voxels is shown in Fig 1*A*. The CP group showed significantly lower FA values throughout the whole brain compared with the TDC group (Fig 1*B*). These areas included the CST, somatosensory cortex, parietal lobe, optic radiation, anterior limb of the internal capsule, external capsule, and CC. Within the CST, FA was significantly lower in the CerPed, PLIC, and motor cortex, but no significant differences were found in the SCR. RD was higher for the CP group throughout the brain, but fewer differences were found anteriorly at the level of the CerPed compared with other regions (Fig 1*C*). Bidirectional results were seen for AD (Fig 1*D*), which was lower for the CP group at the level of the CerPed and cortex (coronal view) but higher for the CP group in the posterior end of the PLIC (axial view) and SCR bilaterally (coronal view). Fewer differences in AD were seen at the level of the motor cortex (right hemisphere) compared with other regions. MD was higher for the CP group within the CC, right CerPed, bilateral PLIC, SCR, and motor cortex (Fig 1*E*).

ROI analysis revealed significant differences between mean DTI outcomes of the CP and TDC groups within specific ROIs located along the CST and CC (Fig 2). Significantly lower FA values in the right sub-CerPed, CerPed bilaterally, and CC body and splenium were found for the CP group. In contrast, RD was significantly higher for the CP group in the CerPed bilaterally and CC body and splenium. AD was significantly lower for the CP group in the left CerPed and higher in the SCR bilaterally. MD was significantly higher for the CP group in the SCR bilaterally and CC body and splenium.

Correlation Analyses

In the whole-brain correlation analyses for the CP group, significant correlations were found for FA and RD but not for AD and MD (Fig 3). Significant positive correlations were found between FA and SCALE for all slices shown in Fig 3*A*. These correlations were associated with motor function regions, including the CST at the level of the CerPed (right > left), PLIC (right > left), motor cortex (left > right), and CC. Fewer voxels within these motor regions exhibited significant positive correlations between FA

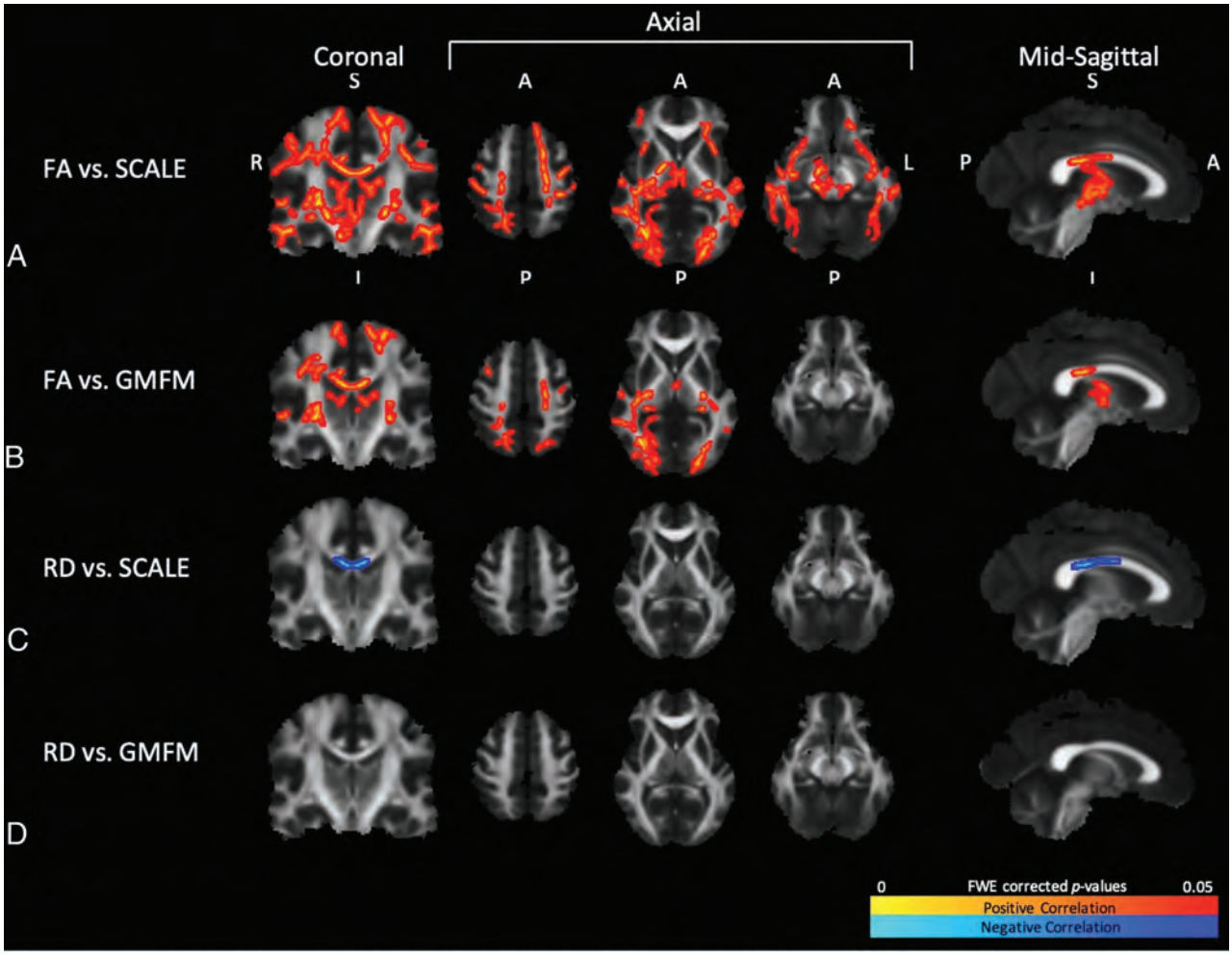

FIG 3. TBSS results show significant correlations ($P < .05$) between DTI measures and clinical measures for the CP group. Coronal slices were selected at the level of the CST. From left to right, axial slices were selected at the level of the motor cortex, PLIC, and CerPed, respectively. Mid-sagittal slices were selected at the level of the CC. Significant correlations are shown for FA vs. SCALE (*A*), FA vs. GMFM (*B*), RD vs. SCALE (*C*), and RD vs. GMFM (*D*). The hot colormaps denote whether the correlations were positive (red-yellow) or negative (blue-light blue). A indicates anterior; FWE, family-wise error; I, inferior; L, left; P, posterior; R, right; S, superior.

and GMFM (Fig 3*B*). In the motor cortex, FA correlated with both SCALE and GMFM for bilateral lower extremity CST and left upper extremity CST as seen from the coronal views. More voxels showed significant correlations with SCALE than with GMFM in these regions. RD exhibited significant negative correlations with SCALE in the CC (Fig 3*C*), but significant correlations with GMFM were not found (Fig 3*D*).

Voxel counts of significant correlations between DTI outcomes and clinical measures within the CST and CC ROIs are shown in the Table. FA correlated positively with SCALE within the right sub-CerPed, CerPed (right > left), PLIC (right > left), SCR (right > left), and CC body and splenium. Compared to SCALE, fewer voxels showed significant positive correlations between FA and GMFM within the PLIC, SCR, CC body and splenium, and throughout the whole brain (30.4% versus 14.4%, respectively). No voxels showed significant correlations between FA and GMFM within the CerPed and sub-CerPed ROIs. RD correlated negatively with SCALE for voxels within all CC ROIs but not CST ROIs. No significant correlations between RD and GMFM were found in voxels for the CST and CC ROIs.

DISCUSSION

This was the first study to associate SCALE, a sensitive measure of SVMC, with DTI outcomes for the CST and other WM tracts in children with spastic bilateral CP. We demonstrated that FA correlated with SCALE in key regions of the CST. A previous DTI study had reported that sensory but not motor tracts correlated with motor function using visual assessment of tract impairment.[23] Motor function in that study, however, was measured using hand-held dynamometry, which is difficult to measure reliably in children with poor motor control.[24] Additionally, the motor skill and ambulatory level were not well-defined. In our analysis, both SCALE and GMFM, which are valid clinical measures for spastic CP, were associated with CST impairment. SCALE emerged as the stronger clinical correlate using TBSS. To quantify the spatial differences, we performed voxel counts in 3D motor ROIs. In comparison with GMFM, the number of voxels with significant correlations between SCALE and FA and the number of voxels with significant correlations between SCALE and RD were greater, establishing SCALE as the more sensitive clinical correlate. Previous studies demonstrating a positive

ROI correlation analyses comparing motor and whole-brain WM regions

Regions	Voxel Count	Voxels with Significant Correlations			
		FA vs. SCALE (%)	FA vs. GMFM (%)	RD vs. SCALE (%)	RD vs. GMFM (%)
CST					
Sub-CerPed R	375	23 (6.1)	0 (0)	0 (0)	0 (0)
Sub-CerPed L	395	0 (0)	0 (0)	0 (0)	0 (0)
CerPed R	598	266 (44.5)	0 (0)	0 (0)	0 (0)
CerPed L	624	74 (11.9)	0 (0)	0 (0)	0 (0)
PLIC R	845	198 (23.4)	74 (8.8)	0 (0)	0 (0)
PLIC L	858	20 (2.3)	18 (2.1)	0 (0)	0 (0)
SCR R	1294	451 (34.9)	387 (29.9)	0 (0)	0 (0)
SCR L	1279	94 (7.3)	25 (2.0)	0 (0)	0 (0)
CC					
Genu	1758	0 (0)	0 (0)	54 (3.1)	0 (0)
Body	3138	1177 (37.5)	692 (22.1)	874 (27.9)	0 (0)
Splenium	2298	904 (39.3)	615 (26.8)	686 (29.9)	0 (0)
Whole brain	126,000	38,251 (30.4)	18,136 (14.4)	2779 (2.2)	0 (0)

Note:—L indicates left; R, right.

relationship between CST FA and functional ability were limited by their use of the GMFCS rating scale, which is a categoric descriptor of mobility.[2,10] In contrast, SCALE and GMFM used in the present study are numeric measures of motor function.

Correlations of FA and RD with SCALE in the CC showed similar trends as reported by Arrigoni et al,[10] in 2016, who reported correlations of FA and RD with GMFCS in the body of the CC. The significant negative correlations between RD and SCALE in the present study suggest that callosal fibers serving interhemispheric sensorimotor communication are better myelinated for children with greater SVMC.[25] These findings may reflect one component of SCALE scoring procedures, the presence of mirroring, which lowers the score. Mirroring occurs when an intentional joint movement on one side of the body is accompanied by an obligatory synkinetic movement on the contralateral side.[4] There are known associations between myelination of the CC and inhibition of mirroring.[26-28] Additionally, transcallosal motor fibers located in the CC body are believed to play an important role in motor control and inhibition of unwanted mirror movements,[29] and lower FA in transcallosal motor fibers has been associated with mirroring in the hands of children with bilateral spastic CP and periventricular leukomalacia. The same mechanism likely occurs in lower extremity mirroring but has not been studied, to our knowledge.

Widespread correlations between SCALE and FA beyond the motor regions were found. In Fig 3, FA correlations with SCALE but not GMFM were seen in the brain stem, visual association pathways, and temporal lobes, suggesting that the integrity of these association pathways was more important for skilled, precise movements than for gross motor activities. Although a direct link between these regions and the ability to execute precise lower extremity movements is difficult to ascertain, such extensive correlations support prior studies demonstrating a relationship between motor function in spastic CP and long-range network connectivity disruptions of various nonmotor networks, including WM regions comprising the visual, limbic, and sensory systems.[1,15] Additionally, lower SCALE scores may be associated with the overall severity of CP, including comorbidities of visual and cognitive impairments.

Consistent with previous studies, children with spastic bilateral CP had lower FA, higher RD, and higher MD in key regions of the CST, specifically the CerPed, PLIC, and motor cortex, compared with TDC.[2,10] While periventricular leukomalacia is a hallmark of spastic CP, no significant between-group differences in FA were found in the periventricular WM. FA values in this region are affected by an abundance of crossing fibers beyond the CST, including the corticopontine, corticobulbar, and thalamocortical tracts, causing more variability in FA. This factor leads to overall reduced measurements of FA in this region and may contribute to the statistically nonsignificant group differences.[1] In spastic CP, WM pathology extends beyond the periventricular WM.[2,10] Accordingly, we found widespread higher RD for the CP group in the somatosensory cortex, parietal lobe, optic radiation, anterior limb of the internal capsule, external capsule, and CC. These higher RD values within the CST and throughout the whole brain are consistent with a lack of mature myelinated fibers and secondary Wallerian degeneration.[3]

Little is known about the relevance of AD differences between the spastic CP and TDC groups. In this analysis, mixed results were found for AD. Unexpectedly, AD was higher in the periventricular WM including the SCR for the CP cohort (Figs 1*D* and 2). This finding may be associated with the radial diffusion of crossing fibers running perpendicular to the ascending/descending tracts in this region.[30] The interpretation of this result is not straightforward because the utility of AD as a putative marker of axonal degeneration or a precise descriptor of tissue microstructure is still under investigation.[25,31]

Statistically significant group differences observed in TBSS were not always reflected in ROI analyses (Figs 1 and 2). This issue can be attributed to the fact that ROI analyses smoothed data over large areas, reducing noise and the number of multiple comparisons. Notably, group-difference analyses in TBSS revealed brain-wide effects in the CP group, suggesting widespread microstructural tissue disruptions. Although motor tracts are deemed the region of injury in CP, WM pathways implicated in vision, hearing, sensation, proprioception, and cognition may be impacted.[32] These findings are consistent with common comorbidities of spastic CP and may also suggest a global

adaptation and neuroplasticity owing to recruitment of different brain regions postdamage.

These widespread differences in the CP group can also be understood in terms of network-connectivity disruptions. Englander et al,[15] in 2013, showed changes to both short- and long-range brain network connectivity not limited to the sensorimotor network in severe-versus-moderate CP, though they did not include a healthy control sample. While we did not have a sufficient sample size to differentiate between severe and moderate cases of CP, our global voxelwise findings implicated similar WM regions including the visual, auditory, and cognitive systems. Ceschin et al,[1] in 2015, found widespread voxelwise reductions of FA in CP and also showed disruption in network connectivity based on global topologic connectivity measures throughout the whole brain. Furthermore, they found alterations in the frontal-striatal and frontolimbic nodes, suggesting compensatory reorganization involving these frontal lobe pathways.[1] Jiang et al,[33,34] in 2019 and 2021, used DTI to show reduced global and nodal network efficiency and increased shortest-path length using the fiber count metrics in infants diagnosed with periventricular WM injury and spastic CP.[33,34] Their study defined nodes as anatomic regions on the cortical gray matter and implicated impairment to the frontal, visual, and cingulate cortices in addition to the supplementary motor area, causing visual spatial or visual perception deficits.[34]

While our hypotheses targeted the CST and WM motor tracts in general, brain-wide WM group differences and brain-wide SCALE correlations suggest both a network-structure disruption effect and a network-region recruitment effort by long-range brain fibers that may serve in a compensatory capacity in response to periventricular leukomalacia injury. Zhou et al,[35] in 2017, suggested the theory of "imperfect compensation," whereby the red nucleus and rubrospinal tract, which are normally inhibited in early life in TDC, further develop to provide compensatory motor control (flexor and extensor synergy patterns) in cases of motor tract injury. While higher FA relative to controls has been reported in the rubrospinal system of adults following stroke,[36,37] higher FA for the CP group in the present study was not found in any WM region. The development of new network-driven hypotheses targeting brain connectivity and compensatory mechanisms in response to perinatal brain injury should be explored.

The study was limited by a small sample size because we could include only participants who could cooperate with MR imaging without sedation. ROI analyses at the level of the primary motor cortex could not be performed because this region was not included in predefined segmentations of the Johns Hopkins University WM atlas labels.

CONCLUSIONS

This study establishes SCALE as a clinical correlate of multiple DTI measures. SCALE was sensitive to WM impairment within the CST and CC and throughout the whole brain. This study supports FA and RD as strong indicators of WM motor injury. It confirmed that children with spastic bilateral CP have altered WM diffusion properties throughout the whole brain, including the CST. Responsiveness to intervention using DTI measures is an important area for future research in CP.

ACKNOWLEDGMENTS

We would like to thank the children and their families for participating in this study, in addition to Dr. Erica Hsu, Mr. Kylen Soriano, and Mr. Vinh Nguyen for their assistance with data processing and analysis.

Disclosures: Eileen G. Fowler—*RELATED*: *Grant*: UCLA Children's Discovery and Innovation Institute, *Comments*: This internal university grant provided funding for the MR images. Also, our institution received donations from individuals that supported salaries.* Joyce Matsumoto—*RELATED*: *Grant*: UCLA Children's Discovery and Innovation Institute, *Comments*: Grant awarded to fund research MR images.* *Money paid to the institution.

REFERENCES

1. Ceschin R, Lee VK, Schmithorst V, et al. **Regional vulnerability of longitudinal cortical association connectivity: associated with structural network topology alterations in preterm children with cerebral palsy.** *Neuroimage Clin* 2015;9:322–37 CrossRef Medline
2. Lee JD, Park HJ, Park ES, et al. **Motor pathway injury in patients with periventricular leucomalacia and spastic diplegia.** *Brain* 2011;134:1199–1210 CrossRef Medline
3. Volpe JJ. **Brain injury in premature infants: a complex amalgam of destructive and developmental disturbances.** *Lancet Neurol* 2009;8:110–24 CrossRef Medline
4. Fowler EG, Staudt LA, Greenberg MB, et al. **Selective Control Assessment of the Lower Extremity (SCALE): development, validation, and interrater reliability of a clinical tool for patients with cerebral palsy.** *Dev Med Child Neurol* 2009;51:607–14 CrossRef Medline
5. Fowler EG, Goldberg EJ. **The effect of lower extremity selective voluntary motor control on interjoint coordination during gait in children with spastic diplegic cerebral palsy.** *Gait Posture* 2009;29:102–07 CrossRef Medline
6. Noble JJ, Gough M, Shortland AP. **Selective motor control and gross motor function in bilateral spastic cerebral palsy.** *Dev Med Child Neurol* 2019;61:57–61 CrossRef Medline
7. MacWilliams BA, Prasad S, Shuckra AL, et al. **Causal factors affecting gross motor function in children diagnosed with cerebral palsy.** *MedRxiv* 2020 https://www.medrxiv.org/content/10.1101/2020.10.26.20217232v1. Accessed December 1, 2020
8. Goldberg EJ, Fowler EG, Oppenheim WL. **Case reports: the influence of selective voluntary motor control on gait after hamstring lengthening surgery.** *Clin Orthop Relat Res* 2012;470:1320–26 CrossRef Medline
9. Staudt LA, Peacock WJ. **Selective posterior rhizotomy for treatment of spastic cerebral palsy.** *Pediatric Physical Therapy* 1989;1:3–9 CrossRef
10. Arrigoni F, Peruzzo D, Gagliardi C, et al. **Whole-brain DTI assessment of white matter damage in children with bilateral cerebral palsy: evidence of involvement beyond the primary target of the anoxic insult.** *AJNR Am J Neuroradiol* 2016;37:1347–53 CrossRef Medline
11. Mailleux L, Franki I, Emsell L, et al. **The relationship between neuroimaging and motor outcome in children with cerebral palsy: a systematic review—Part B diffusion imaging and tractography.** *Res Dev Disabil* 2020;97:103569 CrossRef Medline
12. Assaf Y, Pasternak O. **Diffusion tensor imaging (DTI)-based white matter mapping in brain research: a review.** *J Mol Neurosci* 2008;34:51–61 CrossRef Medline
13. Basser PJ, Jones DK. **Diffusion-tensor MRI: theory, experimental design and data analysis - a technical review.** *NMR Biomed* 2002;15:456–68 CrossRef Medline
14. Winklewski PJ, Sabisz A, Naumczyk P, et al. **Understanding the physiopathology behind axial and radial diffusivity changes: what do we know?** *Front Neurol* 2018;9:92 CrossRef Medline
15. Englander ZA, Pizoli CE, Batrachenko A, et al. **Diffuse reduction of white matter connectivity in cerebral palsy with specific**

vulnerability of long-range fiber tracts. *Neuroimage Clin* 2013;2:440–47 CrossRef Medline
16. Palisano RJ, Rosenbaum P, Bartlett D, et al. **Content validity of the expanded and revised Gross Motor Function Classification System.** *Dev Med Child Neurol* 2008;50:744–50 CrossRef Medline
17. Russell DJ, Rosenbaum PL, Avery LM, et al. *Gross Motor Function Measure (GMFM-66 & GMFM-88) User's Manual*. Mac Keith Press; 2004
18. Smith SM, Jenkinson M, Johansen-Berg H, et al. **Tract-Based Spatial Statistics: voxelwise analysis of multi-subject diffusion data.** *Neuroimage* 2006;31:1487–1505 CrossRef Medline
19. Smith SM, Nichols TE. **Threshold-free cluster enhancement: Addressing problems of smoothing, threshold dependence and localisation in cluster inference.** *Neuroimage* 2009;44:83–98 CrossRef Medline
20. Mori S, Oishi K, Jiang H, et al. **Stereotaxic white matter atlas based on diffusion tensor imaging in an ICBM template.** *Neuroimage* 2008;40:570–82 CrossRef Medline
21. Shapiro SS, Wilk MB. **An analysis of variance test for normality (complete samples).** *Biometrika* 1965;52:591–611 CrossRef
22. Benjamini Y, Hochberg Y. **Controlling the false discovery rate: a practical and powerful approach to multiple testing.** *Journal of the Royal Statistical Society: Series B (Methodological)* 1995;57:289–300 CrossRef
23. Hoon AH Jr, Stashinko EE, Nagae LM, et al. **Sensory and motor deficits in children with cerebral palsy born preterm correlate with diffusion tensor imaging abnormalities in thalamocortical pathways.** *Dev Med Child Neurol* 2009;51:697–704 CrossRef Medline
24. Shortland A. **Editorial: strength, gait and function in cerebral palsy.** *Gait Posture* 2011;33:319–20 CrossRef Medline
25. Song SK, Sun SW, Ramsbottom MJ, et al. **Dysmyelination revealed through MRI as increased radial (but unchanged axial) diffusion of water.** *Neuroimage* 2002;17:1429–36 CrossRef Medline
26. Beaulé V, Tremblay S, Théoret H. **Interhemispheric control of unilateral movement.** *Neural Plast* 2012;2012:627816 CrossRef Medline
27. Nass R. **Mirror movement asymmetries in congenital hemiparesis: the inhibition hypothesis revisited.** *Neurology* 1985;35:1059–62 CrossRef Medline
28. Mayston MJ, Harrison LM, Stephens JA. **A neurophysiological study of mirror movements in adults and children.** *Ann Neurol* 1999;45:583–94 CrossRef Medline
29. Wahl M, Lauterbach-Soon B, Hattingen E, et al. **Human motor corpus callosum: topography, somatotopy, and link between microstructure and function.** *J Neurosci* 2007;27:12132–38 CrossRef Medline
30. Counsell SJ, Shen Y, Boardman JP, et al. **Axial and radial diffusivity in preterm infants who have diffuse white matter changes on magnetic resonance imaging at term-equivalent age.** *Pediatrics* 2006;117:376–86 CrossRef Medline
31. Wheeler-Kingshott CA, Cercignani M. **About "axial" and "radial" diffusivities.** *Magn Reson Med* 2009;61:1255–60 CrossRef Medline
32. Shang Q, Ma CY, Lv N, et al. **Clinical study of cerebral palsy in 408 children with periventricular leukomalacia.** *Exp Ther Med* 2015;9:1336–44 CrossRef
33. Jiang H, Li X, Jin C, et al. **Early diagnosis of spastic cerebral palsy in infants with periventricular white matter injury using diffusion tensor imaging.** *AJNR Am J Neuroradiol* 2019;40:162–68 CrossRef Medline
34. Jiang H, Liu H, Huang T, et al. **Structural network performance for early diagnosis of spastic cerebral palsy in periventricular white matter injury.** *Brain Imaging Behav* 2021;15:855–64 CrossRef Medline
35. Zhou J, Butler EE, Rose J. **Neurologic correlates of gait abnormalities in cerebral palsy: implications for treatment.** *Front Hum Neurosci* 2017;11:103 CrossRef Medline
36. Ruber T, Schlaug G, Lindenberg R. **Compensatory role of the cortico-rubro-spinal tract in motor recovery after stroke.** *Neurology* 2012;79:515–22 CrossRef Medline
37. Yeo SS, Jang SH. **Changes in red nucleus after pyramidal tract injury in patients with cerebral infarct.** *NeuroRehabilitation* 2010;27:373–77 CrossRef Medline

MR Imaging Differences in the Circle of Willis between Healthy Children and Adults

K.P. Guilliams, N. Gupta, S. Srinivasan, M.M. Binkley, C. Ying, L. Couture, J. Gross, A. Wallace, R.C. McKinstry, K. Vo, J.-M. Lee, H. An, and M.S. Goyal

ABSTRACT

BACKGROUND AND PURPOSE: Asymmetries in the circle of Willis have been associated with several conditions, including migraines and stroke, but they may also be age-dependent. This study examined the impact of age and age-dependent changes in cerebral perfusion on circle of Willis anatomy in healthy children and adults.

MATERIALS AND METHODS: We performed an observational, cross-sectional study of bright and black-blood imaging of the proximal cerebral vasculature using TOF-MRA and T2 sampling perfection with application-optimized contrasts by using different flip angle evolution (T2-SPACE) imaging at the level of the circle of Willis in 23 healthy children and 43 healthy adults (4–74 years of age). We compared arterial diameters measured manually and cerebral perfusion via pseudocontinuous arterial spin-labeling between children and adults.

RESULTS: We found that the summed cross-sectional area of the circle of Willis is larger in children than in adults, though the effect size was smaller with T2-SPACE-based measurements than with TOF-MRA. The circle of Willis is also more symmetric in children, and nonvisualized segments occur more frequently in adults than in children. Moreover, the size and symmetry of the circle of Willis correlate with cerebral perfusion.

CONCLUSIONS: Our results demonstrate that the circle of Willis is different in size and symmetry in healthy children compared with adults, likely associated with developmental changes in cerebral perfusion. Further work is needed to understand why asymmetric vasculature develops in some but not all adults.

ABBREVIATIONS: AcomA = anterior communicating artery; CoW = circle of Willis; CoW-area = overall CoW size; CoW-di = CoW deviation index; ICC = intraclass correlation coefficient; pCASL = pseudocontinuous arterial spin-labeling; PcomA = posterior communicating artery

First described by Thomas Willis in the 1600s,[1] the circle of Willis (CoW) is a vascular ring that functionally lies between the distal ICAs and basilar arteries, and the proximal anterior, middle, and posterior cerebral arteries (Fig 1). A complete CoW is often viewed as a mechanism to provide protective collateral flow. Asymmetries in the CoW may be associated with increased stroke risk, particularly in people with carotid stenosis[2-4] or aneurysms.[5] Recent studies have noted an increase in asymmetries with age,[6,7] but these studies have been limited to adults, with most adults reported older than 40 years of age.

In detailed postmortem studies since 1905, completely absent segments of the CoW are rare, on the order of ~3%–5%.[8-10] However, asymmetries of the CoW due to hypoplastic or "functionally absent" segments are much more common, with estimates of approximately 30%–60% in adults.[8,9,11-13] Hypoplastic segments are also common with older age in a heterogeneous clinical population of older adults.[6,7,14] However, despite >3 decades of MRA use, there are presently scant normative CoW imaging data in children. Studies of the CoW in children are limited

Received January 29, 2021; accepted after revision July 19.

From the Department of Neurology (K.P.G., M.M.B., J.-M.L., M.S.G.), Department of Pediatrics (K.P.G., R.C.M.), Mallinckrodt Institute of Radiology (K.P.G., N.G., S.S., C.Y., L.C., R.C.M., K.V., J.-M.L., H.A., M.S.G.), Departments of Biomedical Engineering (J.-M.L.), and Neuroscience (M.S.G.), Washington University School of Medicine, St. Louis, Missouri; Division of Neuroradiology (J.G.), Midwest Radiology, St. Paul, Minnesota; and Department of Neurointerventional Surgery (A.W.), Ascension Columbia St. Mary's Hospital, Milwaukee, Wisconsin.

K.P. Guilliams and N. Gupta contributed equally to this work.

This work is supported by the National Institutes of Health (R01AG057536, MSG; K23NS099472, KPG), the McDonnell Center for Systems Neuroscience (M.S.G), and unrestricted funds from the Mallinckrodt Institute of Radiology (M.S.G.).

Author Contributions: K.P.G.: data acquisition, analysis and interpretation, drafted manuscript; N.G., S.S., J.G., C.Y., L.C.: data acquisition and analysis, critical review of manuscript; M.M.B.: data analysis and interpretation and critical review of manuscript; A.W.: study design, data collection, and critical review of manuscript; R.C.M., K.V., J.-M.L., H.A.: data interpretation and critical review of manuscript; M.S.G.: study design, data collection, analysis and interpretation, drafted manuscript. All authors reviewed and approved the final version of this manuscript.

Please address correspondence to M.S. Goyal, MD, Washington University School of Medicine, 510 South Kingshighway Blvd, St. Louis, MO 63110; e-mail: goyalm@wustl.edu

Indicates open access to non-subscribers at www.ajnr.org

Indicates article with online supplemental data.

http://dx.doi.org/10.3174/ajnr.A7290

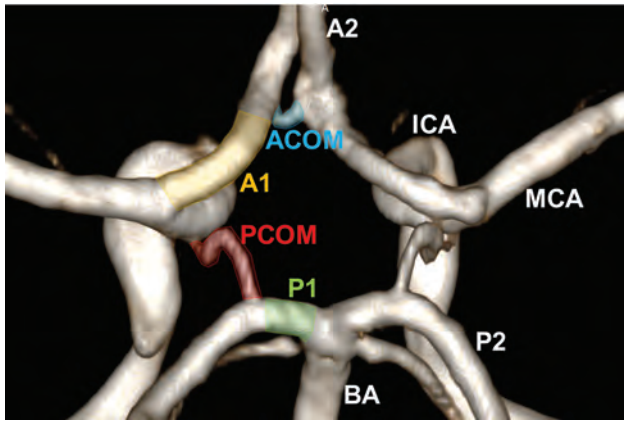

FIG 1. The circle of Willis. 3D volume-rendering of the CoW from a TOF-MRA in a young child. This shows the key segments comprising the vascular ring, including AcomA (blue), the first segment of the anterior cerebral artery (A1, orange), the PcomA (red), and the first segment of the posterior cerebral artery (P1, green). Other arteries feeding the CoW (the ICA and the basilar artery [BA]) and supplied by the CoW (second segment of the anterior cerebral artery [A2], MCA, and second segment of the posterior cerebral artery [P2]) are also labeled.

to a postmortem study[15] and to those with neuropathology, including brain tumors treated with radiation,[16] neurofibromatosis,[17] neonatal stroke,[18] and prematurity.[19] There remains a need for evaluation of the CoW in healthy children in comparison with adults.

The CoW is particularly unique with respect to the possible vascular effects of cerebral perfusion changes because it represents a redundancy in proximal cerebral circulation.[1] Cerebral perfusion and CBF peak in the first decade of life and then decrease substantially both globally and in a regionally specific manner.[20-24] Local CBF is, in part, regulated by arteriolar resistance, though capillaries and large cerebral arteries may also contribute to overall cerebral vascular resistance.[25-27] Moreover, high CBF implies either higher blood velocity, larger arterial cross-section area, or both throughout the cerebral vasculature.[28,29] Yet currently, the effects of CBF, particularly higher CBF in childhood, on the cerebral vasculature are unknown.

The objective of our study was to evaluate the size and topology of the CoW across the life span in healthy children compared with healthy adults using both TOF-MRA and confirmatory T2 sampling perfection with application-optimized contrasts by using different flip angle evolution (SPACE sequence; Siemens) techniques and to investigate possible CBF mechanisms of CoW changes. We hypothesized that the CoW would be larger and more symmetric/complete in healthy children than in adults, primarily in association with increased CBF during childhood.

MATERIALS AND METHODS

Subjects

This study was approved by the institutional review board of Washington University School of Medicine and performed according to provisions within the Declaration of Helsinki. Self-described healthy participants 4–79 years of age were recruited via flyers, word of mouth, and a volunteer data base maintained by our institution. Specific exclusion criteria included any known neurologic or vascular illness or contraindications to MR imaging. In accordance with Strengthening the Reporting of Observational Studies in Epidemiology guidelines for observational cross-sectional studies, we attempted to balance the number of subjects across 3 age groups (children: 4–18, younger adults: 19–40, and older adults: 41–80 years of age) by sex and for them to remain representative of the ethnic composition of the greater St. Louis area to minimize bias.

MR Imaging and Angiography

Recruited participants underwent up to 30 minutes of MR imaging on either a 3T Tim Trio (Siemens) scanner ($n = 58$), or on the same scanner following an upgrade to a 3T Magnetom PrismaFit (Siemens) scanner ($n = 8$), both with a 32-channel head coil. MR imaging protocol specifics are provided in the Online Supplemental Data. Our goal was to produce a protocol that had short-enough sequences to minimize motion artifacts, particularly in young children, yet that could be equally applied to all age groups in this cohort to avoid sequence-specific biases. Participants all underwent the following imaging: 1) isotropic 1-mm^3 sagittal T1-MPRAGE; 2) 3D TOF-MRA with a low flip angle (18°, to minimize intraluminal saturation effects) centered over the CoW with 0.57 × 0.57 × 0.69 cm resolution; 3) 3D T2-SPACE centered over the CoW with 0.53 × 0.53 × 0.50 cm resolution; and 4) a pseudocontinuous arterial spin-labeling (pCASL) sequence (TE/TR = 12/3780 ms, resolution = 3.0 × 3.0 × 5.0 mm, labeling duration = 2000 ms, postlabeling delay = 1500 ms, background suppression not performed). An additional fast inversion recovery sequence of the superior sagittal sinus was obtained to estimate individual blood T1 values for CBF calculations. A subset of participants ($n = 36$) also underwent a phase-contrast sequence of the ICAs and vertebral arteries at the level of the C2–C3 disk space to quantify whole-brain blood flow (TE/TR = 4.06/107.2 ms, resolution = 0.7 × 0.7 × 5.0 mm, flip angle = 25°, 10 averages, velocity encoding = 120 cm/s). Reader 1 (N.G.) reviewed all imaging for excessive noise, motion artifacts, or incomplete imaging.

Vessel Segment Nomenclature

Definition and nomenclature of the vessel segments comprising the CoW and major cerebral arteries follow current clinical convention (Fig 1). On the basis of prior modeling work,[30] we applied a slightly simplified definition of the CoW as comprising 7 segments: bilateral A1, P1, and PcomA segments, and a single anterior communicating artery (AcomA). The ICA termini and basilar apex are defined as inflow segments, and the M1, A2, and P2 segments, as outflow segments, and neither are included in the simplified CoW definition. The ICA segments are labeled from C1 proximally in the upper neck through C7 at the terminus, according to Bouthillier et al,[31] in 1996.

Vessel Diameter Measurement

Vessel measurements were performed on both TOF-MRA and T2-SPACE sequences independently. The source TOF-MRA and T2-SPACE images were analyzed using RadiAnt DICOM Viewer software (Version 4 or 5; Medixant). A board-certified neuroradiologist (M.S.G., with >3 years of postfellowship experience) trained and supervised reader 1 (N.G., an undergraduate student) to perform vessel-diameter measurements. Measurements were

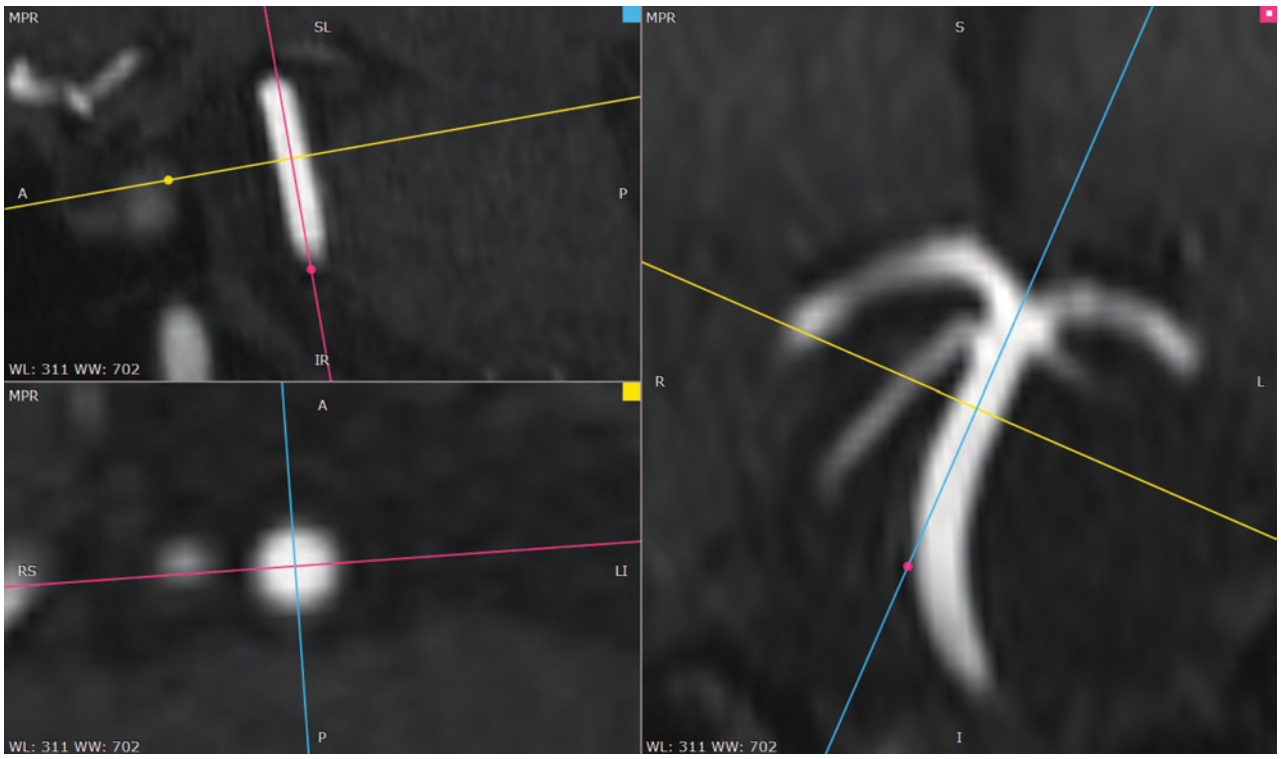

FIG 2. Double-oblique multiplanar reconstruction for vessel-diameter measurement. Two orthogonal planes of reconstruction were aligned along the long axis of each arterial segment to be measured. These were then used to construct a cross-sectional plane through the midportion of the vessel segment on which 2 perpendicular diameters were measured and averaged. Note that partial volume effects at the margins of the artery could result in a slight degree of measurement bias and error. WL indicates window level; WW, window width.

performed using the RadiAnt default window settings to avoid windowing bias. Measurements on all vessel segments from a subset of participants ($n = 15$) were repeated by both reader 1 and reader 2 (J.G., a neuroradiology fellow) to assess intra- and interrater reliability and to confirm the accuracy of measurements by reader 1.

The diameters of C7, distal basilar artery, M1, M2, A1, A2, P1, and P2 segments, AcomA, PcomA, and superior cerebellar arteries were measured on both the TOF-MRA and T2-SPACE images. On the TOF-MRA, the readers made additional measurements of the ICA segments C1–C5/C6, the proximal and mid-basilar artery, anterior inferior cerebellar artery, PICA, and vertebral arteries because the TOF-MRA sequence had a larger craniocaudal FOV. The procedure for measurement included multiplanar reconstruction with the double-oblique technique to identify the mid-cross-section orthogonal to the course of each vessel segment being measured (Fig 2). Care was taken to define the edge of a vessel consistently due to partial volume effects. Readers measured 2 perpendicular diameters at this cross-section using the ruler tool in RadiAnt and then averaged the 2 to produce a final diameter. Nonvisualized segments were assigned a value of zero.

Topologic Analysis of the CoW

We assessed the total summed cross-sectional area of the 7 measured segments of the CoW to determine its overall size (CoW-area). To quantify asymmetries and grade differences between hypoplastic and missing segments while also remaining indifferent to which segments caused asymmetries, we reduced the CoW topology a priori to a single variable defined as the CoW deviation index (CoW-di). We calculated CoW-di as follows: First, we normalized each segment diameter to the mean diameter from all 7 segments within the same CoW. Next, we created a cohort-average CoW, defined as the set of mean segment ratios derived from all participants, children and adults. Finally, a CoW-di for each individual was calculated as the total Euclidean distance between the 7 segment ratios of the individual CoW and the cohort-averaged CoW (Fig 3). A low CoW-di indicates that the relative sizes of the CoW segments are similar to those of the cohort-averaged CoW, whereas a high CoW-di indicates deviation from the group, either due to higher degree of anterior-posterior and/or left-right asymmetry, including that arising from nonvisualized segments (which were assigned a zero diameter).

Cerebral Perfusion Analysis

The pCASL data were first preprocessed using a uniform pipeline that included the following: 1) skull stripping with the FSL Brain Extraction Tool (Version 6.0; http://fsl.fmrib.ox.ac.uk/fsl/fslwiki/BET); 2) motion correction using MCFLIRT from FSL (https://fsl.fmrib.ox.ac.uk/fsl/fslwiki/MCFLIRT), and 3) spatial smoothing using in-house Matlab code (MathWorks). CBF was then calculated from pCASL using Equation 1.[32]

$$1) f = \frac{\lambda \Delta M R_{1a}}{2\alpha M_0 [\exp(-wR_{1a}) - \exp(-(\tau + w)R_{1a}]},$$

where f is CBF, λ (0.9 g/mL) is the blood/tissue water partition coefficient, R_{1a} (1/blood T1 value) is the longitudinal relaxation

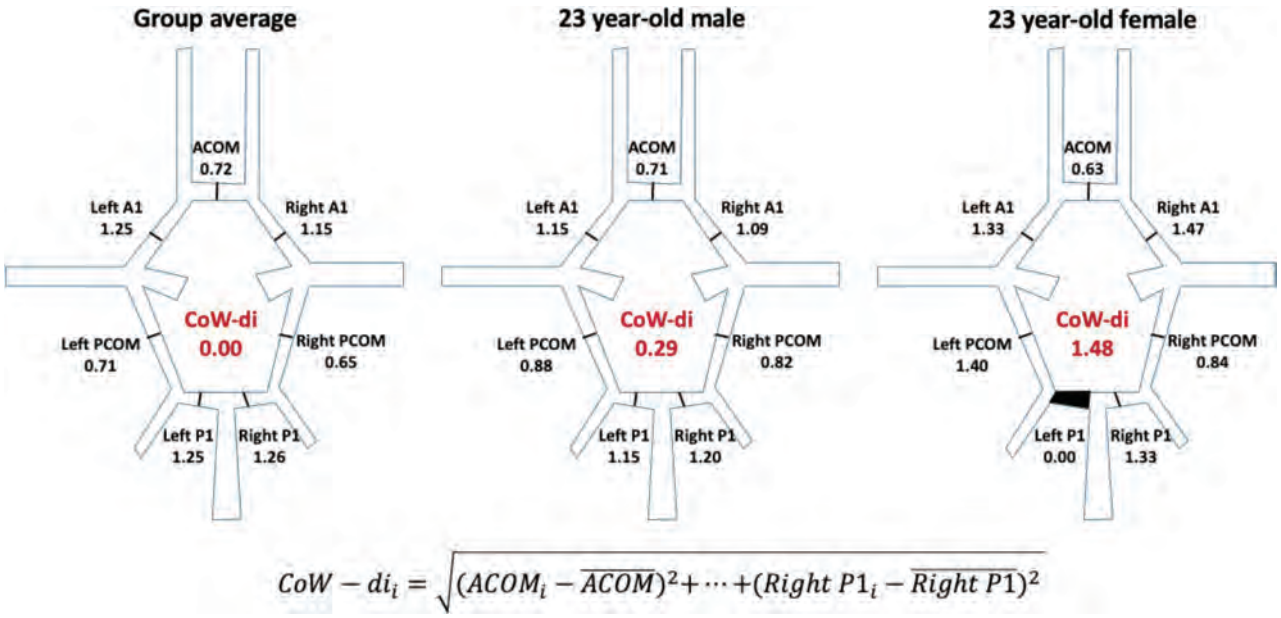

FIG 3. Measurement of the CoW-di. A group average of the ratio of each CoW segment to the mean CoW diameter was calculated. For each individual CoW, similar ratios were calculated for each of the 7 segments. The CoW-di was then calculated as the Euclidean distance between the individual CoW ratios and the group-average ratios, thus representing the degree to which an individual CoW deviated in size from the group average. Examples are shown for two 23-year-old individuals, one with a very low CoW-di (0.29) and another with a high CoW-di (1.48), largely due to a nonvisualized left P1 segment.

rate of blood, α is the tagging efficiency, M_0 is the equilibrium magnetization of brain, τ is the duration of the labeling pulse, and w is the postlabeling delay time. We assigned blood T1 values by age group after measuring them manually from the fast inversion recovery sequence in 56 individuals and averaging them by ages (4–11, 12–20, 21–40, 41–60, 61–80 years of age). The resulting CBF maps were then summarized to ROIs defined by the Desikan-Killiany and subcortical atlases following registration to individual MPRAGE sequences that were processed by FreeSurfer Version 5.3 (http://surfer.nmr.mgh.harvard.edu) as discussed further below.

Whole-Brain Blood Flow Quantitation

We obtained phase-contrast MR imaging sequences to measure blood velocities and cross-section areas of the distal cervical ICAs and vertebral arteries in a subset of individuals. These were measured using the Vitrea software (Version 6.9.2; Vital Images) semi-automated flow-quantification tool within the cardiac flow program. Flow within each vessel was summed to compute whole-brain blood flow.

Brain Structure Volumetric Analysis

Individual MPRAGE image volumes were analyzed with FreeSurfer, Version 5.3 (default options), to provide estimates of intracranial volume, whole-brain volume, gray and white matter volumes, ventricular volumes, and regional cortical and subcortical volumes. Cortical segmentation was performed according to the Desikan-Killiany atlas.

Statistical Analysis

Statistical analysis was performed using the statistical programming language R statistical and computing software, Version 3.5.2 and above (http://www.r-project.org/) and SAS software (Version 9.4; SAS Institute). Despite a priori hypotheses that the CoW would be larger and more symmetric in children, P values are provided for these comparisons first from the conservative 2-tailed t test for initial analysis with TOF-MRA measurements and then the 1-tailed t test for confirmatory analysis with the T2-SPACE measurements because the directionality of difference is already known. The Mann-Whitney U (Wilcoxon rank sum) test was also performed when there was significant skew in the distributions. Descriptive statistics, confidence intervals, and additional specific statistical tests are detailed in the Results section.

Data Availability

Individual numeric measurements and raw imaging data obtained in this study will be provided on reasonable request.

RESULTS

A total of 66 participants underwent MR imaging in this study, ranging from 4 to 74 years of age (children: 4–18 years, $n = 23$; younger adults: 19–40 years, $n = 23$; older adults: 41–74 years, $n = 20$), including a similar number of males and females (34 males, 32 females). Five participants were excluded due to qualitatively noisy or incomplete TOF data, leaving data from 61 participants (19 children, 42 adults) for further analysis. Of these 61 participants, 7 had qualitatively noisy or incomplete T2-SPACE data (4 children, 3 adults) that was not included in subsequent analysis.

Intra- and Interrater Reliability of Manual Vessel Diameter Measurements

Vessel diameter measurements (68 total measurements across both sequences) were repeated for a subset comprising 15 participants (~1000 total measurements) twice by reader 1 and once by

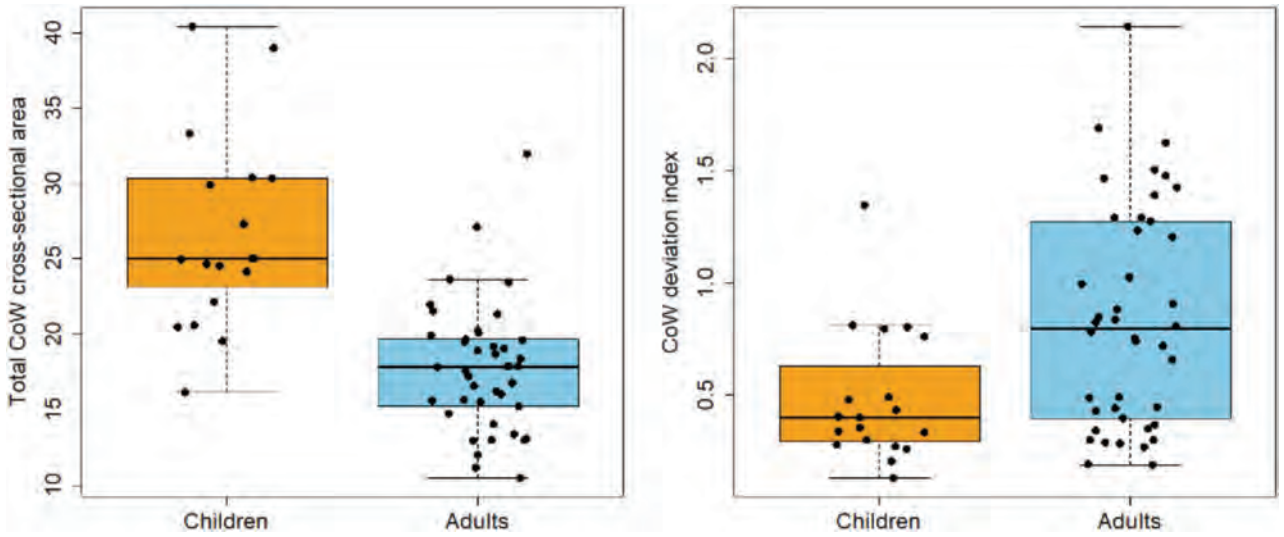

FIG 4. Differences in CoW size and symmetry in children versus adults. The total CoW cross-sectional area was measured in healthy children ($n = 19$) and adults ($n = 42$) on TOF-MRA images as described in the text. The mean total CoW cross-sectional area was larger in children than in adults (children's mean CoW-area = 27.7 mm^2 versus adults' mean CoW-area = 17.8 mm^2, $P < .0001$). Note that T2-SPACE measurements replicated these results, though with a smaller effect size as discussed in the text. CoW topology in children also more closely resembled the average topology found in the whole group, despite there being more adults in the whole group (children's mean CoW-di = 0.48 versus adults' mean CoW-di = 0.84, $P < .001$). As described in the text, the difference in CoW topology is, in part, due to a higher prevalence of nonvisualized CoW segments in adults.

reader 2. Across participants, the intrarater reliability was excellent (intraclass correlation coefficient [ICC] = 0.96, range = 0.89–0.98 across individual participants) with low bias and mean absolute deviation (mean bias = 0.02 mm, mean absolute deviation = 0.216 mm). Interrater reliability was also excellent (ICC = 0.86, range = 0.79–0.92), but there was more bias (mean bias = 0.49 mm); after correcting for this bias, the mean absolute deviation was low (mean absolute deviation = 0.31 mm), suggesting a systematic cause for the bias. After we reviewed the measurement procedure with each reader, this bias likely occurred due to differences in how each reader accounted for partial volume effects at the margins of the vessel lumen. When comparing the mean diameter measurements of C7, M1, and the distal basilar artery with those published recently for a large cohort of adults, the measurements of reader 1 (N.G.) are closer to previously published radii (published: C7 = 1.7 mm, M1 = 1.1 mm, distal basilar = 1.3 mm[33]; reader one: 1.7, 1.3, 1.6 mm; reader two: 2.0, 1.6, 1.7 mm, respectively). Reader 1 also completed measurements in all participants. Primary measurements by reader 1 are, accordingly, used for the remainder of the analysis.

TOF-MRA versus T2-SPACE Measurements

The intra- and interrater reliabilities across all participant data were similar when calculated independently for the TOF-MRA and T2-SPACE measurements (TOF-MRA: intrarater ICC = 0.91, interrater ICC = 0.89; T2-SPACE: intrarater ICC = 0.93, interrater ICC = 0.90). The mean difference between the TOF-MRA and T2-SPACE measurements was 0.147 mm (interquartile range = 0.126–0.168 mm) with limits of agreement ranging from −0.582 to 0.876 mm. Although the overall difference between TOF-MRA and T2-SPACE (TOF-MRA measurements were on average larger) was statistically significant (paired t test, $P < .001$), vessel diameter did not influence the difference between TOF-MRA and T2-SPACE because proportional bias was not significant (slope = 0.0003, $P = .984$). Further analysis of the circle of Willis did, however, reveal an age effect on the differences between TOF-MRA and T2-SPACE on the A1 and P1 segments bilaterally (Pearson $r = -0.33$ to -0.70, all $P < .05$), but not the PcomA and AcomA segments ($r = -0.25$ to -0.08, all $P > .05$), suggesting that age-related CBF differences may mediate differences between TOF-MRA and T2-SPACE.

CoW Size and Topology in Children versus Adults

The total cross-sectional area of the CoW based on TOF-MRA was, on average, 56% larger in children than in adults (CoW-area: children mean = 27.7 mm^2 [95% CI, 24.1–31.2] versus adults mean = 17.8 mm^2 [95% CI, 16.5–19.1]; t test, $P < .001$) (Fig 4*A* and Table). With the T2-SPACE data, the CoW was, on average, 17% larger in children (CoW-area: children mean = 16.6 mm^2 [14.5–18.7 mm^2] versus adults' mean = 14.2 mm^2 [13.0–15.5 mm^2]; t test, $P < .05$). CoW topology also differed between children and adults. Children had a lower CoW-di, reflecting greater symmetry, than adults with both the TOF-MRA measurements (CoW-di: children's mean = 0.48 [95% CI, 0.35–0.62] versus adults' mean = 0.84 [95% CI, 0.69–0.99]; Mann-Whitney U test, $P < .01$) (Fig 3*B*) and T2-SPACE data (CoW-di: children's mean = 0.68 [0.53–0.83] versus adults' mean = 0.93 [0.77–1.08]; $P < .05$, Mann-Whitney U test, $P < .05$). Among 133 potential CoW segments in 19 children, 5 were nonvisualized among 5 children (3.8% of vessel segments, 3 PcomAs and 2 AcomAs; 26% of the 19 children), whereas among 294 potential CoW segments in 42 adults, 31 were nonvisualized among 23 adults (10.5% of vessel segments, 2 A1s, 18 PcomAs, 4 P1s, and 7 AcomAs; 55% of the 42 adults). The odds of a nonvisualized

Summary CoW measurements in healthy children versus adults

	Children (0–18 years of age)	Adults (19–74 years of age)
No. of participants	23	43
Age (range) (yr)	9.5 (4–18)	40.7 (19–74)
Sex (female, male)	11, 12	21, 22
Excluded data	4 of 23	1 of 43
TOF-MRA CoW-area (mean) (mm^2)	27.7 (SD, 7.9)	17.8 (SD, 4.2)
TOF-MRA CoW-di (mean)	0.48 (SD, 0.30)	0.84 (SD, 0.49)
T2-SPACE CoW-area (mean) (mm^2)	16.6 (SD, 4.1)	14.2 (SD, 4.0)
T2-SPACE CoW-di (mean)	0.68 (SD, 0.29)	0.93 (SD, 0.49)
Nonvisualized segments	5/133 (3.8%)	31/294 (10.5%)
Whole-brain CBF (mean) (L/min)	1.10 (SD, 0.24)	0.69 (SD, 0.21)

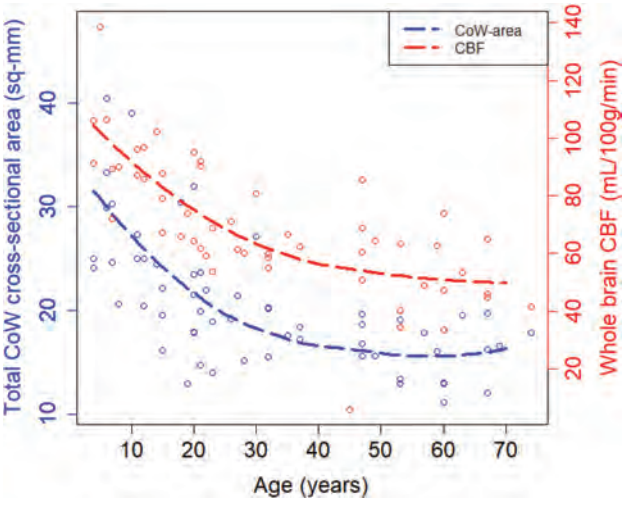

FIG 5. CoW size tracks with CBF changes during development. Total CoW cross-sectional area based on TOF-MRA and whole-brain CBF was measured in participants ranging from 4 to 74 years of age. There is a gradual decrease in whole-brain CBF from childhood to adulthood that parallels the decrease in total CoW cross-sectional area. Across participants, CoW size also correlated with whole-brain CBF (Pearson $r = 0.68$, $P < 10^{-7}$). *Smoothing lines* are for visualization purposes and are based on LOcally WEighted Scatter-plot Smoother fits with span = 1.

segment were thus lower in children compared with adults (Fisher exact test, OR = 0.36; 95% CI, 0.11–0.96; $P < .05$).

Relationship among CoW Segments

In an exploratory analysis of CoW segment-to-segment relationships across all ages, PcomA diameter showed a strong inverse relationship with the ipsilateral P1 diameter (Pearson $r = -0.67$ & -0.71, L & R), as expected. Most interesting, whereas there was a modest inverse correlation between the right A1 and AcomA segments ($r = -0.52$), there was minimal correlation between the left A1 and AcomA segment ($r = -0.05$). Further analysis of other CoW data sets is needed to determine whether this asymmetry in A1-AcomA size relationship is generalizable to other cohorts.

CoW Size and Topology in Relation to Cerebral Perfusion

Whole-brain blood flow estimated using pCASL correlated highly and with minimal bias compared with that measured using phase-contrast MR imaging ($n = 37$ paired comparisons, Pearson $r = 0.84$; 95% CI, 0.70–0.91; linear model slope = 0.96; 95% CI, 0.75–1.17), suggesting that the methods used here to quantify CBF with pCASL are reasonably accurate and unbiased. All subsequent results are thus with the pCASL data, which were available for more of the participants.

Whole-brain CBF decreased significantly with age ($n = 53$, Pearson $r = -0.71$; 95% CI, −0.54 to −0.82) and was, on average, 59% higher in children (children's mean whole-brain CBF = 1.10 L/min ($n = 16$) versus adults' mean = 0.69 L/min [$n = 38$]; t test, $P < .00001$). Based on the TOF-MRA data, the size and topology of the CoW correlate with whole-brain CBF (CoW-area ~ CBF: Pearson $r = 0.68$; 95% CI, 0.50–0.80; CoW-di ~ CBF: $r = -0.41$; 95% CI, −0.16 to −0.61). Across the age span, decreases in TOF-MRA-based measurements of the CoW-area tracked closely with decreases in CBF (Fig 5), and the proportional differences between children and adults are similar for CoW-area (56%) and whole-brain CBF (59%).

To further explore the relationship between CoW topology and CBF, we compared individual diameter asymmetry in PcomA and A1 size with asymmetry in the posterior cerebral artery and anterior cerebral artery territory CBF, respectively, the latter defined on the basis of anatomic ROIs typically within those arterial territories (posterior cerebral artery = cuneus, pericalcarine, lateral occipital regions; anterior cerebral artery = rostral and caudal anterior cingulate, medial orbitofrontal, and superior-frontal). PcomA vessel-size asymmetry correlated modestly with posterior cerebral artery territory CBF asymmetry (Pearson $r = 0.39$; 95% CI, 0.13–0.59). However, there was no correlation between A1 vessel size asymmetry and anterior cerebral artery territory CBF asymmetry (Pearson $r = 0.03$).

DISCUSSION

Since the anatomic and functional exposition of the CoW by Thomas Willis in the 1600s,[1] numerous studies of the CoW have been published in a variety of research domains. The CoW is often viewed in the context of providing protective collateral flow to the cerebral arteries in case of flow restriction within the internal carotid or basilar arteries. The importance of this protection is currently most evident in older patients with atherosclerotic carotid or vertebrobasilar occlusive disease. The CoW may also protect against direct compression of the carotid artery in the neck and thereby reduce the effects of choking or neck trauma—a role that might have been more evolutionarily pertinent.

Yet, the CoW may also have physiologic roles beyond providing protective collateral circulation.[34] The current study suggests that the CoW is both larger and more visibly complete in healthy children than in adults; this feature is associated with developmental differences in CBF. It is possible, then, that the CoW also provides a developmental function, namely in adjudicating flow between the anterior and posterior circulations during normal brain development and maturation. During early infant brain

development, metabolism is higher in the occipital lobes and thalami,[35] which are predominantly supplied by the posterior cerebral arteries and branches arising from the P1 and PcomA segments. As the brain matures, brain metabolism and blood flow increase in other parts of the brain—most prominently in the medial and prefrontal regions.[21,23,36] Thus, there is an overall developmental shift from the posterior-to-anterior circulation–predominant CBF. Although changes in carotid or basilar artery size could accommodate such changes, the CoW is well-positioned to assist in this transition. Indeed, prenatal cerebrovascular development is associated with additional anastomoses between the carotid and vertebrobasilar circulation that typically regress before birth.[37,38] The CoW might represent a later stage of cerebrovascular development, though with limited regression that occurs only in some adults.

Our finding that whole-brain CBF is associated with CoW size and topology is consistent with the relationship between flow and the product of cross-sectional area and blood velocity. The relationship between cerebral artery size and blood flow is further well-established in the context of arteriovenous malformation, in which the feeding arteries are typically much enlarged and then might normalize following obliteration of the arteriovenous malformation. Our study did not include blood-velocity measurements in the CoW. MR imaging–based velocity measurements in the A1 segment do identify mildly higher velocities in children compared with adults, though the difference in 1 study was small.[33] Such newer MR imaging–based flow-quantification methods as well as the transcranial Doppler method would help to fill in this gap and determine whether changes in CBF are also associated with changes in blood velocity within the CoW.[39,40]

Nonvisualized segments in the CoW were notably rare in children (3.8% of all vessel segments) and similar to that reported in postmortem series (~3%–5%). Nonvisualized segments were more common in adults (10.5%), likely due to the overall smaller size of the CoW and decreased CBF that occurs in normal aging. This finding suggests that studies of functionally absent or hypoplastic CoW segments in this context should include measures of both age and CBF as a potential mediator of their findings. Our proportion of adults with nonvisualized segments (55%) is comparable with other studies in adults, though it was less frequent than in a recently reported population-based study suggesting that up to 88% of adults have a nonvisualized segment;[7] however, this study exclusively examined adults 40–90 years of age, whereas half of our adult population was younger than 40 years of age, and we did not include any adults older than 80 years. Our study was also purposefully biased toward healthy individuals. Further work is needed to understand why the older population has decreased CBF and increased asymmetries and whether these might be a result of normal decreasing CBF and metabolic changes in the brain, pathologic changes in the brain such as cerebrovascular disease, or some combination of these factors.

An important strength of our study was the replication of key findings with both a bright-blood, flow-sensitive sequence (TOF-MRA) and a black-blood, anatomic sequence (T2-SPACE). Both sequences demonstrated the CoW to be larger and more symmetric in children than in adults. However, the effect size was considerably larger with TOF-MRA-based measurements than with T2-SPACE (eg, 56% versus 17% difference in CoW-area). Because differences between TOF-MRA- and T2-SPACE-based arterial diameters were, in part, related to the participant's age, we propose that some of this difference might arise from differences in cerebral blood flow exaggerating flow-related enhancement and thereby the apparent vessel diameters in children/adults on the TOF-MRA images. Our findings, thus, prescribe caution when using only TOF-MRA or T2-SPACE to determine vessel diameters, particularly if CBF is expected to vary; applying >1 sequence with different underlying assumptions and artifacts may allow convergent findings.

There are important limitations to the current study. First, whereas the diameter measurements showed excellent intrarater reliability, there was a small systematic interrater bias in these measurements that was likely due to resolution limitations. Future improvements in MR imaging technology and sequence development will likely result in higher resolution methods that provide higher precision and accuracy. Also, whereas these data provide initial measures of the CoW in healthy children in comparison with adults, use of these measures as a normative control for other studies should be avoided because data limitations include reader- and sequence-specific biases, the modest number of children in this study, and a cohort representative of only a single institution and its surrounding community.

CONCLUSIONS

We found that the CoW is larger and more symmetric in children, associated with developmental and aging changes in CBF. Our study suggests that further investigation is warranted into how and why asymmetries arise in the CoW during typical aging or in the context of disease.

Disclosures: Kristin P. Guilliams—*UNRELATED*: *Expert Testimony*: Grant, National Institutes of Health*, *Comments*: expert witness for neonatal stroke (2019, 2020). Adam Wallace–*UNRELATED*: *Expert Testimony*: Hallberg Law, PA, *Comments*: expert testimony provided for malpractice suit. Jin-Moo Lee—*RELATED*: *Grant*: National Institutes of Health*; *UNRELATED*: *Consultancy*: Regnera Medical, *Comments*: consulting on a stroke-recovery drug; *Grants/Grants Pending*: Biogen, *Comments*: funded a study on stroke genetics.* Hongyu An—*UNRELATED*: *Consultancy*: Pfizer; *Grants/Grants Pending*: Siemens. Manu Goyal—RELATED: *Grant*: McDonnell Center for Systems Neuroscience, National Institutes of Health/National Institute of Aging*; *UNRELATED*: *Grants/Grants Pending*: National Institutes of Health*; *Stock/Stock Options*: IBM; *Travel/Accommodations/Meeting Expenses Unrelated to Activities Listed*: Capital Medical University, Shandong Madic Technology, Tancheng Talent Office, *Comments*: honoraria and travel expenses for attending and speaking at the 2019 Linyi Brain PET Conference and Xuanwu Hospital. *Money paid to the institution.

REFERENCES

1. Willis T. ***Cerebri Anatome: Cui Accessit Nervorum Descriptio Et Usus.*** 1663 https://archive.org/details/cerebrianatomecu00will. Accessed April 8, 2020
2. Hoksbergen AW, Legemate DA, Csiba L, et al. **Absent collateral function of the circle of Willis as risk factor for ischemic stroke.** *Cerebrovasc Dis* 2003;16:191–98 CrossRef Medline
3. Kim KM, Kang HS, Lee WJ, et al. **Clinical significance of the circle of Willis in intracranial atherosclerotic stenosis.** *J Neurointerv Surg* 2016;8:251–55 CrossRef Medline
4. Banga PV, Varga A, Csobay-Novak C, et al. **Incomplete circle of Willis is associated with a higher incidence of neurologic events during carotid eversion endarterectomy without shunting.** *J Vasc Surg* 2018;68:1764–71 CrossRef Medline

5. Lazzaro MA, Ouyang B, Chen M. **The role of circle of Willis anomalies in cerebral aneurysm rupture.** *J Neurointerv Surg* 2012;4:22–26 CrossRef Medline
6. Eaton RG, Shah VS, Dornbos D, 3rd, et al. **Demographic age-related variation in circle of Willis completeness assessed by digital subtraction angiography.** *Brain Circ* 2020;6:31–37 CrossRef Medline
7. Hindenes LB, Haberg AK, Johnsen LH, et al. **Variations in the circle of Willis in a large population sample using 3D TOF angiography: the Tromso Study.** *PLoS One* 2020;15:e0241373 CrossRef Medline
8. Kapoor K, Singh B, Dewan LI. **Variations in the configuration of the circle of Willis.** *Anat Sci Int* 008;83:96–106 CrossRef Medline
9. Alpers BJ, Berry RG, Paddison RM. **Anatomical studies of the circle of Willis in normal brain.** *AMA Arch Neurol Psychiatry* 1959;81:409–18 CrossRef Medline
10. Fawcett E, Blachford JV. **The circle of Willis: an examination of 700 specimens.** *J Anat Physiol* 1905;40:63(Pt 1):2–70 Medline
11. Krabbe-Hartkamp MJ, van der Grond J, de Leeuw FE, et al. **Circle of Willis: morphologic variation on three-dimensional time-of-flight MR angiograms.** *Radiology* 1998;207:103–11 CrossRef Medline
12. Hendrikse J, van Raamt AF, van der Graaf Y, et al. **Distribution of cerebral blood flow in the circle of Willis.** *Radiology* 2005;235:184–89 CrossRef Medline
13. Klimek-Piotrowska W, Rybicka M, Wojnarska A, et al. **A multitude of variations in the configuration of the circle of Willis: an autopsy study.** *Anat Sci Int* 2016;91:325–33 CrossRef Medline
14. Zaninovich OA, Ramey WL, Walter CM, et al. **Completion of the circle of Willis varies by gender, age, and indication for computed tomography angiography.** *World Neurosurg* 2017;106:953–63 CrossRef Medline
15. Piechna A, Lombarski L, Krajewski P, et al. **Age dependence of critical pressure in the segments and branches of the circle of Willis.** *Neurol Neurochir Pol* 2017;51:146–48 CrossRef Medline
16. El-Fayech C, Haddy N, Allodji RS, et al. **Cerebrovascular diseases in childhood cancer survivors: role of the radiation dose to Willis circle arteries.** *Int J Radiat Oncol Biol Phys* 2017;97:278–86 CrossRef Medline
17. Bekiesińska-Figatowska M, Braôgoszewska H, Duczkowski M, et al. **Circle of Willis abnormalities in children with neurofibromatosis type 1.** *Neurol Neurochir Pol* 2014;48:15–20 CrossRef Medline
18. Husson B, Hertz-Pannier L, Adamsbaum C, et al. **MR angiography findings in infants with neonatal arterial ischemic stroke in the middle cerebral artery territory: a prospective study using circle of Willis MR angiography.** *Eur J Radiol* 2016;85:1329–35 CrossRef Medline
19. Malamateniou C, Adams ME, Srinivasan L, et al. **The anatomic variations of the circle of Willis in preterm-at-term and term-born infants: an MR angiography study at 3T.** *AJNR Am J Neuroradiol* 2009;30:1955–62 CrossRef Medline
20. Kennedy C, Sokoloff L. **An adaptation of the nitrous oxide method to the study of the cerebral circulation in children; normal values for cerebral blood flow and cerebral metabolic rate in childhood.** *J Clin Invest* 1957;36:1130–07 CrossRef Medline
21. Chiron C, Raynaud C, Maziere B, et al. **Changes in regional cerebral blood flow during brain maturation in children and adolescents.** *J Nucl Med* 1992;33:696–703 Medline
22. Avants BB, Duda JT, Kilroy E, et al. **The pediatric template of brain perfusion.** *Sci Data* 2015;2:150003 CrossRef Medline
23. Satterthwaite TD, Shinohara RT, Wolf DH, et al. **Impact of puberty on the evolution of cerebral perfusion during adolescence.** *Proc Natl Acad Sci U S A* 2014;111:8643–48 CrossRef Medline
24. Goyal MS, Hawrylycz M, Miller JA, et al. **Aerobic glycolysis in the human brain is associated with development and neotenous gene expression.** *Cell Metab* 2014;19:49–57 CrossRef Medline
25. Faraci FM, Heistad DD. **Regulation of large cerebral arteries and cerebral microvascular pressure.** *Circ Res* 1990;66:8–17 CrossRef Medline
26. Heistad DD, Marcus ML, Abboud FM. **Role of large arteries in regulation of cerebral blood flow in dogs.** *J Clin Invest* 1978;62:761–68 CrossRef Medline
27. Willie CK, Tzeng YC, Fisher JA, et al. **Integrative regulation of human brain blood flow.** *J Physiol* 2014;592:841–59 CrossRef Medline
28. Sacks AH, Tickner EG. **The compressibility of blood.** *Biorheology* 1968;5:271–74 CrossRef Medline
29. Wang SH, Lee LP, Lee JS. **A linear relation between the compressibility and density of blood.** *J Acoust Soc Am* 2001;109:390–96 CrossRef Medline
30. Devault K, Gremaud PA, Novak V, et al. **Blood flow in the circle of Willis: modeling and calibration.** *Multiscale Model Simul* 2008;7:888–909 CrossRef Medline
31. Bouthillier A, van Loveren HR, Keller JT. **Segments of the internal carotid artery: a new classification.** *Neurosurgery* 1996;38:425–32; discussion 432–33 CrossRef Medline
32. Wang J, Zhang Y, Wolf RL, et al. **Amplitude-modulated continuous arterial spin-labeling 3.0-T perfusion MR imaging with a single coil: feasibility study.** *Radiology* 2005;235:218–28 CrossRef Medline
33. Mouches P, Forkert ND. **A statistical atlas of cerebral arteries generated using multi-center MRA datasets from healthy subjects.** *Sci Data* 2019;6:29 A CrossRef Medline
34. Vrselja Z, Brkic H, Mrdenovic S, et al. **Function of circle of Willis.** *J Cereb Blood Flow Metab* 2014;34:578–84 CrossRef Medline
35. Goyal MS, Raichle ME. **Glucose requirements of the developing human brain.** *J Pediatr Gastroenterol Nutr* 2018;66(Suppl 3):S46–49 CrossRef Medline
36. Chugani HT, Phelps ME, Mazziotta JC. **Positron emission tomography study of human brain functional development.** *Ann Neurol* 1987;22:487–97 CrossRef Medline
37. Menshawi K, Mohr JP, Gutierrez J. **A functional perspective on the embryology and anatomy of the cerebral blood supply.** *J Stroke* 2015;17:144–58 CrossRef Medline
38. Raybaud C. **Normal and abnormal embryology and development of the intracranial vascular system.** *Neurosurg Clin N Am* 2010;21:399–426 CrossRef Medline
39. Wu C, Honarmand AR, Schnell S, et al. **Age-related changes of normal cerebral and cardiac blood flow in children and adults aged 7 months to 61 years.** *J Am Heart Assoc.* 2016;5:e002657 CrossRef Medline
40. Garcia J, Barker AJ, Murphy I, et al. **Four-dimensional flow magnetic resonance imaging-based characterization of aortic morphometry and haemodynamics: impact of age, aortic diameter, and valve morphology.** *Eur Heart J Cardiovasc Imaging* 2016;17:877–84. Aug CrossRef Medline

Heterotopia in Individuals with 22q11.2 Deletion Syndrome

E. Neuhaus, E. Hattingen, S. Breuer, E. Steidl, N. Polomac, F. Rosenow, T. Rüber, E. Herrmann, C. Ecker, L. Kushan, A. Lin, A. Vajdi, C.E. Bearden, and A. Jurcoane

ABSTRACT

BACKGROUND AND PURPOSE: MR imaging studies and neuropathologic findings in individuals with 22q11.2 deletion syndrome show anomalous early brain development. We aimed to retrospectively evaluate cerebral abnormalities, focusing on gray matter heterotopia, and to correlate these with subjects' neuropsychiatric impairments.

MATERIALS AND METHODS: Three raters assessed gray matter heterotopia and other morphologic brain abnormalities on 3D T1WI and T2*WI in 75 individuals with 22q11.2 deletion syndrome (27 females, 15.5 [SD, 7.4] years of age) and 53 controls (24 females, 12.6 [SD, 4.7] years of age). We examined the association among the groups' most frequent morphologic findings, general cognitive performance, and comorbid neuropsychiatric conditions.

RESULTS: Heterotopia in the white matter were the most frequent finding in individuals with 22q11.2 deletion syndrome ($n = 29$; controls, $n = 0$; between-group difference, $P < .001$), followed by cavum septi pellucidi and/or vergae ($n = 20$; controls, $n = 0$; $P < .001$), periventricular cysts ($n = 10$; controls, $n = 0$; $P = .007$), periventricular nodular heterotopia ($n = 10$; controls, $n = 0$; $P = .007$), and polymicrogyria ($n = 3$; controls, $n = 0$; $P = .3$). However, individuals with these morphologic brain abnormalities did not differ significantly from those without them in terms of general cognitive functioning and psychiatric comorbidities.

CONCLUSIONS: Taken together, our findings, periventricular nodular heterotopia or heterotopia in the white matter (possibly related to interrupted Arc cells migration), persistent cavum septi pellucidi and/or vergae, and formation of periventricular cysts, give clues to the brain development disorder induced by the 22q11.2 deletion syndrome. There was no evidence that these morphologic findings were associated with differences in psychiatric or cognitive presentation of the 22q11.2 deletion syndrome.

ABBREVIATIONS: ADHD = attention deficit/hyperactivity disorder; ASD = autism spectrum disorder; CSP = cavum septi pellucidi; CV = cavum vergae; 22q11.2DS = 22q11.2 deletion syndrome; IQ = intelligence quotient; PNH = periventricular nodular heterotopia

The 22q11.2 deletion syndrome (22q11.2DS, also known as velocardiofacial or DiGeorge syndrome) is the most common microdeletion syndrome, which occurs in ~1 in 3000–6000 live births.[1] Phenotypically, individuals with 22q11.2DS may show a variety of symptoms, including congenital heart defects, velopharyngeal insufficiency, and immunodeficiency.[1] 22q11.2DS is also associated with an elevated risk of psychiatric disorders such as attention deficit/hyperactivity disorder (ADHD), anxiety disorders, autism spectrum disorder (ASD), schizophrenia during adulthood,[2] and epilepsy,[3,4] as well as intellectual disability.[5] To date, structural neuroimaging studies have focused mainly on group differences between individuals with 22q11.2DS and controls in terms of brain volume[6,7] and white matter structural changes.[8] Subjects with 22q11.2DS show widespread volume reductions in multiple gray and white matter regions, particularly in the midline[6,7] and major

Received April 9, 2021; accepted after revision July 19.

From the Institute of Neuroradiology (E.N., E. Hattingen, S.B., E.S., N.P., A.J.), Department of Neurology and Epilepsy Center Frankfurt Rhine-Main (E.N., F.R., T.R.), LOEWE Center for Personalized Translational Epilepsy Research (E.N., F.R., T.R.), Institute of Biostatistics and Mathematical Modelling (E. Herrmann), and Department of Child and Adolescent Psychiatry, Psychosomatics and Psychotherapy (C.E.), Goethe University Frankfurt, Frankfurt am Main, Germany; Department of Epileptology (T.R.), University Hospital Bonn, Bonn, Germany; Department of Forensic and Neurodevelopmental Sciences, Institute of Psychiatry, Psychology and Neuroscience (C.E.), King's College, London, UK; Department of Psychiatry and Biobehavioral Sciences (L.K., A.L., A.V., C.E.B.), Semel Institute for Neuroscience and Human Behavior, and Department of Psychology (C.E.B.), University of California, Los Angeles, Los Angeles, California.

This work was supported by the National Institute of Mental Health R01 MH085953, 1R21MH116473-01A1, and 1U01MH119736-01 (to C.E.B.).

Paper previously presented, in part, as an e-poster at: Annual Conference of the German Society for Neuroradiology–neuroRAD, October 8–9, 2020; Virtual.

Please address correspondence to Elisabeth Neuhaus, MD, Institute of Neuroradiology, University Hospital Frankfurt, Schleusenweg 2-16, 60528 Frankfurt am Main, Germany; e-mail: elisabeth.neuhaus@kgu.de

Indicates open access to non-subscribers at www.ajnr.org

Indicates article with online supplemental data.

http://dx.doi.org/10.3174/ajnr.A7283

Table 1: Summary of psychiatric and cognitive assessment by group

Characteristic	Controls ($n = 53$)	22q11.2DS ($n = 75$)	*P* Value
Mean verbal IQ *T*-score (SD)	59 (13)	36 (9)	<.001[a]
Mean nonverbal IQ *T*-score (SD)	54 (11)	35 (11)	<.001[a]
Mean full-scale IQ (SD)	112 (20)	78 (12)	<.001[a]
ASD (No.) (%)	0 (0%)	14 (19%)	<.001[b]
ADHD (No.) (%)	3 (5.7%)	38 (51%)	<.001[b]
Psychotic disorder (No.) (%)	0 (0%)	4 (5.3%)	.14[b]
Anxiety disorders (No.) (%)	8 (15%)	37 (49%)	<.001[b]

[a]Wilcoxon rank sum test.
[b]Fisher exact test.

corticocortical white matter connections.[8] Neuropathologic reports[9,10] found evidence that the deletion may disrupt neurodevelopment, leading to altered migration of neurons in early developmental stages, which, in turn, results in impaired connectivity or organization of the fiber tracts. Morphologic MR imaging analyses of the brain supported this hypothesis, reporting, among other findings, polymicrogyria[11] and enlarged Sylvian fissures,[12] both indicating a migration disorder during brain development.

Another common malformation of cortical development is periventricular nodular heterotopia (PNH). It is formed by ectopic aggregates of neurons, caused by interruption of neuronal migration from the ventricles to their correct location in the cortex.[13] To our knowledge, only 2 studies found evidence of PNH in 22q11.2DS. One had a small sample size,[10] and the other had a clinical focus.[4] This gap in knowledge prompted us to evaluate and report MR imaging morphologic abnormalities of the brain focused on detection of PNH in a large cohort of 75 individuals with molecularly confirmed 22q11.2DS and in 53 controls. In addition, we investigated the impact of the most frequent neuroradiologic abnormalities found in this study on general cognitive performance and neuropsychiatric conditions.

MATERIALS AND METHODS

Subjects

This is a retrospective analysis of a data set from an originally prospectively acquired DTI and volumetric study at the University of California, Los Angeles. The local ethics committee approved the study, and written informed consent or assent for minors was obtained for all participants. The sample consisted of 80 subjects with molecularly confirmed 22q11.2DS and 57 controls.

Exclusion criteria were neurologic or medical conditions (unrelated to 22q11.2DS) that might affect the brain structure, a history of head injury, insufficient fluency in English, and/or substance or alcohol abuse or dependence within the past 6 months. Controls additionally were excluded if they had intellectual disability or met the criteria for any major mental disorder except ADHD or a past episode of depression.[14]

Nine subjects were excluded from analysis due to motion artifacts. Thus, analyzable data consisted of 75 subjects with 22q11.2DS (37 females, 38 males; mean age, 15.5 [SD, 7.4] years) and 53 controls (24 females, 29 males; mean age, 12.6 [SD, 4.7] years) with a *P* value of .7 for sex and .05 for age.

Psychiatric, Cognitive, and Neurologic Assessment

At the time of MR imaging, all subjects underwent psychiatric and cognitive testing (Structured Clinical Interview for the Diagnostic and Statistical Manual of Mental Disorders and/or Computerized Diagnostic Interview for Children). General intellectual functioning was assessed using the Wechsler Abbreviated Scale of Intelligence or Wechsler Adult Intelligence Scale, 4th ed. The diagnosis of ASD was based on the Autism Diagnostic Observation Schedule[15] and the Autism Diagnostic Interview-Revised.[16] A complete description of the battery is published elsewhere.[14] These assessments are detailed in Table 1. As expected based on prior literature,[2,5] individuals with 22q11.2DS had significantly lower intelligence quotients (IQs) and higher rates of diagnoses of developmental neuropsychiatric disorders. Seizure history was determined by parent interviews. One individual with 22q11.2DS had an epilepsy history and was taking an anticonvulsant medication; 2 individuals had a history of absence seizures in early childhood but no confirmed epilepsy diagnosis. All others had no seizure history. Due to the mere anamnestic survey and the small number of individuals with epilepsy, we have not performed any analyses regarding epilepsy.

Image Acquisition and Analyses

MRIs were acquired on 2 identical 3T MR imaging systems (Trio; Siemens) using a 12-channel head coil. A whole-brain sagittal 3D MPRAGE sequence was acquired with the following parameters: TR/TE/TI = 2300/2.9/900 ms, flip angle = 9°, matrix size = 240 × 256, in-plane resolution = 1 × 1 mm, 160 slices, thickness = 1.2 mm. A T2* sequence was acquired with the following parameters: TR/TE = 5000/33 ms, matrix size = 128 × 128, in-plane resolution = 1.64 × 1.64 mm, 35 slices, thickness = 3 mm.

Three experienced board-certified neuroradiologists (S.B., E. Hattingen, and E.S.) independently evaluated the MR images, blinded to the presence of 22q11.2DS and without having any background information on 22q11.2DS. The first and second raters identified obvious gray matter heterotopia-like lesions (cortex-isointense, round, or ovoid) on T1WI. During their analyses, they also noticed additional morphologic findings: cavum septi pellucidi (CSP) and/or vergae (CV), periventricular cysts, and polymicrogyria. Then, they confirmed heterotopia and cysts by consensus on T2*WI: heterotopia as isointense to cortex and cysts as isointense to CSF. T2*WI was not available for 2 subjects. The third rater independently analyzed the data with respect to the additional morphologic findings, and the final evaluation was performed by consensus by the 3 raters.

The association between the most common morphologic findings in this study and general cognitive performance or comorbid neuropsychiatric conditions was investigated.

Statistical Methods

All analyses were performed in the R statistical environment (Version 3.6; http://www.r-project.org/).[17] Differences in demographics, psychiatric and cognitive assessment, and frequency of

Table 2: Frequency of morphologic anomalies in the 2 groups

Characteristic	Controls ($n = 53$)	22q11.2DS ($n = 75$)	P Value[a] (FDR-Adjusted)
Any morphologic finding	0 (0%)	48 (64%)	<.001
Heterotopia			
Any localization	0 (0%)	34 (45%)	<.001
PNH	0 (0%)	10 (13%)	.007
Heterotopia in the WM	0 (0%)	29 (39%)	<.001
CSP and/or CV	0 (0%)	20 (27%)	<.001
Isolated CSP	0 (0%)	1 (1.3%)	>.9
CSP/CV	0 (0%)	19 (25%)	<.001
Cysts	0 (0%)	10 (13%)	.007
Polymicrogyria	0 (0%)	3 (4.0%)	.30

Note:—FDR indicates false discovery rate.
[a] Fisher exact test.

morphologic anomalies between controls and individuals with 22q11.2DS were tested using the Wilcoxon rank sum test or Fisher exact test. To assess whether certain morphologic findings are more likely to occur together in individuals with 22q11.2DS, we performed the Fisher exact test pair-wise. The conditional maximum likelihood estimate was used to estimate the odds ratios. Cognitive test results of individuals with 22q11.2DS with and without morphologic findings were compared using the 2-sample *t* test or Wilcoxon rank sum test. The Shapiro-Wilk test was used for normality testing; and the Fisher *F*-test, for the equality of variances. A multivariate logistic regression was performed to test the associations between morphologic findings and the prevalence of psychiatric disorders in individuals with 22q11.2DS.

RESULTS

Morphologic Findings

Of the 75 individuals with 22q11.2 DS, 48 (64%) had morphologic findings versus none of the 53 controls (0%; $P < .001$) (Table 2).

Specifically, in this sample, we found the following morphologic abnormalities: heterotopia (periventricular or in the white matter), periventricular cysts, polymicrogyria, and CSP and/or CV (Fig 1 and Table 2).

The heterotopia-like lesions identified on T1WI were also isointense to the cortex on the T2*WI in all individuals with 22q11.2DS and were thus confirmed as heterotopia. The periventricular cyst-like lesions identified on T1WI were isointense to the CSF in all except 1 T2*WI (Online Supplemental Data). In 1 subject, a cystlike lesion proved to be a PNH by additional review of the T2*WI. T2*WI was not available for 1 individual with PNH and 1 with a cyst. Heterotopia and cysts occurred mostly in the frontal regions (10/10 PNH, 28/29 heterotopia in the white matter, 9/10 cysts). In 7/29 individuals with 22q11.2DS, the distribution of heterotopia in the white matter exceeded that in the frontal region. heterotopia-like lesions in the white matter were also found in 4 controls on the T1WI. However, these proved to be isointense to the CSF on T2*WI, so they are most likely enlarged perivascular spaces and not heterotopia (Online Supplemental Data).

Heterotopia and cysts frequently appeared together (Online Supplemental Data; not significant after false discovery rate adjustment). Other findings appeared independently. PNH were in all except 2 individuals, multiple ($n = 2$–13) and bilateral. The cysts were bilateral in 7 individuals, and 6 individuals had multiple cysts ($n = 2$–12). A single cyst or heterotopion was adjacent to the anterior body of the lateral ventricle. When multiple, they appeared arranged in arching, chainlike structures in the sagittal view (Fig 1). In 19/20 individuals with 22q11.2DS, the CSP occurred in combination with CV; in 1 individual, CSP occurred alone. Polymicrogyria was unilateral, right-sided, and located in the peri-Sylvian area in all 3 individuals (Fig 1).

Association with Cognition, Psychiatric Disorders, and Neurology

There were no significant associations between morphologic findings and general cognitive performance for heterotopia (Fig 2), other single findings, or all findings summed together (Online Supplemental Data).

Multivariate logistic regression (Online Supplemental Data) showed no significant association between heterotopia and psychiatric diagnoses (Fig 3) or between other morphologic findings and psychiatric diagnoses.

The subject with confirmed epilepsy had no morphologic abnormalities.

DISCUSSION

We retrospectively examined morphologic abnormalities in a large, originally prospectively assessed cohort of 75 subjects with 22q11.2DS and 53 typically developing controls. We found a significantly higher rate of anomalous morphologic findings in those with 22q11.2DS (64%) than in controls (0%).

We found a significantly elevated rate of PNH in subjects with 22q11.2DS, with a prevalence of 13% versus 0% in controls. A few studies have so far estimated the prevalence of PNH in 22q11.2DS: A study in a sample of 195 subjects (referred for a clinical MR imaging scan) found a 4.1% prevalence,[4] and a study with a sample of 29 subjects (recruited from an epilepsy genetics clinic) found a 17.2% prevalence.[10] Given the originally prospective assessment of our cohort, our prevalence estimate is not biased by clinical referral. In our cohort, all PNH are uncommonly located on top of the dorsal pole of the frontal horn of the lateral ventricles, which is a pattern also reported by Rezazadeh et al.[10] In contrast, "classic" PNH found in other conditions are bilateral, multiple, nearly contiguous, and aligned along the outline of the lateral ventricle walls.[13] Additionally, we identified heterotopia in the white matter with a prevalence of 39%. Heterotopic neurons or nodules in the frontal white matter were described in some neuropathologic case reports of individuals with 22q11.2DS but were, in these cases, only microscopically visible.[9,10]

A DTI study found impaired connectivity, which the authors attributed, among other causes, to ectopic neurons in the white matter.[8] In a study investigating epileptic seizures in individuals with 22q11.2DS, 1 subject with unilateral frontal white matter heterotopion was mentioned,[18] suggesting that the heterotopia visible on MR imaging may be only the tip of the iceberg. The literature describes an accumulation of nonspecific white matter lesions[19,20] in individuals with 22q11.2DS with the same localization and shape as the heterotopia we found in the white matter.

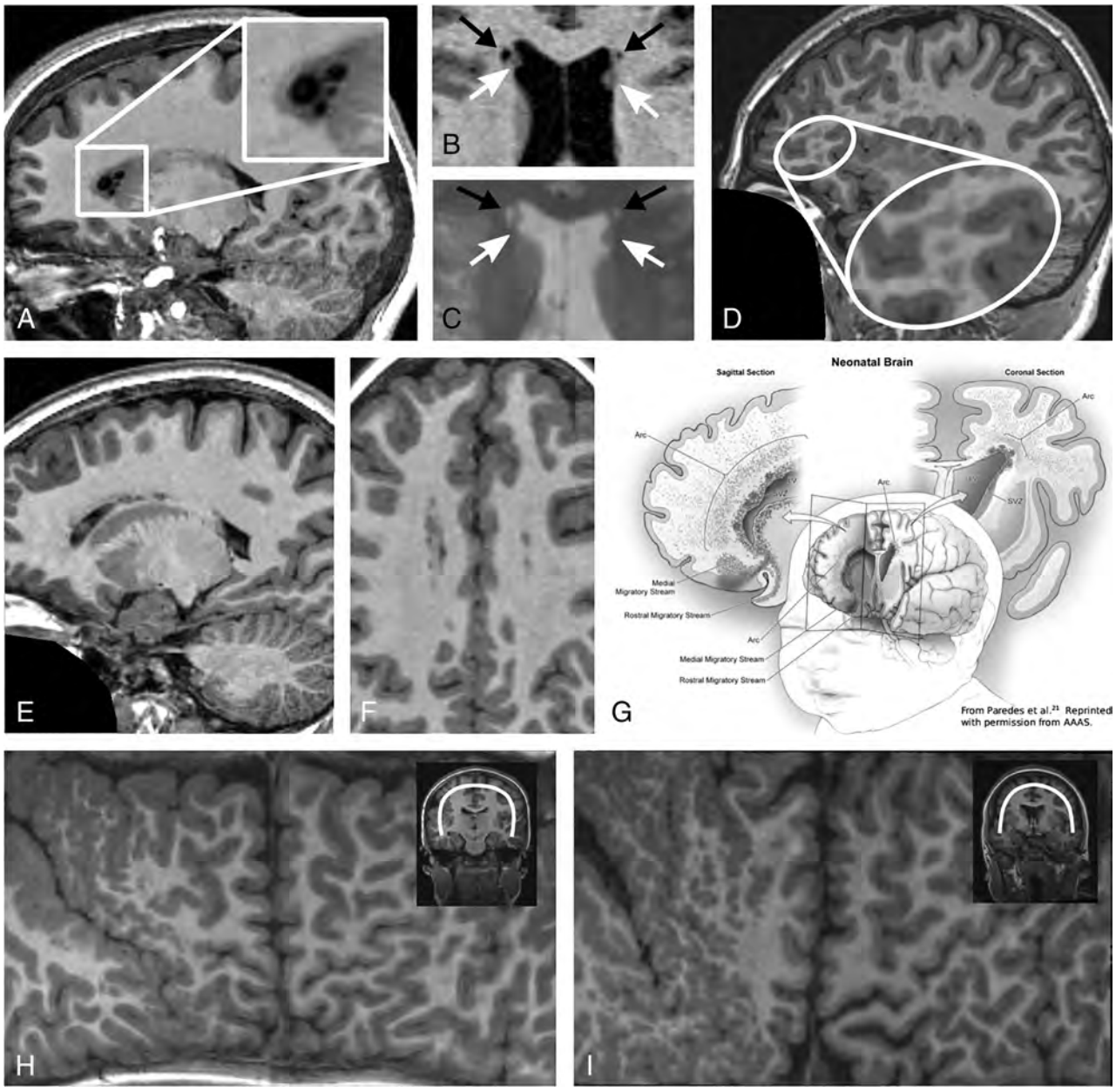

FIG 1. Representative examples of morphometric findings in brain MRIs of 6 subjects with 22q11.2DS. Subject 1: Small cysts adjacent to the anterior horns of the lateral ventricles (*A*). Subject 2: T1WI (*B*) and T2*WI (*C*) of bilateral cysts (*black arrows*, isointense to CSF in both sequences) and periventricular heterotopia (*white arrows*, cortex-isointense in both sequences). Subject 3: Multiple, perivascular, and frontal heterotopia in the white matter (*D*). Subject 4: Multiple periventricular heterotopia forming an arcuate structure in the sagittal view with a remarkable overlap with the migratory stream of the Arc cells outlined in *G* (*E*, *F*, and *G*). The drawing in *G* is taken from Paredes et al[21] (reprinted with permission from American Association for the Advancement of Science), who were the first to identify Arc cells as a population of late-moving neurons at this localization. Subjects 5 and 6: Exemplary Mercator brain projections of 2 of the 3 individuals with polymicrogyria in the peri-Sylvian area of the right hemisphere (*H* and *I*).

The occurrence in the frontal white matter supports the hypothesis of Rezazadeh et al[10] that heterotopia in 22q11.2DS might result from arrested Arc migrating cells. Arc cells are a population of late-migrating neurons, identified by Paredes et al.[21] These neurons form a caplike structure surrounding the anterior body of the lateral ventricle or an arching structure in sagittal sections in the postnatal infant human brain (Fig 1). They continue to migrate along radial glial fibers tangentially to the walls of the lateral ventricles and along blood vessels into the anterior cingulate gyrus and prefrontal cortex in the early postnatal period, when they differentiate and contribute to inhibitory circuits. Paredes et al[21] describe Arc cells as histopathologically organized into 4 tiers from the subventricular zone to the cortex. This distribution of Arc cells led Rezazadeh et al to the hypothesis that the PNH they observed were Arc cells arrested in tiers 1 and 2, and the nodules they observed only microscopically in postmortem examinations were neurons in the Arc tiers 3 and 4. Following this concept, the

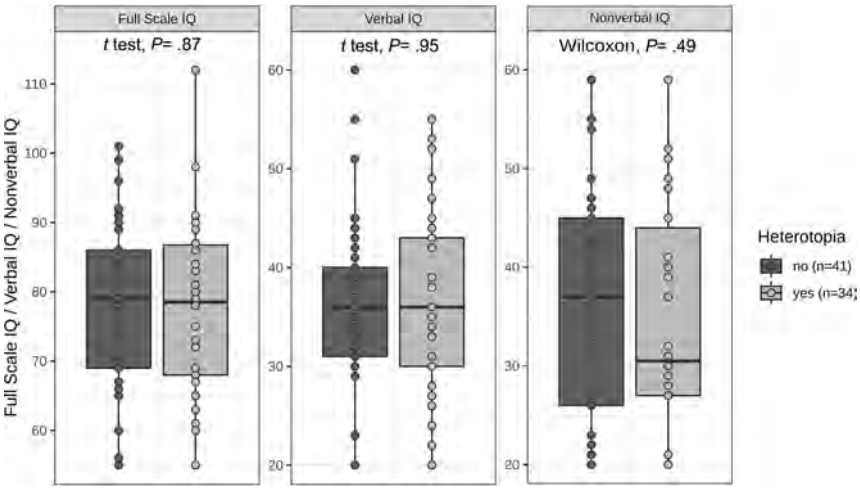

FIG 2. Association between the occurrence of heterotopia and IQ.

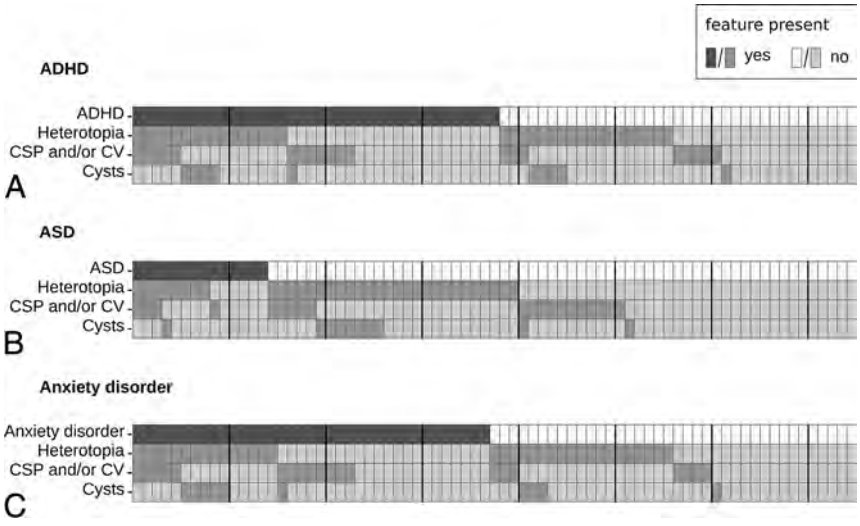

FIG 3. Pattern of distribution of the most frequent morphologic findings by psychiatric diagnosis. Every column represents 1 individual with 22q11.2DS. Ten individuals at a time are separated by a *black line*, and the *shadings* are coding the presence or absence of a finding, whereby the *first row* depicts the presence or absence of ADHD (*A*), ASD (*B*), or anxiety disorder (*C*). Diagnosis of psychosis is not depicted due to the small number of subjects ($n = 4$).

heterotopia in the white matter that we found on MR imaging might represent larger chains of arrested Arc cells in tiers 3 and 4. In addition to the spatial overlap of Arc cells and heterotopia in individuals with 22q11.2DS, there are also immunohistochemical features supporting the hypothesis of Rezazadeh et al.

Our observation of heterotopia in the white matter is limited because we had only 3D T1WI and low-resolution T2*WI at our disposal. Notably, in addition to the signal (cortex-isointense in both T1WI and T2*WI), we also considered the shape (round or ovoid). Furthermore, despite blinded observation, we found no heterotopia in the white matter in controls. The distribution pattern of the heterotopia-like lesions in controls was less concentrated in the frontal lobe than in individuals with 22q11.2DS, and in all 4 of these individuals, the lesions were isointense to the CSF rather than to the cortex in T2*WI, suggesting that these are probably enlarged perivascular spaces. Nevertheless, we cannot exclude some heterotopia in the white matter being nonspecific white matter lesions or enlarged perivascular spaces.

PNH are frequently associated with drug-resistant epilepsy.[13] They often have intrinsic epileptogenicity but may not always be primarily involved in the generation of seizures. Both the heterotopic lesion and particularly the normotopic cortex are involved in the epileptogenic network.[22] Seizures seem to result from complex interactions between PNH and the allo- or neocortex.[23] Ten percent of individuals with 22q11.2DS have a diagnosis of epilepsy.[3] In the study of Rezazadeh et al,[10] 6 of the 7 individuals with 22q11.2DS with PNH had a history of seizures, which suggests that seizures could be the result of PNH. Information concerning epilepsy diagnosis of the subjects in our cohort was unsuitable for use in further analyses.

In 13% of the individuals with 22q11.2DS, we found periventricular cysts, especially adjacent to the anterior horns. Such cysts have been described only in single subjects with 22q11.2DS so far.[19,24] The localization of the cysts is remarkably similar to the localization of PNH, and both seem to occur more often in combination. A reason for the occurrence of cysts could be a vulnerability of the microstructure due to the disturbed Arc cells migration.

We observed another migration disorder, polymicrogyria, in 4% of individuals with 22q11.2DS ($n = 3$) and none of the controls. This corresponds to the reported prevalences between 1%[25] and 7%.[4] Polymicrogyria in all our subjects occurred unilaterally right in the peri-Sylvian region, which is in line with observations by Robin et al.[11]

Another morphologic finding in individuals with 22q11.2DS was persistent CSP and/or CV (27%). In only 1 subject the CSP appeared isolated without CV. CV is normally present in up to 30% of neonates but persists into adulthood in <1% of individuals, while CSP can persist in up to 20%.[26] The increased rates of CSP/CV in individuals with 22q11.2DS are known from prior studies, which reported a prevalence from 19%[19] to 84%.[27] Often no precise distinction is made between CSP and CSP/CV. The mechanisms through which a CSP/CV is maintained are unclear. Consistent with studies that noted an increased

incidence of CSP or CV in patients with schizophrenia compared with healthy subjects,[28,29] there is evidence that CSP is associated with psychosis in individuals with 22q11.2DS.[19,20] Schmitt et al[19] also found a significant association between incidental white matter abnormalities and psychosis. These relationships to psychosis remain unclear in our study due to the young age of the individuals with 22q11.2DS (mean age, 15.5 years). However, the mean age of onset for schizophrenia in individuals with 22q11.2DS is around 20 years.[30]

We did not find any significant relationships between morphologic findings and psychiatric diagnoses or general cognitive performance, consistent with prior studies.[19,20,27] While there was a significant IQ difference between individuals with 22q11.2DS and controls, as expected, no differences were observed between individuals with 22q11.2DS with different morphologic abnormalities.

The functions of the frontal lobe, where most of the morphologic findings were found, are not specifically assessed via IQ tests.

Overall, despite the above-mentioned limitations and the limited sample size for these subgroup analyses, these findings suggest that morphologic findings do not necessarily reflect poorer brain function.

CONCLUSIONS

Taken together, our findings, PNH and heterotopia in the white matter (possibly reflecting interrupted Arc cells migration), persistent CSP/CV, and periventricular cysts, give clues to the brain development disorder induced by 22q11.2DS.

Disclosures: Felix Rosenow—*UNRELATED*: *Consultancy*: UCB, Eisai GmbH, Arvelle Therapeutics, GW Pharmaceuticals, *Comments*: scientific advice; *Grants/Grants Pending*: Deutsche Forschungsgemeinschaft, Hessisches Ministerium für Soziales und Integration (Hessian Ministry for Social Affairs and Integration), Hessisches Ministerium für Wissenschaft und Kunst (Hessian Ministry of Higher Education, Research and the Arts), European Union, Bundesministerium für Bildung und Forschung (Federal Ministry of Education and Research), State of Hessen Landes-Offensive zur Entwicklung Wissenschaftlich-ökonomischer Exzellenz (state offensive for the development of scientific and economic excellence) Program, *Comments*: research grants*; *Payment for Lectures Including Service on Speakers Bureaus*: UCB, GlaxoSmithKline, Arvelle Therapeutics, Eisai GmbH, Medilearn India, *Comments*: for scientific and Continuing Medical Education presentations; *Payment for Development of Educational Presentations*: Eisai GmbH, *Comments*: patient education material. Christine Ecker—*RELATED*: *Grant*: Deutsche Forschungsgemeinschaft, *Comments*: Deutsche Forschungsgemeinschaft research grant.* Carrie E. Bearden—*RELATED*: *Grant*: National Institute of Mental Health, *Comments*: A National Institute of Mental Health grant supported the recruitment and scanning costs of study participants*; *UNRELATED*: *Board Membership*: Neuroscience Novartis, *Comments*: Scientific Advisory Board member. *Money paid to the institution.

REFERENCES

1. McDonald-McGinn DM, Sullivan KE, Marino B, et al. **22q11.2 deletion syndrome.** *Nat Rev Dis Primers* 2015;1:15071 CrossRef Medline
2. Niklasson L, Rasmussen P, Óskarsdóttir S, et al. **Autism, ADHD, mental retardation and behavior problems in 100 individuals with 22q11 deletion syndrome.** *Res Dev Disabil* 2009;30:763–73 CrossRef Medline
3. Eaton CB, Thomas RH, Hamandi K, et al. **Epilepsy and seizures in young people with 22q11.2 deletion syndrome: prevalence and links with other neurodevelopmental disorders.** *Epilepsia* 2019;60:818–29 CrossRef Medline
4. Hopkins SE, Chadehumbe M, Crowley TB, et al. **Neurologic challenges in 22q11.2 deletion syndrome.** *Am J Med Genet A* 2018;176:2140–45 CrossRef Medline
5. Moss EM, Batshaw ML, Solot CB, et al. **Psychoeducational profile of the 22q11.2 microdeletion: a complex pattern.** *J Pediatr* 1999;134:193–98 CrossRef Medline
6. Eliez S, Schmitt JE, White CD, et al. **Children and adolescents with velocardiofacial syndrome: a volumetric MRI study.** *Am J Psychiatry* 2000;157:409–15 CrossRef Medline
7. Bearden CE, van Erp TG, Dutton RA, et al. **Mapping cortical thickness in children with 22q11.2 deletions.** *Cereb Cortex* 2007;17:1889–98 CrossRef Medline
8. Villalón-Reina JE, Martínez K, Qu X, et al. **Altered white matter microstructure in 22q11.2 deletion syndrome: a multisite diffusion tensor imaging study.** *Mol Psychiatry* 2020;25:2818–31 CrossRef Medline
9. Kiehl TR, Chow EW, Mikulis DJ, et al. **Neuropathologic features in adults with 22q11.2 deletion syndrome.** *Cereb Cortex* 2009;19:153–64 CrossRef Medline
10. Rezazadeh A, Bercovici E, Kiehl TR, et al. **Periventricular nodular heterotopia in 22q11.2 deletion and frontal lobe migration.** *Ann Clin Transl Neurol* 2018;5:1314–22 CrossRef Medline
11. Robin NH, Taylor CJ, McDonald-McGinn DM, et al. **Polymicrogyria and deletion 22q11.2 syndrome: window to the etiology of a common cortical malformation.** *Am J Med Genet A* 2006;140:A2416–25 CrossRef Medline
12. Bingham PM, Zimmerman RA, McDonald-McGinn D, et al. **Enlarged Sylvian fissures in infants with interstitial deletion of chromosome 22q11.** *Am J Med Genet* 1997;74:538–43 CrossRef Medline
13. Battaglia G, Chiapparini L, Franceschetti S, et al. **Periventricular nodular heterotopia: classification, epileptic history, and genesis of epileptic discharges.** *Epilepsia* 2006;47:86–97 CrossRef Medline
14. Lin A, Ching CR, Vajdi A, et al. **Mapping 22q11.2 gene dosage effects on brain morphometry.** *J Neurosci* 2017;37:6183–99 CrossRef Medline
15. Lord C, Risi S, Lambrecht L, et al. **The autism diagnostic observation schedule-generic: a standard measure of social and communication deficits associated with the spectrum of autism.** *J Autism Dev Disord* 2000;30:205–23 CrossRef Medline
16. Lord C, Rutter M, Le Couteur A. **Autism Diagnostic Interview-Revised: a revised version of a diagnostic interview for caregivers of individuals with possible pervasive developmental disorders.** *J Autism Dev Disord* 1994;24:659–85 CrossRef Medline
17. Core Team R. *R: A Language and Environment for Statistical Computing. R Foundation for Statistical Computing*; 2019
18. Wither RG, Borlot F, MacDonald A, et al. **22q11.2 deletion syndrome lowers seizure threshold in adult patients without epilepsy.** *Epilepsia* 2017;58:1095–101 CrossRef Medline
19. Schmitt JE, Yi JJ, Roalf DR, et al. **Incidental radiologic findings in the 22q11.2 deletion syndrome.** *AJNR Am J Neuroradiol* 2014;35:2186–91 CrossRef Medline
20. Chow EW, Mikulis DJ, Zipursky RB, et al. **Qualitative MRI findings in adults with 22q11 deletion syndrome and schizophrenia.** *Biol Psychiatry* 1999;46:1436–42 CrossRef Medline
21. Paredes MF, James D, Gil-Perotin S, et al. **Extensive migration of young neurons into the infant human frontal lobe.** *Science* 2016;354: aaf7073 CrossRef Medline
22. Pizzo F, Roehri N, Catenoix H, et al. **Epileptogenic networks in nodular heterotopia: a stereoelectroencephalography study.** *Epilepsia* 2017;58:2112–23 CrossRef Medline
23. Aghakhani Y, Kinay D, Gotman J, et al. **The role of periventricular nodular heterotopia in epileptogenesis.** *Brain* 2005;128:641–51 CrossRef Medline
24. Mitnick RJ, Bello JA, Shprintzen RJ. **Brain anomalies in velo-cardio-facial syndrome.** *Am J Med Genet* 1994;54:100–06 CrossRef Medline
25. McDonald-McGinn DM, Sullivan KE. **Chromosome 22q11.2 deletion syndrome (DiGeorge syndrome/velocardiofacial syndrome).** *Medicine (Baltimore)* 2011;90:1–18 CrossRef Medline
26. Tubbs RS, Krishnamurthy S, Verma K, et al. **Cavum velum interpositum, cavum septum pellucidum, and cavum vergae: a review.** *Childs Nerv Syst* 2011;27:1927–30 CrossRef Medline

27. Beaton EA, Qin Y, Nguyen V, et al. **Increased incidence and size of cavum septum pellucidum in children with chromosome 22q11.2 deletion syndrome.** *Psychiatry Res* 2010;181:108–13 CrossRef Medline
28. DeLisi LE, Hoff AL, Kushner M, et al. **Increased prevalence of cavum septum pellucidum in schizophrenia.** *Psychiatry Res* 1993;50:193–99 CrossRef Medline
29. Galarza M, Merlo AB, Ingratta A, et al. **Cavum septum pellucidum and its increased prevalence in schizophrenia: a neuroembryological classification.** *J Neuropsychiatry Clin Neurosci.* 2004;16:41–46 CrossRef Medline
30. Bassett AS, Chow EW, AbdelMalik P, et al. **The schizophrenia phenotype in 22q11 deletion syndrome.** *Am J Psychiatry* 2003;160:1580–86 CrossRef Medline

MRI Patterns in Pediatric CNS Hemophagocytic Lymphohistiocytosis

P. Malik, L. Antonini, P. Mannam, F.N. Aboobacker, A. Merve, K. Gilmour, K. Rao, S. Kumar, S.E. Mani, D. Eleftheriou, A. Rao, C. Hemingway, S.V. Sudhakar, J. Bartram, and K. Mankad

ABSTRACT

BACKGROUND AND PURPOSE: Neuroimaging has an important role in detecting CNS involvement in children with systemic or CNS isolated hemophagocytic lymphohistiocytosis. We characterized a cohort of pediatric patients with CNS hemophagocytic lymphohistiocytosis focusing on neuroradiologic features and assessed whether distinct MR imaging patterns and genotype correlations can be recognized.

MATERIALS AND METHODS: We retrospectively enrolled consecutive pediatric patients diagnosed with hemophagocytic lymphohistiocytosis with CNS involvement treated at 2 pediatric neurology centers between 2010 and 2018. Clinical and MR imaging data were analyzed.

RESULTS: Fifty-seven children (40 primary, 70%) with a median age of 36 months (interquartile range, 5.5–80.8 months) were included. One hundred twenty-three MR imaging studies were assessed, and 2 broad imaging patterns were identified. Pattern 1 (significant parenchymal disease, 32/57, 56%) was seen in older children ($P = .004$) with worse clinical profiles. It had 3 onset subpatterns: multifocal white matter lesions (21/32, 66%), brainstem predominant disease (5, 15%), and cerebellitis (6, 19%). All patients with the brainstem pattern failed to meet the radiologic criteria for chronic lymphocytic inflammation with pontine perivascular enhancement responsive to steroids. An attenuated imaging phenotype (pattern 2) was seen in 25 patients (44%, 30 studies) and was associated with younger age.

CONCLUSIONS: Distinct MR imaging patterns correlating with clinical phenotypes and possible genetic underpinnings were recognized in this cohort of pediatric CNS hemophagocytic lymphohistiocytosis. Disruptive mutations and missense mutations with absent protein expression correlate with a younger onset age. Children with brainstem and cerebellitis patterns and a negative etiologic work-up require directed assessment for CNS hemophagocytic lymphohistiocytosis.

ABBREVIATIONS: CLIPPERS = chronic lymphocytic inflammation with pontine perivascular enhancement responsive to steroids; HLH = hemophagocytic lymphohistiocytosis; HSCT = hematopoietic stem cell transplant

Recent developments in our understanding of the underlying molecular mechanisms of degranulation defects have revealed hemophagocytic lymphohistiocytosis (HLH) to be a markedly heterogeneous disorder in which there is toxic uncontrolled immune activation. This is often driven by genetic mutations occurring along the perforin-dependent granule exocytosis pathway, termed "primary HLH."[1] Systemic inflammation and immunotherapies may also cause macrophage activation, frequently in the absence of these genetic mutations, termed "secondary HLH."

MR imaging in CNS HLH is a helpful adjunct in diagnosis but does not form a part of the HLH-2004 diagnostic criteria (https://onlinelibrary.wiley.com/doi/10.1002/pbc.21039). However, children with CNS-restricted HLH or in whom CNS HLH precedes systemic involvement often do not satisfy these criteria and have normal blood counts and systemic inflammatory markers.[2] MR imaging findings in these children overlap with infections, demyelination, and other neuroinflammatory disorders, leading to a delayed diagnosis, thus affecting outcomes. Reports of potentially distinct

Received May 12, 2021; accepted after revision July 19.

From the Departments of Diagnostic Imaging (P. Malik, P. Mannam, S.E.M.), Hematology (F.N.A.), and Child Health (S.K.), Christian Medical College, Vellore, India; Department of Paediatric Hemato-Oncology (L.A.), G. Salesi Hospital, Ancona, Italy; Department of Pediatric Neurology (C.H.), Pediatric Neuroradiology Unit (S.V.S., K.M.), Department of Histopathology (A.M.), Bone Marrow Transplant Unit (K.R.), and Departments of Pediatric Hematology (A.R., J.B.), Immunology (K.G.), and Paediatric Rheumatology (D.E.), Great Ormond Street Hospital for Children, London, UK.

P. Malik is first author.

S. Sudhakar, J. Bartram, and K. Mankad are co-senior authors.

Please address correspondence to Kshitij Mankad, MD, Pediatric Neuroradiology unit, Great Ormond St Hospital for Children, Great Ormond St, London WC1N 3JH, UK; e-mail: drmankad@gmail.com; @PrateekM77; @drmankad; @SSudhakar2019

Indicates article with online supplemental data.

http://dx.doi.org/10.3174/ajnr.A7292

neuroimaging patterns exist in the literature.[2,3] However, their incidence, clinical and genotype correlations, and impact on outcomes remain unexplored.

We present clinical profiles, MR imaging findings, and outcomes in a large pediatric cohort of HLH with CNS involvement with the aim to define distinct MR imaging patterns and correlate these with clinical profiles and explore possible genotype correlations.

MATERIALS AND METHODS

This retrospective cohort study recruited children with HLH and CNS involvement presenting to Christian Medical College, Vellore, India, and Great Ormond Street Hospital for Children, London, UK, between 2010 and 2018. Institutional review boards from both centers approved the study. The diagnosis of HLH was defined using the HLH-2004 criteria (https://onlinelibrary.wiley.com/doi/10.1002/pbc.21039),[4] and patients with both primary and secondary HLH were included. The definition of CNS involvement was based on the presence of CSF abnormalities (proteinosis and/or pleocytosis) with or without neurologic symptoms or imaging findings.[4] Children who satisfied the above criteria with available MR images were included for data collection. Children with systemic HLH without CNS involvement based on the above definition or no available MR imaging were excluded from the study.

Demographic, clinical, and outcome data were reviewed. Imaging data collection and pattern allocation (Online Supplemental Data), blinded to the clinical data, was performed by trained neuroradiologists (P.M., S.V.S., with 5–15 years' experience) on separate MR imaging data-collection sheets with consensus agreement. Any disagreement was resolved by a consensus review with a third neuroradiologist (K.M., with 15 years' experience). The supratentorial and infratentorial compartments were further separately assessed for lesion number (single, few, multiple), lesion type (diffuse or focal), level of white matter involvement (subcortical, deep, periventricular), signal characteristics (T2WI/FLAIR, DWI, and T1 postcontrast enhancement), and overall imaging pattern (pattern definitions are elaborated under Results). Flow cytometry data regarding protein expression (NK cell perforin expression and cytotoxic lymphocyte degranulation expression) were also collected and analyzed.

MR Imaging Lesion Definitions

MR imaging was performed on a 1.5T (Magnetom Avanto; Siemens) or a 3T (Intera Achieva; Philips Healthcare) scanner. Signal characteristics were assessed on spin-echo T2WI or FLAIR spin-echo, T1WI, T1 postcontrast, and DWI sequences. They were designated T2 or FLAIR hyperintense when the signal was more than that of normal gray matter, and as T1- and T2-hypointense when it followed the signal or was darker than the signal of gray matter.[5,6]

Diffuse and focal lesions were defined as any lesion involving the gray or white matter measuring ≥2 and <2 cm, respectively.[7] Some focal lesions had T2/FLAIR hypointensity and were further characterized as "target lesions" or "target variants" on the basis of T2/FLAIR and contrast characteristics. In target lesions, the T2 hypointense component formed a middle rim separating central and peripheral T2 hyperintense areas, giving target lesions a trilaminar appearance. In target variants, the hypointense component was present in the central core of the lesion and was surrounded by hyperintense signal. Target lesions with enhancing middle rims formed the ring-enhancing lesions.

Focal patterns of enhancement were termed "nodular" when the enhancing component measured <10 mm and "homogeneous" when ≥10 mm.[8] The perivascular enhancement pattern was defined as small continuous or near-continuous punctate (<3 mm) to nodular (<10 mm) foci of enhancement often merging[8] or heterogeneous/unclassifiable if they did not satisfy the above definitions.

Statistical Analysis

Data from the collected variables were assessed for normality using the Shapiro-Wilk test. Means for normally distributed data were compared using the Student *t* test, while the Mann-Whitney *U* test was used for comparing non-normally distributed unpaired groups. The χ^2 and Fisher exact tests were used for analysis of categoric data when necessary. All statistical tests were 2-sided, and statistical significance was assumed at *P* value of <.05. SPSS Version 25 software package (IBM) was used for the analysis.

RESULTS

Fifty-seven patients satisfied the inclusion criteria. The median age of onset was 36 months with no sex predilection. Neurologic symptoms were reported in 45 patients (79%) (Table 1); seizures and encephalopathy were most common. Of the patients with neurologic symptoms, 27/45 (60%) presented with systemic disease, and 18/45 (40%) following systemic involvement. CSF data was available for 50/57 patients (88%), and 84% ($n = 42$) showed abnormalities, with CSF proteinosis (>45mg/dL) being the most common (64%). In 12 patients (21%), CSF abnormalities, either pleocytosis or proteinosis, were present with no neurologic symptoms or only mild irritability. Thirty-five (61%) patients received either HLH-1994 (etoposide, dexamethasone, with cyclosporine at week 9) or the 2004 treatment protocol (early introduction of cyclosporine along with dexamethasone and etoposide).[9,10] Of the 35 children, 25 went on to receive hematopoietic stem cell transplant (HSCT). The average follow-up in our cohort was 3.7 years ([SD, 3.9]; range 0–15 years). Nineteen of 57 (32%) children died, including 4 from the HSCT group.

Etiology

Seventy percent ($n = 40$) of the patients had primary HLH, with a pathogenic genetic mutation identified in 31. *PRF1* (familial HLH-2) and *UNC13D* (familial HLH-3) mutations were the most common genetic defects, seen in 35% (14) and 20% (8), respectively. Of these 31 patients, data regarding genetic variants were available for 25 patients (Online Supplemental Data). Within these 25 patients, 35 genetic variants were identified. Compound heterozygous (11/25, 44%) and homozygous (11/25, 44%) mutations were nearly equally present, while monoallelic/hemizygous mutations were rare ($n = 3$). Missense (12/17, 71%) and frameshift (8/12, 67%) mutations were the most common in FHLH2 and FHLH3, respectively. In the secondary HLH cohort ($n = 17$),

Table 1: Clinical, treatment, and outcome profiles[a]

Profiles	
Age	
Age at onset (median) (IQR) (mo)	36 (5.5–80.8)
Age at CNS presentation (median) (IQR) (mo)	49.2 (11–96)
Male/female (ratio)	34:23 (1.4:1)
General symptoms	
Fever	45/56 (80)
Hepato-/splenomegaly	46/56 (82)
Abdominal distension	14/56 (25)
CNS symptoms	45/57, 79%
Seizures	28 (62)
Decreased sensorium	22 (49)
Meningismus	13 (29)
Gait ataxia	12 (27)
Hypotonia	11 (24)
Minimal symptoms (mild irritability) or clinically silent patients (no symptoms with CSF abnormalities)	12 (21)
CSF findings	
CSF analyzed at presentation	50/57 (87)
Abnormal CSF	42/50 (84)
CSF pleocytosis (>10 leucocytes/μL)	25/50 (50)
CSF proteinosis (>45 mg/dL)	32/50 (64)
Treatment	
HLH 1994/2004	35/57 (61)
IT methotrexate	17 (30)
HSCT	25 (45)
Outcome profiles	
Death	19 (32)
Death before 8 weeks	7
Death after 8 weeks	12
Alive at last follow-up	36 (63)
Lost to follow-up	2

Note:—IQR indicates interquartile range; IT, intrathecal.

[a] Total ($n = 57$). Data collected are both continuous and categorical, and the analysis method used has been referred to under statistical analysis heading.

infections (10, 59%) and autoimmune etiologies (6, 35%) were the most common.

Imaging Pattern Definitions

We reviewed 123 MR imaging studies from the 57 included patients. On the basis of a pattern-recognition approach, 2 broad imaging patterns were defined (pattern 1 and pattern 2).

Pattern 1, the significant parenchymal disease group, consisted of patients with parenchymal lesions. 93/123 studies (76% of studies; 32/57 patients, 56%) were grouped under pattern 1. The supratentorial and infratentorial compartments were further separately assessed for lesion number, signal, and enhancement characteristics.

Pattern 2 had an attenuated imaging phenotype with no parenchymal lesions at onset and follow-up (if available) and had nonspecific MR imaging findings, isolated cortical atrophy, or normal imaging findings.

Thirty of 123 (24% of studies; 25/57 patients, 44%) studies belonged to pattern 2. These included 10 studies with normal findings, 15 studies with only cerebral atrophy with or without cerebellar atrophy, 3 studies with central tegmental tract T2-hyperintensity as an isolated finding, 2 studies with nonspecific findings (small pons, underopercularization, germinal matrix cysts, and periventricular hemosiderin staining attributable to a remote or perinatal event).

Imaging Findings in Pattern 1

Lesion Type Incidence and Distribution. A near-equal incidence of cerebral and cerebellar involvement was seen, 77/123 (63%) and 71/123 (58%), respectively (Online Supplemental Data). Deep gray nuclear and thalamic involvement was seen in 35/123 studies (28%) and was commonly bilateral and asymmetric (24/35, 68%). Brainstem involvement with a predilection for the dorsal pons was seen in 34/123 (28%), variably extending to involve the midbrain (32/34 studies) and medulla (9/34 studies). Cranial nerve involvement was seen as bilateral nodular enhancement involving multiple nerves in 5 studies. Severe optic nerve swelling, enhancement, and diffusion restriction (Online Supplemental Data) were noted in one. Short-segment enhancing cord lesions were seen in 3 studies, along with cauda equina thickening in one.

Enhancement Characteristics. Enhancement was present in more than half of the studies with cerebral and cerebellar lesions, 52% and 60%, respectively. Both the diffuse (77%) and focal (80%) cerebellar lesions showed a higher proportion of enhancement than their cerebral counterparts (26%, 60%, respectively). Diffuse lesions showed a perivascular pattern of enhancement most commonly, while focal lesions most commonly showed nodular/homogeneous enhancement. Target lesion and target variants were seen in 6 studies with supratentorial lesions and 4 studies with infratentorial lesions. None of the target lesions or variants showed diffusion restriction.

Other Findings. Thirty-two of 123 studies had cortical atrophy along with parenchymal lesions. Eighteen studies showed blooming on SWI within the white matter lesions, representing either microhemorrhages or calcifications. Nineteen studies had ventriculomegaly, which was obstructive due to cerebellar edema in 3.

Subpatterns in Pattern 1

Three onset subpatterns were identified within pattern 1 using an algorithmic approach (Online Supplemental Data) and were divided and assigned to 3 subgroups, 1.1, 1.2, and 1.3.

Subgroup 1.1: Multifocal Cerebral/Cerebellar White Matter Lesions. Patients in subgroup 1.1 showed involvement of cerebral and cerebellar white matter with variable numbers and signal characteristics of the lesions. This subpattern was the most common, identified in 21/32 patients (66%) at onset (Online Supplemental Data). On follow-up, this was again the largest subpattern (21, 37%), with 2 patients of subpattern 1.2 and 4 of subpattern 1.3 evolving into subpattern 1.1.

Subgroup 1.2: Brainstem Predominant Lesions. Subgroup 1.2 pattern was defined as numerous (>3) punctate to nodular enhancing lesions involving the pons with variable extension into the cerebellum, mesencephalon, and deep cerebral white matter and was reminiscent of the radiologic pattern seen in chronic lymphocytic inflammation with pontine perivascular enhancement responsive to steroids (CLIPPERS).[11] These were further assessed for radiologic criteria proposed for CLIPPERS, including the size of the largest T1-enhancing nodule, T2 signal extension beyond

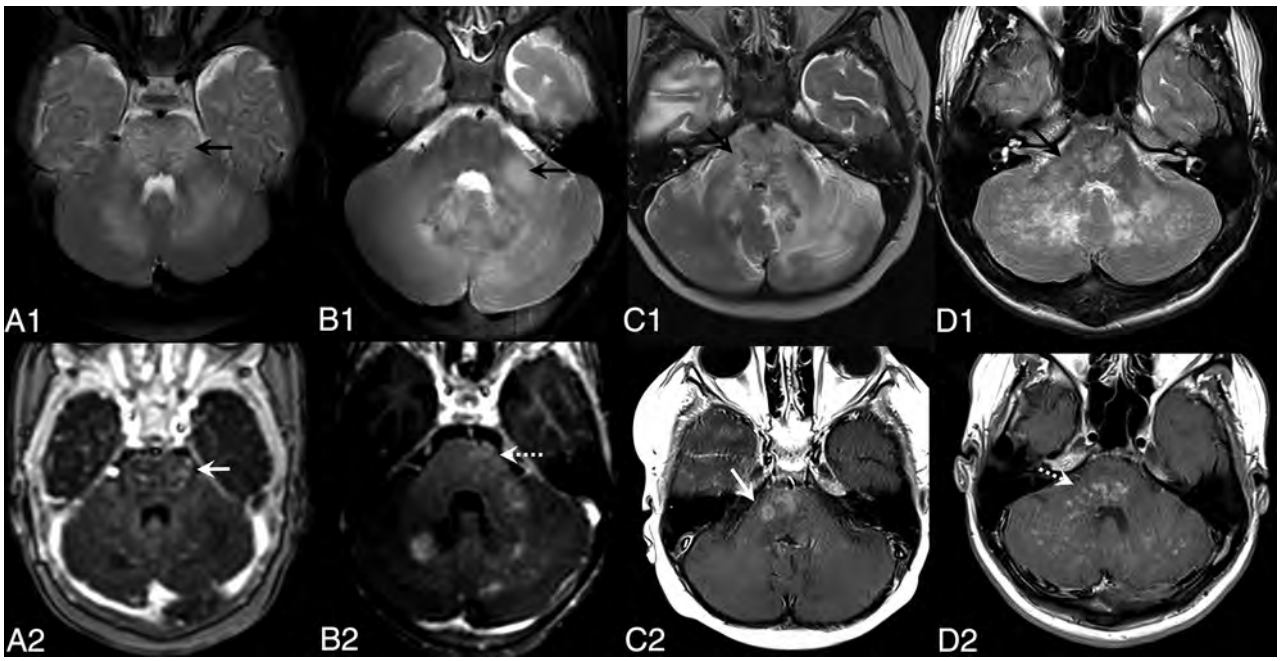

FIG 1. Findings of 4 patients with subpattern 1.2 (brainstem–predominant pattern). Axial T2WI (*A1–D1*) and axial postcontrast TIWI (*A2–D2*) at the level of the pons show multiple punctate (*dashed white arrow*, *B2*, *D2*) to nodular (*solid white arrow*, *A2* and *C2*), enhancing foci and extension of the T2 signal abnormality (*black arrow*, *A1–D1*) beyond the enhancement in all cases.

the T1 enhancing nodule (T2-T1 mismatch), and symmetric or asymmetric involvement of the pons.[12]

This subpattern was seen in 5/32 patients (15%) at the onset of CNS HLH (Online Supplemental Data). In 1 additional patient (patient 47), this pattern was noted on follow-up with the preceding studies showing multifocal white matter lesions. In 2 of these 6 patients, CNS involvement preceded or was within 2 weeks of systemic HLH onset. The underlying genetic defect was variable. Clinically, all had signs of brainstem and/or cerebellar dysfunction along with a variable presence of encephalopathy and seizures. T2 signal abnormality always extended beyond the enhancing nodule (6/6), and in almost all (5/6), the size of the largest T1-enhancing nodule was >3 mm. Four of 6 patients showed an asymmetric involvement of the pons at the middle cerebellar peduncle level (Fig 1). Four of 6 children died (3 received an HLH therapy protocol; one received a steroid-based regimen, and one also received HSCT). For 4 patients, a follow-up imaging was available, and 3/4 developed multifocal white matter lesions.

Representative cerebellar biopsy (patient 57, Online Supplemental Data), obtained before a genetic diagnosis, showed chronic inflammation and nonspecific histologic changes.

Subgroup 1.3: Diffuse Cerebellar Involvement/Cerebellitis. Subgroup 1.3 pattern was defined as diffuse cerebellar cortical swelling/edema with diffuse effacement of cerebellar folia, with or without cerebellar white matter signal change (Fig 2). Mass effect in the form of tonsillar descent, fourth ventricular outflow obstruction, and hydrocephalus was assessed additionally.

This subpattern was seen in 6/32 patients at onset (19%, summarized in the Online Supplemental Data). In these patients, there was diffuse cerebellar edema and effacement of cerebellar folia and/or cerebellopontine cisterns. This was often severe enough to be associated with tonsillar descent (5/6) and proximal hydrocephalus (3/6). In 4/6 children, this was the first manifestation of HLH and preceded systemic involvement. Cerebellitis was the only finding in most, barring 2 children in whom additional white matter lesions were also present. Clinically, all had signs of cerebellar dysfunction and varying degrees of encephalopathy and seizures. The cerebellar edema responded to steroids in all children. Two children had recurrent episodes of cerebellitis. *PRF1* and *UNC13D* mutations were present in 2 patients each. On follow-up, cerebellar edema resolved and evolved into multifocal white matter lesions in all.

Pattern Analysis for Clinicoradiologic Correlation

Patterns 1 and 2, along with the subpatterns, were assessed for clinical and outcome differences. Children with pattern 1 were significantly older (median age, 55.5 versus 16 months, P value = .004) and had a worse symptom profile for most symptoms (Table 2). Both patterns 1 and 2 had a high incidence of CSF abnormalities (90% and 75%, respectively); significant pleocytosis was noted in pattern 1 (P value = .04). Pattern 1 was associated with nearly twice the incidence of mortality and a lower deficit-free survival, though this was not statistically significant (P value = .06). These parameters were not statistically different across the subpatterns.

Genotype Correlations

To analyze possible genotype correlations, we pooled patients with at least 1 disruptive mutation (nonsense, frameshift, or deletion) and missense mutations with absent protein expression together (pooled mutation group) and compared them against children with missense mutations and residual protein expression (Online Supplemental Data). We also assessed the purely disruptive mutation group separately for the same variables.

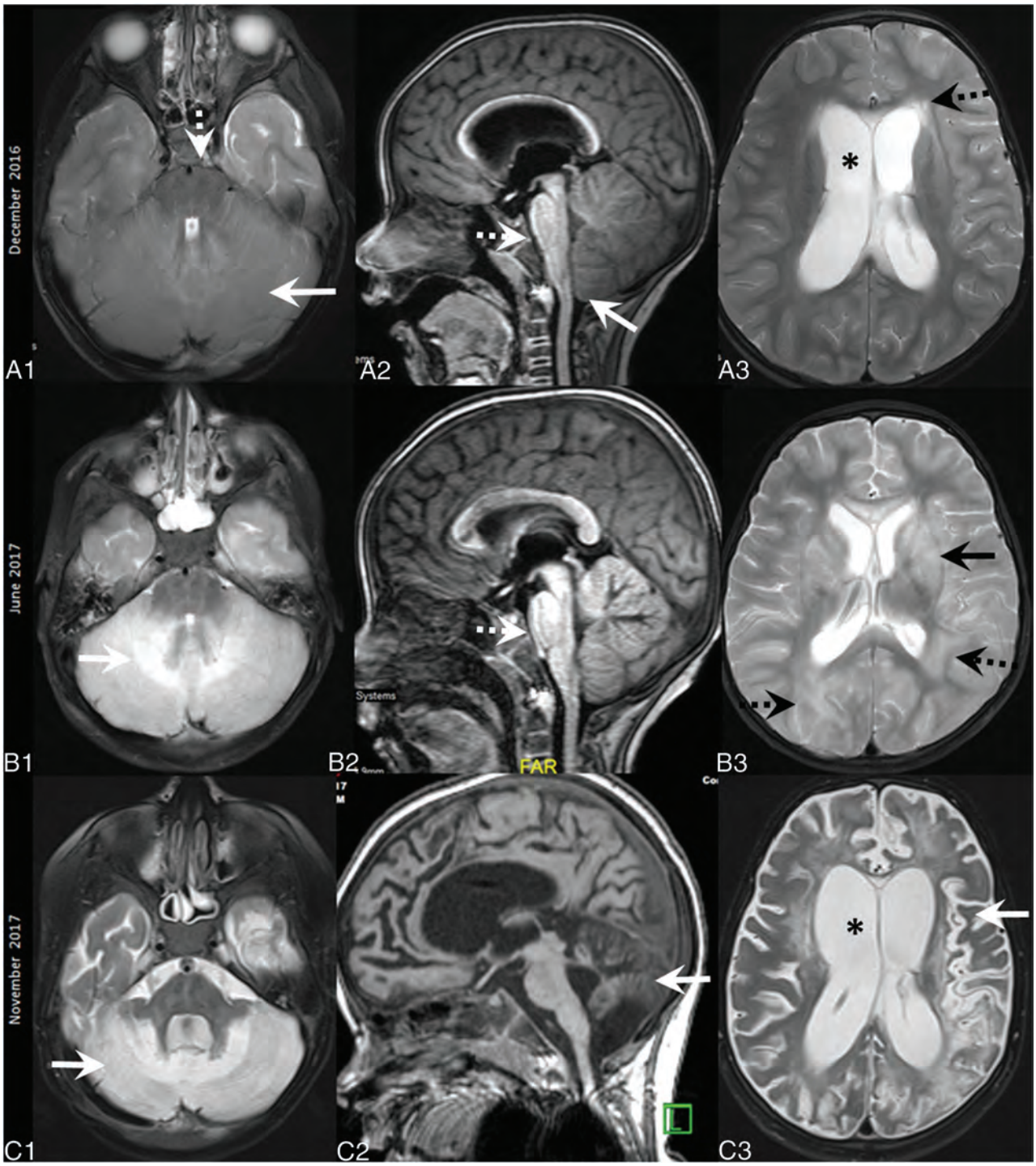

FIG 2. Findings of subpattern 1.3 (cerebellitis). Axial T2WI at the level of the fourth ventricle (*A1–C1*), lateral ventricles (*A3–C3*), and midline sagittal T1WI (*A2–C2*). Onset MR imaging (December 2016) shows severe cerebellar edema and expansion (*white arrow*, *A1*) with mass effect on the brainstem, effacement of the prepontine cistern (*dashed white arrow*, *A2*), and foramen magnum crowding (*white arrow*, *A2*). Lateral ventricular dilation (*asterisk*, *A3*) and transependymal CSF seepage (*dashed black arrow*, *A3*) are also noted. Mild reduction in cerebellar edema and mass effect (*dashed arrow*, *B2*) with new cerebellar (*white arrow, B1*), parieto-occipital (*dashed arrow*, *B3*), and deep gray nuclei (*black arrow*, *B3*) hyperintensities were found in June 2017. Last MR imaging in November 2017 shows cerebral (*white arrow*, *C3*) and cerebellar (*white arrows*, *C1–2*) atrophy, diffuse white matter hyperintensities, and ventriculomegaly (*asterisk*, *C3*).

The age of onset of disease was significantly younger in the purely disruptive mutation group (median age, 3 versus 20 months in children without purely disruptive mutations, P value = .03) and in the pooled mutation group (median age, 4.7 versus 74.4 months in children with missense mutations with residual protein expression, P value = .03). A higher proportion of patients with pattern 2 belonged to the pooled mutation group (13/13) in comparison with pattern 1 (9/12, 75%), with trends toward significance (P

Table 2: Pattern characteristics and analysis[a]

	Subpatterns						
	1.1	1.2	1.3	*P* Value	Pattern 1 Overall	Pattern 2	*P* Value
Median age at onset (mo)	45.4	66	80.5	.5	55.5	16	.004
Symptoms							
Seizures	11/21 (52%)	4/5 (80%)	4/6 (67%)	.5	19/32 (59%)	9/25 (36%)	.08
Encephalopathy	11/21 (52%)	1/5 (20%)	4/6 (67%)	.3	16/32 (50%)	6/25 (24%)	.04
Gait ataxia	5/21 (24%)	3/5 (60%)	3/6 (50%)	.08	12/32 (34%)	0	.001
Limb weakness	6/21 (29%)	1/5 (20%)	1/6 (17%)	.8	8/32 (25%)	1/25 (4%)	.03
Dysarthria	0	2/5 (40%)	1/6 (17%)	.01	3/32 (9%)	1/25 (4%)	.4
Diplopia	01/21 (5%)	2/5 (40%)	2/6 (33%)	.06	5/32 (16%)	0	.03
Abnormal CSF	18/20 (90%)	4/5 (80%)	5/5 (100%)	.6	27/30 (90%)	15/20(75%)	.2
Proteinosis	13 (65%)	4 (80%)	4 (80%)	.5	21 (70%)	11 (55%)	.3
Pleocytosis	10 (50%)	4 (80%)	5 (100%)	.08	19 (63%)	6 (30%)	.04
Pooled mutation group	4/6 (67%)	2/3 (67%)	3/3 (100%)	.32	9/12 (75%)	13/13 (100%)	.09
Mortality	9/20 (45%)	3/5 (60%)	2/6 (33%)	.3	14/31 (45%)	5/24 (21%)	.06
Deficit-free at follow-up	8/20 (40%)	1/5 (20%)	1/6 (17%)	.1	10/31 (32%)	13/25(52%)	.06

[a] Data collected are both continuous and categorical, and the analysis method used has been referred to under statistical analysis heading.

value = .09, Table 2). After an age-based subpattern analysis (Online Supplemental Data), we further noted that patients in the pooled mutation group who presented after 12 months had either posterior fossa patterns 1.2 and 1.3 or pattern 2 (3/6 each). All children with missense mutations with residual protein expression presented after 12 months of age with pattern 1.1 (3/3).

All recurrent mutations in our cohort belonged to the pooled mutation group (Online Supplemental Data) with predominance of pattern 2 except c.50del(p.Leu17Argfs*34, which also had patterns 1.1 and 1.3.

DISCUSSION

CNS HLH, a genetically heterogeneous entity, is neuroradiologically characterized by multifocal parenchymal lesions and atrophy as its most common manifestations. Anecdotal evidence suggests that atypical MR imaging patterns exist; however, these remain unexplored in larger cohort studies. Through our retrospective cohort study, we describe 2 broad MR imaging patterns comprising parenchymal lesions (pattern 1, 32/57 patients, 56%) and an attenuated phenotype with normal-to-nonspecific findings (pattern 2, 25/57 patients; 44%). The attenuated phenotype (pattern 2) affected younger children (16 months, *P* value = .004), had a better symptom profile and a higher deficit-free survival (52%, *P* value = .06). Significant parenchymal disease (pattern 1) was more common in older children (55.5 months) and had 3 distinct imaging subpatterns at onset: multifocal white matter lesions (21/32, 66%), a brainstem–predominant pattern (5/32, 15%), and cerebellitis (6/32, 19%). We summarize their radiologic features, evolution and highlight possible genotype correlations related to these patterns.

CNS involvement in HLH is an independent, poor prognostic factor in children and is associated with significant morbidity and mortality.[13,14] A consensus agreement on a standardized definition of CNS HLH in the literature is lacking, and variable importance has been attached to clinical and imaging findings.[4,15,16] Previous studies have stressed the importance of rigorously evaluating clinical, CSF, and MR imaging findings in assessing CNS involvement.[17] Because MR imaging findings can precede clinical and CSF abnormalities,[17] we used a comprehensive definition, including CSF, clinical, and imaging findings.[4,18] Imaging findings are highly variable, ranging from normal, isolated cortical atrophy to parenchymal lesions. Cortical atrophy is common in CNS HLH[16,17,19] but must be viewed with caution when present in isolation, especially in the background of steroid administration.[17] To address this issue, we used a pattern-recognition approach and segregated the parenchymal lesion group (pattern 1) from patients with nonspecific findings, normal imaging, and isolated cortical atrophy (pattern 2).

Consistent with previous studies, multifocal white matter lesions were the most common finding,[5,20] and frequent cerebral and cerebellar involvement was noted. Multifocal lesions, tumefactive lesions, optic neuritis, and spinal cord lesions can be seen in CNS HLH and overlap with pediatric acquired demyelinating syndromes and infiltrative disorders.[21] While distinct clinicoradiologic syndromes have been described in acquired demyelinating syndromes,[21] such phenotypes remain elusive in CNS HLH. We identified 3 distinct MR imaging subpatterns, 2 of which were seen in children with an acute-to-subacute brainstem and/or cerebellar dysfunction. These subpatterns include multifocal white matter lesions, brainstem–predominant disease, and cerebellitis.

CLIPPERS, a steroid-responsive immune-mediated predominant T-cell perivascular brainstem infiltrative process, has been described mainly in the adult population, and its distinct brainstem radiologic pattern enables identification in the presence of typical features.[8,11] In 2017, clinical, radiologic and pathologic diagnostic criteria were proposed to distinguish CLIPPERS from its mimics,[12] which have been validated in few subsequent studies.[8] Systematic studies evaluating CLIPPERS in pediatric cohorts, however, remain lacking due to differences in disease burden. There is increasing evidence to suggest that unlike in adults, children with a clinicoradiologic phenotype of CLIPPERS have a more aggressive clinical course and higher disability scores on follow-up.[22,23] Pediatric CNS HLH resembling CLIPPERS has been described in the literature (Table 3)[2,24]; however, the radiologic criteria have not been methodically explored. The brainstem–predominant pattern in our cohort was reminiscent of CLIPPERS, though there were important differences (Online Supplemental Data). None of our patients satisfied all the radiologic criteria

Table 3: Relevant literature review of CNS HLH cases with brainstem or cerebellitis patterns with available MR imaging and genetic data

Literature Review	Imaging Pattern	Genetic Variants	Age of Onset, Relation to Systemic HLH	Imaging Findings
Benson et al[2] 3 cases	Brainstem–predominant pattern (CLIPPERS-like)	1 disruptive, 2 with missense mutations and absent protein expression Pt 1: *PRF1* c.452A>T (p.H151L) and c.666C>A (H222Q), Perforin expression 0% Pt 2: *PRF1* c.443C>G (p.A148G) and c.666C>A (H222Q), Perforin expression 0% Pt 3: *UNC13D* c.2346_2349delGGAG (p.R782fs), c.2588G>A (p.G863D)	5–7 yr, all 3 CNS-restricted HLH	CLIPPERS MR imaging criteria NA
Taieb et al[28] 4 patients	Brainstem–predominant pattern (CLIPPERS-like)	4 cases, all with missense mutations and retained-but-decreased protein expression Pt 1: *PRF1* c.272C>T(p.A91V) homozygous, perforin expression 38% Pt 2: *UNC13D* c.919C>T (p.Q307*) and c.2038C>T (p.R680W), not applicable Pt 3: *PRF1* c.116C>A (p.P39H) and c.272C>T (p.A91V), perforin expression 25% Pt 4: *PRF1* c.82C>T (p.R28C) and c.272C>T (p.A91V), perforin expression 38%	Adults (42–73 yr), all had CNS-restricted HLH	Three-fourths had atypical MR imaging CLIPPERS features (confluent contrast-enhancing lesions)
Bhoopalan et al[26] 1 patient	Cerebellitis	1 patient with compound heterozygous *PRF1* gene mutations with at least 1 disruptive mutation *PRF1*: c.50delT (p.L17fs) and c.527G>A(p.C176Y))	8 yr, CNS-restricted HLH	Cerebellitis, tonsillar herniation, no multifocal lesions
Khan et al[27] 1 patient	Cerebellitis	1 patient with homozygous missense mutation c. 173T > C (p.L58P) in STX11 (syntaxin 11) gene	2 yr 7 months, systemic HLH already present	Cerebellitis, tonsillar herniation, diffuse-to-multifocal lesions already present
Astigarraga et al[3] 1 patient	Cerebellitis	1 patient with compound heterozygous missense *PRF* mutations *PRF1*: c.643C>A (p.L215I) and c.785C>A (p.Ala262Asp) (perforin expression data NA)	3 yr, preceded systemic HLH	Recurrent cerebellitis, tonsillar herniation, subsequently multifocal lesions
Taieb et al[28] 1 patient	Cerebellitis	Patient 3's (in CLIPPERS series) brother's; granddaughter, monoallelic *PRF1* mutation (genetic variant NA)	Not specified, self-limited CNS-restricted presentation	NA
Chiapparini et al[29] 1 patient	Cerebellitis	1 patient with homozygous missense *PRF1* mutation c.673C>T (p. Arg225Trp) (perforin expression data NA)	13 yr, preceded systemic HLH	Cerebellitis, tonsillar herniation followed by multifocal lesions

Note:—NA indicates not available; Pt, patient.

for CLIPPERS, and extension of T2 signal change beyond the enhancing nodule was present in all (6/6). Nodular enhancement (5/6) and asymmetric involvement of the pons (4/6) were frequently seen as well. Demyelination work-up, including myelin oligodendrocyte glycoprotein antibody-associated disease,[25] returned negative results, and poor-to-partial responsiveness was noted in those who received steroids. While all cases in literature had CNS-restricted HLH (Table 3), in most (4/6) of our patients, systemic HLH signs were present. After a negative etiologic work-up in this brainstem pattern, CNS HLH evaluation remains imperative in children due to differences in treatment strategies in comparison with other neuroinflammatory disorders.

We also describe 6 children in our cohort (Online Supplemental Data) with cerebellar dysfunction and diffuse cerebellar edema on MR imaging (subpattern 1.3). All children, except 1, presented with this subtype as the first CNS manifestation, and it preceded systemic HLH involvement in most (4/6). In all children, the findings of the diagnostic work-up for cerebellitis were negative, and cerebellar edema responded to steroids. Five similar children with imaging showing cerebellar swelling at the onset of primary HLH have been described previously (Table

3).[3,26-29] Cerebellitis preceded systemic involvement or was followed by CNS-restricted disease in 4 cases. An unfamiliarity with this pattern led to diagnostic delays, and these children subsequently developed multifocal white matter lesions on follow-up. Thus, cerebellar edema and cerebellar dysfunction can be the only finding at the onset of CNS HLH.

Pattern 1 had an older age of onset, worse symptomatology, and trends toward poorer outcomes. The role of hypomorphic missense mutations with residual protein expression is being increasingly recognized in late-onset HLH forms.[20,30] To understand the relationship between onset age and differential brain involvement, we explored possible genotype correlations in our cohort. Consistent with prior studies,[31] both purely disruptive and pooled mutation groups (consisting of children with at least 1 disruptive mutation or missense mutations with absent protein expression) had a younger age of onset. All patients with missense mutations with residual protein expression (hypomorphic mutations) presented after 12 months of age (3/3).

The pooled mutation group also had a higher proportion of patients with pattern 2 (100% versus 75% with pattern 1, *P* value =.09), potentially explaining the younger age of onset with this pattern. This association did not reach statistical significance (*P* value =.09), and we attribute this to the fact that some patients in the pooled mutation group indeed presented after 12 months of age. Interestingly, up to half of the patients with late-onset and disruptive mutations presented with posterior fossa patterns 1.2 and 1.3 (3/6, Online Supplemental Data). Similarly, all patients in the hypomorphic mutation group presented with the more typical pattern. 1.1 (3/3, Online Supplemental Data). We noted many similarities with cases reported in literature. All 8 children with reported MR imaging patterns 1.2 or 1.3 presented after 12 months, between 3 and 13 years of age (Table 3).[2,3,26,27,29] All patients with pattern 1.2 (3/3) had at least 1 disruptive mutation or missense mutations with absent protein expression.[2] Most patients with pattern 1.3 had either disruptive or missense mutations (4/5), but the data regarding protein expression in cases with missense mutations was not available (Table 3). The small number of genetically confirmed patients in the subgroups limits our interpretation. However, the tendency of disruptive mutations and missense mutations with absent protein expression to present with atypical brainstem or cerebellitis patterns in young children after 12 months of age requires further exploration. A CLIPPERS-like pattern has been reported in adult-onset HLH with hypomorphic missense mutations with residual protein expression.[28] This association, thus, may possibly be limited to young children, and there may be other age-related factors, extrinsic triggers, and susceptibility loci influencing MR imaging pattern presentations.

We acknowledge the inherent limitations of our study due to its retrospective nature. Standardizing MR imaging protocols during the 8-year period from which the patients' records were recruited was difficult, and imaging parameters could have differed during this period and between institutions. Interpretation of the genotype correlation analysis remains limited due to small number of patients in the subgroups.

CONCLUSIONS

We systematically described MR imaging findings in a pediatric cohort of CNS HLH. Older children more commonly had a significant parenchymal disease pattern, which was associated with a worse clinical profile and 3 distinct subpatterns. We confirm a genotype correlation between disruptive mutations and a younger age of presentation and expand the same to an attenuated imaging pattern (pattern 2). Larger studies are needed to examine a possible age-related tendency of late-onset disruptive mutations or missense mutations with absent protein expression to present with atypical MR imaging patterns. Finally, because CNS manifestations can precede systemic signs and even remain restricted to the CNS, HLH should be considered in patients with atypical imaging presentations such as brainstem lesions or cerebellar edema and negative findings on work-up for other etiologies because this may be the only finding heralding the onset of HLH.

Disclosure forms provided by the authors are available with the full text and PDF of this article at www.ajnr.org.

REFERENCES

1. Voskoboinik I, Smyth MJ, Trapani JA. **Perforin-mediated target-cell death and immune homeostasis.** *Nat Rev Immunol* 2006;6:940–52 CrossRef Medline
2. Benson LA, Li H, Henderson LA, et al. **Pediatric CNS-isolated hemophagocytic lymphohistiocytosis.** *Neurol Neuroimmunol Neuroinflamm* 2019;6:e560 CrossRef Medline
3. Astigarraga I, Prats JM, Navajas A, et al. **Near fatal cerebellar swelling in familial hemophagocytic lymphohistiocytosis.** *Pediatr Neurol* 2004;30:361–64 CrossRef Medline
4. Koh KN, Im HJ, Chung NG, et al; Korea Histiocytosis Working Party. **Clinical features, genetics, and outcome of pediatric patients with hemophagocytic lymphohistiocytosis in Korea: report of a nationwide survey from Korea Histiocytosis Working Party.** *Eur J Haematol* 2015;94:51–59 CrossRef Medline
5. Deiva K, Mahlaoui N, Beaudonnet F, et al. **CNS involvement at the onset of primary hemophagocytic lymphohistiocytosis.** *Neurology* 2012;78:1150–56 CrossRef Medline
6. Rovaris M, Comi G, Rocca MA, et al. **Relevance of hypointense lesions on fast fluid-attenuated inversion recovery MR images as a marker of disease severity in cases of multiple sclerosis.** *AJNR Am J Neuroradiol* 1999;20:813–20 Medline
7. Mikaeloff Y, Adamsbaum C, Husson B, et al; KIDMUS Study Group on Radiology. **MRI prognostic factors for relapse after acute CNS inflammatory demyelination in childhood.** *Brain* 2004;127:1942–47 CrossRef Medline
8. Taieb G, Mulero P, Psimaras D, et al; French CLIPPERS group. **CLIPPERS and its mimics: evaluation of new criteria for the diagnosis of CLIPPERS.** *J Neurol Neurosurg Psychiatry* 2019;90:1027–38 CrossRef Medline
9. Henter JI, Samuelsson-Horne A, Aricò M, et al; Histocyte Society. **Treatment of hemophagocytic lymphohistiocytosis with HLH-94 immunochemotherapy and bone marrow transplantation.** *Blood* 2002;100:2367–73 CrossRef Medline
10. Bergsten E, Horne A, Aricó M, et al. **Confirmed efficacy of etoposide and dexamethasone in HLH treatment: long-term results of the cooperative HLH-2004 study.** *Blood* 2017;130:2728–38 CrossRef Medline
11. Pittock SJ, Debruyne J, Krecke KN, et al. **Chronic lymphocytic inflammation with pontine perivascular enhancement responsive to steroids (CLIPPERS).** *Brain* 2010;133:2626–34 CrossRef Medline
12. Tobin WO, Guo Y, Krecke KN, et al. **Diagnostic criteria for chronic lymphocytic inflammation with pontine perivascular enhancement**

responsive to steroids (CLIPPERS). *Brain* 2017;140:2415–25 CrossRef Medline
13. Xu XJ, Wang HS, Ju X-L, et al; Histiocytosis Study Group of the Chinese Pediatric Society. **Clinical presentation and outcome of pediatric patients with hemophagocytic lymphohistiocytosis in China: a retrospective multicenter study.** *Pediatr Blood Cancer* 2017;64:e26264 CrossRef Medline
14. Haddad E, Sulis ML, Jabado N, et al. **Frequency and severity of central nervous system lesions in hemophagocytic lymphohistiocytosis.** *Blood* 1997;89:794–800 Medline
15. Jovanovic A, Kuzmanovic M, Kravljanac R, et al. **Central nervous system involvement in hemophagocytic lymphohistiocytosis: a single-center experience.** *Pediatr Neurol* 2014;50:233–37 CrossRef Medline
16. Kollias SS, Ball WS, Tzika AA, et al. **Familial erythrophagocytic lymphohistiocytosis: neuroradiologic evaluation with pathologic correlation.** *Radiology*1994;192:743–54 CrossRef Medline
17. Horne A, Trottestam H, Aricò M, Histiocyte Society, et al. **Frequency and spectrum of central nervous system involvement in 193 children with haemophagocytic lymphohistiocytosis.** *Br J Haematol* 2008;140:327–35 CrossRef Medline
18. Ma W, Li XJ, Li W, et al. **MRI findings of central nervous system involvement in children with haemophagocytic lymphohistiocytosis: correlation with clinical biochemical tests.** *Clin Radiology* 2021;76:159.e9-159–17 CrossRef Medline
19. Rego I, Severino M, Micalizzi C, et al. **Neuroradiologic findings and follow-up with magnetic resonance imaging of the genetic forms of haemophagocytic lymphohistiocytosis with CNS involvement.** *Pediatr Blood Cancer* 2012;58:810–14 CrossRef Medline
20. Blincoe A, Heeg M, Campbell PK, et al. **Neuroinflammatory disease as an isolated manifestation of hemophagocytic lymphohistiocytosis.** *J Clin Immunol* 2020;40:901–16 CrossRef Medline
21. Chhabda S, Malik P, Reddy N, et al. **Relapsing demyelinating syndromes in children: a practical review of neuroradiological mimics.** *Front Neurol* 2020;11:627 CrossRef Medline
22. Sa M, Green LM, Abdel-Mannan O, et al. **Is chronic lymphocytic inflammation with pontine perivascular enhancement responsive to steroids (CLIPPERS) in children the same condition as in adults? Developmental medicine and child neurology.** *Dev Med Child Neurol* 2019;61:490–96 CrossRef Medline
23. Taieb G, Duflos C, Renard D, et al. **Long-term outcomes of CLIPPERS (chronic lymphocytic inflammation with pontine perivascular enhancement responsive to steroids) in a consecutive series of 12 patients.** *Arch Neurol* 2012;69:847–55 CrossRef Medline
24. McCreary D, Omoyinmi E, Hong Y, et al. **Development and validation of a targeted next-generation sequencing gene panel for children with neuroinflammation.** *JAMA Netw Open* 2019;2:e1914274 CrossRef Medline
25. Symmonds M, Waters PJ, Küker W, et al. **Anti-MOG antibodies with longitudinally extensive transverse myelitis preceded by CLIPPERS.** *Neurology* 2015;84:1177–79 CrossRef Medline
26. Bhoopalan SV, Campbell PK, Bag AK, et al. **Haemophagocytic lymphohistiocytosis restricted to the central nervous system.** *Arch Dis Child* 2021;106:527 CrossRef Medline
27. Khan SG, Binmahfoodh M, Alali M, et al. **Cerebellar swelling due to familial hemophagocytic lymphohistiocytosis: an unusual presentation.** *Eur J Paediatr Neurol* 2015;19:603–06 CrossRef Medline
28. Taieb G, Kaphan E, Duflos C, et al. **Hemophagocytic lymphohistiocytosis gene mutations in adult patients presenting with CLIPPERS-like syndrome.** *Neurol Neuroimmunol Neuroinflamm* 2021;8:e970 CrossRef Medline
29. Chiapparini L, Uziel G, Vallinoto C, et al. **Hemophagocytic lymphohistiocytosis with neurological presentation: MRI findings and a nearly miss diagnosis.** *Neurol Sci* 2011;32:473–77 CrossRef Medline
30. Gray PE, Shadur B, Russell S, et al. **Late-onset non-HLH presentations of growth arrest, inflammatory arachnoiditis, and severe infectious mononucleosis, in siblings with hypomorphic defects in *UNC13D*.** *Front Immunol* 2017;8:944.CrossRef Medline
31. Trizzino A, Stadt U. Z, Ueda I, et al; Histiocyte Society HLH Study group. **Genotype-phenotype study of familial haemophagocytic lymphohistiocytosis due to perforin mutations.** *J Med Genet* 2007;45:15–21 CrossRef Medline

Mapping Human Fetal Brain Maturation In Vivo Using Quantitative MRI

V.U. Schmidbauer, G.O. Dovjak, M.S. Yildirim, G. Mayr-Geisl, M. Weber, M.C. Diogo, G.M. Gruber, F. Prayer, R.-I. Milos, M. Stuempflen, B. Ulm, J. Binder, D. Bettelheim, H. Kiss, D. Prayer, and G. Kasprian

ABSTRACT

BACKGROUND AND PURPOSE: On the basis of a single multidynamic multiecho sequence acquisition, SyMRI generates a variety of quantitative image data that can characterize tissue-specific properties. The aim of this retrospective study was to evaluate the feasibility of SyMRI for the qualitative and quantitative assessment of fetal brain maturation.

MATERIALS AND METHODS: In 52 fetuses, multidynamic multiecho sequence acquisitions were available. SyMRI was used to perform multidynamic multiecho–based postprocessing. Fetal brain maturity was scored qualitatively on the basis of SyMRI-generated MR imaging data. The results were compared with conventionally acquired T1-weighted/T2-weighted contrasts as a standard of reference. Myelin-related changes in T1-/T2-relaxation time/relaxation rate, proton density, and MR imaging signal intensity of the developing fetal brain stem were measured. A Pearson correlation analysis was used to detect correlations between the following: 1) the gestational age at MR imaging and the fetal brain maturity score, and 2) the gestational age at MR imaging and the quantitative measurements.

RESULTS: SyMRI provided images of sufficient quality in 12/52 (23.08%) (range, 23 + 6–34 + 0) fetal multidynamic multiecho sequence acquisitions. The fetal brain maturity score positively correlated with gestational age at MR imaging (SyMRI: $r = 0.915$, $P < .001$/standard of reference: $r = 0.966$, $P < .001$). Myelination-related changes in the T2 relaxation time/T2 relaxation rate of the medulla oblongata significantly correlated with gestational age at MR imaging (T2-relaxation time: $r = -0.739$, $P = .006$/T2-relaxation rate: $r = 0.790$, $P = .002$).

CONCLUSIONS: Fetal motion limits the applicability of multidynamic multiecho–based postprocessing. However, SyMRI-generated image data of sufficient quality enable the qualitative assessment of maturity-related changes of the fetal brain. In addition, quantitative T2 relaxation time/T2 relaxation rate mapping characterizes myelin-related changes of the brain stem prenatally. This approach, if successful, opens novel possibilities for the evaluation of structural and biochemical aspects of fetal brain maturation.

ABBREVIATIONS: GA = gestational age; MDME = multidynamic multiecho; PD = proton density; R1 = T1-relaxation rate; R2 = T2-relaxation rate; SI = signal intensity; T1R = T1-relaxation time; T2R = T2-relaxation time

Ultrasonography is considered the mainstay of antenatal imaging and serves as the technique of choice for the structural examination of the human fetus in utero.[1-5] However, the sonography-based assessment of prenatal brain development has some specific limitations.[6-9] Foremost among these is that current sonography imaging systems do not allow a tissue-specific quantitative characterization of fetal brain maturity.[10]

Physical MR imaging properties have been proved to provide noninvasive biomarkers for the assessment of brain maturation[11] and may offer new possibilities in the prenatal detection of neurodevelopmental anomalies. Until now, the acquisition of quantitative parameters, underlying visually perceptible MR imaging signal intensity (SI) values, was considered a highly time-consuming process, which limited its applicability in a clinical setting.[12-16] Recent developments in quantitative MR imaging enable the generation of various MR imaging contrasts and quantitative maps based on a single multidynamic multiecho (MDME) sequence acquisition and, therefore, in a clinically acceptable imaging time.[17-19] The MDME data-postprocessing software SyMRI (Synthetic MR; Version 11.1.5) provides information about tissue-specific MR imaging properties such as proton density (PD) and relaxation

Received April 17, 2021; accepted after revision July 19.

From the Departments of Biomedical Imaging and Image-Guided Therapy (V.U.S., G.O.D., M.S.Y., M.W., M.C.D., F.P., R.-I.M., M.S., D.P. G.K), Neurosurgery (G.M.-G.), and Obstetrics and Gynecology (B.U., J.B., D.B., H.K.), Medical University of Vienna, Vienna, Austria; and Department of Anatomy and Biomechanics (G.M.G.), Karl Landsteiner University of Health Sciences, Krems an der Donau, Austria.

Paper previously presented at: Annual Meeting of the European Congress of Radiology, March 3–7, 2021; Virtual.

Please address correspondence to Gregor Kasprian, MD, Department of Biomedical Imaging and Image-Guided Therapy, Medical University of Vienna, Waehringer Guertel 18-20, 1090 Vienna, Austria; e-mail: gregor.kasprian@meduniwien.ac.at

Indicates article with online supplemental data.

http://dx.doi.org/10.3174/ajnr.A7286

Demographics and clinical characteristics

Fetal MDME Sequence Acquisitions ($n = 12$)	GA at MR Imaging	Sex	Position	Brain MR Imaging Findings
1	23 + 6	♀	Breech	Dolichocephaly
2	24 + 6	♂	Cephalic	Asymmetry of lateral ventricles
3	25 + 4	♂	Cephalic	No pathologic findings
4	25 + 4	♂	Cephalic	No pathologic findings
5	25 + 5	♀	Cephalic	No pathologic findings
6	25 + 5	♂	Breech	Altered signal of periventricular crossroads
7	26 + 6	♀	Cephalic	No pathologic findings
8	27 + 4	♂	Breech	No pathologic findings
9	29 + 6	♂	Cephalic	No pathologic findings
10	30 + 1	♂	Breech	No pathologic findings
11	32 + 4	♀	Cephalic	Agenesis of septum pellucidum
12	34 + 0	♀	Cephalic	Agenesis of corpus callosum, ventriculomegaly, hemorrhage (left cella media)

parameters (T1-relaxation time [T1R]/T1-relaxation rate [R1]; T2-relaxation time [T2R]/T2-relaxation rate [R2]).[17] Furthermore, this method allows the adjustment of TR, TE, and TI in retrospect, which enables an individual modulation of the MR imaging contrasts after data acquisition.[19] MDME-based imaging proved beneficial in a neonatal neuroimaging setting because this technique allows a reduction in examination time, while providing a variety of imaging data beyond the standard neonatal MR imaging protocol.[11,15,16] However, currently, the full potential of this technology for the investigation of brain maturation at early developmental stages is widely unexplored.

The aim of this study was to evaluate the feasibility of quantitative MDME-based postprocessing for human fetal brain imaging. For this purpose, qualitative neuroradiologic assessments of brain maturation based on SyMRI-generated and conventionally acquired MR imaging data were compared. The visual evaluation of fetal brain maturity was complemented by a self-assessment of confidence by the investigating radiologists. In addition, tissue-specific properties of the fetal brain stem were quantified, to investigate whether the described approach is sensitive to the detection of myelin-related changes.

MATERIALS AND METHODS

Ethics Approval

The Ethics Commission of the Medical University of Vienna approved the protocol of this study. All women provided written informed consent for fetal MR imaging before scanning and agreed to the scientific use of the acquired data.

Study Cohort

Between December 2019 and October 2020, a total of 52 fetal MR images, including MDME sequence acquisitions of the fetal brain, were collected at the Neuroradiology Department of a tertiary care hospital. All fetuses included in this study were referred for MR imaging by the Department of Obstetrics and Gynecology after a detailed sonographic examination by a fetal medicine specialist, according to European standards. Congenital abnormalities of the central nervous system were the most common indications for fetal MR imaging (Online Supplemental Data). A detailed overview of demographic and clinical characteristics of included fetuses is given in the Table. Fetal gestational age (GA) (weeks) was determined at the first trimester ultrasonographic screening.

Fetal MR Imaging Data Acquisition and SyMRI-Based MDME Postprocessing

Imaging was performed in accordance with the fetal MR imaging guidelines of the International Society of Sonography in Obstetrics and Gynecology.[20] All fetuses were examined using a standardized fetal MR imaging protocol of the brain (Online Supplemental Data) on the same Ingenia 1.5T MR imaging system (Philips Healthcare) equipped with a body coil. An MDME sequence (Online Supplemental Data) (acquisition time: 3 minutes and 20 seconds) was acquired (axial plane) by applying 2 repeat acquisition phases: phase a: saturation of 1 section by a section-selective saturation pulse (flip angle = 120°); and phase b: section-selective excitation pulses (flip angle = 90°) and section-selective refocusing pulses (flip angle = 180°) to generate a train of spin-echoes for another section.[17,21,22] Via the mismatch between the saturated section and the image section, a matrix with a variety of effects of R1/R2 was acquired.[21,22] Echo-trains, characterized by different saturation delays, were used to estimate T1-/T2-relaxation parameters.[17,21,22] The T1-relaxation constants allowed the local radiofrequency field (B_1) to be calculated.[21] On the basis of the acquired relaxation parameters and B_1, the PD can be computed.[17] SyMRI-based MDME postprocessing (postprocessing time: <1 minute) was applied to generate conventional MR imaging contrasts (Fig 1) and quantitative MR imaging maps (Fig 2) for qualitative and quantitative analysis. Color-coded voxels, according to the physical MR imaging properties, were used to generate quantitative maps.[21]

Fetal Brain Maturity Assessment

Before the evaluation of the MR imaging data, a visual review was performed. On the basis of the subjective judgment made by 1 fetal imaging specialist with 15 years of experience, fetuses were excluded from this study if qualitative and quantitative analyses were not possible due to severely degraded images by fetal motion. To assess fetal brain maturity, we used a qualitative scoring system based on existing brain-maturation scores.[15,23] Developmental aspects were evaluated on both conventionally acquired MR imaging contrasts (T1-weighted/snapshot inversion recovery, T2-weighted) (axial plane) and SyMRI-generated image

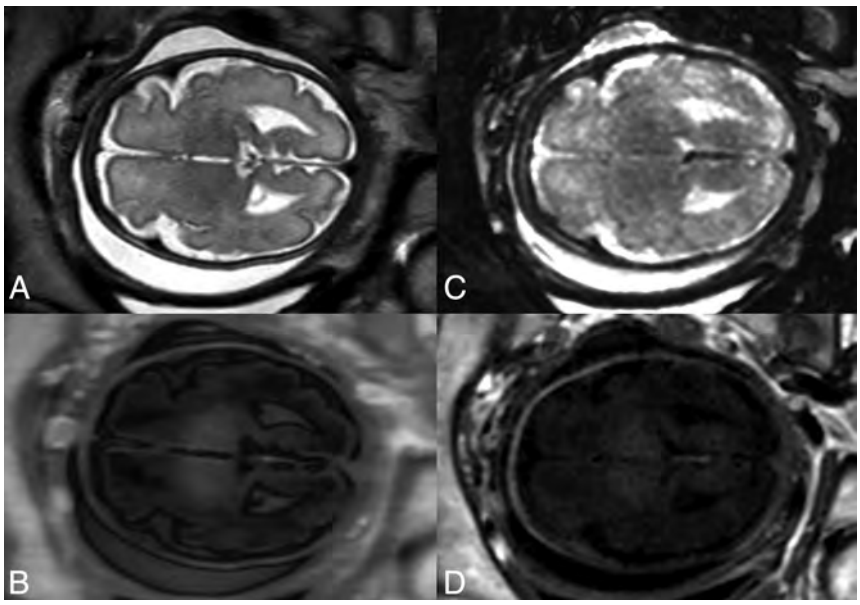

FIG 1. Conventionally acquired (*A* and *B*) and SyMRI-generated (*C* and *D*) fetal MR image data of comparable SIs: T2-weighted (*A*); snapshot inversion recovery (*B*); T2-weighted STIR (TR = 15,000 ms, TE = 100 ms, TI = 300 ms) (*C*); and T1-weighted inversion recovery (TR = 2500 ms, TE = 10 ms, TI = 1050 ms) (*D*). Presentation of SyMRI-generated MR imaging contrasts based on the default software settings for TR, TE, and TI.

data (T1-weighted/T1-weighted inversion recovery, T2-weighted/T2-weighted STIR, quantitative MR imaging maps) (axial plane) by 2 independent neuroradiologists (rater 1, with 15 years of experience, and rater 2, with 30 years of experience with fetal MR imaging), who were blinded to GA at MR imaging. The criteria used to determine brain maturity were the following: morphologic presentation of the frontal, occipital, and insular cortices according to Vossough et al;[23] the presence of the germinal matrix; identifiability of the primary sulci;[24] and fetal brain myelination (medulla oblongata, midbrain and inferior colliculus, thalamus, posterior limb of the internal capsule, and central region).[15]

SyMRI-generated quantitative MR imaging maps based on T1R/R1 and T2R/R2 were available for the assessment of brain myelination. The observers had the opportunity to adjust the windowing (conventionally acquired and SyMRI-generated MR imaging contrasts); TR, TE, and TI (SyMRI-generated MR imaging contrasts); and the color-coding scale (SyMRI-generated quantitative MR imaging maps) at their discretion during fetal brain maturity assessment. The scoring system is explained in the Online Supplemental Data. The points allocated for each evaluated developmental aspect were totaled, resulting in a fetal brain maturity total score for each included subject. Furthermore, both raters performed a Likert scale–based self-assessment of confidence with regard to the evaluation of fetal brain maturity. For this purpose, both raters allocated a minimum of 1 (not very confident) and a maximum of 4 (highly confident) points when assessing the 10 components of the score. The allocated points were totaled, resulting in a total score for confidence (minimum: 10 [lowest level of confidence]; maximum: 40 [highest level of confidence]) for each included subject.

Determination of Physical Properties of the Brain Stem

T1R (ms), R1 (s^{-1}), T2R (ms), R2 (s^{-1}), PD (%), and MR imaging SI values were determined by manual delineation of the medulla oblongata and the midbrain on SyMRI-generated image data (T1R/R1, T2R/R2, PD) and conventionally acquired T2-weighted contrasts (MR imaging SI values) (axial plane). The provided average values of the physical properties were calculated on the basis of the voxels within the drawn ROI. The ROI placement (Online Supplemental Data) was performed separately from fetal brain maturity assessment by 2 different investigators (investigator 1, with 2 years of experience and investigator 2, with 1 year of experience with fetal MR imaging), who were blinded to GA at MR imaging.

Statistical Analyses

Statistical analyses were performed using SPSS Statistics for Macintosh, Version 25.0 (2017; IBM) at a significance level of $\alpha = 5\%$ ($P < .05$).

To detect concordances of the fetal brain maturity assessment of both raters and the quantitative measurements of both investigators, we calculated an intraclass correlation coefficient. The intraclass correlation coefficient values of ≥0.75 were considered a strong correlation.[25] In case of high concordances, the results of 1 rater were reported.

Pearson correlation analyses were performed to assess correlations between the GA at MR imaging and the fetal brain maturity total score, and the quantitative measurements of the fetal brain stem.

RESULTS

Feasibility of SyMRI for Human Fetal Brain Imaging

Image data perceived to be of sufficient quality for qualitative and quantitative analysis were provided in 12/52 (23.08%) (mean GA at fetal MR imaging: 27 + 5 [SD, 3 + 1] weeks; range, 23 + 6–34 + 0 weeks) fetal MDME sequence acquisitions (Table and Online Supplemental Data). In 40/52 (76.92%) cases, the image quality of SyMRI-generated image data was highly degraded by fetal motion (Online Supplemental Data).

Interrater Reliability

There was a strong correlation between the fetal brain maturity total score assessed by both raters on SyMRI-generated MR imaging data, 0.798 (95% CI, 0.279–0.943). There was no strong correlation between the fetal brain maturity total score assessed by both raters on conventionally acquired MR imaging data, 0.587 (95% CI, −0.055–0.898). There were strong correlations between the quantitative measurements determined by both investigators,

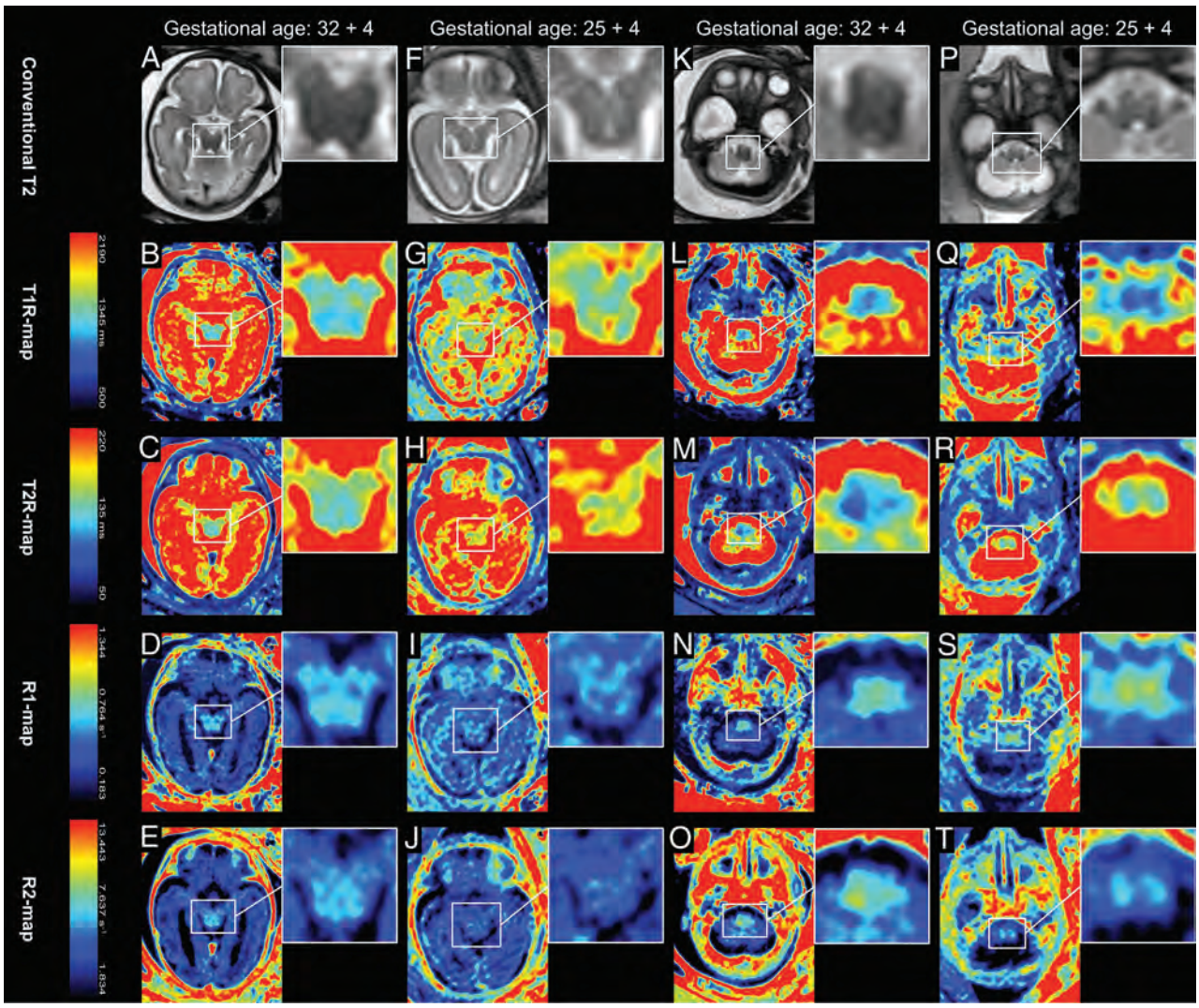

FIG 2. Presentation of conventionally acquired T2-weighted MR imaging contrasts (*A*, *F*, *K*, *P*) and quantitative MR imaging maps based on T1R (*B*, *G*, *L*, *Q*), T2R (*C*, *H*, *M*, *R*), R1 (*D*, *I*, *N*, *S*), and R2 (*E*, *J*, *O*, *T*). The color-coding, according to the T1-/T2-relaxation parameters, is indicated by the colored bars. The first (*A*, *B*, *C*, *D*, *E*) and the third columns (*K*, *L*, *M*, *N*, *O*) show MR imaging data from a fetus imaged at 32 + 4 weeks' GA. The second (*F*, *G*, *H*, *I*, *J*) and the fourth columns (*P*, *Q*, *R*, *S*, *T*) show MR imaging data from a fetus imaged at 25 + 4 weeks' GA. Brain myelination is indicated by a shortening of T1R/T2R (blue color-coding) and a prolongation of R1/R2 (yellow/orange color-coding). The color-coding of T1-relaxation parameters shows a distinct myelination of the medulla oblongata (*L*, *N*) and the midbrain tegmentum/tectum (*B*, *D*) at 32 + 4 weeks' GA. At 25 + 4 weeks' GA, only the medulla oblongata shows remarkable myelination (*Q*, *S*). The color-coding of T2-relaxation parameters indicates myelination of the medulla oblongata (*M*, *O*) at 32 + 4 weeks' GA. Beginning T2R-shortening and R2-prolongation are visible in the medulla oblongata (*R*, *T*) at 25 + 4 weeks' GA and in the midbrain tegmentum/tectum (*C*, *E*) at 32 + 4 weeks' GA.

ranging from 0.879 (95% CI, 0.643–0.963) to 0.989 (95% CI, 0.962–0.997) (Online Supplemental Data).

Assessment of Fetal Brain Maturity

The fetal brain maturity total score based on the assessment of SyMRI-generated MR imaging data showed a positive correlation with the GA at fetal MR imaging ($r = 0.915$, $P < .001$). The fetal brain maturity total score based on the assessment of conventionally acquired MR imaging data showed a positive correlation with the GA at fetal MR imaging (rater 1: $r = 0.966$, $P < .001$; rater 2: $r = 0.915$, $P < .001$) (Fig 3 and Online Supplemental Data).

The self-assessment of confidence by the investigating radiologists revealed a higher level of confidence for the assessment of fetal brain maturity on the basis of conventionally acquired MR imaging data (rater 1: median, 34; range, 33–34; and rater 2: median, 34.5; range, 31–40) compared with SyMRI-generated MR imaging data (rater 1: median, 32.5; range, 19–38, and rater 2: median, 33; range, 16–34) (Online Supplemental Data).

Physical Tissue Properties of the Brain Stem

Significant correlations were observed between the GA at fetal MR imaging and the T2R ($r = -0.739$, $P = .006$) and R2 ($r = 0.790$, $P = .002$) determined in the medulla oblongata. No significant correlations were observed between the GA at fetal MR imaging and the T1R ($r = -0.340$, $P = .280$), R1 ($r = 0.467$, $P = .126$), PD ($r = -0.071$, $P = .826$), or MR imaging SI ($r = -0.264$, $P = .408$) determined in the medulla oblongata. No significant correlations were observed between the GA at fetal MR imaging and the T1R ($r =$

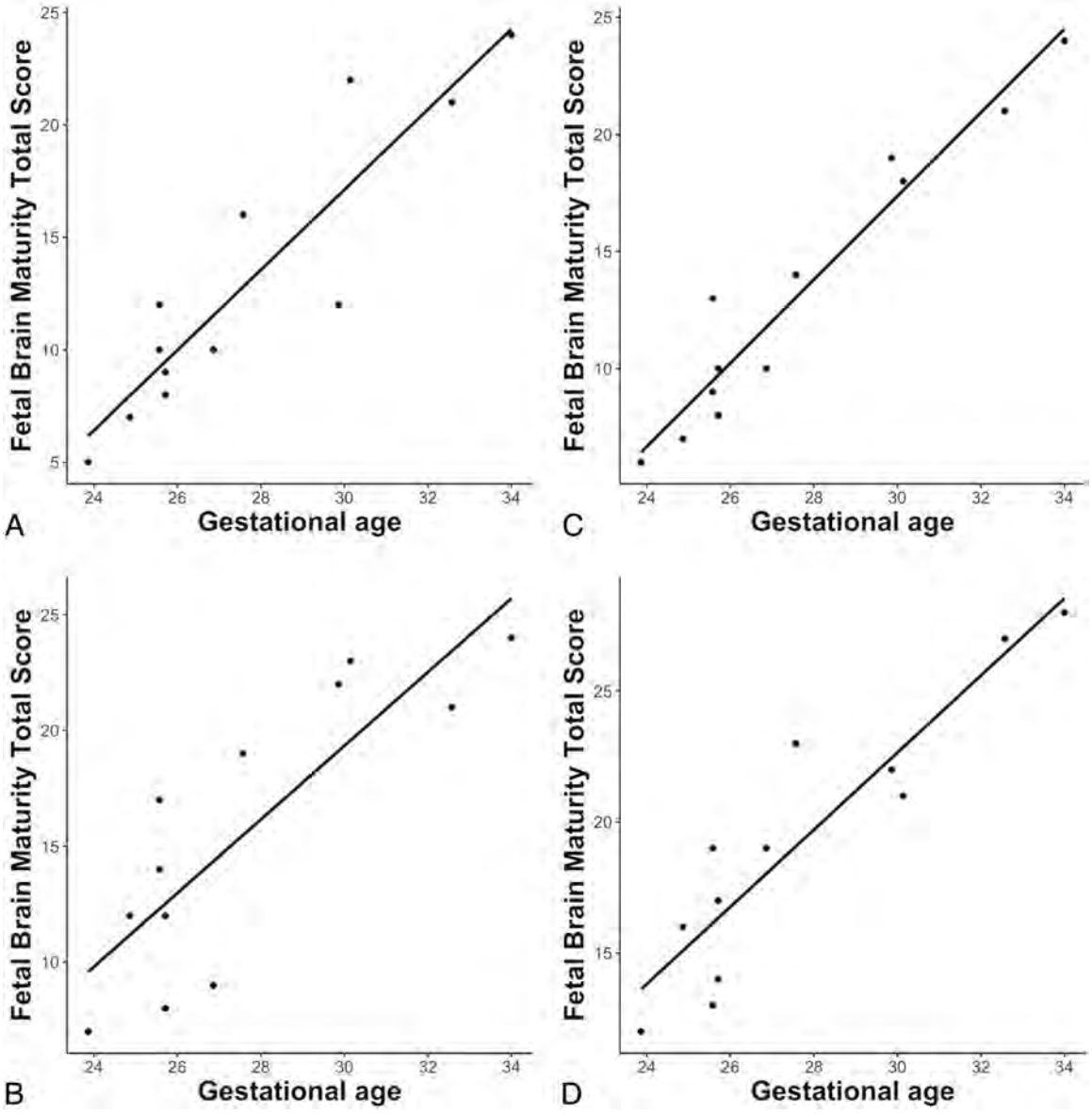

FIG 3. Pearson correlation between GA at MR imaging (x-axis) and the fetal brain maturity total score (y-axis) on the basis of SyMRI-generated (*A* and *B*) and conventionally acquired MR imaging data (*C* and *D*). Rater 1: *A* and *C*; rater 2: *B* and *D*.

−0.349, $P = .266$), R1 ($r = 0.363$, $P = .247$), T2R ($r = -0.461$, $P = .131$), R2 ($r = 0.567$, $P = .054$), PD ($r = -0.187$, $P = .561$), or MR imaging SI ($r = -0.376$, $P = .229$) determined in the midbrain (Fig 4 and Online Supplemental Data).

DISCUSSION

In this study, a novel quantitative MR imaging technique was used in prenatal neuroimaging. Due to the time-consuming acquisition of MDME sequences, the investigated approach was commonly limited by fetal motion. However, in a certain fraction of successful acquisitions, this technique provides multiple MR imaging data based on a single scan. The results presented here suggest that provided that an MDME sequence acquisition of sufficient quality is feasible, SyMRI-based image data supply additional multiparametric information to the assessment of fetal brain maturation.

The prenatal radiologic assessment of brain maturity is based on morphologic features and changes in physical tissue properties that lead to MR signal alterations.[23,26] Cortical development begins in the first trimester of pregnancy by cell proliferation in the ganglionic eminence, followed by neuronal migration through the hemispheres to the surface of the brain.[9,23,27] With time, postmigrational maturation becomes evident by opercularization, gyration, and sulcation.[28,29] In fetuses, primarily myelination processes alter the appearance of white matter.[30,31] Myelin is first seen in the spinal cord and proceeds rapidly cephalad in its dorsal portions.[26] In the sixth month of pregnancy, myelination is already detectable in the brain stem.[26] At 32 weeks of gestation, myelin-induced MR signal changes appear supratentorially.[26,32] Thus, cerebral development progresses through a predictable pattern, underlying the scoring system used in this study.[15,23]

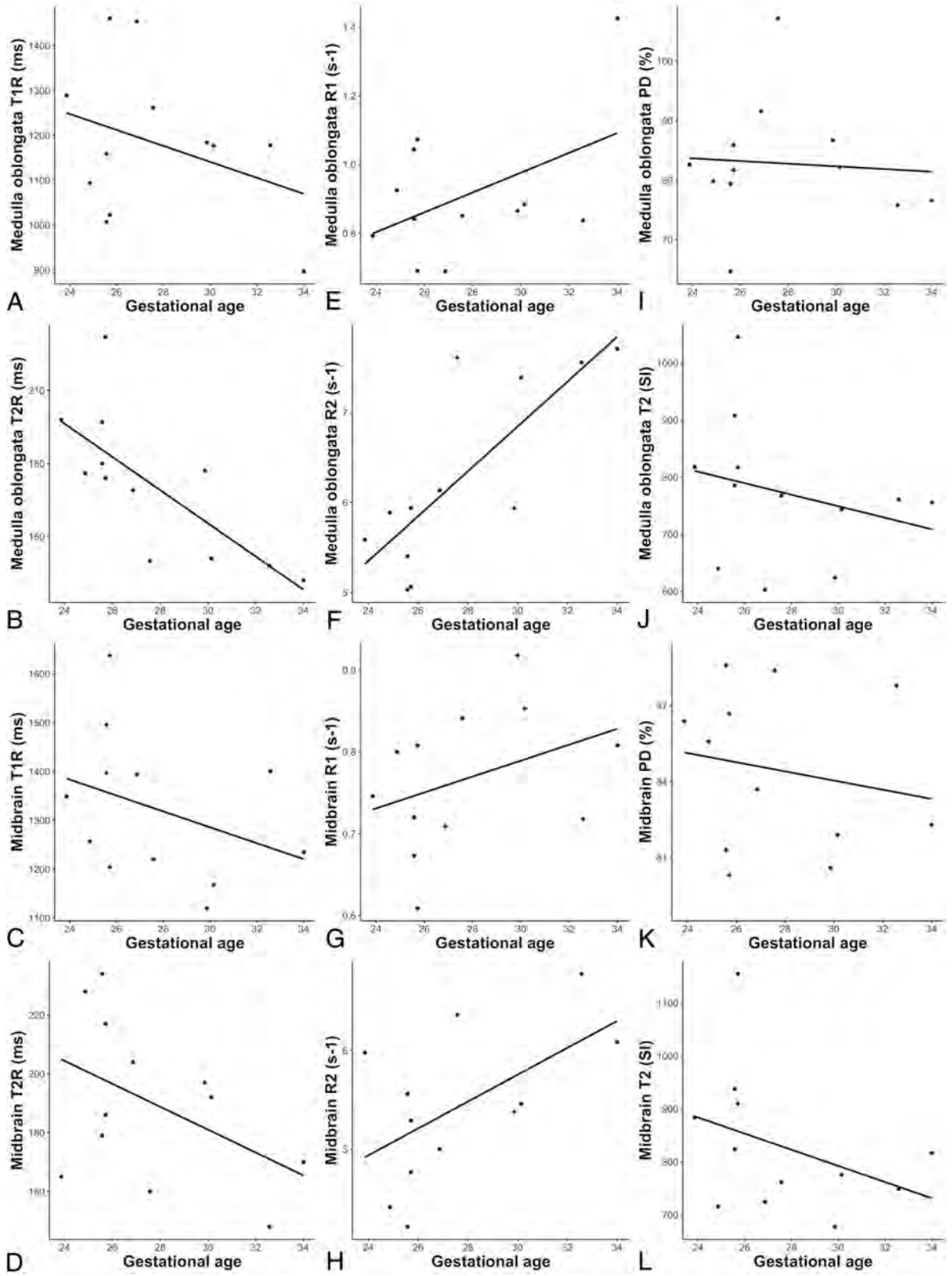

FIG 4. Pearson correlation between GA at MR imaging (x-axis) and quantitative MR imaging metrics (*y*-axis) determined by rater 1 (medulla oblongata [*A*, *B*, *E*, *F*, *I*, *J*]; midbrain [*C*, *D*, *G*, *H*, *K*, *L*]).

The assessment of fetal brain maturity based on SyMRI-generated and conventionally acquired MR imaging data revealed comparable results. However, overall, both investigating radiologists reported a higher level of confidence when structural aspects of brain maturation were evaluated on the basis of standard-of-care images, because this technique achieves higher spatial resolution.

Most interesting, relatively high levels of confidence were observed when SyMRI-generated maps were available for the evaluation of brain myelination. Quantitative MR imaging mapping has already been proved beneficial for the qualitative assessment of neonatal brain myelination because the color-coding visualizes myelin-induced changes more clearly.[15] The availability of various MR imaging maps for the evaluation of myelination might allow a more consistent neuroradiologic assessment of fetal brain maturity. In the present study, good/excellent concordances were observed between the raters when SyMRI-generated data were used for the evaluation of brain maturation.[25,33] In contrast, on the basis of the assessment of conventionally acquired MR imaging contrasts, there was only moderate/fair agreement.[25,33]

However, future development in sequence acceleration and *k*-space sampling are needed to improve the applicability of this technique in a clinical, fetal imaging setting.[34,35] Nonetheless, the principle of MDME-based postprocessing would be of great benefit in prenatal imaging. Moreover, this technique provides information about tissue-specific properties, which enables the characterization of brain myelination by a quantitative approach.[11,17]

In fetuses, the maximum quantities of myelin deposition are detectable in the brain stem.[26,32] Thus, this region best reflects myelin-induced changes in tissue-specific properties. These physical characteristics are linked to visually perceptible MR imaging SI values, which serve as the basis for the qualitative evaluation of brain myelination.[26] However, there was only a nonsignificant decrease of the T2 SI values of the brain stem. This finding highlights the limitations of a visual evaluation of myelination based on conventional MR imaging contrasts.[15] Most interesting, significant changes in T2-relaxation parameters of the medulla oblongata were found within the developing brain stem. There is evidence that the tightening of fully developed myelin sheaths induces T2R-shortening/R2-prolongation.[36-38] The medulla oblongata shows beginning myelination at 24 weeks' GA.[26] Hence, in contrast to other substructures of the brain stem, this section already contains a relatively huge amount of fully developed fibers at the end of the third trimester.[26,32] This fact could also explain that T2R-shortening and R2-prolongation were less pronounced in the midbrain. However, even though T1 MR imaging metrics proved sufficient to quantify brain myelination in neonates, T1R/R1 did not reveal significant changes prenatally.[11] Generally, similar to T1R/T2R, the PD decreases as myelin development proceeds.[30] In this study, there were no significant correlations between GA and spin density, confirming that PD does not allow a reliable quantitative characterization of brain myelination at early developmental stages.[11,30]

Delayed brain maturation is associated with neuropsychiatric disorders.[39,40] Quantitative MR imaging techniques generate valuable image data for the qualitative assessment of fetal brain maturity. Furthermore, these MR imaging data provide novel imaging biomarkers that allow a more differentiated assessment of prenatal brain development. The evaluation of fetal brain maturity is considered challenging in clinical neuroradiology, and current qualitative assessment strategies are limited by the low sensitivity of conventional MR imaging to small myelin quantities.[26] Thus, imaging modalities that enable a more reliable characterization of early developmental stages are greatly needed because these may help clinicians predict future neurodevelopmental disabilities. Quantitative MR imaging metrics could provide the opportunity to track prenatal brain maturation and detect developmental anomalies at an early stage, even though these subtle signal alterations may not be detected qualitatively.[26] However, this topic was outside the scope of this study but should be addressed in the future.

This study has several limitations. By default, the fetal MR imaging protocol did not include axial T1-weighted/snapshot inversion recovery MR image acquisitions, limiting a direct comparison of both imaging modalities to a certain extent. The investigated cohort was small and included pathologic brain scans. Furthermore, the limited sample impeded a reliable between-group comparison (fetuses with normal versus pathologic brains). Although only MDME-based image data of superior quality were included in this study, movement-related artifacts were still present in most cases. These limitations might have had an impact on both qualitative and quantitative analyses. Although strong correlations were observed, there is still an impact of movement-related artifacts on qualitative and quantitative analysis that needs to be clearly stated. Nonetheless, the results presented in this work are in line with findings of previous studies that investigated the characteristics of tissue-specific MR imaging properties at the early stages of cerebral development.[11,30]

CONCLUSIONS

The results of this study indicate that given ideal imaging conditions, MDME-based image data allow a qualitative assessment of maturity-related changes of the fetal brain in utero. In addition, this method makes tissue-specific quantitative information available and, therefore, provides quantitative imaging biomarkers for fetal neuroimaging. Future technical advances in accelerating multiecho sequence acquisitions will help to address current fetal motion-related limitations of this approach. Together with other recent advances in multicontrast, multiparametric estimation techniques such as STrategically Acquired Gradient Echo (STAGE),[41] our data indicate that this line of research is promising and is likely to evolve as a new radiologic strategy to provide complementary MR imaging information to the continuously improving quality of fetal sonography.

Disclosures: Gudrun Mayr-Geisl—*UNRELATED*: *Employment*: Medical University of Vienna, Department of Neurosurgery, *Comments*: University Assistant. Mariana C. Diogo—*RELATED*: *Grant*: Austrian Science Fund*; *Support for Travel to Meetings for the Study or Other Purposes*: Austrian Science Fund*; *UNRELATED*: *Employment*: Hospital Garcia de Orta, in the meantime, *Comments*: working as a neuroradiologist. Gregor Kasprian—*UNRELATED*: *Employment*: Medical University of Vienna, *Comments*: employed as Faculty; *Grants/Grants Pending*: Austrian Science Fund, *Comments*: I 3925-B27. *Money paid to the institution.

REFERENCES

1. Bonacquisto L. **Antenatal screening: the first and second trimester.** *Aust Fam Physician* 2011;40:785–87 Medline
2. Whitworth M, Bricker L, Mullan C. **Ultrasound for fetal assessment in early pregnancy.** *Cochrane Database Syst Rev* 2015;2015:CD007058 CrossRef Medline
3. Sylvan K, Ryding EL, Rydhstroem H. **Routine ultrasound screening in the third trimester: a population-based study: late ultrasound screening and prognosis.** *Acta Obstet Gynecol Scand* 2005;84:1154–58 CrossRef Medline

4. Karim JN, Roberts NW, Salomon LJ, et al. **Systematic review of first-trimester ultrasound screening for detection of fetal structural anomalies and factors that affect screening performance.** *Ultrasound Obstet Gynecol* 2017;50:429–41 CrossRef Medline
5. Malinger G, Paladini D, Haratz KK, et al. **ISUOG practice guidelines (updated): sonographic examination of the fetal central nervous system, Part 1: performance of screening examination and indications for targeted neurosonography.** *Ultrasound Obstet Gynecol* 2020;56:476–84 CrossRef Medline
6. Malinger G, Kidron D, Schreiber L, et al. **Prenatal diagnosis of malformations of cortical development by dedicated neurosonography.** *Ultrasound Obstet Gynecol* 2007;29:178–91 CrossRef Medline
7. Whitby EH, Paley MN, Sprigg A, et al. **Comparison of ultrasound and magnetic resonance imaging in 100 singleton pregnancies with suspected brain abnormalities.** *BJOG* 2004;111:784–92 CrossRef Medline
8. Whitby E, Paley MN, Davies N, et al. **Ultrafast magnetic resonance imaging of central nervous system abnormalities in utero in the second and third trimester of pregnancy: comparison with ultrasound.** *BJOG* 2001;108:519–26 CrossRef Medline
9. Jarvis DA, Griffiths PD. **Current state of MRI of the fetal brain in utero.** *J Magn Reson Imaging* 2019;49:632–46 CrossRef Medline
10. Rix A, Lederle W, Theek B, et al. **Advanced ultrasound technologies for diagnosis and therapy.** *J Nucl Med* 2018;59:740–46 CrossRef Medline
11. Schmidbauer V, Dovjak G, Geisl G, et al. **Impact of prematurity on the tissue properties of the neonatal brainstem: a quantitative MR approach.** *AJNR Am J Neuroradiol* 2021;42:581–89 CrossRef Medline
12. Deoni SCL, Peters TM, Rutt BK. **High-resolution T1 and T2 mapping of the brain in a clinically acceptable time with DESPOT1 and DESPOT2.** *Magn Reson Med* 2005;53:237–41 CrossRef Medline
13. Deoni SCL, Mercure E, Blasi A, et al. **Mapping infant brain myelination with magnetic resonance imaging.** *J Neurosci* 2011;31:784–91 CrossRef Medline
14. McKenzie CA, Chen Z, Drost DJ, et al. **Fast acquisition of quantitative T2 maps.** *Magn Reson Med* 1999;41:208–12 CrossRef Medline
15. Schmidbauer V, Geisl G, Diogo M, et al. **SyMRI detects delayed myelination in preterm neonates.** *Eur Radiol* 2019;29:7063–72 CrossRef Medline
16. Schmidbauer V, Geisl G, Diogo MC, et al. **Validity of SyMRI for assessment of the neonatal brain.** *Clin Neuroradiol* 2021;31:315–23 CrossRef Medline
17. Warntjes JB, Leinhard OD, West J, et al. **Rapid magnetic resonance quantification on the brain: optimization for clinical usage.** *Magn Reson Med* 2008;60:320 29 CrossRef Medline
18. McAllister A, Leach J, West H, et al. **Quantitative synthetic MRI in children: normative intracranial tissue segmentation values during development.** *AJNR Am J Neuroradiol* 2017;38:2364–72 CrossRef Medline
19. Tanenbaum LN, Tsiouris AJ, Johnson AN, et al. **Synthetic MRI for clinical neuroimaging: results of the Magnetic Resonance Image Compilation (MAGiC) prospective, multicenter, multireader trial.** *AJNR Am J Neuroradiol* 2017;38:1103–10 CrossRef Medline
20. Prayer D, Malinger G, Brugger PC, et al. **ISUOG practice guidelines: performance of fetal magnetic resonance imaging.** *Ultrasound Obstet Gynecol* 2017;49:671–80 CrossRef Medline
21. Hagiwara A, Warntjes M, Hori M, et al. **SyMRI of the brain: rapid quantification of relaxation rates and proton density, with synthetic MRI, automatic brain segmentation, and myelin measurement.** *Invest Radiol* 2017;52:647–57 CrossRef Medline
22. Kang KM, Choi SH, Kim H, et al. **The effect of varying slice thickness and interslice gap on T1 and T2 measured with the multidynamic multiecho sequence.** *MRMS* 2019;18:126–33 CrossRef Medline
23. Vossough A, Limperopoulos C, Putt ME, et al. **Development and validation of a semiquantitative brain maturation score on fetal MR images: initial results.** *Radiology* 2013;268:200–07 CrossRef Medline
24. Garel C, Chantrel E, Brisse H, et al. **Fetal cerebral cortex: normal gestational landmarks identified using prenatal MR imaging.** *AJNR Am J Neuroradiol* 2001;22:184–89 Medline
25. Cicchetti D. **Guidelines, criteria, and rules of thumb for evaluating normed and standardized assessment instruments in psychology.** *Psychol Assess* 1994;6:284–90 CrossRef
26. van der Knaap MS, Barkhof F, Valk J. *Magnetic Resonance of Myelination and Myelin Disorders*. 3rd ed. Springer-Verlag; 2005
27. Prayer D, Kasprian G, Krampl E, et al. **MRI of normal fetal brain development.** *Eur J Radiol* 2006;57:199–216 CrossRef Medline
28. van der Knaap MS, van Wezel-Meijler G, Barth PG, et al. **Normal gyration and sulcation in preterm and term neonates: appearance on MR images.** *Radiology* 1996;200:389–96 CrossRef Medline
29. Poon LC, Sahota DS, Chaemsaithong P, et al. **Transvaginal three-dimensional ultrasound assessment of Sylvian fissures at 18–30 weeks' gestation.** *Ultrasound Obstet Gynecol* 2019;54:190–98 CrossRef Medline
30. Lee SM, Choi YH, You SK, et al. **Age-related changes in tissue value properties in children: simultaneous quantification of relaxation times and proton density using synthetic magnetic resonance imaging.** *Invest Radiol* 2018;53:236–45 CrossRef Medline
31. Ding XQ, Kucinski T, Wittkugel O, et al. **Normal brain maturation characterized with age-related T2 relaxation times: an attempt to develop a quantitative imaging measure for clinical use.** *Invest Radiol* 2004;39:740–46 CrossRef Medline
32. Yakovlev P, Lecours A. The myelogenetic cycles of regional maturation of the brain. In: Minkowski A, ed. *Regional Development of the Brain in Early Life*. Blackwell; 1967:3–70
33. Koo TK, Li MY. **A guideline of selecting and reporting intraclass correlation coefficients for reliability research.** *J Chiropr Med* 2016;15:155–63 CrossRef Medline
34. Roy CW, Seed M, Macgowan CK. **Accelerated MRI of the fetal heart using compressed sensing and metric optimized gating.** *Magn Reson Med* 2017;77:2125–35 CrossRef Medline
35. Senel LK, Kilic T, Gungor A, et al. **Statistically segregated k-space sampling for accelerating multiple-acquisition MRI.** *IEEE Trans Med Imaging* 2019;38:1701–14 CrossRef Medline
36. Wang S, Ledig C, Hajnal JV, et al. **Quantitative assessment of myelination patterns in preterm neonates using T2-weighted MRI.** *Sci Rep* 2019;9:12938 CrossRef Medline
37. Barkovich AJ, Lyon G, Evrard P. **Formation, maturation, and disorders of white matter.** *AJNR Am J Neuroradiol* 1992;13:447–61 Medline
38. Dubois J, Dehaene-Lambertz G, Kulikova S, et al. **The early development of brain white matter: a review of imaging studies in fetuses, newborns and infants.** *Neuroscience* 2014;276:48–71 CrossRef Medline
39. Wu Y, Stoodley C, Brossard-Racine M, et al. **Altered local cerebellar and brainstem development in preterm infants.** *Neuroimage* 2020;213:116702 CrossRef Medline
40. Fitzgerald E, Boardman JP, Drake AJ. **Preterm birth and the risk of neurodevelopmental disorders: is there a role for epigenetic dysregulation?** *Curr Genomics* 2018;19:507–21 CrossRef Medline
41. Qu F, Sun T, Chen Y, et al. **Fetal brain tissue characterization at 1.5 T using STrategically Acquired Gradient Echo (STAGE) imaging.** *Eur Radiol* 2021;31:5586–94 CrossRef Medline

Prenatal Diagnosis of Third and Fourth Branchial Apparatus Anomalies: Case Series and Comparison with Lymphatic Malformation

Y. Li, A. Mashhood, M.D. Mamlouk, C.E. Lindan, V.A. Feldstein, and O.A. Glenn

ABSTRACT

BACKGROUND AND PURPOSE: Third and fourth branchial apparatus anomalies are rare congenital anomalies. The purpose of this study was to investigate imaging features of these lesions on fetal MR imaging in comparison with lymphatic malformations, the major competing differential diagnosis in these cases.

MATERIALS AND METHODS: A retrospective review of our institutional fetal MR imaging database between 1997 and 2019 resulted in 4 patients with confirmed third and fourth branchial apparatus anomalies and 14 patients with confirmed lymphatic malformations. The imaging features were reviewed by consensus, and the Fisher exact test was used to evaluate statistically significant differences between these 2 populations.

RESULTS: Four cases of third and fourth branchial apparatus anomalies were imaged at 29 weeks 1 day (range, 23 weeks 1 day to 33 weeks 4 days). All 4 cases demonstrated unilateral, unilocular cysts without reduced diffusion or hemorrhage and a medially directed beaked contour that tapered between the spine and airway at the level of the piriform sinus. Compared with 14 cases of fetal lymphatic malformations imaged at 27 weeks 6 days (range, 21 weeks 3 days to 34 weeks 6 days), third and fourth branchial apparatus cysts were significantly more likely to be unilocular ($P < .005$) and to have a medially beaked contour ($P < .005$). The combination of features of unilateral, unilocular, and medially beaked contour was observed only in the fetuses with third and fourth branchial apparatus cysts ($P < .001$).

CONCLUSIONS: The presence of a left-sided unilocular cyst with a medially beaked contour tapering at the level of the piriform sinus suggests the diagnosis of third and fourth branchial apparatus anomaly. Accurate diagnosis in the prenatal period allows proper counseling, genetic work-up, and treatment, potentially sparing patients from recurrent infections and associated morbidity.

ABBREVIATION: SS = single-shot

Anomalies of the branchial apparatus are among the most common congenital abnormalities of the head and neck, second only to thyroglossal duct cysts, and are thought to represent failure of obliteration of the branchial clefts or cervical sinus of His.[1] Third and fourth branchial apparatus anomalies are rare, comprising only 1%–10% of all branchial apparatus anomalies.[2-4] These anomalies arise from the piriform sinus and course through the deep spaces of the neck, often descending into the mediastinum along the tracheoesophageal groove. Although third and fourth branchial apparatus anomalies are relatively less common, they are clinically important to recognize because they can present acutely with abscess, suppurative thyroiditis,[5,6] and even life-threatening airway compromise and need to be appropriately treated.[7,8] These anomalies typically manifest postnatally as fistulas or sinuses but can sometimes manifest in utero. There are few published reports on the prenatal imaging appearance of these lesions.

We present 4 cases of third or fourth branchial apparatus anomalies diagnosed prenatally with MR imaging and describe the prenatal MR imaging features suggestive of this diagnosis. We compare these imaging features with those seen in lymphatic malformations, the most common cystic lesion in the posterior cervical space, to investigate distinguishing features of these entities. Last, we correlate our prenatal findings with postnatal imaging, surgery, pathology, and clinical follow-up.

Received April 13, 2021; accepted after revision July 19.

From the Department of Radiology and Biomedical Imaging (Y.L., C.E.L., V.A.F., O.A.G.), University of California San Francisco, San Francisco, California; Palo Alto Veteran Affairs Medical Center (A.M.), Stanford University, Palo Alto, California; and The Permanente Medical Group (M.D.M.), Kaiser Permanente Medical Center Santa Clara, Santa Clara, California.

Paper previously presented at: Annual Meeting of the American Society of Pediatric Neuroradiology, January 10–12, 2020; Miami, Florida; it won a Cum Laude Award in Scientific Posters.

Please address correspondence to Yi Li, MD, Neuroradiology Section, Department of Radiology and Biomedical Imaging, University of California, San Francisco, 505 Parnassus Ave, M-391, San Francisco, CA 94143-0628; e-mail: yi.li@ucsf.edu; @YiLi MD

Indicates article with online supplemental video.

http://dx.doi.org/10.3174/ajnr.A7293

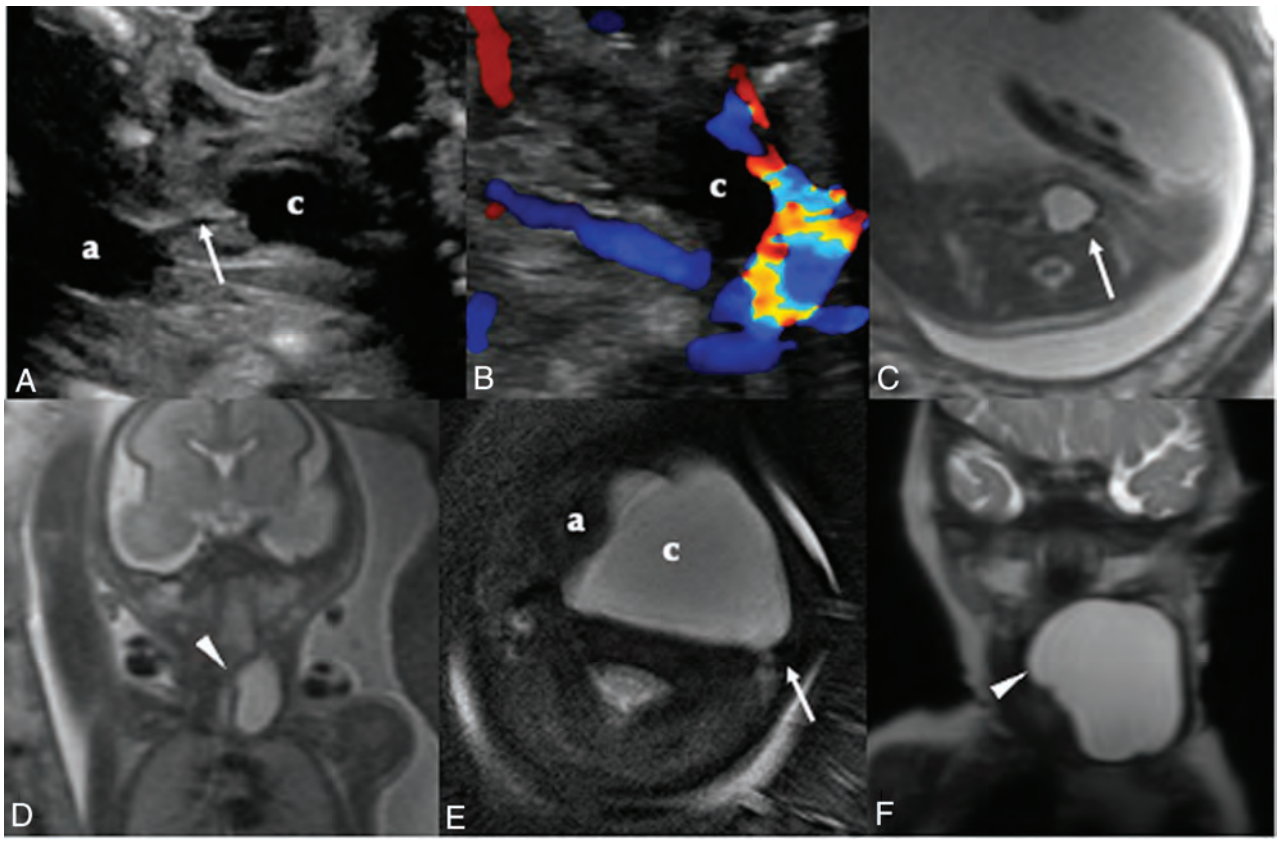

FIG 1. Patient 1 was initially identified as having a cystic neck mass on prenatal sonography. *A*, Sonography at 23 weeks demonstrates a left-sided cystic neck mass and communication (*arrow*) between the airway (a) and cyst (c). Doppler imaging (*B*) confirms the absence of intralesional vascular flow. Cine sonography imaging (Online Supplemental Video) shows fluctuation in the size of the cystic lesion with fetal breathing motion. Fetal MR imaging at 23 weeks' gestation with axial T2 SS FSE demonstrates (*C*) a left-sided unilocular cystic lesion that approaches but does not displace the airway on the axial image. The carotid sheath (*arrow*) is posterior to the cyst (*arrow*). Coronal image (*D*) from the same scan highlights the tubular shape of the lesion with a medial beak (*arrowhead*). Postnatal axial T2 image (*E*) shows interval growth of the lesion, with better visualization of the posteriorly displaced carotid sheath (*arrow*) relative to the cyst (c). The airway is displaced to the right (a). Coronal T2 image (*F*) from the same postnatal scan demonstrates the medial beak (*arrowhead*) and tubular shape of the lesion.

MATERIALS AND METHODS

In this institutional review board–approved, Health Insurance Portability and Accountability Act–compliant study, we searched the University of California San Francisco fetal MR imaging database for all reports of fetal neck MR imaging with cystic neck masses performed between 1997 and 2019. After correlation with available postnatal surgical reports and/or pathology, we identified 4 patients with surgically and/or pathologically confirmed third and fourth branchial apparatus anomalies and 14 patients with confirmed lymphatic malformations. Of the 4 patients with third and fourth branchial apparatus anomalies, 1 patient was scanned with 1.5T MR imaging (GE Healthcare Signa, Waukesha, WI) and the 3 others were scanned with 3T MR imaging (GE Healthcare Discovery 750, Waukesha, WI). One of the 4 patients underwent 2 fetal MRIs, both at 3T. Of the 14 cases of lymphatic malformation, 7/14 (50%) cases were imaged at 1.5T (GE Healthcare Signa, Waukesha, WI) and 7/14 (50%) were imaged at 3T (GE Healthcare Discovery 750, Waukesha, WI). The fetal neck MR imaging protocol at our institution includes a sagittal maternal large FOV single-shot (SS) FSE for localization, and then 2 or 3 acquisitions in each of the 3 planes of T2-weighted real-time SS FSE centered over the fetal neck (TR = 4000 ms, TE = 100 ms, 3-mm section thickness/0-mm section spacing, FOV = 24.0, matrix = 224 × 256). Additional sequences include axial and coronal diffusion-weighted imaging (b = 800, TR = 4000 ms, TE = minimum, 3-mm section thickness/0-mm section spacing, FOV = 32.0, matrix = 64 × 128) and axial echo-planar imaging (TR = 4000 ms, TE = 90 ms, 3-mm section thickness/0-mm section spacing, FOV = 25.0, matrix = 100 × 100).

Two radiologists with expertise in pediatric neuroradiology (Y.L., O.A.G.) and 1 radiologist with expertise in obstetric sonography (V.A.F.) reviewed the imaging by consensus and rated the location, size, locularity, laterality, vascular displacement, the presence of a medial beak, airway displacement, thyroid and mediastinal involvement, as well as T1, T2, DWI, and EPI characteristics of the masses. The Fisher exact test was used to evaluate statistically significant differences in these characteristics between third and fourth branchial apparatus anomalies and lymphatic malformations. Postnatal surgical and pathology reports were also reviewed, and clinical follow-up was obtained when available.

RESULTS

Fetal MR Imaging of Third and Fourth Branchial Apparatus Anomalies

We identified 4 cases of prenatally diagnosed third and fourth branchial apparatus anomalies. In all 4 cases, the patients were referred

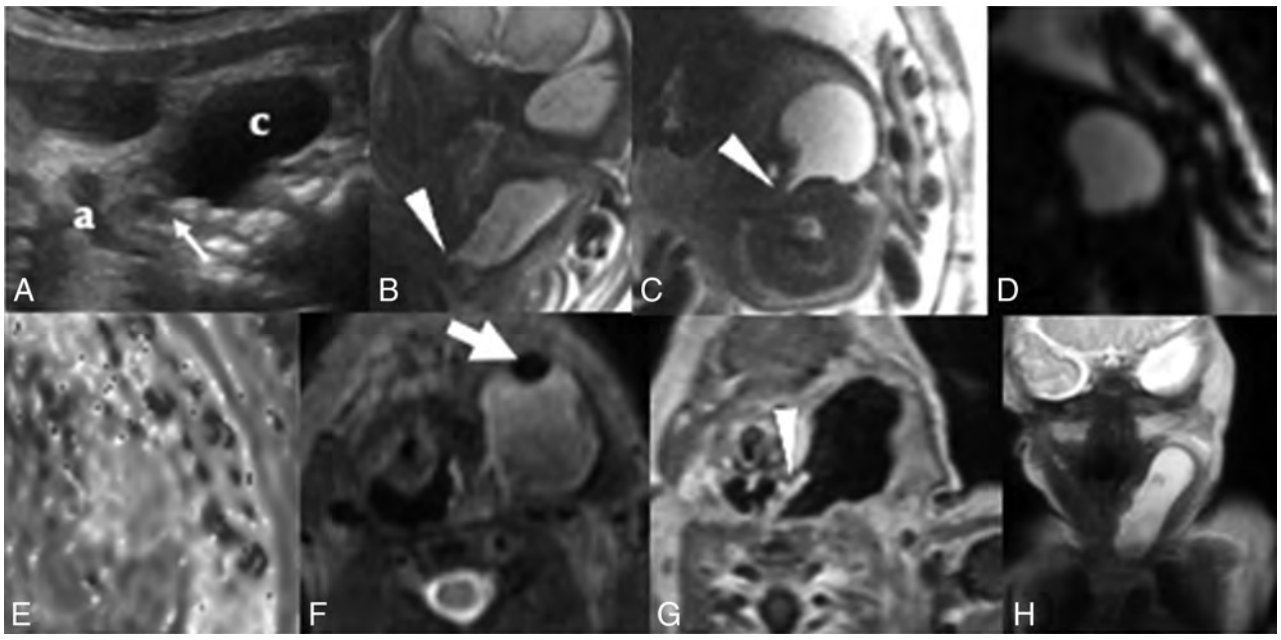

FIG 2. Prenatal sonography in patient 2 (*A*) demonstrates a left-sided cystic lesion in the neck. The lesion (c) lies lateral to the airway (a) and courses posterior to the airway as it extends medially (*white arrow*). Coronal (*B*) and axial (*C*) T2 SS FSE fetal MR images at 31 weeks' gestation show a tubular cystic neck lesion with a beak (*arrowhead*) that extends medially and posterior to the airway. Axial EPI diffusion-weighted imaging (*D*) and an ADC map (*E*) demonstrate no abnormal susceptibility or reduced diffusion. Postnatal T2 imaging (*F*) in the same patient shows a nondependent hypointensity (*white arrow*) within the lesion after birth, compatible with air. Postcontrast T1 image (*G*) shows a communication with the airway (*white arrowhead*), confirmed intraoperatively following the postnatal scan. Coronal T2 image (*H*) demonstrates the tubular shape of the sinus.

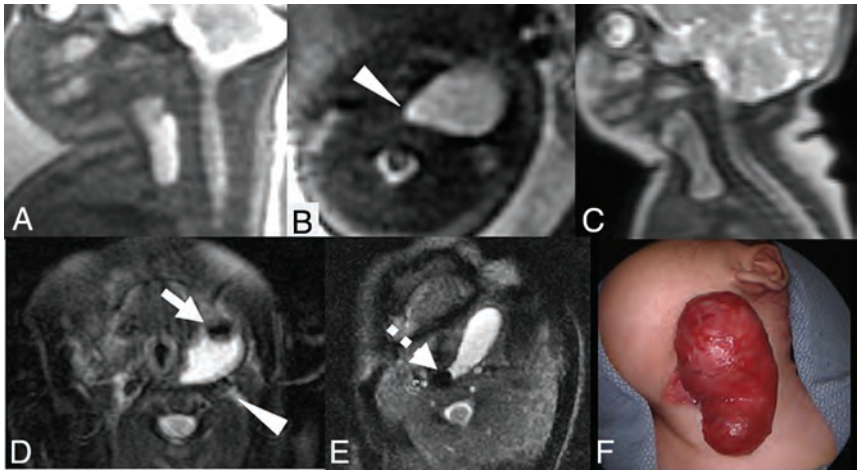

FIG 3. Fetal MR imaging for patient 3 at 20 weeks demonstrates a unilocular left-sided cystic neck lesion extending into the mediastinum in the sagittal (*A*) and axial (*B*) planes. The lesion tapers toward the midline with a medial beak (*arrowhead*) and extends into the mediastinum. Postnatal imaging demonstrates a similar craniocaudal extent of the cystic lesion (*C*) compared with the prenatal image (*A*). T2 fat-saturated postnatal imaging (*D*) demonstrates a focus of air (*white arrow*) within the lesion, with posterior displacement of the carotid artery (*white arrowhead*). Positioning the patient in the left lateral decubitus position (*E*) shows movement of the air bubble (*dashed arrow*) with repositioning. Postoperative photograph (*F*) of the cystic lesion in the neck before excision. Operative findings confirmed a sinus tract communicating with the piriform sinus.

for fetal MR imaging for evaluation of a unilateral, unilocular, cystic neck mass detected on routine prenatal sonography (Figs 1–4) at a mean gestational age of 20 weeks 3 days (range, 18 weeks 6 days to 21 weeks 0 days). Fetal MRIs were performed following the ultrasounds at a mean gestational age of 29 weeks 1 day (range, 23 weeks 1 day to 33 weeks 4 days). In the case in which a second fetal MR imaging was performed to assist with delivery planning, the second MR imaging occurred 9 weeks after the first, at 37 weeks gestational age.

In all 4 cases, on sonography, the cysts were unilocular and anechoic without internal debris. Features of the cysts by fetal MR imaging are listed in the Table. On fetal MR imaging, the cysts were homogeneously T2-hyperintense and T1-hypointense. In the 2 cases in which DWI was performed, the lesions demonstrated increased diffusivity. No hemorrhage was seen on EPI in any of the 4 cases. All cysts were unilateral, left-sided, and involved the deep spaces of the neck and displaced the ipsilateral carotid space in a posterior-medial direction and the sternocleidomastoid muscle laterally. All 4 cases demonstrated a medially directed beaked contour that tapered between the spine and the airway at the level of the piriform sinus. There were varying degrees of mass effect on the airway in 3 cases, and the lesions crossed the midline posterior to the airway in 2 cases. In all 4 cases, the lesion extended inferiorly to contact the thyroid gland, and in 3 cases, the lesion extended into the mediastinum.

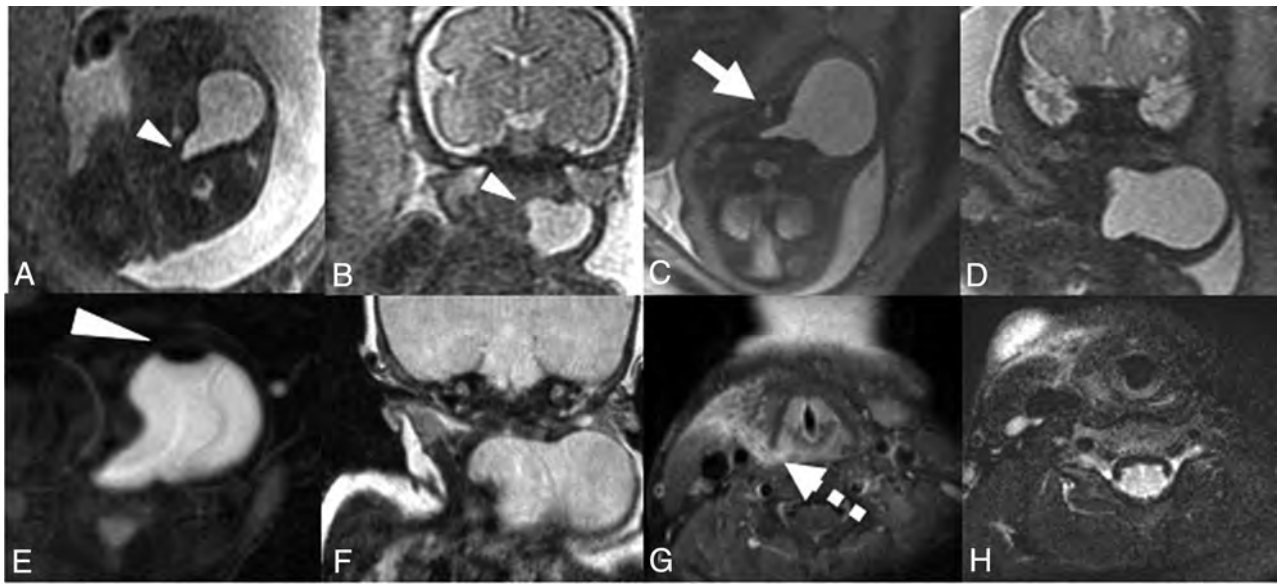

FIG 4. Fetal MR imaging of patient 4 in the axial (*A*) and coronal (*B*) planes at 28 weeks demonstrates a left-sided unilocular cystic lesion, with medial beaking (*arrowhead*), extending medially posterior to the airway, without mass effect on the airway. Axial (*C*) and coronal (*D*) T2 SS FSE fetal MR imaging at 37 weeks demonstrates interval growth of the cystic lesion, now displacing the airway (*white arrow*) to the right. Postnatal axial T2 fat-saturated image (*E*) demonstrates a nondependent hypointensity (*white arrowhead*), compatible with air within the cyst, which appears to have continued to enlarge on the coronal image (*F*) compared with the fetal MR imaging at 37 weeks' gestation (*D*). A contralateral right-sided fistula in the same patient presented at 5 years of age, superiorly involving the piriform sinus (*dashed arrow*) on the axial T1 fat-saturated postcontrast image (*G*) and extending to the skin on the T2 fat-saturated image (*H*) more inferiorly. Bilateral third and fourth branchial anomalies are rare, but occur in 2%–3% of cases and are often familial.[26] The right-sided fistula was also hypothesized to represent a pseudofistula acquired through multiple repeat infections of the branchial apparatus anomaly.

Imaging characteristics of postnatally confirmed fetal third or fourth branchial apparatus anomalies compared with consecutive cases of fetal lymphatic malformation

	Third or Fourth Branchial Apparatus Anomalies ($n = 4$)	Lymphatic Malformation ($n = 14$)	*P* Value
Unilateral	4/4 (100%)	5/14 (36%)	$P = .08$
Unilocular	4/4 (100%)	2/14 (14%)	$P = .005$
Medial beak	4/4 (100%)	2/14 (14%)	$P = .005$
Combination of findings: unilateral, unilocular, with medial beaking	4/4 (100%)	0/14 (0%)	$P < .001$
Vascular displacement	4/4 (100%)	7/14 (50%)	$P = .12$
Mediastinal involvement	3/4 (75%)	5/14 (36%)	$P = .28$
Displaces airway	3/4 (75%)	11/14 (79%)	$P = 1.00$
Extends posterior to airway	4/4 (100%)	7/14 (50%)	$P = .07$
Contacts thyroid	4/4 (100%)	9/14 (64%)	$P = .12$
Areas of susceptibility on EPI	0/4 (0%)	4/11 (36%)	$P = .41$
Areas of T1 hyperintensity	0/3 (0%)	3/12 (25%)	$P = 1.00$

In the case with a follow-up fetal MR imaging 9 weeks later, the cyst demonstrated interval growth, but there was no change in its morphology or signal characteristics.

In one case on prenatal sonography, the lesion was noted to fluctuate in size with swallowing, suggesting communication with the airway (Online Supplemental Video).

Comparison with Fetal Lymphatic Malformation

Fourteen cases of fetal lymphatic malformations were imaged by fetal MR imaging at a mean gestational age of 27 weeks 6 days (range, 21 weeks 3 days to 34 weeks 6 days).

In comparison with the cases of fetal lymphatic malformations, the third and fourth branchial apparatus cysts demonstrated several distinguishing features (Table). Third/fourth branchial apparatus cysts were significantly more likely to be unilocular ($P < .005$) and to have a medially beaked contour ($P < .005$). Cystic lateral neck masses that demonstrated all 3 features in combination (unilateral, unilocular, with a medially beaked contour) were all subsequently confirmed to be third and fourth branchial apparatus cysts ($P < .001$). Two of the 14 lymphatic malformations were unilocular, but neither were in the expected location of the third and fourth branchial apparatus anomalies. One was in the left suboccipital region extending into the posterior neck, and the other involved the scalp near the vertex. Additionally, of the unilateral cystic lymphatic malformations that involved the deep spaces of the neck that were in reasonable locations for third or fourth branchial apparatus anomalies, none were unilocular or demonstrated the medially beaked appearance (Fig 5).

Postnatal Follow-up

In all 4 cases of third and fourth branchial apparatus anomalies, the diagnosis was suggested prenatally on the basis of these imaging

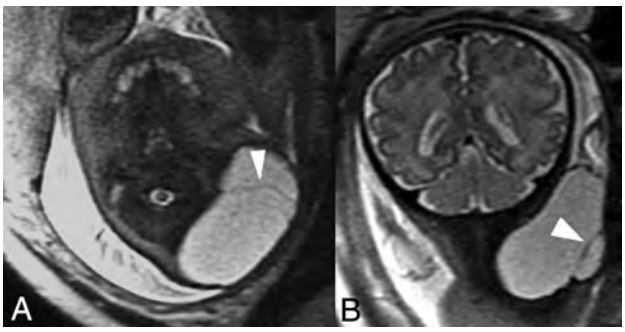

FIG 5. Axial (*A*) and coronal (*B*) T2 SS FSE fetal MR imaging from a representative patient with a postnatally confirmed lymphatic malformation, imaged at 34 weeks 6 days. Although the left-sided cystic neck lesion is in a location in which third and fourth branchial apparatus anomalies occur, the lesion is multiloculated with internal septations (*arrowheads*) and does not demonstrate a medially beaked contour, thus differentiating this case from the cases of third and fourth branchial apparatus anomalies.

characteristics. All subjects underwent postnatal MR imaging after delivery to confirm the prenatally described findings and for surgical planning. In all subjects, the cyst had grown by postnatal MR imaging, and in 1 patient, the cyst demonstrated new extension across the midline. One of the 4 patients received contrast, which revealed thin peripheral enhancement typical of a cyst. Most interesting, postnatal imaging demonstrated air in the cyst in 3 of the 4 cases, indicating communication with the airway.

Operative reports, surgical pathology, and clinical follow-up were available for review in all patients. In patient 1 (Fig 1), the left neck cyst was noted to approximate the left piriform sinus, but no discrete tract was noted to ascend to the sinus, and no epithelialized tract was found by pathology. Pathology in this case initially diagnosed a thyroglossal duct cyst on the basis of the presence of thyroid tissue within the cyst. After we compared the pathologic findings with imaging findings, however, the cyst was thought more likely to represent a piriform sinus fistula. The thyroid tissue within the specimen was thought to be ectopic, likely due to a common embryologic origin. In patient 2 (Fig 2), microdirect laryngoscopy revealed a fistulous tract in the left piriform sinus that tracked directly to the cystic left neck mass. The mass was initially decompressed of air and fluid via the fistulous tract, and the tract was cauterized and oversewn. Several days later, the cyst recurred as an abscess, which was drained percutaneously and subsequently re-excised. In patient 3 (Fig 3), an operation confirmed the presence of a fistula to the piriform sinus in association with a cystic neck mass, establishing the diagnosis of third or fourth branchial apparatus anomaly. Patient 4 (Fig 4) underwent surgical repair of a left-sided third or fourth branchial cleft cyst in infancy, which was confirmed to communicate with the piriform sinus. This patient presented later in childhood with an abscess in the contralateral right side of the neck, and imaging demonstrated a fistulous tract extending from the surface of the skin to the airway. This fistula had not been detected prenatally or in infancy. On resection, this anomaly was also diagnosed as a branchial cleft remnant, and the fistula tract was thought most likely to represent a pseudofistula acquired through multiple infections.[9]

DISCUSSION

Third and fourth branchial apparatus anomalies are rare developmental anomalies that often present as cystic lateral neck masses, sinus tracts, or fistulas, most frequently on the left side.[6] We present a series of 4 cases in which the diagnosis of third and fourth branchial apparatus anomaly was suggested prenatally on the basis of the appearance by fetal MR imaging. All lesions presented as homogeneously T2 hyperintense, unilateral, left-sided, unilocular cystic masses, extending posterior to the airway, with a medially beaked contour that tapered toward the piriform sinus. These cysts were typically located deep to the sternocleidomastoid muscle, anterior to the carotid sheath, and lateral to the visceral space of the neck. One cyst was noted to fluctuate in size on prenatal sonography, suggesting communication with the airway. In our cohort, the combination of a unilocular, unilateral cyst with a medial beak directed toward the region of the piriform sinus was seen only in patients with confirmed third or fourth branchial apparatus anomalies and not in any of the lymphatic malformations. This finding is consistent with previously published literature that stated that lymphatic malformations are only rarely unilocular.[10]

The differential diagnosis of congenital cystic lesions of the neck can be quite broad and includes thyroglossal duct cysts, branchial sinus anomalies, lymphatic malformations, dermoid/epidermoid cysts, ranulas, cervical thymic cysts, and cervical bronchogenic cysts.[11] It is important to differentiate third and fourth branchial cleft cysts from these entities because treatment options may vary, and third and fourth branchial apparatus cysts are associated with specific genetic disorders.

Branchial apparatus cysts may become infected, leading to abscess formation and airway compromise; therefore, they are commonly surgically excised when they come to medical attention.[11] Because branchial apparatus anomalies do not spontaneously regress with time, surgical excision is considered the definitive therapy.[12] Although sclerosis has been shown to be safe[13] and has been used in those with contraindications to an operation, sclerosis is not considered a definitive treatment because multiple sessions may be necessary and the fistulous connection to the piriform sinus must be definitively sclerosed to prevent recurrent infection.

Lymphatic malformations, though a more common cause of a lateral neck cyst,[10,11] are not commonly superinfected, and at some institutions, they may be observed or sclerosed as opposed to resected, if they are otherwise not leading to immediate complications such as respiratory distress, because some rare cases may spontaneously regress in size with time.[14]

Furthermore, branchial apparatus anomalies can be associated with Treacher Collins syndrome, DiGeorge syndrome, Pierre Robin sequence, Goldenhar syndrome, and branchio-oto-renal syndrome.[15] Lymphatic malformations involving the dorsal neck, commonly referred to as "cystic hygromas," are often associated with underlying genetic abnormalities such as Turner syndrome, Noonan syndrome, or Trisomy 21. Macrocystic lymphatic malformations in the lateral neck, on the other hand, are not associated with these genetic abnormalities.[14]

Cervical thymic cysts, another entity on the differential diagnosis of cervical cystic lesions, account for 0.3% of all congenital

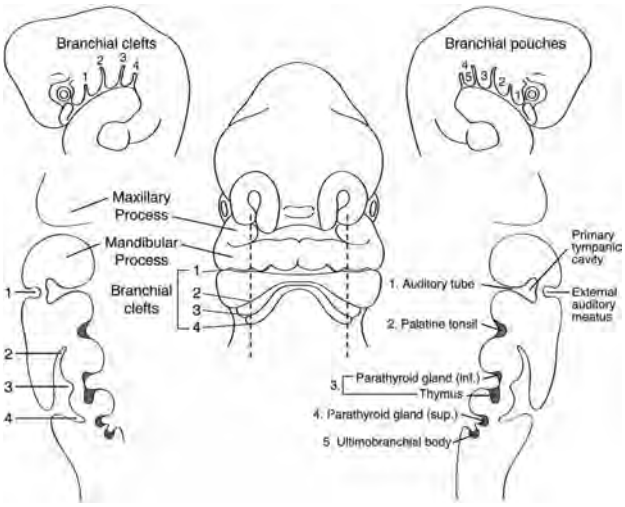

FIG 6. Frontal and sagittal schematic representations of a 5-mm human embryo at the fifth week of gestation. The branchial apparatus with clefts and internal pouches is depicted, as well as the derivations of the major head and neck structures. Reprinted with permission from Waldhausen.[12]

neck masses[16] and occur in the same location as third and fourth branchial apparatus anomalies because they arise from the thymopharyngeal duct but embryologically derive from the third branchial apparatus.[17] Prior reports of thymic cysts have shown that they can be unilocular or multiloculated, are also more commonly left-sided, and can extend into the mediastinum and retropharyngeal space.[18] Some authors have also described communication with the piriform sinus.[17] Prenatally diagnosed cases have included prenatal sonography reports of mediastinal cysts,[19] but to the best of our knowledge, there have been no published cases of prenatally diagnosed cervical thymic cysts or cases diagnosed with fetal MR imaging. Patients often present in childhood with swelling or mass effect on the airway.[20] On the basis of imaging characteristics, cervical thymic cysts may be indistinguishable from third or fourth branchial apparatus anomalies but are exceedingly rare and are managed similarly with surgical excision. Thus, precise distinction of this entity from third and fourth branchial apparatus anomalies may not be possible or necessary.

Additionally, tracheoesophageal fistulas can present as a cystic midline neck mass anterior to the fetal spine. The cyst represents the dilated upper blind end of an atretic esophagus and is typically midline as opposed to the lateral neck and, thus, can be distinguished from third and fourth branchial apparatus anomalies on the basis of location.[21] Tracheoesophageal fistulas are most commonly prenatally diagnosed on the basis of secondary findings of polyhydramnios and a small gastric bubble.[22]

The branchial apparatus is an embryologic structure that appears during the fourth week of gestation in the walls of the embryologic pharyngeal digestive tract, forming 5 paired arches (Fig 6). The arches are separated by clefts and pouches, which reflect indentations of the ectoderm and endoderm, respectively. The arches are composed of embryonic mesoderm and neural crest cells and contain a neurovascular bundle. Thus, these structures serve as the embryonic origin of many different osseous, cartilaginous, muscular, vascular, neural, endocrine, mucosal, and cutaneous structures in the head and neck. By the seventh week of development, the second arch has overgrown the lower arches and, thus, creates the cervical sinus of His, an ectoderm-lined space that is obliterated during the course of normal development. The third branchial arch eventually gives rise to the stylopharyngeus muscle, internal and common carotid arteries, glossopharyngeal nerve, hyoid bone, inferior thyroid gland, and thymus.[15] The fourth branchial cleft eventually forms the laryngeal cartilages, laryngeal and pharyngeal constrictor muscles, superior laryngeal nerve, calcitonin-secreting cells of the thyroid gland, superior parathyroid glands, left thoracic aorta, and the right proximal subclavian artery.[23]

Prior publications of third or fourth branchial cleft anomalies report they are approximately 80% left-sided, the reason being not fully understood but possibly due to asymmetric vascular development of the branchial arches.[24] Bilateral anomalies, such as in one of our patients, are rare and occur in 2%–3% of cases, and, when present, are often familial.[25,26] Imaging remains an important component of diagnosis of third and fourth branchial apparatus anomalies. As the case of the pathologically misdiagnosed thyroglossal duct cyst demonstrates, pathology can be misleading in the isolation of imaging findings. In one prior study, 88% of surgically excised third or fourth branchial anomalies contained ectopic thyroid tissue.[9] In the absence of imaging, these cysts may be easily mistaken for thyroglossal duct cysts.

While both third and fourth branchial arch anomalies communicate with the piriform sinus, third branchial arch anomalies originate from the base of the piriform fossa and fourth branchial arch anomalies originate from the apex.[27] Additionally, third branchial cleft anomalies originate cranial to the superior laryngeal nerve, whereas fourth branchial cleft anomalies originate caudal to the superior laryngeal nerve.[11] While theoretically these features help to distinguish between third and fourth branchial apparatus anomalies, the size of the abnormality relative to the fetal or infant neck often results in difficulty resolving these anatomic differences.[15] In practice, therefore, these entities are typically discussed together.

CONCLUSIONS

Our review of this series of surgically and pathologically proved cases of prenatal presentations of third and fourth branchial apparatus anomalies identified several features on fetal MR imaging that are highly suggestive of this entity. Namely, the presence of a medially beaked contour that tapers between the spine and airway at the level of the piriform sinus in a left-sided, unilocular cyst suggests the diagnosis of third and fourth branchial apparatus anomaly. Fetal MR imaging allows the prenatal diagnosis of these congenital anomalies, and accurate prenatal diagnosis allows proper counseling, genetic work-up, and earlier definitive management. Because these lesions do not spontaneously regress and carry the risk of superinfection, surgical excision is considered the definite therapy, and earlier treatment may potentially spare these patients from associated morbidity.

Disclosures: Yi Li—*UNRELATED*: *Grants/Grants Pending*: Radiological Society of North America, *Comments*: I am a recipient of the Radiological Society of North America Scholar Grant. Vicki A. Feldstein—*UNRELATED*: *Employment*:

University of California, San Francisco, Department of Radiology and Biomedical Imaging, *Payment for Lectures Including Service on Speakers Bureaus*: University of California, San Francisco, Department of Radiology. Office of Postgraduate Education.

REFERENCES

1. Bansal AG, Oudsema R, Masseaux JA, et al. **US of pediatric superficial masses of the head and neck.** *Radiographics* 2018;38:1239–63 CrossRef Medline
2. Nicollas R, Guelfucci B, Roman S, et al. **Congenital cysts and fistulas of the neck.** *Int J Pediatr Otorhinolaryngol* 2000;55:117–24 CrossRef Medline
3. Choi SS, Zalzal GH. **Branchial anomalies: a review of 52 cases.** *Laryngoscope* 1995;105:909–13 CrossRef Medline
4. Ford GR, Balakrishnan A, Evans JN, et al. **Branchial cleft and pouch anomalies.** *J Laryngol Otol* 1992;106:137–43 CrossRef Medline
5. Shiniciro T, Akira M, Fumio M, et al. **Internal fistula as a route of infection in acute suppurative thyroiditis.** *Lancet* 1979;1:751–52 Medline
6. Madana J, Yolmo D, Kalaiarasi R, et al. **Recurrent neck infection with branchial arch fistula in children.** *Int J Pediatr Otorhinolaryngol* 2011;75:1181–85 CrossRef Medline
7. Minhas SS, Watkinson JC, Franklyn J. **Fourth branchial arch fistula and suppurative thyroiditis: a life-threatening infection.** *J Laryngol Otol* 2001;115:1029–31 CrossRef Medline
8. Schmidt K, Leal A, McGill T, et al. **Rapidly enlarging neck mass in a neonate causing airway compromise.** *Proc (Bayl Univ Med Cent)* 2016;29:183–84 CrossRef Medline
9. James A, Stewart C, Warrick P, et al. **Branchial sinus of the piriform fossa: reappraisal of third and fourth branchial anomalies.** *Laryngoscope* 2007;117:1920–24 CrossRef Medline
10. White CL, Olivieri B, Restrepo R, et al. **Low-flow vascular malformation pitfalls: from clinical examination to practical imaging evaluation, Part 1: lymphatic malformation mimickers.** *AJR Am J Roentgenol* 2016;206:940–51 CrossRef Medline
11. Koeller KK, Alamo L, Adair CF, et al. **From the archives of the AFIP. Congenital cystic masses of the neck: radiologic-pathologic correlation.** *Radiographics* 1999;19:121–46 CrossRef Medline
12. Waldhausen JH. **Branchial cleft and arch anomalies in children.** *Semin Pediatr Surg* 2006;15:64–69 CrossRef Medline
13. Ha EJ, Baek SM, Baek JH, et al. **Efficacy and safety of ethanol ablation for branchial cleft cysts.** *AJNR Am J Neuroradiol* 2017;38:2351–56 CrossRef Medline
14. Elluru RG, Balakrishnan K, Padua HM. **Lymphatic malformations: diagnosis and management.** *Semin Pediatr Surg* 2014;23:178–85 CrossRef Medline
15. Mandell DL. **Head and neck anomalies related to the branchial apparatus.** *Otolaryngol Clin North Am* 2000;33:1309–29 CrossRef Medline
16. Hsieh YY, Hsueh S, Hsueh C, et al. **Pathological analysis of congenital cervical cysts in children: 20 years of experience at Chang Gung Memorial Hospital.** *Chang Gung Med J* 2003;26:107–13 Medline
17. Prosser JD, Myer IM. **Branchial cleft anomalies and thymic cysts.** *Otolaryngol Clin North Am* 2015;48:1–14 CrossRef Medline
18. Statham MM, Mehta D, Willging JP. **Cervical thymic remnants in children.** *Int J Pediatr Otorhinolaryngol* 2008;72:1807–13 CrossRef Medline
19. McEwing R, Chaoui R. **Fetal thymic cyst: prenatal diagnosis.** *J Ultrasound Med* 2005;24:127–30 CrossRef Medline
20. Khariwala SS, Nicollas R, Triglia JM, et al. **Cervical presentations of thymic anomalies in children.** *Int J Pediatr Otorhinolaryngol* 2004;68:909–14 CrossRef Medline
21. Hochart V, Verpillat P, Langlois C, et al. **The contribution of fetal MR imaging to the assessment of oesophageal atresia.** *Eur Radiol* 2015;25:306–14 CrossRef Medline
22. Houben CH, Curry JI. **Current status of prenatal diagnosis, operative management and outcome of esophageal atresia/tracheoesophageal fistula.** *Prenat Diagn* 2008;28:667–75 CrossRef Medline
23. Patel AB, Hinni ML. **The fourth branchial complex anomaly: a rare clinical entity.** *Case Rep Otolaryngol* 2011;2011:1–4 CrossRef Medline
24. Thomas B, Shroff M, Forte V, et al. **Revisiting imaging features and the embryologic basis of third and fourth branchial anomalies.** *AJNR Am J Neuroradiol* 2010;31:755–60 CrossRef Medline
25. Rea PA, Hartley BEJ, Bailey CM. **Third and fourth branchial pouch anomalies.** *J Laryngol Otol* 2004;118:19–24 CrossRef Medline
26. Clevens RA, Weimert TA. **Familial bilateral branchial cleft cysts.** *Ear Nose Throat J* 1995;74:419–21 CrossRef Medline
27. Carta F, Sionis S, Mascia L, et al. **Fourth branchial cleft anomaly: management strategy in acute presentation.** *Int J Pediatr Otorhinolaryngol* 2014;78:1480–84 CrossRef Medline

Filtered Diffusion-Weighted MRI of the Human Cervical Spinal Cord: Feasibility and Application to Traumatic Spinal Cord Injury

S.A. Murphy, R. Furger, S.N. Kurpad, V.E. Arpinar, A. Nencka, K. Koch, and M.D. Budde

ABSTRACT

BACKGROUND AND PURPOSE: In traumatic spinal cord injury, DTI is sensitive to injury but is unable to differentiate multiple pathologies. Axonal damage is a central feature of the underlying cord injury, but prominent edema confounds its detection. The purpose of this study was to examine a filtered DWI technique in patients with acute spinal cord injury.

MATERIALS AND METHODS: The MR imaging protocol was first evaluated in a cohort of healthy subjects at 3T ($n = 3$). Subsequently, patients with acute cervical spinal cord injury ($n = 8$) underwent filtered DWI concurrent with their acute clinical MR imaging examination <24 hours postinjury at 1.5T. DTI was obtained with 25 directions at a b-value of 800 s/mm^2. Filtered DWI used spinal cord–optimized diffusion-weighting along 26 directions with a "filter" b-value of 2000 s/mm^2 and a "probe" maximum b-value of 1000 s/mm^2. Parallel diffusivity metrics obtained from DTI and filtered DWI were compared.

RESULTS: The high-strength diffusion-weighting perpendicular to the cord suppressed signals from tissues outside of the spinal cord, including muscle and CSF. The parallel ADC acquired from filtered DWI at the level of injury relative to the most cranial region showed a greater decrease (38.71%) compared with the decrease in axial diffusivity acquired by DTI (17.68%).

CONCLUSIONS: The results demonstrated that filtered DWI is feasible in the acute setting of spinal cord injury and reveals spinal cord diffusion characteristics not evident with conventional DTI.

ABBREVIATIONS: AD = axial diffusion; DDE = double diffusion encoding; $fADC_{||}$ = filtered parallel ADC; fDWI = filtered DWI; NODDI = neurite orientation dispersion and density imaging; PRESS = point-resolved spectroscopy sequence; SCI = spinal cord injury

Reliable biomarkers of spinal cord injury (SCI) severity could aid long-term functional prognosis and facilitate therapeutic decision-making. DWI has shown promise as a noninvasive tool to detect injury severity. DTI, the most widely used DWI model, has revealed important changes to the tissue microstructure that provide insight to function post-SCI in experimental models;[1-6] however, technical challenges and difficulties in interpreting the data are central reasons for the lack of DTI application within clinical settings and for investigations after human SCI.[7-10] To address these challenges, a recent filtered DWI (fDWI) technique, originally developed on the basis of principles of double diffusion encoding (DDE), has shown promise in animal models[3,11] and simulations,[12] providing information about axonal injury after a spinal cord trauma. The purpose of this study was to examine the feasibility and efficacy of an fDWI scheme in the healthy human spinal cord with initial applications in the acutely injured cervical spinal cord.

DTI is uniquely sensitive to the microstructure of the spinal cord with an ability to reveal changes caused by injury that remain undetectable by other MR imaging schemes and contrasts. Axial diffusivity (AD), a directionally specific DTI metric quantifying diffusion parallel to the spinal cord, typically decreases after SCI and is specifically attributed to axonal damage.[2] In the acute SCI setting, decreased AD is likely caused by the formation of axonal beading that restricts water mobility,[2,12-14] though end-bulbs and other microscopic features of acutely injured axons may also contribute (Fig 1). Unfortunately, additional tissue responses to the injury, particularly edema and hemorrhage, confound AD measurements by DTI.[15] Edema is an evolving pathology in the early acute stage, and the logistics of patient transport and monitoring

Received February 8, 2021; accepted after revision July 7.

From the Department of Neurosurgery (S.A.M., R.F., S.N.K., M.D.B.), Center for Neurotrauma Research (R.F., S.N.K., M.D.B.), and Center for Imaging Research (V.E.A., A.N., K.K.), Medical College of Wisconsin, Milwaukee, Wisconsin.

This work was supported by the Craig H. Neilsen Foundation (546624) and a Merit Review Award (I01RX002751) from the United States Department of Veterans Affairs Rehabilitation Research and Development Service.

Please address correspondence to Spencer A. Murphy, PhD, 8701 Watertown Plank Rd. Wauwatosa, WI 53226; e-mail: spamurphy@mcw.edu

Indicates open access to non-subscribers at www.ajnr.org

Indicates article with online supplemental data.

http://dx.doi.org/10.3174/ajnr.A7295

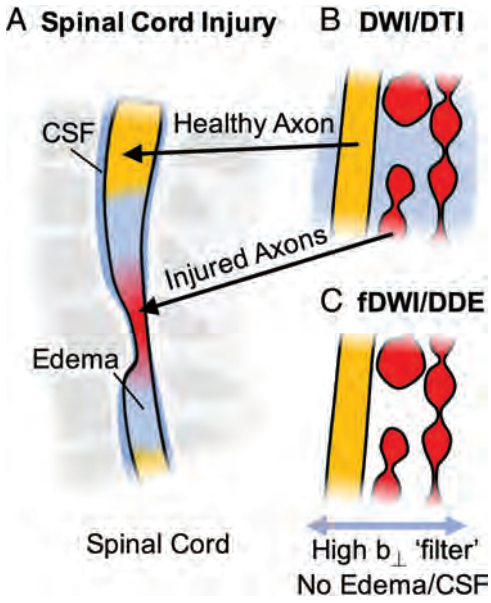

FIG 1. Schematic representation of the fDWI/DDE MR imaging technique for spinal cord injury. Traumatic injury to the spinal cord (*A*) results in microscopic damage to axons, illustrated here as beading and end-bulbs that reflect the underlying acute pathology (*B*). A prominent edema response (light blue) is typical surrounding the injury site. Traditional DWI/DTI derives measures reflecting the bulk sum of all features. With fDWI/DDE, a high-strength diffusion-weighting perpendicular to the spinal cord suppresses extracellular edema (and CSF) to estimate tissue-specific diffusivity metrics less confounded by edema.

after SCI complicate measures of edema.[16,17] Thus, a prominent limitation for the efficacy of DTI in the clinic is differentiating true axonal injury from the inflammatory response.

The goal of this study was to disambiguate healthy and injured axons using DWI. While DTI is confounded by extracellular edema,[5] through prior simulations and preclinical studies we have shown that the fDWI approach diminishes the effects of edema on the DWI metrics and is more sensitive to diffusion within axons (Fig 1). We compared AD measured by DTI with the filtered parallel ADC (fADC$_{||}$) measured by fDWI within healthy and injured cords. Additionally, we used another DDE variant, a point-resolved spectroscopy sequence (DDE-PRESS) readout for single voxel, whole-cord measurements. The results demonstrated that both fDWI and DDE-PRESS are feasible MR imaging schemes with sensitivity to white matter diffusivity.

MATERIALS AND METHODS

Participants

All procedures were approved by the institutional review board at the Medical College of Wisconsin, and written consent was obtained from all participants. To first establish the protocol and demonstrate the feasibility on human systems, we tested the sequence on 3 healthy individuals with an intact spinal cord on a 3T scanner (mean age, 43.0 [SD, 16.4] years). Subsequently, the protocol was ported to a 1.5T clinical MR imaging system and evaluated in 8 patients with acute SCI (mean, 4.66 [SD, 3.23] hours from hospital admittance to scan time) (mean age, 51.9 ± [SD, 12.1] years). The Online Supplemental Data include participant characteristics.

MR Imaging

For healthy subjects, cervical spine imaging was performed on a research-dedicated 3T Premier scanner with a 45-channel Head Neck Spine array (GE Healthcare). For subjects with acute SCI, imaging was performed on a clinical 1.5T Signa Optima MR450w GEM scanner with a 24-channel Head Neck Spine array (GE Healthcare). Participants were in the supine position with cushions/padding to limit head tilting and lordosis in the cervical (imaging) region. The participant was instructed to limit motion, such as swallowing, to breaks in the acquisition series.

To first characterize signal attenuation and illustrate the effects of diffusion filtering in the spinal cord, experiments in healthy subjects used diffusion-weighting perpendicular to the cord at b-values of 0, 200, 500, 1000, and 2000 s/mm^2, using a pulsed gradient spin-echo acquisition with a diffusion separation (Δ) of 32.5 ms and duration (δ) of 25.4 ms. An EPI readout (TR = 2500 ms; TE = 64 ms) was used with an FOV of 200 mm^2 and 11 slices at a thickness of 5 mm and 0.2-mm gap.

For all participants, a DTI and fDWI protocol was used for an EPI readout. The DTI acquisition used 25 directions distributed along a sphere all at a b-value of 800 s/mm^2. The diffusion-encoding for fDWI consisted of a diffusion-weighting "filter" gradient perpendicular to the spinal cord axis with a b-value of 2000 s/mm^2. A separate diffusion-weighting "probe" gradient was applied parallel to the main axis of the spinal cord from 0 to 1000 s/mm^2. A total of 26 directions was acquired that accounts for both a positive and negative combination of the filter and probe gradient directions. Scan times were similar for DTI and fDWI at 5 minutes 27 seconds and 5 minutes 35 seconds, respectively. For the healthy spinal cord, slices were centered at C4, while in the SCI group, slices were centered at the level of the lesion.

Because the diffusion filter pulse suppresses signals outside the spinal cord, the fDWI acquisition was additionally coupled with a single-voxel DDE-PRESS as a separate acquisition (TR = 2000 ms; TE = 145 ms). For individuals with SCI, this voxel (20 × 20 × 10 mm^3) was placed at the epicenter of the lesion for 1 acquisition and above the lesion for a second acquisition, both maintaining alignment with the main axis of the spinal cord. The diffusion parameters for the DDE-PRESS sequence were identical to those in DWI-EPI to the extent possible. A b-value of 2000 s/mm^2 was used for the diffusion filter pair, and 9 different b-values from 0 to 2000 s/mm^2 in increments of 250 s/mm^2 were used for the diffusion probe (in addition to 1 non-diffusion-weighted spectrum). The full DDE-PRESS acquisition was repeated 4 times with a single average for each b-value and was acquired in 2 minutes 56 seconds. DDE-PRESS was performed on 6 of the 8 participants with SCI.

As part of the clinical MR imaging protocol, T2-weighted sagittal images were acquired and used for quantification of anatomic lesion features.

Image Processing and Data Analysis

The Spinal Cord Toolbox (SCT; https://spinalcordtoolbox.com/) was used for the following postacquisition processing of the DWI-EPI data: 1) section-wise motion correction to correct for

translations in the axial plane; 2) DTI parameter maps of the whole FOV using linear least-squares fitting; 3) spinal cord segmentation; 4) spinal cord registration to the PAM50 template to automate ROIs for the CSF, gray matter, and white matter. Segmentation and registration were performed using the non-diffusion-weighted ($b = 0$ s/mm^2) image for DTI and the filtered, non-diffusion-weighted image ($b = 2000$ s/mm^2, $b_{||} = 0$ s/mm^2) for the fDWI acquisition. A pipeline was established to fully automate the tasks performed by the SCT, and the outputs were visually inspected to ensure its effectiveness and reliability. Mean cord values were obtained from the combined white and gray matter (ie, whole cord) because they could not be reliably discerned within the spinal cord injury setting, likely due to injury responses and the lower resolution on the 1.5T system. The noise and muscle ROIs were manually selected for healthy individuals and patients with SCI.

Maps of the diffusivity measured parallel to the cord in the presence of the perpendicular diffusion filter (fADC$_{||}$) were estimated in Matlab (MathWorks) using a least-squares fit to the equation:

$$S_i = S_o \times \exp(-b \times D),$$

where S_o is the signal measured without diffusion-weighting and reflects the signal in the presence of the diffusion filter with no parallel diffusion weighting ($b = 2000$ s/mm^2, $b_{||} = 0$ s/mm^2), S_i reflects the measured signal at each of the $b_{||}$-values with $b = q^2\left(\Delta - \frac{\delta}{3}\right)$. DTI and fDWI parameter maps were evaluated using an ROI analysis. Quantification of fADC$_{||}$ and AD consisted of averages from each section and an average of all 11 slices for the specified ROI. Linear regression was used to relate fADC$_{||}$ and AD across all slices for both the intact spinal cord group and the acute SCI group, with whole-cord values used for both groups for similar comparisons.

The average SNR of all slices within the ROIs was also measured and obtained from the non-diffusion-weighted images for DTI and fDWI by dividing images by the SD measured from a region of pure noise:

$$SNR = \frac{S_i}{SD(noise)}.$$

Analysis of DDE-PRESS data used custom Matlab scripts for derivation of diffusion parameters. The complex signals were Fourier-transformed, and the water peak within the single non-diffusion-weighted spectra (S_o) was set as the frequency reference point for the subsequent integration of the other diffusion spectra. Integration of the absolute valued signal was performed between ±2 ppm of the water peak to exclude the lipid contribution at approximately +3.5 ppm from the water peak. The integrated and normalized signal (S_i/S_o) was fit to a biexponential model:[3]

$$S_i = S_0 \times f_R \times \exp(-b \times D_R) + S_0(1 - f_R) \times \exp(-b \times D_{fast}),$$

where D_R and D_{fast} capture the slow or restricted diffusion component (D_R) and the fast or more freely diffusing component (D_{fast}). The f_R reflects the fraction of the restricted signal. SNR was computed and defined as the mean signal divided by the SD from a region of pure noise.

The lesion length and hemorrhage extent were also measured from the cranial-to-caudal extents of the spinal cord hyperintensity and hypointensity, respectively, evaluated on sagittal T2-weighted images. consistent with the National Institutes of Health Common Data Elements.[18]

Statistics

Statistical tests were performed using SPSS Statistics 27 (IBM). Data are reported as mean (SD). In the healthy subjects, a linear regression analysis was performed to compare fADC$_{||}$ and AD across all slices from the same ROIs. A Wald–Wolfowitz runs test for randomness was used to determine whether linear regression was an appropriate fit to the data, with significance indicating the presence of a nonrandom distribution of residuals. For the subjects with acute injury, paired t tests were performed to compare each section with the most cranial section for each of the diffusivity metrics separately. The linear regression and runs test were also performed to directly relate fADC$_{||}$ and AD. No direct comparisons between fADC$_{||}$ and AD were performed because while they reflect similar features of parallel diffusivity, they are obtained from a different set of b-values and directions and are estimated differently using single-axis or tensor estimation.

RESULTS

Single-Axis Diffusion-Weighted Behavior in the Intact Spinal Cord

A pulsed gradient spin-echo applied perpendicular to the cord axis in the intact spinal cord exhibited a characteristic exponential decay within each of the tissue types captured by the ROIs (Online Supplemental Data). With increasing b-values, WM signal was less attenuated compared with that of the GM signal. There was nearly complete signal attenuation to the noise floor for the CSF and muscle at $b = 2000$ s/mm^2. At the b-value 2000 s/mm^2, the mean SNR values from the WM (24.0 [SD, 3.4]) were greater compared with GM (14.0 [SD, 4.2]). The mean SNR for both CSF (6.77 [SD, 6.01]) and muscle (3.97 [SD, 4.10]) were indistinguishable from the noise floor (3.77 [SD, 2.11]). Collectively, these results demonstrate a diffusion gradient applied perpendicular to the cord (2000 s/mm^2) that resulted in a signal consisting primarily of spinal cord white matter without a contribution from non-neural tissues.

Filter-Probe Diffusion-Encoding in the Intact Spinal Cord

In the intact cervical spinal cord, fDWI was compared with DTI (Fig 2). Mean fADC$_{||}$ measured in the white matter (1.16 [SD, 0.38] μm^2/s) was lower compared with the mean AD (1.45 [SD, 0.40] μm^2/s) (Fig 2*C*), which equates to a reduction of 20.00%.

Filter-Probe Diffusion-Encoding in the Injured Cervical Spinal Cord

fDWI, DTI, and DDE-PRESS were obtained in subjects with acute spinal cord injury. In a sample image of a single subject (Fig 3), fADC$_{||}$ decreased at the injury site compared with AD. Averaged across all acquired slices, mean fADC$_{||}$ values were lower (0.81 [SD, 0.42] μm^2/s) than mean AD values (1.36 [SD, 0.42] μm^2/s) (see examples for all participants in the Online Supplemental Data). A paired t test comparing each section with the most cranial section revealed a significant decrease at the injury epicenter

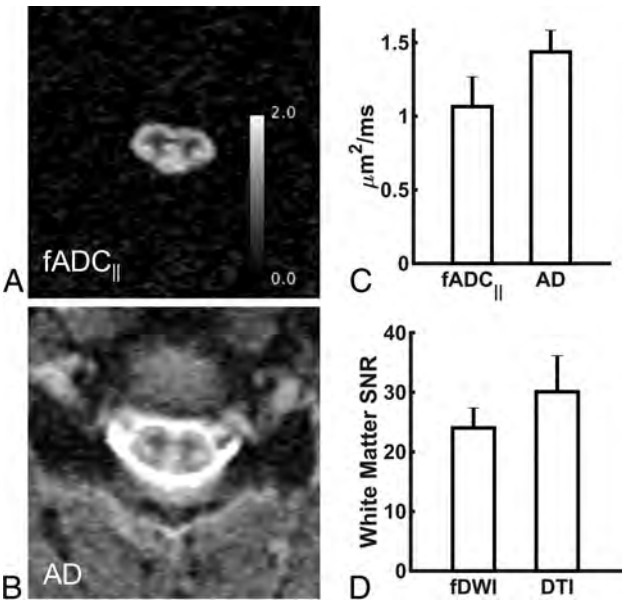

FIG 2. $fADC_{||}$ and AD maps for the healthy spinal cord. Single-subject $fADC_{||}$ (*A*) and AD maps (*B*) at C4 for a healthy individual on a 3T system. Comparison of the mean white matter $fADC_{||}$ or AD values (*C*) and SNR (*D*).

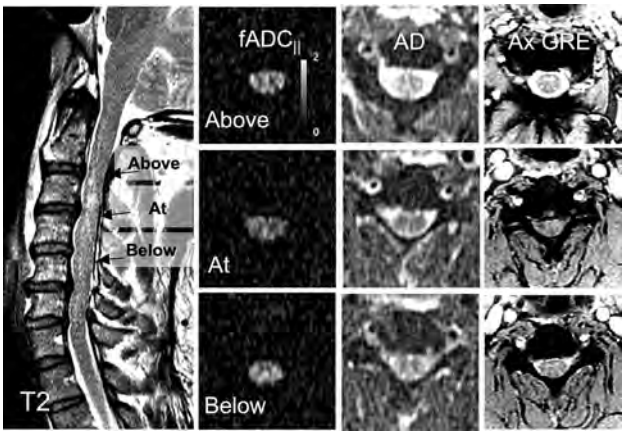

FIG 3. $fADC_{||}$ and AD maps for an individual (subject 3) with an acute spinal cord injury. A T2-weighted image for an individual with an acute spinal cord injury on a 1.5T system. Single slices above, at, and below the injury site (as labeled in the T2 image) for $fADC_{||}$ and AD maps. Ax GRE indicates axial gradient recalled-echo.

compared with above the injury for both $fADC_{||}$, $t(7) = 3.115$, $P = .017$, and AD, $t(7) = 2.881$, $P = .024$. The most caudal section showed no significant differences compared with the most cranial section for $fADC_{||}$, $t(7) = 1.117$, $P = .301$, or AD, $t(7) = -0.045$, $P = .965$. AD also decreased, though to a lesser extent, at the injury site compared with above and below the injury (Fig 4). When normalized to the first section above the injury, $fADC_{||}$ values decreased an average of 38.71% at the injury epicenter, while AD decreased by 17.68% at the same section. However, AD also exhibited localized increases above and below the injury (Fig 5). Together, these results showed an overall decrease in diffusion measured parallel to the cord using 2 different DWI methods at the injury site, with a greater decrease in $fADC_{||}$ compared with AD.

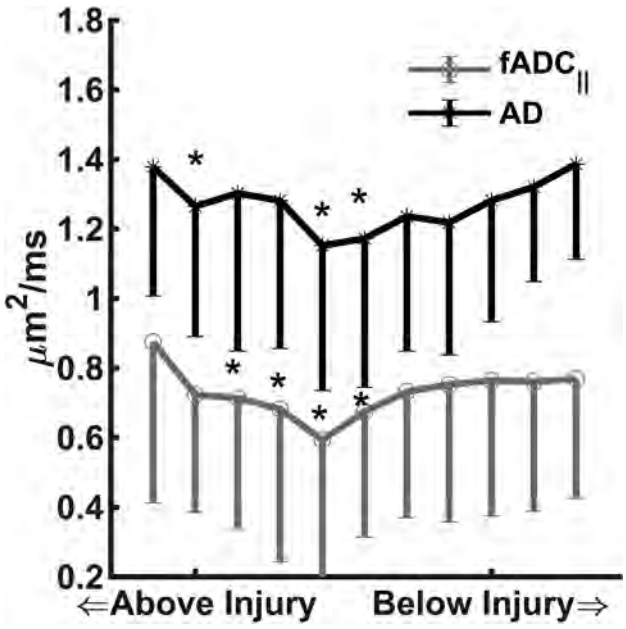

FIG 4. $fADC_{||}$ and AD compared at each individual section for acute spinal cord injury ($n = 8$). There is a large, unidirectional decrease in $fADC_{||}$ at the injury site compared with a lesser, multidirectional decrease in AD values. The *asterisk* indicates significance compared with the first section ($P < .05$).

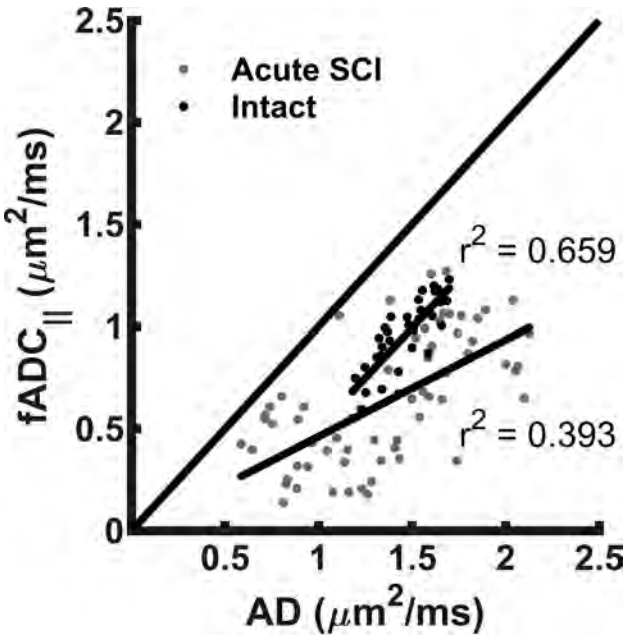

FIG 5. Correlations of $fADC_{||}$ and AD at each individual section for the intact spinal cord and acute spinal cord injury. Correlations are significant for the intact spinal cord; however, a lower correlation and nonrandom residuals for the acute SCI setting indicate that $fADC_{||}$ and AD do not have a simple linear relationship, suggesting that they provide differing information.

The relationship between $fADC_{||}$ and AD was also evaluated to examine their differential effects. In the intact spinal cord, $fADC_{||}$ and AD have a linear relationship with one another ($r^2 = 0.659$, $P < .001$) (Fig 5*A*), with a runs test confirming that the

residuals exhibit a random distribution ($P = .344$, Fig 5*A*). In acute injury, $fADC_{||}$ and AD do not exhibit a similar relationship (Fig 5*B*) because the linear regression reveals a lower slope ($r^2 = 0.393$, $P < .001$), and the runs test indicates that the residuals are nonrandom ($P < .001$). Together, these data showed that in the healthy, intact spinal cord, $fADC_{||}$ and AD provide similar information, but after acute SCI, they exhibit differing information.

The same metric of $fADC_{||}$ was also obtained from DDE-PRESS, though with differences in spatial positioning and coverage. In a patient with acute SCI (Online Supplemental Data), the EPI readout was complicated by artifacts and low image quality. However, the spectra exhibited a clear water peak and a lipid peak at both the injury site and above the injury site. $fADC_{||}$ measured from DDE-PRESS demonstrated significantly lower mean values at the injury site (0.61 [SD, 33] $\mu m^2/ms$) compared with the more remote location above the injury (1.10 [SD, 0.34] $\mu m^2/ms$), $t(5) = 2.89$, $P = .034$, showing trends similar to that of $fADC_{||}$ obtained from EPI. These data together show that the estimated $fADC_{||}$ from the DDE-PRESS for participants with low image quality was similar to that of fDWI.

DISCUSSION

The results of this feasibility study demonstrated the efficacy and applicability of the filtered diffusion encoding scheme in the acute human spinal cord injury setting. The pathologic ambiguity of DTI hinders its utility to specifically evaluate axonal integrity in acute SCI.[5,19] The filtered diffusion approach exploits the spinal cord anatomy and known diffusion properties to suppress or filter predominantly extracellular signals as shown in prior animal and simulation studies.[3,11,12] In this study, we directly compared $fADC_{||}$ measured by fDWI with AD measured by DTI in the same healthy subjects and a cohort of subjects with acute spinal cord traumatic injury. First, the results demonstrate that a b-value of 2000 s/mm^2 sufficiently suppressed signals outside the cord while retaining white matter signal (Fig 2). Second, decreases in $fADC_{||}$ at the injury site of acute injury were more pronounced than those of AD. Similarly, while AD showed inconsistent fluctuations across the injured cord, $fADC_{||}$ showed a unidirectional change compared with above and below the injury (Fig 5). Last, DDE-PRESS was able to capture similar measures of $fADC_{||}$ indicative of axonal integrity for acute SCI (Online Supplemental Data), particularly useful in cases in which EPI quality was unusable.

In acute spinal cord injury, axonal integrity is believed to be the best indicator of functional outcome after a spinal cord injury,[20] and parallel or axial diffusivity is the diffusion metric most closely associated with the underlying cytotoxic edema consistent with swollen and beaded axons.[2,12,21] Indeed, in prior DTI studies of acute SCI, AD was the strongest correlate of long-term outcome.[22] The diffusion protocol in this study used multiple b-values along a single direction parallel to the spinal cord, enabling a more direct approach but with certain limitations. After traumatic SCI, axonal injury is also accompanied by a prominent edema response evident on T2-weighted images,[23] including both vasogenic or cytotoxic edema. Vasogenic edema is presumed to be extracellular, and as a consequence, it confounds DTI, resulting in counterintuitive increases in AD.[2,12-14,24] In the proposed fDWI approach, $fADC_{||}$ has a minimal contribution from vasogenic edema and is more specific to cytotoxic edema. These differential effects explain the greater sensitivity of $fADC_{||}$ to the acutely injured cord (Fig 4).

Other approaches to resolving these diffusion properties have used multicompartment modeling of the diffusion signal. Notably, neurite orientation dispersion and density imaging (NODDI) is 1 example that estimates compartment volume fractions[25] but is based on the assumption of a single diffusion coefficient of 1.7 $\mu m^2/ms$ for the intra-axonal parallel diffusivity. This is likely to misattribute a prominent decrease in diffusivity to other estimated parameters. Furthermore, NODDI and other models require considerably more images for reliable estimates. Prior studies applying NODDI to the cervical spinal cord of patients with MS used approximately 18 minutes of imaging and nearly 100 images,[26] generally infeasible in a trauma setting. The primary advantage of fDWI in this context is that the filtering is achieved during data acquisition, improving feasibility. Moreover, fDWI has other favorable features including suppression of noncord tissue, most notably CSF and muscle. The suppression of CSF reduces artifacts attributable to motion such as CSF pulsation and reduces Gibbs ringing and partial volume effects in the spinal cord. Although fDWI inextricably has decreased SNR compared with similar DTI, it is countered by improvements in contrast and specificity.

The fDWI approach is also compatible with a straightforward single-voxel spectroscopic readout, and because noncord signals are suppressed, voxel dimensions can be larger than the cord axial cross-section. Previously, $fADC_{||}$ derived from DDE-PRESS was shown to have a high degree of tolerance to magnetic field inhomogeneity artifacts that render EPI unusable.[27] In this study, similar results were evident in a subset of patients with poor EPI quality in which DDE-PRESS achieved decreased $fADC_{||}$ values in the voxel at the injury site relative to one above the injury. As expected, DDE-PRESS sacrificed spatial information for greater SNR compared with EPI.

The primary limitation of this study is the small sample size. Further studies are needed in a larger cohort of patients and with long-term follow-up to appreciate the added value of fDWI in predicting neurologic outcome, because this is an important concern for both the patient and for improving stratification for clinical trials. This study was also limited in that healthy controls and patients with acute SCI were not scanned on the same magnet due to logistical limitations in equipment availability for the healthy population. Additionally, demonstrating the utility of these techniques within other clinical populations is needed. In particular, it may be suited to other conditions that impact the spinal cord such as multiple sclerosis and myelopathy, which have complex and evolving pathologies and in which diffusion metrics have been shown to be beneficial.[28,29]

CONCLUSIONS

The results demonstrate that a diffusion acquisition tailored to the acutely injured spinal cord using filtered diffusion encoding improves sensitivity to white matter damage. The filtered diffusion metric $fADC_{||}$ has a reduced dependence on vasogenic edema, and the results of this study show a greater decrease at the site of acute spinal cord injury compared with DTI metrics. Furthermore, a single-voxel method using the same diffusion filtering allowed estimates of $fADC_{||}$ in cases in which more

conventional EPI had diminished quality. Future studies on a larger cohort of patients with acute and chronic SCI are needed to relate the improved sensitivity to functional outcomes. The fDWI scheme demonstrated in this study improved specificity to axonal damage, and it is believed that these advances will help in more accurately predicting long-term functional outcomes after spinal cord injury.

ACKNOWLEDGMENTS

We would like to thank Victoria Slomski and all the MR imaging technologists at Froedtert Hospital and the Medical College of Wisconsin for acquiring the data in this study. We also thank Sarah Cornell for help recruiting patients to participate in the study.

Disclosures: Spencer A. Murphy—*RELATED*: *Grant*: The Craig H. Neilsen Foundation and Department of Veterans Affairs;* *UNRELATED*: *Employment*: Medical College of Wisconsin. Robyn Furger—*RELATED*: *Grant*: The Craig H. Neilsen Foundation and Department of Veterans Affairs*, *Comments*: grant to fund the research study. Shekar Kurpad—*UNRELATED*: *Grants/Grants Pending*: Bryon Riesch Paralysis Foundation.* Andrew Nencka—*UNRELATED*: *Grants/Grants Pending*: GE Healthcare*, *Comments*: My lab receives research funding from GE Healthcare for development, dissemination, and support of MR imaging pulse sequences for neurocognitive imaging studies. These pulse sequences were not used in the submitted work. *Stock/Stock Options*: VasoGnosis, *Comments*: I hold stock in a privately held company that focuses on image processing and communication in the field of neurovascular imaging of the head. No products or derivatives of work associated with that company were used in the submitted work. Kevin Koch—*UNRELATED*: *Grants/Grants Pending*: GE Healthcare*, *Comments*: My lab receives research funding from GE Healthcare for development, dissemination, and support of MR technology development for orthopaedic and neurocognitive imaging studies. These technologies were not used in the submitted work. *Stock/Stock Options:* VasoGnosis, *Comments*: I hold stock in a privately held company that focuses on image processing and communication in the field of neurovascular imaging of the head. No products or derivatives of work associated with that company were used in the submitted work. *Money paid to the institution.

REFERENCES

1. Zhao C, Rao JS, Pei XJ, et al. **Longitudinal study on diffusion tensor imaging and diffusion tensor tractography following spinal cord contusion injury in rats.** *Neuroradiology* 2016;58:607–14 CrossRef Medline
2. Kim JH, Loy DN, Wang Q, et al. **Diffusion tensor imaging at 3 hours after traumatic spinal cord injury predicts long-term locomotor recovery.** *J Neurotrauma* 2010;27:587–98 CrossRef Medline
3. Skinner NP, Kurpad SN, Schmit BD, et al. **Rapid in vivo detection of rat spinal cord injury with double-diffusion-encoded magnetic resonance spectroscopy.** *Magn Reson Med* 2017;77:1639–49 CrossRef Medline
4. Patel SP, Smith TD, VanRooyen JL, et al. **Serial diffusion tensor imaging in vivo predicts long-term functional recovery and histopathology in rats following different severities of spinal cord injury.** *J Neurotrauma* 2016;33:917–28 CrossRef Medline
5. Chiang CW, Wang Y, Sun P, et al. **Quantifying white matter tract diffusion parameters in the presence of increased extra-fiber cellularity and vasogenic edema.** *Neuroimage* 2014;101:310–19 CrossRef Medline
6. Jirjis MB, Kurpad SN, Schmit BD. **Ex vivo diffusion tensor imaging of spinal cord injury in rats of varying degrees of severity.** *J Neurotrauma* 2013;30:1577–86 CrossRef Medline
7. Cheran S, Shanmuganathan K, Zhuo J, et al. **Correlation of MR diffusion tensor imaging parameters with ASIA motor scores in hemorrhagic and nonhemorrhagic acute spinal cord injury.** *J Neurotrauma* 2011;28:1881–92 CrossRef Medline
8. Cohen-Adad J, Buchbinder B, Oaklander AL. **Cervical spinal cord injection of epidural corticosteroids: comprehensive longitudinal study including multiparametric magnetic resonance imaging.** *Pain* 2012;153:2292–99 CrossRef Medline
9. Vedantam A, Eckardt G, Wang MC, et al. **Clinical correlates of high cervical fractional anisotropy in acute cervical spinal cord injury.** *World Neurosurg* 2015;83:824–28 CrossRef Medline
10. Shanmuganathan K, Zhuo J, Bodanapally UK, et al. **Comparison of acute diffusion tensor imaging and conventional magnetic resonance parameters in predicting long-term outcome after blunt cervical spinal cord injury.** *J Neurotrauma* 2020;37:458–65 CrossRef Medline
11. Budde MD, Skinner NP, Muftuler LT, et al. **Optimizing filter-probe diffusion weighting in the rat spinal cord for human translation.** *Front Neurosci* 2017;11:706 CrossRef Medline
12. Skinner NP, Kurpad SN, Schmit BD, et al. **Detection of acute nervous system injury with advanced diffusion-weighted MRI: a simulation and sensitivity analysis.** *NMR Biomed* 2015;28:1489–506 CrossRef Medline
13. Budde MD, Frank JA. **Neurite beading is sufficient to decrease the apparent diffusion coefficient after ischemic stroke.** *Proc Natl Acad Sci U S A* 2010;107:14472–77 CrossRef Medline
14. Steffensen AB, Sword J, Croom D, et al. **Chloride cotransporters as a molecular mechanism underlying spreading depolarization-induced dendritic beading.** *J Neurosci* 2015;35:12172–87 CrossRef Medline
15. Sundberg LM, Herrera JJ, Narayana PA. **In vivo longitudinal MRI and behavioral studies in experimental spinal cord injury.** *J Neurotrauma* 2010;27:1753–67 CrossRef Medline
16. Sliker CW, Mirvis SE, Shanmuganathan K. **Assessing cervical spine stability in obtunded blunt trauma patients: review of medical literature.** *Radiology* 2005;234:733–39 CrossRef Medline
17. Leypold BG, Flanders AE, Schwartz ED, et al. **The impact of methylprednisolone on lesion severity following spinal cord injury.** *Spine (Phila Pa 1976)* 2007;32:373–78; discussion 379–81 CrossRef Medline
18. Biering-Sørensen F, Alai S, Anderson K, et al. **Common data elements for spinal cord injury clinical research: a National Institute for Neurological Disorders and Stroke project.** *Spinal Cord* 2015;53:265–77 CrossRef Medline
19. Surey S, Berry M, Logan A, et al. **Differential cavitation, angiogenesis and wound-healing responses in injured mouse and rat spinal cords.** *Neuroscience* 2014;275:62–80 CrossRef Medline
20. Medana IM, Esiri MM. **Axonal damage: a key predictor of outcome in human CNS diseases.** *Brain* 2003;126:515–30 CrossRef Medline
21. Fieremans E, Jensen JH, Helpern JA. **White matter characterization with diffusional kurtosis imaging.** *Neuroimage* 2011;58:177–88 CrossRef Medline
22. Shanmuganathan K, Zhuo J, Chen HH, et al. **Diffusion tensor imaging parameter obtained during acute blunt cervical spinal cord injury in predicting long-term outcome.** *J Neurotrauma* 2017;34:2964–71 CrossRef Medline
23. Leypold BG, Flanders AE, Burns AS. **The early evolution of spinal cord lesions on MR imaging following traumatic spinal cord injury.** *AJNR Am J Neuroradiol* 2008;29:1012–16 CrossRef Medline
24. Williams PR, Marincu BN, Sorbara CD, et al. **A recoverable state of axon injury persists for hours after spinal cord contusion in vivo.** *Nat Commun* 2014;5:5683 CrossRef Medline
25. Grussu F, Schneider T, Zhang H, et al. **Neurite orientation dispersion and density imaging of the healthy cervical spinal cord in vivo.** *Neuroimage* 2015;111:590–601 CrossRef Medline
26. By S, Xu J, Box BA, et al. **Application and evaluation of NODDI in the cervical spinal cord of multiple sclerosis patients.** *Neuroimage Clin* 2017;15:333–42 CrossRef Medline
27. Budde MD, Skinner NP. **Diffusion MRI in acute nervous system injury.** *J Magn Reson* 2018;292:137–48 CrossRef Medline
28. Nukala M, Abraham J, Khandige G, et al. **Efficacy of diffusion tensor imaging in identification of degenerative cervical spondylotic myelopathy.** *Eur J Radiol Open* 2019;6:16–23 CrossRef Medline
29. Farrell JA, Smith SA, Gordon-Lipkin EM, et al. **High b-value q-space diffusion-weighted MRI of the human cervical spinal cord in vivo: feasibility and application to multiple sclerosis.** *Magn Reson Med* 2008;59:1079–89 CrossRef Medline

Celebrating 35 Years of the AJNR

November 1986 edition

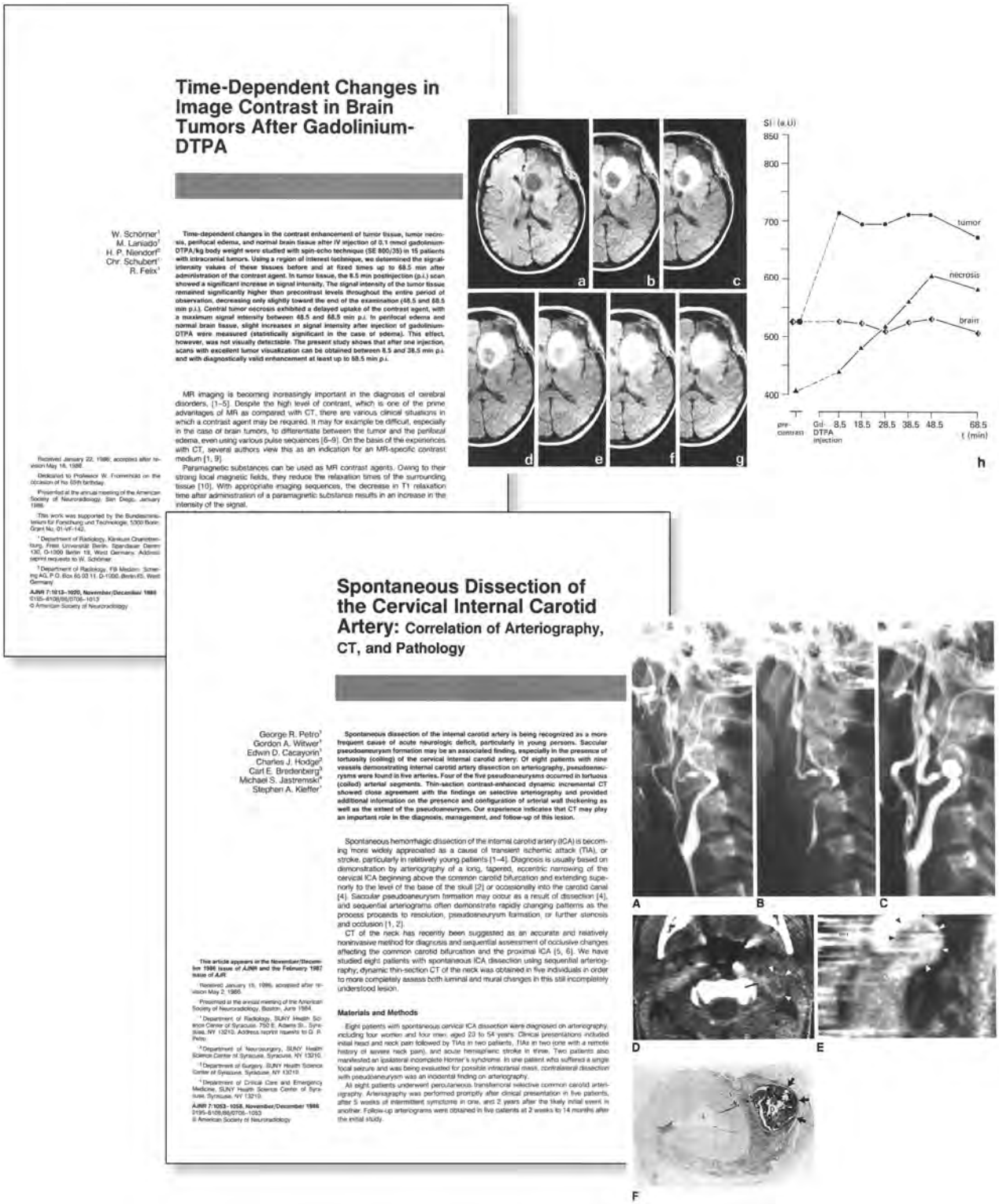

Time-Dependent Changes in Image Contrast in Brain Tumors After Gadolinium-DTPA

W. Schörner[1]
M. Laniado[1]
H. P. Niendorf[2]
Chr. Schubert[1]
R. Felix[1]

Time-dependent changes in the contrast enhancement of tumor tissue, tumor necrosis, perifocal edema, and normal brain tissue after IV injection of 0.1 mmol gadolinium-DTPA/kg body weight were studied with spin-echo technique (SE 800/35) in 15 patients with intracranial tumors. Using a region of interest technique, we determined the signal-intensity values of these tissues before and at fixed times up to 68.5 min after administration of the contrast agent. In tumor tissue, the 8.5 min postinjection (p.i.) scan showed a significant increase in signal intensity. The signal intensity of the tumor tissue remained significantly higher than precontrast levels throughout the entire period of observation, decreasing only slightly toward the end of the examination (48.5 and 68.5 min p.i.). Central tumor necrosis exhibited a delayed uptake of the contrast agent, with a maximum signal intensity between 48.5 and 68.5 min p.i. In perifocal edema and normal brain tissue, slight increases in signal intensity after injection of gadolinium-DTPA were measured (statistically significant in the case of edema). This effect, however, was not visually detectable. The present study shows that after one injection, scans with excellent tumor visualization can be obtained between 8.5 and 28.5 min p.i. and with diagnostically valid enhancement at least up to 68.5 min p.i.

MR imaging is becoming increasingly important in the diagnosis of cerebral disorders, [1–5]. Despite the high level of contrast, which is one of the prime advantages of MR as compared with CT, there are various clinical situations in which a contrast agent may be required. It may for example be difficult, especially in the case of brain tumors, to differentiate between the tumor and the perifocal edema, even using various pulse sequences [6–9]. On the basis of the experiences with CT, several authors view this as an indication for an MR-specific contrast medium [1, 9].

Paramagnetic substances can be used as MR contrast agents. Owing to their strong local magnetic fields, they reduce the relaxation times of the surrounding tissue [10]. With appropriate imaging sequences, the decrease in T1 relaxation time after administration of a paramagnetic substance results in an increase in the intensity of the signal.

Received January 22, 1986; accepted after revision May 16, 1986.

Dedicated to Professor W. Frommhold on the occasion of his 65th birthday.

Presented at the annual meeting of the American Society of Neuroradiology, San Diego, January 1986.

This work was supported by the Bundesministerium für Forschung und Technologie, 5300 Bonn (Grant No. 01-VF-142).

[1] Department of Radiology, Klinikum Charlottenburg, Freie Universität Berlin, Spandauer Damm 130, D-1000 Berlin 19, West Germany. Address reprint requests to W. Schörner.

[2] Department of Radiology, Fa Medizin. Schering AG, P.O. Box 65 03 11, D-1000 Berlin 65, West Germany.

AJNR 7:1013–1020, November/December 1986
0195-6108/86/0706–1013

Spontaneous Dissection of the Cervical Internal Carotid Artery: Correlation of Arteriography, CT, and Pathology

George R. Petro[1]
Gordon A. Witwer[1]
Edwin D. Cacayorin[1]
Charles J. Hodge[2]
Carl E. Bredenberg[3]
Michael S. Jastremski[4]
Stephen A. Kieffer[1]

Spontaneous dissection of the internal carotid artery is being recognized as a more frequent cause of acute neurologic deficit, particularly in young persons. Saccular pseudoaneurysm formation may be an associated finding, especially in the presence of tortuosity (coiling) of the cervical internal carotid artery. Of eight patients with nine vessels demonstrating internal carotid artery dissection on arteriography, pseudoaneurysms were found in five arteries. Four of the five pseudoaneurysms occurred in tortuous (coiled) arterial segments. Thin-section contrast-enhanced dynamic incremental CT showed close agreement with the findings on selective arteriography and provided additional information on the presence and configuration of arterial wall thickening as well as the extent of the pseudoaneurysm. Our experience indicates that CT may play an important role in the diagnosis, management, and follow-up of this lesion.

Spontaneous hemorrhagic dissection of the internal carotid artery (ICA) is becoming more widely appreciated as a cause of transient ischemic attack (TIA), or stroke, particularly in relatively young patients [1–4]. Diagnosis is usually based on demonstration by arteriography of a long, tapered, eccentric narrowing of the cervical ICA beginning above the common carotid bifurcation and extending superiorly to the level of the base of the skull [2] or occasionally into the carotid canal [4]. Saccular pseudoaneurysm formation may occur as a result of dissection [4], and sequential arteriograms often demonstrate rapidly changing patterns as the process proceeds to resolution, pseudoaneurysm formation, or further stenosis and occlusion [1, 2].

CT of the neck has recently been suggested as an accurate and relatively noninvasive method for diagnosis and sequential assessment of occlusive changes affecting the common carotid bifurcation and the proximal ICA [5, 6]. We have studied eight patients with spontaneous ICA dissection using sequential arteriography; dynamic thin-section CT of the neck was obtained in five individuals in order to more completely assess both luminal and mural changes in this still incompletely understood lesion.

Materials and Methods

Eight patients with spontaneous cervical ICA dissection were diagnosed on arteriography, including four women and four men, aged 23 to 54 years. Clinical presentations included initial head and neck pain followed by TIAs in two patients, TIAs in two (one with a remote history of severe neck pain), and acute hemispheric stroke in three. Two patients also manifested an ipsilateral incomplete Horner's syndrome. In one patient who suffered a single focal seizure and was being evaluated for possible intracranial mass, contralateral dissection with pseudoaneurysm was an incidental finding on arteriography.

All eight patients underwent percutaneous transfemoral selective common carotid arteriography. Arteriography was performed promptly after clinical presentation in five patients, after 5 weeks of intermittent symptoms in one, and 2 years after the likely initial event in another. Follow-up arteriograms were obtained in five patients at 2 weeks to 14 months after the initial study.

This article appears in the November/December 1986 issue of AJNR and the February 1987 issue of AJR.

Received January 15, 1986; accepted after revision May 2, 1986.

Presented at the annual meeting of the American Society of Neuroradiology, Boston, June 1984.

[1] Department of Radiology, SUNY Health Science Center of Syracuse, 750 E. Adams St., Syracuse, NY 13210. Address reprint requests to G. R. Petro.

[2] Department of Neurosurgery, SUNY Health Science Center of Syracuse, Syracuse, NY 13210.

[3] Department of Surgery, SUNY Health Science Center of Syracuse, Syracuse, NY 13210.

[4] Department of Critical Care and Emergency Medicine, SUNY Health Science Center of Syracuse, Syracuse, NY 13210.

AJNR 7:1053–1058, November/December 1986
0195-6108/86/0706–1053

From Dysembryoplastic Neuroepithelial Tumors to Myxoid Glioneuronal Tumors, a New Entity

Dysembryoplastic neuroepithelial tumors (DNETs) in the septum pellucidum are now considered a distinct type of lesion: myxoid glioneuronal tumors (MGTs). On the basis of DNA-methylation profile differences between these 2 entities, the c-IMPACT-NOW[1] update 6 decided to call this new entity, MGT. Initially described in 2018, MGTs are slow-growing lesions that involve the anterior septum pellucidum.[2] MGTs have a mutation in the *PDGFRA* gene that is unique to them. Included in the family of "neuronal and mixed neuronal-glial tumors," they are considered grade I by the World Health Organization and thus are cured by complete surgical excision.

The differential diagnosis includes subependymoma, central neurocytoma, and colloid cyst. Based on the scant literature available, MGTs are adult lesions and distinguishable from subependymoma because the latter tends to arise mostly in the fourth ventricle in this age group. Central neurocytoma is a solid cystic mass that shows variable contrast enhancement, but the latter is not present in MGT. While colloid cysts are midline lesions, MGTs are eccentric. Nevertheless, MGTs have a cystlike appearance and may be confused with colloid and simple ependymal cysts.

In fact, in 3 recent cases seen at our institution, the initial impression on MR imaging studies was intraventricular cyst. Reappraisal of the studies showed that MGTs are solid masses if findings in all sequences are correctly interpreted. Although MGTs show low T1 and high T2 in a cystlike fashion, they show high FLAIR signal (especially in the periphery, similar to that in DNET) and are solid on high-resolution heavily T2-weighted sequences such as CISS and FIESTA (Figure).[3] In accordance with the findings in a small published series, none of our cases showed contrast enhancement.[4] In that publication, contrast-enhanced was normal, but arterial spin-labeling showed mildly elevated perfusion.[4] Susceptibility images showed no blood or calcium, a finding similar to that in our cases. In 1 case, MR spectroscopy showed low NAA but normal choline and creatine levels.[4] FLAIR images may show artifacts in a location similar to that of MGT, and although artifacts are commonly bilateral, they can also be unilateral. These artifacts show a mixed FLAIR signal, while MGTs show high signal probably due to mucinous contents.

In conclusion, neuroradiologists need to be aware of MGT, a newly recognized neoplasia. This new entity is important to keep in mind when lesions in the frontal horns of the ventricles have a cystlike appearance. Their features on FLAIR and heavily weighted T2 images suggest the diagnosis, alert the neuropathologist, and may influence treatment.

http://dx.doi.org/10.3174/ajnr.A7273

REFERENCES

1. Louis DN, Wesseling P, Aldape K, et al. **cIMPACT-NOW update 6: new entity and diagnostic principle recommendations of the cIMPACT-Utrecht meeting on future CNS tumor classification and grading.** *Brain Pathol* 2020;30:844–56 CrossRef Medline
2. Lucas CH, Villanueva-Meyer JE, Whipple N, et al. **Myxoid glioneuronal tumor, PDGFRA p.K385-mutant: clinical, radiologic, and histopathologic features.** *Brain Pathol* 2020;30:479–94 CrossRef Medline
3. Parmar HA, Hawkins C, Ozelame R, et al. **Fluid-attenuated inversion recovery ring sign as a marker of dysembryoplastic neuroepithelial tumors.** *J Comput Assist Tomogr* 2007;31:348–53 CrossRef Medline
4. de Oliveira Narvaez E, Inada BS, Frota de Almeida PR, et al. **Myxoid glioneuronal tumour: report of three cases of a new tumor in a typical location and review of the literature.** *BJR Case Reports* 2021;7:20200139 CrossRef

C. Zamora
M. Castillo
Division of Neuroradiology, Department of Radiology
University of North Carolina School of Medicine
Chapel Hill, North Carolina

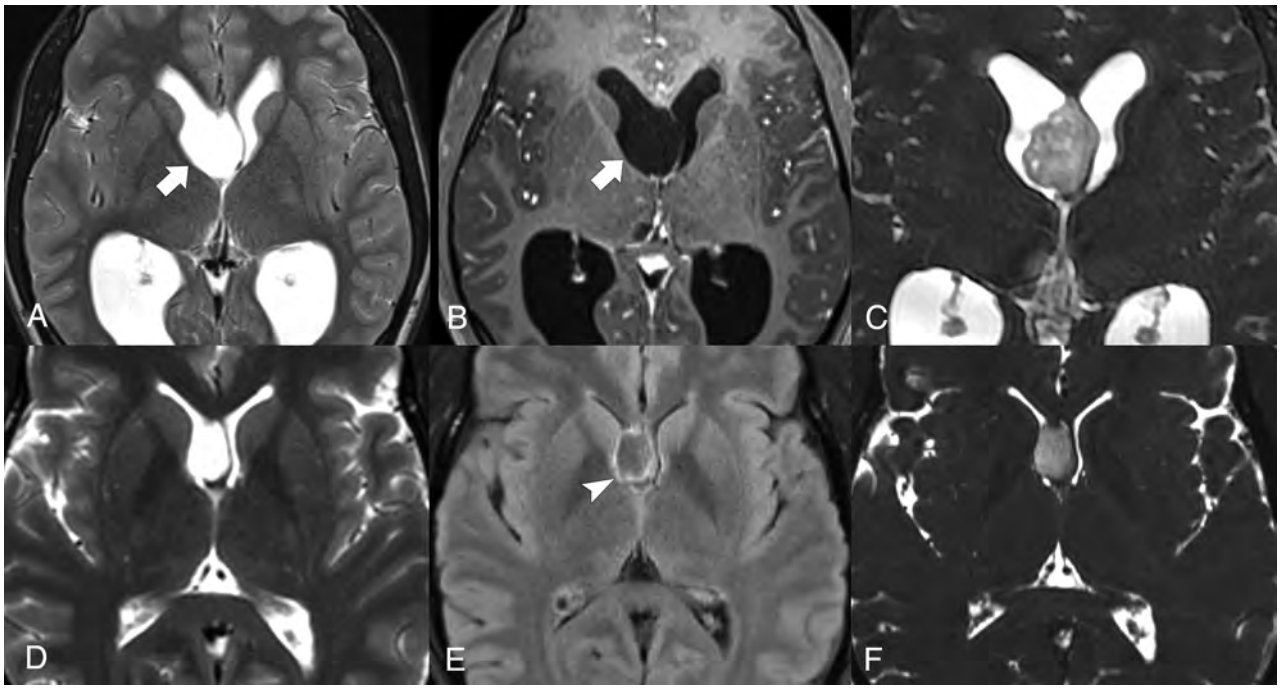

FIGURE. A 15-year-old boy presenting with migraines (*A–C*). Axial T2- and postcontrast T1-weighted images (*A* and *B*) show a cystic-appearing mass in the right lateral ventricle (*arrows*) without contrast enhancement. The mass appears solid on the CISS sequence (*C*). There is obstructive ventriculomegaly. Axial T2-weighted (*D*), FLAIR (*E*), and CISS (*F*) sequences in a 24-year-old asymptomatic woman. Images show a similar mass in the right lateral ventricle with a bright rim on FLAIR (*E*, *arrowhead*) and a solid texture on CISS (*F*).